Evaluation of the anti-cancer effects of a novel guanidinium-based compound, VP79s, in multiple myeloma

Trinity College Dublin

The University of Dublin

Thesis submitted to the University of Dublin, Trinity College

for the Degree of Doctor of Philosophy

By

Rebecca Amet, B.A (Mod)

School of Biochemistry and Immunology,

Trinity College Dublin

March 2020

Supervised by

Prof. Daniela M. Zisterer

Co-supervised by

Dr Tony McElligott, Prof Isabel Rozas and Prof Paul Browne

Declaration

I declare that this thesis has not been submitted as an exercise for a degree at this or any other university and it is entirely my own work. Figure 3.1 was carried out with Emily Sheridan and Patricia Hannon and Figure 4.31 which was carried out with Caoimhe O'Connell. I agree to deposit this thesis in the University's open access institutional repository or allow the library to do so on my behalf, subject to Irish Copyright Legislation and Trinity College Library conditions of use and acknowledgement

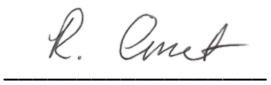

Rebecca Amet

Acknowledgments

First and foremost, I would like to thank my amazing supervisor Danny. I honestly wouldn't have been able to do it without your constant help, guidance, support and belief in me over the years. Thank you for your constant encouragement and keeping me calm throughout my whole PhD. Words can't express how grateful I am for your patience and kindness (and correcting every typo in this thesis). Tony, you were a super co-supervisor! I can't thank you enough for all the time and effort you put into helping me. You always made me feel like my PhD was on track and I was doing great. Thank you for all the opportunities to go to conferences and thank you for all the commas you put into this thesis (I'm going to be honest, I'm still not 100% sure on when I should use a semicolon). Isabel, thank you for your continued guidance, support and kindness. Paul, thank you for always being so kind and encouraging.

To everyone past and present in the sixth floor reading room: Gillian, Ewelina, Rachel, Marilena, Ciara, Stefania, Emma, Jill, Patricia, Sinead, Tania, Magda, Louie, Callum, Claire, Mary, Catriona, Brian, Joan, Nick and Vinnie. Thank you will never be enough for all the support, laughter and cake we've shared over the years. I've made some amazing friends over the past three and a half years and I wouldn't have made it through without you all. I'd like to especially thank the DZ girls: Rachel, Stefania and Patricia. I couldn't have shared the lab with a better group of people. Thank you for making the lab a fun and enjoyable place through your constant friendship and support. Rachel, I couldn't have done this PhD without your invaluable help and support in the beginning and throughout my PhD. Thank you for always answering my questions even if they were a bit silly. To Gillian, my long-term lab partner, thank you for always being someone to talk to and doing everything with me. To Helene and Viola, thank you for your friendship, kindness and help over the years.

A huge thank you to everyone in the School of Biochemistry and Immunology and the School of Medicine for all their help over the years, in particular Barry and Eamon for their help with flow cytometry. I'd especially like to thank Liam Cross and Noel Breslin for their

ability to fix absolutely everything. I don't know what we would have done without you both! Thank you to Ailish and Jane for all of your help with the John Scott fund and to everyone in the school office and the teaching lab. A special thank you to Liam McCarthy for helping me with many, many things over the years.

To Deirdre Teeling, thank you for always believing in me, your kind words and support. You'll never know how much it means to me.

To my friends - Nicole, Amy, Jade, Nadia, Lee-Anne and Huda, thank you for the constant support and encouragement, I'm forever grateful. Thank you for always listening to me rant about an experiment not working. Thank you for reminding me the end was in sight and thank you for all the fun times. I can't wait to start living my best post-PhD life.

To Michael, thank you for your constant love, support and strength, especially over the past year. Thank you for always listening to my rants and making me laugh. I couldn't have done it without you.

To my family, thank you for your constant love and support. Mam, thanks for always looking after me. Dad, thanks for all the lifts to and from St James. To my brothers, Stevie and Alex, and my loving nanny, thanks for all the fun, love and support. A special mention to Tessa and Peppa for always giving me the best greeting when I got home from the lab.

I'd like to thank the John Scott PhD fellowship and Multiple Myeloma Ireland for funding my PhD.

Summary

Multiple myeloma (MM) is an incurable haematological malignancy accounting for 300-350 cancer diagnoses in Ireland each year. Mainly a disease of the elderly, MM is most prevalent in Western societies where aging populations are rising, and the likelihood of MM is increasing. MM is an extremely arduous malignancy to treat due to the marked clonal heterogeneity among patients. A better understanding of the pathophysiology of MM and advancements in the development of novel therapeutics have allowed the median survival of patients to increase from 3 to 6 years in the past decade. However, despite the effectiveness of the first-line treatments, patients invariably relapse and become refractory to treatment; therefore, novel therapeutics which target this incurable cancer are still required.

The Janus kinase (JAK)/Signal transducer and activator of transcription 3 (STAT3) pathway in MM can be both constitutively active due to autonomous mutations or activated by growth and survival factors, such as interleukin-6 (IL-6), secreted by bone marrow stromal cells (BMSCs) and other cells within the bone marrow microenvironment. Increasing evidence has demonstrated that STAT3 is upregulated in MM and that STAT3 increases the expression of genes involved proliferation, angiogenesis and evasion of apoptosis. Consequently, STAT3 has emerged as a therapeutic target in various cancers including MM. In the present study, the anti-MM activity of an optimised series of novel aryl-guanidinium compounds were initially tested in a representative pair of MM cell lines, NCI-H929 and U266B1, and a lead compound, VP79s, was identified. Results with VP79s compared very favourably with those obtained with a panel of standard and emerging therapeutics used to treat MM. In contrast to these therapeutic agents, VP79s equipotently reduced the viability of a panel of myeloma cells with no resistance observed. Following on from this, VP79s was found to induce apoptosis in NCI-H929 and U266B1 cell lines in a dose- and time-dependent manner resulting in caspase 3 activation.

The RAS/RAF/MEK/ERK, JAK/STAT, PI3K/AKT and NFκB signalling pathways are known to play a key role in the pathogenesis of MM. Examination of these pathways found that VP79s rapidly inhibited both constitutively active and IL-6-induced STAT3 signalling in

U266B1 and NCI-H929 cells respectively. Examination of upstream mediators of STAT3 signalling suggested that VP79s may inhibit STAT3 via inhibition of JAK2 phosphorylation and downregulation of the IL-6 receptors, CD126 and CD130. Analysis of downstream STAT3 targets demonstrated a decrease in the expression levels of anti-apoptotic Bcl-2 family member, Mcl-1; inhibitor of apoptosis protein, survivin; and the cell cycle protein, cyclin D1. In particular, treatment with VP79s resulted in a rapid time-dependent decrease in Mcl-1, a critical survival factor in MM, suggesting that VP79s may be a promising anti-MM therapeutic.

Examination of the translational capacity of VP79s demonstrated that VP79s was able to enhance cell death induced by the proteasome inhibitor; bortezomib, a standard MM treatment. VP79s was also found to induce minimal cytotoxicity of peripheral blood mononuclear cells, T, B and Natural Killer cells from healthy donors at concentrations which are lethal to MM cell lines suggesting selective anti-myeloma activity.

MM cells have an intricate relationship with the bone marrow microenvironment and in particular with BMSCs. MM cells rely heavily on this relationship for growth, survival and drug resistance *in vivo* and is mediated through the secretion of soluble factors, such as IL-6, and adhesion of MM cells to BMSCs. In contrast to bortezomib, VP79s was shown to overcome both soluble and adhesion mediated drug resistance when myeloma cells were co-cultured with the stromal cell line HS5. Finally, VP79s significantly reduced the viability of *ex vivo* MM patient samples in a dose-responsive manner suggesting its potential as an anti-MM therapeutic.

In conclusion, a novel aryl-guanidium compound, VP79s, was identified as a lead compound capable of inhibition of the STAT3 signalling pathway and inducing potent anti-MM activity in MM cell lines and *ex vivo* patient samples. These data warrant further translational and pre-clinical studies into the efficacy and mechanism of action of VP79s.

Table of Contents

List of Figures

Chapter 1:

Chapter 2:

Chapter 3:

Chapter 4:

Chapter 5:

Chapter 6:

Appendix:

List of Tables

Chapter 1:

Chapter 2:

Chapter 3:

Chapter 5:

Abbreviations

µM	Micromolar
ADCC	Antibody-dependent cellular cytotoxicity
ADCP	Antibody-dependent cellular phagocytosis
AIF	Apoptosis inducing factor
AKT	Protein kinase B
AML	Acute myeloid leukaemia
AP-1	Activator protein-1
APAF-1	Apoptotic protease-activating factor 1
APC	Allophycocyanin
ASCT	Autologous haematopoietic stem cell transplant
ATP	Adenosine triphosphate
AVOVA	Analysis of variance
BAFF	B cell activating factor
BAK	Bcl-2 antagonist/killer
BAX	Bcl-2-associated X protein
Bcl-2	B cell lymphoma-2
Bcl-xL	B-cell lymphoma-extra large
BCMA	B cell maturation antigen
BH	Bcl-2 homology
BID	BH3 interacting-domain death agonist
BMM	Bone marrow microenvironment
BMSC	Bone marrow stromal cell
CAM-DR	Cell adhesion mediated drug resistance
CAR T cells	Chimeric antigen receptor T cells
CARD	Caspase recruitment domains
Caspase	Cysteine-aspartic proteases
CCD	Coiled-coiled domain

CDC	Complement-dependent cytotoxicity
CDK	Cyclin dependent kinase
CI	Combination index
CLL	Chronic lymphocytic leukaemia
CRAB	Hypercalcaemia, renal insufficiency, anaemia and bone lesions
DCFH-DA	2',7'-Dichlorofluorescin diacetate
dH_2O	Deionised water
Diablo	Direct inhibitor of apoptosis-binding protein with low pI
DMEM	Dulbecco's modified eagle medium
DMSO	Dimethyl sulfoxide
DNA	Deoxyribonucleic acid
DSS	Durie-salmon staging system
DTT	Dithiothreitol
EC	Endothelial cell
ECL	Electrochemiluminescence
ECM	Extracellular matrix
EDTA	Ethylene-diamine-tetra-acetic acid
EGFR	Epidermal growth factor receptor
ER	Endoplasmic reticulum
ERK	Extracellular signal-regulated kinase
EtOH	Ethanol
EU	Europium
Fa	Fractional Affect
FACS	Fluorescence-activated Cell Sorting
FADD	Fas-associated protein with death domain
FAS	First apoptotic signal
FBS	Foetal bovine serum
FDA	Federal drug agency
FITC	Fluorescein isothiocyanate

FSC	Forward scatter
GAPDH	Glyceraldehyde 3-phosphate dehydrogenase
GC	Glucocorticoid
gp130/CD130	Glycoprotein 130
h	Hour
H_2O_2	Hydrogen peroxide
HDACI	Histone deacetylase inhibitor
HEPES	4-(2-hydroxyethyl)-1-piperazineethanesulfonic acid
HRP	Horse radish peroxidase
IAP	Inhibitor of apoptosis protein
IC_{50}	50% inhibitory concentration
ICAM1	Intracellular adhesion molecule 1
Ig	Immunoglobulin
IGF-1	Insulin growth factor-1
IL-	Interleukin-
IL-6Rα/CD126	IL-6 receptor alpha
IMiD	Immunomodulatory agent
ISS	International staging system
JAK	Janus kinase
JNK	c-Jun N-terminal kinase
kDa	KiloDalton
LDH	Lactate dehydrogenase
LFA1	Lymphocyte function associated antigen 1
mAb	Monoclonal antibody
MAPK	Mitogen-activated protein kinase
Mcl-1	Myeloid cell leukaemia-1
MEK	Mitogen activated protein kinase kinase
MGUS	Monoclonal gammopathy of undetermined significance
min	Minute

miRNA	MicroRNA
mL	Millilitre
MM	Multiple myeloma
mM	Millimolar
MMP	Matrix metalloproteinases
MOMP	Mitochondrial outer membrane permeabilization
mRNA	Messenger RNA
mTOR	Mammalian target of rapamycin
MUC1	Mucin-1
NAC	N-acetyl L-cysteine
NFκB	Nuclear factor kappa B
nM	nanomole
NO	Nitric oxide
Noxa	Phorbol-12-myristate-13-acetate-induced protein 1
OMM	Outer mitochondrial membrane
OS	Overall survival
PARP	Poly ADP ribose polymerase
PBS	Phosphate buffered saline
PCL	Plasma cell leukaemia
PCR	Polymerase chain reaction
PDGF	Platelet derived growth factor
PE	R-phycoerythrin
PerCP	Peridinin chlorophyll protein
PEST domain	Proline/glutamic acid/serine/threonine domain
PI	Propidium iodide
PI3K	Phosphatidylinositol 3 kinase
PS	Phosphatidyl serine
Puma	p53 upregulated modulator of apoptosis
PVDF	Polyvinylidene difluoride

RAF	Rapidly accelerated fibrosarcoma
RANKL	Receptor activator of NFKB ligand
RAS	Rat sarcoma
RIPA	radio immunoprecipitation assay
RISS	Revised international staging system
RNA	Ribonucleic acid
ROS	Reactive oxygen species
RPMI	Roswell park memorial institute medium
RTK	Receptor tyrosine kinase
S.E.M	Standard error of the mean
SCID	severe combined immunodeficiency
SDS	Sodium dodecyl sulfate
SDS-PAGE	Sodium dodecyl sulfate-polyacrylamide gel electrophoresis
SH-2 Domain	SRC homology-2 domain
siRNA	small interfering ribonucleic acid
SMAC	Second mitochondria-derived activator of caspase
SMM	Smouldering multiple myeloma
SPEP	Serum protein electrophoresis
STAT3	Signal transducer and activator of transcription 3
tBid	Truncated Bid
TBS	Tris buffered saline
TBST	Tris buffered saline tween
T-cell ALL	T-cell acute lymphoblastic leukaemia
TEMED	Tetramethylethylenediamine
TGF-β	Transforming growth factor-β
TNF- α	Tumour necrosis factor-alpha
TNFR1	TNF-α receptor 1
TNFRSF	Tumour necrosis factor receptor super family
TRAIL	TNF-related apoptosis inducing ligand

UPP	Ubiquitin-proteasome pathway
VCAM1	Vascular cell adhesion molecule 1
VEGF	Vascular endothelial growth factor
VLA4	Very-late antigen 4
x g	Times gravity

Thesis outputs: Publications, Presentations and Awards

Publications

Published:

Previtali, V. Trujillo, C. **Amet, R.** Zisterer, DM. and Rozas, I. Effect of isouronium/guanidinium substitution on the efficacy of a series of novel anti-cancer agents. MedChemComm, 2018. 9(4): p. 735-743.

Brindisi M, Ulivieri C, Alfano G, Gemma S, de Asís Balaguer F, Khan T, Grillo A, Chemi G, Menchon G, Prota AE, Olieric N, Lucena-Agell D, Barasoain I, Diaz JF, Nebbioso A, Conte M, Lopresti L, Magnano S, **Amet R**, Kinsella P, Zisterer DM, Ibrahim O, O'Sullivan J, Morbidelli L, Spaccapelo R, Baldari C, Butini S, Novellino E, Campiani G, Altucci L, Steinmetz MO, Brogi S. Structure-activity relationships, biological evaluation and structural studies of novel pyrrolonaphthoxazepines as antitumor agents. Eur J Med Chem. 2019 Jan 15;162:290-320.

Under Review and in preparation:

Saraswati, P. Brindisi, M. Relitti, N. Grillo, A. Chemia, G Federicoa, S. Gemma, S. McCabe, N. Turkington, R, O'Sullivan, J. Lamponia, S. Ghanim, M. Kelly, V. Amet, R. Hannon, P. Zisterer, DM. Jungg, M. Herp, D, Altucci, L. Ruberti, G. Christianson, DW. Campiani, G, and Butini, S.

Spiroindoline-capped selective HDAC6: design, synthesis, structural analysis and biological evaluation. ACS Medicinal Chemistry Letters.

Previtali, V. Mihigo, H. Amet, R. McElligott, AM. Zisterer, DM and Rozas, I.

Diaromatic guanidinium derivatives as cancer cell growth inhibitors. Eur J Med Chem.

Amet, R. Previtali, V. Mihigo, H. Sheridan, E. Brophy, S. Hayden, P. Browne, V. Rozas, I. McElligott, AM. and Zisterer, DM.

A novel aryl-guanidinium derivative, targets the STAT3 signalling pathway and exhibits preclinical activity against multiple myeloma.

Awards

- Multiple Myeloma Ireland Educational Grant, 2018.
  Awarded €10,000 to examine the translational capacity of VP79s.
- League of European Research Universities Doctoral Summer School, 2017. Zurich, Switzerland.
  Awarded a scholarship to attend the LERU Doctoral Summer School on citizen science and represent Trinity College.
- Best Poster Award - The 11th International Cancer Conference, 2019. Trinity St. James's Cancer Institute, Dublin, Ireland.
  Awarded a best poster prize.
- Trinity Travel Trust Award to attend "A Matter of Life or Death: From Basic Cell Death Mechanisms to Novel Cancer Treatments", 2018. Amsterdam, The Netherlands.
  Awarded a bursary to travel to The Netherlands to present my research.

Conference Presentations

Oral Presentations

- *"Novel therapeutics for multiple myeloma which target the STAT3 signalling pathway" Young Cancer Researcher Network Meeting, 2018.* Cork, Ireland.
- *"Novel agent VP79s targets STAT3 signalling in myeloma cells overcoming microenvironment induced drug resistance" Haematology Association of Ireland Annual meeting, 2019.* Galway, Ireland.

Poster Presentations

- *Haematological Association of Ireland annual Meeting, 2017.* Belfast, Ireland.
- *"A Matter of Life or Death: From Basic Cell Death Mechanisms to Novel Cancer Treatments", 2018. European Association for Cancer Research.* Amsterdam, The Netherlands.

- *Irish Association for Cancer Research Annual Meeting, 2018.* Dublin, Ireland.
- *Blood Cancer Network Ireland Annual Meeting, 2018.* Dublin, Ireland.
- *Haematological Association of Ireland annual Meeting, 2018.* Cork, Ireland.
- *"Advances and Future Directions in Personalised Medicine". The 11th international Cancer Conference, 2019.* Dublin, Ireland.

Conferences Attended

- *Blood Cancer Network Ireland Annual Meeting 2017.* Dublin, Ireland.
- *Sci:Com Conference 2017.* Dublin, Ireland.

Modules Completed

Science in Society, School of Education, Trinity College Dublin.

Science Communication and Education, School of Education, Trinity College Dublin (15 Credits).

Chapter 1:
Introduction

1.1. Multiple myeloma

Multiple myeloma (MM) is a haematological malignancy characterised by the accumulation of malignant plasma cells in the bone marrow and the presence of monoclonal immunoglobulins (Igs) in the urine and blood causing characteristic osteolytic lesions, anaemia, renal failure, and hypercalcemia [1]. Usually affecting older populations, the median age for diagnosis is 65 to 70 years, accounting for approximately 1% of all cancers and 10% of all haematologic malignancies [2]. MM is an insidious disease which evolves from the asymptomatic premalignant plasma cell MM dyscrasia stages; monoclonal gammopathy of undetermined significance (MGUS) [3] and/or smouldering multiple myeloma (SMM) [4]. The first known documented case of myeloma is thought to be that of a 39-year-old woman, Sarah Newbury, in 1844 as described by Solly [5]. Since then, the prevalence of MM in the population has been steadily rising with approximately 300 newly diagnosed cases in Ireland each year [6].

A better understanding of the pathophysiology of myeloma and advancements in the development of novel treatments have seen patient survival steadily increase over the past two decades, allowing the median survival of patients to increase from 3 to 6 years. However, despite the effectiveness of the first-line treatments, patients invariably relapse and become drug refractory; therefore, novel therapeutics which target this incurable disease are still required. Indeed, ageing populations in Western societies indicate that the incidence of MM is likely to double over the next 15 years, necessitating the pursuit of novel anti-myeloma therapeutics [7].

1.1.1. Classification and staging

MM arises from premalignant proliferation of monoclonal plasma cells that are derived from post–germinal-centre B cells [8]. Progression of an asymptomatic plasma cell disorder involves a multistep transformation process: accumulating chromosomal abnormalities, mutations, and epigenetic alterations leading to altered gene expression. Unlike other haematological malignancies, MM is often preceded by an age-progressive

premalignant condition termed MGUS, progressing to SMM and, finally, progressing to symptomatic MM (See Table 1.1). Currently, there are no reliable predictors for the progression of MGUS to MM. In MM, patients display the pathological CRAB symptoms (hypercalcaemia, renal insufficiency, anaemia and bone lesions) along with plasma cell infiltration and increased monoclonal protein distinguishing MM from its precursor counterparts [4].

	Pre-Malignant		Malignant	
Condition	**MGUS**	**SMM**	**Myeloma**	**Plasma Cell Leukaemia**
% Clonal plasma cells in bone marrow	**<10%**	**10-60%**	**>60%**	**>10% plus >20% circulating plasma cells**
Presence of myeloma defining events	**No**	**No**	**Yes**	**Yes**
Likelihood of progression	**~ 1% per year**	**~ 10% per year**	**N/A**	**N/A**
Treatment	**None**	**None**	**Yes**	**Yes**

Table 1. 1 Classification of Multiple Myeloma.

MM has two distinct premalignant stages, monoclonal gammopathy of undetermined significance (MGUS) and smouldering multiple myeloma (SMM), distinguishable by the likelihood of progression and percentage of clonal cells in the bone marrow. Once patients present with myeloma defining events the malignant disease can diagnosed. Plasma cell leukaemia is an advanced stage of the disease which has a higher percentage of circulating plasma cells. MM patients can advance to this stage of the disease from MM or present with primary PCL. Adapted from Rajkumar, Am Soc Clin Oncol Educ Book, 2016 [9].

1.1.1.1. Monoclonal gammopathy of undetermined significance

MGUS was first described by Kyle *et al.* after noting that asymptomatic patients with increased levels of monoclonal protein had an increased risk of developing MM [10]. Monoclonal protein are monoclonal Igs produced by the plasma cells [11]. This is thought

to be the first pathogenic step in the progression to malignant myeloma. A 2009 study by Landgren *et al.* on a cohort of 77,000 MM patients showed that almost all had previously been diagnosed with MGUS [12], illustrating the correlation between MGUS diagnosis and progression to MM. However, currently there are a lack of appropriate biological markers to make definitive diagnostic predictions [4]. Progression of MGUS to MM is thought to occur at a rate of 1% per year [13].

1.1.1.2. Smouldering multiple myeloma

SMM is thought to represent an intermediate stage between MGUS and MM; however, it is distinguishable from MGUS with a much higher risk of progression to MM at 10% per year (in the first 5 years). The development of SMM to MM is mainly characterised by the progression from asymptomatic plasma cell dyscrasia to the presence of end-organ damage attributed to the underlying plasma cell proliferative disorder [14]. In recent years there have been major advances in the diagnosis, progression and management of SMM. Recently, clinical trials have been exploring early prophylactic treatment for high-risk SMM which may be of benefit to patients; however, thus far, no significant improvement in overall survival was found with early therapy [15]. One trial assessing early treatment with melphalan and prednisone versus treatment once MM had progressed in asymptomatic patients demonstrated no difference in response rates or overall survival [16]. Some evidence may suggest an improvement in overall patient survival; however, this has not been conclusively proven [17].

1.1.1.3. Multiple myeloma

In MM, patients display the pathological CRAB symptoms along with plasma cell infiltration and increased monoclonal protein distinguishing MM from its precursor counterparts. The heterogenous nature of MM means that almost 25% of patients only survive up to 3 years while their counterparts can survive up to 10 years with the disease. For this reason, the development of a robust staging system was required to properly assess the disease burden and to predict survival. Unlike staging in solid tumours such as lung and breast

cancer, once myeloma has been diagnosed it is systemic. Up to 2016, there were two main staging systems: The International Staging System (ISS) and the Durie-Salmon Staging System (DSS), until the development of the Revised International Staging System (RISS) which amalgamated the two systems. RISS combines prognosis of high-risk cytogenetic abnormalities ((Del(17p), translocation t(4;14), and translocation t(14;16)) and lactate dehydrogenase (LDH)) with ISS score and gives a better differentiation of MM patients into three survival subgroups, stages I to III [18, 19]. LDH levels give an indication of tumour mass and high LDH is associated with a larger tumour burden (Table 1.2) [9, 18, 20].

RISS stage	**Staging Criteria**	**Percentage of Myeloma Patients**	**Survival Rate (5 year)**
Stage I	• ISS Stage I (Serum albumin >3.5, Serum beta-2-microglobulin <3.5) and • No high-risk cytogenetics • Normal LDH	**28 %**	**82 %**
Stage II	• Not aligning to stage I or Stage III criteria	**62 %**	**62 %**
Stage III	• ISS Stage III (Serum beta-2-microglobulin >5.5) and • High risk cytogenetics [t(4;14), t(14;16), or del(17p)] and/or elevated LDH	**10 %**	**40 %**

Table 1. 2 Staging in Multiple Myeloma

The Revised International Staging System (RISS) divides myeloma patients into three survival subgroups based on criteria such as cytogenetic abnormalities and serum lactate dehydrogenase (LDH) levels. Adapted from Palumbo et al., J Clin Oncol, 2015 [18].

1.1.1.4. Plasma cell leukaemia

PCL is a rare variant of MM which is characterised by the presence of circulating malignant MM cells. It is subdivided into primary and secondary PCL: primary occurring at diagnosis and secondary PCL in patients with refractory/relapsed MM. Diagnostic criteria includes > 20% circulating malignant plasma cells and a count greater than 2×10^9/L plasma cells in peripheral blood. The molecular basis of PCL is poorly understood although current evidence suggests that it is cytogenetically different to typical MM. Thus far, the heterogeneous and scarce nature of PCL means that little is known of the malignancy except that it has a shorter refractory times and typically negative outcomes [21].

1.1.2. Progression to multiple myeloma and cytogenetic abnormalities

The cause of MM is unknown with no known hereditary genetic component or definitive environmental risk factor making MM a highly heterogeneous disease. As previously described, MM is preceded by largely asymptomatic precursors MGUS and SMM. Why some individuals with MGUS and SMM can remain asymptomatic for decades while others develop symptomatic MM is unknown, but the current and most plausible explanation is the accumulation of aberrant genetic events in evolving patients. It is believed an initiating hit is required to immortalise a plasma cell, followed by a series of genetic hits which lead to the development of the myeloma clone (Figure 1.1). These aberrant events include those that take place during normal B-cell development, as well as in the tumour microenvironment such as loss of heterozygosity, gene amplification, mutations and possibly epigenetic changes. This accumulation of anomalous events is thought to give rise to MM. Until recently our knowledge of myeloma genetics was limited, however; with the advancements of molecular techniques such as microarrays and next generation-sequencing, our understanding of the biology and pathophysiology of MM has improved vastly over the past decade [22].

There are two main types of cytogenetic abnormalities: primary and secondary. Primary genetic events are thought to be the initial factor which drives the plasma cell into the monoclonal premalignant stage known as MGUS. These primary genetic events include

translocations and hyperdiploidy which are usually mutually exclusive. Translocations which affect the immunoglobulin heavy chain (IgH) locus, such as the t(11;14) translocation, leads to the amplification of oncogenes. For example, the t(11;14) translocation juxtaposes the cyclin D1 (*CCND1*) gene to the IgH gene leading to amplified expression [23]. Cyclin D1 is a cell cycle protein which together with its cyclin-dependent kinase (CDK) partner is responsible for transition to S phase, the actively replicating phase of the cell cycle [24, 25]. While patients with hyperdiploidy present with trisomies of odd numbered chromosomes (3, 5, 7, 9, 11, 15 and 17). The variety of secondary cytogenetic abnormalities, such as the rearrangement of c-MYC, found in MM is much larger than primary. Frequently MM patients present with one or more of these secondary genetic events which include gains of chromosomes, secondary translocations, epigenetic events and deletions. Monosomy of chromosome 13 or 13/del(13q) is an early genetic event in MM development and is frequently found in approximately 50% of MGUS patients. Later cytogenetic events include the deletions of chromosome 17p which is a high-risk indicator of the progression of SMM to MM and duplication of chromosome 1q21 which has an approximate incidence rate of 40% in SMM and MM suggesting that this gain plays a role in disease progression [26].

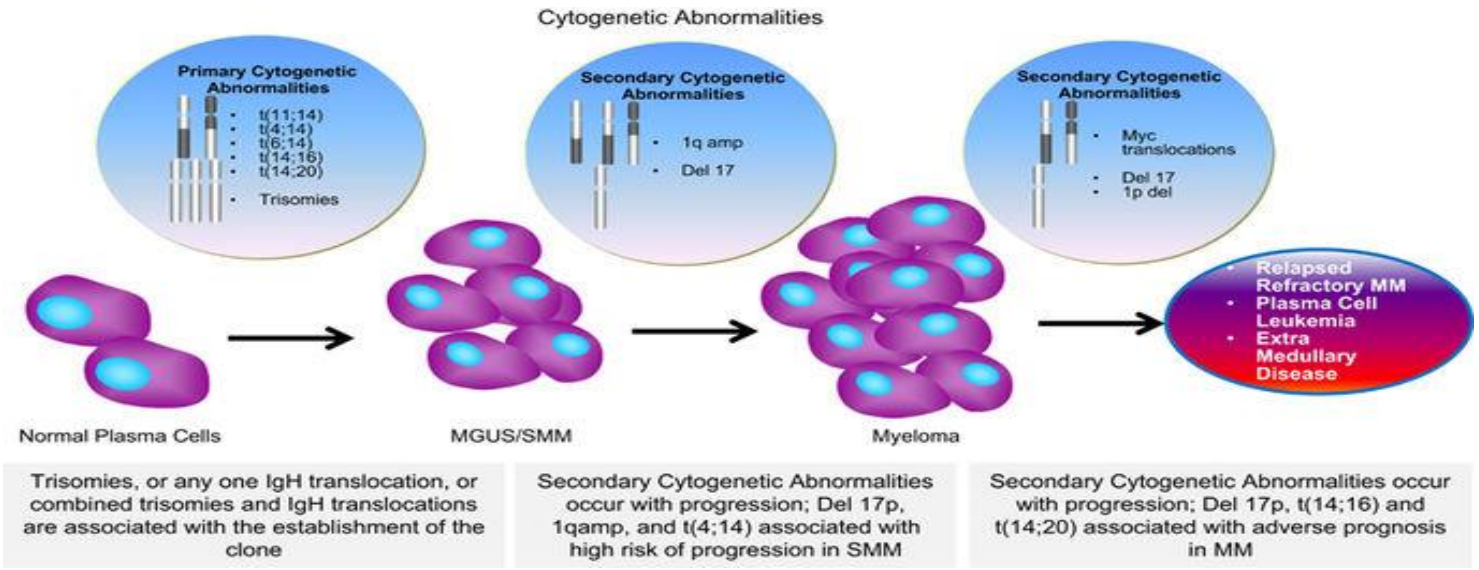

Figure 1. 1 Cytogenetic abnormalities and disease progression.

There are two main types of cytogenetic abnormalities: Primary and secondary. Primary genetic events are thought to be the initial factor which drives the plasma cell into the monoclonal premalignant stage known as monoclonal gammopathy of undetermined significance (MGUS). These primary genetic events include translocations such as the t(11;14) which is thought to upregulate cyclin D1 and hyperdiploidy such as trisomies of odd numbered chromosomes. The variety of secondary cytogenetic abnormalities found in MM is much larger than primary which include gains, secondary translocations, epigenetic events and deletions. Image from Rajan et al., Blood Cancer Journal, 2015 [24].

1.1.3. Diagnosis

As aforementioned, the distinction between MGUS, SMM and MM is the development of end-organ damage associated with increased monoclonal plasma cells and monoclonal Igs. Whilst MGUS and SMM are largely asymptomatic, the detection of monoclonal protein in the blood and urine is most often the first indication of precursor plasma cell dyscrasia. Proteins in the blood can be measured by serum protein electrophoresis (SPEP). The presence of a monoclonal spike (or M spike) is an indicator of large amounts of monoclonal Igs present in the serum of the patient. Tests such as serum immunofixation, and the serum free light chain assay are also carried out to determine mAb presence. To be diagnosed with MGUS patients must possess three simultaneous criteria as in line with the International Myeloma Working Group standards: monoclonal protein of less than 3g per decilitre, plasma cell infiltration of less than 10% and no signs of end-organ damage. Similarly, SMM can be diagnosed by similar means; however, with higher cut off levels of serum protein (>3 g per decilitre) and plasma cell infiltration (> 10 %) and no signs of end organ damage.

Patients with MM present with clonal bone marrow plasma cells > 10 % and one or more symptoms including back pain, fatigue, pallor, renal failure, proteinuria, lytic bone lesions and increased susceptibility to respiratory infections. As with MGUS and SMM, SPEP will be carried out to assess monoclonal protein accumulation whilst full blood counts assess myeloma associated anaemia, hypercalcemia, creatinine, urea and nitrogen levels. Urinary tests can also be carried out to assess the presence of antibody light chains which filter through the kidneys known as Bence Jones proteins. If further tests are warranted bone marrow aspiration may be carried out to assess plasma cell infiltration, as well as X-ray and computed tomography (CT) scans for the presence of osteoporosis and lytic bone lesions. At the time of initial diagnosis, fluorescent *in situ* hybridisation should be carried out to detect high risk chromosomal abnormalities t(11;14), t(4;14), t(14;16), t(6;14), t(14;20), trisomies, monosomies and del(17p) [27]. Following initial diagnosis of MM, the RISS staging group will be applied based on the presence or absence of high risk chromosomal abnormalities and serum LDH levels (Reviewed in [2, 27]).

1.2. Bone marrow microenvironment

Myeloma cells have an intricate relationship with the bone marrow microenvironment (BMM) as myeloma cells rely on signals from the BMM in order to survive and proliferate. Substantial study into the area of the bone marrow tumour microenvironment has elucidated the important role that it plays in differentiation, migration, proliferation, survival and drug resistance [28, 29]. Some key pathological effects are also caused by this complex relationship including bone lesions and hypercalcemia. The BMM can be divided into two main compartments: the cellular and non-cellular compartments. The cellular compartment is comprised of haematopoietic and non-haematopoietic cells including fibroblasts/bone marrow stromal cells (BMSC), endothelial cells (ECs), osteoclasts, osteoblasts and immune cells such as macrophages, natural killer cells and T cells (Table 1.3). The non-cellular compartment is comprised of the extracellular matrix (ECM) and liquid milieu including cytokines, growth factors and chemokines (Table 1.4) [30]. MM cells grow and multiply in the BMM, where they adhere to BMSCs and ECM proteins which upregulate signalling pathways in both cell types. MM cells also home to the BMM which allows the progression of the disease as it infiltrates new areas of the BMM [31, 32].

1.2.1. Cellular compartment

The cellular compartment is comprised of haematopoietic and non-haematopoietic cells. These cells play a major role in drug resistance and MM cell proliferation (Table 1.3) [33, 34]. BMSCs are often considered to be one of the most important players in MM survival and progression as interactions between adhesion molecules on the BMSCs and cytokines produced by the BMSCs promote the proliferation of MM cells (Figure 1.2). MM cells bind to BMSCs via adhesion molecules such as mucin-1 (MUC1) on MM cells and intracellular adhesion molecule 1 (ICAM1) on BMSCs. This binding induces the activation of mitogen-activated protein kinase (MAPK) and nuclear factor kappa B (NFκB) pathways in BMSCs. In turn, this activation of NFκB upregulates transcription of adhesion molecules on myeloma cells including, very-late antigen 4 (VLA4), lymphocyte function associated antigen 1 (LFA1) and MUC1 and BMSC adhesion proteins, ICAM1 and vascular cell adhesion molecule 1

(VCAM1) [35, 36]. Binding of BMSC to MM cells leads to interleukin-6 (IL-6) secretion from BMSCs via activation of NFκB [35]. A recent study by Bar-Natan *et al*. has shown that BMSCs protect MM cells from alkylating agents through the upregulation of MUC1. This resistance was not due to cell-to-cell contact and was thought to be induced through soluble factors secreted by the BMSCs, in particular, MUC1 expression was shown to be mediated through IL-6-dependent upregulation of the Janus kinase (JAK)/signal transducer and activator of transcription 3 (STAT3) pathway [37]. MM cells have been shown to secrete vascular endothelial growth factor (VEGF) and tumour necrosis factor-alpha (TNF-α) independently, however, MM-BMSC interactions have been shown to promote BMSCs to secrete IL-6, VEGF, insulin growth factor-1 (IGF-1) and stromal cell-derived factor-1α [38]. BMSC-MM interactions are also mediated through Notch signalling pathways which leads to an induction of IL-6, VEGF and IGF-1 in both MM cells and BMSCs [39]. BMSC-MM cell interactions have also been shown to modify the kinomic activity of MM cells causing an upregulation in ERK (extracellular signal-regulated kinases) 1/2 and STAT3 creating a more drug resistant cell type [40].

Osteoclasts are cells which break down bone by secreting hydrochloric acid. Under normal physiological conditions there is a tightly regulated balance between bone reabsorption and bone formation with osteoblasts, bone building cells, however, this balance is lost in MM. This ultimately leads to the development of osteolytic lesions and increased calcium levels in the blood, an indicator of active myeloma. Osteoclasts also produce pro-angiogenic factors such as VEGF and osteopontin [41] which promotes the formation of new vasculature and tumour cell growth. Osteoblasts may also have a pathogenic role in MM. A study by Karadag *et al*. has shown that osteoblasts produce IL-6 when in co-culture with myeloma cells, promoting the growth of MM cells [42](Reviewed in [43]).

Bone Marrow Microenvironment	Microenvironment Components	Interactions with Myeloma Cells
Cellular Compartment	***Bone Marrow Stromal Cells***	MM cells bind to BMSCs via adhesion molecules such as MUC1 on MM cells and ICAM1 on BMSCs. This binding induces the activation of MAPK and NFκB pathways in BMSCs. Activation of NFκB upregulates adhesion molecules on MM cells including, VLA4, LFA1 and MUC1 and BMSC adhesion proteins ICAM1 and VCAM1.
	Endothelial Cells	In MM, ECs may play a role in bone remodelling, cell adhesion, chemotaxis, angiogenesis, resistance to apoptosis and cell-cycle regulation.
	Osteoblasts	Osteoblasts may have a pathogenic role in MM. Dickkopf-related protein 1 produced by MM cells suppresses differentiation of osteoblasts.
	Osteoclasts	Signals from MM cells such as IL-6, RANKL and IL-3 activate osteoclasts and induce osteoclastic activity. Osteoclasts play a key role in the pathogenesis of MM. Under normal physiological conditions there is a tightly regulated balance between bone reabsorption with osteoclasts and bone formation with osteoblasts, however, this balance is lost in MM.

Table 1. 3 Summary of important interactions between cellular components and MM cells in the bone marrow microenvironment

1.2.2. Non-Cellular compartment

The non-cellular compartment is rich in cytokines, growth factors and chemokines which maintain the MM cell population through upregulation of signalling pathways associated with growth, survival and drug resistance. Cytokines found in the BMM are mainly pro-inflammatory, a shift which promotes the growth of cancer cells while hindering anti-tumour immune responses. [44].

One key cytokine involved in MM progression is IL-6. It is a pleiotropic cytokine with multiple functions from acute immune response, haematopoiesis and inflammation [45]**.** In MM, the main sources of IL-6 are autocrine (MM-cell derived) or paracrine (BMM-derived). Clinically, elevated IL-6 levels in MM patients is often associated with poor

prognosis and reflect a highly proliferative cell population [46]. Frassanito *et al.* has shown that autocrine IL-6 production in MM cells is indicative of a highly malignant phenotype as IL-6 producing cells were resistant to both dexamethasone and spontaneous apoptosis, whereas non-IL-6 producing cells were dexamethasone-sensitive [47]. Under normal conditions, basal IL-6 expression is low, however, in the tumour microenvironment there is a massive shift in IL-6 production. Amplified IL-6 levels also play a role in renal disease, thrombocytosis, anaemia and bone reabsorption [48]**.** IL-6 leads to activation of the JAK/STAT and RAS/RAF/MAPK pathways which play a role in MM growth and survival. Upregulation of anti-apoptotic B cell lymphoma-2 (Bcl-2) members such as myeloid cell leukaemia-1 (Mcl-1) and B-cell lymphoma-extra-large (Bcl-xL), is mediated through active STAT3 which leads to protection from various therapeutics [29, 49, 50]. NFκB also plays a critical role in cytokine and adhesion mediated IL-6 upregulation; NFκB is upregulated in BMSC and MM cells through cytokines, such as IL-6 and VEGF, produced by both cell types. Critically, IL-6 can also inhibit the anti-proliferative effects of CDK inhibitors p21 and p27 through the phosphatidylinositol 3 kinase (PI3K)/protein kinase B (AKT) pathway [51].

Multiple growth factors play a role in MM pathogenesis and progression including IGF-1 and VEGF [52]. Similarly, MM cell interaction with BMM derived growth factors play an intrinsic role in MM cell survival through the upregulation of anti-apoptotic proteins and proliferative signalling pathways. IGF-1 is a growth factor which has been shown to be critically involved in solid and haematological malignancies [53]. Activation of the PI3K pathway promotes cell survival through upregulation of Bcl-2 and Bcl-xL whilst downregulating the pro-apoptotic Bcl-2 family member, Bim. VEGF is another well-known key pro-angiogenic factor in cancer and MM. Tumours require nutrients and oxygen to grow, therefore, they require a constant blood supply. VEGF increases angiogenesis introducing new vasculature into the environment [54]. Increased levels of VEGF are particularly prevalent in haematological malignancies [55], and in MM, amplified VEGF levels and increased microvessel density is associated with poor prognosis [56]. VEGF is produced by cells from the BMM and MM cells themselves, stimulated by other cytokines and growth factors such as IL-6, transforming growth factor-β (TGF-β) and TNF-α. Several studies have shown that VEGF enhances MM cell survival through the upregulation of

anti-apoptotic proteins such as Mcl-1 and survivin [57] by activating the Rat Sarcoma (RAS)/ Rapidly Accelerated Fibrosarcoma (RAF)/Mitogen Activated Protein Kinase Kinase (MEK)/ERK pathway ([58], Reviewed in [43]). These cytokines activate the MAPK, JAK/STAT and the PI3K/AKT pathways and their downstream targets in MM which will ultimately lead to angiogenesis, bone lesions and drug resistance [59]. These oncogenic signalling pathways will be discussed in more detail in section 1.3 below. IL-6 production in turn increases VEGF production in MM cells creating a paracrine loop which optimises the BMM for MM cell growth and survival [60] [56], thus, serving as a link between the BMM and tumour progression.

Bone Marrow Microenvironment	**Microenvironment Components**	**Interactions with Myeloma Cells**
Non-Cellular Compartment	***Interleukin-6***	IL-6 leads to activation of the JAK/STAT and RAS/MAPK pathways which play a role in MM growth and survival through upregulation of anti-apoptotic proteins and inhibition of p21 and p27.
	Vascular endothelial growth factor	Activation of VEGF receptor -1 and -2 leads to proliferation, migration and differentiation of BMSC and EC cells. It also promotes angiogenesis.
	Transforming growth factor beta	TGF-β inhibits proliferation and IL-2 responsiveness in T lymphocytes. It also contributes to bone destruction.
	Insulin growth factor 1	IGF-1 is involved in the homing process of MM cells, upregulates anti-apoptotic proteins and stimulates the production of VEGF.

Table 1. 4 Summary of important cytokines in the myeloma bone marrow microenvironment

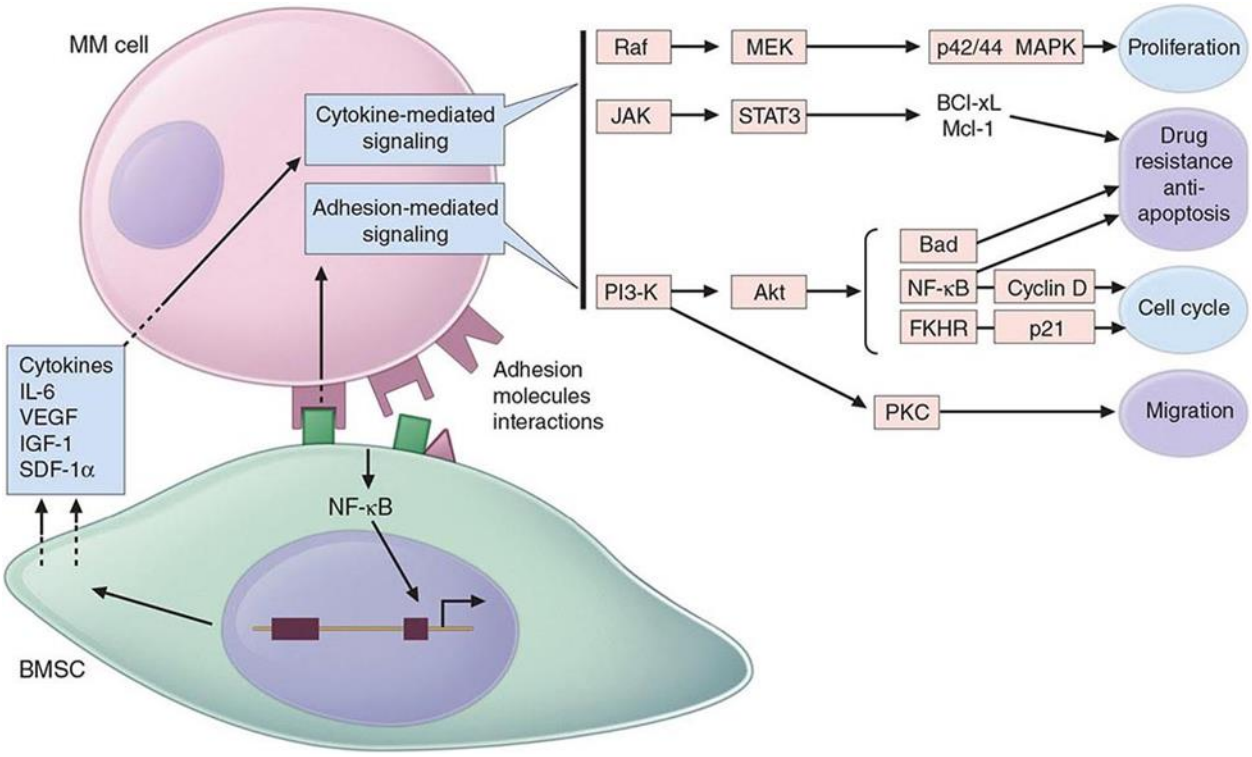

Figure 1. 2 Bone marrow stromal cell induced oncogenic signalling in myeloma.

Myeloma cells have an intricate relationship with the bone marrow microenvironment and in particular, with bone marrow stromal cells (BMSC). When BMSCs bind to the myeloma cell via adhesions molecules, this leads to the activation of signalling pathways within the BMSC. This in turn leads to the secretion of cytokines and growth factors which leads to the activation of oncogenic signalling pathways within the myeloma cell. Activation of these pathways lead to enhanced drug-resistance, proliferation, cell cycle progression and migration. Image from Tefferi et al., Harrison's Principles of Internal Medicine, 2015 [61].

1.3. Oncogenic signalling in multiple myeloma

As described in section 1.1.2., there are numerous frequently mutated genes in MM. The absence of a single unifying genetic mutation makes treating this widely diverse disease with a single drug or treatment unlikely. Recently, efforts into understanding frequently dysregulated and oncogenic signalling pathways in MM are underway in the hope of developing a more unified treatment strategy. MM cells multiply in bone marrow and rely heavily on signals from both the cellular and non-cellular compartments of the BMM to proliferate and survive through upregulation of signalling pathways such as the JAK/STAT, PI3K/AKT, NFκB and RAS/RAF pathways. The collective effects of aberrant activation and BMM induced activation leads to increased proliferation and resistance to apoptosis [62].

1.3.1. JAK/STAT pathway

The JAK/STAT pathway plays a critical role in immune regulation, haematopoiesis and cell growth. Various cytokines and growth factors such as IL-6, interferon, VEGF and platelet derived growth factor (PDGF) activate the pathway [63]. The signalling cascade is composed of a cell surface receptor, a JAK and two STAT proteins. In the canonical pathway, following engagement of IL-6 to the IL-6 receptor alpha (IL-6Rα or CD126) [64] there is ligand-induced homo or hetero-dimerisation of signal transducing receptor subunits and auto-phosphorylation of tyrosine residues on the JAKs. The JAKs are activated which increases its kinase activity, resulting in phosphorylation of tyrosine residues on the receptor creating binding sites for Src Homology-2 (SH-2) domains. The SH-2 domain on STAT binds to these phosphorylated sites. Subsequently, these STATs are recruited to the receptor where they are phosphorylated, homo or hetero-dimerise and translocate to the nucleus where they modulate the expression of target genes by binding to promoter regions [65, 66].

1.3.1.1. The IL-6 receptors

IL-6 signalling in MM is complex. IL-6 can activate JAK/STAT signalling in MM through two different signalling pathways: The classical signalling pathway and the *trans*-signalling pathway [67]. As aforementioned, the classical or canonical signalling pathway involves the engagement of IL-6 with the IL-6Rα (CD126) on the cell surface. The IL-6Rα is a single

membrane-spanning protein around 80 kDa. This complex recruit's glycoprotein 130 (gp130, CD130 or IL-6 Receptor-Beta) to form a hexameric IL-6/IL-6Rα/gp130 complex which initiates downstream signalling (Figure 1.3). Classical signalling is restricted to few cell types, mainly immune cells and hepatocytes as the IL-6Rα is only expressed on these cells. Conversely, *trans*-signalling is possible in all cell types due to the ubiquitous expression of gp130 as a co-receptor for many other cytokines and growth factors. In *trans*-signalling, IL-6 and a soluble form of the IL-6R known as sIL-6R form a complex and bind with membrane bound gp130 to elicit signalling. sIL-6R can be produced by alternative splicing of IL-6Rα messenger RNA (mRNA) and/or by the proteolytic shedding of the IL-6Rα by the disintegrin and metalloproteinase domain-containing protein 17 (ADAM17) from cells which express IL-6Rα. Therefore, *trans*-signalling is possible in all cell types that lack IL-6Rα but express gp130 (Reviewed in [68]).

Each pathway regulates distinct biological effects in cells. Classical signalling has been shown to play an important role in immunological responses, haematopoiesis and homeostasis while *trans*-signalling is thought to play an essential role in the tumour microenvironment; controlling the recruitment of immune cells to the area. The key element in both types of signalling is the presence of gp130, as engagement of gp130 is essential in both classical and *trans*-signalling. The activation of gp130 is a major event in controlling the proliferation and survival of MM cells [69].

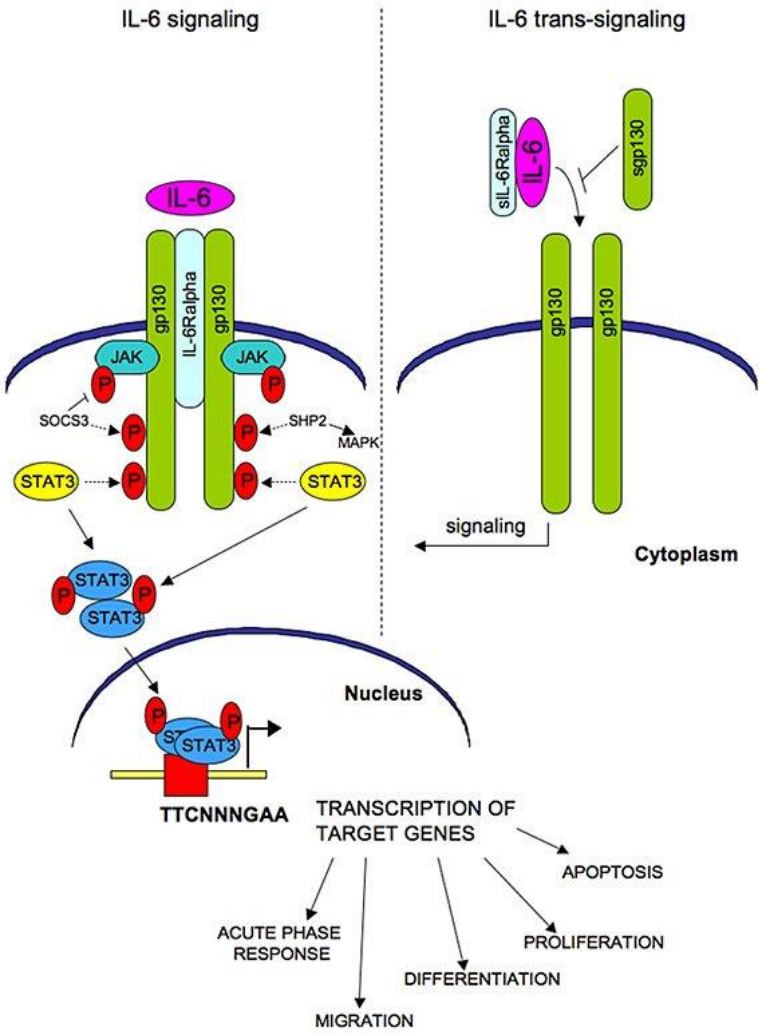

Figure 1. 3 Classical and trans signalling initiated by IL-6.

IL-6 binds to the IL6-Rα or sIL-6Rα forming a complex which associates with gp130 triggering its dimerisation. This leads to consequent activation of the associated JAK kinases. The JAKs phosphorylate specific tyrosine residues on the gp130 cytoplasmic tail, which in turn act as docking sites for STAT3 src homology-2 domain, leading to JAK-mediated STAT3 phosphorylation. The STATS then dimerise and translocate to the nucleus, where it regulates transcription of target genes. Image from Camporeale et al., Frontiers in Bioscience, 2012 [70].

1.3.1.2. JAKs

As previously discussed, IL-6 signalling via both the classical and *trans*-signalling pathways involves engagement of gp130 which leads to gp130-associated activation of the JAKs. The JAKs are a family of kinases which play an important role in cytokine signalling with aberrant activation associated with autoimmune diseases and haematological malignancies. In humans, four JAKs have been identified: JAK1, JAK2, JAK3 and TYK2. JAK1, JAK2 and TYK2 (Tyrosine Kinase 2) are widely expressed across many cell types whilst JAK3 is mainly expressed on haematopoietic cell types [68].

Many cytokine receptors, such as the IL-6R, lack intrinsic kinase activity and therefore depend on the JAKs which associate with the cytoplasmic tail of the receptor to potentiate downstream signalling [71]. The tyrosine kinase domain of the JAK is located in the JAK homology domain of the carboxyl-terminus. Formation of the IL-6/IL-6Rα/gp130 complex results in full activation of associated JAKs by disruption of inhibitory controls. The JAKs then go on to phosphorylate multiple sites on the cytoplasmic tail of gp130. These phosphorylated sites act as docking sites for effector proteins involved in major myeloma oncogenic signalling pathways, including the PI3K/AKT pathway, the RAS/RAF/MEK/ERK pathways and the JAK/STAT3 pathway.

Mutations in all four JAKs have been associated with human pathologies [72]. Inactivation of the JAKs is often associated with immune deficiencies whilst hyperactivation of JAK1, JAK2 and TYK2 is associated with myeloproliferative disorders and blood cancers [72]. For example, somatic activations in JAK1 are present in almost 20% of all adult T-cell acute lymphoblastic leukaemia (T-cell ALL). Overexpression of JAK2 has also been implicated in many haematological disorders. JAK2 overexpression can be caused by mutations such as a point mutation where valine is substituted for phenylalanine at position 617 (V617F) in the JAK Homology-2 domain of *JAK2* which leads to constitutive tyrosine activation. However, the V617F mutation, which is associated with many other myeloproliferative disorders such as polycythaemia vera, is absent in MM [73-75], despite reports that up to 57% of MM patients exhibit overexpression of JAK2 [76]. Considering the importance of activation of the JAK2/STAT3 pathway in MM cell survival, activation of this pathway must occur

through mechanisms other than *JAK2* mutations, most likely through the BMM. Regardless, the potent anti-MM activity of many JAK inhibitors is widely reported making these kinases a promising target for the treatment of MM [77-79].

1.3.1.3. STATs

The STATs (1, 2, 3, 4, 5A, 5B and 6) are a seven-membered family of cytoplasmic proteins which play a key role in cell fate. They relay signals from cell surface receptors to the nucleus where they elicit their activity as transcription factors. Structurally STAT proteins all contain an N-terminal domain, a coiled-coiled domain (CCD), a deoxyribonucleic acid (DNA) binding domain, a linker domain, a SH-2 domain, and a C-terminal transactivation domain (Figure 1.4) [80]. The core fragment contains the linker domain, CCD, DNA binding domain and the SH-2 domain which all play an integral role in the transcriptional activity of STAT3. Mounting evidence has demonstrated that aberrant activation of STAT3 contributes to tumourigenesis in both haematological cancers, such as MM and leukaemia, and solid cancers such as breast and prostate cancers [81, 82]. It should also be noted that constitutively active STAT5 has additionally been implicated in oncogenesis although in terms of neoplastic cellular transformation STAT3 is more frequently involved in oncogenic transformation [83, 84].

Inactive STAT3 exists as a monomer in the cytoplasm. Following phosphorylation of gp130 by the JAKs, the SH-2 domain of STAT3 binds to the phosphorylated tyrosine residues. The active JAK enzymes then subsequently phosphorylate STAT3 at tyrosine 705 (Y705). This phosphorylation results in head-to-tail dimerisation of STAT3 and translocation to the nucleus where STAT3 carries out its function as a transcription factor. STAT3 binds to the promotor regions of STAT3 responsive genes involved in cell survival, proliferation and migration; such as cyclin D1, Mcl-1 and matrix metalloproteinase-1 (MMP-1) respectively [85]. This induction of target genes by STAT3 is largely how STAT3 promotes the growth of tumour cells. One key aspect is that STAT3 can induce a positive feedback loop through binding to the IL-6 promotor region leading to the induction of IL-6 which, in turn, leads to the upregulation of proteins associated with cell survival, proliferation, angiogenesis,

metastasis and immune suppression [86]. Therefore, targeting the JAK/STAT3 pathway may be a promising anti-myeloma target.

Dysregulated STAT3 signalling has been implicated in nearly all features of cancer biology. Constitutive and induced activation of STAT3 signalling promotes initiation and progression of cancers by driving proliferation, angiogenesis and invasion whilst inhibiting apoptosis [87]. STAT3 modulates the expression of target genes such as survivin, cyclins and Bcl-2 proteins which play an integral role in cell proliferation and survival (Figure 1.5). This will be discussed in more detail below. In particular, Mcl-1, an anti-apoptotic Bcl-2 family member, plays a critical role in MM cell survival through both constitutive activation through mutations and microenvironment-induced activation of STAT3 signalling [29], making STAT3 a favourable target for MM and many other cancers [88].

In addition to canonical-STAT3 signalling, STAT3 activity can be modulated through phosphorylation on alternate sites and acetylation. The STATs can be phosphorylated on serine residues, however, much less frequently than tyrosine amino acids [89]. The role of phosphorylation of STAT3 on serine 727 is unclear and its function may depend on the cell type being investigated. Previously phosphorylation on this site has been shown to play a role in enhancing the transcriptional activity of STAT3 in CLL however, conversely, serine phosphorylation has also been shown to inhibit the transcriptional activity of STAT3 demonstrating the promiscuous nature of phosphorylation on this site. In CLL, STAT3 is constitutively phosphorylated on serine 727 but not tyrosine 705 [90]. Serine phosphorylated STAT3 in CLL has been found to translocate to the nucleus, bind to DNA and activate transcription of STAT3 target genes [91]. Similarly, Sakaguchi *et al.* have shown that serine 727 is phosphorylated in melanoma suggested that phosphorylation on this site plays a role in the transcriptional activity of STAT3 and cell survival [92]. The group also demonstrated that constitutive phosphorylation of serine was in part mediated BRAF/MEK/ERK pathway [92]. Interestingly, RAS-dependent proliferation requires phosphorylation of STAT3 on serine but not tyrosine. Activation of serine 727 by RAS has been shown to potentiate RAS transformation as it leads to increased mitochondrial respiration. Gough *et al.* have shown that mitochondrial STAT3 supports this transformation by maintaining altered glycolytic and oxidative phosphorylation respiration,

a hallmark of cancer [93]. In the mitochondria STAT3 influences respiration via its interaction with electron transport chain components and phosphorylation on serine has been shown to be essential for this process. The chaperone protein GRIM-19 promotes incorporation of STAT3 into the electron transport chain complex. This inhibits the localisation and transcriptional activity of STAT3 and has been demonstrated to lead to an increase in reactive oxygen species (ROS) production and the induction of apoptosis [89].

In addition to phosphorylation, STAT3 has been shown to be acetylated on lysine 685. Acetylation of STAT3 is mediated by the histone acetyltransferase p300 and this modification has been shown to be essential for its transcriptional activity as its required for the formation of stable dimers which translocate to the nucleus and bind DNA [94].

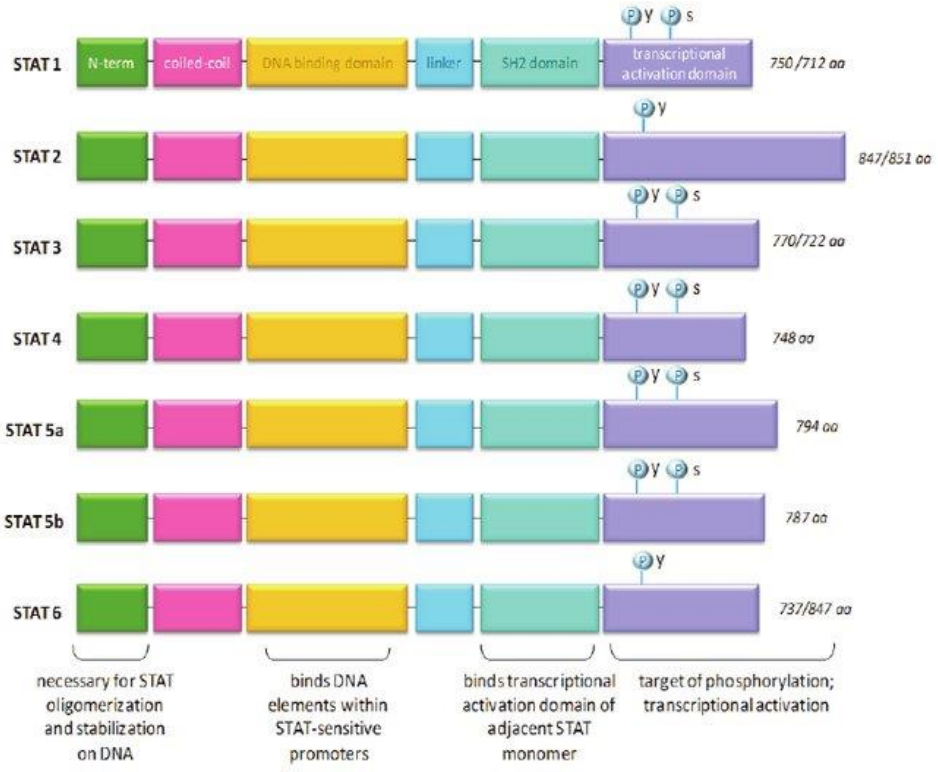

Figure 1. 4 Structural homology of the STAT3 family.

The STATs (1, 2, 3, 4, 5A, 5B and 6) are a seven-member family of transcription factors. Structurally STAT proteins all contain an N-terminal domain, a coiled-coiled domain (CCD), a deoxyribonucleic acid (DNA) binding domain, a linker domain, an SH-2 domain, and a C-terminal transactivation domain. Image from Nicholas et al., Breakthroughs in Melanoma Research, 2011 [95].

1.3.1.4. Downstream targets of STAT3

STAT3 has multiple downstream targets such as cell cycle proteins, proinflammatory cytokines, MMPs, growth factors and anti-apoptotic proteins (Figure 1.5). These downstream targets all play a vital role in MM cell survival. Key proteins include survivin, cyclin D1 and Mcl-1, as well as pro-survival growth factors and cytokines as previously discussed. Mcl-1 will be discussed in detail in section 1.6.3 below.

Survivin is a member of the inhibitor of apoptosis protein (IAP) family which include NAIP, cIAP1, cIAP2, XIAP, survivin, livin, apollon and ILP-2. They can mediate protein-protein interactions and are thought to play a role in the inhibition of cysteine-aspartic protease (caspase) cleavage and activation. Caspase proteases are known as the death executioners in apoptosis. Consequentially, IAPs are also thought to play a critical role in regulation of apoptosis. Previous studies have shown that IAPs are overexpressed in multiple malignancies including small cell lung cancer, pancreatic cancer, breast cancer and MM [96]. Survivin, the smallest member of the IAP family may also have implications in MM [97]. It functions not only as an IAP but also as a component of the chromosome passenger complex where it plays a role in mitotic checkpoint regulation. It has emerged as a target in cancers due to its restricted expression in normal tissues but high expression in malignancies [98]. Survivin is overexpressed in many MM cell lines and high expression of survivin in patient samples is considered to indicate poor prognosis [97, 99]. Moreover, constitutive or induced STAT3 signalling can lead to an upregulation in survivin gene expression which may play a role in BMM induced drug resistance [100].

Another major downstream target of STAT3 in MM is cyclin D1. Cyclin D1 is the protein product of the *CCND1* gene and upregulation of cyclin D1 is an early and unifying event in MM [101]. Cyclin D1 is an important regulator of the cell cycle, regulating G1 to S phase progression in many cell types. The cell cycle is a highly controlled process, the activation of which is controlled by CDKs and several checkpoint pathways. The function of these CDK is regulated by cyclins and CDK inhibitors [102]. CDK4 and 6 bind to cyclin D1 forming an active complex that promotes cell cycle progression by inactivating retinoblastoma protein [103]. Perturbations in the cell cycle are a common feature of most cancers and in MM this

deregulation is mainly caused by dysfunction of cyclin D and Inhibitors of CDK4 (INK4) family of inhibitors [102, 104]. As previously discussed, the most common translocation in MM is t(11;14), which results in the upregulation of cyclin D1 expression. Increased cyclin D1 expression is not restricted to non-hyperdiploid MM as it also occurs in hyperdiploid MM, likely caused by trisomic chromosome 11 [101, 105]. Studies have shown that STAT3 promotes proliferation of cells through direct association with the promotor of the *CCND1* gene to induce cyclin D1 expression and enhance proliferation [104, 106, 107].

In addition, the transcription factor c-MYC and PIM kinases have been shown to lie downstream of STAT3. Activation of the transcription factor c-MYC has been shown to play an important role in myeloma [108]. c-MYC is thought to be expressed in 40% of cancers and MYC family oncogenes, especially c-MYC, is associated with late MM disease progression . Many cancer cells can develop an addiction to MYC and therefore may be a promising therapeutic target in MM [109]. The Pim kinases are a small family of kinases that are constitutively expressed in haematological malignancies and have been shown to play a role in the development of drug resistance. Previous studies have demonstrated that the Pim kinases lie downstream of STAT3 and that inhibition of STAT3 results in downregulation of Pim2 [110]. Moreover, inhibition of the Pims by a pan pim kinase inhibitor induced apoptotic cell death in MM cells suggesting its potential as a MM target [111].

To summarise, STAT3 activation leads to the transcription of many genes involved in tumour progression and survival. Key players involved in MM progression include cyclin D1, the anti-apoptotic Bcl-2 family members, IL-6 and VEGF.

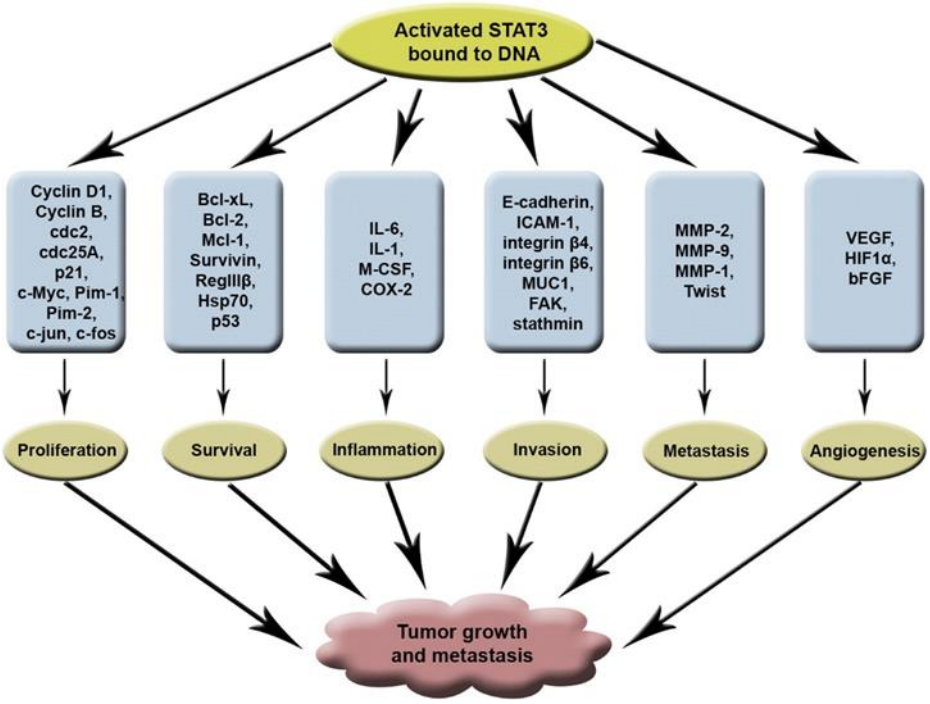

Figure 1. 5 The role of downstream STAT3 targets in cancer development.

STAT3 has multiple downstream targets such as anti-apoptotic proteins, cytokines and adhesion molecules which play a role in tumour growth, survival and metastasis. Targeting aberrant STAT3 signalling in cancer is therefore a promising target. From Siveen et al., Biochm Biophys Acta, 2014 [81].

1.3.2. Mitogen-activated protein kinase pathways

The MAPKs are a family of protein kinases with diverse biological functions from cell differentiation, proliferation and survival to cell death. MAPKs link extracellular signals to the intracellular machinery which controls these cellular processes. They are divided into distinct groups in mammals, the most well studied being the RAS/RAF/MEK/ERK, p38 and JNK pathways (Figure 1.6).

1.3.2.1. The RAS/RAF/MEK/ERK pathway

Activation of the RAS/RAF/MEK/ERK pathway in MM can be caused by autonomous mutations and mediated by cytokines such as IL-6, IGF-1 and VEGF from the BMM. Ras

proto-oncogenes are frequently mutated in MM and other malignancies such as ovarian, pancreatic, and lung cancers [112]. Ras proteins are encoded by three ubiquitously expressed genes: *HRAS*, *KRAS* and *NRAS*. These proteins are GTPases that function as molecular switches regulating pathways responsible for proliferation and cell survival. Activation of this pathway contributes significantly to MM cell growth, survival, angiogenesis and the development of drug resistance. In MM, *KRAS* and *NRAS* activating mutations occur at a high frequency of up to 50% in newly diagnosed patients [113]. Evidence is emerging to suggest that patients with activating *KRAS* mutations have a much poorer prognosis than those with the *NRAS* variant [114]. However, a more recent 2014 study by Mulligan *et al*. demonstrated that activating mutations of *NRAS* but not *KRAS* significantly reduced MM cell sensitivity to bortezomib, highlighting the promiscuous nature of mutant *RAS* variants [115]. One recurrent difference between MGUS and MM is the frequency of *RAS* mutations, they tend to be much more common in MM and not in MGUS which indicates that *RAS* mutations may play a role in the pathogenesis of MM and disease progression [116]. Indeed, there appears to be a dominant mutation cluster in *RAS/RAF* genes in MM highlighting this signalling pathway as a promising therapeutic target. Since approximately 50% of newly diagnosed MM patients have mutations in *NRAS*, *KRAS* and *BRAF* and the frequency of other mutated genes is much lower, targeting these key signalling pathways as a therapeutic strategy against MM may be a more viable tactic in treating such a genetically diverse disease [117, 118].

Currently, there are no drugs approved for the treatment of MM which target the RAS/RAF/MEK/ERK pathway directly. Sorafenib, a multi-kinase inhibitor which targets BRAF and VEGFR2 has shown promising effects against MM as a single agent and in combination with anti-myeloma drugs warranting further studies [119, 120]. More recently, preliminary studies testing vemurafenib, a BRAF inhibitor, in MM patients with $BRAF^{V600E}$ mutations have shown promising results. $BRAF^{v600E}$ mutations can be seen in around 4% of MM patients and are associated with an unusually aggressive clinical course [121]. Trametinib, a MEK inhibitor has shown some promising anti-MM activity as both a mono- and combination therapy with complete responses seen in some patients with

activating MAPK mutations. However, despite these promising results in some patients, no long-term responses were observed (Reviewed in [122]).

1.3.2.2. The c-Jun N-Terminal kinase Pathway

The c-Jun N-Terminal kinase (JNK) family, also known as stress-activated protein kinase (SAPK) family, is comprised of three proteins; JNK1, JNK2 and JNK3. They control a diverse range of cellular responses such as differentiation, cell death and survival [123]. JNK1 and JNK2 are almost ubiquitously expressed in all tissues while JNK3 is confined to the brain, heart and testes [124]. Similar to other MAPKs, they are activated by stimuli such as growth factors, cytokines, chemicals and pathogens culminating in a phosphorylation cascade. Like all MAPKs, JNKs are phosphorylated by MAP2Ks such as MKK4 and MKK7, MAP2Ks are in turn phosphorylated by upstream MAP3Ks such as the apoptosis signal-regulating kinase family member, TAK1 (Figure 1.6). Following phosphorylation of JNK, this kinase in turn phosphorylates and, thus, activates a number of proteins, including the transcription factor activator protein-1 (AP-1) which forms via the dimerisation of a Jun protein and a Fos protein [125].

The role of JNK in cancer and disease progression is under debate. One view point of JNK hyperactivation being involved in tumourigenesis is supported by studies illustrating that sustained JNK1 activation is associated with tumour formation in liver cancer [126]. Similarly, in MM, a study by Barbarulo *et al.* illustrated that JNK2 activation is associated with enhanced cell survival [127]. Conversely, numerous studies have implicated JNK signalling in tumour suppression. One murine study by She *et al*. demonstrated that JNK1 null mice had enhanced tumour formation in comparison to their wild type counterparts [128]. This tumour suppressive function was further supported by studies which have shown that JNK1/2 deficient mice have enhanced mammary tumour formation, driven in part by decreased p53 expression [129]. The tumour suppressive function of JNK1 signalling is likely mediated through initiation of apoptosis through the intrinsic apoptotic pathway [130]. These conflicting viewpoints indicate that the role of JNK activation may be specific to the cancer or even cell type.

1.3.2.3. The p38 MAP kinase pathway

Similar to the JNK signalling pathway, the p38 MAPK pathway plays a pivotal role in multiple biological functions from development to cell death. Unlike the ERK pathway, the p38 pathway is strongly activated by cytokines and extracellular stresses. p38 MAPK is activated by upstream kinases MKK3, MKK6 and sometimes MKK4 kinase which are capable of phosphorylating p38 on threonine and tyrosine residues concurrently. p38 regulates the transcription factors p53 and activating transcription factor 2 (ATF-2), as well the protein kinases mitogen- and stress-activated protein kinase 1 (MSK1) and MAPK-activated kinase 2 (MK2) [131]. There is evidence to suggest that p38 acts as a tumour-suppressor through the inhibition of cell cycle progression and induction of apoptosis. In addition, like JNK signalling, there is evidence to suggest that p38 activation may also have oncogenic functions. The p38β isoform is thought to increase the activation of AP-1, whilst the p38γ and p38δ isoforms have been shown to inhibit AP-1 transcription [132].

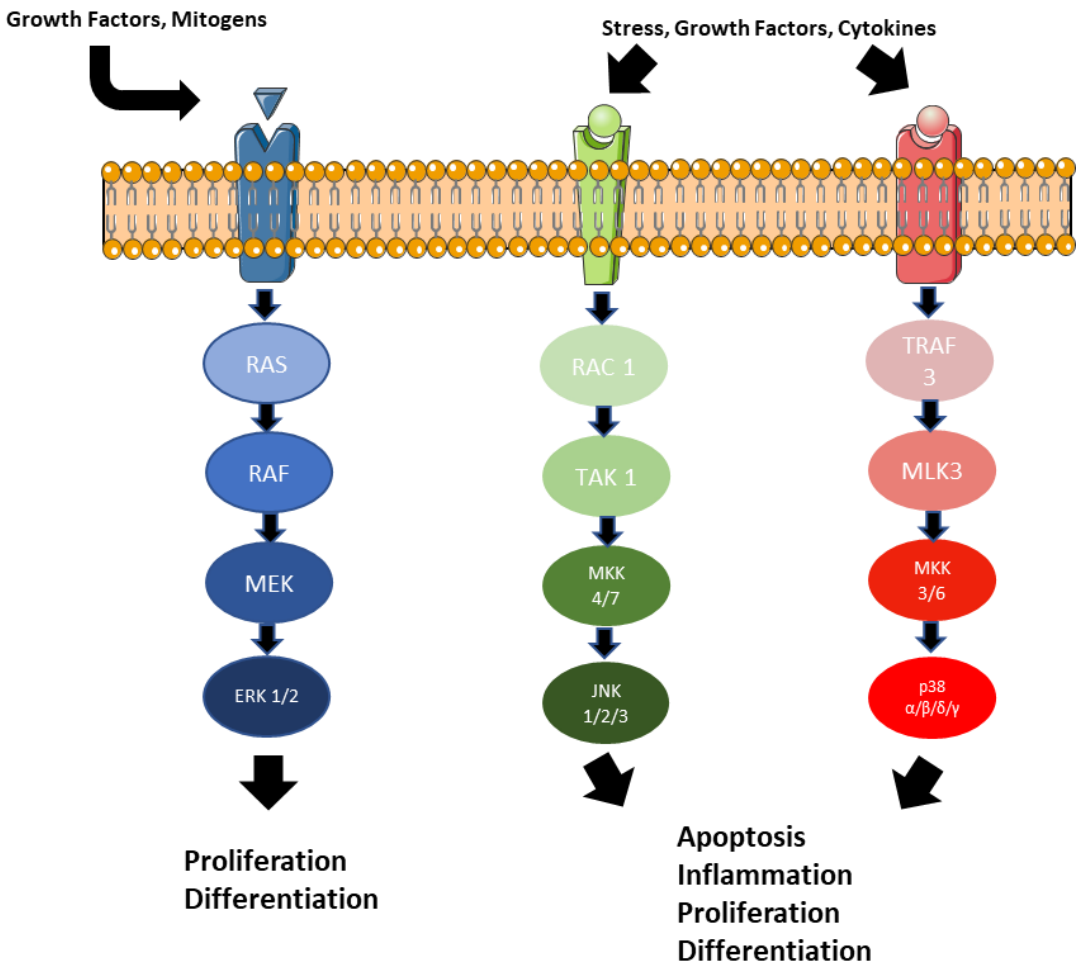

Figure 1. 6 The MAP kinase signalling pathways.

The MAPKs are a family of protein kinases with diverse biological functions from cell differentiation, proliferation and survival to cell death. MAPKs link extracellular signals to the intracellular machinery which controls these cellular processes. They are divided into distinct groups in mammals, the most well studied being the RAS/RAF/MEK/ERK, p38 and JNK pathways. The RAS/RAF/MEK/ERK pathway traditionally plays a role in cell proliferation and differentiation whilst the p38 and JNK pathways are more associated with cell death, however, the pathways can act in an opposing manner depending on the cell type and the circumstances.

1.3.3. PI3K/AKT pathway

Studies have shown that multiple genes involved in the PI3K pathway are mutated in cancer and, in particular, MM [133, 134]. PI3Ks are a large and complex family of lipid kinases which phosphorylate the 3'-OH position of the inositol ring of inositol phospholipids [135], producing 3 lipid products which bind to the pleckstrin homology domains of proteins and control the activity and subcellular localisation of a wide variety of signal transduction molecules. Under normal conditions the PI3K pathway is tightly regulated through multiple mechanisms. There are three different classes of PI3K (I, II and III), as well as the different isoforms within each class. There is increasing evidence of the importance of distinct roles for each of the three different classes. Oncogenic signalling is mainly mediated through kinase activated group 1A of the class I PI3Ks. The PI3K pathway is activated through ligands, such as IL-6 and IGF-1, binding a receptor tyrosine kinase (RTK) on the plasma membrane. Following receptor-ligand binding a p85 regulatory subunit binds to the p110 catalytic subunit, forming the p85-p110 complex which moves to the cytoplasmic tail of the RTK receptor leading to activation of PI3K kinase. This results in a conformational change and leads to the generation of PtdIns(3,4,5)P3 (PIP3), a second messenger, which activates multiple downstream pathways through recruitment of pleckstrin homology domain containing proteins, such as AKT (Figure 1.7) [135, 136]. AKT activation leads to increased survival, proliferation and growth of tumour cells, and possibly angiogenesis by signalling through epithelial cells [137]. In MM, deregulated cytokines and growth factors such as IL-6 and IGF-1 activate this signalling pathway leading to survival, migration and proliferation [51, 138, 139]. Mammalian target of rapamycin (mTOR), a major survival checkpoint regulator downstream of AKT, has shown significant anti-apoptotic activity in MM resulting in myeloma cell survival and proliferation [140].

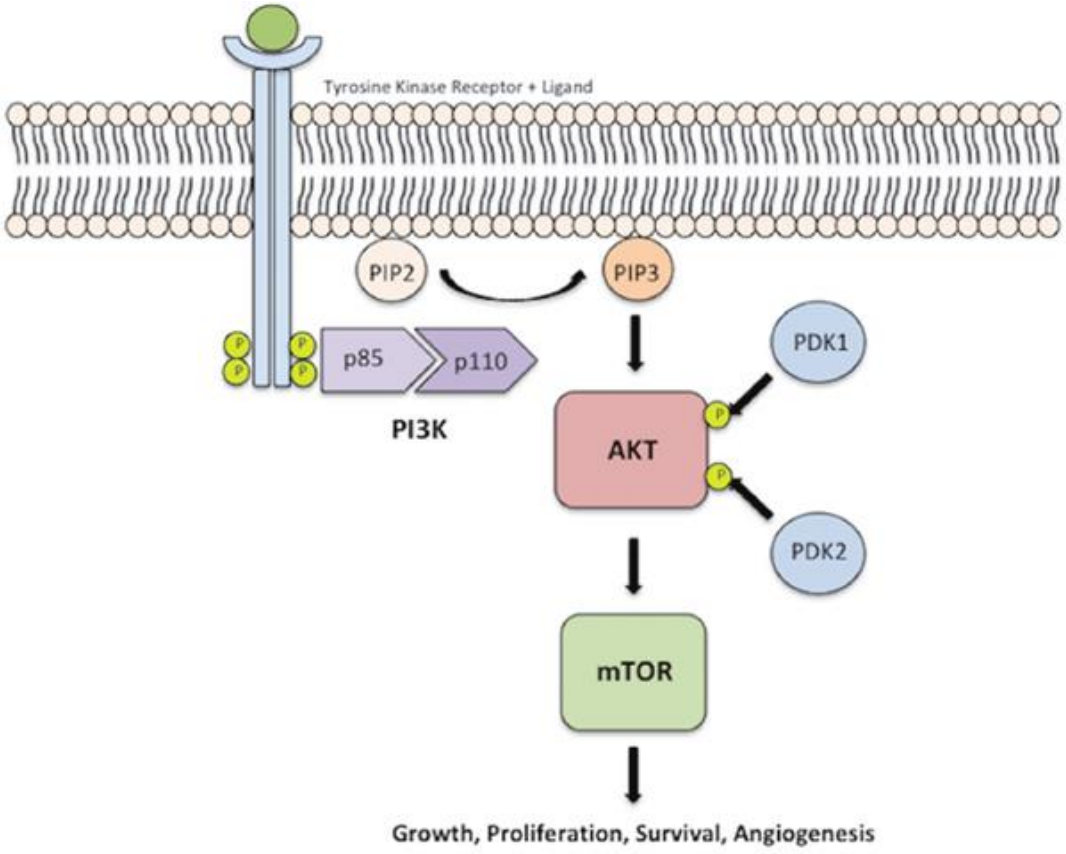

Figure 1. 7 The PI3K/AKT signalling pathway.

The PI3K pathway is activated through ligands such as IL-6 and IGF-1 binding a receptor tyrosine kinase on the plasma membrane. Following receptor-ligand binding a p85 regulatory subunit binds to the p110 catalytic subunit, forming the p85-p110 complex which moves to the cytoplasmic tail of the RTK receptor leading to activation of PI3K kinase. This results in a conformational change and leads to the generation of PtdIns(3,4,5)P3 (PIP3), a second messenger, which activates multiple downstream pathways through recruitment of pleckstrin homology domain containing proteins such as AKT. Mammalian target of rapamycin (mTOR), a major survival checkpoint regulator downstream of AKT. Image from Adimonye et al., Oncotarget, 2018 [141].

1.3.4. The Nuclear Factor Kappa B pathway

The NFκB family of transcription factors play a critical role in the proliferation and survival of many malignancies including MM. NFκB is essential for proper cellular functions and aberrant NFκB activation can lead to many autoimmune diseases, inflammatory conditions and malignancies; therefore, inhibiting its activation is an important therapeutic strategy [142]. The family is composed of NFκB1, NFκB2, RelA (p65), RelB and c-Rel which all share a conserved N-terminal Rel homology domain. These transcription factors act dimerically to modulate the function of biological processes through two pathways known as the canonical and non-canonical pathways. The canonical pathway mainly coordinates inflammatory signalling and is primarily known for defence against microorganisms. The non-canonical NFκB pathway mainly mediates activation of p52/RelB dimer and dysregulation is often associated with lymphoid malignancies (Figure 1.8) [143].

Mutations in the NFκB pathways are extremely common in haematological malignancies, including MM. Mutations in several components of the NFκB pathway in MM have been identified with around 17% of primary MM samples expressing mutations and 42% of all MM cell lines. NFκB controls the expression of molecules, such as IL-6 and B cell activating factor (BAFF) which are important for MM cell growth as previously discussed. BAFF and NFκB can create a positive feedback loop leading to the activation of oncogenic signalling pathways. Cell cycle proteins, such as cyclin D1, are also thought to be regulated by NFκB. Another key role NFκB plays in MM pathogenesis is the process of angiogenesis which has been shown to be partially regulated by NFκB as it can lead to the secretion of VEGF from BMSCs. As previously discussed, NFκB plays a key role in BMM induced resistance in MM and this, combined with the frequency of mutations, makes this pathway an interesting target (Reviewed in [144]).

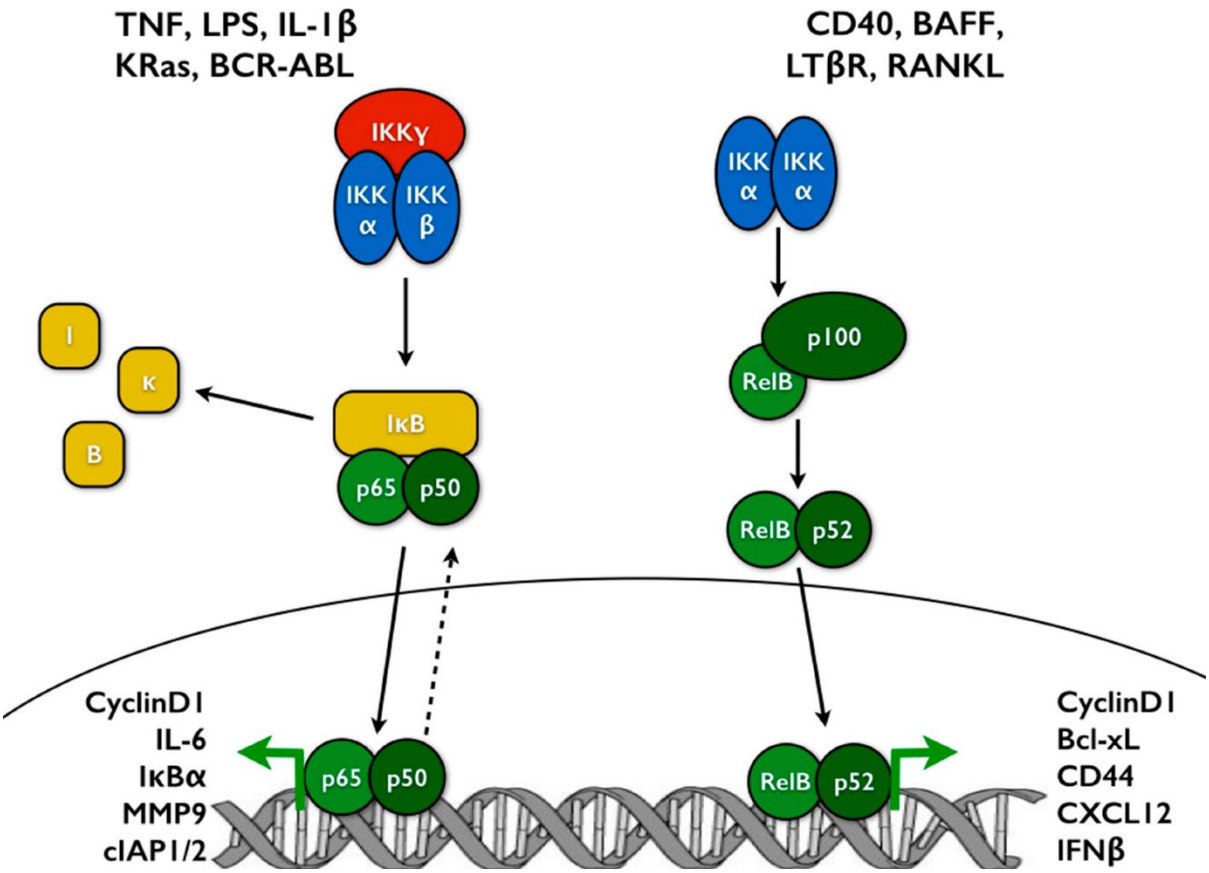

Figure 1. 8 Nuclear Factor Kappa B signalling pathway.

The NFκB family of transcription factors act dimerically to modulate the function of biological processes through two pathways known as the canonical and non-canonical pathways. The canonical pathway coordinates inflammatory signalling mainly and is primarily known for defence against microorganisms. The non-canonical NFκB pathway mainly mediates activation of p52/RelB dimer and dysregulation is often associated with lymphoid malignancies and adaptive immunity. Image from Rinkenbaugh et al., Cells, 2016 [145].

1.4. Current treatments for multiple myeloma

Although MM is currently considered a single malignancy, it is in fact, a collection of several different plasma cell malignancies characterised by marked cytogenetic, proliferative and molecular heterogeneity [146, 147]. As a result, treatment of the disease has changed dramatically over the past two decades with the introduction of new drugs and drug combinations for the treatment of both newly diagnosed and relapsed myeloma. Historically, MM was treated with alkylating agents, such as melphalan, in combination with corticosteroids, such as prednisone (MP), which achieved a median survival of 2 to 3 years. The introduction of autologous haematopoietic stem cell transplant (ASCT) with high-dose chemotherapy in the 1990s, demonstrated a marked increase in overall survival at a median of 5 years [148]. However, with the approval of new drugs and therapeutic strategies over the past decade there has been an almost 3-fold improvement in the median overall survival rate which now approaches 6-10 years [149]. Current treatments regimens for newly diagnosed MM patients include a doublet or triplet combination such as lenalidomide, dexamethasone and bortezomib followed by ASCT or maintenance therapy for ASCT-ineligible patients [150]. Eligibility for ASCT is based upon a number of factors including age, co-morbidities and disease related factors such as the presence of certain cytogenetic abnormalities [151]. These patients are categorised as “fit” or “unfit”. “Fit” patients receive full-dose therapy, whilst “unfit” patients receive a reduced-dose treatment. Patients younger than 65 years with no co-morbidities often receive ASCT with high-dose therapy whilst those older than 65 years do not, however, these criteria are guidelines and individual “fitness” varies from patient to patient with different therapeutic approaches adopted based on the patient [152].

Several new drugs have been approved over the past 10 years, such as third generation immunomodulatory agents (IMiDs), pomalidomide and lenolidamide, the second generation proteasome inhibitors , carfilzomib and ixazomib, the histone deacetylase inhibitor (HDACI), panobinostat and two mAbs, elotuzumab and daratumumab, and as a result, there are now 6 different classes of agents that can be used in combination to treat this heterogeneous malignancy (Table 1.5) [153]. A focus on novel immunomodulatory

agents, and drugs which target MM in the context of the BMM, have transformed the treatment archetype and have vastly improved patient survival overall. Yet, as previously described, even patients with excellent responses to front-line treatments frequently, if not always, relapse requiring further treatment. This strengthens the pursuit of novel drugs which can improve patient outcomes.

Disease Stage	Drug Regimens
Front-line	• Bortezomib/melphalan/prednisone (VMP) • Lenalidomide/low-dose dexamethasone (Rd) • Melphalan/prednisone/thalidomide (MPT) • Bortezomib/cyclophosphamide/dexamethasone (VCD) • Bortezomib/thalidomide/dexamethasone (VTD) • Bortezomib/lenalidomide/dexamethasone (VRD)
Relapsed and Refractory	• Carfilzomib/lenalidomide/dexamethasone (KRD) • Bortezomib/dexamethasone/panobinostat (VD-Pano) • Carfilzomib/dexamethasone (Kd) • Lenalidomide/dexamethasone/elotuzuman (Rd-Elo) • Lenalidomide/dexamethasone/ixazomib (IRd) • Bortezomib/dexamethasone/daratumumab (DVd) • Lenalidomide/dexamethasone/daratumumab (DRd)

Table 1. 5 Current Treatments for primary and relapsed/refractory myeloma

Adapted from Moreau, Blood 2017 [2]

1.4.1. Proteasome inhibitors

Proteasome inhibition first emerged as a promising therapeutic strategy against MM after the first phase 1 clinical trials of the first-in-class proteasome inhibitor, bortezomib, in the early 2000s [154]. Since these promising preclinical trials, proteasome inhibitors have become a pivotal anti-myeloma therapy. Undeniably, bortezomib and, more recently, second generation inhibitors, carfilzomib and ixazomib, have contributed substantially to the observed improvement in overall survival of MM patients over the past 15 years [155].

Although, bortezomib was primarily approved as a single agent, it is most commonly used in combination with other drugs as previously described.

The ubiquitin-proteasome pathway (UPP) plays an essential role in maintaining cellular homeostasis. This is a normal cellular process and it is responsible for degradation of regulatory proteins in cells, including proteins involved in cell-cycle progression, DNA repair and apoptosis making it an important anticancer target [156]. The UPP also plays an important role in the removal of damaged and defective proteins. The 26S proteasome is made up of two sub-complexes: a catalytic core particle (20S proteasome) and two terminal 19S regulatory particles that serve as a proteasome activator [157]. Proteins that are destined to be degraded by the proteasome are recognised by the 19S cap and are directed to the 20S core where proteolytic cleavage of the proteins takes place. Disruption of proteasome activity leads to an increase of regulatory proteins within the cell. This accumulation of incompatible proteins within the cell leads to induction of an apoptotic cascade [158]. In some cancers, such as MM, proteasomal activity can be increased, possibly due to aberrancies in the UPP which may lead to the degradation of pro-apoptotic proteins thus inhibiting the induction of apoptosis. MM cells are particularly susceptible to proteasome inhibition as they over-produce defective proteins which need to be degraded by the proteasome, and they up-regulate signalling pathways dependent on the 26S proteasome [159]. Bortezomib, a boronate, targets chymotrypsin and caspase-like sites of the 20S core inhibiting the proteasome and inducing apoptosis through multiple mechanisms [160]. Bortezomib has also been shown to directly induce apoptosis through modulation of NFκB activity and by blocking IL-6 signalling. This leads to the suppression of downstream survival and pro-angiogenic signalling pathways, in both MM cells and in cells of the BM microenvironment, through caspase-dependent downregulation of gp130 [161]. Additionally, the endoplasmic reticulum (ER) stress response is also thought to be triggered by bortezomib in MM cells which is an important mechanistic action due to the production of Ig by myeloma cells [162].

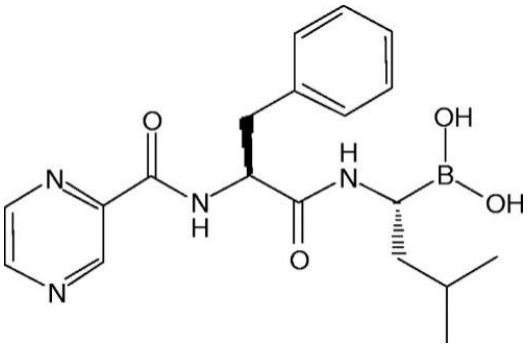

Figure 1. 9 Chemical structure of the proteasome inhibitor bortezomib.

Structure of bortezomib, Image from PubChem, 2019 [163].

1.4.2. Alkylating agents

Alkylating agents such as melphalan and cyclophosphamide, are the most widely used anti-cancer drugs and have been used in the treatment of MM for decades due to their broad anti-tumour activity [164]. These agents attach an alkyl group to the guanine base of DNA, most frequently at position N7. The exact mechanism of action of these widely-acting alkylating agents is unclear but it is thought that since cancer cells replicate at a much higher rate than non-cancerous cells, alkylating agents will target these rapidly proliferative cells [165]. Once melphalan is administered, efforts by the cell to replicate or repair DNA damage cause the formation of double-stand breaks or single-strand gaps in the DNA. These lesions can lead to chromosomal abnormalities and breakage during mitosis. The subsequent DNA damage caused by the lesions may trigger apoptosis or other mechanisms of cell death. With more drugs becoming frequently available to treat MM, clinicians are less likely to treat newly diagnosed patients with alkylating agents due to their non-specific activity and harsh side effects unless they are unsuitable for ASCT. If patients are suitable for ASCT, melphalan is often used in preparative regimens due to its ability to destroy the bone marrow and to exhibit immunosuppressive effects (Reviewed in [166]).

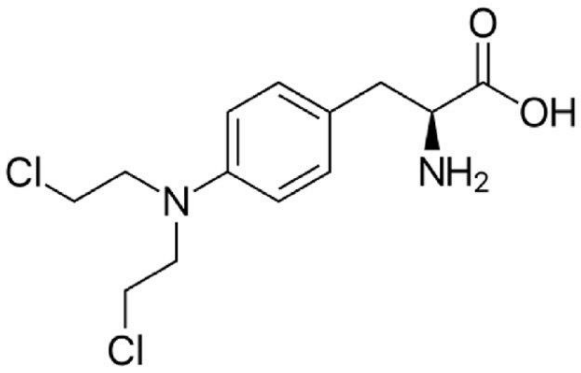

Figure 1. 10 Structure of melphalan.

Chemical structure of melphalan.
Image from Powar et al., Indian Jour Ed and Research, 2019 [167].

1.4.3. Corticosteroids

Glucocorticoids (GC) are steroid hormones that are produced by the adrenal glands [168]. Synthetic steroidal GCs, such as dexamethasone and prednisone, have been used in medicine for their immunosuppressive and antiproliferative effects for decades, despite this, their precise mechanism of action is unknown [169]. GCs such as dexamethasone have been shown to induce apoptosis in many haematological cancers, including lymphomas and MM, and hormone responsive cancers such as breast and prostate, becoming a staple in many treatment regimens [170]. How GCs elicit their antiproliferative effects is still unclear; however, there are two main proposed mechanisms. The first mechanism proposes that GCs induce the apoptotic cascade via activation of transcription of death specific genes. The second mechanism proposes that apoptosis is mediated via downregulation of proinflammatory cytokines or survival genes, which occurs via inhibition of transcription [171]. While both mechanisms are plausible, evidence is mounting towards the latter mechanism in which dexamethasone induces apoptosis with direct interaction between the GC receptor and NFκB and AP-1 being the most likely causative events for GC induced apoptosis [171].

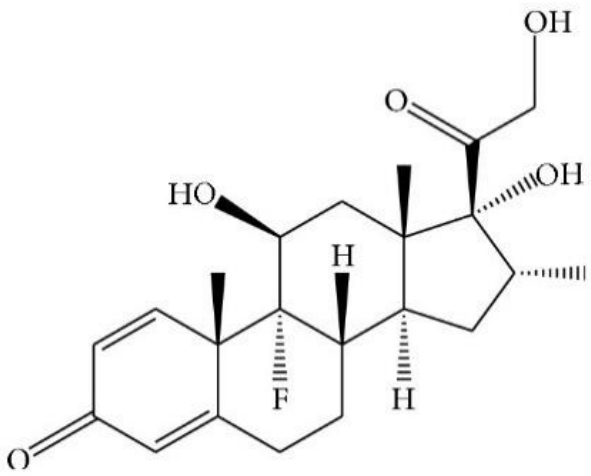

Figure 1. 11 Structure of dexamethasone.

Chemical structure of dexamethasone. Image from Duarte et al., European Polymer Journal, 2009 [172].

1.4.4. Immunomodulatory agents

The development and introduction of IMiDs such as thalidomide, pomalidomide and lenalidomide, for the treatment of MM has contributed greatly to the improvement in patient outcomes [173]. Controversially, thalidomide was the first IMiD approved for use in MM due to its anti-angiogenic capabilities. Following the pioneering work of Judah Folkman and Robert D'Amato into angiogenesis, a study by Singhal *et al*., illustrated that thalidomide could induce marked cell death in refractory MM patients who had become resistant to other chemotherapies, paving the way for the approval of thalidomide in MM treatment in 2006 [174]. The thalidomide analogues, lenalidomide and pomalidomide, were developed as safer and more potent alternatives to thalidomide. IMiDs are thought to elicit multiple anti-tumour effects in MM including the induction of apoptosis and cell cycle arrest. IMiDs bind to the cereblon E3 ubiquitin ligase complex, resulting in the ubiquitination, and subsequent degradation, of transcription factors such as the Ikaros family member, IKZF1. IKZF1 has been shown to be important for B cell development [175].

IMiDs also disrupt MM-BMM interactions through the modulation of anti-angiogenic and anti-inflammatory cytokines and adhesion molecules. They are thought to inhibit BMSC production of cytokines, such as IL-6 and TNF-α, and growth factors such as VEGF and basic fibroblast growth factor which inhibit myeloma cell proliferation and angiogenesis. IMiDs are also thought to act as co-stimulatory molecules of T cell activation inducing proliferation, cytokine production and cytotoxic responses in CD8+ cytotoxic T cells. The activated T cells produce natural killer cell activating cytokines, such as IL-2 and interferon-gamma. The activated NK cells go on to kill the MM cells through cytolytic granule mediated apoptosis and/or antibody dependent cellular cytotoxicity (ADCC) [176].

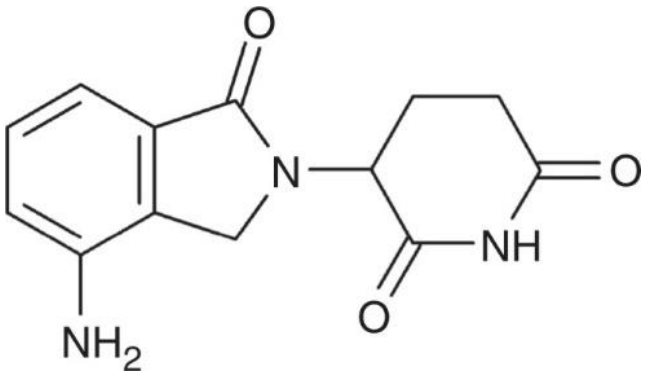

Figure 1. 12 Chemical structure of lenalidomide.

Image from Saxema et al., INDO American Journal of Pharmaceutical Research, 2017 [177].

1.4.5. Histone deacetylase inhibitors

DNA methylation and histone modifications are the primary epigenetic changes that can drive oncogenesis in cells. These epigenetic modifications are post-translational adaptations which are thought to alter gene expression whilst not having an impact on the genetic sequence. Acetylation is generally associated with elevated transcription, while deacetylated histones are often associated with gene repression and this acetylation/deacetylation is controlled by histone acetyltransferases and histone deacetylases [178, 179]. Studies by Choudhary *et al.* have shown that HDACs target not

only histones but also target non-histone proteins; therefore, HDAC inhibitors have emerged as a potential treatment approach for MM as they can hyperacetylate MM-relevant proteins including p53, STAT3 and the NFκB subunit RelA [180]. Subsequently, two HDACIs, panobinostat and vorinostat, have been approved for use in MM [181]. These HDACIs inhibit MM cell proliferation and survival by numerous mechanisms. Non-specific HDACIs induce cell cycle arrest through the upregulation of cell cycle proteins such as p53 and p21. Apoptotic and non-apoptotic cell death mechanisms can also be induced by HDACIs. Apoptosis has been shown to be induced through intrinsic and extrinsic pathways by upregulating pro-apoptotic proteins, like phorbol-12-myristate-13-acetate-induced protein 1 (Noxa) and downregulating anti-apoptotic Bcl-2 family members, like Mcl-1 and Bcl-2 [182], whilst also upregulating death receptor expression making the MM cells more susceptible to TNF-related apoptosis inducing ligand (TRAIL)-induced killing. Vorinostat has also been shown to suppress insulin growth factor-1 signalling which is vital for MM cell growth and survival [183, 184].

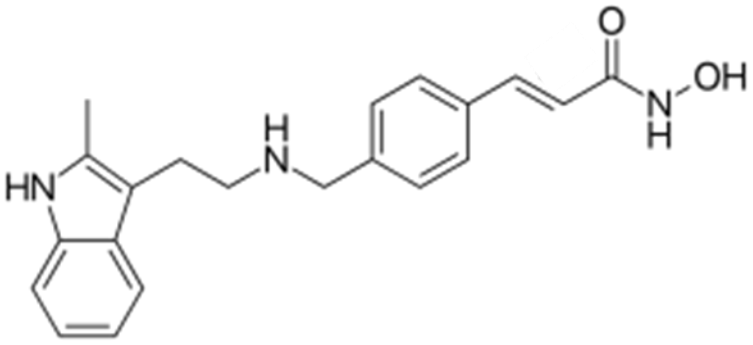

Figure 1. 13 Structure of panobinostat.

Chemical structure of the histone deacetylase inhibitor panobinostat. Image from, PubChem, 2020 [185].

1.4.6. Monoclonal antibodies

Two mAbs have recently been approved for use in relapsed MM, elotuzumab and daratumumab [186]. Daratumumab is a monoclonal IgG-k antibody which binds to the glycoprotein, CD38, on the surface of the myeloma cells. The main anti-myeloma activity of daratumumab is ADCC via NK cells and complement-dependent cytotoxicity (CDC); however, daratumumab has been shown to induce apoptosis directly, suggesting an alternative mechanism of action is the induction of apoptosis via Fc receptor (FcR)-mediated crosslinking. Cell death through antibody-dependent cellular phagocytosis (ADCP), which is mediated by macrophages, is also thought to be induced by daratuzumab [186, 187]. The glycoprotein CD38 has both cyclase and hydrolase enzymatic activity. Daratuzumab has been shown to inhibit the cyclase activity of CD38 *in vitro* and to stimulate the activity of CD38 to hydrolyse cyclic ADP-ribose [188]. Similarly, elotuzumab induces cell death in MM cells through multiple mechanisms. Elotuzumab binds to signalling lymphocytic activation molecule F7 (SLAMF7) on malignant MM cells. The primary action of the mAb is thought to be the induction of ADCC, via formation of a complex with CD16 and activation of the adaptor protein, Ewing's sarcoma-associated transcript 2 (EAT-2), on the surface of NK cells [187].

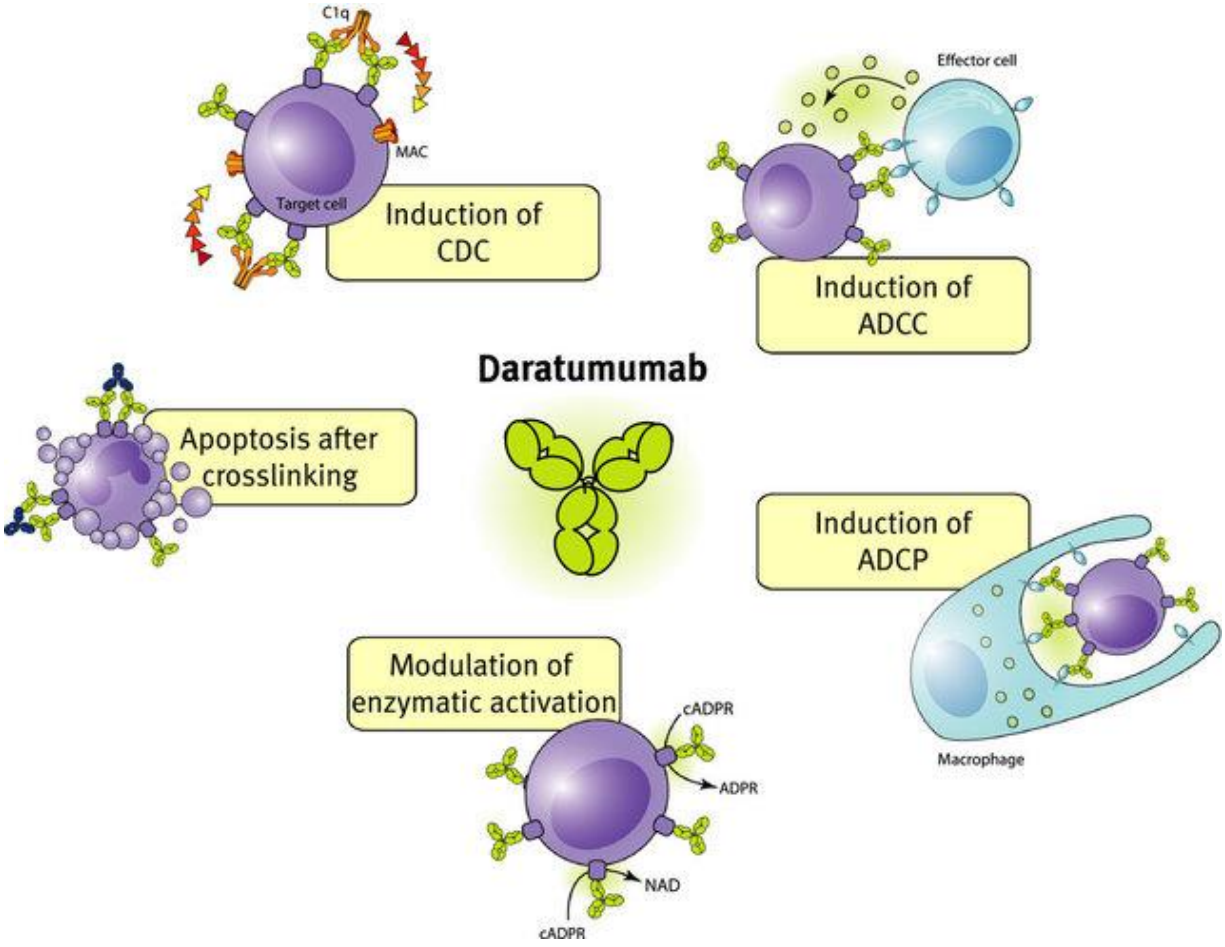

Figure 1. 14 Mechanism of action of daratumumab.

The main anti-myeloma activity of daratumumab is antibody dependent cellular cytotoxicity and complement dependent cytotoxicity however, daratumumab has been shown to induce apoptosis suggesting another mechanism of action is the induction of apoptosis via FcR-mediated crosslinking. Cell death through antibody dependent cellular phagocytosis which is mediated by macrophages is also thought to be induced by daratuzumab. Daratuzumab has also been shown to have some enzymatic activity. Image from van de Donk et al., Immunol Rev, 2016 [188].

1.5. Multidrug resistance

Despite advances in the understanding of MM and the development of novel treatment strategies MM remains a generally incurable disease. A hallmark of myeloma is its ability to evolve drug resistance phenotypes throughout the course of treatment. Patients who may initially respond well to a certain treatment may often become resistant to the drug at a later stage. This is a feature that is common not only in MM but also in other haematological cancers and in solid malignancies such as breast, gastrointestinal tract and lung cancers. The exact mechanism by which cancer cells develop drug resistance is often unknown but multiple mechanisms are suggested, such as drugs being prevented from entering the cell or pumped out before exerting their effects, a mutation which alters the drug target, senescence or DNA repair (Reviewed in [189]).

Multidrug resistance in MM is thought to be initiated through multiple mechanisms. Conventional MM chemotherapy, such as vincristine and doxorubicin, induces the expression of multidrug resistance genes and p-glycoprotein in haematological malignancies which leads to resistance in myeloma cells [190]. MicroRNAs (miRNA) have also been implicated in myeloma drug resistance by modulating proteins, such as drug transporter system related proteins and cell cycle proteins as well as modulating apoptotic signalling and autophagy [191]. For example, Roccaro *et al.* demonstrated that cell cycle regulating *miR-15* and *-16* are decreased in myeloma patients. These miRNAs inhibit the expression of cyclin D1 and other cell cycle proteins inducing G1 arrest and therefore, maybe a mechanism of resistance in MM cells [192]. Clonal evolution is another mechanism by which myeloma cells evade chemotherapeutic cell death. During treatment patients may acquire new translocations which confer resistance against previously effective drugs [193].

The proteasome inhibitor bortezomib has become routinely used in myeloma treatment regimens since its approval in the early 2000s; however, many patients are intrinsically resistant or subsequently develop resistance following treatment [194]. The exact cause of this resistance in debated. It is suggested that a mutation in the β5-subunit of the proteasome may be involved in resistance as this is targeted by bortezomib. Derangement

of stress response, survival and anti-apoptotic pathways have been indicated to be involved in bortezomib resistance too [195]. One 2017 study by Zaal *et al*. suggests that bortezomib resistance in MM may be associated with increased serine synthesis. Resistant cells demonstrated higher activity of both the pentose phosphate pathway and the serine synthesis pathway. This led to increased antioxidant activity in these cells. Interestingly, starving the bortezomib resistant cells of serine desensitised the myeloma cells to bortezomib [196].

The heterogeneous nature of MM means that treating the malignancy with one individual drug is highly unlikely. However, developing drugs which can overcome critical myeloma survival mechanisms and BMM induced resistance are highly sought-after [36]. As previously discussed, the BMM-MM cell relationship is a powerful player in MM cell survival through upregulation of key oncogenic signalling pathways and anti-apoptotic proteins.

1.6. Cell death and cancer

The ability of cancer cells to evade cell death is one of the hallmarks of cancer. Typically, most chemotherapies induce cell death via the controlled cell suicide mechanism known as apoptosis. However, other cell death mechanisms in the context of cancer cell death, such as autophagy and necroptosis are becoming more widely explored as possible treatment approaches for MM [197].

1.6.1. Apoptosis

Inherent or developed resistance to apoptosis is considered one of the hallmarks of cancer [198]. Apoptosis is an evolutionary conserved, highly regulated form of cell death and is a key mechanism involved in maintaining cellular homeostasis [199]. It is defined by its morphological features including cell shrinkage, cell rounding, plasma membrane blebbing, fragmentation of the nucleus, retraction of pseudopods and phagocytic recognition [200]. Activation of apoptotic signalling pathways can be initiated in cancer cells through both the intrinsic and extrinsic pathways and usually culminates in the triggering of a caspase cascade. Current cancer therapies such as chemotherapy, immunotherapy and radiation

can induce apoptosis through both pathways which will be discussed in further detail [201].

1.6.2. Caspases

Caspases are a family of cytosolic cysteine proteases which cleave intracellular substrates at the C-terminal side of aspartic acid residues [202]. They are composed of 3 domains: a C-terminal small subunit (p10), a large subunit (p20) and an N-terminal pro-domain. The mammalian caspases can be broadly divided into two groups: the inflammatory or apoptotic caspases. The inflammatory caspases consist of caspases 1, 4, 5, 11 and 12 whilst the apoptotic caspases consist of 2, 3, 6, 7, 8, 9 and 10. Apoptotic caspases play a vital role in caspase cascades involved in cell death which are activated by stimuli from both the intrinsic and extrinsic pathways of apoptosis. Initially they are found as inactive zymogens, in the pro-enzyme form (pro-form). Activation, or maturation, of caspases involves cleavage of the N-terminal pro-domain, causing the caspase to mature into an active enzyme. The mature caspase then dimerises with other monomers in a head-to-tail fashion. Caspase activation results from cleavage of the linker region between the small and large subunits of the caspase. Apoptotic caspases are further subdivided into two groups: initiator or effector caspases. Initiator caspases, such as caspase 8 and caspase 9 cleave downstream effector caspases 3, 6 and 7 initiating the caspase cascade associated with apoptotic cell death. Effector caspases, are activated by cleavage of the aspartate-X sites between the small and large subunits and between the pro-domain and large subunit by initiator caspases [202, 203]. Once the effector caspases are activated, they cleave cellular substrates which in turn leads to cell death.

1.6.3. Extrinsic pathway

Extrinsic apoptosis involves the binding of extracellular ligands belonging to the tumour necrosis factor (TNF) superfamily to “death receptors” also known as the TNF receptor superfamily. These structurally similar endogenous ligands include first apoptosis signal (FAS) ligand, TNF-α and TRAIL. The sequence starts when ligands bind to various death

receptors on the cell surface such as TNF-α receptor 1 (TNFR1) and FAS (Figure 1.15). This results in death receptor aggregation and the recruitment of signalling molecules to the death receptor's intracellular domain followed by a series of events leading to apoptotic cell death [204]. The two best characterised pathways are FAS/FASL and TNF-α/TNFR1. Upon ligation of FAS/FASL the adaptor protein Fas-associated protein with death domain (FADD) is recruited to the death effector domain of FADD and goes on to recruit pro-caspase 8, which becomes activate caspase 8, initiating the caspase cascade. The death inducing signalling complex is a multiprotein signalling complex formed from recruited signalling proteins and from here the caspase cascade commences. The initiator caspase, caspase 8 cleaves pro-caspase 3 to active caspase 3 and apoptosis is executed [204]. Alternatively, caspase 8 can lead to the engagement of the intrinsic pathway by the proteolytic cleavage of BH3 interacting-domain death agonist (Bid) to truncated Bid (tBid). tBid migrates to the outer mitochondrial membrane (OMM) initiating mitochondrial outer membrane permeabilisation (MOMP), as discussed further below [205].

1.6.4. Intrinsic pathway

The intrinsic apoptotic pathway, or mitochondrial pathway, is characterised by permeabilisation of the OMM by pro-apoptotic members of the Bcl-2 family [206]. The initiation of intrinsic apoptosis is activated by various non-receptor mediated stimuli which act directly on targets within the cell by producing signals which act in a positive or negative manner. These stimuli include radiation, chemotherapy and growth factor withdrawal. Once apoptosis is triggered, Bcl-2-associated X protein (Bax) and Bcl-2 antagonist/killer (Bak), two pro-apoptotic Bcl-2 family members oligomerise on the OMM initiating MOMP. This leads to the release of pro-apoptotic factors from the mitochondria, such as cytochrome C and second mitochondria-derived activator of caspase/direct inhibitor of apoptosis-binding protein with low pI (SMAC/DIABLO), into the cytoplasm stimulating cell death (Figure 1.15.). Cytochrome C interacts with apoptotic protease-activating factor 1 (Apaf-1) causing a conformational change in caspase recruitment domains (CARD) of initiator caspases forming a multimeric complex known as the

apoptosome with cytochrome C and Apaf-1. Pro-caspase 9 is recruited to the CARD motif within the apoptosome and it is cleaved into active caspase 9 which initiates the caspase cascade, activating effector caspases 3 and 7. In turn, these effector caspases cleave cellular proteins such as poly ADP ribose polymerase (PARP), a DNA repair enzyme, resulting in cell death (Reviewed in [207, 208]).

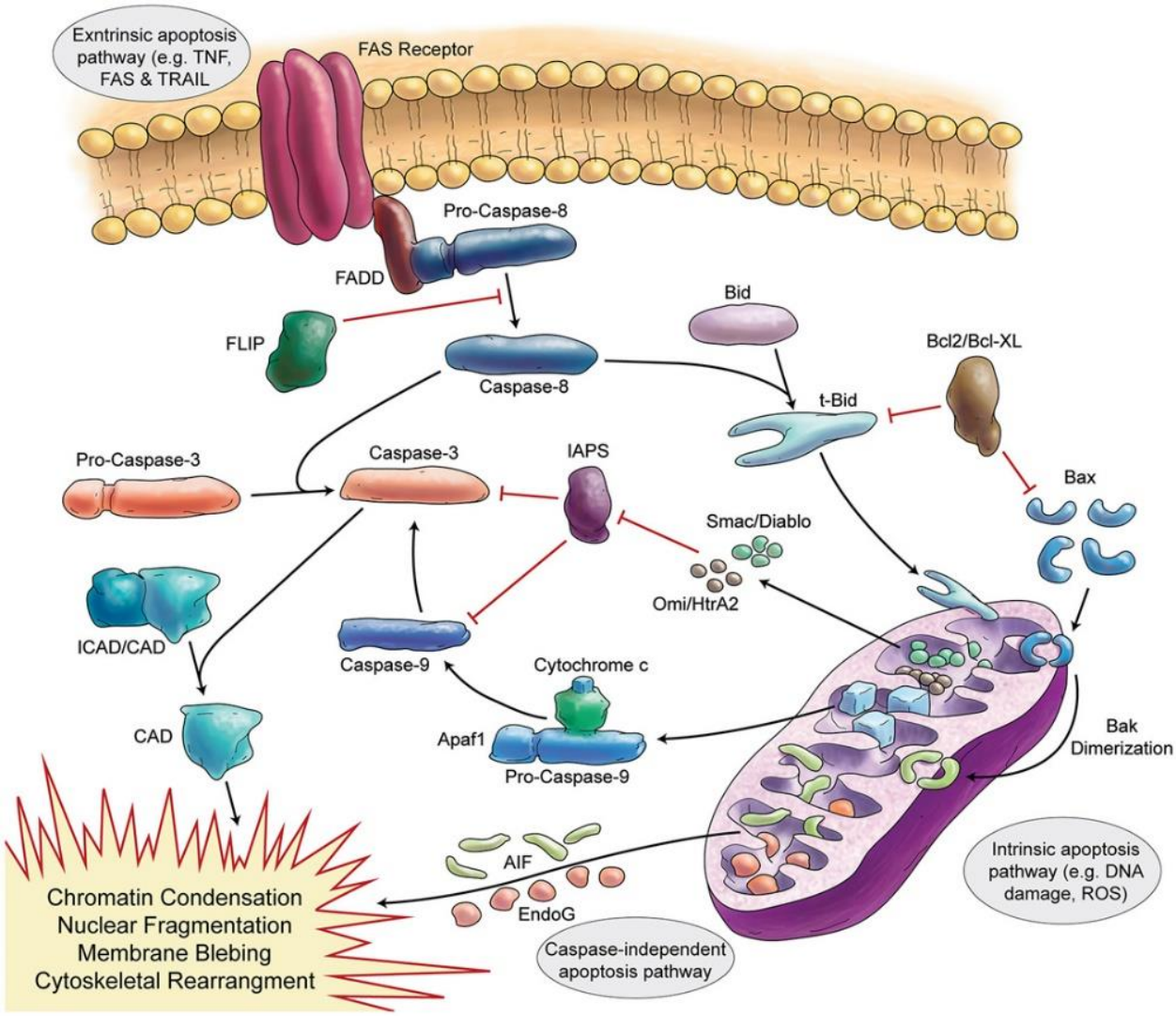

Figure 1. 15 Apoptotic signalling pathways.

Caspase dependent apoptotic cell death occurs through two main pathways: the intrinsic and extrinsic pathways. The intrinsic pathway is activated by stimuli such as chemotherapy, radiation and growth factor withdrawal. The extracellular pathway is activated by extracellular ligands binding to so-called death receptors on the cell surface thus initiating cell death. Caspase-independent pathways also exist. Image from Marzban et al., Front Cell Neurosci, 2014 [209].

1.6.5. Bcl-2 family of proteins

The Bcl-2 family are evolutionarily conserved proteins which control intrinsic apoptosis by controlling MOMP. They are divided into two categories based on their ability to induce or

inhibit apoptosis. The balance between pro-apoptotic and anti-apoptotic Bcl-2 family members determines whether a cell lives or dies. These proteins all share Bcl-2 homology (BH) domains but are subdivided into three groups of structurally related proteins: the pro-apoptotic BH3-only proteins, the anti-apoptotic Bcl-2-like proteins and finally the multi-BH3 domain pro-apoptotic Bax/Bak proteins (Figure 1.16). Bcl-2 was first identified from the break point region of a recurrent chromosomal translocation in human follicular lymphoma, normally present on chromosome 18; the Bcl-2 gene is translocated next to an IgH heavy chain locus on chromosome 14 [210, 211].

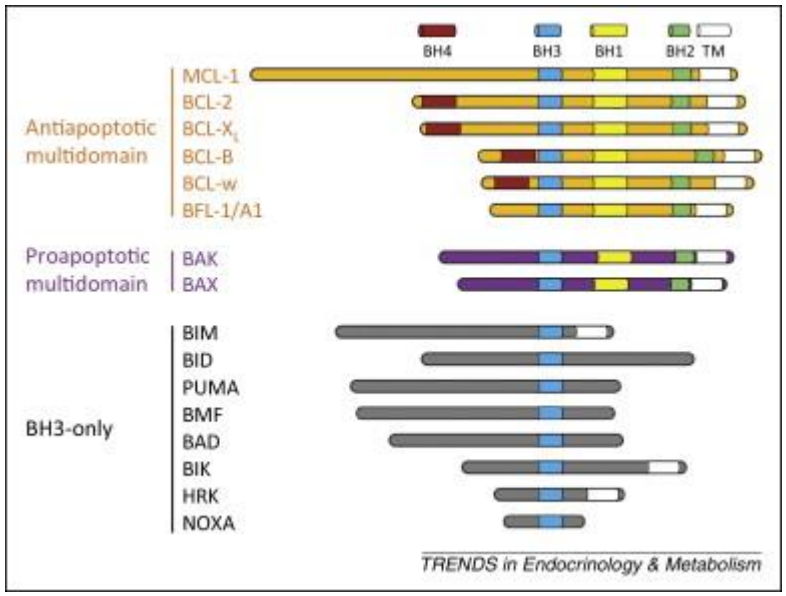

Figure 1. 16 Structure and functional classification of Bcl-2 proteins.

Bcl-2 proteins all share Bcl-2 homology (BH) domains but are subdivided into three groups of structurally related proteins: the pro-apoptotic BH3-only proteins, the anti-apoptotic Bcl-2-like proteins and finally the multi-BH3 domain pro-apoptotic Bax/Bak proteins. Image from Gimenez-Cassina et al., Trends in Endocrinology & Metabolism, 2016 [210].

1.6.5.1. Anti-apoptotic Bcl-2 family proteins

Anti-apoptotic Bcl-2 family members have a dual role in cancer, in addition to their inhibitor effects on the intrinsic apoptotic pathway Bcl-2 proteins have an inhibitory effect

on cell cycle progression. They contain four BH domains and a C-terminal transmembrane domain which allows them to be tethered to the outer mitochondrial membrane and possibly to other organelles. These proteins include, Bcl-2, Mcl-1, Bcl-xL, Bcl-2-like protein 2 (Bcl2L2 or Bcl-W) and Bcl-2-related protein A1 (BLFL-1), and BCL2L10 (Bcl-B).

1.6.5.1.1. Bcl-2

Bcl-2 was the first member of the Bcl-2 family to be identified and is often referred to as the gatekeeper of the apoptotic response. Unlike Mcl-1 which has multiple cellular locations, Bcl-2 is localised to the cytoplasmic face of the OMM, the ER and the nuclear envelope. Bcl-2 elicits its anti-apoptotic function by preventing the oligomerisation of Bid to Bax and thereby preventing the formation of a pore in the OMM and subsequent release of cytochrome C, caspase activation and ultimately cell death [212]. BH3 only proteins such as p53 upregulated modulator of apoptosis (Puma) and Noxa, have been shown to bind to Bcl-2 preventing it from binding to Bax or Bak (Reviewed in [213, 214]). Bcl-2 is highly expressed in multiple tissue types but it is of particular interest in B cell malignancies as it is highly expressed in pro-B cells and mature B cells. However, as previously described, Bcl-2 is not considered to play a pivotal role in MM as loss of Bcl-2 still allows for tumour cell survival due to Mcl-1 induced resistance [215]. BH3 mimetics such as ABT-737 and ABT-263, selectively inhibit Bcl-2, however since MM cells often overexpress Mcl-1, drug resistance often occurs [216, 217]. Venetoclax (ABT-199) is a selective Bcl-2 inhibitor which is approved for use in chronic lymphocytic leukaemia (CLL) and is currently undergoing clinical trials for use in MM patients [218]. MM cells with t(11;14) translocations express relatively higher levels of Bcl-2 compared to Bcl-xL and Mcl-1 indicating that it may be a useful treatment for those with the cytogenetic abnormality, moreover, venetoclax is well tolerated in most MM patients [219].

1.6.5.1.2. Mcl-1

Mcl-1 was the second member of the Bcl-2 family to be discovered and is essential for the survival of most cancer cells [220]. Landscape studies by Beroukhim *et al*. demonstrated

amplifications in MCL1 genes in 10.9% of cancers across multiple tissue types, highlighting its critical role in cell survival [221]. Unlike other Bcl-2 family members Mcl-1 has distinguishing features including its ability to oppose a wide variety of pro-apoptotic stimuli, a much larger N-terminus and it contains two proline/glutamic acid/serine/threonine (PEST) domains. PEST domains are a key feature of rapidly degrading proteins. Under normal physiological conditions Mcl-1 has a short half-life and its expression is tightly regulated at multiple levels including transcriptional, post-transcriptional and translational [222]. It is likely that PEST sequences play a role in the regulation of Mcl-1. These regions are subject to ubiquitination, phosphorylation and caspase cleavage which modulate the function of Mcl-1 [222-224]. Various extracellular stimuli, such as GFs, like VEGF and cytokines such as IL-6 and IL-3, activate pathways which modify its expression [222]. Signalling pathways which are triggered by these proteins alone or in combination affect downstream Mcl-1 expression. For example, as described previously, the JAK/STAT, p38/MAPK, MEK/ERK and the PI3K/AKT pathways can lead to an upregulation in Mcl-1 expression. IL-6 from the BMM triggers Mcl-1 upregulation in MM cells through the JAK/STAT3 pathway [29].

Mcl-1 blocks apoptosis by interacting with and sequestering pro-apoptotic Bcl-2 family members. Disruption of binding with Bax, Bak or Bim can lead to apoptosis as pro-apoptotic Bak and Bax dimerise to form pores in the OMM causing release of cytochrome C from the mitochondria which leads to activation of the intrinsic apoptotic pathway. Mcl-1 is thought to play an important role in tumorigenesis in MM. The frequency of abnormalities involving chromosome 1q21 in MM is quite high and the *MCL1* gene is thought to map to this region [225]. Despite most plasma cells expressing Bcl-2, Bcl-xL and Mcl-1, Mcl-1 has been identified as being critical for plasma cells, and therefore, MM cell survival [215, 226, 227]. Mice who were treated with the Bcl-2/Bcl-xL inhibitor ABT-737 saw a massive decrease in B cells however there was a minimal effect on non-malignant plasma cells. Moreover, inhibition of Mcl-1 caused a dramatic decrease in MM cells present in the bone marrow [228]. Furthermore, antisense oligonucleotide studies by Zhang *et al.* demonstrated that Mcl-1 plays a key role in MM survival as rapid downregulation of Mcl-1 protein levels coincided with induction of apoptosis [215].

Similarly, Gong *et al*. demonstrated that only a minority of myeloma cell lines are killed with the selective inhibition of Bcl-2 and Bcl-xL, thus demonstrating a pivotal role for Mcl-1 in MM cell survival [229]. Interestingly, IL-6-upregulated Mcl-1 in myeloma is thought to be mediated through the JAK/STAT pathway rather than the RAS/MAPK pathway indicating that targeting JAK/STAT in myeloma may be a more favourable therapeutic strategy in MM [230].

1.6.5.1.3. Bcl-xL

Bcl-xL was the third member of the anti-apoptotic Bcl-2 family of proteins to be discovered. It is expressed on the OMM and similarly to Bcl-2, prevents apoptosis through heterodimerisation with Bak and Bax preventing formation of OMM pores. Similar to Mcl-1, Bcl-xL lies downstream of STAT3 signalling and is thought to play a role in cell proliferation and survival of MM cells. Bcl-xL has four BH domains with the fourth domain thought to be essential for its anti-apoptotic effects. Bcl-xL is cleaved by caspases during cell death and no longer contains the anti-apoptotic BH4 domain. Some studies suggest that the cleaved Bcl-xs fragment may exert pro-apoptotic effects, however, further studies to confirm this have yet to be undertaken [206, 231].

1.6.6. Reactive oxygen species

ROS is the collective term for unstable, reactive oxygen derivatives which are the cellular by-products of normal metabolic functions. These by-products often act as second messengers in cell signalling and immune responses forming essential parts of many biological functions. There are two main classifications of these mediators; the radicals, which include superoxide, hydroxyl radical and nitric oxide (NO) and non-radicals, which include hydrogen peroxide and peroxynitrite [232, 233].

In cancer, ROS is often seen as a double-edged sword, manifesting a dual role as both a cancer promoting and suppressing agent. Cancer cells show increased levels of ROS production compared to non-malignant cells. In cancer, ROS levels are increased due to the external environment and internal cellular processes. It is believed that during cancer

development this leads to a significant survival advantage as it has been shown to enhance proliferation and invasion. ROS are an inevitable consequence of metabolism. Cancer cells require enhanced metabolism in order to meet the energy requirements of a highly proliferative cell; these cells undergo anaerobic glycolysis, producing excessive levels of lactic acid. This lactic acid is released into the environment round the cancer cell leading to acidosis. Normal cells are unable to survive in this acidic environment leading to the selection of more aggressive cancer cell clones (Reviewed in [234]). ROS is also generated following activation of a number of oncogenes known to play a role in cancer and cancer progression, such as *KRAS,* which is known to play a critical role in myeloma cell survival [115, 235, 236]. The hypoxic environment of many cancer cells lacking appropriate neovascularisation can also lead to enhanced ROS production and activation of integrins associated with cancer cell metastasis.

Conversely, many chemotherapeutic agents have been shown to induce ROS dependent cell death [232]. As aforementioned, cancer cells are under large amounts of oxidative stress due to enhanced levels of ROS production. It is hypothesised that chemotherapeutics induce cell death as they push the level of ROS over the already amplified threshold (Figure 1.17). Cancer cell ROS production is due to mitochondrial ROS production and inhibition of the normal cellular antioxidant system whereby, glucose is metabolised into pyruvate, a potent antioxidant. Of the various drugs used to treat MM, anthracyclines such as doxorubicin are thought to induce the largest amounts of ROS production, whilst alkylating agents and taxanes have been shown to generate varying levels of ROS [232]. The proteasome inhibitor bortezomib has also been shown to induce ROS production in myeloma cells via the induction of ER stress [237]. The excessive production of Igs and cytokines by many MM cells mean that they are heavily reliant on the ability of the ER to tolerate stress. Severely misfolded proteins are transported from the ER to the proteasome to be degraded, however, inhibition of the proteasome by bortezomib leads to an accumulation of proteins in the ER and enhanced stress [162]. This also leads to overproduction of ROS in the ER. ROS induced cell death is thought to be one of the main mechanisms by which bortezomib induces cell death in myeloma cells [238].

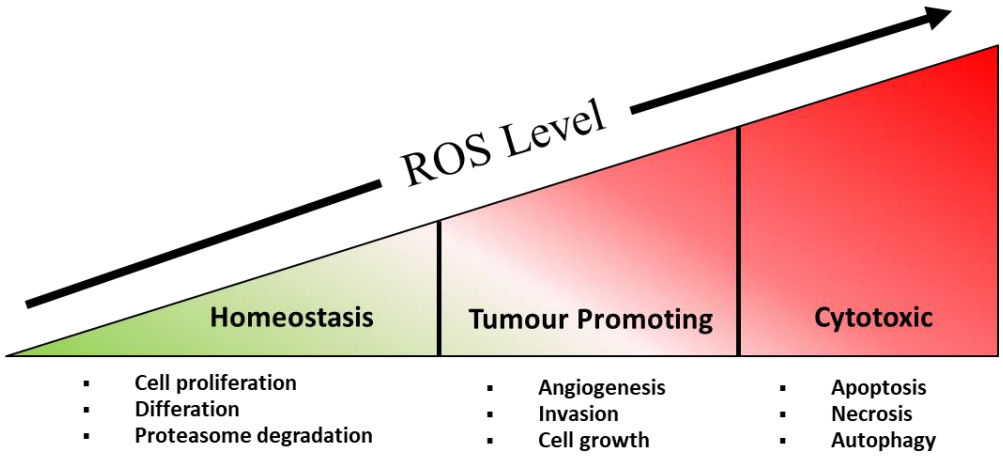

Figure 1. 17 The balance of ROS in cancer.

In cancer, ROS is often seen as a double-edged sword, manifesting a dual role as both a cancer promoting and suppressing agent. Cancer cells show increased levels of ROS production compared to non-malignant cells. In cancer, ROS levels are increased due to the external environment and internal cellular processes. It is believed that during cancer development this leads to a significant survival advantage as it has been shown to enhance proliferation and invasion. Some chemotherapeutics are thought to induce ROS and push cancer cells over the threshold towards cell death. Adapted from Yang et al., J Exp Clin Cancer Res, 2018 [232].

1.7. Novel treatment strategies

The development of new drugs for MM over the past decade has vastly improved patient survival rates. Despite this, MM remains a largely incurable disease supporting the quest for novel drugs and treatment strategies. The introduction of T cell immunotherapies has improved the lives of patients with lymphomas; however, this success has not been seen in MM patients. Most mAbs have shown little to no benefit as single agents or in combination with standard treatments in early trials with the exception of daratumumab and elotuzumab when in combination with IMiDs and proteasome inhibitors which have greatly improved patient outcomes. Immune checkpoint inhibitors such as the PD-1 inhibitor nivolumab, has shown disappointing results as a single agent with only 4% of patients responding to treatment (Reviewed in [239]). One of the most promising results in the field of novel MM treatment strategies is anti-B-cell maturation antigen (BCMA) chimeric antigen receptor (CAR) T-cell therapy which has been shown to be highly efficacious and safe in MM patients where other treatments options have been exhausted. Despite these impressive results, the majority of patients relapse [240]. XPOVIO, also known as selinexor, is a first-in-class, oral small molecule inhibitor of exportin-1 that is approved for the treatment of relapsed and refractory MM in combination with dexamethasone [241]. Exportin-1 is a major exporter of tumour suppressor proteins such as p53, growth regulators and oncoprotein mRNAs. Inhibition of exportin-1 results in accumulation of tumour suppressors within the cell resulting in apoptosis. XPOVIO was demonstrated to have minimal effects on non-malignant cells and; therefore, it's efficacy in other haematological malignancies is now being examined (Reviewed in [241]).

As previously mentioned, since up to 50% of newly diagnosed MM patients present with mutations in *RAS,* targeting the MAPK pathway may be a promising approach. Moreover, since IL-6, a key survival cytokine in MM, activates both the RAS/RAF/MEK/ERK and JAK/STAT3 pathways; targeting upstream signalling molecules may be a viable treatment option. Nevertheless, overwhelming evidence indicates that MM is a malignancy with huge clonal heterogeneity most likely requiring combination treatments to combat the disease.

1.7.1. Inhibiting STAT3

To date, there are no STAT3 inhibitors approved for the treatment of MM. However, there are numerous preclinical studies that demonstrate the potent anti-myeloma effects that occur when targeting this transcription factor. Strategies for targeting STAT3 signalling include inhibition of upstream events such as IL-6 and ligand binding, receptor activation and kinase phosphorylation, STAT3 (SH-2-SH-2) dimerisation, STAT3 transcription, localisation of STAT3 to the nucleus and DNA binding (Reviewed in [85]).

1.7.1.1. Targeting the IL-6 receptors

Constitutive STAT3 signalling is rarely caused by a mutation directly affecting STAT3, rather, STAT3 phosphorylation is usually mediated through activation of upstream signalling molecules such as RTKs (e.g. epidermal growth factor receptor) or non-RTKs (e.g. SRC and JAK). Therefore, targeting upstream signalling molecules can be an effective means of inhibiting STAT3 activation [242]. For example, IL-6 can be inhibited with siltuximab, a chimeric mouse-human antibody. Siltuximab has been extensively studied as an IL-6 targeting agent and preclinical studies using siltuximab have shown enhanced anti-myeloma activity when in combination with melphalan in *in vitro* models. However, these promising preclinical results did not improve overall progression-free survival rates in clinical trials when in combination with bortezomib, melphalan and prednisone [243, 244]. Of note, a clinical trial using siltuximab for high-risk SMM suggested that treatment may delay the progression of SMM [245]. Tocilizumab is a mAb which competitively inhibits the binding of IL-6 to the IL-6R blocking both sIL-6R and IL-6Rα [246]. To date, no preclinical studies have been carried out to determine the efficacy of tocilizumab as an anti-myeloma agent. However, a phase I clinical trial has shown efficacy in combination with carboplatin/doxorubicin in the treatment of ovarian cancer [247]. There are currently trials examining the efficacy of tocilizumab for the treatment of breast cancer (NCT03135171) and melanoma (NCT03999749) amongst others. Targeting gp130 may also be a favourable anti-myeloma target as MM cells can undergo both classical and *trans*-signalling as described previously. Atovaquone is an anti-microbial agent which has recently been

shown to inhibit STAT3 signalling in MM cells *in vitro* in part via rapid downregulation of gp130 on the cell surface [248].

1.7.1.2. Kinase inhibitors for the treatment of multiple myeloma

Inhibiting the kinase activity of upstream kinases such as the JAK and SRC kinases is another possible mechanism for inhibiting STAT3 activation. Small molecule protein kinase inhibitors have recently become an area of interest with modulating kinase function becoming an important goal in modern drug discovery due to the important functions that the kinase super-family play in disease [249]. To date, 52 kinase inhibitors have been approved by the FDA; eleven target non-RTKs, twenty-eight block RTKs, cobimetinib and trametinib are two dual specificity protein kinase inhibitor and eleven target serine/threonine protein kinases. Of the 52 kinase inhibitors, 46 have been approved for the treatment of cancers such as sorafenib for thyroid cancer and vemurafenib for $BRAF^{V600E}$ positive melanoma. In 2019 alone, four new kinase inhibitors were approved targeting: tropomyosin receptor kinase A, fibroblast growth factor receptor 1, colony-stimulating factor 1 receptor, and JAK2. Currently there are no kinase inhibitors approved for use in MM (Reviewed in [250]). Given that multiple kinases are involved in the malignancy, kinase inhibitors offer a promising treatment option. Possible targets in MM include RTKs and non-RTKs, cell cycle kinases, the PI3K/AKT pathway, the MAPK pathway and the JAK/STAT pathway. Numerous preclinical studies have demonstrated the effectiveness of JAK inhibitors for the treatment of MM; however, there have been limited clinical trials carried out with JAK inhibitors which have already been approved for the treatment of other conditions such as the recently approved JAK2 inhibitor, fedratinib, for the treatment of myelofibrosis [251].

1.7.1.2.1. Protein kinases

The human kinome is comprised of 540 kinases which were initially mapped by Manning *et al*. in 2002 [252]. Many TKs are primarily components of the cytosolic domains of plasma membrane receptors, while serine/threonine kinases are often found dispersed

throughout the cell [253]. Many kinases have been implicated in cancer development and other diseases such as rheumatoid arthritis and aberrant alteration of signal transduction pathways is one of the key mechanisms involved in the progression of cancer. Kinases can also target non-proteins such as PI3K and sphingosine. In MM as described previously, kinases are involved in the constitutive upregulation of many signalling pathways such as MAPK and PI3K/AKT pathways, similarly, factors produced by the tumour microenvironment can lead to activation of many pro-survival signalling pathways. Constitutively activated kinases have a transforming capacity and are, therefore, often considered oncogenic, in some cancer cases upregulation of a single signalling pathway is often enough to drive cancer cell survival. In these cases where the cancer cells have a so-called "oncogene addiction", they are much more susceptible to drugs which target that oncogene, thus, kinase inhibitors which can target these particular mutations are a promising treatment strategy [253].

1.7.1.2.2. Kinase inhibitors

Kinase inhibitors fall into four main categories: type I, type II, type III (allosteric inhibitors) and type IV (allosteric inhibitors) (see Figure 1.18). Type I inhibitors such as silmitasertib are ATP competitive inhibitors which recognise the active conformation of the kinase and occupy the ATP binding site. Type II inhibitors such as imatinib are ATP competitive inhibitors that recognise the inactive conformation of the kinase and occupy a hydrophobic binding site directly adjacent to the ATP binding site. Type III bind to an adjacent pocket to the ATP binding site and type IV allosteric inhibitors, such as trametinib, bind to a remote binding site away from the ATP binding site and modulate kinase activity; these kinase inhibitors are thought to exert the highest selectivity due to their ability to bind to sites that are unique to that kinase. Finally, covalent inhibitors such as ibrutinib, form an irreversible covalent bond with the kinase active site by, most frequently, reacting with a nucleophilic cysteine residue; these inhibitors are sought after due to their high binding ability and selectivity (Reviewed in [254]).

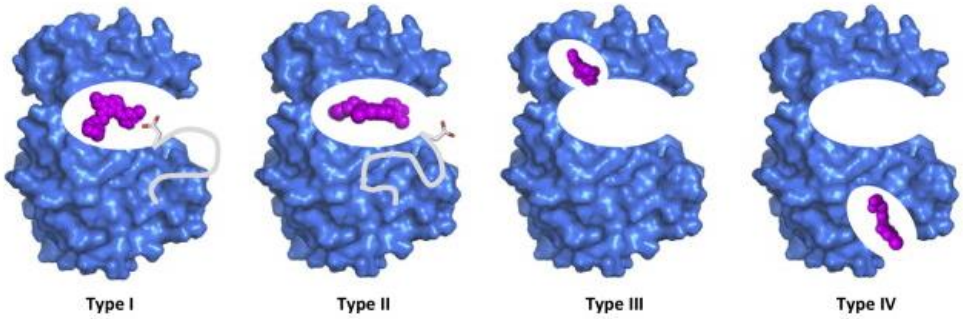

Figure 1. 18 Examples of various classes (Type I to IV) of kinase inhibitors.

Type I inhibitors are ATP competitive and recognise the active confirmation of the kinase. Type II inhibitors recognise the inactive confirmation of the kinase. Type III inhibitors occupy an allosteric site adjacent to the ATP binding site. Type IV inhibitors bind to the kinase outside of the ATP binding site. Allosteric inhibitors, types III and IV, are thought to be the most selective. From Wu et al., Trends in Pharmacological Sciences, 2015 [255].

1.7.1.3. Targeting kinases upstream of STAT3

Ruxolitinib is a JAK1/2 inhibitor which has shown efficacy against MM. Preclinical studies have shown that ruxolitinib induced limited cell death in MM cell lines as a single agent but synergised with the proteasome inhibitor bortezomib. Interestingly, the combination of ruxolitinib, bortezomib and lenalidomide induced similar cell death as the dexamethasone, bortezomib and lenalidomide combination, which is a regimen currently used in the clinic [76]. A phase I clinical trial has also shown that ruxolitinib in combination with lenalidomide and steroids can overcome refractoriness in relapsed and refractory MM patients (NCT03110822). Tofactinib is a pan JAK inhibitor with lower affinity for JAK2. Preclinical studies have demonstrated that tofacitinib can synergise with venetoclax to overcome BMM-induced drug resistance in *in vitro* models of MM highlighting the essential role of the JAKs in BMM-induced drug resistance [256]. NS-018 is an ATP

competitive inhibitor of JAK2 and SRC, both of which lie upstream of STAT3. Preclinical studies have shown that NS-018 reduced MM cell viability in cell lines even in the presence of IL-6 and reduced osteolysis in an *in vivo* mouse model suggesting the important role for both kinases in IL-6 induced drug resistance and the pathology of MM [257]. Similarly, a study by Heusschen *et al.* demonstrated that inhibition of SRC by saracatinib limited the development of osteolysis in the 5TGM.1 and 5T2MM MM mouse models [258].

1.8. Design and synthesis of novel tyrosine kinase inhibitors

The Rozas group in the School of Chemistry at Trinity College Dublin in collaboration with the Zisterer group have rationally designed and synthesised numerous novel multi-tyrosine kinase inhibitors as potential anti-cancer agents. Previously, the group identified ED73a, a 3,4'-bis-guanidinium di-phenyl compound, as a protein kinase inhibitor capable of inhibiting the MAPK/ERK pathway by binding to, and thus inhibiting, BRAF [259]. ED73a shows structural similarities to the kinase inhibitor sorafenib (See Figure 1.19) suggesting that it may also act through similar mechanisms. Sorafenib (trade name Nexavar) is a multi-kinase inhibitor approved for use in hepatocellular carcinoma, renal cell carcinoma and radioactive iodine resistant advanced thyroid carcinoma [260-262]. Sorafenib has been shown to have multiple targets including VEGF, BRAF, PDGF and STAT3 [263, 264] and is thought to act through a type II mechanism. Early studies have shown that sorafenib has potential anti-MM activity [119, 120].

It was suggested, however, that ED73a works through a type III allosteric mechanism and as a consequence would not have to overcome the selectivity issues of ATP competitive kinase inhibitors, possibly resulting in a greater degree of specificity and less off-target effects. ED73a exhibited cytotoxic activity in human leukaemia and colorectal cancer cell lines in the micromolar range suggesting its potential as a novel anti-cancer agent [265]. Twenty-five new derivatives were next synthesised to identify the structural motifs that determine the allosteric inhibition of the RAS/RAF/MEK/ERK pathway by ED73a. These new derivatives of ED73a were rationally designed and synthesised based on three different moieties identified in ED73a: the hydrophobic moiety, the linker and the polar

moiety. These derivatives are currently under investigation as potential anti-cancer agents. In a preliminary study VP79s, one of these promising derivatives was found to reduce the viability of a panel of human cancer cell lines including breast MCF-7, promyelocytic leukaemia HL60 and cervical HeLa cells (Viola Previtali Thesis, unpublished data). As activation of the RAS/RAF/MEK/ERK pathway contributes significantly to MM cell growth, survival, angiogenesis and drug resistance it was hypothesised in the present study that these novel compounds, and in particular VP79s, may exhibit potent anti-myeloma activity.

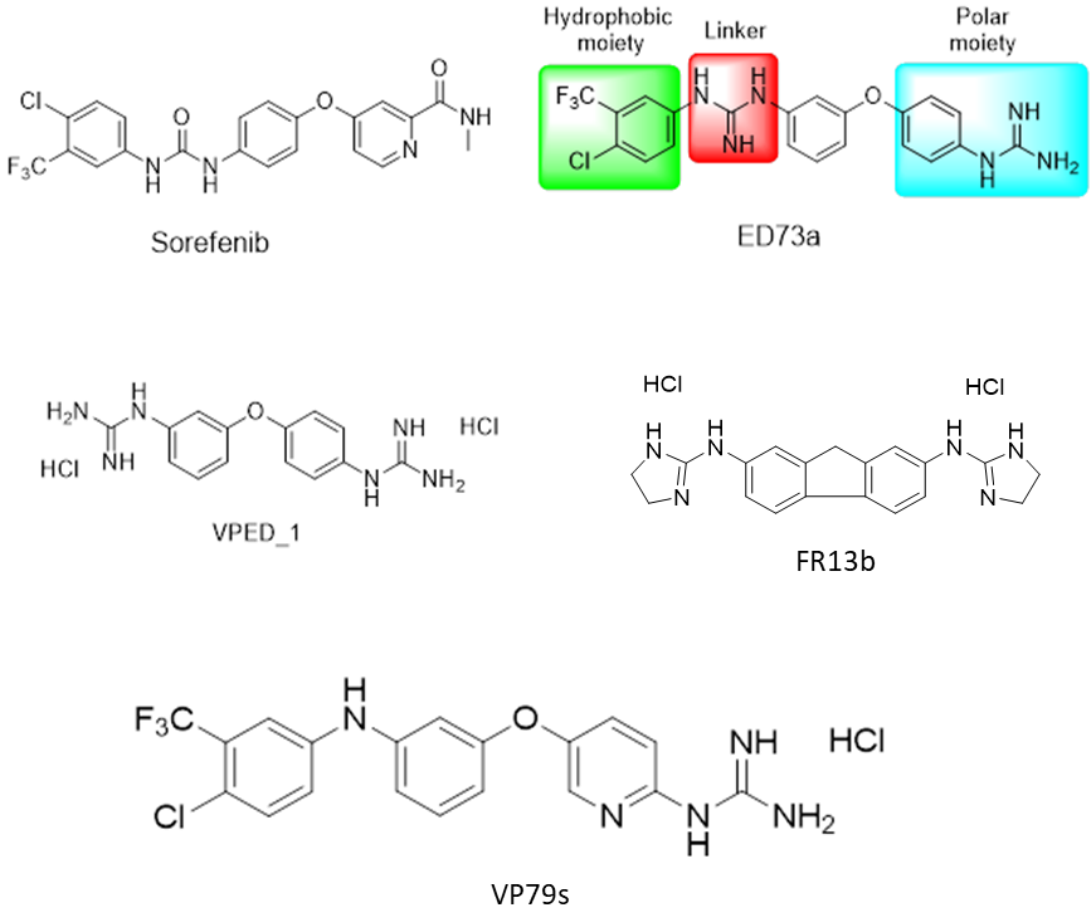

Figure 1. 19 Chemical structures of sorafenib, ED73a, VPED_1, FR13b and VP79s.

Structure of ED73a and sorafenib indicating the three moieties identified in ED73a: the hydrophobic moiety, the linker and the polar moiety. Chemical structure of VPED_1, FR13b and VP79s derivatives of ED73a. Images adapted from Diez-Cecilia, Bioorg Med Chem let, 2015 [259] and Diez-Cecilia, Eur J Med Chem, 2014 [265] and unpublished data.

1.9 Objectives

MM is a haematological malignancy that is largely incurable. Despite advances in the therapeutic options available to MM patients over the past two decades, patients almost always relapse and become refractory to treatment. Therefore, new therapeutic options and strategies are desperately needed to combat this malignancy. This project sought to evaluate the anti-myeloma effects of a series of novel guanidinium diaryl derivatives and to identify a lead compound that was capable of inducing cell death in MM cell lines, *ex vivo* patient samples and of overcoming BMM induced drug resistance.

More specifically the aims of the project were:

1. To screen a series of novel drugs (derivatives of ED73a) on the viability of two MM cell lines in order to identify a potential lead anti-myeloma compound. To determine the cytotoxic effects of that lead compound in a panel of drug susceptible and drug resistant MM cell lines and compare the effects of that lead compound with standard and emerging treatments for MM.
2. To elucidate the molecular basis of cytotoxicity by evaluating the effect of the lead compound on oncogenic signalling pathways known to play a role in the progression of MM; in particular, the RAS/RAF/MEK/ERK, NFκB, PI3K/AKT and JAK/STAT3 pathways.

   To evaluate the ability of the lead compound to overcome BMM induced drug resistance through co-culture of a representative MM cell line with the HS5 stomal cell line. To assess the synergistic effect of the lead compound in combination with a standard MM treatment (bortezomib), and finally, to evaluate the cytotoxic effects of the lead compound in healthy donor peripheral blood mononuclear cells and *ex vivo* MM patient samples.

Therefore; it is hypothesised that VP79s is eliciting its anti-myeloma activity via modulation of key signalling pathways known to play a role in the progression of MM.

Chapter 2:
Materials and methods

2.1. Materials and suppliers

100 mM DTT (qPCR)	Invitrogen
4',6-diamidino-2-phenylindole (DAPI)	Sigma-Aldrich
5,6-dichloro-2-[3-(5,6-dichloro-1,3-diethyl-1,3-dihydro-2H-benzimidazol-2-ylidene)-1-propen-1-yl] -1,3-diethyl-1H-benzimidazolium, monoiodide (JC-1)	Sigma-Aldrich
ABT-199 (Venetoclax)	Selleck Chemicals
Alamar Blue	Life Technologies
Ammonium Persulfate	Sigma-Aldrich
Annexin V-Fluorescein Isothiocyanate (FITC)	iQ Products
Anti-AKT	Cell Signaling
Anti-AKT (S473)	Cell Signaling
Anti-Alpha-Tubulin	Calbiochem
Anti-Bcl-2	Calbiochem
Anti-Bcl-xL	BD Pharminogen
Anti-Beta-Actin	Sigma-Aldrich
Anti-caspase 3	Cell Signaling
Anti-Caspase 8	Cell Signaling
Anti-Caspase 9	Cell Signaling
Anti-CD126 (PE)	Biolegend
Anti-CD130 (APC)	Biolegend
Anti-CD138 (PE)	BD Biosciences
Anti-CD19 (PE)	Miltenyi Biotec
Anti-CD3 (PerCP)	Miltenyi Biotec
Anti-CD56 (APC)	Miltenyi Biotec
Anti-Cleaved Caspase 3	Cell Signaling
Anti-Cyclin D1	Cell Signaling
Anti-GAPDH	Calbiochem
Anti-IκBα	Cell Signaling
Anti-JAK1	Sigma-Aldrich
Anti-JAK2	Cell Signaling

Anti-Mcl-1	Cell Signaling
Anti-p38	Cell Signaling
Anti-p44/42 MAPK (Erk1/2)	Cell Signaling
Anti-Phospho- Stress-activated protein kinase/Jun-amino-terminal kinase (SAPK/JNK) (Thr183/Tyr185)	Cell Signaling
Anti-Phospho-IκBα (S32)	Cell Signaling
Anti-Phospho-JAK1 (Y1022)	Sigma-Aldrich
Anti-Phospho-JAK2 (Y1007/Y1008)	Cell Signaling
Anti-Phospho-p38 (Thr180/Tyr182)	Cell Signaling
Anti-Phospho-p44/42 MAPK (Erk1/2) (Thr202/Tyr204)	Cell Signaling
Anti-Phospho-SRC (PTYR418)	Sigma-Aldrich
Anti-Phospho-STAT3 Serine (S727)	Cell Signaling
Anti-Phospho-STAT3 Serine 727 (APC)	BD Biosciences
Anti-Phospho-STAT3 Tyrosine (Y705)	Cell Signaling
Anti-Phospho-STAT3 Tyrosine 705 (PE)	BD Biosciences
Anti-SOCS-1	Cell Signaling
Anti-SRC	Sigma-Aldrich
Anti-STAT3	Cell Signaling
Anti-Stress-Activated Protein Kinase/Jun-Amino-Terminal Kinase (SAPK/JNK)	Cell Signaling
Anti-Survivin	Cell Signaling
BCA Protein Reagents A and B	Pierce
Bortezomib	Selleck Chemicals
Bromophenol Blue	Sigma-Aldrich
BSA	Sigma-Aldrich
BSA Protein Standards	Pierce
Carbonyl Cyanide-p-Trifluoromethoxyphenylhydrazone	Sigma-Aldrich
Cell Culture Plastics	Cruinn
Chloroquine	Sigma-Aldrich
Complete Ultra Inhibitor Tablets	Roche
Cryogenic Tubes	Nalgene
Deoxyribonucleotide Triphosphate (dNTPs)	Invitrogen

Dexamethasone	Sigma-Aldrich
Dichloro-Dihydro-Fluorescein Diacetate (DCFH-DA)	Sigma-Aldrich
Dimethyl Sulfoxide	Sigma-Aldrich
Dithiothreitol (DTT)	Sigma-Aldrich
Dulbecco's Modified Eagle Medium	Biosciences
ECL Detection Kit	Pierce
Ethanol	Lennox
Filter Paper	Whatman
Foetal Bovine Serum	Sigma
Glycerol	Sigma-Aldrich
Glycine	Sigma-Aldrich
Human Recombinant IL-6	Biolegend
Hydrochloric Acid	Sigma-Aldrich
Hydrogen Peroxide (H_2O_2)	Sigma-Aldrich
Isopropanol	Sigma-Aldrich
Lenalidomide	Selleck Chemicals
LY294002	Sigma-Aldrich
Lymphoprep	Stem cell technologies
Menadione	Fluorochem
Methanol	Lennox
MicroAmp Optical 96 well reaction plate and Adhesive film	Qiagen
N-Acetyl-L-Cysteine	Sigma-Aldrich
Non-Fat Dried Milk	Marvel
PBS Tablets	Sigma-Aldrich
Penicillin Streptomycin	Invitrogen
Phosphatase Inhibitor Cocktail 2	Sigma-Aldrich
Phosphatase Inhibitor Cocktail 3	Sigma-Aldrich
Polyvinylidene difluoride (PVDF)	Millipore
Propidium Iodide	Sigma-Aldrich
Protein Ladder	Sigma-Aldrich
Protogel	Sigma-Aldrich

Random Hexamers	Promega
RIPA Lysis Buffer	Sigma-Aldrich
RNase A	Sigma-Aldrich
RNase-Free DNase kit	Qiagen
RNeasy Mini Kit	Qiagen
Roswell Park Memorial Institute (RPMI)-1640	Biosciences
Ruxolitinib	Selleck Chemicals
SB203580	Selleck Chemicals
Secondary HRP-linked anti-mouse	Promega
Secondary HRP-linked Anti-Rabbit	Promega
Sodium Chloride	Sigma-Aldrich
Sodium Dodecyl Sulfate	Sigma-Aldrich
Sorafenib	LC Laboratories
SP600125	Fluorochem
Sterile H_2O	Sigma Aldrich
Sterile Phosphate Buffered Saline	Biosciences
Stripping Buffer	Pierce
Superscript First Strand Buffer	Invitrogen
TaqMan Gene Expression Assay - BCL2	Applied Biosystems
TaqMan Gene Expression Assay - Beta-2-Microglobulin	Applied Biosystems
TaqMan Gene Expression Assay - CCND1	Applied Biosystems
TaqMan Gene Expression Assay - MCL1	Applied Biosystems
TaqMan Gene Expression Assay - STAT3	Applied Biosystems
TaqMan Universal PCR Master mix	Applied Biosystems
TEMED	Sigma-Aldrich
Transwell 12 well inserts	Corning
Trizma Base	Sigma-Aldrich
TrypLE	Biosciences
Tween-20	Sigma-Aldrich
U0126	Sigma-Aldrich
Z-VAD-fmk	Calbiochem

2.2. Contact details of distributors

Brennan Co: Stillorgan Industrial Park, Dublin, Ireland
enquiries@brennanco.ie
Calbiochem: La Jolla, California 92-39-2087, U.S.A.
CUSTOMER.SERVICE@MERCKBIOSCIENCES.CO.UK
Cell Signaling Technology: 3 Trask Lane, Denvers, Massachusetts 09123, U.S.A.
enquiries@brennanco.ie
Cruinn Diagnostics Ltd: 5b/6b Hume Centre, Park West Industrial Estate, Dublin 12, Ireland. info@cruinn.ie
DSMZ cell bank: Inhoffenstraße 7B, 38124 Braunschweig, Germany.
contact@dsmz.de
Fluorochem Ltd: Unit 14, Graphite Way, Hadfield, Derbyshire, SK13 1QH U.K.
Enquiries@Fluorochem.co.uk
GraphPad Software Inc: 2236 Avendia de la Playa, La Jolla, California 90237, U.S.A.
sales@graphpad.com
Greiner Bio-One-Ltd: Brunel Way, Stroudwater Business Park, Stonehouse, Gloustershire L10 3SX, U.K.
orders@cruinn.ie
Invitrogen Ltd: 3 Fountain Drive, Inchinnan Business Park, Paisley PA4 9RF, U.K.
ukorders.lifesci@thermofisher.com
Qiagen Ltd: Skelton House, Lloyd Street North Manchester M15 6SH, U.K.
orders-uk@qiagen.com
Millipore: Tullagreen, carrigtwohill, Co. Cork, Ireland
eiorders@europe.sial.com
MyBio: Kilkenny Research and Innovation Centre, Kilkenny, Ireland
info@mybio.ie
Pierce Biotechnology Ltd.: P.O. Box 117, Rockford, Illinois 61105, U.S.A.
info@medical-supply.ie
R&D Systems: 19 Barton Lane, Abingdon Science Park, OX14 3NB, U.K.
info@RnDSystems.co.uk
Roche Diagnostics Ltd.: Burgess Hill, West Sussex, RH159RY, U.K.
burgesshill.ras@roche.com
Sigma-Aldrich Ireland Ltd: Vale Road, Arklow, Wicklow, Ireland
EIRCustsupport@sial.com
VWR: Northwest Business Park, Dublin 15, Ireland
sales@ie.vwr.com

2.3. Cell maintenance

2.3.1. Cell culture

Human multiple myeloma cell lines NCI-H929 and U266B1 were obtained from the Deutsche Sammlung von Mikroorganismen und Zellkulturen GmbH (DSMZ) cell bank (Braunschweig, Germany). MM1.S and MM1.R were a gift from Dr Eva Szegezdi, NUI Galway. The NCI-H929 cell line are CD138 positive MM cells established from a malignant effusion from a 62 year old, female, Caucasian patient [266]. The U266B1 cell line was isolated from a 53 year old male and are reported to produce IL-6 [267, 268]. The paired dexamethasone resistant (MM1.R) and susceptible (MM1.S) were isolated from the parent cell line, MM.1, which was established from peripheral blood of a 42 year old, black, female MM patient who had become resistant to steroid-based therapy [269]. The MM1.R cell line lacks the glucocorticoid receptor, while the receptor is expressed in the MM1.S cell line. All myeloma cell lines were cultured in complete RPMI-1640 GlutaMAX^{TM} at 37°C in a humified atmosphere containing 5% CO_2. All cell culture media was purchased from Gibco (Grand Island, NY, USA). All media was supplemented with 10% (v/v) foetal bovine serum (FBS) (Gibco) and 100 U/mL penicillin and 100 ug/mL streptomycin (complete media). NCI-H929 and U266B1 cells were seeded into pre-warmed complete medium (2.5 x 10^5 cells/mL) and maintained at a cell density of 2.5-10 x 10^5 cells/mL by centrifuging cells, decanting supernatant and routinely sub-culturing cells 1:2 or 1:3, three times a week. MM1.S and MM1.R cell lines grow both as a lightly attached monolayer and in suspension. Cells were sub-cultured by gently scraping adherent cells into the medium with suspension cells, centrifuging cells, decanting supernatant and replacing with fresh media.

The HS5 cell line was obtained from American Type Culture Collection (ATCC®) (Manassas, VA, USA). This cell line is an HPV-16 E6/E7 transformed bone marrow stomal cell line established from a 30-year-old, Caucasian male. HS5 cells can be used to maintain *ex vivo* bone marrow cultures in colony forming assays and in co-culture models as the cell line produces multiple cytokines and growth factors [270]. HS5 cells were cultured in Dulbecco's Modified Eagle Medium (DMEM) GlutaMAX^{TM} supplemented with 10% (v/v) foetal bovine serum (FBS), 100 U/mL penicillin and 100 µg/mL streptomycin. Cell lines

were passaged twice weekly. The media was removed from the cells and the cells were washed with 5 mL of PBS. In order to detach the cells from the base of the flask, 5 mL of the disassociation reagent, TrypLe Express, was added. Cells were incubated at 37^{o}C with the TrypLe Express for 2-3 minutes. The TrypLe Express was neutralised with 5 mL of fresh medium, transferred to a falcon and centrifuged at 300 x g for 5 minutes in a Sorvall T centrifuge. The supernatant was decanted; cells were resuspended in the appropriate amount of media and transferred to new flasks.

Cell lines	**NCI-H929**	**U266B1**	**MM1.S**	**MM1.R**
Mutations	NRAS	TP53	CDKN2C	CDKN2C
	PRKD2	BRAF	KRAS	KRAS
	FAM46C	TRAF3	FAM46C	FAM46C
	RECQLS	RB1	TRAF3	TRAF3
	BRCA2	BLM	LTB	LTB
	NLRX1	CHD2	MSH3	MSH3
	TYK2	HIST1H1C	TLR2	TLR2
	KDM5A	FRANCF	CDKN2A	CDKN2A
	WHSC1	-	TYK2	TYK2
	-	-	TLR6	TLR6
	-	-	WHSC1	WHSC1
Translocations	t(4;14)	t(11;14)	t(14;16)	t(14;16)
IL-6 production	No	Yes	No	No
Drug resistance				
Dexamethasone	No	Yes	No	Yes
Melphalan	No	Yes	No	No
Lenalidomide	Yes	No	Yes	Yes

Table 2. 1 Characteristics of NCI-H929, U266B1, MM1.S and MM1.R cell lines.
Table adapted from Tessoulin et al., Journal of Haematology and Oncology, 2019 [271-274].

2.3.2. Counting cells

Cells were counted using a haemocytometer (counting chamber) to determine the concentration of cells in a liquid sample. The gridded area of the haemocytometer is engraved with 1 x 1 mm squares. To count cells, a coverslip (Sigma) is placed on the slide which creates a chamber 0.1 mm high. The design of the chamber means that the total concentration of cells in the cell suspension can be determined using a simple calculation. A 10 µL aliquot of diluted (1:10) cell suspension was pipetted onto the edge of the haemocytometer, which covers the gridded area underneath the coverslip by capillary action. Cells within the four outer squares of the grid were counted and the mean value of cells was calculated. The volume of each large square is 1×10^{-4} mL; therefore, the total cell concentration (mL^{-1}) of the sample was determined by multiplying the mean number of cells counted by the dilution factor 10 and by 10^4.

2.3.3. Cryopreservation

Low passage number stocks of each cell type were stored in liquid nitrogen (-196°C). Freezing medium consisted of 90% FBS and 10% dimethyl sulfoxide (DMSO). Cell lines were harvested by centrifugation and pellets were resuspended in freezing medium. 1 mL aliquots were then transferred to cryotubes (3×10^6 cells in 1 mL). The cells were frozen down in a freezing container filled with isopropyl alcohol at -70°C for at least 24 hours. This ensured that the cells were frozen down at a rate of 1°C per minute. After initial freezing, cryotubes were transferred to liquid nitrogen for long term storage at -196°C. When cells were required, cells were rapidly defrosted and transferred to 10 mL of complete medium heated to 37°C before being centrifuged at 300 x g for 5 minutes. Pellets were resuspended in 5 mL of complete RPMI medium and incubated at 37°C + 5% CO_2 until confluent. Once cells were at a suitable growth rate (approximately 2-3 passages) they were used in experimentation.

2.4. Preparation of stock solutions of drugs, inhibitors and recombinant proteins

2.4.1. Novel drugs

Novel guanidinium-based compounds ED73a, VP79s, VPED_1 and FR13b were provided by Prof. Isabel Rozas (School of Chemistry, Trinity College Dublin). Compounds were dissolved in 100% ethanol and made up to 10 mM stocks. Working dilutions were made up with ethanol to the concentration required. All stock concentrations and dilutions in ethanol were stored at 4°C.

2.4.2 Dexamethasone

Dexamethasone was purchased from Sigma-Aldrich and dissolved in 100% ethanol to make a 10 mM stock and stored at 4°C. Working concentrations were made up in complete-RPMI on the day of the experiment.

2.4.3 Ruxolitinib, venetoclax, lenalidomide and bortezomib

Ruxolitinib, venetoclax, lenalidomide and bortezomib were purchased from SelleckChem and dissolved in cell culture grade DMSO to make high concentration stocks. The stocks were aliquoted and stored at -70°C until necessary to avoid freeze-thawing. Working concentrations of each drug were made up in DMSO. Dilutions were prepared fresh on the day with DMSO and sterile H_2O or complete media.

2.4.4 Inhibitors

The general caspase inhibitor Z-VAD-FMK (Calbiochem) was dissolved in DMSO to make a stock concentration of 50 mM and stored at -20°C. Dilutions were prepared fresh on the day in sterile deionised H_2O with the final DMSO concentration applied to the cells at 0.2% for the NCI-H929 cell line and 0.05% for the U266B1 cell line. The MEK inhibitor U0126 (Sigma-Aldrich) was made up to a 100 mM stock in DMSO, aliquoted and stored at -20°C. The JNK inhibitor SP600125 (Fluorochem) was made up to a 30 mM stock in DMSO, aliquoted and stored at -20°C. The p38 inhibitor SB203580 (SelleckChem) was made up to a 50 mM stock in DMSO, aliquoted and stored at -20°C.

2.4.5. Recombinant proteins

Recombinant Human IL-6 (Biolegend) was reconstituted in 0.5% BSA in PBS and made up to a stock concentration of 50 ng/µL and stored at -70°C. On the day, IL-6 was made up to a working concentration of 1 ng/µL in complete RPMI medium.

2.5. Assessment of the purity of VP79s by high-performance liquid chromatography

High-performance liquid chromatography (HPLC) analysis was carried out using a Varian ProStar system in order to assess the purity of each batch of VP79s used in this study. The system is equipped with a Varian Prostar 335 diode array detector and a manual injector. In order to detect the purity of VP79s, detection was performed at 254 nm and peak purity was assessed using a purity channel. The stationary phase consisted of an ACE 5 C18-AR column (150 × 4.6 mm), and the mobile phase used the following gradient system, eluting at 1 mL/min: aqueous formate buffer (30 mM, pH 3.0) for 10 minutes, linear ramp to 85% methanol buffered with the same system over 25 minutes, hold at 85% buffered methanol for 10 minutes. Minimum requirement for purity was set at 95.0%. Experiments to assess purity were carried out by Viola Previtali and Helene Mihigo (Appendix Figures 1-4).

2.6. Alamar Blue viability assay

Alamar Blue© (Invitrogen) is a non-toxic, soluble, REDOX indicator used to quantitatively measure the viability of cells in response to toxic agents. The active ingredient of Alamar Blue is resazurin which is cell permeable and blue in colour. Upon entering the cells, resazurin is reduced to resorufin, which produces red fluorescence. Viable cells convert resazurin to resorufin giving a quantitative measure of viability as damaged and non-viable cells have lower innate metabolic activity and therefore produce less resorufin.

The purpose of the Alamar Blue© viability assay was to assess the cytotoxic and cytostatic effects of the novel guanidinium-diaryl derivates provided by the Rozas group and chemotherapeutic drugs on MM cell lines and to calculate the relative IC_{50} value for each

compound. Cells were seeded in 96-well plates at a density of 2.5 x 10^5 cells/mL in a total volume of 200 µL per well (5 x 10^4 cells/well). Cells were treated with 100X dilutions of each compound in triplicate to yield a 1X final concentration in the well. Ethanol was used as a vehicle control and cells were treated with 0.5% ethanol (v/v). Plates were incubated for 24, 48 and 72 hours at 37°C in 5% CO_2 after which 20 µL of Alamar Blue was added to each well. The plates were then incubated in the dark for up to 5 hours. Alamar Blue added to complete RPMI medium was used as a blank control. Plates were read after the appropriate time on the Spectramax Gemini Plate Reader using SOFTmax Pro version 4.9 (Molecular Devices, Sunnyville, C.A) at excitation and emission wavelengths of 544 nm and 590 nm respectively.

Vehicle treated cells were taken as 100% viability and wells treated with compounds were calculated as a percentage of the vehicle control. The mean of each triplicate was calculated. Dose response curves were plotted in order to obtain IC_{50} values using Prism GraphPad 5.

2.7. Flow cytometry

2.7.1. Cell cycle analysis by propidium iodide staining

Cell cycle analysis by DNA quantification was one of the earliest applications of flow cytometry [275]. Propidium iodide (PI) is a DNA intercalating agent which binds stoichiometrically to DNA. PI fluorescence intensity increases 20-fold when bound to DNA (excitation 488 nm and emission 600 nm). Following treatment, cells were harvested and fixed in 70% ethanol/30% phosphate buffered saline (PBS) and stored at -20°C until required. When samples were required 5 µL of FBS was added to each sample and samples were centrifuged at 1000 x g for 10 minutes to obtain a cell pellet. The ethanol containing supernatant was discarded and the pellet was resuspended in 200 µL of PBS supplemented with 10 µg/mL of RNase A (Sigma Aldrich, St Louis, MO, USA) and 100 µg/mL propidium iodide (Sigma Aldrich, St Louis, MO, USA). Cells were incubated in the dark at 37°C for 30 minutes. Analysis was performed using a BD Accuri™ C6 flow cytometer using BD Accuri™ C6 software. Samples were first gated on vehicle controls to remove debris and cell

aggregates (Figure 2.1). Cells (1 x 10^4) from each sample were counted and results were visualised on histograms. PI was detected using 585/40 bandpass filter.

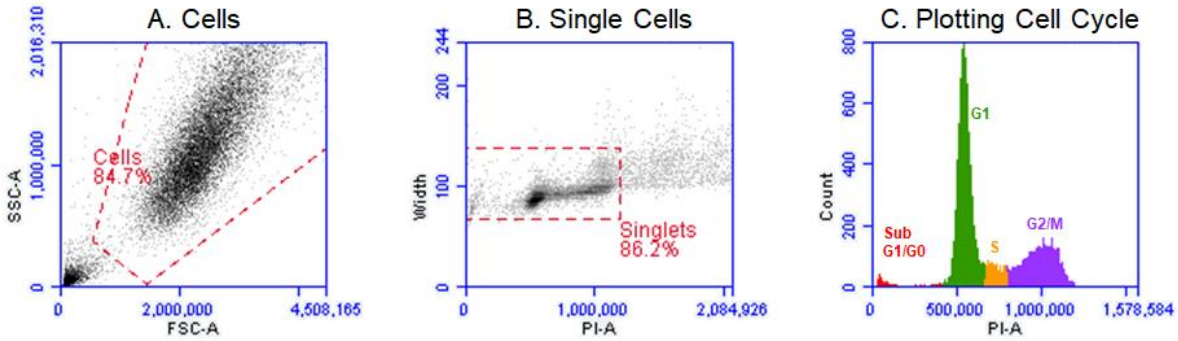

Figure 2. 1 Gating strategy for cell cycle (PI) flow cytometric analysis.

Representative image of the gating strategy for PI staining using the BD Accuri™ flow cytometer. ***A.*** *Cells were gated by plotting forward scatter area (FSC-A) against side scatter area (SCC-A) on a dot plot.* ***B.*** *A single cell gate was then created to exclude doublets and polyploid cells by plotting width vs PI (488 nm, FL-2 channel: 585/40 bypass filter) area (PI-A).* ***C.*** *To determine cell cycle stages, single cells were plotted on a PI-A histogram based on PI intensity.*

2.7.2. Detection of cell death by annexin V/PI staining

In order to detect cell death by apoptosis or necrosis the annexin V/PI assay was employed. The apoptotic cell undergoes a series of characteristic changes which distinguish it from a viable cell, this includes the translocation of the phospholipid phosphatidyl serine (PS) from the inner membrane to the outer leaflet of the plasma membrane. This generally occurs early on in the apoptotic process prior to other features of apoptosis, such as loss of mitochondrial membrane potential. Annexin V has a high binding affinity for PS and in this assay, fluorescein isothiocyanate (FITC) bound annexin V binds PS exposed to the extracellular environment. PI is a dye capable of binding tightly to nucleic acids and emitting a red fluorescence. PI is incapable of permeabilising non-apoptotic and early apoptotic membranes and, thus, cells which are in the early stages of apoptosis or non-apoptotic cells are not stained by PI. Therefore, cells which display PS to

the extracellular environment but still maintain their membrane integrity (early apoptosis), stain positive for annexin V-FITC and negative for PI (annexin V^+/PI^-), while cells undergoing late apoptosis/necrosis stain positive for annexin V-FITC and PI (annexin V^+/PI^+) [276].

Cells were seeded in 12 well plates at a density of 3 x 10^5 cells/mL in a total volume of 2 mL, allowed to rest for 1 hour and then treated for the required amount of time. Following treatment, cells were transferred to a 30 mL falcon tube. Cells were centrifuged at 300 x g for 5 minutes to obtain a cell pellet. The cell pellet was then washed with 0.5 mL of annexin V Binding Buffer (20X Binding buffer: 0.1 M HEPES, 1.4M NaCl, 25 mM $CaCl_2$ pH7.4, diluted 1 in 20 in PBS to give 1 X solution) and centrifuged at 300 x g for 5 minutes to obtain a pellet. The supernatant was discarded, and the pellet stained with 50 µL of annexin V-FITC (1:33.3 dilution in 1X annexin binding buffer) for 30 minutes in the dark on ice. 0.5 mL of annexin V binding buffer was added, and the samples centrifuged at 300 x g for 5 minutes at 4^{o}C. The supernatant was discarded, and the pellet resuspended in 2.5 mL PI (1 mg/mL diluted 1:2000 in annexin V binding buffer). The samples were then analysed immediately on a BD Accuri^{TM} C6 flow cytometer using BD Accuri^{TM} C6 software. Samples were first gated on vehicle controls (unstained, annexin V-FITC only, PI only and annexin V^+/PI^+) to remove debris and cell aggregates. These gates were then analysed on an annexin V-FITC (535 nm – FL1 channel using a 530/30 bandpass filter) vs PI (488 nm – FL2 using a 585/40 bandpass filter) dot plot. Single stained vehicles were used as compensation controls (Figure 2.2).

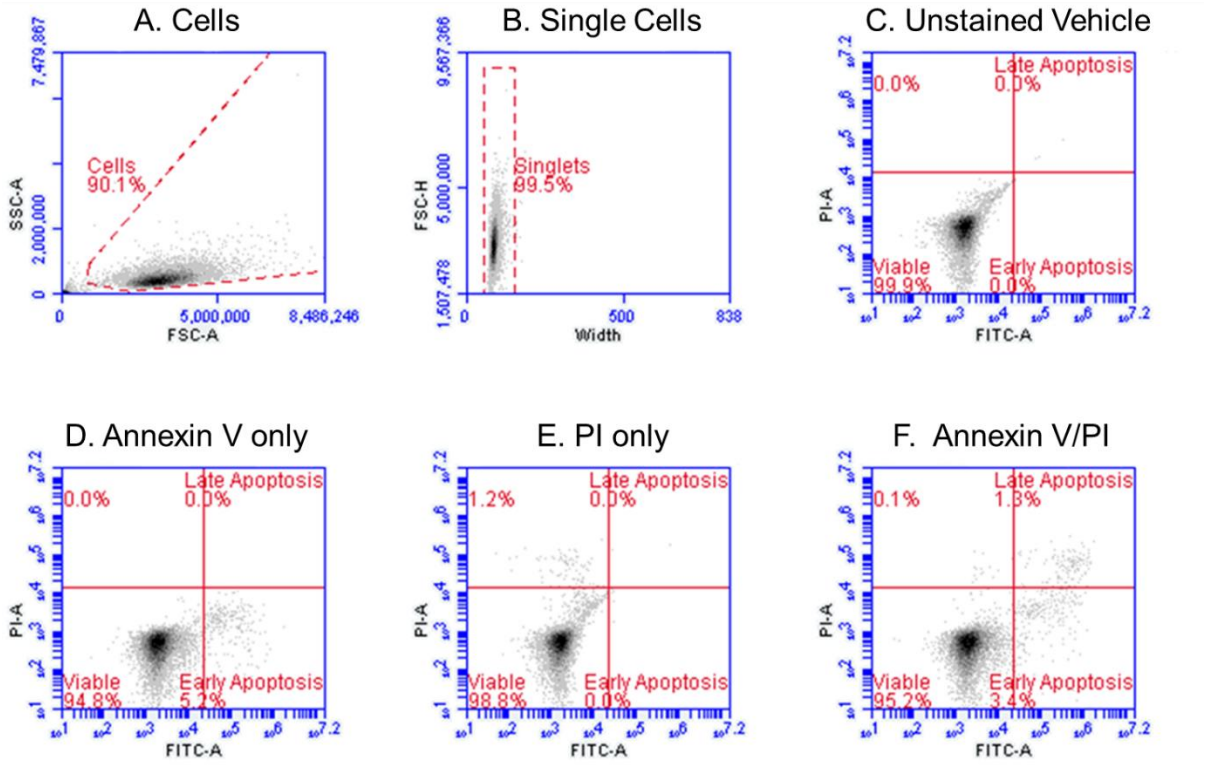

Figure 2. 2 Gating Strategy for annexin V/propidum iodide flow cytometric analysis.

Representative image of gating strategy for annexin V-FITC and propidium iodide (PI) staining using BD Accuri™ flow cytometer. ***A.*** *Cells were gated by plotting forward scatter area (FSC-A) against side scatter area (SCC-A) on a dot plot.* ***B.*** *A single cell gate was then created to remove doublets and triplets by plotting forward scatter height (FSC-H) versus width. Cells were then gated based on vehicle controls:* ***C.*** *unstained,* ***D.*** *annexin V only,* ***E.*** *PI only and* ***F.*** *annexin V/PI by plotting PI area (PI-A) versus FITC area (FITC-A).*

2.7.3. Detection of reactive oxygen species

ROS production was detected using the 2',7'-Dichlorofluorescin diacetate (DCFH-DA) assay (Sigma), a fluorescent assay that measures intracellular ROS. 2',7'-Dichlorofluorescin diacetate is a cell permeable fluorescent dye which is converted to non-fluorescent H_2DCFDA by esterases within the cell. H_2DCFDA can be rapidly oxidized and converted into fluorescent DCF by intracellular ROS which can be detected by flow cytometry.

3 X 10^5 cells/mL were seeded into 24 well plates wells and stained with 20 µM DCFH-DA for 30 minutes. After 30 minutes each well was treated with 10 µM VP79s for 0, 15, 30, 45, 60, 90, 120 and 240 minutes. Menadione (100 µM) and H_20_2 (100 µM) were used as positive controls and N-acetyl L-cysteine pH 7 (NAC) (5 mM) was used as a negative control. After the appropriate treatment time, cells were transferred to FACS (Fluorescence-activated Cell Sorting) tubes and analysed on a BD FACSCanto™ II by gating on cells, single cells and FITC-A cells (using a 530/30 bandpass filter).

2.7.4. Determination of mitochondrial membrane potential by the JC-1 assay

As well as PS exposure, depolarisation of the inner mitochondrial membrane is thought to be an early irreversible event in apoptotic cell death, induced via the intrinsic or mitochondrial apoptotic pathways [277].

JC-1 (5,6-dichloro-2-[3-(5,6-dichloro-1,3-diethyl-1,3-dihydro-2H-benzimidazol-2-ylidene)-1-propen-1-yl] -1,3-diethyl-1H-benzimidazolium, monoiodide) is a cationic carbocyanine dye that accumulates in mitochondria. In healthy mitochondria (high membrane potential), JC-1 accumulates in the mitochondria and forms complexes known as J-aggregates which fluoresce orange/red. In contrast, in mitochondria with low membrane potential, JC-1 forms monomers which fluoresce green. Therefore, mitochondrial membrane potential can be measured by flow cytometry by measuring a decrease from red to green fluorescence.

NCI-H929 and U266B1 cells were seeded at 1.5x10^5 cells/500 µL in 24 well plates and were treated for the required time in duplicate. Cells were collected, washed once with warm PBS and centrifuged at 400 x g for 5 minutes. Cells were resuspended in 500 µL of 2 µM JC-1 (1% DMSO) and incubated for 30 minutes at 37 °C. After incubation 500 µL of warm PBS was added to each tube and samples were centrifuged at 400 x g for 5 minutes. The supernatant was decanted, and cells were resuspended in 400 µL of warm PBS. Cells were analysed using a BD FACSCanto™ II flow cytometer by gating on cells, single cells and the JC-1 aggregates/monomers (red-585/43/green-530/30 fluorescence). Carbonilcyanide p-

triflouromethoxyphenylhydrazone (*FCCP*) was used as a positive gating control (Figure 2.3). Data analysis was performed using FlowJo software.

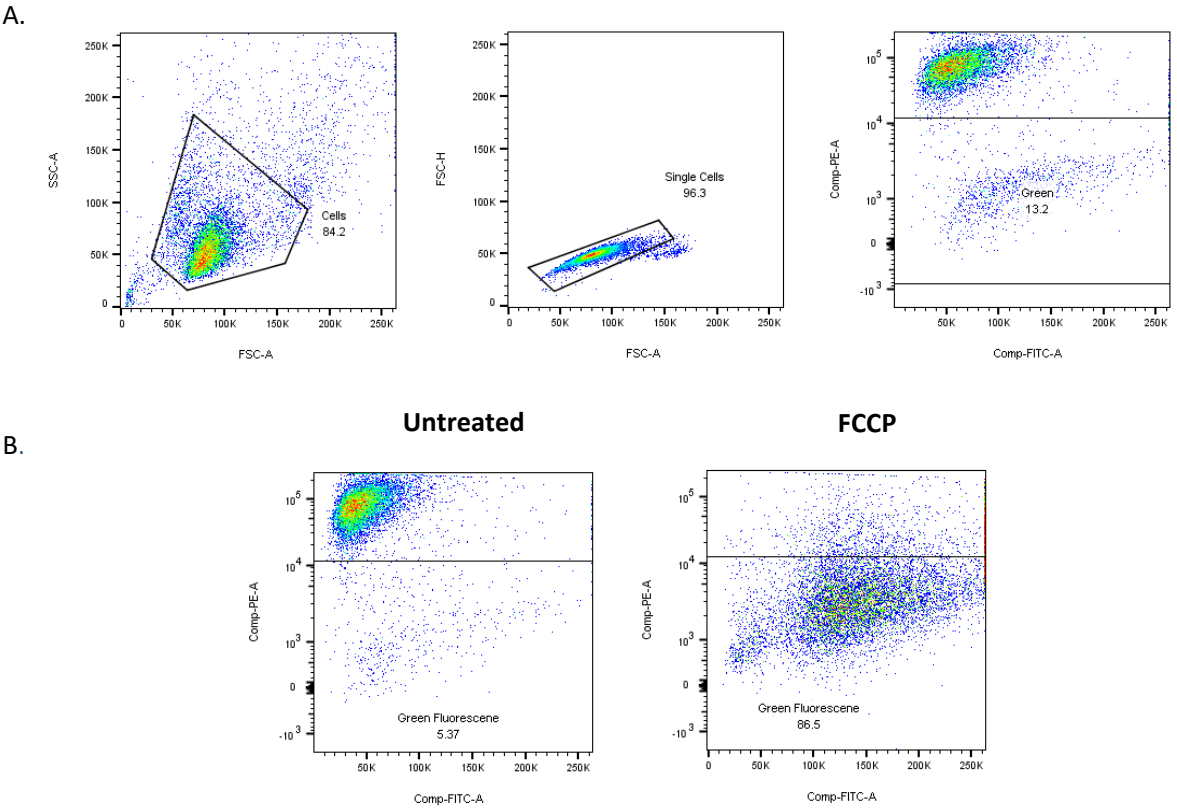

Figure 2. 3 Gating strategy for JC-1 assay.

Representative image of gating strategy for JC-1 assay using the BD FACSCanto™ II flow cytometer. Cells were gated by plotting forward scatter area (FSC-A) against side scatter area (SCC-A) on a dot plot. ***A.*** *A single cell gate was then created to remove doublets and triplets by plotting forward scatter height (FSC-H) versus area (FSC-A).* ***B.*** *Cells were gated based on healthy control cells; unstained and stained, and on cells treated with 25 µM carbonilcyanide p-triflouromethoxyphenylhydrazone (FCCP) as a positive control for mitochondrial membrane depolarisation (green fluorescence).*

2.7.5. STAT3 intracellular flow cytometry staining

3 x 10^5 cells/mL were seeded in 12 well plates and treated with either vehicle (0.5% EtOH) or 10 µM VP79s for 1 hour. Cells were transferred to labelled FACS tubes and wells were

washed with 500 µL of FACS buffer (2% FBS and 1 mM EDTA in PBS). Cells were centrifuged at 400 x g for 5 minutes, the supernatant was removed and cells were washed with 500 µL of FACS buffer. The supernatant was removed again and cells were resuspended in 100 µL of FACS buffer. 250 µL of fixation buffer (BD Cytofix Fixation Buffer) was added to each tube while vortexing. Samples were then incubated for 20 minutes in the fridge in the dark. Following incubation cells were washed twice with 500 µL of FACS buffer. 500 µL of -20°C permeabilisation buffer (BD Phosflow Perm Buffer III) was added to each sample slowly while vortexing. Samples were incubated on ice in the dark for 30 minutes. Following incubation, cells were centrifuged at 300 x g for 10 minutes. The supernatant was carefully removed and cells were washed with 1 mL of FACS buffer. Cells were resuspended in 100 µL of FACS buffer. 20 µL of each antibody (Phospho-STAT3 serine Alex Fluor 647 and Phospho-STAT3 Tyrosine PE) was added to the appropriate tubes and were incubated in the dark at room temperature for 30 minutes. After incubation, 500 µL of FACS buffer was added, samples were centrifuged and supernatant was removed. Samples were resuspended in 400 µL of FACS buffer and were analysed on the BD FACSCanto™ II flow cytometer gating on cells, single cells and cells phosphorylated on serine 727 (660/20 nm bandpass filter) and tyrosine 705 (585/42 bandpass filter). Single stained controls were used to set compensation.

2.7.6. Myeloma cell lines in co-culture with HS5 stromal cell line

2.7.6.1. Cell-to-cell contact

1 x10^5 HS5 cells were seeded in 12 well plates and left to adhere overnight. The next day the media was carefully removed and 3x10^5 NCI-H929 cells were seeded on top of the HS5 cells in 1 mL complete RPMI (a 1:3 cell ratio). Cells were left adhere for 2 hours. Cells were then treated with either vehicle (0.5% EtOH or 0.01% DMSO), 5 µM VP79s or 1.5 nM bortezomib for 24 hours. Cells were carefully collected by pipetting up and down ensuring no disruption of the adherent HS5 cells. Cells were recovered, washed with 500 µL of annexin V binding buffer, centrifuged at 600 x g and were then stained with annexin V-FITC and anti-CD138 for 20 minutes. Following incubation, cells washed and stained with PI just

prior to analysis by flow cytometry. CD138 is a MM cell marker, therefore, the induction of apoptosis in NCI-H929 cells was quantified by gating on CD138 positive cells to exclude any HS5 cells which may have been inadvertently detached and assessing annexin V/ propidium iodide stained cells on the BD FACSCanto™ II flow cytometer.

2.7.6.2. Transwell

1 x10^5 HS5 cells were seeded in 12 well plates and left to adhere overnight. The next day the media was carefully removed and replaced with 1 mL of complete RPMI containing 1.5 x10^5 NCI-H929 cells were seeded in 500 µL of complete RPMI in transwell inserts and placed on top of the HS5 cells. Cells were left to incubate for 2 hours. Cells were then treated with either vehicle (0.5% EtOH) or 5 µM VP79s for 24 hours. Induction of apoptosis in NCI-H929 cells was then quantified by gating on with the myeloma cell marker CD138 and then gating on annexin V/ propidium iodide stained cells on the BD FACSCanto™ II flow cytometer.

2.7.7. PBMC isolation

Peripheral Blood Mononuclear Cells (PBMCs) were isolated from healthy donor blood following informed consent by density gradient centrifugation using Lymphoprep® (Axis-Shield, UK). The donor blood (10 mL) was diluted 1 in 2 with wash buffer in a 50 mL Falcon tube (RPMI medium supplemented with 100 units/mL penicillin and 0.1 mg/mL streptomycin) and mixed by inverting. Diluted blood was then layered carefully on top of the Lymphoprep®. Samples were then centrifuged at 800 x g for 30 minutes with no brake at room temperature. After centrifugation, the PBMC layer at the sample/medium interface was carefully removed with a Pasteur pipette and placed into a new Falcon tube. The sample was brought up to 30 mL with wash buffer and then centrifuged at 300 x g for 10 minutes at room temperature at break 9. Samples were washed 3 times with wash buffer before being resuspended in the appropriate volume of complete RPMI. Cells were counted and seeded at 1x10^5 cells/well in U bottomed 96 well plates to assist with pelleting and left to rest for 4 hours prior to treatment. Cells were then treated with various concentrations of VP79s for 24 hours. After treatment time, cells were collected,

stained with antibodies against CD3-PerCP cy5.5, CD19-PE and CD56-APC for gating of T cells, B cells and NK cells respectively. DAPI (gated on Pacific blue) was used as an indicator of cell viability as DAPI cannot penetrate healthy cells. Samples were analysed by flow cytometry on the BD FACSCanto™ II flow cytometer.

2.7.8. Cell surface staining of CD126 and CD130

U266B1 cells were seeded at 3 x 10^5 cells/mL in 12 well plates and were treated with either vehicle (0.5% EtOH) or VP79s (5 or 10 µM) for 15 minutes to 4 hours. Following treatment, cells were collected and transferred to labelled FACS tubes and wells were washed with 500 µL of cold PBS. Cells were then centrifuged at 400 x g for 5 minutes, supernatant was removed and cells were washed with 500 µL of FACS buffer followed by centrifugation as before. The supernatant was removed, and cells were resuspended in 90 µL of FACS buffer (PBS with 2% FBS and 1 mM EDTA) with 5 µL of each antibody (Anti-CD126 PE and anti-CD130 APC- BD biosciences). Cells were stained in the dark at room temperature for 15 minutes. 500 µL of FACS buffer was then added to each sample and they were centrifuged at 400 x g for 5 minutes. The supernatant was discarded and samples were resuspended in 250 µL of FACS buffer. Samples were analysed on the BD FACSCanto™ II flow cytometer gating on cells, single cells and cells positive for CD130 (660/20 nm bandpass filter) and CD126 (585/40 bandpass filter). Single stained controls were used to set compensation.

2.8. Western blotting

2.8.1. Preparation of cell lysates

NCI-H929 and U266B1 cells were seeded at a density of 3 x 10^5 cells/mL in 25 cm^2 flasks in 10 mL of media. Cells were treated with the required concentration of each drug for varying amounts of time. Cells and media were transferred to universal tubes and flasks were washed with 1 mL PBS. Samples were centrifuged at 600 x g for 5 minutes. The supernatant was discarded, and samples were resuspended in 1 mL non-sterile PBS. The resuspended pellet was centrifuged at 600 x g for 5 minutes at 4°C. After centrifugation the supernatant was removed, and pellets were stored at -70°C until required.

Cell pellets were removed from the -70°C freezer and kept on ice during the lysis process. The lysis of the samples was performed using ice-cold radioimmunoprecipitation (RIPA) buffer supplemented with 10% (v/v) protease inhibitor and 1% (v/v) phosphatase inhibitor cocktail 2 and 3. RIPA lysis buffer was obtained from Sigma. A 10 X concentrated protease inhibitor cocktail was prepared by diluting 1 tablet (cOmplete™ tablets mini EASYpack) in 1 mL of dH_2O. This solution was distributed into 100 µL aliquots and stored at -20 °C until required. The 10 X protease inhibitor cocktail was diluted to 1 X concentration in RIPA buffer. Phosphatase inhibitor cocktails 2 and 3 (Sigma) were also added to lysis buffer at a dilution of 1 in 100. RIPA buffer was kept on ice until required.

Sample pellets were resuspended in an appropriate volume of RIPA buffer and left on ice for 30 minutes. Following incubation with RIPA lysis buffer protein concentration was quantified by BCA assay.

2.8.2. Determination of protein concentration

Protein concentration was determined using a BCA assay kit from Pierce. BSA standards were prepared as described in Table 2.2 from a 2 mg/mL stock. BCA working reagent was prepared by diluting reagent B 1:50 with reagent A. 20 µL of each standard or diluted sample was added to a 96 well plate followed by 200 µL of the BCA working reagent. This was performed in duplicate. The plate was wrapped in tinfoil and left for 30 minutes at 37°C in a non-sterile incubator. Absorbance was read at 562 nm using a molecular devices microplate reader and the mean of the standards was determined and a standard curve was constructed (Figure 2.4). The standard curve was used to determine the protein concentration of each sample and the volume of sample required to make 100 ug/100 µL lysate was determined to ensure equal loading.

Vial	Volume of Diluent (µL)	Volume and Source of BSA (µL)	Final concentration BSA mg/mL
1	0	Stock solution	2
2	250	250 of 1	1
3	250	250 of 2	0.5
4	250	250 of 3	0.25
5	250	250 of 4	0.125
6	250	250 of 5	0.0625
7	250	0	0

Table 2. 2 Preparation of BSA standards.

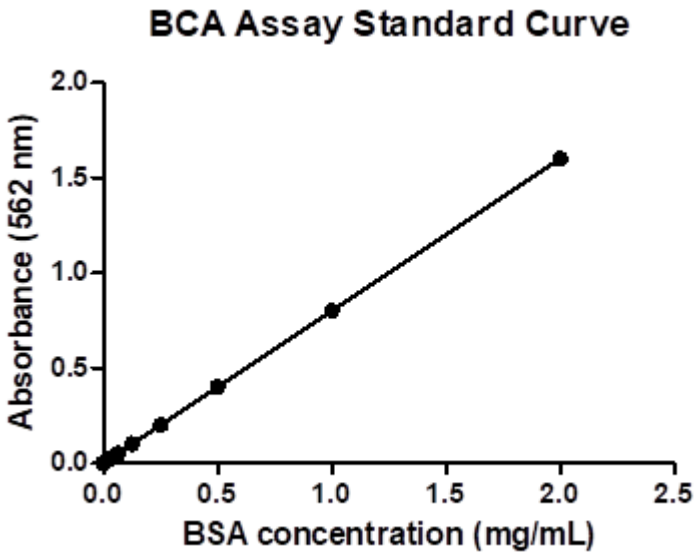

Figure 2. 4 BCA assay standard curve.

BSA standards from a 2 mg/mL stock were prepared as described in Table 2.2. 20 µL of each standard or diluted sample was added to a 96 well plate in duplicate followed by 200 µL of the BCA working reagent. Absorbance was read at 562 nm and the mean of the standards was determined and a standard curve was constructed.

2.8.3. Sodium dodecylsulphate-polyacrylamide gel electrophoresis (SDS-PAGE)

Cell lysates were boiled with 5x Laemmli sample buffer [Tris-HCl 62.5 mM (pH 6.7), glycerol 10% (v/v), sodium dodecyl sulphate 2% (w/v), bromophenol blue 0.002% (w/v) containing DTT (50 µM)] for 10 minutes at 80°C. Following boiling, lysates were vortexed and placed on ice or frozen until required.

Bio-rad 1.5 mm glass plates were washed, dried and assembled. Resolving gel was prepared as in Table 2.3, 7.5 mL of the resolving gel mix was pipetted between the plates 1 mL at a time to minimise bubbles. 200 µL of isopropanol was pipetted onto the gel to prevent bubbles and even out the surface layer of the gel. Once the resolving gel had set, the isopropanol was poured off and the top of the gel was washed with deionised water. The stacking gel was prepared as per Table 2.3 and was poured on top of the resolving gel. A comb was then placed into the gel to create wells in the gel. Once the gel had set it was ready for use. If not needed immediately, the gel was wrapped in wet tissue paper and clingfilm and stored at 4°C.

When ready to use, the 2 gels were placed into a Bio-rad rig (mini-PROTEAN II) creating a chamber and the chamber was then filled with 1X running buffer diluted from 10X solution (25 mM Tris, 192 mM glycine, 0.1 % (v/v) SDS in dH_2O). The comb in the gel was then removed to create wells in which the lysate would be added. Molecular weight marker (7 µL) was loaded into the first well. Lysate samples were then added to each well (10-20 µg of protein). The chamber was then filled with 1X running buffer and a current was applied. The gel was run at 80 V for 30 minutes to allow samples to travel through the stacking gel and then the voltage was increased to 120 V. The gel was run until samples reached the bottom of the resolving gel.

Components (mL)	6% Resolving Gel	8% Resolving Gel	10% Resolving Gel	12% Resolving Gel	15% Resolving Gel	5% Stacking
H_2O	15.9	13.9	11.9	9.9	6.9	6.8
30 % acrylamide mix	6.0	8.0	10	12.0	15.0	1.7
1.5 M Tris (pH 8.8)	7.5	7.5	7.5	7.5	7.5	_
10% SDS	0.3	0.3	0.3	0.3	0.3	0.1
10% ammonium persulfate	0.3	0.3	0.3	0.3	0.3	0.1
TEMED	0.024	0.018	0.012	0.012	0.012	0.01
1 M Tris (pH 6.8)	_	_	_	_	_	1.25

Table 2. 3 Solutions for preparing 30 mL resolving and stacking 10 mL gels used in SDS-PAGE.

2.8.4. Transfer

Polyvinylidene difluoride (PVDF) membrane was activated in methanol for 2 minutes and left soaking in 1 X transfer buffer diluted from 10X solution (25 mM Tris, 192 mM glycine in dH_2O) along with 4 pieces of filter paper. A sponge was placed on a transfer cassette, followed by 2 pieces of filter paper. The gel was removed from the gasket and was carefully excised from in-between the glass plates. The gel was then placed on the filter paper followed by activated PVDF membrane, taking care to avoid bubbles forming between the gel and PVDF. Two pieces of filter paper were then placed on top of the PVDF followed by a sponge. The assembled cassette was then placed into the transfer rig (Bio-rad) and filled to 50% with 1X transfer buffer, an icepack was placed in the rig and the 1X transfer buffer was topped up. The gel was transferred for 60-100 minutes at 150 mA depending on protein size.

2.8.5. Probing membranes for proteins

Following transfer of proteins onto a PVDF membrane, non-specific binding sites on the membrane were blocked by washing the membrane in 5% non-fat dried milk (Marvel) in

TBST (20 mM Tris, 0.15 mM NaCl, 0.1% Tween, pH 7.6) for 1 hour at room temperature. Following blocking, membranes were washed once in TBST and incubated overnight in primary antibody at 4°C. Antibodies were diluted in either 5% (w/v) dried milk for total proteins or 5% (w/v) BSA for phosphorylated proteins in TBST. Dilution factors varied for each antibody ranging from 1:500 – 1:5000. Following incubation, the membrane was washed in TBST 3 for 10 minutes each time. The membrane was then incubated in secondary antibody (anti-rabbit or anti-mouse, conjugated to horseradish peroxidase (HRP)) for 1 hour at room temperature and was then washed 3 times in TBST to remove any non-bound secondary antibody. The presence of bound antibodies on the membrane was detected by electrochemiluminescence (ECL). The membrane was covered in ECL detection reagent which consists of luminol and peroxide. The presence of HRP and peroxide results in the oxidation of luminol and the release of light that can be detected with the Bio-rad Gel Doc ^{TM} XR + system with Image Lab software. GAPDH, beta-actin and alpha-tubulin were used as loading controls in order to ensure equal loading of protein across the gel. If a protein was a similar size to the loading control, the membrane was stripped for 15 minutes in stripping buffer (Thermo Fisher), washed X3 times in TBST and blocked in 5% (w/v) dried milk as before. The membrane was then re-probed with anti-GAPDH (1:5000), for 1 hour at room temperature. Following incubation, the membrane was washed X3 in TBST and placed in anti-mouse secondary (1:5000) for 1 hour at room temperature. The membrane was then washed X3 in TBST and proteins were detected as above.

2.9. Gene expression assays

2.9.1. RNA extraction and quantification

U266B1 cells were seeded at 3 x 10^5 cells/mL in 6 well plates (3 mL per well) and were treated with either vehicle or VP79s (2.5 µm) for 2 or 8 hours. RNA was extracted using RNeasy Mini Kit from Qiagen (Hilden, Germany) as per manufacturer's instructions. Prior to first use, ethanol was added to Buffer RPE as per manufacturer's instructions. Before each extraction, 20 µL of 2M DTT was added per 1 mL of RLT Lysis Buffer. DTT contributes

to denaturing RNases released after cell lysis thus preventing RNA degradation. Cells were collected as usual and were pelleted by centrifuging at 400 x g for 5 minutes. Cells were then washed twice by resuspending the pellet in 1 mL ice-cold PBS and centrifuging at 600 x g for 3 minutes at 4°C. After washing cells were resuspended in 350 µL of RTL buffer and cells were lysed by pipetting. The lysate was then added to a labelled QIAshredder column and centrifuged at 8000 x g for 2 minutes at 4°C to homogenise the lysate. At this point the flow-through was stored at minus 80°C overnight.

350 µL of 70% ethanol was added to the flow-through, to promote binding, and was transferred to a RNeasy spin column. The RNeasy column was then centrifuged at 8200 x g for 15 seconds and flow-through was discarded. The nucleic acid remained bound to the column. The column was then washed with 350 µL of Buffer RW1 and centrifuged at 8000 x g for 15 seconds and flow-through was discarded. DNA digestion was then performed on the column using RNase-Free DNase Kit from Qiagen (Hilden, Germany). The DNase I stock solution was prepared by reconstituting lyophilised DNase I with RNase-free water. The DNase I was aliquoted and stored at -20°C. 10 µL of DNase I stock was added to 70 µL of Buffer RDD and mixed gently by inversion. 40 µL of the DNase mixture was then added to the column and left for 15 minutes at room temperature. The column was then washed by adding 350 µL of Buffer RW1 to the column and centrifuging at 8000 x g for 15 seconds. The column was then washed twice with 500 µL of Buffer RPE to elute any contaminants and was then transferred to a collection tube and centrifuged at 8000 x g to dry the membrane. 30 µL of RNA free water was then added to the column and centrifuged at 8000 x g for 1 minute to elute the RNA. RNA quality and quantity were then assessed by using a Nanodrop ND 1000 UV-Vis Spectrophotometer (Thermo Fisher Scientific (MA, USA)).

2.9.2. cDNA preparation

500 ng of RNA was converted to DNA as follows. The required amount of RNA was made up to 11 µL using sterile RNase/DNase free water. A master mix containing 5 X Superscript First Strand Buffer, 25 mM dNTPs, water, 100 mM DTT and 3 µg/µL Random hexamers was

made up and 11 µL was aliquoted per sample (Table 2.4). 11 µL of the diluted RNA was added. Samples were heated to 96°C for 2 minutes and chilled on ice for 5 minutes. 1 µL of RNase out and 1 µL of superscript II was added to each sample and samples were vortexed. Samples were heated to 42°C for 90 minutes, 96°C for 2 minutes and then were placed on ice for 5 minutes. cDNA samples were stored at -20°C.

Components	Volume per sample (µL)
cDNA	11
3 µg/µL Random Hexamers	1
100 mM DTT	2.5
5 x Superscript First Strand Buffer	5
25 mM dNTPs	1
Sterile H_2O	1.5

Table 2. 4 cDNA master mix.

2.9.3. Quantitative reverse transcription PCR (RT-qPCR)

In order to determine the gene expression of *STAT3* related genes (Table 2.5), gene expression was assessed using TaqMan Gene Expression Assays (Applied Biosystems, Netherlands). TaqMan probes are dual-labelled, containing a FAM (6-carboxyfluorescein) reporter dye at the 5' end and a non-fluorescent quencher with a minor groove binding moiety at the 3´ end. When the probe anneals between primer sites of the target gene, the probe is cleaved at the 5´ end due to the nuclease activity of the DNA polymerase. This cleavage separates the dye from the quencher leading to increased fluorescence. Therefore, fluorescence intensity is proportional to the amount of amplicon produced.

PCR preparation was carried out in a designated class II laminar flow hood. PCR master mix was prepared by adding 1 µL of gene expression assay per sample to 10 µL of TaqMan Universal PCR Master mix per sample. 11 µL of the mix was added per well in MicroAmp Optical 96 well Reaction plates (Qiagen, Netherlands). cDNA was diluted to 50 ng/well (per 9 µL) in nuclease free water. Samples were added to each well of the plate in duplicate. The plate was covered in a MicroAmp Optical Adhesive Film and each individual well was sealed. The plate was gently vortexed and centrifuged at 100 x g for 60 seconds.

Amplification was run on an ABI 7500 Real Time PCR System (Applied Biosystems, Netherlands).

Gene	Assay Number
MCL1	Hs01050896_m1
BCL2	Hs00608023_m1
CCND1	Hs00765553_m1
STAT3	Hs01047580_m1
Beta-2-microglobulin	Hs00187842_m1

Table 2. 5 TaqMan Gene Expression Assays (Applied Biosystems) used for RT-qPCR.

2.9.4. RT-qPCR analysis

Analysis was performed using the Delta-Delta CT method ($2^{-\Delta\Delta Ct}$) was used to quantify changes in gene expression in one sample relative to another sample [278]. The comparative Ct equation is defined as $2^{-\Delta\Delta Ct}$= [Ct gene of interest- Ct endogenous control] Sample 1 - [Ct gene of interest- Ct endogenous control] Sample. 2β-2 microglobulin (B2M) was used as an endogenous control.

2.10. Drug combination studies

For the analysis of bortezomib in combination with VP79s a constant ratio was utilised. Therefore, a ratio of 1000:1 was used in combination. $3x10^5$ cells/mL U266B1 cells were seeded in 12 well plates and treated either alone or with a combination of VP79s and Bortezomib (Table 2.6). Each condition was treated in duplicate. After 16 hours cells were collected and stained with annexin V/ PI. Cell death induced by each drug alone and in combination was determined by annexin V/PI staining by flow cytometry on the BD FACSCanto™ II flow cytometer.

Single treatment concentrations		Combination
VP79s (µM)	Bortezomib (µM)	VP79s + Bortezomib (µM)
1	0.001	1.001
2	0.002	2.002
3	0.003	3.003
7	0.007	7.007
10	0.01	10.01

Table 2. 6 Drug concentrations used for combination studies

2.10.1 Analysis of drug interactions

The computer program Compusyn was used to determine the interactions between drugs. The programme utilises the Chou-Talalay method to determine Combination Index (CI) values for each drug combination [279]. CI values <1, =1 and >1 indicate synergistic, additive and antagonistic effects of the drugs of interest respectively. Higher CI values indicate antagonism, while lower CI values indicate synergism (Table 2.7).

Combination Index (CI)	Description
<1	Synergism
=1 (0.9-1.1)	Additive
>1	Antagonistic

Table 2. 7 Drug Combination Descriptions.

2.11. Myeloma patient samples

MM cells were isolated from patients presenting at the Department of Haematology, St James's Hospital, Dublin following informed consent. This project was approved by the St James's Hospital and Adelaide and Meath incorporating the National Children's Hospital (AMNCH) Joint Ethics committee. 15 mL of bone marrow aspirate was obtained from 5 treatment naïve patients at diagnosis and diluted 1:3 in RPMI-1640 media. Bone marrow

mononuclear cells were isolated by density gradient centrifugation. The diluted bone marrow aspirate was layered carefully on 0.5 volume of Lymphoprep®. Samples were then centrifuged at 800 x g for 30 minutes with no brake at room temperature. After centrifugation, the bone marrow mononuclear cells (BMMCs) were carefully removed, washed in RPMI-1640 media and centrifuged at 300 x g for 10 minutes at room temperature.

Cell count and viability of the BMMCs were assessed by staining with acridine orange and ethidium bromide and using a haemocytometer. 10mg/mL ethidium bromide and 100 ug/mL acridine orange were diluted 1:100 in PBS to make the staining solution. Prior to use, an aliquot of cell suspension was diluted 1:20 or 1:50 with PBS and stained with acridine orange/ethidium bromide. 10 µL of cell suspension was loaded onto a haemocytometer and placed under the blue light of a fluorescent microscope. Cell count and viability were noted in 4 squares with live cells appearing green and dead cells appearing orange under the fluorescent microscope. $CD138^+$ (syndecan-1) cells were isolated from the BMMCs by positive selection using the EasySep™ Human CD138 Positive Selection Kit II (Stemcell Technologies) according to the manufacturer's protocol. The CD138 antigen is expressed on normal and malignant plasma cells but not mature B cells. In brief, 1 x 10^8/mL BMMCs were incubated with tetrameric antibody complexes recognizing CD138 and dextran-coated magnetic particles and separated using an EasySep™ magnet. Purity assessment of CD138+ cells was determined by flow cytometry and all samples were >90% $CD138^+$. $CD138^+$ cells were suspended in 90% FBS containing 10% DMSO and cryopreserved in liquid nitrogen.

When required, an anonymised sample was quickly thawed and resuspended in warm complete RPMI-1640. Cells were then counted as described previously and simultaneously, viability was determined by the trypan blue exclusion assay, whereby, dead cells uptake the trypan blue stain whilst live cells do not. 50 µL of trypan blue was added to 50 µL of cells. 10 µL of the mix was then pipetted onto a haemocytometer and cell viability was determined. 5 x 10^4 cells/well of viable MM cells were seeded into 96 well plates and left to rest for 1 hour at 37°C. MM cells were then treated with various concentrations of VP79s (0.625 – 5 µM) for 24 hours. Following treatment, samples were collected and

stained with annexin V/PI. Samples were then analysed on a BD FACSCanto™ II flow cytometer.

2.12. Data analysis

2.12.1. Densitometry

Densitometric analysis of protein expression on western blots was carried out using the Image Lab programme. This programme compared the density (pixels) of one band with that of another. Lanes on the membrane were defined and a box of equal size was placed around each band to assign an equal area to ensure equal analysis. The programme removes any background automatically. The relative density of each band of interest was calculated against a reference band (vehicle or control). The relative density of the loading control was also calculated, and values were normalised against the loading control.

2.12.2 Statistical analysis

All statistical analysis was performed on GraphPad Prism 5. Results are displayed as the mean ± the standard error of the mean (S.E.M.). For comparisons of more than two groups, a one-way ANOVA followed by Tukey's or Dunnett's multiple comparison tests were performed. For comparisons between two groups a two-tailed paired t-test was performed. Values of *$p<0.05$, **$P<0.01$ and ***$p<0.001$ were considered to be significant.

Chapter 3:
Identification of a novel compound, VP79s, which elicits anti-myeloma activity

3.1 Introduction

The treatment landscape for MM has changed dramatically over the past two decades. Significant advances in our understanding of the disease along with the introduction of novel therapeutics and treatment strategies have nearly doubled overall survival rates [280]. Despite momentous advances in therapeutic approaches to combat MM, prognosis for patients is still very poor [281]. The burden of MM in Europe accounted for around 1.2% of all new cancer diagnoses and 1.6% of all cancer deaths in 2018 [282], and the worldwide incidence of MM has increased by 126% from 1990 to 2016 with the highest occurrences in Western societies [283]. The heterogenous nature of MM suggests that treating MM with a single therapeutic agent is highly unlikely and therefore, it is not surprising that all recently approved therapeutics belong to unique treatment classes including proteasome inhibitors, HDAC inhibitors and mAbs [284-286]. Novel treatment strategies have led to unprecedented responses and progression free survival for many patients [287]. Despite this, patients still frequently relapse following treatment and many receive four or five lines of therapy throughout the duration of their treatments [288].

As previously discussed, for decades MM was treated with an alkylating agent, such as melphalan, in combination with a steroid. Such a combination attained a median survival of 2-3 years at the expense of treatment-related toxicity [289]. The introduction of better treatment strategies, namely ASCT and novel therapeutics have greatly improved the lives of MM patients extending overall survival to between 8-10 years. However, long term progression free survival is still not achieved by the majority [288, 290]. Indeed, it is likely that the forthcoming years will see the introduction of novel drugs and immunotherapies that are desperately needed to enhance the treatment battery [291].

Kinases are involved in the constitutive upregulation of many signalling pathways involved in the pathogenesis of MM, namely, the RAS/RAF, JAK/STAT and PI3K/AKT pathways [49, 134, 292]. The frequency and influence of dysregulated kinase activation in disease and cancer development has led to the design and synthesis of protein kinase inhibitors as novel therapeutic agents [253]; so much so, that the design of novel kinase inhibitors has become one of the most dynamic areas in modern drug discovery [293]. To date, 52 small

molecule protein kinase inhibitors have been approved by the FDA for the treatment of human diseases, six of which are direct targets of the RAS/RAF/MEK/ERK pathway: binimetinib, cobimetinib, trametinib, dabrafenib, encorafenib and vemurafenib. Binimetinib, cobimetinib and trametinib are MEK 1/2 inhibitors while dabrafenib, encorafenib and vemurafenib target BRAF [250]. The RAS/RAF/MEK/ERK kinase cascade is highly conserved and regulates many biological processes from proliferation and differentiation to cell death. Thus, aberrations in the activation of this pathway can lead to disease and cancer. Mutations in RAS genes constitute the most frequently mutated oncogene family in human cancers, with a high frequency of mutations being observed in melanoma, colorectal adenocarcinoma, pancreatic cancer and MM [112, 294]. Therefore, targeting this pathway may be of therapeutic benefit to many cancers. The aforementioned kinase inhibitors have all been approved for the treatment of malignant melanomas where activating BRAF mutations are present in 40-60% of patients [295]. Interestingly, there is a dominant mutation cluster in RAS/RAF genes present in MM [292]. Up to 50% of newly diagnosed MM patients present with mutations in *NRAS, KRAS and HRAS* emphasising that targeting this pathway may be of benefit in the treatment of MM. A recent clinical trial assessing the efficacy of vemurafenib in MM patients with BRAF mutations (NCT01524978) demonstrated an overall response rate of 33%; however, not all patients with BRAF mutations responded [296]. Similarly, a trial investigating BRAF/MEK inhibition with encorafenib in combination with binimetinib in relapsed and refractory MM is currently underway (NCT02834364).

Despite the success of small molecule kinase inhibitors which target the MAPK pathway in other cancers, selectivity and resistance are two of the most prominent challenges affecting drugs currently available and the development of novel inhibitors. As previously described, kinases play a vital role in many physiological functions and processes, therefore, controlled inhibition of specific kinases is essential in avoiding any unwanted off target affects [297].

The Rozas group in the School of Chemistry at Trinity College Dublin have rationally designed and synthesised numerous novel multi-tyrosine kinase inhibitors as potential anti-cancer agents. Previously, the group identified ED73a, as a protein kinase inhibitor

capable of inhibiting BRAF, an isoform of RAF kinase [259, 265]. ED73a exhibited efficacious cytotoxic activity in multiple human cancer cell lines including acute promyelocytic leukaemia HL60 cells [265], breast adenocarcinoma MCF-7 cells, cervical adenocarcinoma HeLa cells and the colorectal carcinoma cell lines, HCT116 cells and HK-2, with IC_{50} values in the low micromolar range suggesting its potential as an anti-cancer agent ([259, 265] and unpublished data).

ED73a shows structural similarities to the kinase inhibitor sorafenib [265]. Sorafenib is a multi-kinase inhibitor that was originally designed to target BRAF [120]. More recently it has been shown to have multiple targets including VEGFR and STAT3 [263]. Preclinical studies have demonstrated that sorafenib induces potent anti-myeloma activity *in vitro* and induces apoptotic cell death in both a murine model and *ex vivo* MM patient samples [298]. However, unlike sorafenib, it was suggested that ED73a worked through a type III allosteric mechanism [265], meaning, the inhibitor would bind to a site outside the ATP-binding site and therefore modulate kinase activity in an allosteric manner. Type III inhibitors are considered to exhibit much more specificity against a particular kinase unlike ATP competitive inhibitors as they are binding to a site that is particular to that specific kinase [297]. Therefore, Type III inhibitors are expected to display little to no off-target effects. Following on from the success of ED73a, the Rozas group synthesised a series of derivatives of ED73a in order to optimise binding to RAF and therefore, inhibition of the RAS/RAF/MEK/ERK pathway.

In this chapter, a series of guanidinium diaryl derivatives were screened in a representative drug-sensitive (NCI-H929) and drug-resistant MM (U266B1) cell lines to determine their anti-myeloma activity. Following this preliminary screen, a lead compound, VP79s, was identified and the anti-myeloma activity of that compound was then determined in a panel of drug-sensitive and drug-resistant MM cell lines. The effects of standard and emerging chemotherapeutic drugs used to treat MM were also tested in the panel of MM cell lines, and results were compared with VP79s. Finally, the effects of VP79s on the cell cycle and its ability to induce apoptotic cell death in the MM cell lines were also examined in order to understand the molecular mechanisms underlying its cytotoxic activity.

3.2. Experimental results

3.2.1. Optimisation of seeding density for the alamar blue assay using a panel of myeloma cell lines

The alamar blue assay was employed to determine the cytotoxic effects of multiple drugs in myeloma cell lines NCI-H929, U266B1, MM1.S and MM1.R. Viable cells metabolise resazurin to resofurin through a reduction reaction which results in a colour change from blue to pink/purple [299]. The alamar blue assay is only quantitative if there is a linear correlation between fluorescence and the cell density in the well. Thus, optimisation of the cell density is required to ensure that cells are within the correct range due to variations in the growth rate of each cell type and their ability to metabolise resofurin.

In order to determine the validity of the assay NCI-H929, U266B1, MM1.S and MM1.R cells were seeded at various densities from 12,500-200,000 cells per well. Cells were left for 72 hours to mimic maximum treatment time, and then 10% (v/v) alamar blue was added to each well. Following a 4 - 5 hour incubation time, fluorescence was read on a SpectraMax Gemini plate reader at an excitation wavelength of 544 nm and emission wavelength of 590 nm. A linear correlation between cell density and fluorescence was observed up to 100,000 cells/well in both the NCI-H929 and U266B1 cells and up to 50,000 cells/well for the MM1.S and MM1.R (Figure 3.1). For subsequent experiments, all myeloma cell lines were seeded at 50,000 cells per well.

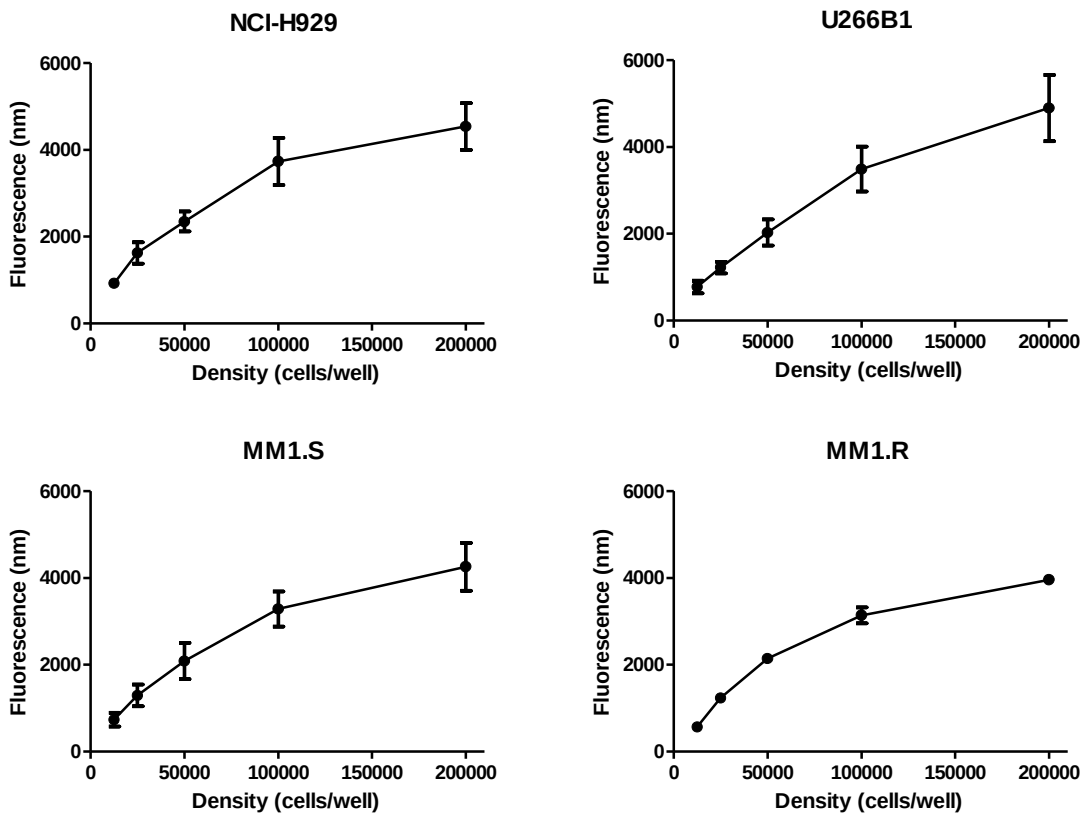

Figure 3. 1 Optimisation of seeding density for the alamar blue assay in a panel of MM cell lines. *Multiple myeloma cell lines (NCI-H929, U266B1, MM1.S and MM1.R) were seeded at various densities (12,500-200,000 cells/well) in 96 well plates with a volume of 200 µL media in each well. Cells were incubated for 72 hours. Following incubation, 10% (v/v) Alamar Blue™ (20 µL) was added to each well. Plates were incubated in the dark for up to 5 hours until a colour change was observed in the vehicle. Fluorescence was measured using the SpectraMax Gemini plate reader with SOFTmax Pro version 4.9 at excitation wavelength 544 nm and an emission wavelength of 590 nm. Results were plotted using GraphPad Prism 5. Results are representative of 3 independent experiments with values representing the mean ± S.E.M.*

3.2.2. A series of novel guanidinium-based compounds reduce the viability of myeloma cell lines in a dose responsive manner

Despite advances in the understanding of the molecular pathogenesis of MM and promising new therapies there is still an unmet need for novel anti-myeloma treatments. The effect of a series of novel guanidinium-based compounds synthesised by the Rozas group in TCD on the viability of two myeloma cell lines was examined. Viability was assessed through the use of the alamar blue viability assay. Initially, the MM cell lines were screened with 2 to 3 concentrations of novel compounds to assess general sensitivity. A lower concentration was used for VP79s (up to 20 μM) as the cell lines appeared more sensitive. Concentrations up to 50 μM were used for the other novel compounds. The myeloma cell lines NCI-H929 and U266B1 were treated with a range of concentrations of the novel compounds ED73a (1.25 – 50 μM), VP79s (0.625 – 20 μM), VPED_1 (1.25 – 50 μM) and FR13b (1.25 – 50 μM) for 72 hours. Typically, the NCI-H929 cell line is considered to be more drug susceptible while the U266B1 cell line is considered to be more drug resistant [49, 273].

Both ED73a and VP79s decreased the viability of myeloma cell lines in a dose-dependent manner. The IC_{50} values of 3.3 ± 0.2 μM and 3.9 ± 0.4 μM in NCI-H929 and U266B1 cells respectively were obtained following treatment with VP79s (Figure 3.2, Table 3.1). ED73a also reduced the viability of the myeloma cell lines in a dose-dependent manner (Figure 3.2). The IC_{50} values obtained for the NCI-H929 and U266B1 were 4.4 ± 0.5 μM and 17.5 ± 2.1 μM respectively (Figure 3.2, Table 3.1), demonstrating that the U266B1 cell line appears to be more resistant to ED73a.

Both VPED_1 and FR13b reduced the viability of the NCI-H929 cell line in a dose-dependent manner with IC_{50} values of 11.5 ± 1 μM and 14.9 ± 1.7 μM obtained respectively. The U266B1 cell line showed resistance to both VPED_1 and FR13b with minimal effects on viability visible up to 50 μM (Figure 3.3, Table 3.1).

From this preliminary screen VP79s was identified as the lead compound as it exhibited the most potent effects in both cell lines tested (Table 3.1).

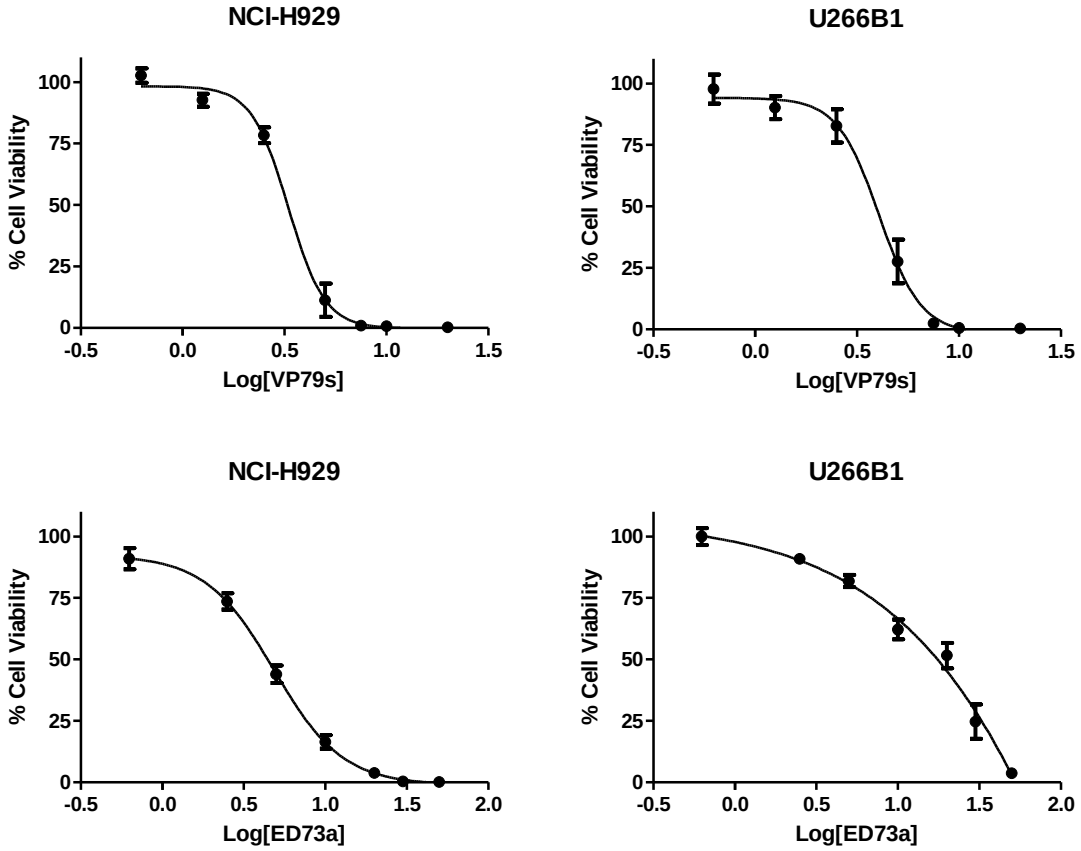

Figure 3. 2 VP79s and ED73a reduce the viability of myeloma cell lines

Myeloma cell lines NCI-H929 and U266B1 were seeded at 5x10^4 cells/well in 96 well plates. Cells were treated with a vehicle (0.5% (v/v) ethanol) or a range of concentrations of VP79s (0.625 – 20 µM) or ED73a (0.625 – 50 µM). After 72 hours 10% alamar blue (v/v) was added to each well. Plates were incubated in the dark for up to 5 hours until a colour change was observed in the vehicle. Fluorescence was measured using a SpectraMax Gemini plate reader at excitation wavelength 544 nm and emission wavelength 590. Values represent the mean ± S.E.M of four independent experiments for VP79s and three independent experiments for ED73a.

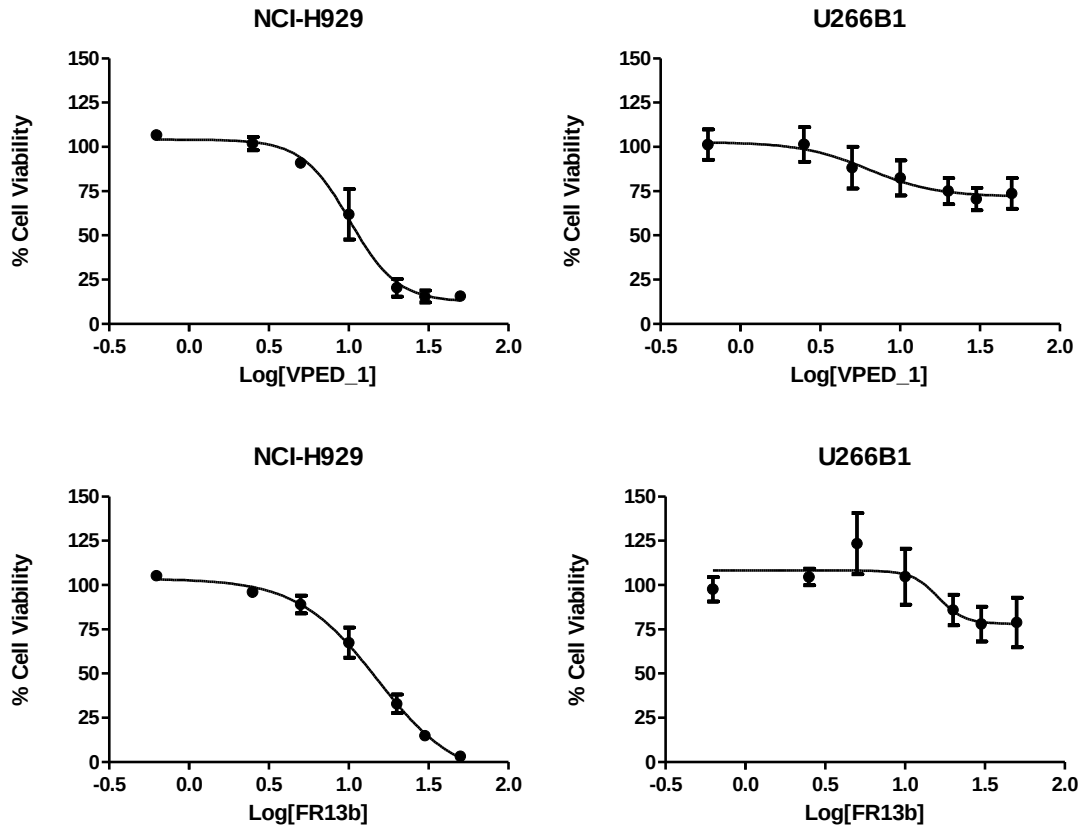

Figure 3. 3 VPED_1 and FR13b reduce the viability of myeloma cell lines.

Myeloma cell lines NCI-H929 and U266B1 were seeded at 5x10^4 cells/well in 96 well plates. Cells were treated with a vehicle (0.5% (v/v) ethanol) or a range of concentrations of VPED_1 (0.625 – 50 µM) or FR13b (0.625 – 50 µM). After 72 hours 10% alamar blue (v/v) was added to each well. Plates were incubated in the dark for up to 5 hours until a colour change was observed in the vehicle. Fluorescence was measured using a SpectraMax Gemini plate reader at excitation wavelength 544 nm and emission wavelength 590. Values represent the mean ± S.E.M of three independent experiments.

Compound	IC_{50} (μM)	
	NCI-H929	**U266B1**
VP79s	3.3 ± 0.2	3.9 ± 0.4
ED73a	4.4 ± 0.5	17.5 ± 2.1
VPED_1	11.5 ± 1.0	> 50
FR13b	14.9 ± 1.7	> 50

Table 3. 1 IC_{50} values for a series of guanidinium-based compounds in NCI-H929 and U266B1 cells.

IC_{50} values were calculated by plotting the mean percentage viability at each drug concentration relative to the vehicle of three independent experiments. The graph was then transformed to logarithmic values and the IC_{50} value was extrapolated from the graph as the concentration which caused a 50% reduction in cell viability.

3.2.3. VP79s reduces the viability of a panel of myeloma cell lines in a time-dependent manner

VP79s was identified as the lead compound warranting further studies. The alamar blue viability assay was again utilised to evaluate the anti-myeloma activity of VP79s in a panel of myeloma cell lines over various time points. The MM1.S and MM1.R cell lines are a paired cell line which exhibit dexamethasone susceptibility (MM1.S) and resistance (MM1.R) [269]. Therefore, this panel of myeloma cells contains two drug susceptible cell lines, MM1.S and NCI-H929 and two drug resistant cell lines, MM1.R and U266B1 cells.

NCI-H929, U266B1, MM1.S and MM1.R cells were treated with a range of concentrations VP79s (0.625 – 20 µM) for 24, 48 and 72 hours. VP79s reduced the viability of myeloma cell lines in a dose- and time-dependent manner (Figure 3.4). The IC_{50} values obtained were all in the low micromolar range with effects on viability observed as early as 24 hours. The NCI-H929 cell line appeared to be the most sensitive at 24 hours, however, there were no statistical differences observed in the IC_{50} values obtained in drug-sensitive versus drug-resistant cell lines with IC_{50} values ranging 3.3 to 4 µM at the later 72 hour timepoint.

These results warranted further study into the mechanistic action by which VP79s elicits a reduction in cell viability.

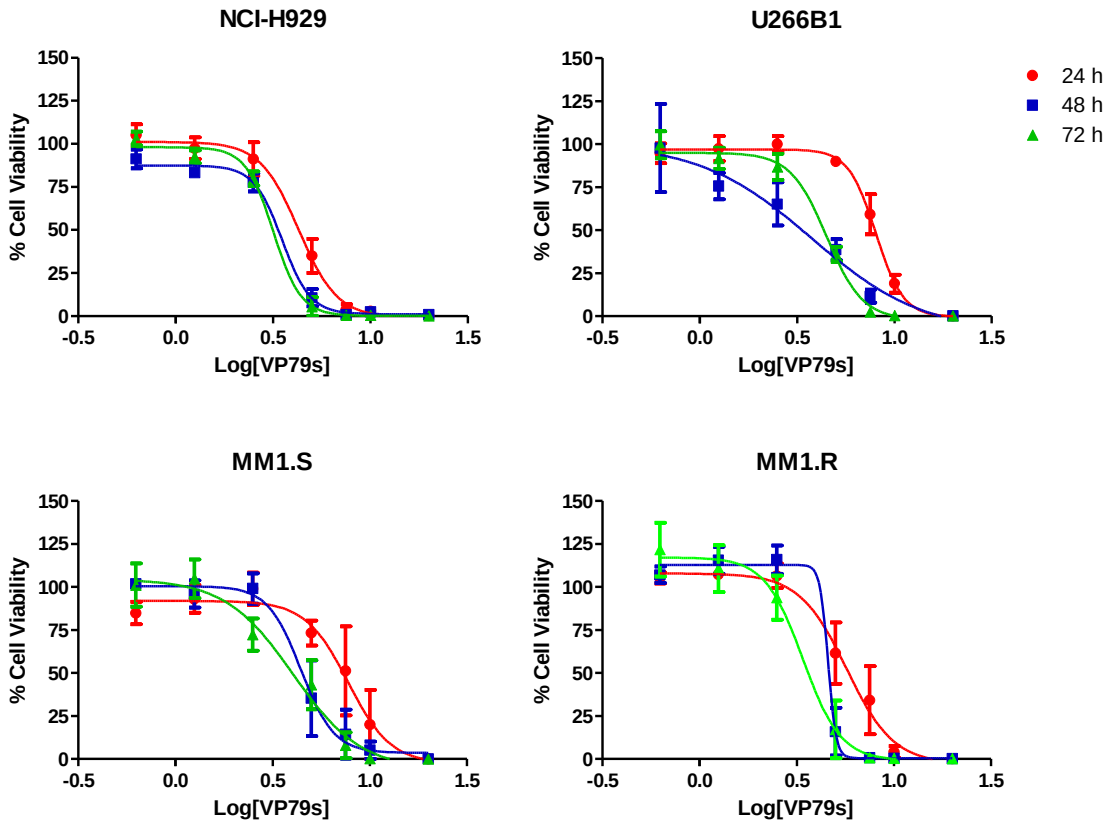

Timepoint	NCI-H929	U266B1	MM1.S	MM1.R
24 h	4.3 ± 0.5 µM	7.7 ± 0.9 µM	7.3 ± 1.4 µM	6.3 ± 0.7 µM
48 h	3.4 ± 0.2 µM	3.8 ± 0.7 µM	4.9 ± 0.7 µM	4.3 ± 0.3 µM
72 h	3.3 ± 0.2 µM	3.9 ± 0.4 µM	4.0 ± 1 µM	3.6 ± 0.7 µM

Figure 3. 4 VP79s reduces the viability of a panel of myeloma cell lines.

MM1.S and MM1.R cells were seeded at 5x10^4 cells/well in 96 well plates and left overnight to adhere. NCI-H929 and U266B1 cells were seeded at 5x10^4 cells/well on the day. Cells were treated with vehicle (0.5% (v/v) ethanol) or a range of concentrations of VP79s (0.625 – 20 µM). After 24, 48 or 72 hours 10% alamar blue (v/v) was added to each well. Plates were incubated in the dark for up to 5 hours until a colour change was observed in the vehicle. Fluorescence was measured using a SpectraMax Gemini plate reader at excitation wavelength 544 nm and emission wavelength 590. IC_{50} values represent the mean ± S.E.M of three independent experiments.

3.2.4. The effect of dexamethasone, lenalidomide, venetoclax, ruxolitinib and bortezomib on the viability of myeloma cell lines

The alamar blue viability assay was next utilised to assess the anti-myeloma activity of dexamethasone, lenalidomide, venetoclax, ruxolitinib and bortezomib in MM cell lines and to determine how the IC_{50} values compared to those obtained with VP79s. Dexamethasone, lenalidomide and bortezomib represent standard chemotherapeutics used for the treatment of MM whilst venetoclax and ruxolitinib are drugs which have shown preclinical efficacy in the treatment of MM [31, 300].

The cytotoxic effects of dexamethasone on the dexamethasone-sensitive cell line MM1.S and dexamethasone-resistant cell line MM1.R as well as the NCI-H929 and U266B1 cells was next determined utilising the alamar blue viability assay. Cells were treated with various concentrations of dexamethasone (31.25 – 2000 nM) for 72 hours (Figure 3.5 and Table 3.2). As expected, the MM1.S cell line was susceptible to dexamethasone with an IC_{50} value of 52.4 ± 10 nM. In accordance with reports in the literature, the MM1.R cell line was found to be completely dexamethasone resistant up to 2000 nM [269]. IC_{50} values could not be determined for NCI-H929 and U266B1 cell lines. The U266B1 cell line was completely dexamethasone-resistant while the NCI-H929 cell line exhibited only a 20% decrease in viability at the highest concentration tested.

Similarly, IC_{50} values could not be determined across all myeloma cell lines treated with lenalidomide (1.25 – 10 μM) for 72 hours (Figure 3.6 and Table 3.2). Lenalidomide caused around a 40% decrease in viability in the NCI-H929, MM1.R and MM1.S cell lines. The U266B1 cell line appeared to be completely lenalidomide resistant up to the top concentration tested of 10 μM.

Venetoclax induced potent anti-myeloma activity in three of the four cell lines tested with IC_{50} values in the low micromolar range of 4.76 ± 0.78 μM for the NCI-H929 cell line, 6.76 ± 0.23 μM for the MM1.S cell line and 6.5 ± 0.25 μM for the MM1.R cell line (Figure 3.7 and Table 3.2). The IC_{50} value for the U266B1 cell line appeared to be greater than 10 μM following treatment for 72 hours.

Ruxolitinib reduced the viability of all four cell lines in a dose-responsive manner following treatment for 72 hours, with the NCI-H929 cells exhibiting the lowest IC_{50} value at 11.5 ± 5

μM. Similar IC_{50} values within error were obtained in the U266B1, MM1.S and MM1.R cell lines (Figure 3.8 and Table 3.2).

In the case of bortezomib treatment, the panel of cell lines were treated for 24 hours. Bortezomib induced similar IC_{50} values in the low nanomolar range at 2.8 ± 0.55 nM and 2.7 ± 0.36 nM in the MM1.S and MM1.R respectively (Figure 3.9 and Table 3.2). The NCI-H929 cell line were the most sensitive with an IC_{50} value of 1.54 ± 0.2 nM while the U266B1 cell line appeared to be completely resistant up to 100 nM at 24 hours. The result obtained with the U266B1 cell line appeared to be in conflict with reports in the literature [301, 302]. This could be due to a different assay being used as the two cited reports above used the XTT and WST-1 viability assays respectively to assay the effect of bortezomib on U266B1 cells. Therefore, in order to validate the results of the alamar blue assay, U266B1 cells were treated with bortezomib and cell viability was analysed using the alamar blue assay and annexin V/PI staining on the same day. These results demonstrated that whilst the alamar blue assay had shown no decrease in cell viability, almost 50% of the U266B1 cells were early apoptotic at all concentrations tested (Appendix Figure 1).

In conclusion, results obtained with VP79s compared very favourably with those obtained with small molecules or drugs currently in use in MM or in development. VP79s equipotently reduced the viability of both drug-resistant and -sensitive cell lines examined with no resistance observed. This is in contrast to some of the other compounds tested such as venetoclax (Table 3.2).

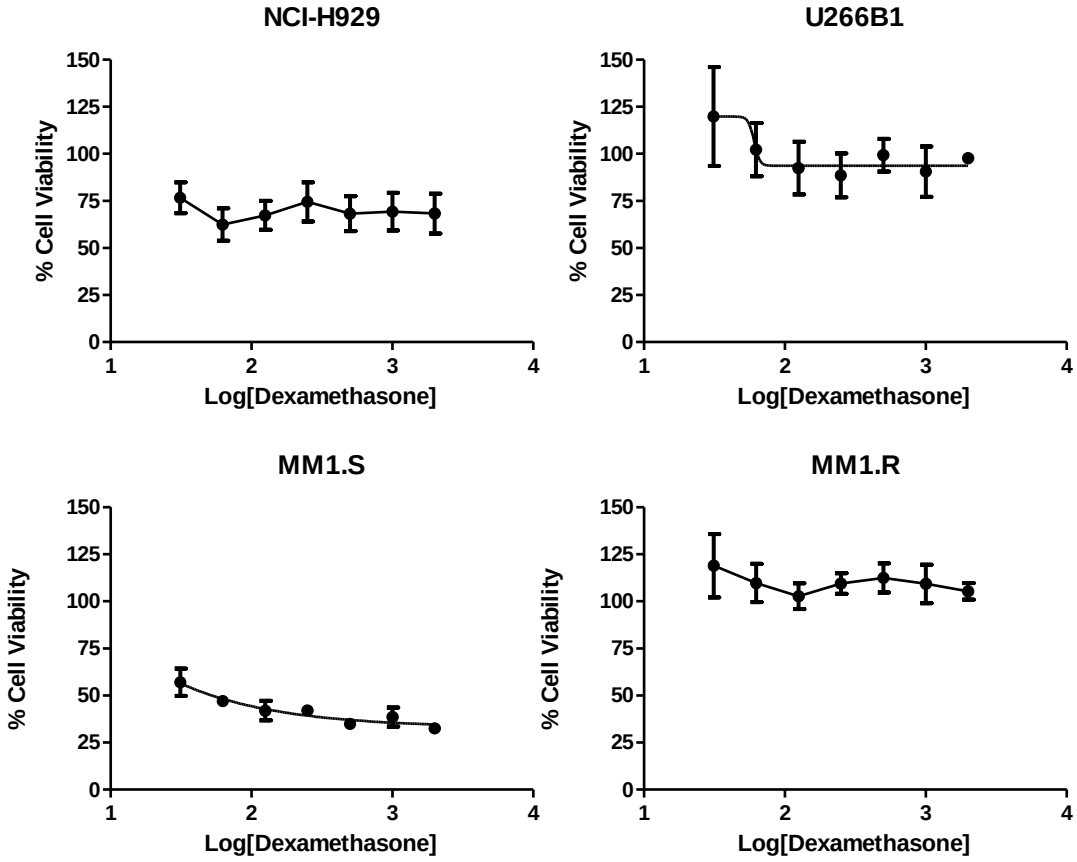

Figure 3. 5 Effect of dexamethasone on the viability of a panel of myeloma cell lines.

Myeloma cell lines NCI-H929, U266B1, MM1.S and MM1.R were seeded at 5x10^4 cells/well in 96 well plates. Cells were treated with vehicle [0.5% EtOH (v/v)] or a range of concentrations of dexamethasone (31.25 – 2000 nM). After 72 hours 10% alamar blue (v/v) was added to each well. Plates were incubated in the dark for up to 5 hours until a colour change was observed in the vehicle. Fluorescence was measured using a SpectraMax Gemini plate reader at excitation wavelength 544 nm and emission wavelength 590. IC_{50} values represent the mean ± S.E.M of three independent experiments.

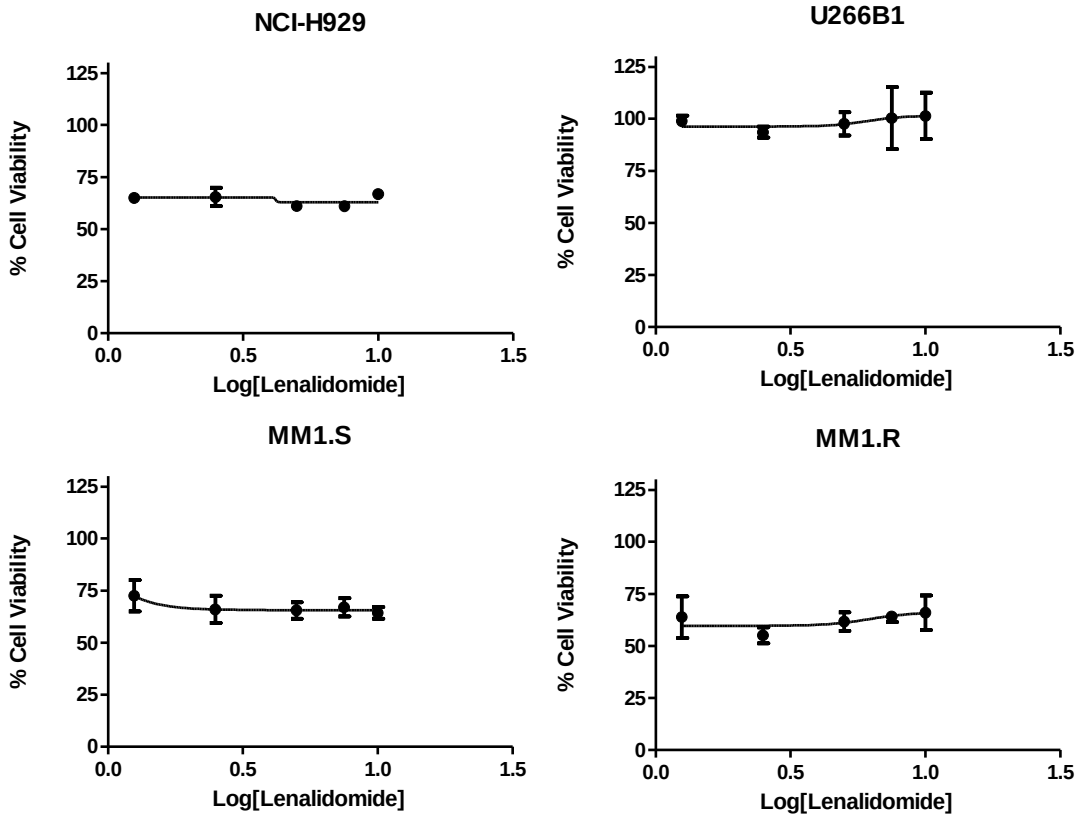

Figure 3. 6 Effect of lenalidomide on the viability of a panel of myeloma cell lines.

Myeloma cell lines NCI-H929, U266B1, MM1.S and MM1.R were seeded at 5x10^4 cells/well in 96 well plates. Cells were treated with vehicle [0.1% DMSO (v/v)] or a range of concentrations of lenalidomide (1.25 – 10 µM) for MM1.S, MM1.R, U266B1 and NCI-H929. After 72 hours 10% alamar blue (v/v) was added to each well. Plates were incubated in the dark for up to 5 hours until a colour change was observed in the vehicle. Fluorescence was measured using a SpectraMax Gemini plate reader at excitation wavelength 544 nm and emission wavelength 590. Values represent the mean ± S.E.M of three independent experiments for MM1.S, MM1.R and U266B1 and the mean ± range of two independent experiments for NCI-H929.

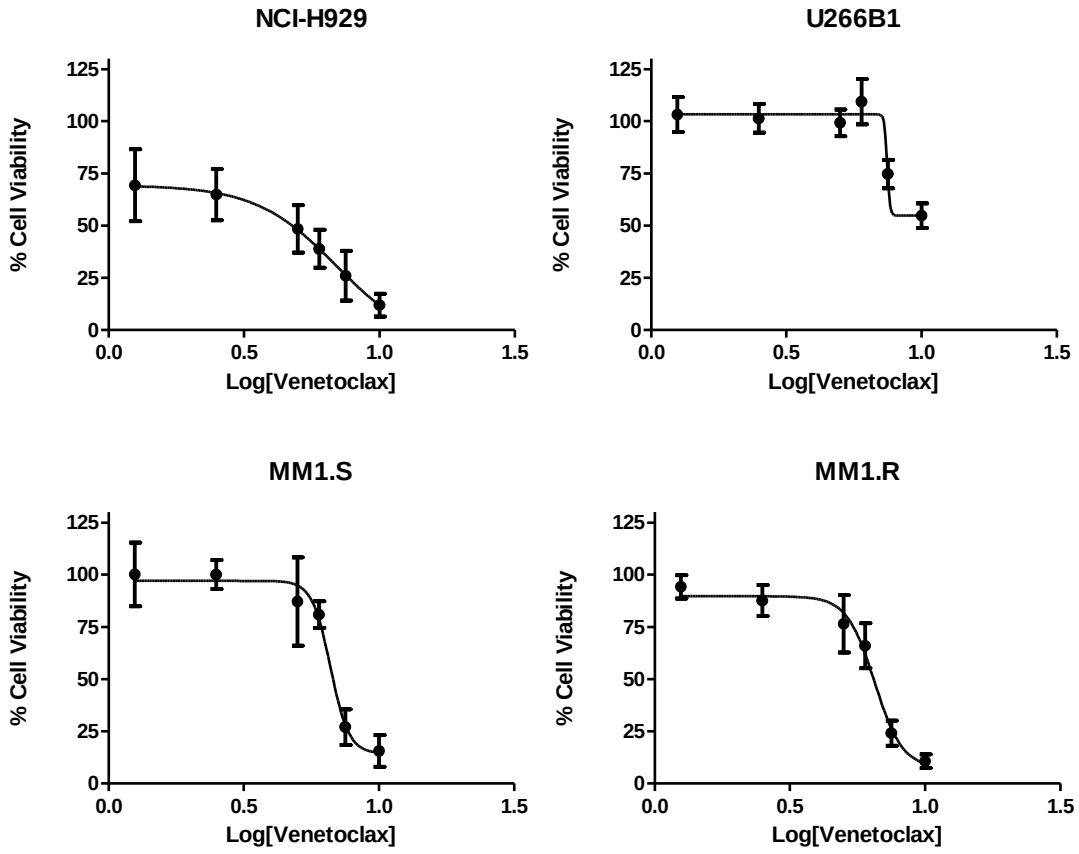

Figure 3. 7 Effect of venetoclax on the viability of a panel of myeloma cell lines.

MM1.S and MM1.R cells were seeded at 5x10^4 cells/well in 96 well plates and left overnight to adhere. NCI-H929 and U266B1 cells were seeded at 5x10^4 cells/well on the day. Cells were treated with vehicle [0.5% DMSO (v/v)] or a range of concentrations of venetoclax (1.25 – 10 µM). After 72 hours 10% alamar blue (v/v) was added to each well. Plates were incubated in the dark for up to 5 hours until a colour change was observed in the vehicle. Fluorescence was measured using a SpectraMax Gemini plate reader at excitation wavelength 544 nm and emission wavelength 590. Values represent the mean ± S.E.M of three independent experiments.

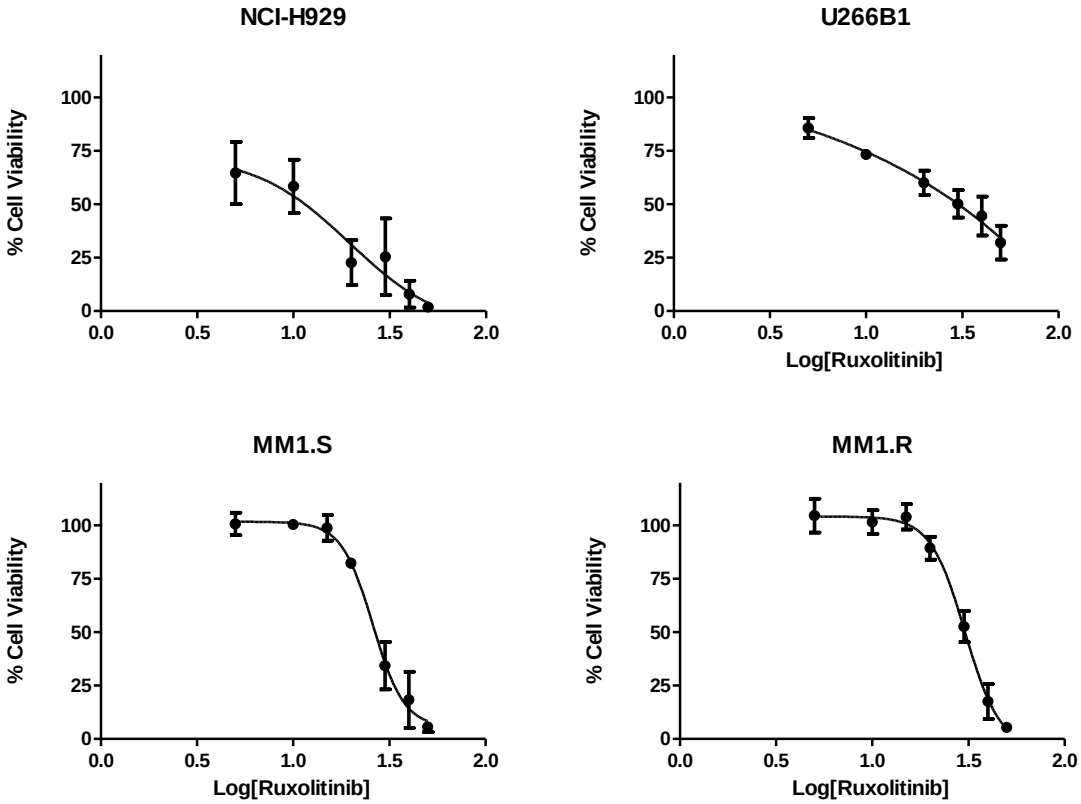

Figure 3. 8 Effect of ruxolitinib on the viability of a panel of myeloma cell lines.

MM1.S and MM1.R cells were seeded at 5x10^4 cells/well in 96 well plates and left overnight to adhere. NCI-H929 and U266B1 cells were seeded at 5x10^4 cells/well on the day. Cells were treated with vehicle [0.5% DMSO (v/v)] or a range of concentrations of ruxolitinib (5 – 50 µM). After 72 hours 10% alamar blue (v/v) was added to each well. Plates were incubated in the dark for up to 5 hours until a colour change was observed in the vehicle. Fluorescence was measured using a SpectraMax Gemini plate reader at excitation wavelength 544 nm and emission wavelength 590. Values represent the mean ± S.E.M of three independent experiments for NCI-H929, MM1.S and MM1.R and four independent experiments for U266B1.

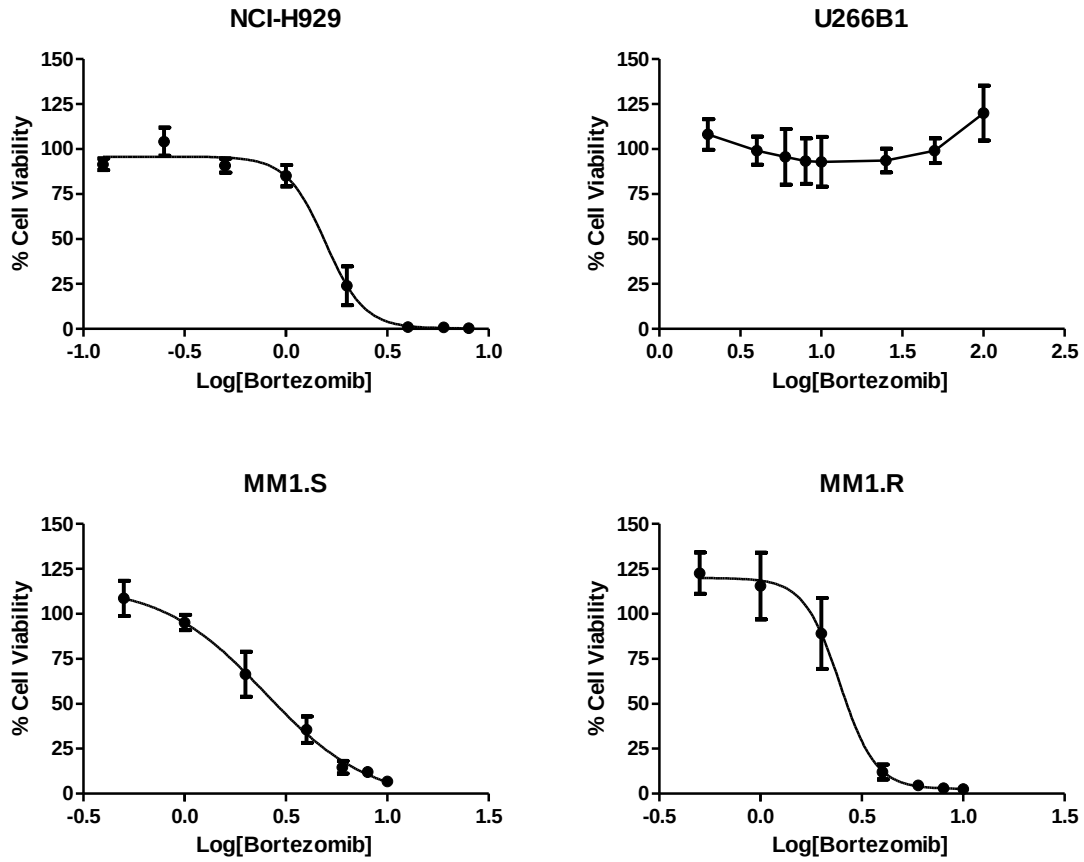

Figure 3. 9 Effect of bortezomib on the viability of a panel of myeloma cell lines.

MM1.S and MM1.R cells were seeded at 5x10^4 cells/well in 96 well plates and left overnight to adhere. NCI-H929 and U266B1 cells were seeded at 5x10^4 cells/well on the day. Cells were treated with vehicle [0.1% DMSO (v/v)] or a range of concentrations of bortezomib (0.125 – 8 nM) for NCI-H929 cells, (2 – 100 nM) for U266B1 cells and (0.5 – 10 nM) for MM1.S and MM1.R cells. After 24 hours 10% alamar blue (v/v) was added to each well. Plates were incubated in the dark for up to 5 hours until a colour change was observed in the vehicle. Fluorescence was measured using a SpectraMax Gemini plate reader at excitation wavelength 544 nm and emission wavelength 590. Values represent the mean ± S.E.M of three independent experiments.

Compound	NCI-H929	U266B1	MM1.S	MM1.R
VP79s	3.3 ± 0.2 μM	3.9 ± 0.4 μM	4.0 ± 1 μM	3.6 ± 0.7 μM
Dexamethasone	>2 μM	>2 μM	0.05 ± 0.01 μM	>2 μM
Lenalidomide	>10 μM	>10 μM	>10 μM	>10 μM
Venetoclax	4.8 ± 0.8 μM	>10 μM	6.8 ± 0.2 μM	6.5 ± 0.3 μM
Ruxolitinib	11.5 ± 5.0 μM	30.1 ± 3.9 μM	28.2 ± 3.2 μM	30.8 ± 2.1 μM
Bortezomib	1.54 ± 0.2 nM	> 100 nM	2.8 ± 0.6 nM	2.7 ± 0.4 nM

Table 3. 2 IC_{50} values of VP79s and standard/emerging myeloma therapeutics in a panel of myeloma cell lines.

3.2.5. The effect of VP79s treatment on the cell cycle of NCI-H929 and U266B1 cells

Results from the alamar blue assays showed a decrease in cell viability following treatment of MM cells with novel compound VP79s. It was then necessary to determine whether the observed decrease in cellular viability was due to cell cycle arrest, cell death or a combination of both. Flow cytometric analysis of PI stained cells was therefore employed.

The ability of VP79s to induce cell cycle arrest was determined by flow cytometric analysis of the G1, S, G2/M and sub G1/G0 peaks of PI stained cells. No increase in the percentage of cells in G1, S or G2/M was observed indicating that VP79s does not induce cell cycle arrest. However, there was an observable increase in the percentage of cells in sub G1/G0 indicative of cell death from as early as 8 hours, however, this was not statistically significant until 24 hours post treatment in both cell lines. For example, in the NCI-H929 cells at the 24 hour timepoint following VP79s treatment approximately 33.1% of cells were found in the sub G1/G0 peak in comparison to vehicle treated cells where only 4.3% of cells were found in the sub G1/G0 peak (Figure 3.10). The percentage of cells in sub G1/G0 increased with time following VP79s treatment reaching a maximum of 58.3% in NCI-H929 cells and 53.4% in U266B1 cells at 72 hours (Figure 3.11). The increase in the percentage of cells in sub G1/G0 was concomitant with a statistically significant decrease in cells in G1 and G2/M phases, most notably in G1 in both the NCI-H929 and U266B1 cells (Table 3.3).

Next in order to determine the concentration at which VP79s first elicits cell death U266B1 cells were treated with a range of concentrations of the compound (1.25-10 μM) for 16 hours. As observed from Figure 3.12, VP79s induced an increase in the percentage of cells in sub G1/G0 indicative of cell death in a dose-responsive manner with effects first observed at 5 μM however, this was not significant until 10 μM. No statistical differences were observed in G1, S or G2/M phases. These results suggested that VP79s induced apoptotic and/or necrotic cell death justifying further flow cytometric analysis with annexin V/PI staining.

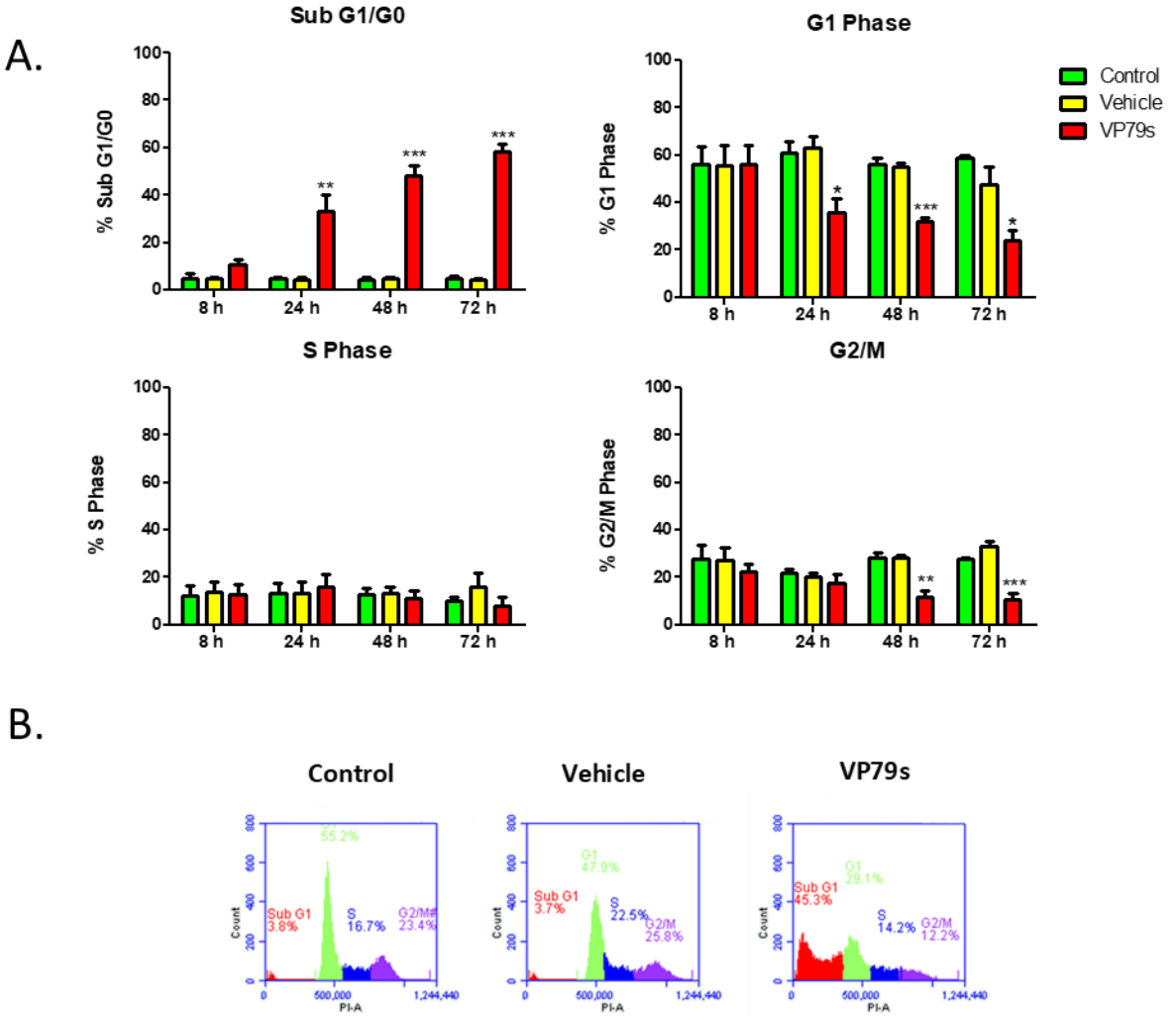

Figure 3. 10 The effect of VP79s on the DNA profile of NCI-H929 cells.

NCI-H929 cells were seeded at 30x10^4 cells/mL in 12 well plates. Cells were left untreated (control) or treated with a vehicle [0.5% EtOH (v/v)] or 10 µM VP79s for 8, 24, 48 and 72 hours. Following the appropriate incubation time cells were harvested and fixed with 70% ethanol and stained with propidium iodide. Cells were analysed by flow cytometry using BD Accuri™ C6 software. 10,000 single cells were gated on control and vehicle treated cells and the percentage of cells in sub G1/G0 peak was determined by quantification of DNA content. ***A.*** *Values represent the mean ± S.E.M of three independent experiments. Statistical analysis was performed using one-way ANOVA with Tukey's post hoc test comparing vehicle to treatment. *p< 0.05, ** p<0.01.and ***p< 0.001* ***B.*** *Representative DNA profile of treatments at 48 hours.*

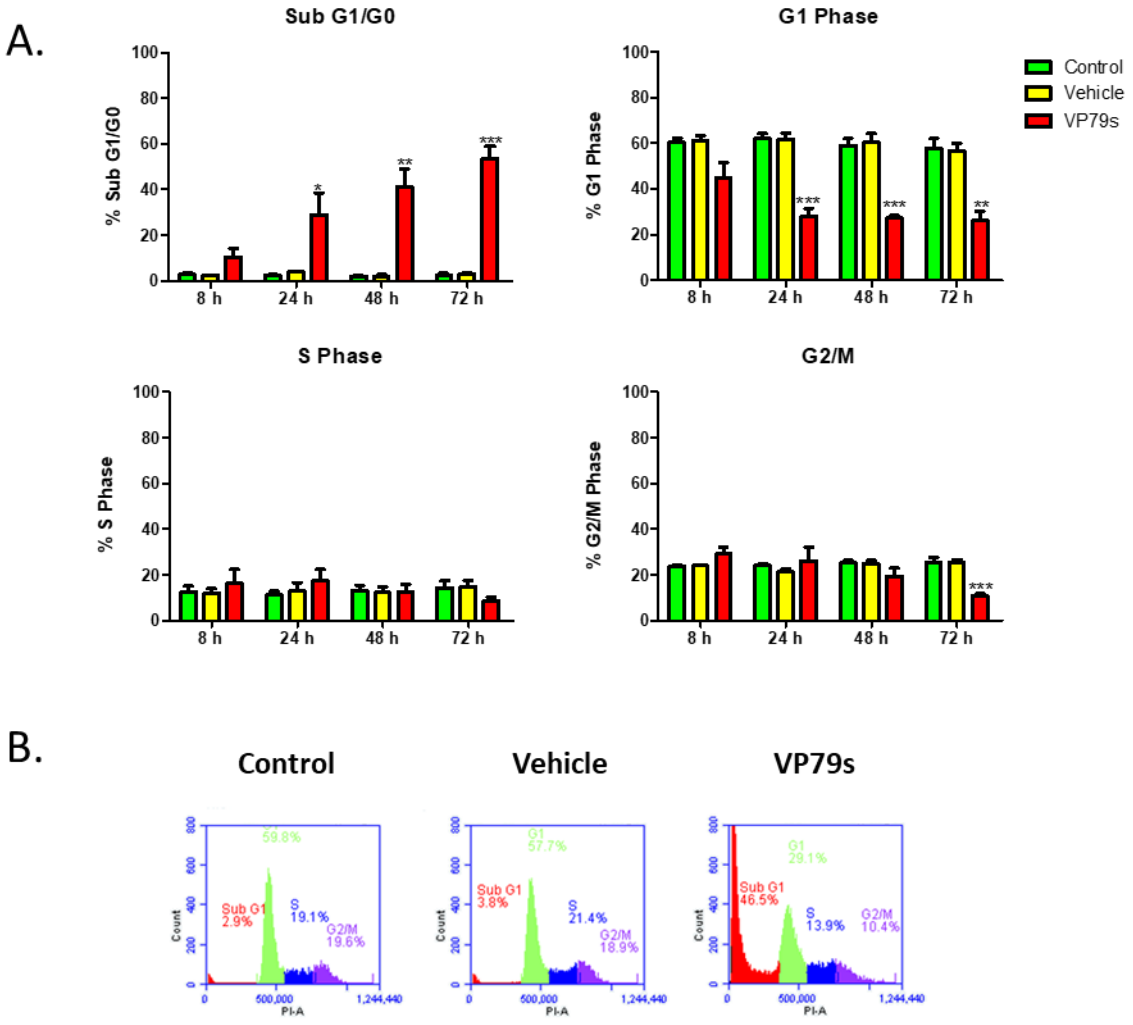

Figure 3. 11 The effect of VP79s on the DNA profile of U266B1 cells.

U266B1 cells were seeded at 30x10^4 cells/mL in 12 well plates. Cells were left untreated (control) or treated with a vehicle [0.5% EtOH (v/v)] or 10 µM VP79s for 8, 24, 48 and 72 hours. Following the appropriate incubation time cells were harvested and fixed with 70% ethanol and stained with propidium iodide. Cells were analysed by flow cytometry using BD Accuri™ C6 software. 10,000 single cells were gated on control and vehicle treated cells and the percentage of cells in sub G1/G0 peak was determined by quantification of DNA content. ***A.*** *Values represent the mean ± S.E.M of three independent experiments. Statistical analysis was performed using one-way ANOVA with Tukey's post hoc test comparing vehicle to treatment. *p< 0.05, ** p<0.01, ***p<0.001.* ***B.*** *Representative DNA profile of treatments at 48 hours.*

	NCI-H929				U266B1			
8 hours								
	Sub G1/G0	**G1**	**S**	**G2/M**	**Sub G1/G0**	**G1**	**S**	**G2/M**
Control	5.03 ± 1.8	56.3 ± 7.5	12.8 ± 4	27.5 ± 5.8	2.8 ± 0.6	60.2 ± 2.3	12.5 ± 2.6	23.6 ± 0.6
Vehicle	4.8 ± 0.8	55.3 ± 9.1	13.5 ± 4.4	27 ± 5.4	2.4 ± 0.3	60.9 ± 2.3	12 ± 1.9	24 ± 0.4
VP79s	10.5 ± 2.3	55.8 ± 8.3	3.9 ± 4.7	22.2 ± 3.4	10.5 ± 3.8	44.9 ± 6.5	16.2 ± 6	29.1 ± 2.9
24 hours								
	Sub G1/G0	**G1**	**S**	**G2/M**	**Sub G1/G0**	**G1**	**S**	**G2/M**
Control	4.7 ± 0.9	60.9 ± 4.8	13.3 ± 4.2	21.9 ± 1.5	2.6 ± 0.4	62.1 ± 2.1	11.2 ± 1.8	24 ± 0.8
Vehicle	4.3 ± 1.1	63 ± 4.7	13.3 ± 4.6	20.2 ± 1.8	4 ± 0.1	61.7 ± 2.7	13.1 ± 3.6	21.3 ± 1.3
VP79s	33.1 ± 7	35.4 ± 6	15.7 ± 5.3	17.5 ± 3.7	29.2 ± 9.4	27.8 ± 3.5	17.3 ± 5	26.2 ± 6
48 hours								
	Sub G1/G0	**G1**	**S**	**G2/M**	**Sub G1/G0**	**G1**	**S**	**G2/M**
Control	4.1 ± 1.3	55.7 ± 3	12.6 ± 2.9	28.4 ± 1.7	2.2 ± 0.4	59.1 ± 3.1	13.1 ± 2.3	25.4 ± 1.2
Vehicle	4.6 ± 1	54.9 ± 1.6	12.9 ± 2.9	28.4 ± 0.8	2.2 ± 0.6	60.5 ± 3.8	12.2 ± 2.7	24.9 ± 1.5
VP79s	48 ± 4.25	31.8 ± 2.1	10.9 ± 3.4	11.8 ± 2.5	41.2 ± 7.8	27.4 ± 1.1	12.5 ± 3.4	19.4 ± 3.6
72 hours								
	Sub G1/G0	**G1**	**S**	**G2/M**	**Sub G1/G0**	**G1**	**S**	**G2/M**
Control	4.5 ± 1.2	58.7 ± 0.8	9.7 ± 1.9	27.7 ± 0.5	2.7 ± 0.6	57.7 ± 4.4	14.3 ± 3.1	25.5 ± 2
Vehicle	4.4 ± 0.6	47.7 ± 7	15.7 ± 5.9	32.9 ± 2	3 ± 0.6	56.8 ± 3.2	14.8 ± 2.6	25.6 ± 1.1
VP79s	58.3 ± 3.3	23.7 ± 4.8	8 ± 3.4	10.6 ± 2.6	53.4 ± 5.4	26.2 ± 3.8	8.6 ± 1.8	10.9 ± 0.9

Table 3. 3 Analysis of cell cycle profile of NCI-H929 and U266B1 cells treated with VP79s – percentage of cells in sub G1/G0, G1, S and G2/M peaks.

Values represent the mean ±S.E.M of three independent experiments.

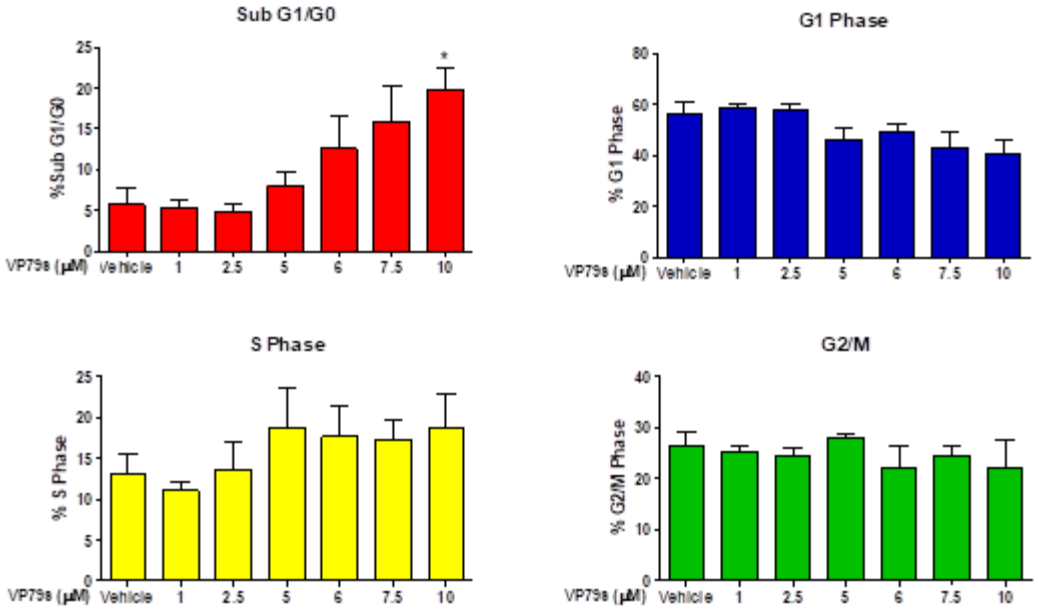

Figure 3. 12 VP79s induces cell death in U266B1 cells in a dose-responsive manner.

*U266B1 cells were seeded at 30x10^{4} cells/mL in 12 well plates. Cells were treated with either vehicle [0.5% EtOH (v/v)] or various concentrations of VP79s (1-10 µM) for 16 hours. Cells were harvested and fixed with 70% ethanol and stained with propidium iodide. Cells were analysed by flow cytometry using BD Accuri™ C6 software. 10,000 single cells were gated on vehicle treated cells and the percentage of Sub G1/G0, G1 phase, S phase and G2/M phase cells was determined by quantification of DNA content. Values represent the mean ±S.E.M of three independent experiments. Statistical analysis was performed using one-way ANOVA with Dunnett's post hoc test comparing vehicle to treatment. *p< 0.05.*

3.2.6. VP79s induces apoptotic cell death in a panel of myeloma cell lines

Cell death was further analysed by flow cytometric analysis of annexin V/PI stained cells. Utilisation of this method allows for the identification of apoptosis. Viable cells exclude both annexin V and PI (lower left quadrant), early apoptotic cells exclude PI (lower right quadrant) and late apoptotic/necrotic cells stain positive for both (upper right quadrant) [303]. An observable increase in early and late apoptosis was detected in all cell lines from concentrations of 5 µM VP79s however, cell death was not significant until 7.5 µM.

In the case of NCI-H929 cells, VP79s (1.25 - 10µM) induced apoptosis in a dose-dependent manner with significant apoptosis observed at the two highest concentrations tested (Figure 3.13 A). A concentration of 7.5 µM resulted in over 50% of cells undergoing apoptosis while at 10 µM over 80% of cells had succumbed (Figure 3.13 B). More apoptosis was detected by the annexin V/PI staining than PI staining alone (Figure 3.11). This may be due the PI staining only detecting late apoptotic or necrotic cells whilst annexin V/PI staining detects early phosphatidylserine exposure and is considered to be more sensitive. It has been reported that PI staining cannot be used to quantify the exact percentage of cells undergoing apoptosis. Rather, it is an indication of apoptosis as apoptotic cells do not always have distinctly lower DNA content [69]. Similarly, VP79s induced apoptotic cell death in the U266B1 cell line in a dose-dependent manner. Again, significant apoptosis was observed at the 7.5 µM and 10 µM treatments with 36.8% and 49.8% apoptosis induced respectively (Figure 3.14 B). The overall percentage of cells undergoing apoptosis was somewhat reduced when compared to the NCI-H929 cells.

Likewise, VP79s induced apoptotic cell death in both the MM1.S and MM1.R cell lines in a dose-dependent manner with significant apoptosis observed at the higher concentrations of 7.5 µM and 10 µM (Figure 3.15 B and Figure 3.16 B). These results correlate with alamar blue viability assay and cell cycle analysis results.

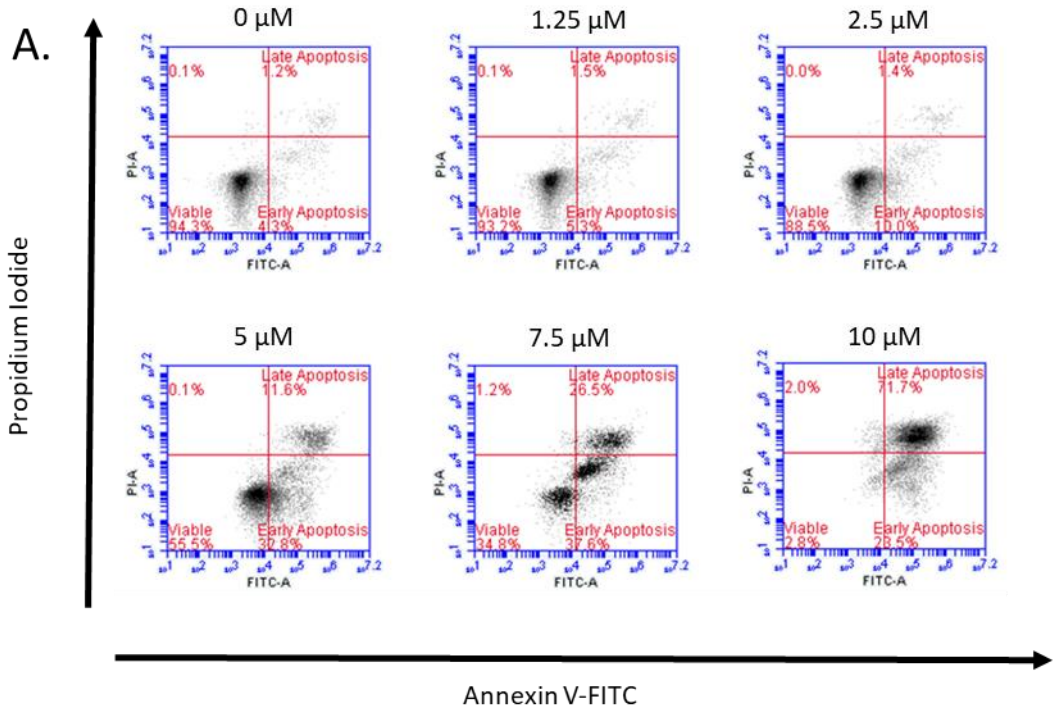

Figure 3. 13 VP79s induces apoptosis in a dose-dependent manner in NCI-H929 cells.

NCI-H929 cells were seeded at a density of 30x10^4 cells/mL and were treated with either vehicle control [0.5% EtOH (v/v)] or various concentrations of VP79s (1.25-10 µM) for 24 hours. After incubation cells were harvested and stained with annexin V/propidium iodide (PI) and were analysed by flow cytometry using BD Accuri™ C6 software. 10,000 cells were gated on vehicle treated cells. ***A.*** *Representative dot plot of treated samples.* ***B.*** *Values represent the mean ± S.E.M. of three independent experiments. Statistical analysis was performed using one-way ANOVA with Dunnett's multiple comparisons test comparing vehicle to treatments. *** p< 0.001.*

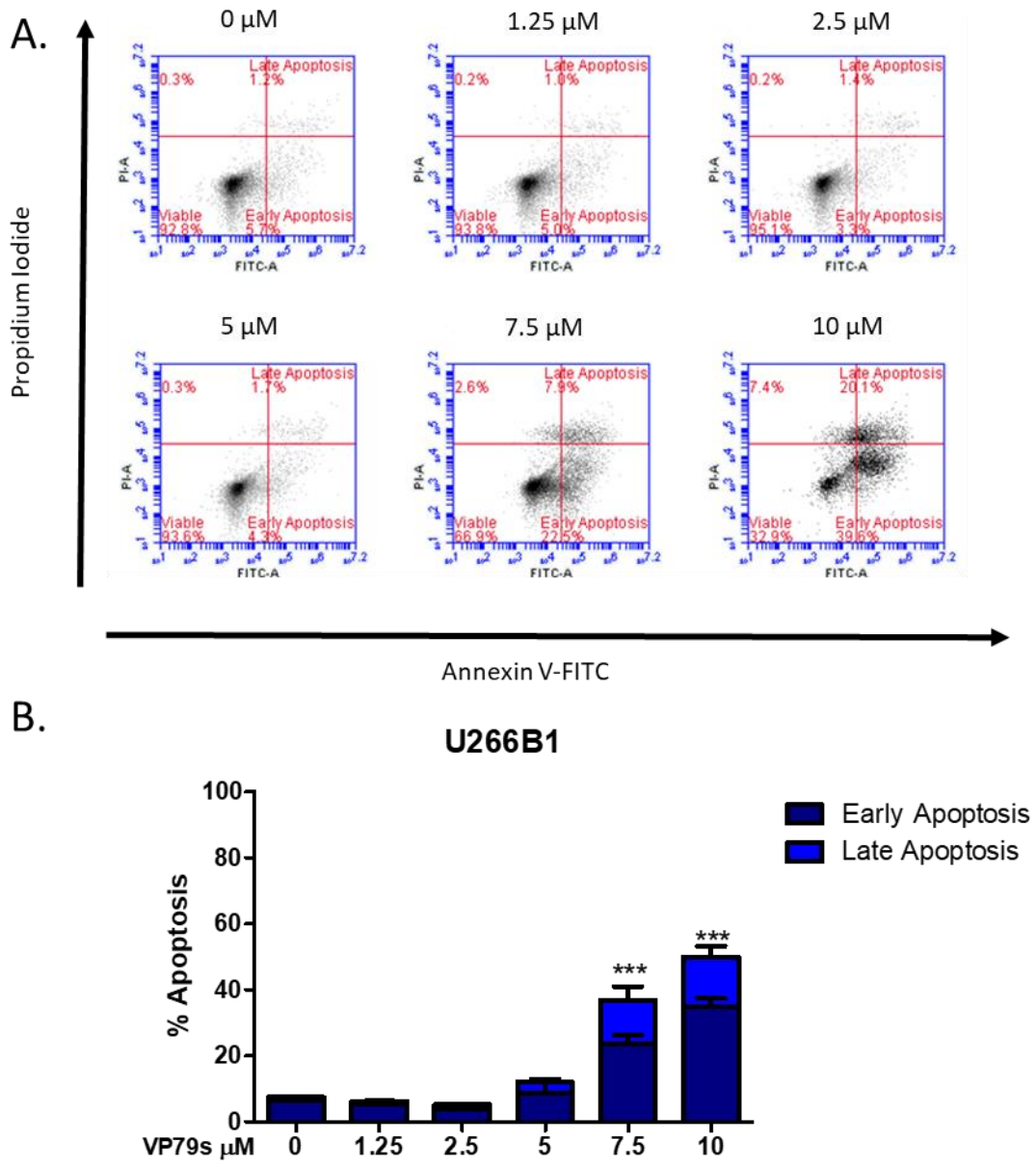

Figure 3. 14 VP79s induces apoptosis in a dose-dependent manner in U266B1 cells.

U266B1 cells were seeded at a density of 30x10^4 cells/mL and were treated with either vehicle control [0.5% EtOH (v/v)] or various concentrations of VP79s (1.25-10 µM) for 24 hours. After incubation cells were harvested and stained with annexin V/propidium iodide (PI) and were analysed by flow cytometry using BD Accuri™ C6 software. 10,000 cells were gated on vehicle treated cells. ***A.*** *Representative dot plot of treated samples.* ***B.*** *Values represent the mean ± S.E.M. of three independent experiments. Statistical analysis was performed using one-way ANOVA with Dunnett's multiple comparisons test comparing vehicle to treatments. *** p< 0.001.*

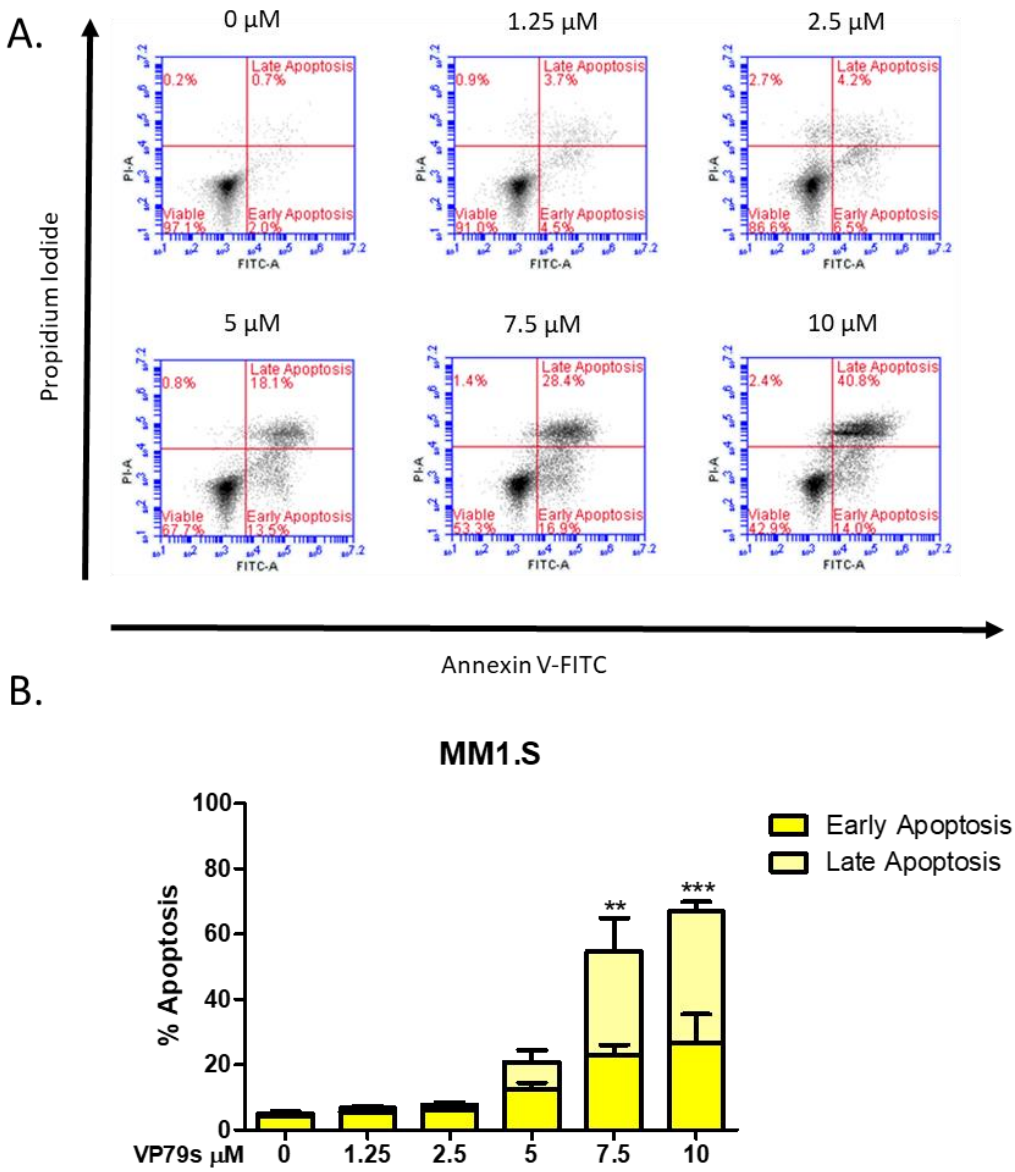

Figure 3. 15 VP79s induces apoptosis in a dose-dependent manner in MM1.S cells.

MM1.S cells were seeded at a density of 30x10^4 cells/mL and left to adhere overnight. The following day cells were treated with either vehicle control [0.5% EtOH (v/v)] or various concentrations of VP79s (1.25-10 µM) for 24 hours. After incubation cells were harvested and stained with annexin V/propidium iodide (PI) and were analysed by flow cytometry using BD Accuri™ C6 software. 10,000 cells were gated on vehicle treated cells. ***A****. Representative dot plot of treated samples.* ***B.*** *Values represent the mean ± S.E.M. of three independent experiments. Statistical analysis was performed using one-way ANOVA with Dunnett's multiple comparisons test comparing vehicle to treatments. **p < 0.01, *** p< 0.001.*

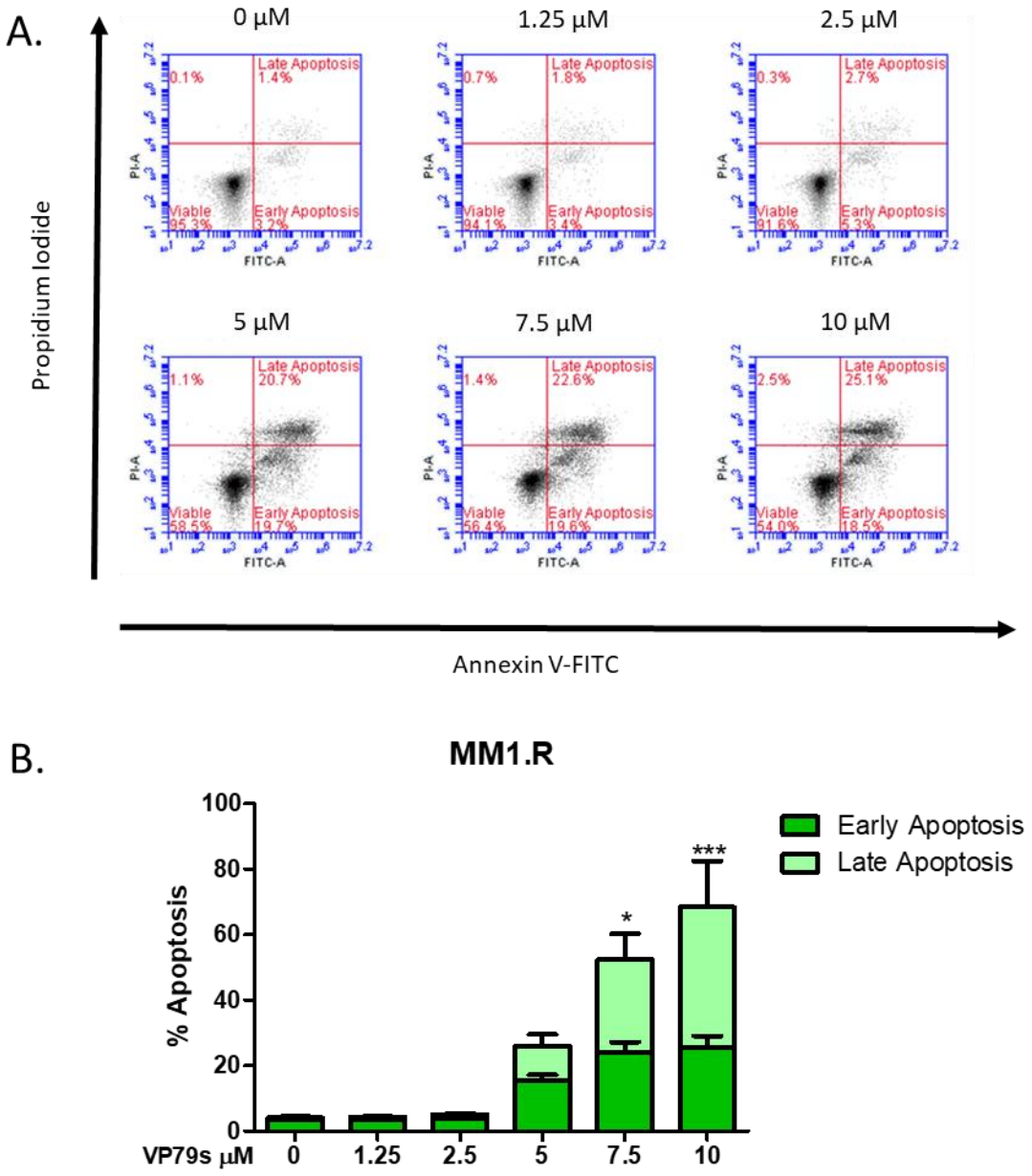

Figure 3. 16 VP79s induces apoptosis in a dose-dependent manner in MM1.R cells.

MM1.R cells were seeded at a density of 30x10^4 cells/mL and left to adhere overnight. The following day cells were treated with either vehicle control [0.5% EtOH (v/v)] or various concentrations of VP79s (1.25-10 µM) for 24 hours. After incubation cells were harvested and stained with annexin V/propidium iodide (PI) and were analysed by flow cytometry using BD Accuri™ C6 software. 10,000 cells were gated on vehicle treated cells. ***A****. Representative dot plot of treated samples.* ***B.*** *Values represent the mean ± S.E.M. of three independent experiments. Statistical analysis was performed using one-way ANOVA with Dunnett's multiple comparisons test comparing vehicle to treatments. *p< 0.05, *** p< 0.001.*

3.2.7. VP79s induces caspase 3 activation

Apoptotic cell death is mediated through the cleavage and thus activation of initiator (e.g. caspase 8 and 9) and effector (e.g. caspase 3) caspases. A series of experiments was undertaken to determine the involvement of caspases in VP79s-induced apoptosis.

NCI-H929 cells were treated with either vehicle (0.5% EtOH) or VP79s (1.25 – 10 µM) for 16 hours. Lysates were prepared and run on a 15% SDS-PAGE gel before being probed for full-length pro-form caspase 3 and cleaved active fragments of caspase 3.

Treatment with VP79s resulted in an observable decrease in full length caspase 3 at 10 µM and the presence of the active cleaved fragments of caspase 3 at 10 µM (Figure 3.17 A). Following densitometric analysis, a statistically significant decrease of full-length caspase 3 and cleavage of caspase 3 was observed at 10 µM (Figure 3.17 B). Similar results were observed in the U266B1 cell line with an observable increase in cleaved caspase 3 at 5 and 10 µM (Figure 3.18 A). A statistically significant increase in cleaved caspase 3 was observed at 10 µM (Figure 3.18 B).

In order to determine the involvement of the extrinsic and/or intrinsic apoptotic pathway in VP79s-induced cell death, the reduction of full-length initiator caspases 8 and 9 respectively was also examined. As before, NCI-H929 and U266B1 cells were treated with either vehicle (0.5% EtOH) or VP79s (1.25 – 10 µM) for 16 hours. A visible decrease in the pro-forms of both caspase 8 and 9 was observed in both cell lines following treatment with 10 µM VP79s (Figure 3.19 A and B). This would suggest that VP79s induces apoptosis through both the intrinsic and extrinsic pathways. The role of caspase cleavage in myeloma cell death was further examined. The NCI-H929 cells were pre-treated with 100 µM of the pan-caspase inhibitor Z-VAD-fmk for 1 hour prior to treatment with 10 µM VP79s. Western blot analysis of the pro- and cleaved forms of caspase 3 validated the effects of the caspase inhibitor as Z-VAD-fmk inhibited caspase 3 cleavage (Figure 3.20 A). Pre-treatment of cells with the caspase inhibitor failed to protect the cells from apoptosis indicating that cell death may be mediated through caspase independent means (Figure 3.20 B). Conversely, pre-treatment with 25 µM Z-VAD-fmk in the U266B1 cells substantially

inhibited cell death induced by VP79s suggesting the caspases play a significant role in VP79s induced cell death in the U266B1 cell line (Figure 3.21 B).

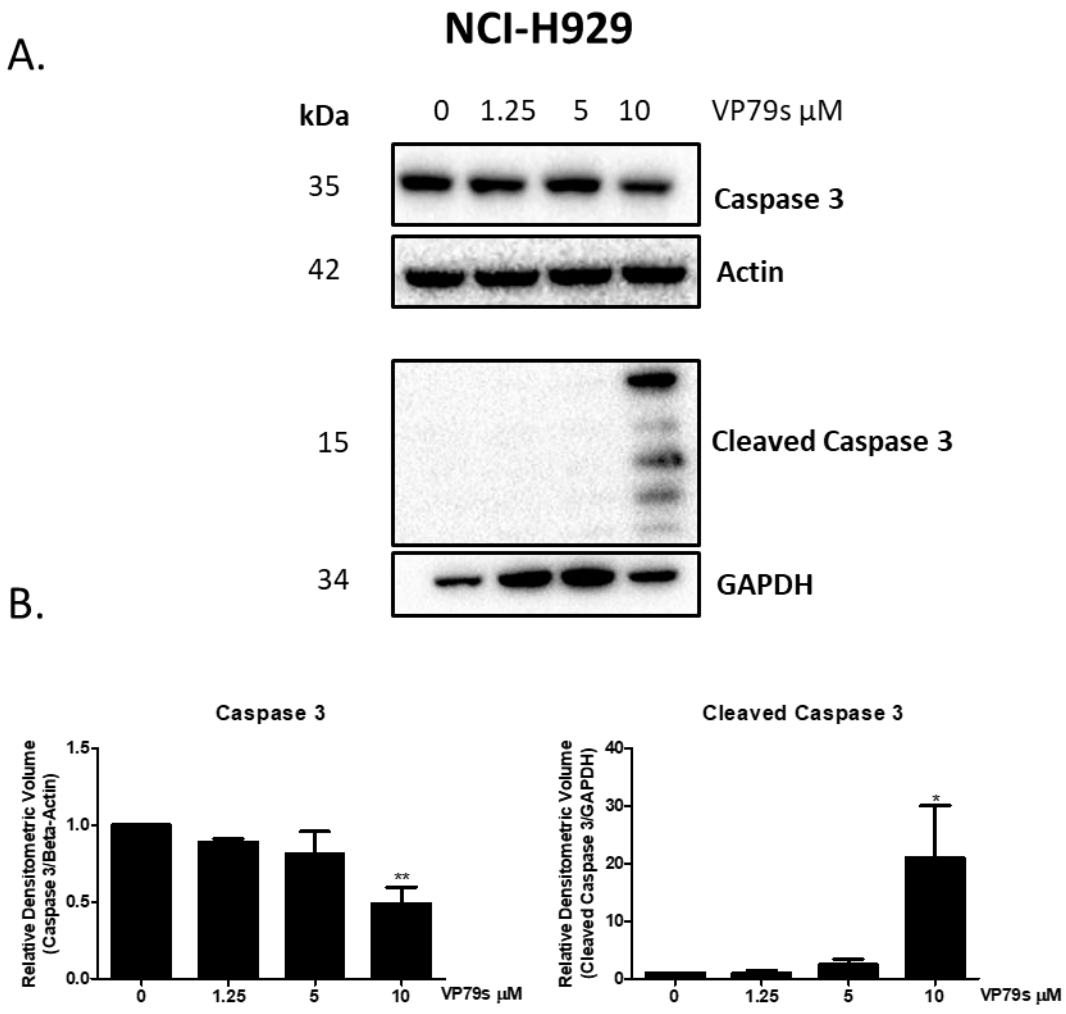

Figure 3. 17 VP79s induces caspase 3 cleavage in NCI-H929 cells.

NCI-H929 cells were seeded at a density of 30x10^4 cells/mL. Cells were treated with either vehicle [0.5% EtOH (v/v)] or VP79s (1.25, 5 and 10 µM) for 16 hours. ***A.*** *Cells were lysed and 20 µg of protein was loaded and separated on 15% SDS-page gels, transferred to PVDF membrane and probed with the appropriate antibody. Anti-GAPDH and anti-beta-actin were used as loading controls. Results are representative of 3 independent experiments. Western blots were normalised to GAPDH or beta-actin as a loading control.* ***B.*** *Densitometric analysis of bands was carried out using image lab software. Statistical analysis was performed using one-way ANOVA with Dunnett's post hoc test. *p<0.05, **p<0.01.*

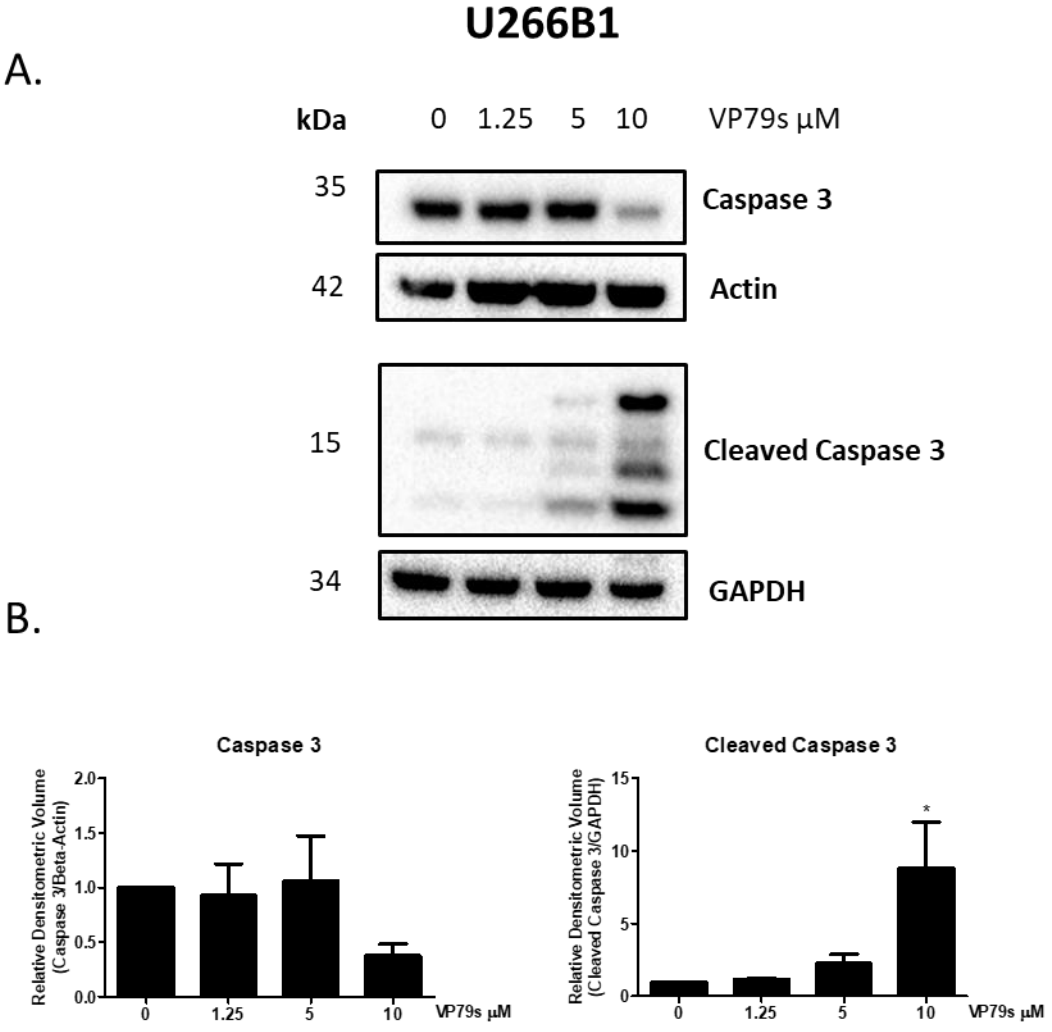

Figure 3. 18 VP79s induces caspase 3 cleavage in U266B1 cells.

U266B1 cells were seeded at a density of 30x10^4 cells/mL. Cells were treated with either vehicle [0.5% EtOH (v/v)] or VP79s (1.25, 5 and 10 µM) for 16 hours. ***A.*** *Cells were lysed and 20 µg of protein was loaded and separated on 15% SDS-page gels, transferred to PVDF membrane and probed with the appropriate antibody. Anti-GAPDH and anti-beta-actin were used as loading controls. Results are representative of 3 independent experiments. Western blots were normalised to GAPDH or beta-actin as a loading control.* ***B.*** *Densitometric analysis of bands was carried out using image lab software. Statistical analysis was performed using one-way ANOVA with Dunnett's post hoc test. *p<0.05.*

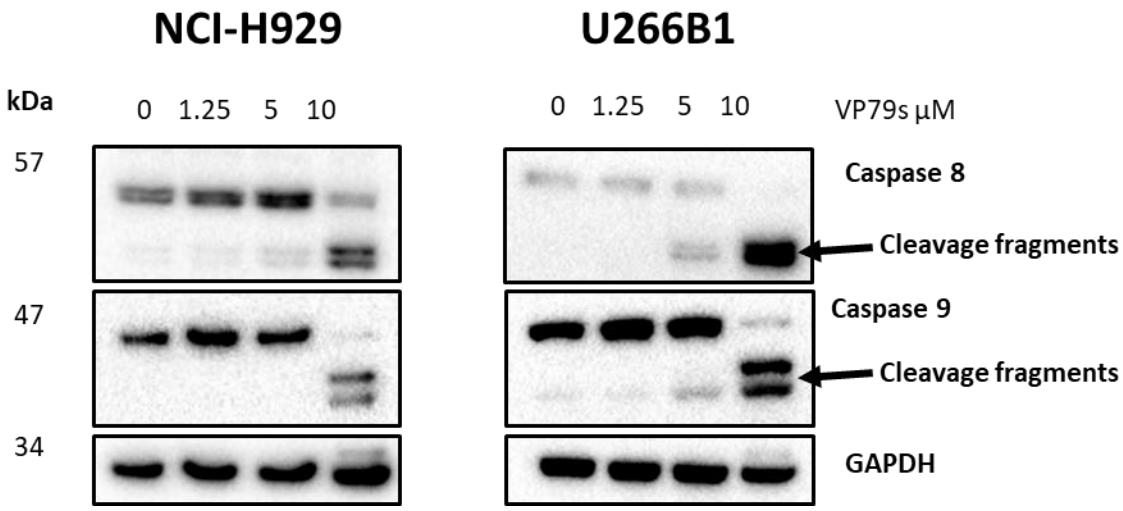

Figure 3. 19 VP79s induces caspase 8 and 9 cleavage in NCI-H929 and U266B1 cells.

NCI-H929 and U266B1 cells were seeded at a density of 30x10^4 cells/mL. Cells were treated with either vehicle [0.5% EtOH (v/v)] or VP79s (1.25, 5 and 10 µM) for 16 hours. A. Cells were lysed and 20 µg of protein was loaded and separated on 15% SDS-page gels, transferred to PVDF membrane and probed with the appropriate antibody. Anti-GAPDH was used as a loading control. Results are representative of 3 independent experiments. Western blots were normalised to GAPDH as a loading control.

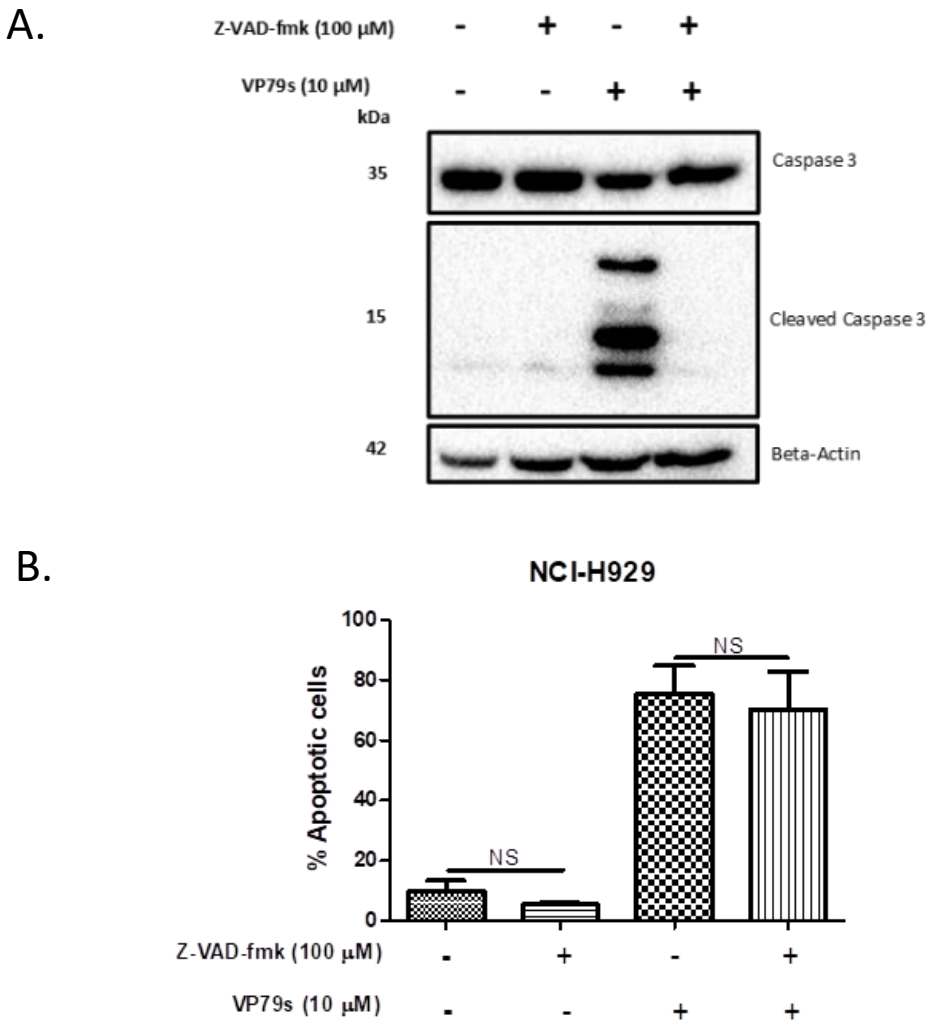

Figure 3. 20 VP79s induces caspase-independent cell death in NCI-H929 cells.

NCI-H929 cells were seeded at a density of 30x10^4 cells/mL and were treated with either vehicle control [0.5% EtOH (v/v) + 0.05% DMSO (v/v)], vehicle + Z-VAD-fmk (100 µM), VP79s (10 µM) or VP79s (10 µM) + Z-VAD-fmk (100 µM). ***A.*** *After incubation for 16 hours cells were harvested, lysed and 20 µg of protein was loaded and separated on 15% SDS-page gel, transferred to PVDF membrane and probed with the appropriate antibody. Anti-beta-actin was used as a loading control. Results are representative of 2 independent experiments.* ***B.*** *After incubation cells were harvested and stained with annexin V/propidium iodide (PI) and were analysed by flow cytometry using BD Accuri™ C6 software. 10,000 cells were gated on vehicle treated cells. Values represent the mean and S.E.M. of three independent experiments. Statistical analysis was performed using a paired two-tailed t-test. NS = no significance.*

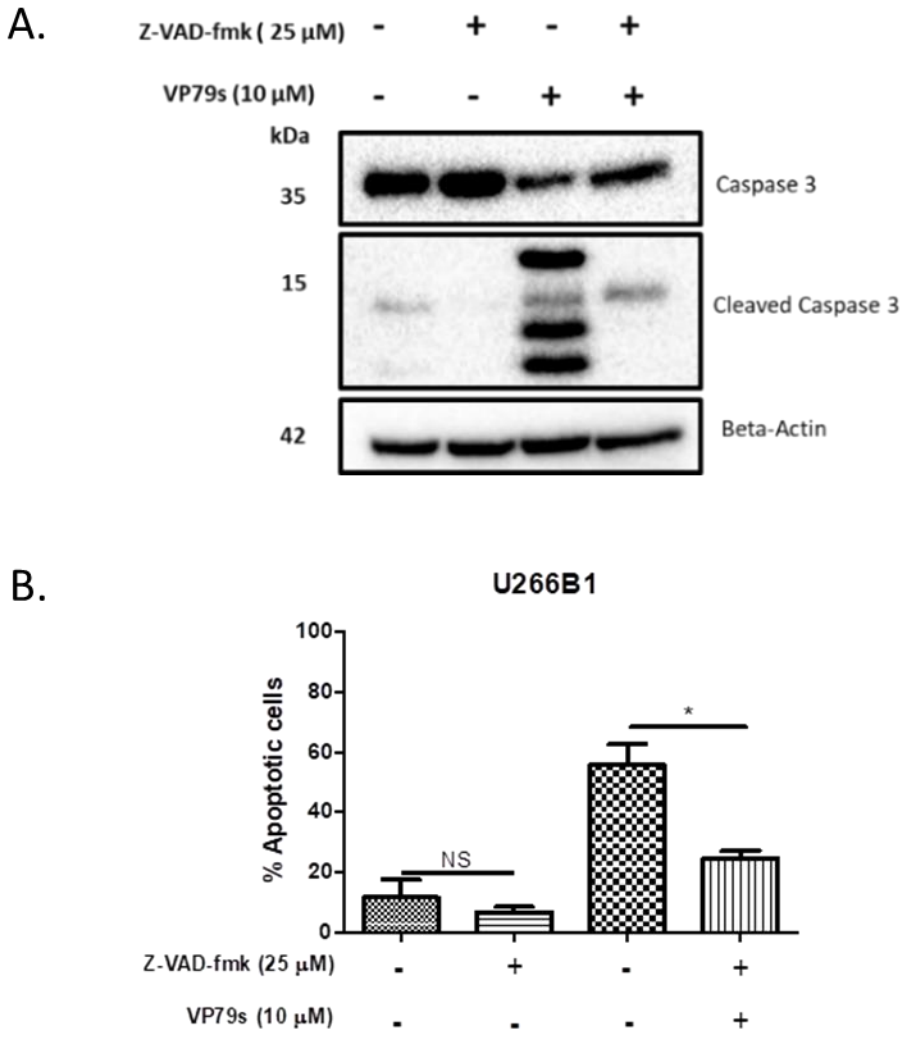

Figure 3. 21 VP79s induces caspase-dependent cell death in U266B1 cells.

U266B1 cells were seeded at a density of 30x10^4 cells/mL and were treated with either vehicle control [0.5% EtOH (v/v) + 0.05% DMSO (v/v)], vehicle + Z-VAD-fmk (25 µM), VP79s (10 µM) or VP79s (10 µM) + Z-VAD-fmk (100 µM). ***A.*** *After incubation for 16 hours cells were harvested, lysed and 20 µg of protein was loaded and separated on 15% SDS-page gel, transferred to PVDF membrane and probed with the appropriate antibody. Anti-beta-actin was used as a loading control. Results are representative of 2 independent experiments.* ***B.*** *After incubation cells were harvested and stained with annexin V/propidium iodide (PI) and were analysed by flow cytometry using BD Accuri™ C6 software. 10,000 cells were gated on vehicle treated cells. Values represent the mean and S.E.M. of three independent experiments. Statistical analysis was performed using a paired two-tailed t-test. *p<0.05, NS = no significance.*

3.3. Discussion

MM is an incurable malignancy with no unifying genetic mutations or environmental risk factors [285]. Despite improvements in the current therapies available for the treatment of MM and the improvement in overall survival time, drug resistance is still a foremost issue, therefore novel therapeutics and treatment strategies are required to target this heterogeneous disease [287]. The nature of B cells is to allow for genetic diversity; consequently, clonal evolution and genetic instability play a direct role in the development of myeloma drug resistance and pathogenesis [304]. Along with clonal diversity in MM, the bone marrow microenvironment plays an integral role in resistance mediated by activation of the PI3K/AKT, JAK/STAT and RAS/RAF pathways leading to the inhibition of cell death through upregulation of anti-apoptotic Bcl-2 proteins, IAP proteins and cell cycle proteins [28, 29, 305]. Therefore, novel drugs which can target both autonomous and microenvironment-dependent resistance are required for the treatment of MM.

In this study, a series of novel guanidinium based compounds designed and synthesised by the Rozas group (School of Chemistry, Trinity College Dublin) were screened for their anti-myeloma activity initially in two myeloma cell lines, NCI-H929 and U266B1. Typically, the NCI-H929 cell line is considered to be more drug susceptible while the U266B1 cell line is typically more resistant [49, 273, 306]. VP79s was found to elicit the most potent anti-myeloma activity with similar median inhibitory values in the low micromolar range in both cell lines compared to other novel compounds in the screen. This prompted further study into the drug's mechanism of action and potency in other myeloma cell lines. The anti-myeloma activity of current and emerging treatments for MM was also evaluated in the MM cell line panel. Dexamethasone, lenalidomide and bortezomib represent standard therapeutics used for the treatment of MM whilst venetoclax and ruxolitinib have shown preclinical efficacy in the treatment of MM [31, 76, 219, 300].

Prednisone and dexamethasone remain the archetypal treatments for MM and dexamethasone is still considered the most effective single agent therapy in the treatment of MM [307]. As a single agent, dexamethasone has limited anti-myeloma activity but when used in combination with novel agents it has an enhanced clinical response. Severe

toxicities limit the use of high dose treatments in patients and resistance is common in the relapsed and refractory setting, therefore, there is a need for novel treatment strategies [308]. Multiple mechanisms for steroid resistance have been observed in MM. The paired MM1.S and MM1.R cell lines express an identical immunohistochemical profile [269], but the MM1.R cell line displays loss of the normal glucocorticoid receptor (GR) making it resistant to dexamethasone. Dexamethasone resistance can also occur through dysfunctional GRs. A study by Moalli *et al.* in the MM1.R cell line has shown that the cells possess a truncated form of the GR which lacks the C-terminal hormone binding domain conferring dexamethasone resistance [309]. Dexamethasone susceptibility and resistance was confirmed in the MM1.S and MM1.R cell lines in this study. The susceptibility of NCI-H929 and U266B1 cells to dexamethasone was also examined. The U266B1 cell line was completely dexamethasone resistant at concentrations up to 2 µM whilst the NCI-H929 cell line demonstrated only a 20% decrease in viability. These results corroborate with previous studies which have demonstrated dexamethasone resistance in both the U266B1 and NCI-H929 cell lines [310-312]. It is not unexpected that dexamethasone does not largely reduce the viability of the MM cell lines examined herein as it is believed that the main therapeutic function of dexamethasone is its anti-inflammatory functions. At high doses, dexamethasone is capable of induces apoptosis in MM cells however, it is associated with toxicities. Therefore, dexamethasone is mainly used in combination treatment for MM [313].

Lenalidomide, a thalidomide analogue, is an IMiD which induces cell death in haematological malignancies through multiple mechanisms including direct cytotoxic effects and indirect effects on the microenvironment and immune cells [314]. In this study, lenalidomide reduced the viability of NCI-H929, MM1.S and MM1.R cells by approximately 40% while the U266B1 cells were completely resistant at concentrations up to 10 µM. Similar results with lenalidomide were observed by Chauhan *et al.* in U266B1, MM1.S and MM1.R cell lines [274]. Recently, a study by Zhu *et al*. demonstrated a novel mechanism of lenalidomide resistance associated with autocrine IL-6 and activation of STAT3 [315]. SGC-CBP30 is a small molecule that selectively targets the interferon regulatory factor 4 (IRF4) network in MM. In the study Zhu *et al.* demonstrated that co-treatment of SGC-CBP30 with

lenalidomide overcame resistance in myeloma cell lines. Interestingly, SGC-CBP30 was also shown to inhibit IL-6 autocrine production and STAT3 activation in the lenalidomide resistant cell line, XG1LenRes. Since the U266B1 cell line possesses constitutively active STAT3 due to autocrine IL-6 production, this may suggest a mechanism of resistance to lenalidomide induced cell death [49]. A study by Moros *et al*. illustrated that the anti-tumoural activity of lenalidomide in mantle cell lymphoma requires the destabilisation of the cyclin D1/p27KIP1 complexes [316]. It could be speculated that increased expression of cyclin D1 leads to resistance of lenalidomide in the U266B1 cell line as cyclin D1 lies downstream of STAT3 [49, 106]. Similar to dexamethasone, the main therapeutic function of lenalidomide is its immunomodulatory functions, therefore, it is not unexpected that it has limited effects on the viability of the MM cells. Lenalidomide is largely used in combination with other anti-myeloma therapeutics [314].

Venetoclax is a highly selective Bcl-2 inhibitor which has been approved for the treatment of relapsed and refractory chronic lymphocytic leukaemia (CLL) and acute myeloid leukaemia (AML) but has shown efficacy in many other haematological malignancies [317, 318]. Venetoclax acts as a BH3 mimetic and binds to the BH3-binding groove of anti-apoptotic Bcl-2 and displaces pro-apoptotic BH3-only proteins such as BIM. This frees these BH3-only proteins to bind to BAK or BAX encouraging their oligomerisation and the formation of pore in the OMM thus inducing MOMP [319]. A study by Touzeau *et al*. has demonstrated that venetoclax is highly effective in MM cell lines and patients with the t(11;14) translocation [320]. As previously discussed, the t(11;14) translocation leads to overexpression of cyclin D1 and high levels of Bcl-2 compared to Mcl-1 and Bcl-xL [101]. Herein, venetoclax reduced the viability of three MM cell lines; the NCI-H929 cell line was the most sensitive with an IC_{50} value of 4.76 µM. An IC_{50} value could not be obtained in the U266B1 cell line due to the limits of solubility but there was a 45% reduction in cell viability at 10 µM. These results are in line with previous studies [321-323]. Similar to lenalidomide, the resistance observed in the U266B1 cell line may be due to the overexpression of cyclin D1 due to constitutively active STAT3. Alternatively, a study by Valdez *et al.* which has shown similar results in the MM1.R and U266B1 cells, directly correlated resistance to venetoclax with anti-apoptotic Bcl-2 family member expression as the U266B1 cells

expressed higher levels of Bcl-2, Bcl-xL and Mcl-1 compared to other cell lines examined [322]. Another more extensive study then demonstrated that response to venetoclax can be predicted by the expression profile of anti-apoptotic Bcl-2, Bcl-xL and Mcl-1. The study demonstrated that cell lines which express lower levels of Mcl-1 compared to Bcl-2 and Bcl-xL are more sensitive to treatment with venetoclax [323]. Touzeau *et al.* have also demonstrated that MM is a heterogenous disease in relation to anti-apoptotic Bcl-2 family expression with the majority of cell lines examined demonstrating co-dependency on two or more family members [324]. Several clinical trials assessing the effects of venetoclax as a monotherapy and in combination with other therapeutics for the treatment of MM are currently underway (NCT03539744, NCT03314181) [325].

Ruxolitinib is a kinase inhibitor which inhibits JAK 1 and 2. It is used mainly for the treatment of myeloproliferative disorders [326]. Previous studies by de Oliveira *et al*. have demonstrated that 57% of myeloma patients in a cohort overexpressed JAK2. Moreover, ruxolitinib was shown to elicit synergistic effects in combination with bortezomib providing a rationale for targeting the JAK/STAT pathway in the treatment of MM [76]. In the present study, it has been shown that ruxolitinib reduced the viability of the MM cell line panel with similar IC_{50} values of around 30 µM in the U266B1, MM1.S and MM1.R cell lines. This is consistent with previous studies [76]. Currently there are phase 1 clinical trials exploring ruxolitinib, steroids and lenalidomide for relapsed/refractory MM (NCT03110822).

Bortezomib is a front-line treatment for MM patients who are not eligible for stem cell transplantation. Introduction of bortezomib into treatment regimens has greatly improved overall patient survival [327], but despite this, bortezomib resistance is a growing problem for MM patients [328]. Herein, bortezomib exhibited IC_{50} values in the low nanomolar range in the MM1.S, MM1.R and NCI-H929 cell lines which is in line with previous studies. For example, Shabaneh *et al.* demonstrated that MM1.S and MM1.R cells treated with bortezomib for 48 hours exhibit IC_{50} values in the low nanomolar range [329]. In *in vitro* studies, bortezomib and its analogues induce potent anti-myeloma activities in the low nanomolar range; however, in a clinical setting bortezomib resistance is common in MM patients highlighting the need for new drugs to overcome this resistance [330]. The viability results obtained with the U266B1 cell line are not in line with previous reports in

the literature. Herein, bortezomib did not reduce the viability of U266B1 cells up to 100 nM. It has been previously reported that bortezomib reduces the viability of U266B1 cell line in a dose-responsive manner with an IC_{50} value of around 5-10 nM [301, 331]. In order to try to understand this anomaly, U266B1 cells were treated with a 5, 10 and 100 nM bortezomib and cell viability was determined via alamar blue and annexin V/PI staining concurrently. Surprisingly, it was demonstrated that while bortezomib appeared to have no effect on cell viability using the alamar blue assay, annexin V/PI staining demonstrated that 47% of cells treated with 5 nM bortezomib were early apoptotic. The reason for this discrepancy between assays was not examined further. However, it could be postulated that since the majority of the cells are early apoptotic, they may still be able to metabolise resazurin to resoflurin. The reports which demonstrated the low IC_{50} values in U266B1 cells utilised different assays such as the XTT assay and WST-1 assay. This may also account for differences observed with IC_{50} values.

In conclusion, results obtained with VP79s compared very favourably with those obtained with small molecules and drugs currently in use in the treatment of MM and in development. In contrast to many of the other compounds tested, VP79s equipotently reduced the viability of all cell lines examined with no resistance observed. Further studies were then carried out to elucidate the mechanism by which VP79s induced anti-myeloma activity.

Several cytotoxicity assays are required for determining the response of a cancer cell to a given drug and are vital for the pre-clinical evaluation of novel compounds, such as VP79s, where the mechanism of cell death is completely unknown. Therefore, flow cytometric analysis of both cell cycle progression and cell death were employed. Results from the alamar blue assay indicated that VP79s reduced the viability of MM cells, although it was not clear whether this reduction in cell viability was due to cell cycle arrest, cell death or a combination of both. Therefore, the effect that VP79s had on the DNA profile of NCI-H929 and U266B1 cells over 8, 24, 48 and 72 hours was examined through quantitation of DNA content using PI staining. No cell cycle arrest in G1, G2/M or S phase was observed, however, in both cell lines VP79s induced an accumulation of cells in the sub G1/G0 peak in a time- and dose-responsive manner. Sub G1/G0 peaks is indicative of apoptosis

although it cannot be considered quantitative analysis as apoptotic cells do not always have distinctly lower DNA content [332]. No cell cycle arrest in G1, G2/M or S phase was observed. These findings were in agreement with the alamar blue viability assays which showed a time- and dose-dependent decrease in cell viability. The presence of early and late apoptosis was confirmed by flow cytometric analysis of annexin V/PI stained cells. VP79s induced apoptotic cell death in all four MM cell lines in a dose-responsive manner. The NCI-H929 cell line were the most sensitive to VP79s. Of note, VP79s induced equipotent apoptosis in the paired MM1.S and MM1.R cell lines, suggesting that cell death induced by VP79s does not involve the GR.

To confirm that the results obtained by annexin V/PI staining were truly representative of an apoptotic cell population, western blot analysis of the full length and cleaved forms of caspase 3 was examined. Dose-responsive cleavage of caspase 3 to active caspase 3 was observed in both the NCI-H929 and U266B1 cell lines correlating with the annexin V/PI staining results. It was also determined that VP79s induced apoptosis through both the extrinsic and intrinsic pathways as demonstrated by a reduction in the pro-form of both caspase 8 and caspase 9 respectively.

Programmed cell death is essential for many biological processes and in maintaining cellular homeostasis. Whilst apoptosis is arguably the most well studied form of cell death, other forms of cell death also exist, including autophagy, necroptosis, pyroptosis and caspase independent cell death (CICD) [333]. In this study, it was determined that caspases appear to play a role in VP79s induced cell death in the U266B1 cell line as pre-treatment with the pan-caspase inhibitor Z-VAD-fmk significantly abrogated apoptotic cell death induced by VP79s. Conversely, in the NCI-H929 cell line, pre-treatment with 100 µM Z-VAD-fmk did not alter the cell death induced by VP79s. MOMP is often considered a pivotal step in the initiation of cell death. CICD occurs when apoptotic triggers lead to permeabilisation of the outer mitochondrial membrane in the absence of caspase activity. During CICD, apoptosis inducing factor (AIF) and endonuclease G relocate to the nucleus where they mediate DNA fragmentation [334]. It is differentiated from caspase-dependent intrinsic apoptosis by the extent of cryoprotection conferred by inhibition of caspase activation, through pharmacological or other means [333]. Indeed, numerous

chemotherapeutics have been shown to induce both caspase dependent and independent cell death in cancer cells including MM cells [335-337].

To conclude, viability results obtained with VP79s compared very favourably with those obtained with standard and emerging therapeutics used to treat MM. In contrast to many other myeloma drugs and small molecules tested, VP79s equipotently reduced the viability of a panel of myeloma cells with no resistance observed. VP79s appeared to induce apoptosis through both the intrinsic and extrinsic apoptotic pathways but caspase-dependence appeared to be cell type specific. The promising anti-myeloma activity exhibited by VP79s, warranted further study to try to elucidate the molecular mechanisms underpinning VP79s induced cell death in MM cell lines.

Chapter 4:
Investigation into the molecular mechanisms underlying the anti-myeloma activity of VP79s

4.1. Introduction

In the era of modern medicine and novel therapeutics, MM is still an extremely arduous malignancy to treat. The heterogenous nature of MM and the unremitting development of drug resistance makes treating MM with a single drug or treatment strategy highly unlikely [285]. MM is thought to arise through genetic lesions such as translocations between Ig enhancers and oncogenes, followed by a series of secondary events which leads to the activation of growth and survival pathways creating the immortal MM clone [338]. The nature of B cells allows for the accumulation of such mutations, which results in the development of resistance to chemotherapy and treatments through upregulation of anti-apoptotic proteins and the activation of oncogenic signalling pathways [339]. Whilst these initial mutations can play a key role in the development of MM, the influence of the bone marrow microenvironment (BMM) also plays a critical role in the pathogenesis of the disease and occurrence of drug resistance [340]. The BMM mediates drug resistance through the production of cytokines and growth factors as well as the engagement of adhesion molecules on cells, such as bone marrow stromal cells (BMSCs), which are thought to be of particular importance [33, 38, 341]. Binding of MM cells to BMSCs prompts the secretion of cytokines and growth factors which activate oncogenic signalling pathways. Activation of these pathways leads to enhanced cell proliferation, survival, differentiation and drug resistance [34, 36, 43]. Therefore, it can be suggested that the influence of the BMM on MM is one of the most important factors in the development of drug resistance and cell survival.

Protection from drug-induced apoptosis in MM is mainly mediated through four main pathways, the RAS/RAF/MEK/ERK, PI3K/AKT, NFκB and JAK/STAT3 pathways. Activation of these pathways is facilitated by cytokines such as IL-6 and the presence of activating oncogenic mutations [60, 340]. A 2015 genomic study identified 15 frequently mutated genes in MM patients with a dominant mutation cluster in RAS/MAPK associated genes. The study demonstrated that the RAS/MAPK pathway is the most frequently mutated in MM with 43.2% of patients presenting with mutations in this pathway (*NRAS, KRAS* and *BRAF*), suggesting that MM may be driven by mutations within the RAS signalling cascade

[113]. Since activation of this pathway has been shown to be present in up to 50% of MM patients, inhibiting key components of the cascade is thought to be of therapeutic potential with numerous studies underway examining the potential of established and novel inhibitors of the pathway [292, 342].

As mentioned above, the JAK/STAT3 pathway also plays a key role in MM pathogenesis due to the involvement of the BMM. In particular, the IL-6R/JAK/STAT3 pathway has been demonstrated to contribute largely to the multistep transformation process and pathogenesis of MM through upregulation of key angiogenic and anti-apoptotic proteins [343]. IL-6 binds to either the IL6-Rα (CD126) or shedded sIL-6Rα, forming a complex which associates with CD130 (gp130) triggering its dimerisation. CD130 is a transmembrane glycoprotein which acts as the common signal transducing component for many cytokines including oncostatin M, leukaemia inhibitory factor and IL-6 [344]. Binding of IL-6 to CD126 and CD130 results in the activation of the associated JAK kinases; JAK1, JAK2 and Tyrosine Kinase-2. The JAKs then phosphorylate specific tyrosine residues on the CD130 cytoplasmic tail, which in turn act as docking sites for the STAT3 SH-2 domain, leading to JAK-mediated STAT3 phosphorylation. Phosphorylation of STAT3 on tyrosine 705 is the first cited event for STAT3 activation and has been convincingly demonstrated to be essential for its transcriptional activity in MM [81]. The biological role of STAT3 phosphorylation on serine 727 is unclear. Some studies have demonstrated that its activation is required for maximum phosphorylation, whilst others have suggested its activation can lead to inhibition of phosphorylation on tyrosine 705 [345, 346]. In contrast, in chronic lymphocytic leukaemia (CLL), the serine site is constitutively phosphorylated and serine phosphorylation has been shown to be important for STAT3 transcriptional activity [91]. In addition to the JAK kinases, SRC kinase has also been demonstrated to activate STAT3 directly [347]. The kinase activity of SRC is controlled by its phosphorylation on three tyrosine residues: tyrosine 534, tyrosine 529 and tyrosine 418. Phosphorylation of SRC on tyrosine 418 is required for the full catalytic activity of SRC and inhibition of phosphorylation on this amino acid has been reported to lead to a decrease in STAT3 phosphorylation [348].

Following phosphorylation on tyrosine 705, the STATs then dimerise and translocate to the nucleus, where it regulates transcription of target genes which play a vital role in MM cell survival. STAT3 regulates genes involved in the control of cell cycle proteins, proinflammatory cytokines, matrix metalloproteinases, growth factors and anti-apoptotic proteins [88]. Key proteins whose expression is regulated by STAT3 include the IAP survivin, the cell cycle protein, cyclin D1 and anti-apoptotic Bcl-2 family member, Mcl-1 as well as pro-survival growth factors and cytokines, such as VEGF and IL-6. As previously discussed, upregulation of cyclin D1 is an early and unifying event in MM. Cyclin D1 regulates G1 to S phase progression in many cell types and studies have shown that STAT3 promotes cell growth through upregulation of cyclin D1. Additionally, STAT3 has been shown to directly associate with the promotor of the *CCND1* gene to enhance cyclin D1 protein expression and cell proliferation [104, 106, 107]. Inarguably, Mcl-1 is considered one of the most critical survival proteins for MM cells and overexpression of Mcl-1 is associated with relapse and shorter overall survival [215, 226]. Despite co-expression of other anti-apoptotic proteins, MM cells largely depend on Mcl-1 for survival. Mcl-1 expression in MM cells can be independent of external factors such as cytokines; however, Mcl-1 protein expression can be upregulated following treatment with IL-6, as well as insulin growth factor-1 (IGF-1) and interferon [349, 350]. Therefore, targeting this pathway may be a favourable therapeutic strategy for MM. Indeed, previous reports in the literature have demonstrated that upregulation of the JAK/STAT pathway has been implicated in drug-resistance to multiple agents, including dexamethasone, lenalidomide, melphalan and bortezomib [315, 351-353].

The IL-6R/JAK/STAT pathway can be targeted at multiple levels; from IL-6 and the IL-6 receptors (CD126 and CD130), to upstream kinases and even STAT3 directly. Yet, to date there are no licenced inhibitors of the pathway approved for the treatment of MM. Inhibiting the kinase activity of upstream kinases such as the JAK and SRC kinases is a promising mechanism for inhibiting STAT3 activation [257, 354]. The suppressor of cytokine signalling (SOCS) family are negative feedback inhibitors of signalling induced by the cytokines and SOCS-1 and SOCS-3 have the unique ability to inhibit the kinase activity of JAKs via its kinase inhibitory domain [355]. Therefore, STAT3 phosphorylation can also

be inhibited through upregulation of SOCS, inhibition of upstream kinases or downregulation of the IL-6 receptors.

The aberrant activation of the PI3K/AKT pathway is a common feature in many cancers and, in particular, MM [133, 134]. AKT activation in cancer has been shown to lead to increased survival, proliferation and growth of tumour cells, and possibly angiogenesis by signalling through epithelial cells [137]. In MM, deregulated cytokines and growth factors, such as IL-6 and IGF-1, activate this signalling pathway leading to enhanced survival, migration and proliferation through upregulation of key survival proteins including Mcl-1 [51, 138, 139].

The NFκB transcription factors have also been shown to play a critical role in the proliferation and survival of many malignancies including MM. NFκB is essential for proper cellular functions and abnormal NFκB activation has been shown to play an important role in the development of malignancies [142]. Approximately 17% of primary MM samples and 42% of all MM cell lines have been found to express mutations in NFκB [356, 357]. NFκB controls the expression of molecules, such as IL-6 and B cell activating factor (BAFF), which are important for MM cell growth as previously discussed. Cell cycle proteins, such as cyclin D1, are also thought to be regulated by NFκB [358]. Therefore, targeting NFκB may be a potential therapeutic target in MM.

In the previous chapter, VP79s, a novel guanidinium based compound, was shown to induce apoptotic cell death in MM cell lines through caspase-dependent and -independent mechanisms. ED73a, a precursor of VP79s, was previously shown to be capable of inhibiting the RAS/RAF/MEK/ERK signalling pathway through the allosteric inhibition of BRAF in colorectal cancer cell lines [259]. In addition to inhibiting RAF, ED73a was shown to inhibit STAT3 and AKT phosphorylation; however, the mechanism of inhibition of these kinases by ED73a was not delineated. Therefore, given the collective data, the effect of VP79s on the activation of key oncogenic signalling pathways known to play a role in MM pathogenesis was examined in order to elucidate the molecular mechanisms underlying the anti-myeloma activity of VP79s in this chapter.

4.2. Results

4.2.1. VP79s modulates the expression of AKT in a time responsive manner in NCI-H929 and U266B1 cells

In the previous chapter, VP79s was shown to induce apoptosis in a panel of drug-sensitive and drug-resistant MM cell lines. Given these promising results, the effects of VP79s on oncogenic signalling pathways known to play a role in pathogenesis and survival of MM cells were examined. As previously described, activation of the PI3K/AKT signalling pathway is a key oncogenic signalling pathway in MM which can be activated by both autonomous mutations and by the BMM. NCI-H929 and U266B1 cells were treated with 10 µM VP79s for 30 minutes, 2, 4 or 8 hours. Cells were collected, lysed and ran on 12% SDS-PAGE gel before being transferred to PVDF membrane and probed for total AKT and phosphorylated-AKT (serine 473). Anti-GAPDH was used as a loading control. U266B1 cells were treated with 30 µM LY294002, a known PI3K inhibitor, for 30 minutes as a positive control.

Treatment with LY294002 in the U266B1 cells resulted in a decrease in phosphorylation on serine 473 and no change in total AKT levels, thus validating the assay.

Surprisingly, VP79s was shown to transiently increase the phosphorylation of AKT on serine 473 in both NCI-H929 and U266B1 cells. An initial increase was observed at 30 minutes with phosphorylation returning to basal levels at around 8 hours in the NCI-H929 cells and at the earlier timepoint of 2 hours in the U266B1 cells (Figure 4.1 A and B). No significant decrease in total or phosphorylated AKT was observed in the NCI-H929 cells at any of the time points examined. However, in the U266B1 cell line there was a significant decrease in total and phosphorylated AKT observed at 4 and 8 hours when analysed by densitometry (Figure 4.2)

AKT may play a role the anti-myeloma activity of VP79s in MM, however, due to the contrasting data obtained in the two myeloma cell lines no firm conclusions could be drawn.

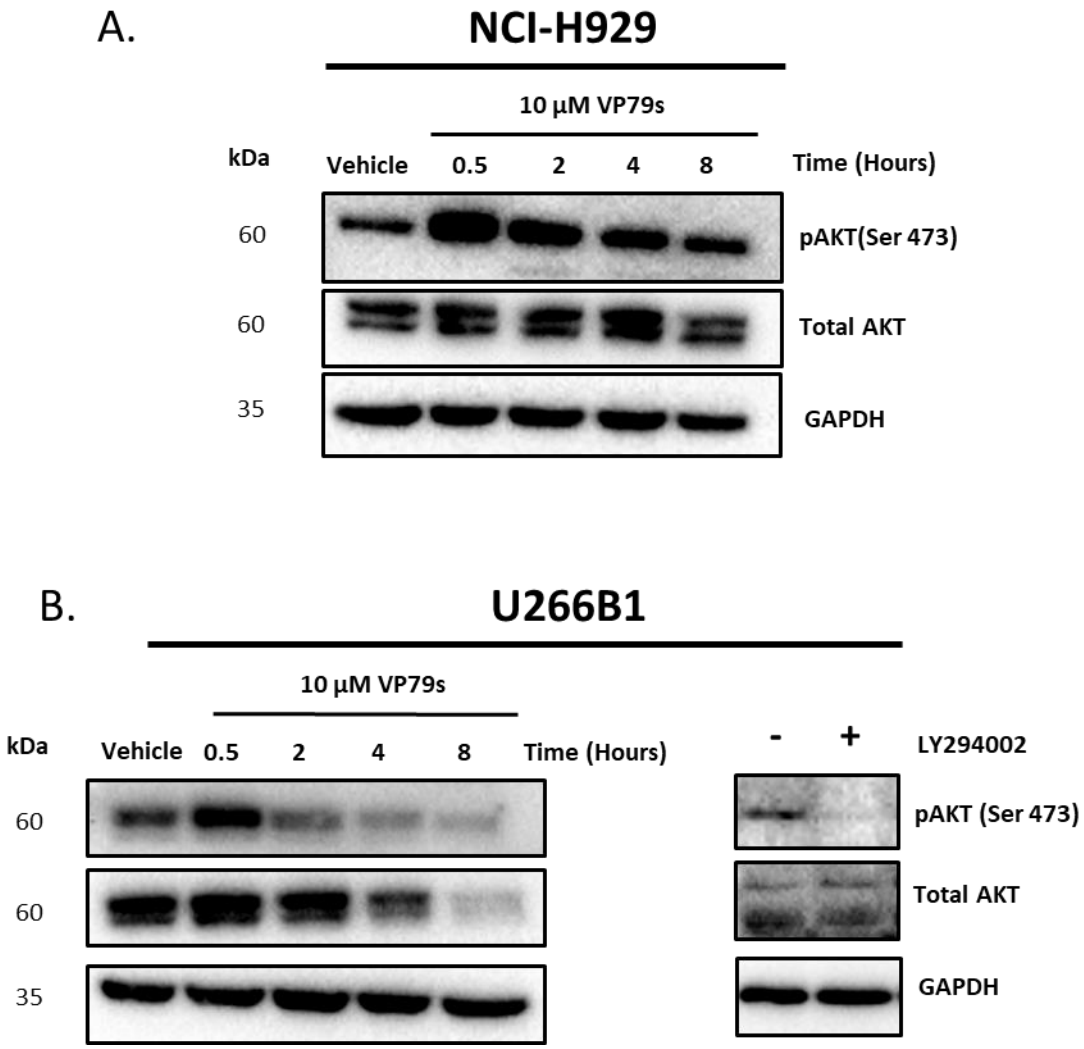

Figure 4. 1 VP79s alters the expression of phospho- and total AKT in NCI-H929 and U266B1 cells.

U266B1 and NCI-H929 cells were seeded at a density of 30x10^4 cells/mL. ***A.*** *NCI-H929 cells were treated with either vehicle [0.5% EtOH (v/v)] or 10 µM VP79s for 30 minutes, 2, 4 or 8 hours.* ***B.*** *U266B1 cells treated with 30 µM LY294002 for 30 minutes was used as a positive control. Cells were also treated with either vehicle [0.5% EtOH (v/v)] or 10 µM VP79s for 30 minutes, 2, 4 or 8 hours. Cells were lysed and equal amounts of protein were loaded and separated on 12% SDS-page gels, transferred to PVDF membrane and probed with the appropriate antibody. Anti-GAPDH was used as a loading control. Results are representative of 3 independent experiments. Western blots were normalised to total GAPDH as a loading control.*

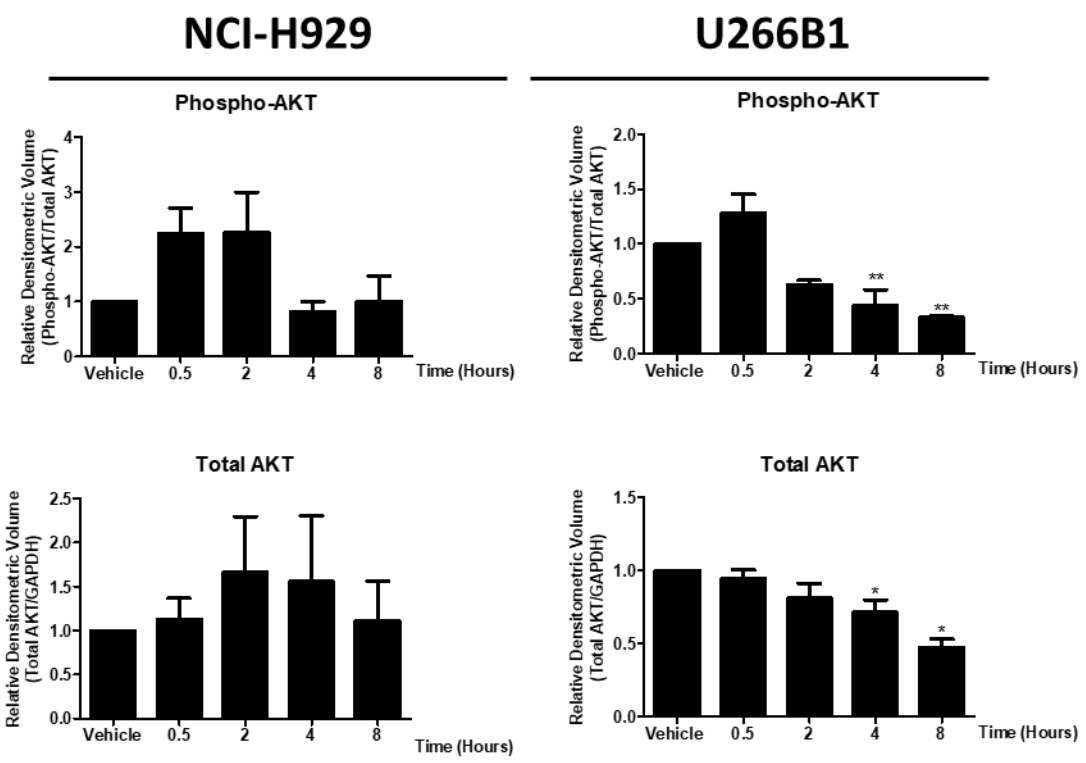

Figure 4. 2 VP79s downregulates phospho- and total AKT in U266B1 cells.

*Cells were seeded at a density of 30x10^4 cells/mL and treated with either vehicle [0.5% EtOH (v/v)] or 10 µM VP79s for 30 minutes, 2, 4 or 8 hours. Cells were lysed and equal amounts of protein were loaded and separated on 12% SDS-page gels, transferred to PVDF membrane and probed with the appropriate antibody. Results are representative of 3 independent experiments. Western blots were normalised to total GAPDH as a loading control. Densitometric analysis was carried out using image lab software. Statistical analysis was performed using one-way ANOVA with Dunnett's post hoc test comparing vehicle to treatments. *p<0.05 and **p<0.01.*

4.2.2. VP79s treatment has no effect on the canonical NFκB pathway in U266B1 cells

The role of the NFκB pathway was next examined. NFκB transcription factors have been implicated in the survival and proliferation of many B-cell tumours, including MM, and the NFκB pathway has been demonstrated to play a role in the pathogenesis of MM. Activating and inactivating mutations in 11 regulators of the NFκB pathway have been identified in 20% of treatment naive MM tumours causing the cells to become less dependent on ligand-mediated NFκB activation [359]. Moreover, genome sequencing has identified apparent NFκB activating mutations in 17-29% of MM tumours [118, 356, 357]. Similarly, 50% of MM cell lines have been shown to have high NFκB activity. Therefore, modulation of this pathway may be of therapeutic potential in MM [357].

Degradation of the inhibitor of NFκB, IκBα, by the proteasome is indicative of activation of the classical pathway whereas an increase in expression of IκBα signals inhibition of the pathway [360]. Of note, bortezomib has been demonstrated to activate NFκB in U266B1 cells through phosphorylation on serine residues and degradation of IκBα by ubiquitination and subsequent proteasomal degradation [361]. In order to first confirm the ability of U266B1 cells to activate the NFκB pathway in this study, bortezomib was used as a positive control. Cells were treated with 20 nM bortezomib or 10 μM VP79s for 8 hours. Phosphorylated and total levels of Iκbα were assessed by western blotting. A marked increase in the expression of phosphorylated IκBα on serine 32 was observed in response to bortezomib indicating activation of the NFκB pathway (Figure 4.3 A) and validation of the assay. No effect was observed with VP79s treatment for 8 hours (Figure 4.3 A). Earlier timepoints from 0 to 120 minutes were next examined. U266B1 cells were treated with either vehicle (0.5% EtOH) or 10 μM VP79s for 0, 15, 30, 45, 60, 90 or 120 minutes. Lysates were prepared and samples were run on 12% SDS-PAGE gel, transferred to PVDF membrane and probed for levels IκBα. No differences in IκBα levels were seen at any timepoint tested indicating that VP79s does not appear to target the NFκB pathway (Figure 4.3 B).

To summarise, VP79s appeared to have no effect on the canonical NFκB pathway at any of the time points examined.

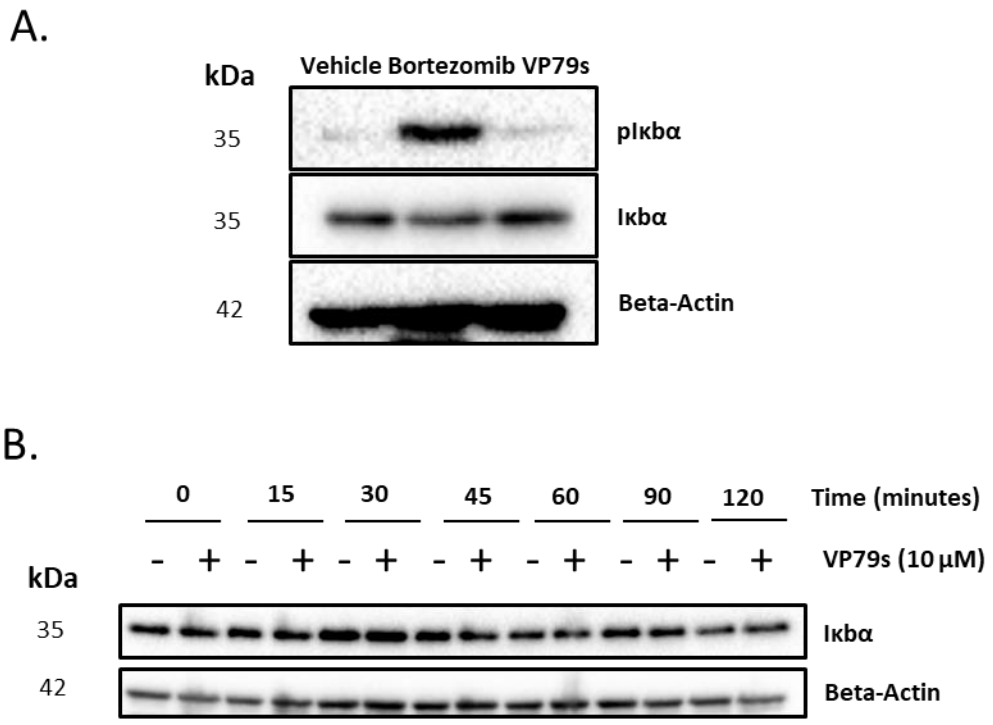

Figure 4. 3 VP79s has no effect on Iκbα, the inhibitory subunit of NFκB.

*U266B1 cells were seeded at a density of 30x10^4 cells/mL and were treated with **A.** Vehicle [0.01% DMSO (v/v) and 0.5% EtOH (v/v)], 20 nM bortezomib or 10 µM VP79s for 8 hours or **B.** either vehicle [0.5% EtOH (v/v)] or 10 µM VP79s for 0, 15, 30, 45, 60, 90 or 120 minutes. Cells were lysed and equal amounts of protein were loaded and separated on 12% SDS-page gels, transferred to PVDF membrane and probed with the appropriate antibody. Anti-beta-actin was used as a loading control. Results are representative of **A.** 2 and **B.** 3 independent experiments with similar results.*

4.2.3. VP79s inhibits constitutively active STAT3 phosphorylation on tyrosine 705 in U266B1 cells

STAT3 signalling has been found to be involved in oncogenesis and constitutive activation of STAT3 has been associated with tumourigenesis in various types of human cancers including MM by stimulating target genes that enhance cell proliferation and prevent apoptosis [88, 362]. The U266B1 cell line harbours a mutation leading to the constitutive activation, and therefore, phosphorylation of STAT3 on residues tyrosine 705 and serine 727 via an IL-6 dependent autocrine loop [49]. Phosphorylation of STAT3 on tyrosine 705 is the first cited event for its activation and has been convincingly demonstrated to correlate with STAT3 DNA binding and transcriptional activity [81]. Therefore, the effect of VP79s on STAT3 signalling was initially examined in the U266B1 cell line by western blot analysis to assess the levels of phosphorylated STAT3 prior to and post drug treatment. U266B1 cells were treated with 10 µM VP79s for 30 minutes, 2, 4 or 8 hours. Cells were collected, lysates were prepared, and proteins were separated out on a 12% SDS-PAGE gel. Gels were probed with anti-phospho-STAT3 (Y705), anti-phospho-STAT3 (S727) and anti-total STAT3 antibodies. Anti-GAPDH was used as a loading control.

VP79s was found to inhibit STAT3 phosphorylation on tyrosine 705 in a time-dependent manner. An observable decrease in STAT3 phosphorylated on tyrosine 705 was seen from 30 minutes and this band was no longer visible from 2 hours. (Figure 4.4 A). Densitometric analysis of western blots demonstrated a significant decrease in STAT3 phosphorylation from 2 hours in VP79s treated cells (Figure 4.4 B). In contrast, there were no observable differences in the levels STAT3 phosphorylation on serine 727 or total STAT3 (Figure 4.4 A). Densitometric analysis confirmed that no statistical differences were observed in phospho-STAT3 serine 727 or in total STAT3 when VP79s cells were compared to the vehicle (Figure 4.4 B).

The effect of VP79s on STAT3 phosphorylation in the NCI-H929 cell line was next examined. The NCI-H929 cell line does not possess constitutively active phosphorylation on tyrosine 705, however, it is phosphorylated on serine 727. Similar to the U266B1 cell line, VP79s elicited no visible effects on the expression levels of serine 727 or total STAT3 (Figure 4.5 A). Of note, phosphorylated STAT3 on serine 727 appeared as a double band in

these cells, possibly indicative of acetylation [89, 94]. Densitometric analysis confirmed that no statistical differences were observed in phospho-STAT3 serine 727 or in STAT3 (Figure 4.5 B).

Given that the tumour microenvironment protects myeloma cells against the cytotoxic effects of various drugs, the ability of VP79s to overcome this resistance was examined. As previously discussed, MM cells rely heavily on pro-survival factors from the BMM in order to facilitate their survival and proliferation. One key survival factor which is known to play a role in MM cell survival through the activation of the JAK2/STAT3 pathway is IL-6 [48]. As aforementioned, the NCI-H929 cell line does not possess constitutively active phosphorylation on tyrosine 705. Therefore, in order to induce STAT3 phosphorylation on tyrosine 705 the NCI-H929 cells were pre-treated with 1 ng/mL human recombinant IL-6 for 30 minutes prior to treatment with VP79s for 30 minutes, 4 or 16 hours. Cells were collected and prepared for western blotting for the indicated timepoints. Cells were collected at 16 hours for flow cytometric analysis of cell death with annexin V/PI staining.

Western blot analysis illustrated that VP79s was capable of inhibiting IL-6-induced STAT3 phosphorylation from as early as 4 hours and sustained this inhibition at 16 hours (Figure 4.6 A). Moreover, flow cytometric analysis of IL-6 treated cells and VP79s alone treated cells by annexin V/PI staining demonstrated that VP79s could induce significant apoptotic cell death even in the presence of the cell survival cytokine IL-6 (Figure 4.6 B). Of note, IL-6 did appear to elicit some survival advantage to the NCI-H929 cells demonstrating the importance activation of this pathway has on MM cell survival; however, the difference was not significant.

Having determined that VP79s inhibits phosphorylation of STAT3 on tyrosine 705 in U266B1 cells but had no effect on serine 727 in either cell line, flow cytometric analysis of NCI-H929 and U266B1 cells was carried out to confirm the results obtained by western blotting. NCI-H929 and U266B1 cells were treated with 10 µM VP79s for 1 hour. Following treatment, cells were harvested, fixed with paraformaldehyde, permeabilised and stained with antibodies against phosphorylated STAT3 on serine 727 (pSTAT3 S727 fluorochrome FITC-510-550 nm) and tyrosine 705 (pSTAT3 Y705 fluorochrome PE-562.5-587.5 nm). NCI-H929 cells were also treated with 10 ng/mL IL-6 for 1 hour as a positive control for STAT3

tyrosine phosphorylation in the NCI-H929 cells. Cells were then gated on serine and tyrosine phosphorylation whereby the top left quadrant (Q1) indicates cells phosphorylated on serine 727, the top right indicates dual phosphorylation on serine and tyrosine (Q2), the bottom left indicates no phosphorylation on serine on serine 727 or tyrosine 705 (Q3) and the bottom right indicates cells phosphorylated on tyrosine (Q4). In line with the results obtained by western blotting, it was observed in the NCI-H929 cells that the cells expressed constitutively active phosphorylation on serine 727 but not on tyrosine 705 as 90% of cells were present in Q1 and only 5% in Q2 (Figure 4.7 A). It was also observed that VP79s treatment had no effect on serine 727 phosphorylation in line with western blot results. IL-6 treatment increased double phosphorylation of STAT3 on tyrosine 705 and serine 727 from 5% to 30% (see Q2) (Figure 4.7 A). Similarly, the U266B1 flow cytometry results reflected the results obtained by western blotting. The U266B1 cell line was demonstrated to have constitutively active phosphorylation of STAT3 on serine 727 and tyrosine 705 as 68.7% were phosphorylated on serine (Q1) and 29.7% of cells were dually phosphorylated on both tyrosine 705 and serine 727 (Q2). Treatment with VP79s resulted in a decrease in dual phosphorylation from 29.7% to 3.5%. Treatment with VP79s also resulted in total loss of phosphorylation on both sites in 16.8% of cells post treatment with VP79s (Q3) (Figure 4.7 B). Therefore, VP79s is affecting STAT3 phosphorylation on tyrosine 705 but has limited affect on serine 727 phosphorylation.

To conclude, VP79s was shown to inhibit both constitutively active and IL-6 induced STAT3 phosphorylation on tyrosine 705 but not on serine 727 as evidenced by western blotting and flow cytometric analysis. Moreover, VP79s was capable of inducing significant apoptotic cell death even in the presence of the pro-survival cytokine IL-6.

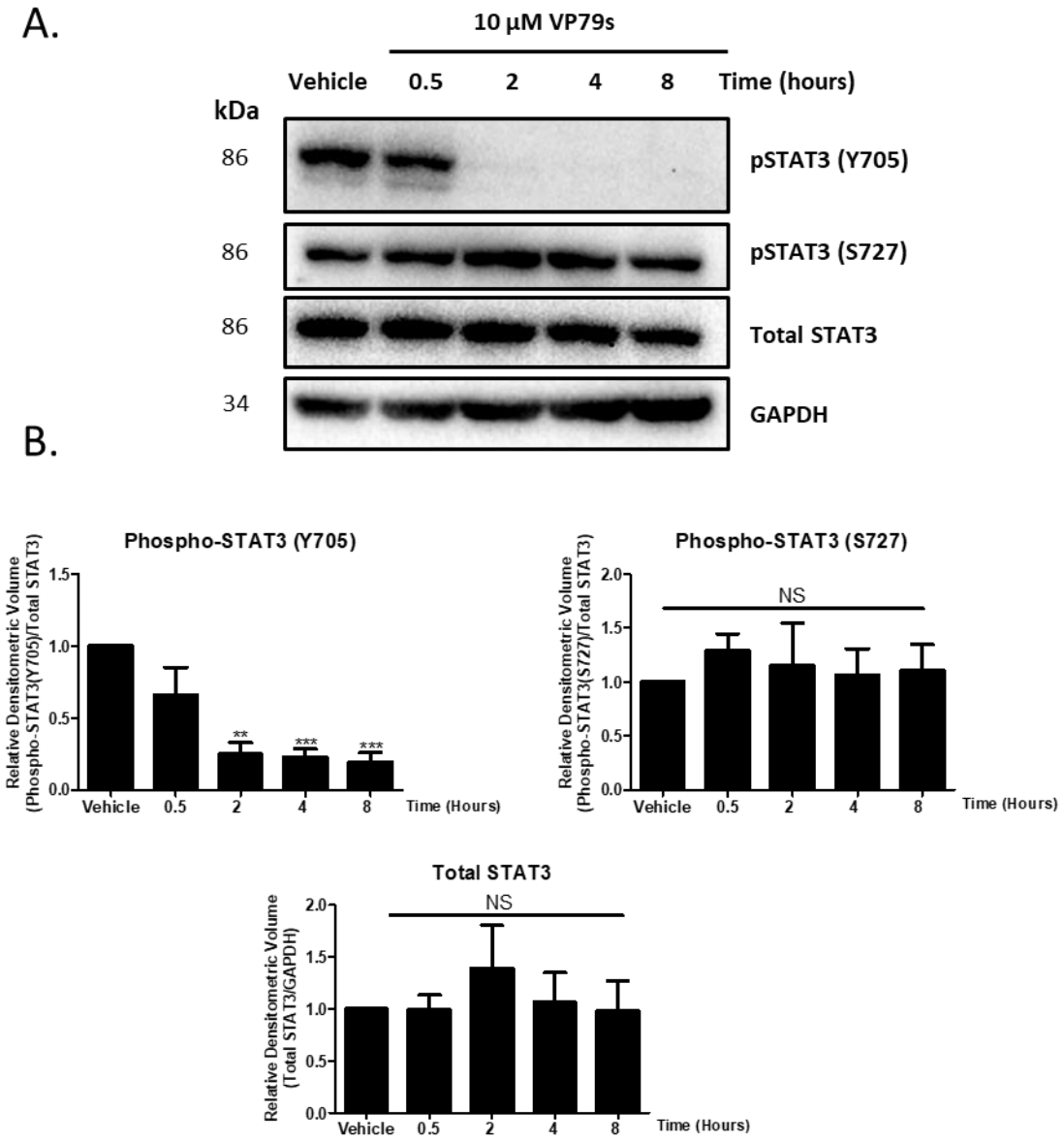

Figure 4. 4 VP79s inhibits constitutively active STAT3 signalling in U266B1 cells.

U266B1 cells were seeded at a density of 30x10^4 cells/mL. Cells were treated with either vehicle [0.5% EtOH (v/v)] or VP79s (10 µM) for 30 mins, 2, 4 or 8 hours. Cells were lysed and equal amounts of protein were loaded and separated on 12% SDS-page gel, transferred to PVDF membrane and probed with the appropriate antibody. ***A.*** *Representative images of phospho-STAT3 (Y705), phospho-STAT3 (S727) and total STAT3. Anti-GAPDH was used as a loading control. Results are representative of 3 independent experiments.* ***B.*** *Densitometric analysis was carried out using image lab software. Statistical analysis was performed using one-way ANOVA with Dunnett's post hoc test. **p<0.01, ***p<0.001, NS = No significance.*

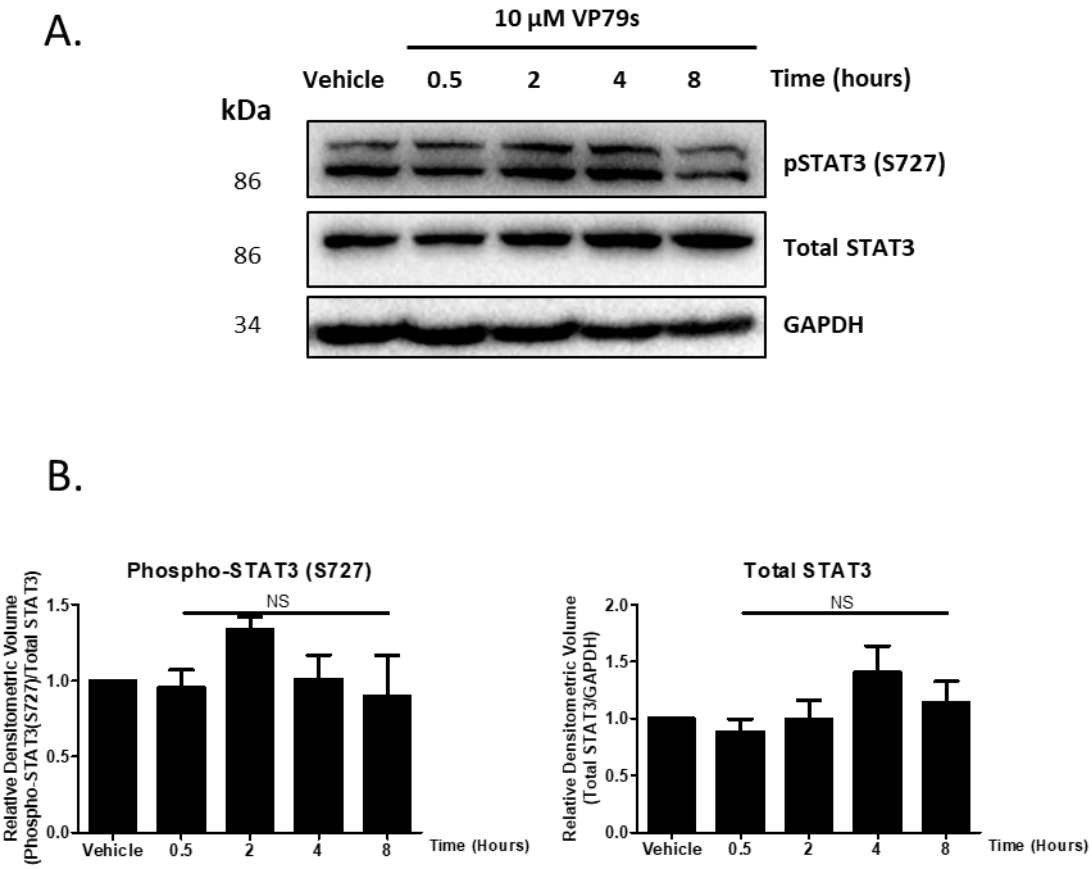

Figure 4. 5 VP79s has no effect on phospho-STAT3 (S727) in NCI-H929 cells.

NCI-H929 cells were seeded at a density of 30x10^4 cells/mL. Cells were treated with either vehicle [0.5% EtOH (v/v)] or VP79s (10 µM) for 30 mins, 2, 4 or 8 hours. Cells were lysed and equal amounts of protein were loaded and separated on 12% SDS-page gel, transferred to PVDF membrane and probed with the appropriate antibody. ***A.*** *Representative images of phospho-STAT3 (S727) and total STAT3. Anti-GAPDH was used as a loading control. Results are representative of 3 independent experiments.* ***B.*** *Densitometric analysis was carried out using image lab software. Statistical analysis was performed using one-way ANOVA with Dunnett's post hoc test. NS = No significance.*

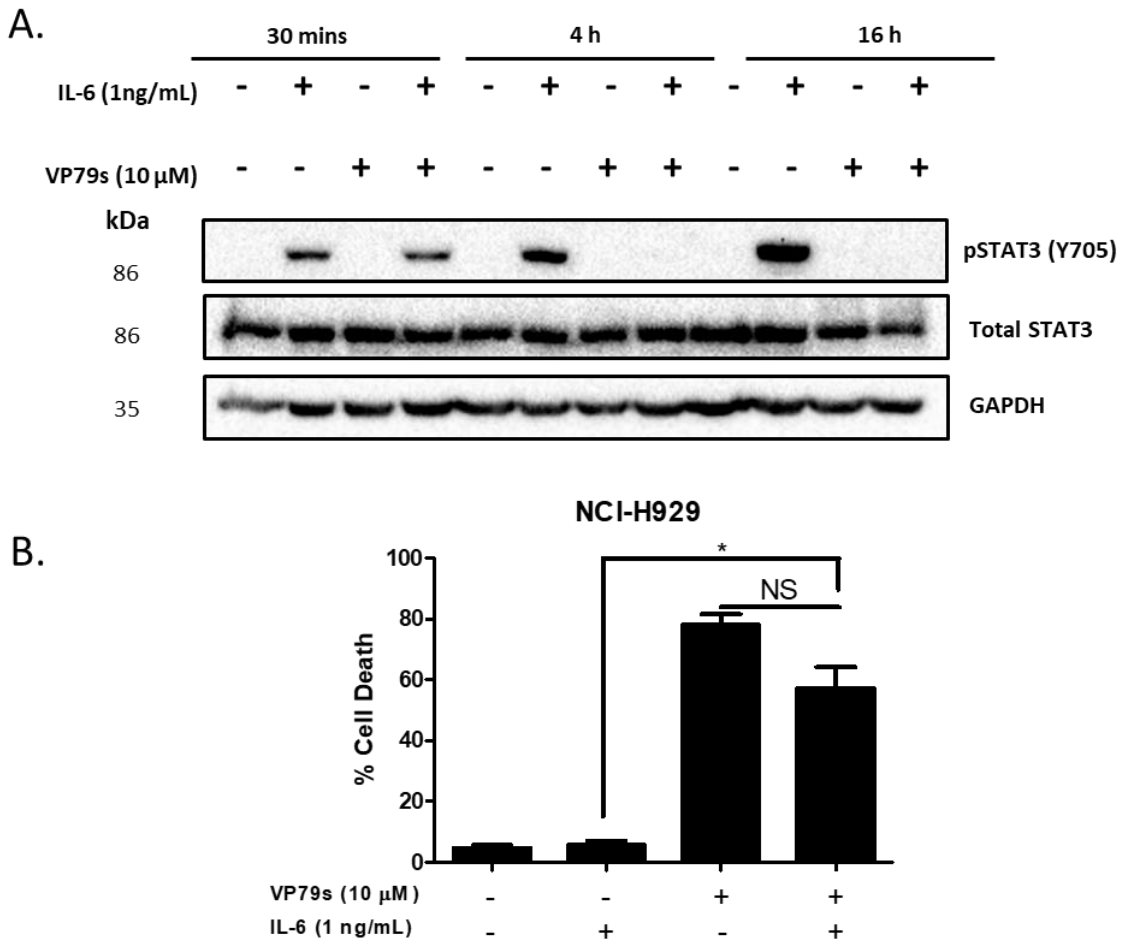

Figure 4. 6 VP79s can inhibit IL-6 induced STAT3 signalling and induce cell death in NCI-H929 cells in the presence of pro-survival IL-6.

NCI-H929 cells were seeded at a density of 30x10^4 cells/mL. Cells were treated with either vehicle [0.5% EtOH (v/v)] or VP79s (10 µM) with or without 1ng/mL IL-6 for 30 minutes, 4 hours or 16 hours. ***A.*** *Cells were lysed and 20 µg of protein was loaded and separated on 10% SDS-page gel, transferred to PVDF membrane and probed with and antibodies against phospho-STAT3 (Y705) and total STAT3 antibodies. Anti-GAPDH was used as a loading control.* ***B.*** *After incubation cells were harvested and stained with annexin V/propidium iodide (PI) and were analysed by flow cytometry using BD Accuri™ C6 software. 10,000 cells were gated on vehicle treated cells. Results are representative of 3 independent experiments where values represent the mean ± S.E.M. Statistical analysis was performed using a paired two-tailed t-test. NS = No significance, *p<0.05.*

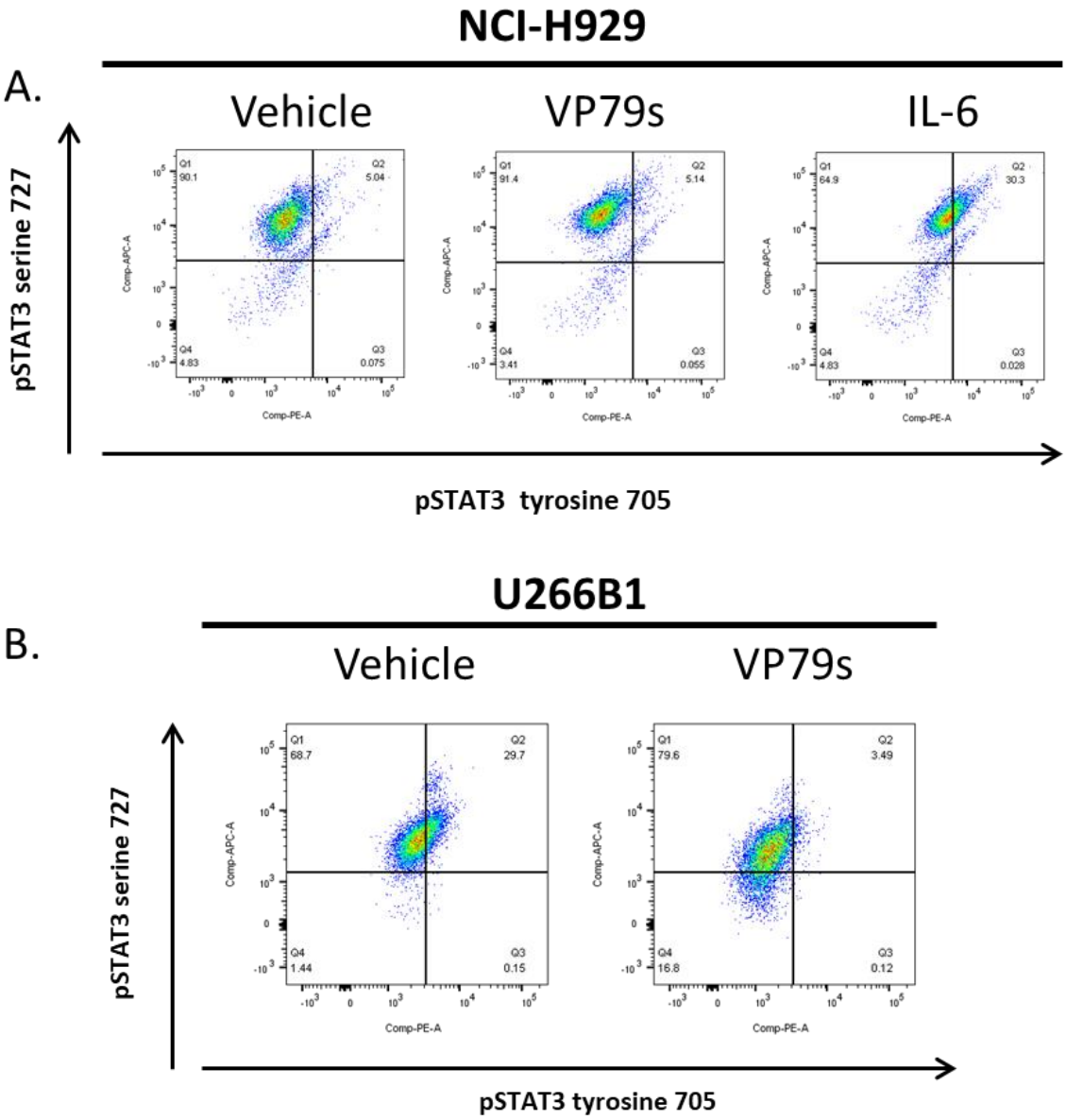

Figure 4. 7 VP79s inhibits STAT3 tyrosine 705 phosphorylation as evidenced by flow cytometry.

NCI-H929 and U266B1 cells were seeded at 30 x 10^4 cells/mL in 12 well plates and treated with either vehicle [0.5% EtOH (v/v)] or 10 µM VP79s for 60 minutes. Cells were collected, fixed, permeabilised and stained with anti-phospho-STAT3 Serine 727 and anti-phospho-STAT3 Tyrosine 705. Cells were compensated on unstained and single stained controls. ***A.*** *Representative plots of 10,000 single NCI-H929 cells gated on pSTAT3 (tyrosine 705 conjugated to PE) and pSTAT3 (serine 727 conjugated to APC). Cells were pre-treated with 10 ng/mL IL-6 for 30 minutes as a positive control.* ***B.*** *Representative plots of 10,000 single U266B1 cells gated on pSTAT3 (tyrosine 705 conjugated to PE) and pSTAT3 (serine 727 conjugated to APC). Results are representative of three independent experiments with similar results.*

4.2.4. VP79s has no effect on SOCS-1 expression

Having established that VP79s inhibits STAT3 phosphorylation, upstream targets that are known to be involved in STAT3 activation were next examined. The suppressor of cytokine signalling (SOCS) family are negative feedback inhibitors of signalling induced by cytokines which activate the JAK/STAT pathway. The SOCS family can act as ubiquitin ligases but SOCS-1 and SOCS-3 have the unique ability to inhibit the kinase activity of JAKs via their kinase inhibitory domain [355]. SOCS-1 is a tumour suppressor and downregulation of SOCS-1 is thought to play in role in cancer progression. Moreover, SOCS-1 has been shown to be silenced by methylation in 62% of MM patients [363]. Therefore, the effect that VP79s had on the expression of SOCS-1 in U266B1 cells was examined. U266B1 cells were treated with 10 μM VP79s for 30 minutes, 2, 4 or 8 hours. Cells were collected, lysates were prepared, and proteins were separated out on a 12% SDS-PAGE gel. Gels were probed with anti-SOCS-1 and anti-GAPDH was used as a loading control.

Western blot analysis demonstrated no observable differences in SOCS-1 protein expression following treatment with VP79s (Figure 4.8 A). Densitometry analysis confirmed that no statistically significant differences were observed (Figure 4.8 B).

In conclusion, VP79s had no effect on the expression of SOCS-1 therefore, suggesting that VP79s does not inhibit STAT3 phosphorylation through SOCS-1 inhibition of the JAKs.

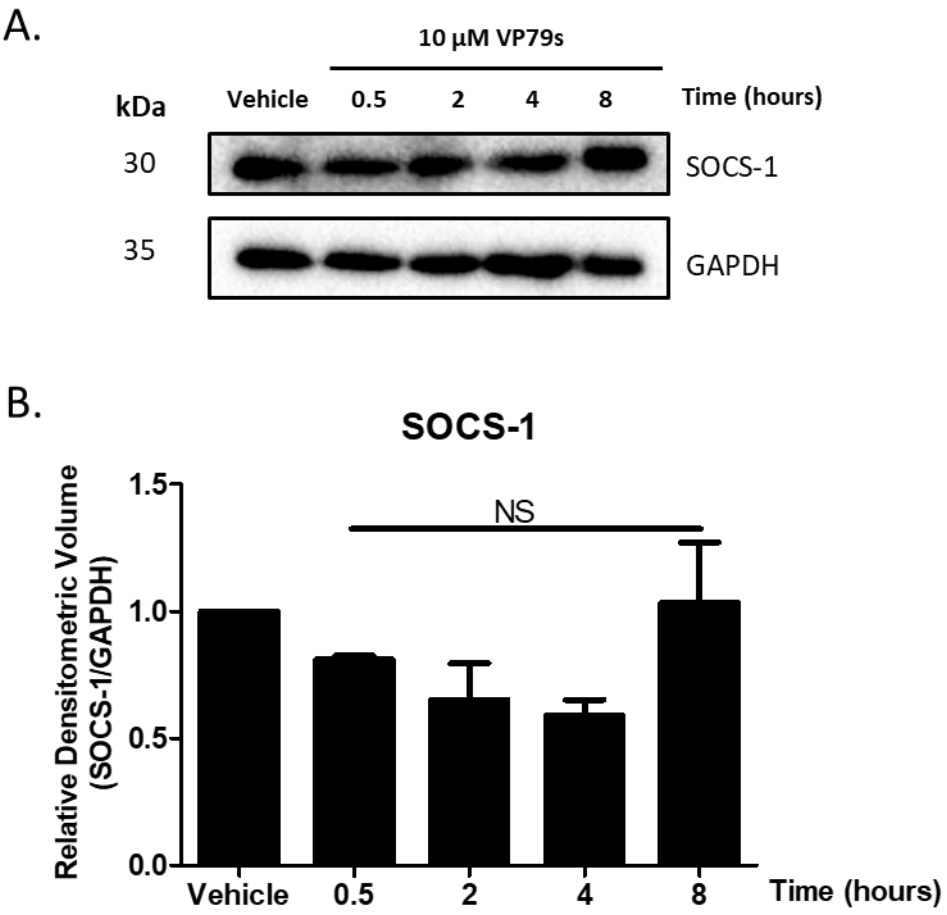

Figure 4. 8 VP79s does not affect SOCS-1 expression levels in U266B1 cells.

U266B1 cells were seeded at a density of 30x10^4 cells/mL. Cells were treated with either vehicle [0.5% EtOH (v/v)] or VP79s (10 µM) for 30 mins, 2, 4 or 8 hours. Cells were lysed and equal amounts of protein were loaded and separated on 12% SDS-page gel, transferred to PVDF membrane and probed with the appropriate antibody. ***A.*** *Representative images of SOCS-1. Anti-GAPDH was used as a loading control. Results are representative of 3 independent experiments.* ***B****. Densitometric analysis was carried out using image lab software. Statistical analysis was performed using one-way ANOVA with Dunnett's post hoc test. NS = no significance.*

4.2.5. VP79s appears to inhibit JAK2 phosphorylation but not JAK1 or SRC phosphorylation

Having established that SOCS-1 does not play a significant role in the STAT3 inhibitory activity of VP79s, kinases known to lie upstream of STAT3 were next examined. Aberrant STAT3 activation in cancer is not fully understood. However, in most instances, hyper-phosphorylation of STAT3 is mediated by unchecked intrinsic tyrosine kinase activity of kinases, such as JAK and SRC rather than a mutation in STAT3 itself [343, 364]. As such, intense efforts focusing on the inhibition of kinases that drive STAT3 phosphorylation are underway.

SRC is a tyrosine kinase that has been demonstrated to lie upstream of STAT3 [354]. It has been reported that SRC plays key roles in cell growth, division, migration, and survival signalling pathways. Consequently, the ability of VP79s to inhibit SRC phosphorylation was examined. NCI-H929 and U266B1 cells were treated with 10 μM VP79s for 30 minutes, 2, 4 or 8 hours. Cells were collected, lysates were prepared, and proteins were separated out on a 12% SDS-PAGE gel. Gels were probed with anti-total SRC and anti-phospho-SRC (Y418). Phosphorylation of SRC on tyrosine 418 (Y418) was examined as it is required for the full catalytic activity of SRC and inhibition of phosphorylation on this residue has been reported to lead to a decrease in STAT3 phosphorylation [348]. Anti-GAPDH was used as a loading control.

No visible differences were observed in SRC phosphorylated on tyrosine 418 at any timepoint examined in both the U266B1 and NCI-H929 cell line (Figure 4.9). Interesting, on the total SRC blot, a band approximately 65-70 kilodaltons in size was visible at 4 and 8 hours post treatment with VP79s in both the NCI-H929 and U266B1 cell lines which may be a modified form of SRC such as phosphorylation or ubiquitinated SRC (Figure 4.9).

JAK 1 and 2 lie upstream of STAT3 and are an essential component of the IL-6R/JAK/STAT3 signalling cascade and moreover, numerous compounds such as ruxolitinib have been shown to inhibit JAK 1/2 phosphorylation and consequently STAT3 phosphorylation. Therefore, the effect of VP79s on JAK1 and JAK2 was also examined. As such, U266B1 cells were treated with 10 μM VP79s or 30 μM ruxolitinib for 4 hours. Cells were collected, lysates were prepared, and proteins were separated on a 10% SDS-PAGE gel. Gels were

probed with antibodies against JAK1, phospho-JAK1, JAK2, phospho-JAK2, and STAT3 and phospho-STAT3. Anti-GAPDH was used as a loading control.

The effect of VP79s and ruxolitinib on phospho-JAK2 was firstly examined. VP79s and ruxolitinib were shown to inhibit phospho-JAK2 in the U266B1 cell line (Figure 4.10 A). Inhibition of phosphorylated JAK2 by ruxolitinib is in line with previous reports [365]. Due to time constraints owing to a longer optimisation period than expected, clear results for this experiment were only obtained on two occasions due to technical issues arising with western blots. Optimisation was carried out over many months with changes including: different RIPA buffer constituents, increasing the concentration of phosphatase and protease inhibitors, not removing cellular debris after lysing the cells, boiling the lysates at various temperatures, avoiding freezing the lysates completely, transferring overnight, blocking in 5% non-fat milk or 5% bovine serum albumin or 5% foetal bovine calf serum, incubating for 1 h to 3 days with primary antibody, increasing the concentration of primary antibody and changing the concentration of secondary antibody and incubation times. A time course from 0-120 minutes was also carried out and demonstrated that JAK2 phosphorylation on Y1007/Y1008 was inhibited from 15 minutes following treatment with VP79s. However, this result is only representative of one experiment as it could not be replicated (Figure 4.10 B). Although results from three independent experiments demonstrated inhibition of JAK2 phosphorylation by VP79s, due to technical issues with the assay more studies are required to confirm this.

The effect of VP79s on JAK1 and STAT3 was next examined. Interestingly, neither VP79s nor ruxolitinib elicited any effect on JAK1 phosphorylation in the U266B1 cells (Figure 4.11). STAT3 and phosphorylated STAT3 on tyrosine 705 were also examined as ruxolitinib has previously been shown to inhibit STAT3 phosphorylation [256, 366]. Both VP79s and ruxolitinib inhibited STAT3 phosphorylation with no visible effects on total STAT3 (Figure 4.11).

To summarise, VP79s appeared to inhibit JAK2 phosphorylation but had no effect JAK1. Whilst VP79s had no effect on SRC phosphorylation on tyrosine 418, it was shown to modulate the expression of total SRC with the appearance of a band approximately 65-70

kilodaltons in size. More studies are required to delineate the nature of this modification and the role that it may play, if any, in VP79s induced cell death.

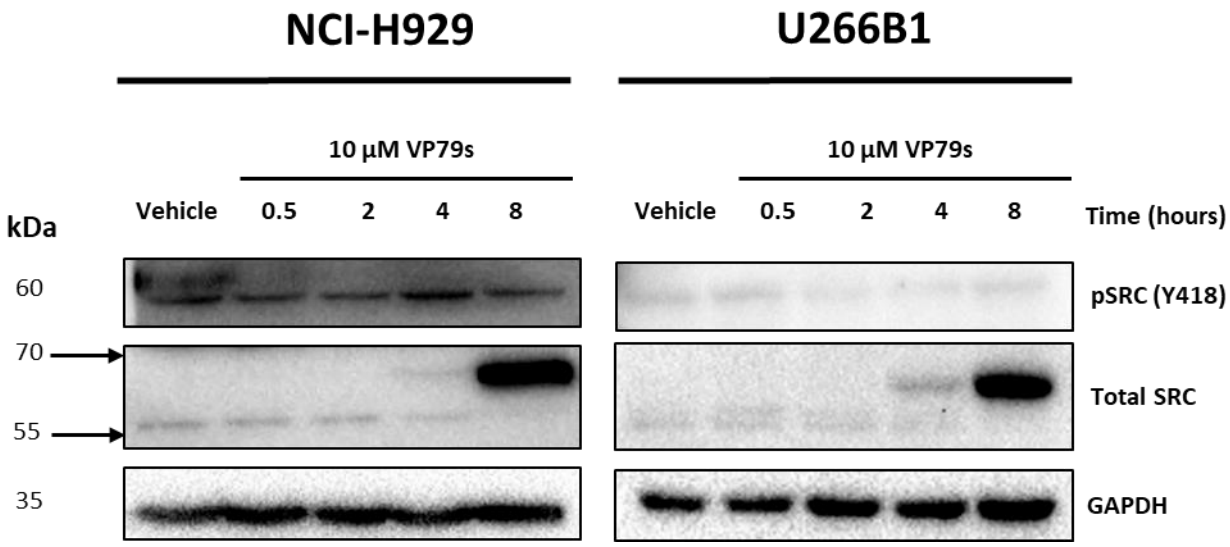

Figure 4. 9 VP79s Modulates total SRC but not phospho-SRC in NCI-H929 and U266B1 cells in a time responsive manner.

NCI-H929 and U266B1 cells were seeded at a density of 30x10^4 cells/mL. Cells were treated with either vehicle [0.5% EtOH (v/v)] or 10 µM VP79s for 30 minutes, 2, 4 or 8 hours. Cells were lysed and equal amounts of protein were loaded and separated on 12% SDS-page gels, transferred to PVDF membrane and probed with the appropriate antibody. Anti-GAPDH was used as a loading control. Results are representative of 2 independent experiments for pSRC NCI-H929 and 3 independent experiments for all other blots. GAPDH was used as a loading control. Arrows indicate where the 55 and 70 kilodalton (kDa) markers are on the blot relative to the bands on the blot.

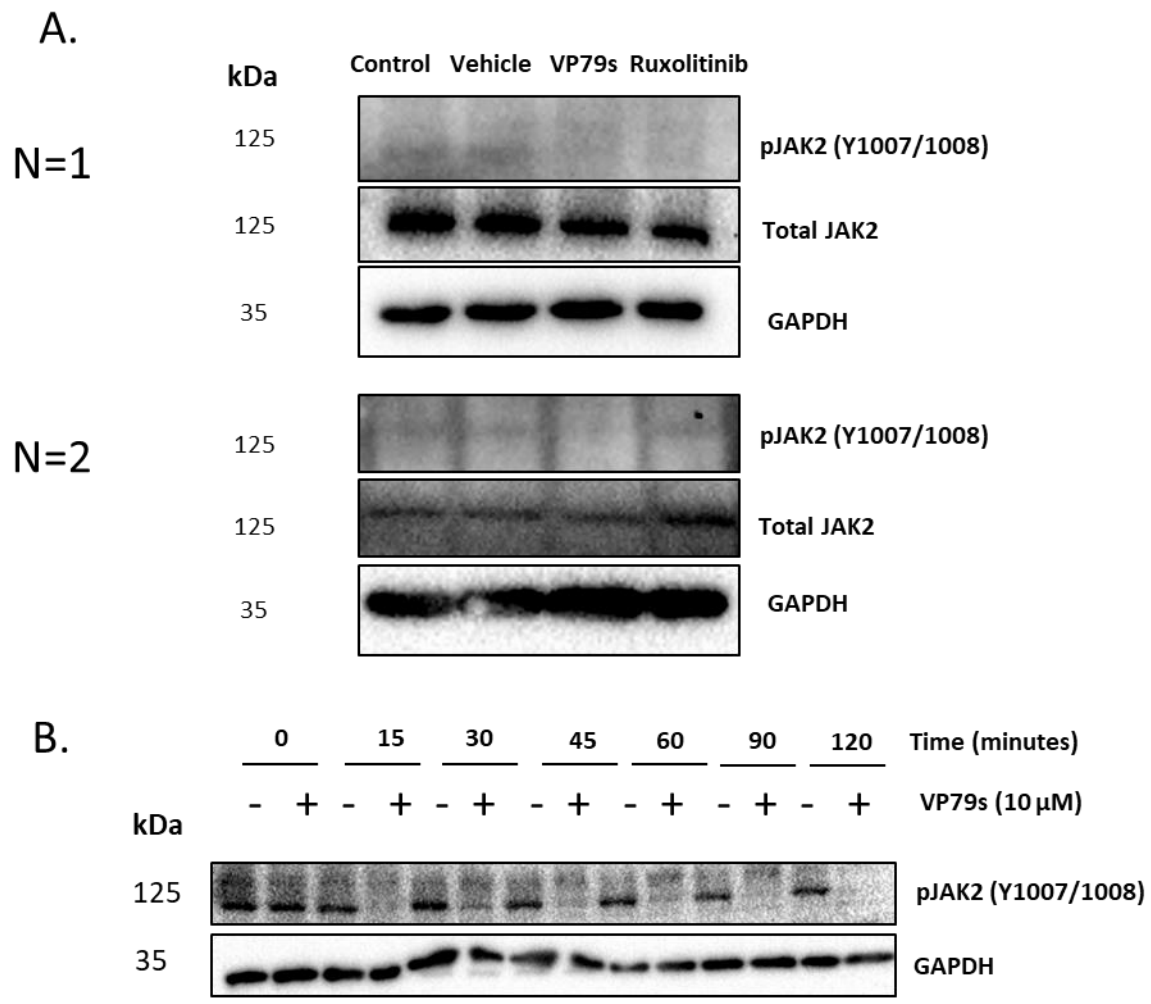

Figure 4. 10 VP79s inhibits JAK2 phosphorylation in U266B1 cells.

U266B1 cells were seeded at a density of 30x10^4 cells/mL ***A.*** *Cells were left untreated (control) or treated with either vehicle [0.5% EtOH (v/v) + 0.1% DMSO (v/v)] or 10 µM VP79s or 30 µM ruxolitinib for 4 hours or* ***B.*** *cells were treated with either vehicle [0.5% EtOH (v/v)] or 10 µM VP79s for 0, 15, 30, 45, 60, 90 or 120 minutes. Cells were lysed and 20 µg of protein was loaded and separated on 10% SDS-page gels, transferred to PVDF membrane and probed with the appropriate antibody. Anti-GAPDH was used as a loading control. Results show 2 independent experiments for* ***A.*** *and 1 experiment for* ***B.***

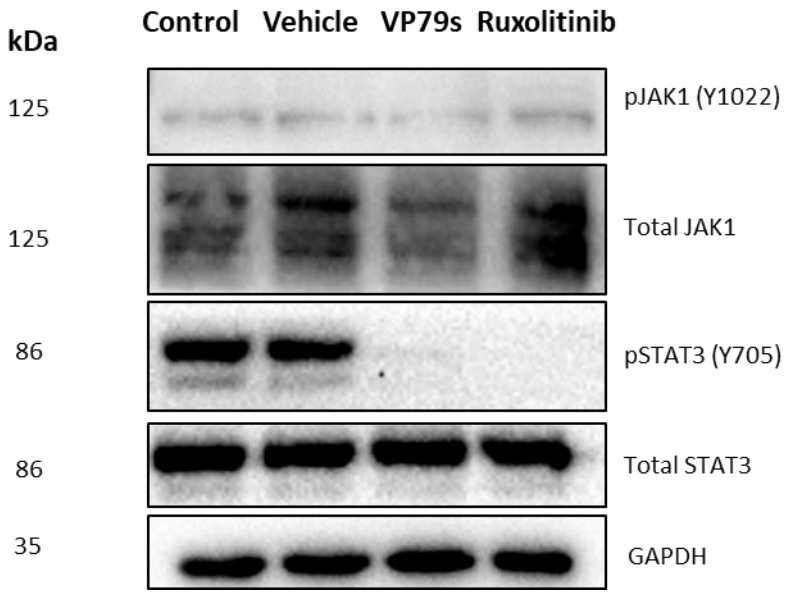

Figure 4. 11 VP79s does not affect JAK1 phosphorylation in U266B1 cells.

U266B1 cells were seeded at a density of 30x10^4 cells/mL. Cells were left untreated (control) or treated with either vehicle [0.5% EtOH (v/v) + 0.1 % DMSO (v/v)], 10 µM VP79s or 30 µM ruxolitinib for 4 hours. Cells were lysed and 20 µg of protein was loaded and separated on 10% SDS-page gels, transferred to PVDF membrane and probed with the appropriate antibody. Anti-GAPDH was used as a loading control. Results are representative of 3 independent experiments.

4.2.6. VP79s downregulates cell surface expression of CD126 and CD130 in U266B1 cells

The IL-6R/JAK2/STAT3 pathway is known to play an important role in the development of many human cancers including MM, and IL-6 is reported to be central in the pathogenesis of MM [68, 367]. CD126 (IL-6 receptor alpha) and the co-receptor CD130 (IL-6 Receptor beta or gp130) are two cell surface receptors that are required for IL-6 activation of the JAK/STAT3 pathway. Having established that VP79s can inhibit STAT3 phosphorylation in U266B1 cells (Figure 4.4 A), and that it can inhibit IL-6 induced STAT3 phosphorylation in the NCI-H929 cell line (Figure 4.6 A), the effect of VP79s on the cell surface expression of CD126 and CD130 was next investigated.

U266B1 cells were treated with 5 or 10 µM VP79s for 1 or 4 hours. After treatment, cells were collected and stained with antibodies for CD126 (Fluorochrome PE-562.5-587.5 nm) and CD130 (Fluorochrome APC-655-675 nm) and analysed by flow cytometry. With regard to CD130, VP79s induced an observable decrease the surface expression of CD130 in a dose- and time-dependent manner as a shift in fluorescence to the left indicates a decrease in expression (Figure 4.12 A). The fold change was determined by comparing the median fluorescence intensity of the vehicle to each treatment. These results were statistically significant at both time points and concentrations examined (Figure 4.12 B). Similar results were obtained for cell surface expression of CD126 with a statistically significant decrease demonstrated in a time- and dose-responsive manner (Figure 4.12 A and B).

In order to determine if CD130 and CD126 expression was downregulated prior to or post STAT3 inhibition a time course experiment was conducted. Thereby, U266B1 cells were treated with either vehicle or 10 µM VP79s for 15, 30, 45 or 60 minutes. As before, and following the appropriate time, cells were collected and stained with antibodies for CD126 and CD130 and were analysed by flow cytometry. An observable time-responsive decrease in both CD130 and CD126 was evident from 30 minutes as indicated by a shift in fluorescence to the left (Figure 4.13 A). The fold change in median fluorescence intensity comparing vehicle to treatments indicated an observable decrease at 30 minutes;

however, this decrease was not statistically significant until the 60 minute timepoint (Figure 4.13 B).

In summary, VP79s was found to downregulate both CD130 and CD126 in a dose- and time-responsive manner. CD130 and CD126 were downregulated concurrently with a significant decrease in expression observed at 60 minutes.

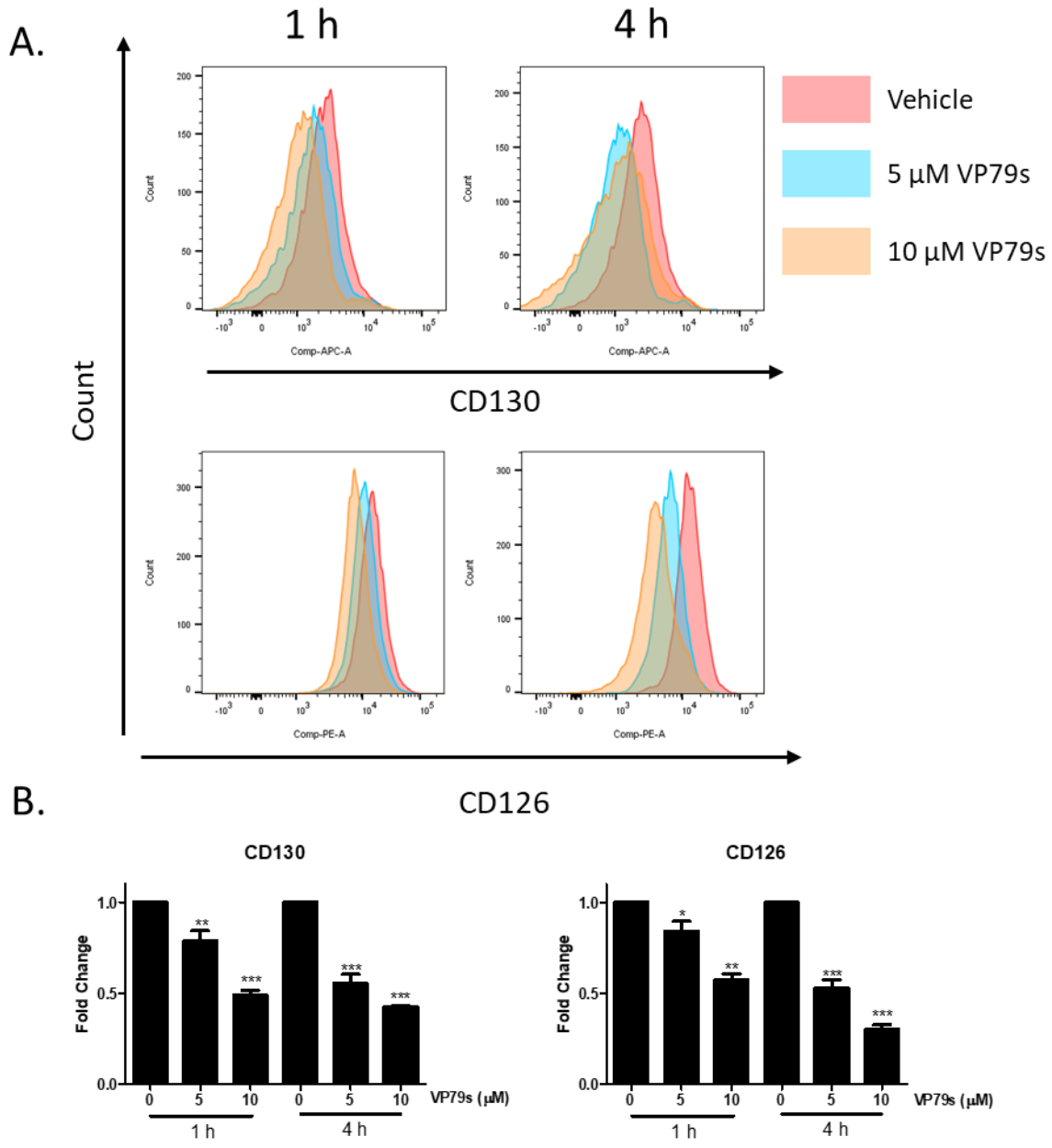

Figure 4. 12 VP79s downregulates CD130 and CD126 in a dose- and time-responsive manner. *30 x 10^4 cells/mL of U266B1 cells were seeded in 24 well plates and were treated with either vehicle [0.5% EtOH (v/v)], 5 µM or 10 µM VP79s for 1 or 4 hours. After treatment, cells were collected and stained with antibodies for CD126 (Conjugated to PE) and CD130 (Conjugated to APC). Samples were analysed on BD FACSCanto™ II flow cytometer.* ***A.*** *Representative histograms showing the effect of VP79s treatment of CD126 and CD130 surface expression****. B.*** *Bars represent the fold change in median fluorescence intensity of vehicle and treatments. Error bars represent the mean ± the S.E.M. of 3 independent experiments. Statistical analysis was performed using one-way ANOVA with Dunnett's post hoc test comparing vehicle to treatments. *p<0.05, **p <0.01 and *** p < 0.001.*

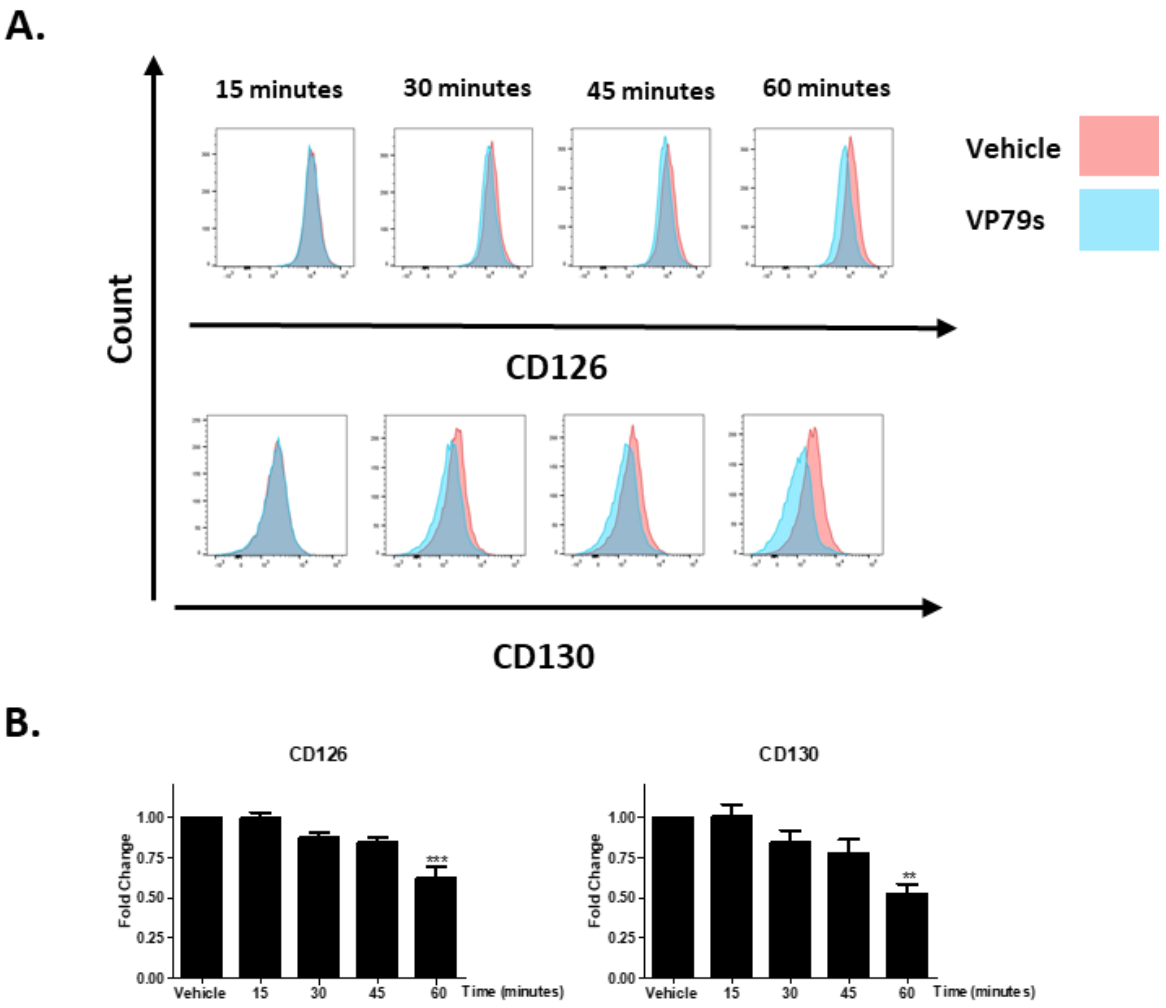

Figure 4. 13 VP79s downregulates CD130 and CD126 in a time-responsive manner.

30 x 10^4 cells/mL of U266B1 cells were seeded in 24 well plates and were treated with either vehicle [0.5% EtOH (v/v)] or 10 µM VP79s for 15 – 60 minutes. After treatment, cells were collected and stained with antibodies for CD126 (Conjugated to PE) and CD130 (Conjugated to APC). Samples were analysed on BD FACSCanto™ II flow cytometer. ***A.*** *Representative histograms showing the effect of VP79s treatment on CD126 and CD130 surface expression****.*** ***B.*** *Bars represent the fold change in median fluorescence intensity of vehicle and treatments. Error bars represent the mean ± the S.E.M. of 3 independent experiments. Statistical analysis was performed using one-way ANOVA with Dunnett's post hoc test comparing vehicle to treatments. **p <0.01.*

4.2.7. STAT3 inhibition by VP79s results in a decrease in the expression of downstream STAT3 target genes

Following activation of the JAK/STAT3 signalling pathway, the active JAK enzymes phosphorylate STAT3 at tyrosine 705 (Y705). This phosphorylation results in head-to-tail dimerisation of STAT3 and translocation to the nucleus where STAT3 carries out its function as a transcription factor. STAT3 binds to the promotor regions of STAT3 responsive genes involved in proliferation, cell survival and migration; such as cyclin D1, the anti-apoptotic Bcl-2 family members, IAPs and metalloproteinase 1 respectively [78]. Having previously demonstrated that VP79s inhibits STAT3 phosphorylation on tyrosine 705, the effect of VP79s on STAT3 regulated genes was determined by quantitative PCR.

U266B1 cells were treated with 2.5 µM VP79s for 2 or 8 hours. This concentration of VP79s was chosen in order to ensure that any changes in gene expression were not due to cell death. Following treatment, cells were collected, samples were prepared and STAT3 regulated genes, *MCL1*, *BCL2*, *CCND1* (Cyclin D1) and *STAT3* were examined at the mRNA level. Beta-2-microglobulin (B2M) was used as a housekeeping gene. Minimal effects were observed 2 hours post treatment. At the 8 hour timepoint, VP79s had caused a decrease in *STAT3*, *MCL1* and *CCND1*, with a fold decrease of 0.98, 0.67 and 0.81 respectively. No decrease was observed in the expression of *BCL2* (Figure 4.14). No significant differences were observed in the gene expression of STAT3 responsive genes examined however a trend towards the downregulation of *STAT3*, *MCL1* and *CCND1* was observed. This was likely due to the lower concentration of 2.5 µM VP79s being used to avoid any changes in gene expression caused by the induction of cell death.

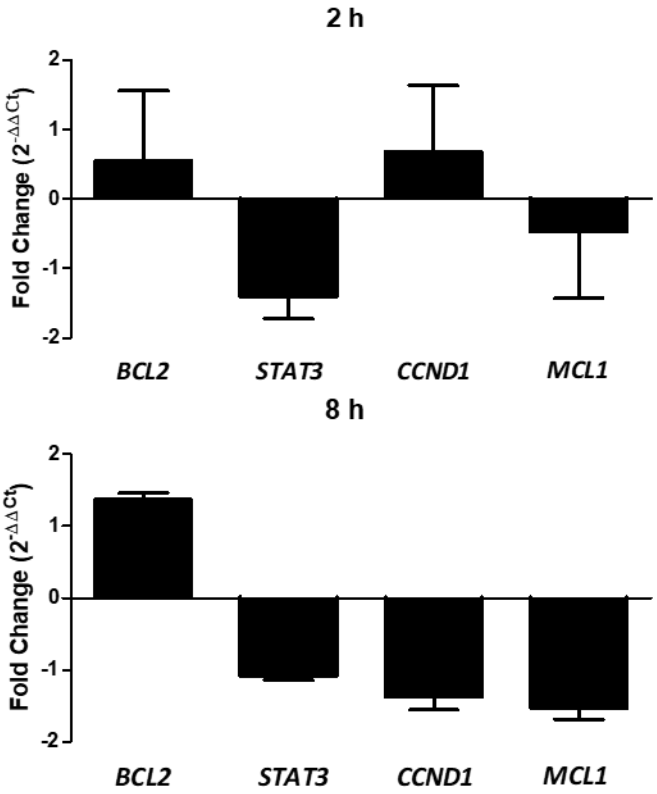

Relative mRNA expression compared to vehicle ($2^{-\Delta\Delta Ct}$)					
	Vehicle	*BCL2*	*STAT3*	*CCND1*	*MCL1*
2 hours	1	1.25 ± 0.37	0.82 ± 0.17	1.34 ± 0.38	0.96 ± 0.34
8 hours	1	1.367 ± 0.1	0.98 ± 0.08	0.81 ± 0.15	0.67 ± 0.08
Fold Change					
2 hours	n/a	0.55 ± 1.7	-1.4 ± 0.54	0.67 ± 1.7	-0.5 ± 1.6
8 hours	n/a	1.37 ± 0.96	-1.07 ± 0.07	-1.37 ± 0.2	-1.5 ± 0.2

Figure 4. 14 The effect of VP79s on the gene expression of downstream STAT3 target genes.

U266B1 cells were seeded at 30 x 10^4 cells/mL and were treated with either vehicle [0.5% EtOH (v/v)] or 2.5µM VP79s for 2 or 8 hours. Samples were analysed by RT-qPCR performed using TaqMan Assays for STAT3, BCL2, CCND1 (cyclin D1) and MCL1. Beta-2-microglobulin (B2M) was used as an endogenous control. Error bars represent the S.E.M of three independent experiments. Relative fold change was calculated using the delta-delta ct method.

4.2.8. VP79s results in the downregulation of the expression of anti-apoptotic Mcl-1 in NCI-H929 and U266B1 cells

Since VP79s was shown to induce apoptotic cell death in the panel of drug-sensitive and -resistant MM cell lines (Chapter 3) and quantitative PCR indicated a possible decrease in Mcl-1 gene expression, the protein expression of a number of anti-apoptotic Bcl-2 family members was next examined in order to further elucidate the mechanism by which VP79s induces cell death. The effect of VP79s on anti-apoptotic Bcl-2 family members Mcl-1, Bcl-2 and Bcl-xL was assessed. As before, NCI-H929 and U266B1 wells were treated with VP79s (1.25, 5 or 10 µM) for 16 hours. Lysates were prepared and ran on 12% SDS-PAGE gels.

Following treatment with VP79s the expression of Mcl-1 was significantly downregulated at 10 µM in the NCI-H929 cell line (Figure 4.15 A and B); however, following the 5 µM treatment a band of approximately 25 kilodaltons was observed (Figure 4.15 A). This band may possibly be a cleaved form of Mcl-1. It has been demonstrated that such cleavage fragments not only abrogate the anti-apoptotic function of Mcl-1 but also generate a pro-apoptotic truncated fragment [368]. In contrast, VP79s was shown to have no significant effects on the level of expression of anti-apoptotic Bcl-2 or Bcl-xL in the NCI-H929 cell line (Figure 4.15 A and B).

VP79s caused downregulation of the expression of Mcl-1 in the U266B1 cell line in a dose-responsive manner (Figure 4.16 A) with statistically significant inhibition observed following treatment with both 5 µM and 10 µM VP79s (Figure 4.16 B). Similar to the NCI-H929 cell line, no visible change in the expression levels of either Bcl-2 or Bcl-xL was observed. However, significant cleavage of Bcl-2 was observed in the U266B1 cell line following treatment with 10 µM VP79s with a cleaved band evident at approximately 20 kilodaltons (Figure 4.16 A and B). Similar to cleaved Mcl-1, it is suggested that such cleaved fragments represent pro-apoptotic forms of the protein [369].

Mcl-1 is a key anti-apoptotic survival protein which has been found to be overexpressed in MM and is associated with patient relapse and shorter survival time, therefore novel drugs which can downregulate Mcl-1 in MM are required [226]. Since VP79s downregulated Mcl-1 protein expression levels at 16 hours, earlier time points were next examined to determine when this downregulation begins. NCI-H929 and U266B1 cells were treated

with 10 μM VP79s for 30 minutes, 2, 4 or 8 hours. Cells were collected, lysates were prepared, and proteins were separated on a 12% SDS-PAGE gel. Gels were probed with antibodies against Mcl-1. Anti-GAPDH was used as a loading control.

Mcl-1 was found to be downregulated in the NCI-H929 cell line in a time-dependent manner as early as 2 hours post treatment with significant inhibition observed at 8 hours. Similarly, in U266B1 cells, significant downregulation of Mcl-1 protein expression occurred from 2 hours, with complete abrogation of Mcl-1 protein expression at 8 hours (Figure 4.17 A and B).

To summarise, VP79s downregulated the protein expression of Mcl-1 in both the NCI-H929 cells and U266B1 cells with no significant differences observed in the full-length forms of Bcl-2 and Bcl-xL. Cleavage of Mcl-1 and Bcl-2, to possible truncated pro-apoptotic forms of the proteins were observed in the NCI-H929 and U266B1 cell lines, respectively.

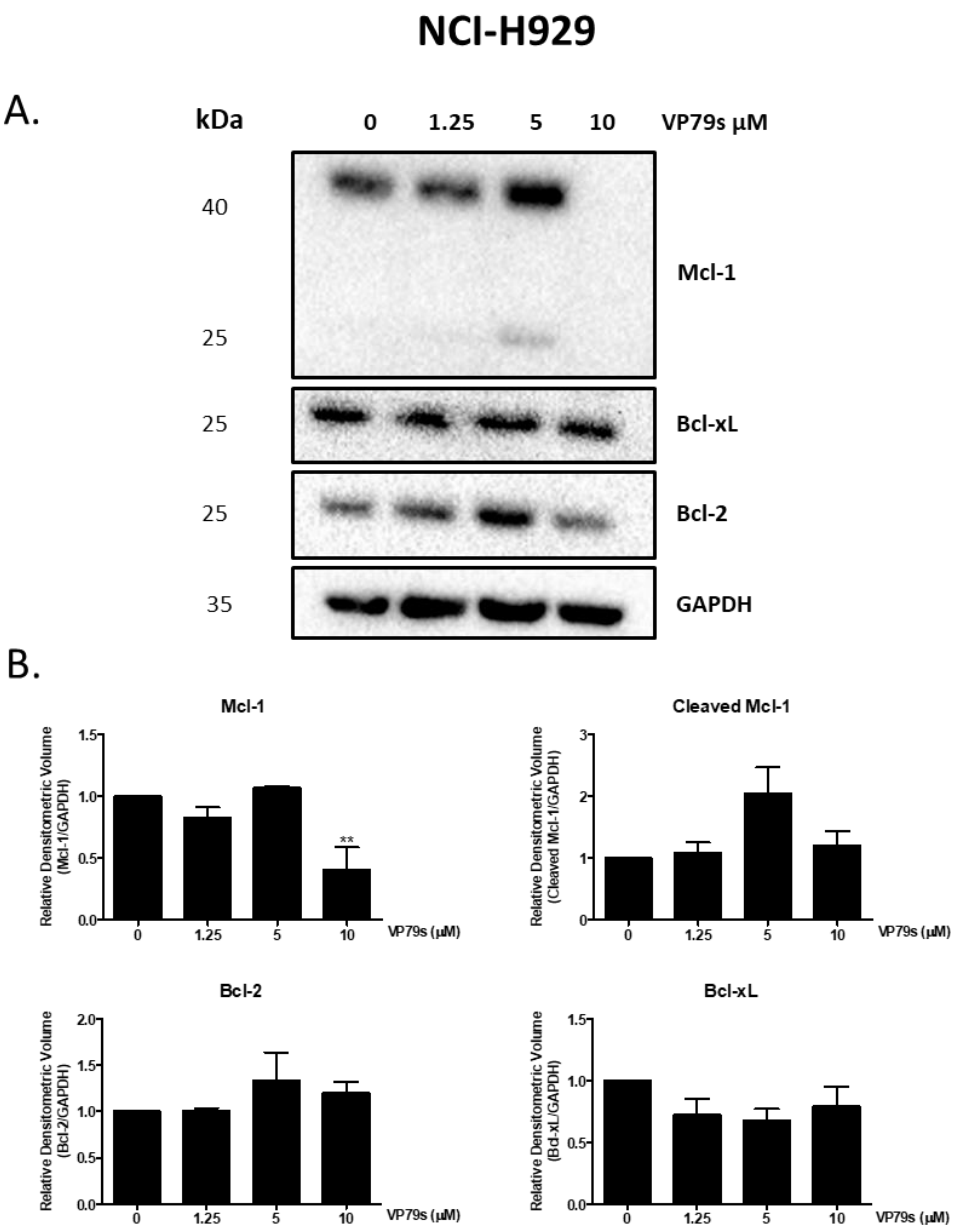

Figure 4. 15 VP79s downregulates the expression level of anti-apoptotic Mcl-1 in NCI-H929 cells.

NCI-H929 cells were seeded at a density of 30x10^4 cells/mL. Cells were treated with either vehicle [0.5% EtOH (v/v)] or VP79s (1.25, 5 and 10 µM) for 16 hours. Cells were lysed and 20 µg of protein was loaded and separated on 15% SDS-page gels, transferred to PVDF membrane and probed with the appropriate antibody. ***A.*** *Representative images of Mcl-1, Bcl-2 and Bcl-xL. Anti-GAPDH was used as a loading control. Results are representative of 3 independent experiments.* ***B.*** *Densitometric analysis of bands was carried out using image lab software. Statistical analysis was performed using one-way ANOVA with Dunnett's post hoc test comparing vehicle to treatments. **p<0.01.*

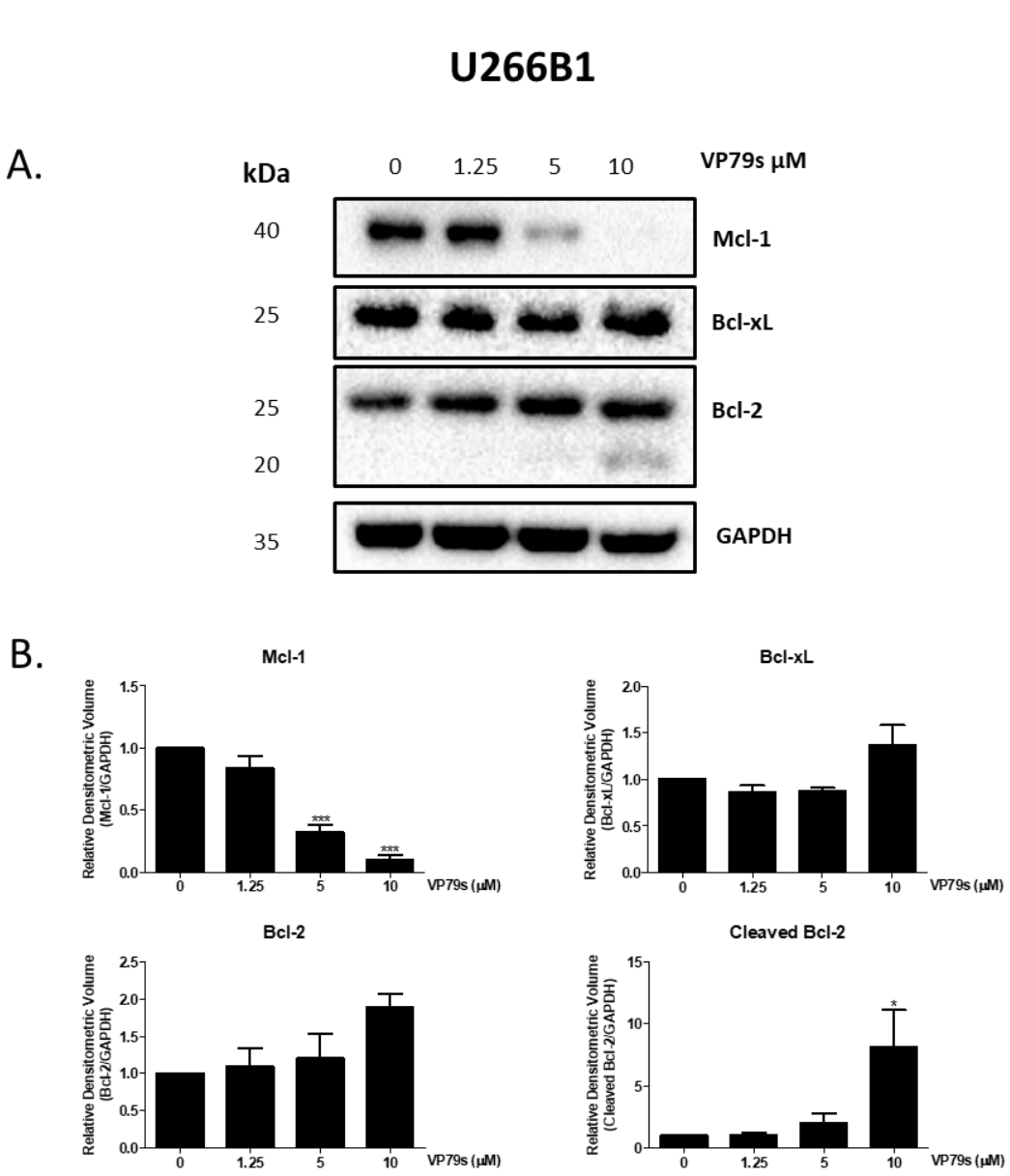

Figure 4. 16 VP79s downregulates the expression level of anti-apoptotic Mcl-1 in U266B1 cells in a dose responsive manner.

U266B1 cells were seeded at a density of 30x10^4 cells/mL. Cells were treated with either vehicle [0.5% EtOH (v/v)] or VP79s (1.25, 5 and 10 µM) for 16 hours. Cells were lysed and 20 µg of protein was loaded and separated on 15% SDS-page gels, transferred to PVDF membrane and probed with the appropriate antibody. ***A.*** *Representative images of Mcl-1, Bcl-2 and Bcl-xL. Anti-GAPDH was used as a loading control. Results are representative of 3 independent experiments.* ***B.*** *Densitometric analysis of bands was carried out using image lab software. Statistical analysis was performed using one-way ANOVA with Dunnett's post hoc test comparing vehicle to treatments. *p<0.05, ***p<0.001.*

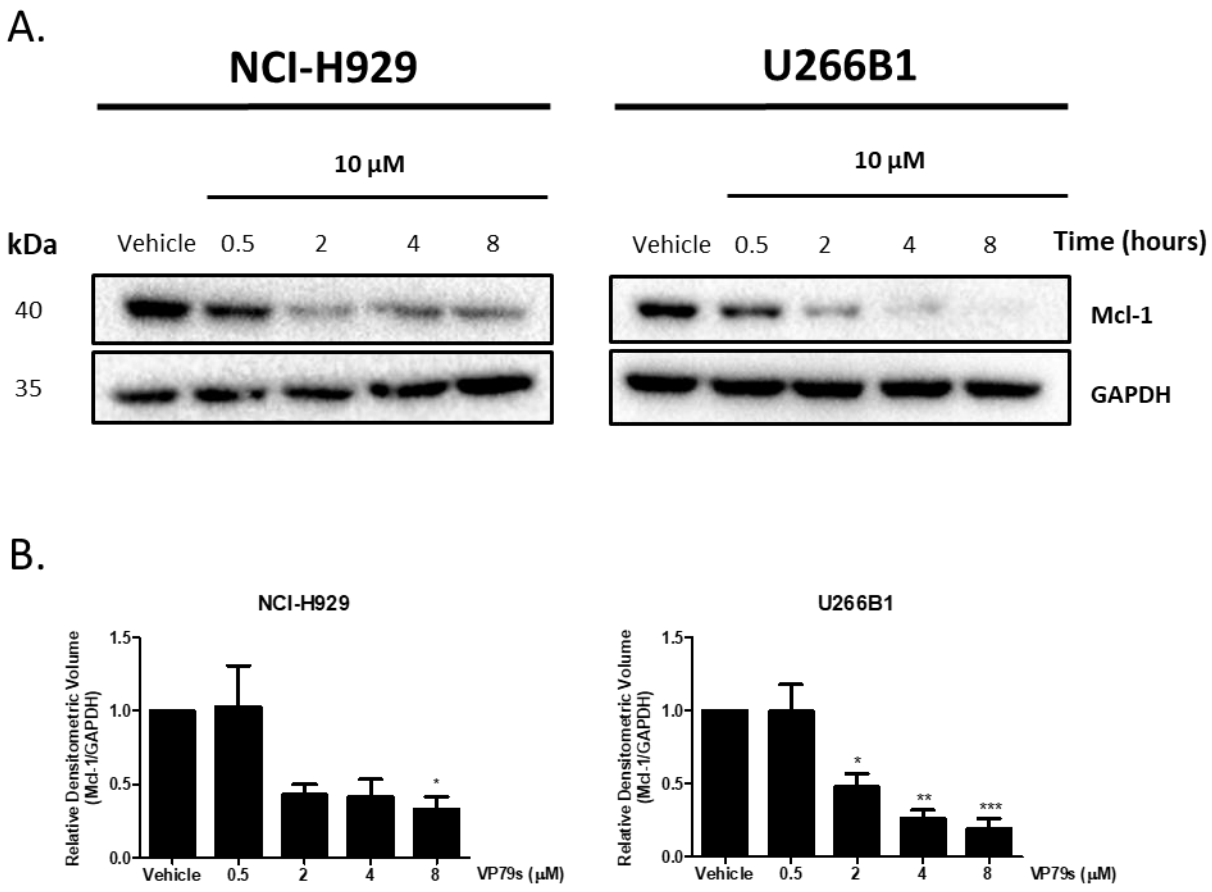

Figure 4. 17 VP79s downregulates Mcl-1 in NCI-H929 and U266B1 cells in a time-responsive manner.

NCI-H929 and U266B1 cells were seeded at a density of 30x10^4 cells/mL. Cells were treated with either vehicle [0.5% EtOH (v/v)] or 10 µM VP79s for 30 minutes, 2, 4 or 8 hours. Cells were lysed and equal amounts of protein were loaded and separated on 12% SDS-page gels, transferred to PVDF membrane and probed with the appropriate antibody. Anti-GAPDH was used as a loading control. ***A.*** *Results are representative of 3 independent experiments. Western blots were normalised to total GAPDH as a loading control.* ***B.*** *Densitometric analysis of bands was carried out using image lab software. Statistical analysis was performed using one-way ANOVA with Dunnett's post hoc test. *p<0.05, **p<0.05 and ***p<0.001.*

4.2.9. VP79s downregulates the expression level of downstream STAT3 targets cyclin D1 and survivin

Having demonstrated an apparent decrease in cyclin D1 gene expression in the U266B1 cell line, expression of cyclin D1 at the protein level was next examined in both the NCI-H929 and U266B1 cell lines. As previously discussed in detail above, cyclin D1 has been shown to be a STAT3 responsive gene and upregulation of cyclin D1 is an early and unifying event in MM which is thought to play a key role in the survival and proliferation of MM cells through modulation of the cell cycle [101]. Survivin is also another downstream STAT3 target that has been shown to play a role in cell survival acting as an inhibitor of apoptosis protein [100]. Survivin has also been demonstrated to be overexpressed in MM, therefore, its expression was also examined [97]. NCI-H929 and U266B1 wells were treated with VP79s (1.25, 5 or 10 μM) for 16 hours. Cells were collected, lysates were prepared and ran on 15% SDS-PAGE gels before being transferred to PVDF membrane. Membranes were then probed for antibodies against cyclin D1 and survivin. Anti-beta-actin and anti-GAPDH were used as loading controls respectively.

Treatment with 5 and 10 μM VP79s in the NCI-H929 cell line resulted in an observable decrease in cyclin D1 expression; however, this decrease did not reach statistical significance until 10 μM. VP79s appeared to have no observable effect on the expression of survivin in the NCI-H929 cells with densitometric analysis of three separate western blots confirming this result (Figure 4.18).

VP79s caused an observable decrease in cyclin D1 expression in a dose-responsive manner in the U266B1 cells. When results from three separate western blots were combined, densitometric analysis illustrated a statistically significant decrease at both 5 and 10 μM (Figure 4.18 B). Treatment with 5 μM VP79s resulted in a statistically significant decrease in survivin following densitometric analysis (Figure 4.18 B).

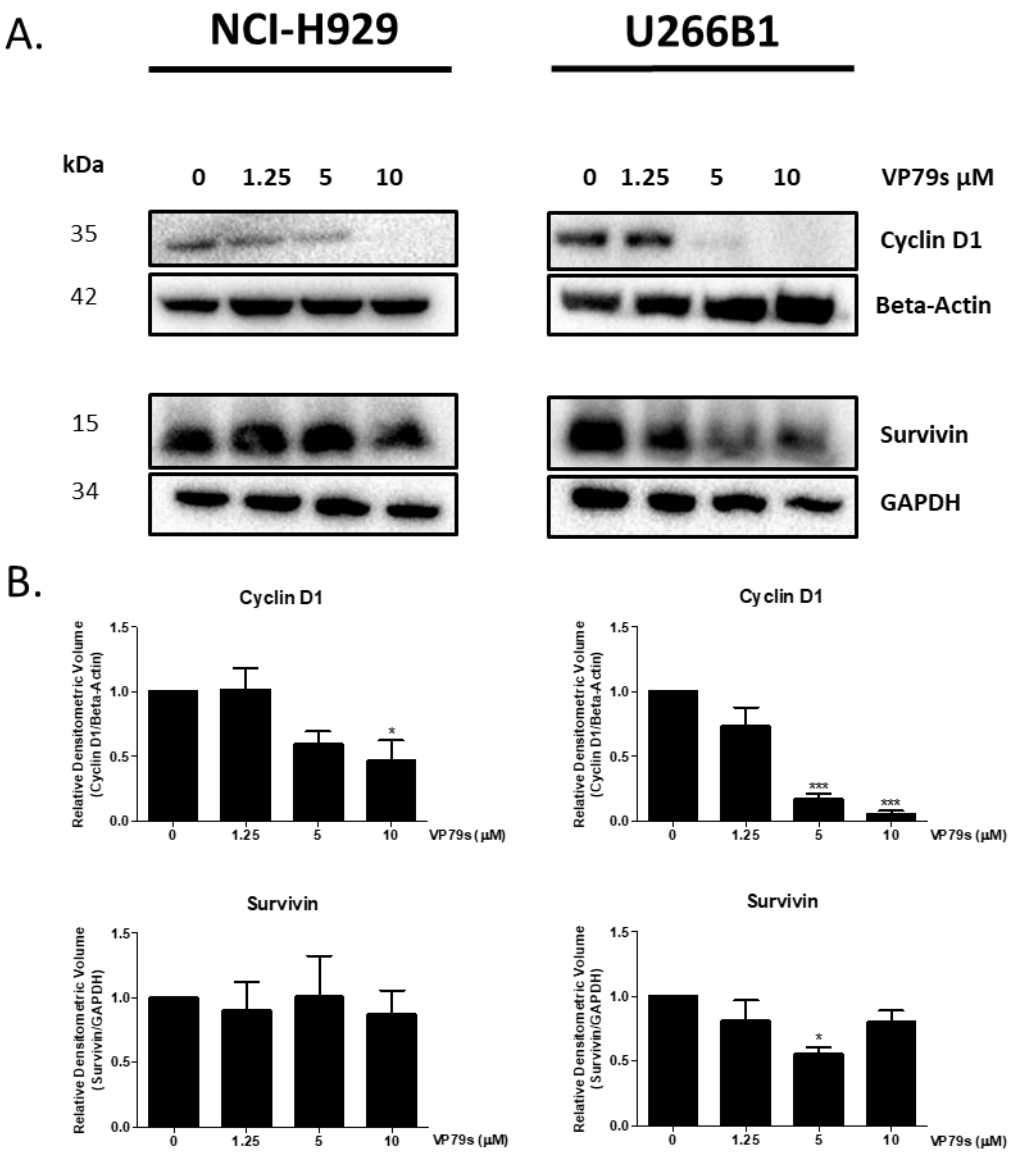

Figure 4. 18 The effect of VP79s on the expression levels of cyclin D1 and survivin.

U266B1 and NCI-H929 cells were seeded at 30 x 10^4 cells/mL and were treated with either vehicle [0.5% EtOH (v/v)] or VP79s (1.25, 5 and 10 µM) for 16 hours. ***A.*** *Cells were lysed and 20 µg of protein was loaded and separated on 15% SDS-page gels, transferred to PVDF membrane and probed with the appropriate antibody. Anti-GAPDH and anti-beta-actin were used as loading controls. Results are representative of 3 independent experiments. Western blots were normalised to GAPDH or beta-actin as a loading control.* ***B.*** *Densitometric analysis of bands was carried out using image lab software. Statistical analysis was performed using one-way ANOVA with Dunnett's post hoc test. *p<0.05 and ***p<0.001.*

4.2.10. VP79s activates MAPK signalling pathways in NCI-H929 and U266B1 cells

Since VP79s was rationally designed to allosterically target BRAF and ED73a, a precursor of VP79s, was demonstrated to target BRAF, the effects of VP79s on the RAS/RAF/MEK/ERK signalling pathway were next examined. ERK is a serine/threonine kinase which lies downstream of BRAF and its phosphorylation was used as a read out for any effects VP79s may have had on this signalling pathway. Initially, NCI-H929 cells were treated with 10 µM VP79s for 30 minutes, 2, 4 and 8 hours. Cells were collected, lysates were prepared, ran on a 12% SDS-PAGE gel before being transferred to PVDF membrane. Membranes were then probed for antibodies against ERK and phosphorylated ERK. Anti-GAPDH was used as loading control.

Interestingly, VP79s was shown to distinctly increase ERK phosphorylation from 2 hours with a marked increase in phosphorylation in the NCI-H929 cells. An increase in total ERK was also observed at the later timepoints of 4 and 8 hours (Figure 4.19).

Having observed this increase in ERK activation, the effect of VP79s on JNK and p38 activation was also examined. JNK and p38 are also members of the MAPK family which link extracellular signals to the intracellular machinery which controls cellular processes. Unlike ERK, whose activation is associated with cell survival, JNK and p38 activation is most often associated with cell death [123, 131]. Samples were treated and processed as before and membranes were then probed for antibodies against p38, JNK and their phosphorylated forms. Anti-GAPDH was used as a loading control.

As with ERK, a marked increase in phosphorylation of p38 and JNK was observed from 2 hours. Total levels of p38 and JNK did not appear to increase as substantially as total ERK (Figure 4.19).

Following on from this, the effect of VP79s on the MAPK pathways was examined in the U266B1 cells. Cells were treated with 10 µM VP79s for 30 minutes, 2, 4 and 8 hours. Cells were collected, lysates were prepared, ran on a 12% SDS-PAGE gel before being transferred to PVDF membrane. Membranes were then probed for antibodies against the total and phosphorylated forms of ERK, p38 and JNK. Anti-GAPDH was used as loading control.

The U266B1 cells possess much higher levels of constitutively activated ERK compared to the NCI-H929 cell line, likely due to the U266B1 possessing a mutation in *BRAF [370]*. However, an observable increase in both the total and phosphorylated forms of ERK was seen following treatment with VP79s (Figure 4.20). An observable increase in p38 and JNK phosphorylation was also seen from 2 hours post treatment in the U266B1 cells (Figure 4.20).

To summarise, VP79s treatment led to a sustained increase in phosphorylation of ERK, JNK and p38 in the NCI-H929 and U266B1 cells from 2 hours.

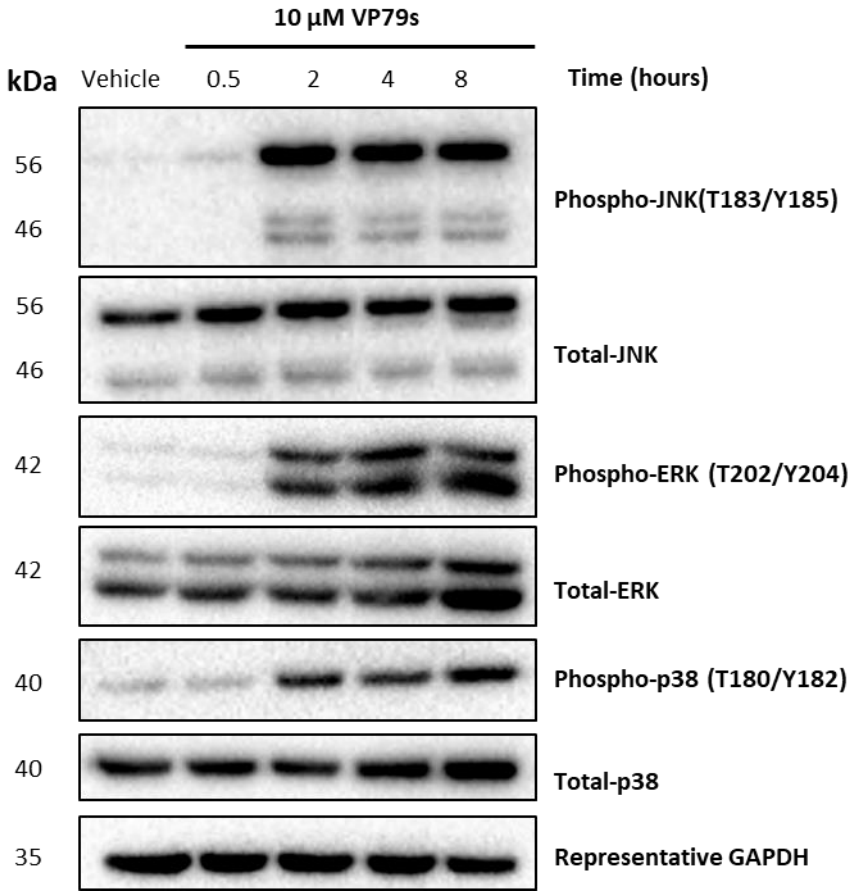

Figure 4. 19 VP79s activates ERK, JNK and p38 signalling in NCI-H929 cells.

NCI-H929 cells were seeded at a density of 30x10^4 cells/mL. Cells were treated with either vehicle [0.5% EtOH (v/v)] or VP79s (10 µM) for 30 mins, 2, 4 or 8 hours. Cells were lysed and equal amounts of protein were loaded and separated on 12% SDS-page gel, transferred to PVDF membrane and probed with the appropriate antibody. Representative images of phospho-JNK, total JNK, phospho-ERK, total ERK, phospho-p38 and total p38. Anti-GAPDH was used as a loading control. Results are representative of 3 independent experiments.

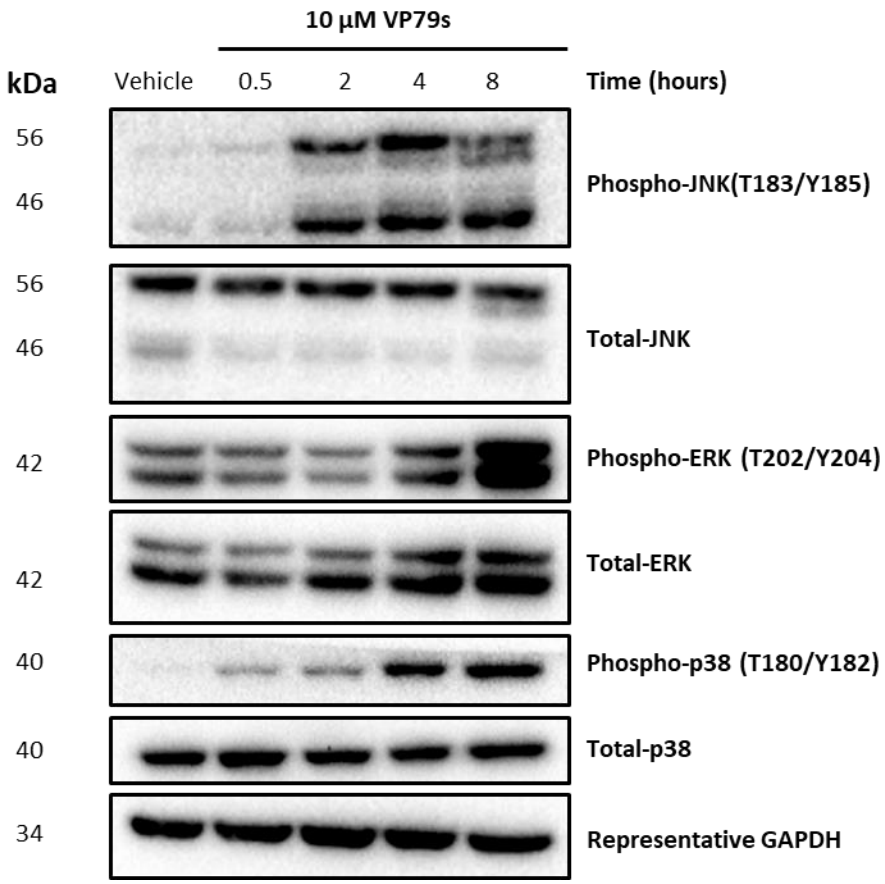

Figure 4. 20 VP79s activates ERK, JNK and p38 signalling in U266B1 cells.

U266B1 cells were seeded at a density of 30x10^4 cells/mL. Cells were treated with either vehicle [0.5% EtOH (v/v)] or VP79s (10 µM) for 30 mins, 2, 4 or 8 hours. Cells were lysed and equal amounts of protein were loaded and separated on 12% SDS-page gel, transferred to PVDF membrane and probed with the appropriate antibody. Representative images of phospho-JNK, total JNK, phospho-ERK, total ERK, phospho-p38 and total p38. Anti-GAPDH was used as a loading control. Results are representative of 3 independent experiments.

4.2.11. VP79s inhibits STAT3 phosphorylation prior to activation of MAPK pathways in U266B1 cells

Having determined that VP79s inhibits both STAT3 phosphorylation and activates MAPK pathways from as early 2 hours, an earlier time course was carried out to try to elucidate the sequence of events following treatment with VP79s. As such, U266B1 cells were treated with 10 μM VP79s for 0, 15, 30, 45, 60, 90 and 120 minutes. Following the appropriate time, samples were collected and lysates were prepared. Samples were run on 10% or 12% SDS-PAGE gels before being transferred to PVDF membrane and being probed with antibodies to the total and phosphorylated forms of STAT3, ERK, p38 and JNK. Anti-GAPDH was used as a loading control

VP79s was shown to rapidly and significantly inhibit STAT3 phosphorylation on tyrosine 705 from as early as 30 minutes (Figure 4.21 and 4.22). In contrast, a significant increase in JNK and p38 phosphorylation was not observed until 120 minutes post treatment (Figure 4.21 and 4.22). This suggests that STAT3 inhibition may occur prior to the induction of MAPK activation. In regard to ERK activation, no significant increases in ERK phosphorylation up to 2 hours post treatment were observed (Figure 4.21 and 4.22).

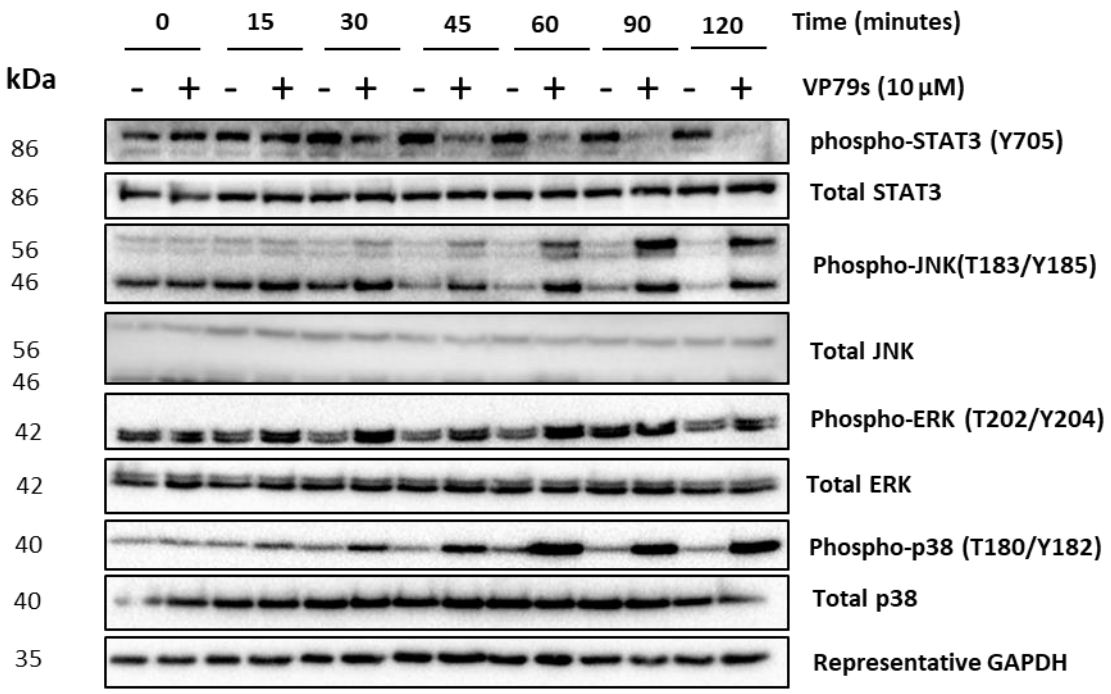

Figure 4. 21 Effects of VP79s within two hours on the STAT3 and MAPK signalling pathways.

U266B1 cells were seeded at a density of 30x10^4 cells/mL and were treated with either vehicle [0.5% EtOH (v/v)] or 10 µM VP79s for 0, 15, 30, 45, 60, 90 or 120 minutes. Cells were lysed and equal amounts of protein were loaded and separated on 10% SDS-page gels, transferred to PVDF membrane and probed with antibodies for the total and phosphorylated forms of STAT3, JNK, ERK and p38. Anti-GAPDH was used as a loading control. Results are representative of 3 independent experiments with similar results.

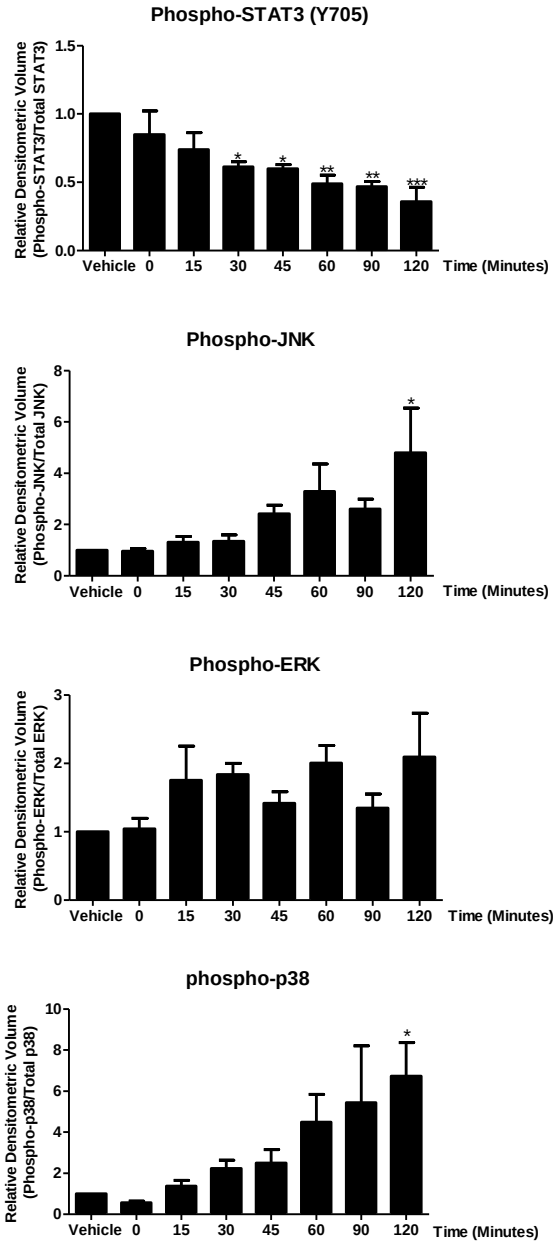

Figure 4. 22 Densitometric analysis of the effects of VP79s within two hours on the STAT3 and MAPK signalling pathways.

*U266B1 cells were seeded at a density of 30x10^4 cells/mL and were treated with either vehicle [0.5% EtOH (v/v)] or 10 µM VP79s for 0, 15, 30, 45, 60, 90 or 120 minutes. Cells were lysed and equal amounts of protein were loaded and separated on 10% SDS-page gels, transferred to PVDF membrane and probed with antibodies for the total and phosphorylated forms of STAT3, JNK, ERK and p38. Anti-GAPDH was used as a loading control. Results are representative of three independent experiments. Densitometric analysis of bands was carried out using image lab software. Statistical analysis was performed using one-way ANOVA with Dunnett's post hoc test comparing vehicle to treatments. *p<0.05, **p<0.01 and ***p<0.001.*

4.2.12. MAPK activation does not play a vital role in the anti-myeloma activity of VP79s

In order to determine if MAPK activation plays a significant role in the anti-myeloma activity of VP79s specific inhibitors of ERK, p38 and JNK were utilised. NCI-H929 cells were pre-treated with 20 µM U0126, SB203580 or SP600125, inhibitors of ERK, p38 and JNK respectively, for 30 minutes prior to treatment with 10 µM VP79s for 8 hours. Following the incubation time, cells were harvested for both western blotting and annexin V/PI staining. For western blotting, membranes were probed with antibodies for the phosphorylated forms of ERK, JNK and p38. Alpha-tubulin and GAPDH were used as loading controls. Cells were collected, stained with annexin V/PI and samples were analysed by flow cytometry.

Pre-treatment of cells with U0126 completely abrogated activation of ERK induced by VP79s (Figure 4.23 A), thus validating the efficacy of the inhibitor. However, inhibition of ERK activation did not prevent cell death induced by VP79s (Figure 4.23 B).

Similar results were obtained with the p38 inhibitor SB203580. Pre-treatment with the inhibitor abrogated activation of p38 induced by VP79s (Figure 4.24 A), thus validating the efficacy of the inhibitor. However, inhibition of p38 activation did not prevent cell death induced by VP79s (Figure 4.24 B).

As with U0126 and SB203580, pre-treatment with the JNK inhibitor SP600125 abrogated activation of JNK induced by VP79s (Figure 4.25 A), thus validating the efficacy of the inhibitor. However, inhibition of JNK activation did not prevent cell death induced by VP79s (Figure 4.25 B).

In conclusion, these data suggest that MAPK activation does not play a significant role in cell death induced by VP79s.

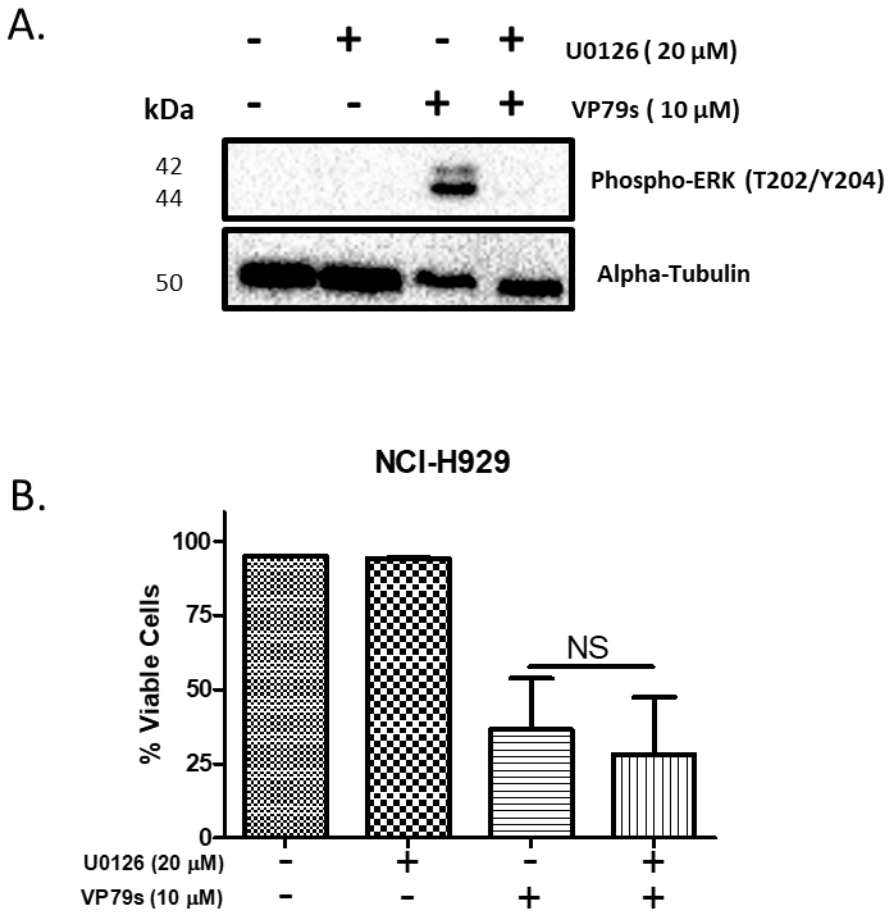

Figure 4. 23 The ERK inhibitor U0126 does not affect VP79s induced cell death in NCI-H929 cells.

30 x 10^4 cells/mL NCI-H929 cells were pre-treated with 20 µM U0126 for 30 minutes prior to treatment with either vehicle [0.5% EtOH (v/v)] or 10 µM VP79s for 8 hours. After the required treatment time cells were collected and ***A.*** *Cells were lysed and equal amounts of protein were loaded and separated on 12% SDS-page gel, transferred to PVDF membrane and probed with the appropriate antibody. Anti-alpha-tubulin was used as a loading control. Results are representative of 2 independent experiments.* ***B.*** *After incubation cells were harvested, stained with annexin V/PI and were analysed by flow cytometry using BD Accuri™ C6 software. 10,000 cells were gated on vehicle treated cells. Columns and error bars represent the mean ± S.E.M. of cells in the viable gate three independent experiments. Statistical analysis was performed using a paired two-tailed t-test. NS = No significance.*

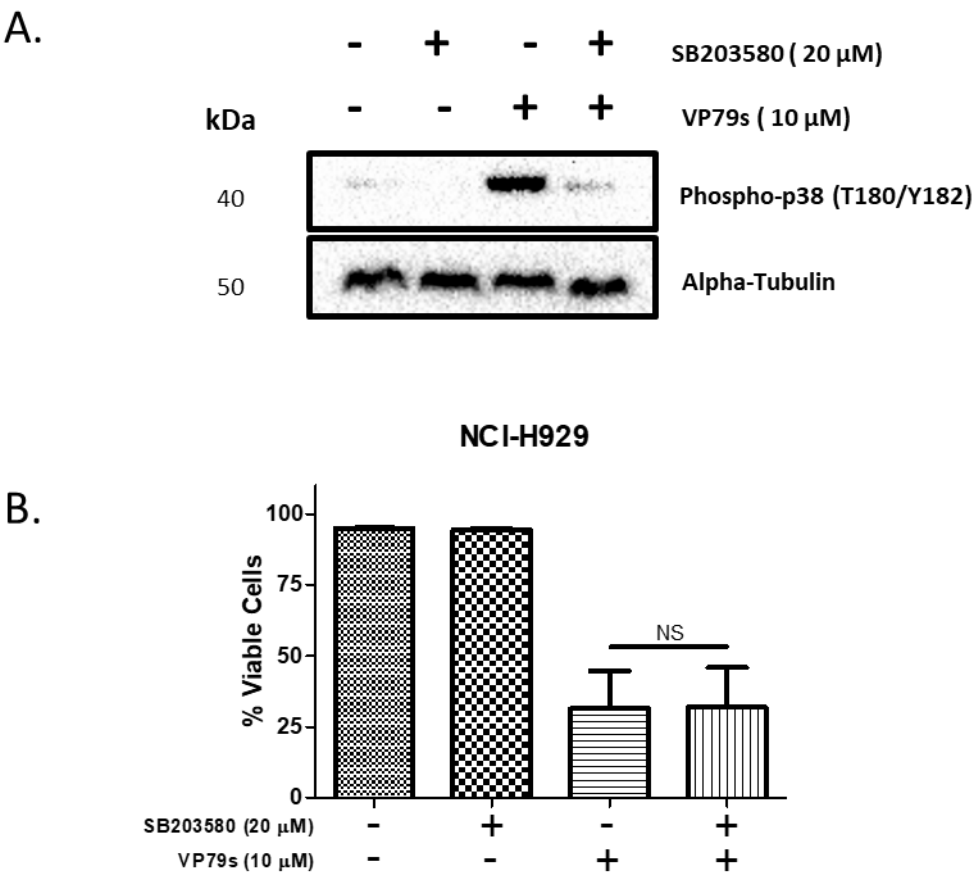

Figure 4. 24 The p38 inhibitor SB203580 does not affect VP79s induced cell death in NCI-H929 cells.

30 x 10^4 cells/mL NCI-H929 cells were pre-treated with 20 µM SB203580 for 30 minutes prior to treatment with either vehicle [0.5% EtOH (v/v)] or 10 µM VP79s for 8 hours. After the required treatment time cells were collected and ***A.*** *Cells were lysed and equal amounts of protein were loaded and separated on 12% SDS-page gel, transferred to PVDF membrane and probed with the appropriate antibody. Anti-alpha-tubulin was used as a loading control. Results are representative of 3 independent experiments* ***B.*** *After incubation cells were harvested, stained with annexin V/PI and were analysed by flow cytometry using BD Accuri™ C6 software. 10,000 cells were gated on vehicle treated cells. Columns and error bars represent the mean ± S.E.M. of cells in the viable gate of four independent experiments. Statistical analysis was performed using a paired two-tailed t-test. NS = No significance.*

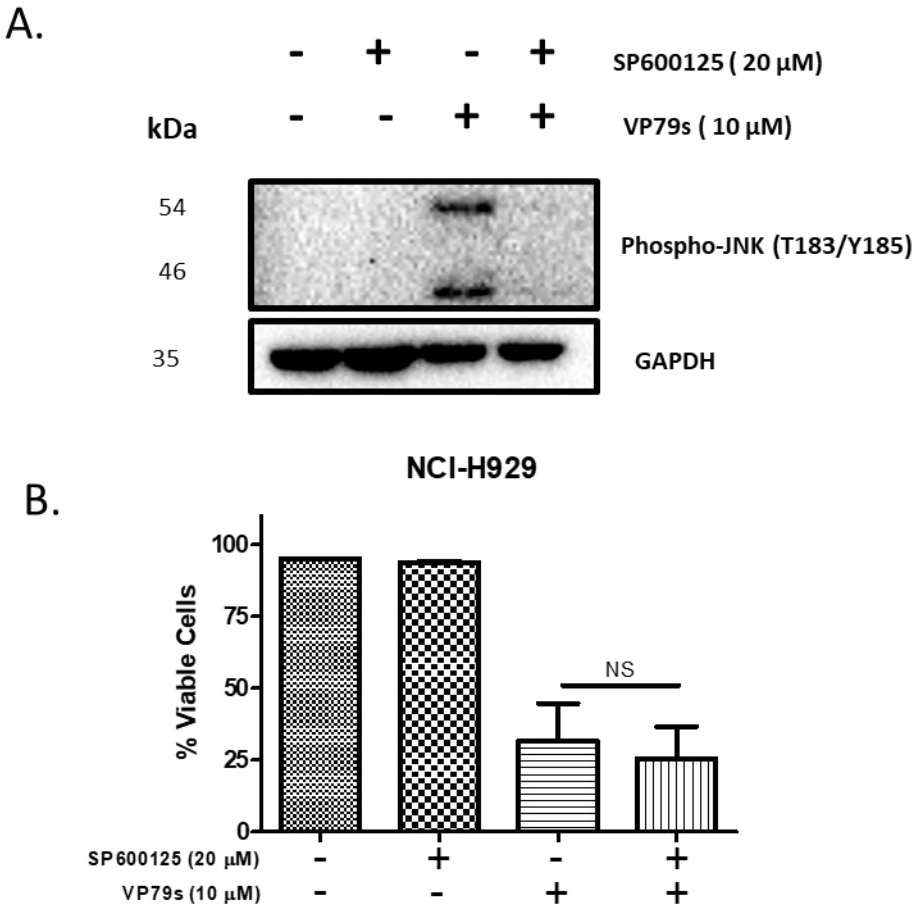

Figure 4. 25 The JNK inhibitor SP600125 does not affect VP79s induced cell death in NCI-H929 cells.

30 x 10^4 cells/mL NCI-H929 cells were pre-treated with 20 μM SP600125 for 30 minutes prior to treatment with either vehicle [0.5% EtOH (v/v)] or 10 μM VP79s for 8 hours. After the required treatment time cells were collected and ***A.*** *Cells were lysed and equal amounts of protein were loaded and separated on 12% SDS-page gel, transferred to PVDF membrane and probed with the appropriate antibody. Anti-GAPDH was used as a loading control. Results are representative of three independent experiments.* ***B.*** *After incubation cells were harvested, stained with annexin V/PI and were analysed by flow cytometry using BD Accuri™ C6 software. 10,000 cells were gated on vehicle treated cells. Columns and error bars represent the mean ± S.E.M. of cells in the viable gate of four independent experiments. Statistical analysis was performed using a paired two-tailed t-test. NS = no significance.*

4.2.13. VP79s induces early mitochondrial depolarisation of NCI-H929 and U266B1 cells

In order to further elucidate the sequence of events leading to VP79s induced cell death the JC-1 assay was employed. Depolarisation of the inner mitochondrial membrane is thought to be an early and irreversible event in apoptotic cell death induced via the intrinsic or mitochondrial apoptotic pathway [277]. JC-1 is a cationic carbocyanine dye that accumulates in mitochondria. In mitochondria with high membrane potential JC-1 aggregates and fluoresces orange/red. In contrast, in mitochondria with low membrane potential, JC-1 forms monomers which fluoresce green. Therefore, mitochondrial membrane potential can be measured by flow cytometry by measuring a change from red to green fluorescence [371].

NCI-H929 and U266B1 cells were treated with 10 µM VP79s for 0, 15, 30, 45, 60, 90 and 120 minutes. Following the appropriate time, samples were collected, stained with JC-1 dye and analysed by flow cytometry.

In the NCI-H929 cells, a change from red to green fluorescence was observed from 60 minutes with statistically significant depolarisation observed at 90 and 120 minutes (Figure 4.26 A and B). At the 45 minute timepoint cells appeared to shift to the right of the plot suggesting an increase in red fluorescence as they do not move into the lower green fluorescence gate (Figure 4.26 A). Reports in the literature have suggested that this increase in red fluorescence is associated with hyperpolarisation [372].

Similarly, in the U266B1 cells, depolarisation of the mitochondrial membrane began around 45 minutes with a statistically significant increase in green fluorescence observed at 120 minutes (Figure 4.27 A and B). As with the NCI-H929 cells, a shift in cells to the right of the plot, suggesting in increase in red fluorescence, was observed at the earlier timepoint of 30 minutes (Figure 4.27 A).

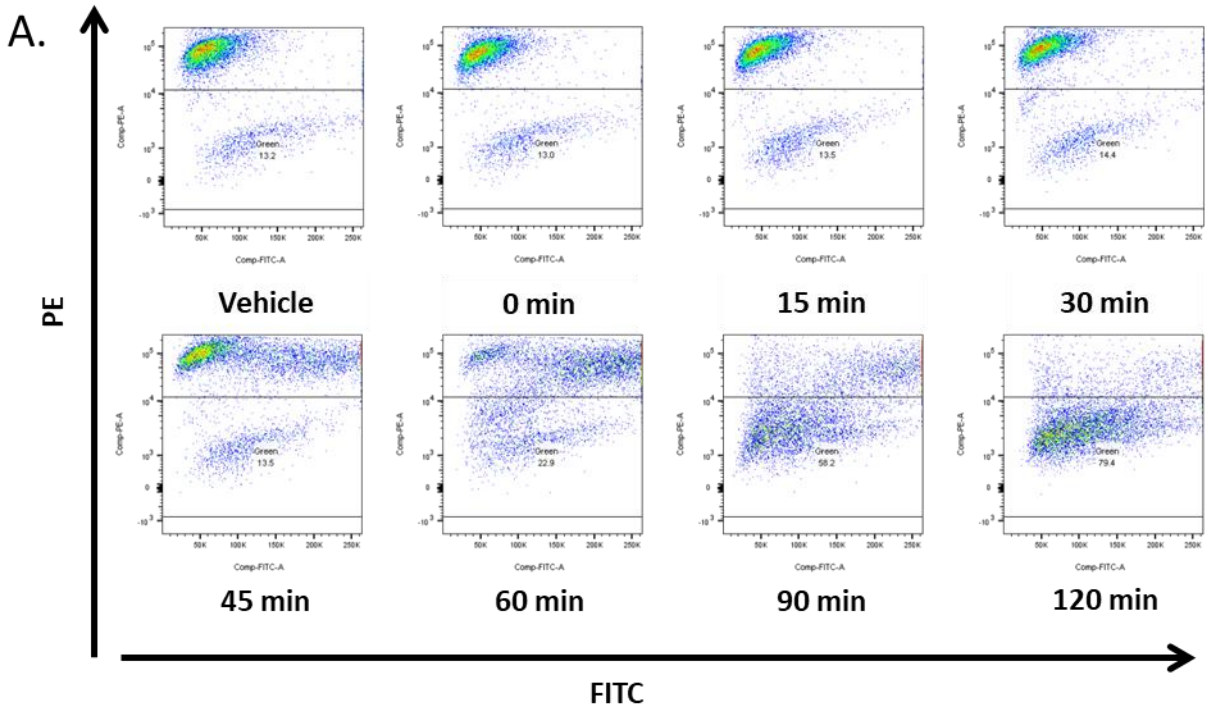

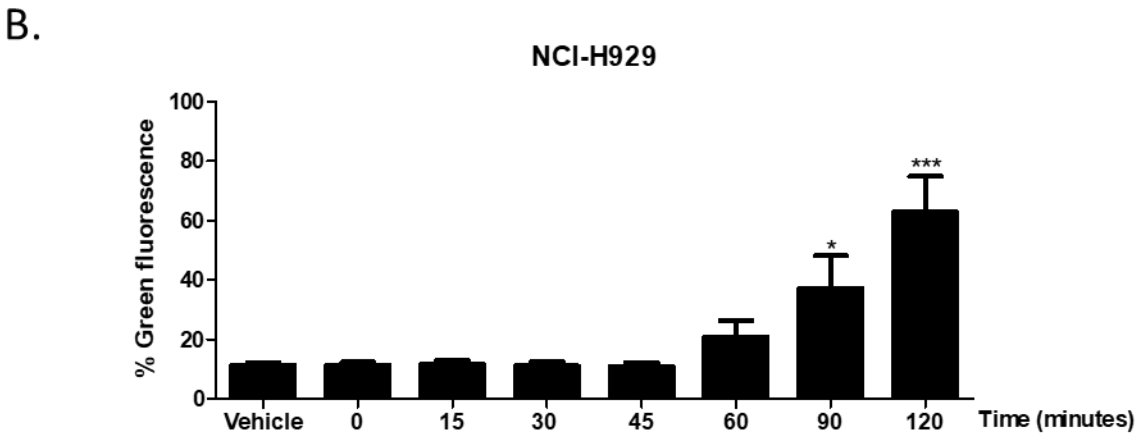

Figure 4. 26 Effect of VP79s on mitochondrial depolarisation in NCI-H929 cells.

30 x 10^4 cells/mL cells were seeded in 24 well plates and treated in duplicate with either vehicle [0.5% EtOH (v/v)] or 10 µM VP79s for 0-120 minutes. After the required treatment time cells were collected and stained with 2 µM JC-1 and analysed by flow cytometry. ***A.*** *Representative plots of 10,000 single NCI-H929 cells gated on PE (562.5-587.5 nm) and FITC (510-550 nm). Cells were compensated on unstained, healthy control cells and FCCP treated cells to determine the depolarised population.* ***B.*** *Columns and bars represent the mean ± S.E.M. of cells emitting green fluorescence from three independent experiments. Statistical analysis was performed using one-way ANOVA with Dunnett's post hoc test. *p<0.05, ***p<0.001.*

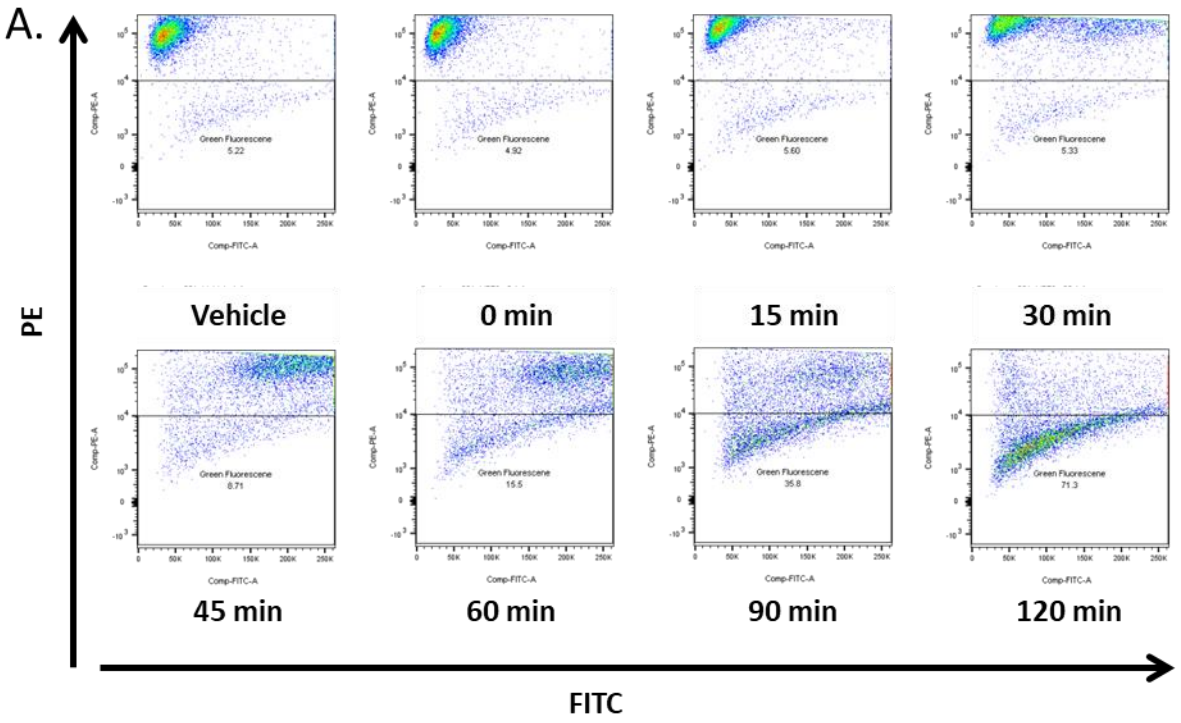

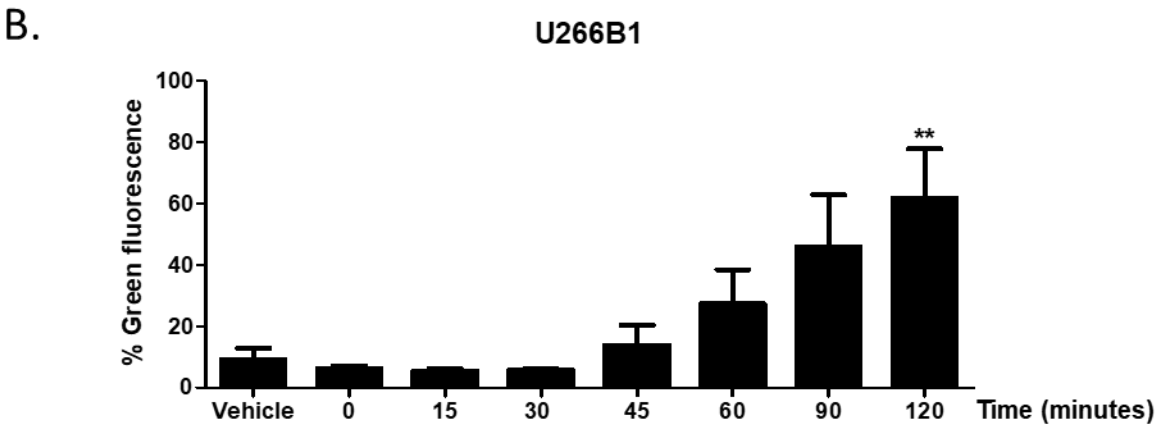

Figure 4. 27 Effect of VP79s on mitochondrial depolarisation in U266B1 cells.

30 x 10^4 cells/mL cells were seeded in 24 well plates and treated in duplicate with either vehicle [0.5% EtOH (v/v)] or 10 µM VP79s for 0-120 minutes. After the required treatment time cells were collected and stained with 2 µM JC-1 and analysed by flow cytometry. ***A.*** *Representative plots of 10,000 single U266B1 cells gated on PE (562.5-587.5 nm) and FITC (510-550 nm). Cells were compensated on unstained, healthy control cells and FCCP treated cells to determine the depolarised population.* ***B.*** *Columns and bars represent the mean ± S.E.M. of cells emitting green fluorescence from three independent experiments. Statistical analysis was performed using one-way ANOVA with Dunnett's post hoc test. **p<0.01.*

4.2.14. VP79s induces the production of reactive oxygen species in NCI-H929 and U266B1 cells

VP79s was shown to increase the fluorescence intensity of cells prior to mitochondrial depolarisation at 30 and 45 minutes in U266B1 and NCI-H929 cells respectively (Figure 4.26 and 4.27). Reports in the literature have demonstrated that hyperpolarisation of mitochondria occurs concurrently with the induction of reactive oxygen species (ROS) [373, 374]. Therefore, the DCFH-DA assay was utilised in order to determine if ROS was induced in line with the observed hyperpolarisation of the mitochondria.

In order to determine the efficacy of the assay a number of controls were utilised. The ROS scavenger, N-acetyl-L-cysteine (NAC), was used as a negative control, whilst hydrogen peroxide (H_2O_2) and menadione were used as positive controls. H_2O_2 was indicative of extracellular ROS, while menadione was used as a positive control for intracellular ROS. NCI-H929 and U266B1 cells were treated with 5 mM NAC, 100 µM menadione or 100 µM H_2O_2 for 15 minutes and 4 hours. Both positive controls and the negative control appeared effective. Treatment with NAC resulted in a shift to the left of the plot indicative of a decrease in fluorescence and therefore no ROS production whilst menadione and H_2O_2 resulted in a shift to the right suggesting an increase in fluorescence and therefore production of ROS, thus validating the efficacy of the assay in detecting ROS (figure 4.28 A and B).

Having validated the assay, NCI-H929 and U266B1 cells were treated with 10 µM VP79s for for 0, 15, 30, 45, 60, 90 and 120 minutes. Following the appropriate time, samples were collected and analysed by flow cytometry. A visible increase in ROS production was first observed at 45 minutes in the NCI-H929 cells (Figure 4.29 A), however the increase in ROS production was not statistically significant until 90 minutes post-treatment (Figure 4.29 B).

Similarly, in the U266B1 cells, an observable increase in ROS production was evident at 30 minutes (Figure 4.30 A), with a significant increase in ROS observed from 60 minutes (Figure 4.30 B).

In conclusion, VP79s induced a statistically significant increase in ROS production in U266B1 and NCI-H929 cells at 60 and 90 minutes respectively. This increase in ROS

concurrent with the increase in fluorescence observed in the JC-1 assay suggesting ROS may play a role in VP79s induced cell death.

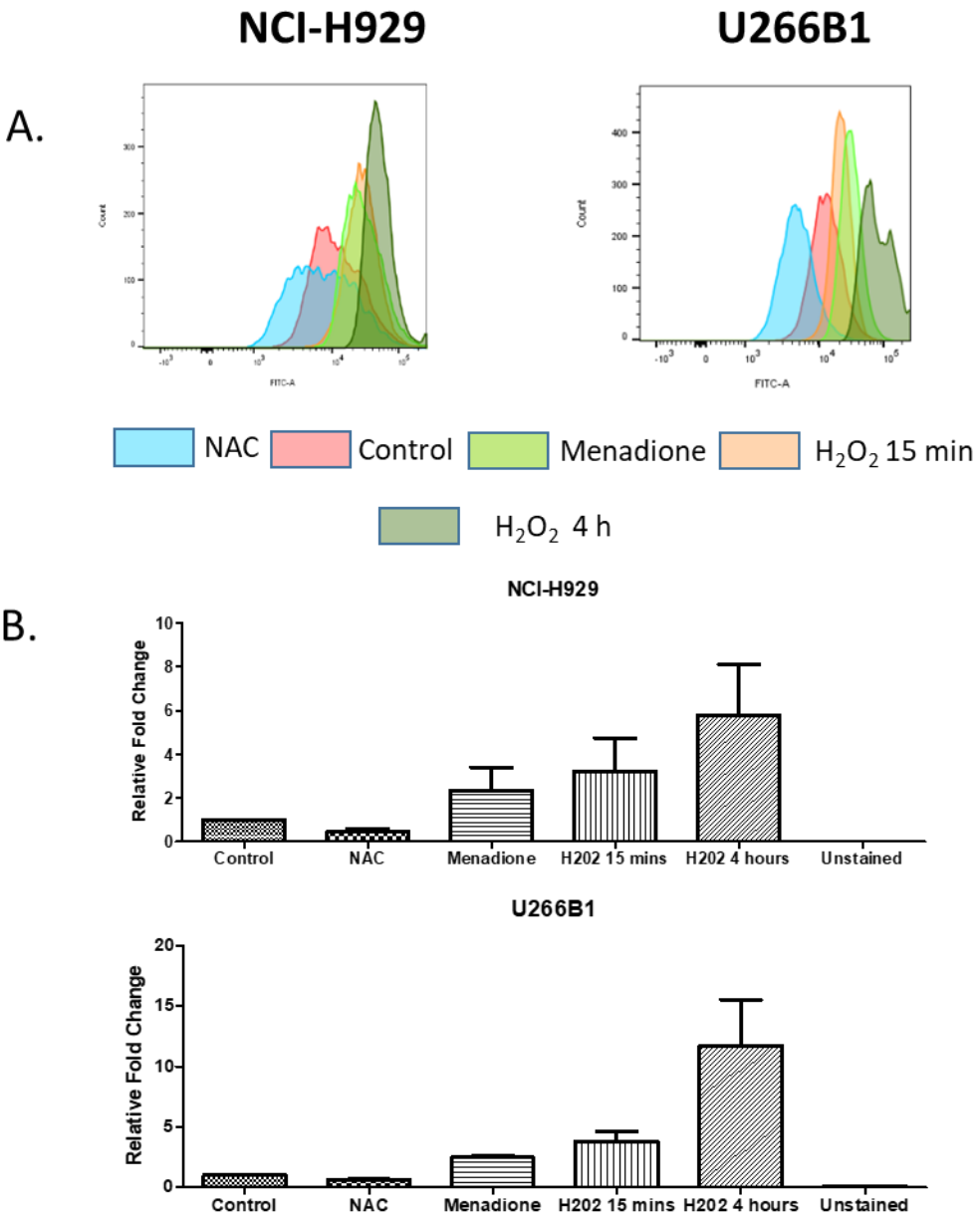

Figure 4. 28 Validation of the DCFH-DA assay to measure ROS production.

15 x 10^4 cells/well of U266B1 and NCI-H929 cells were seeded in 24 well plates and were pre-stained with 20 µM DCF-DA for 30 minutes. Cells were then treated with either 5 mM NAC, 100 µM menadione, or 100 µM H_2O_2 for 4 hours. Cells were also treated with 100 µM H_2O_2 for 15 minutes in duplicate. After the required treatment time cells were collected analysed by flow cytometry. ***A.*** *Representative histograms of 10,000 single NCI-H929 and U266B1 cells gated on FITC.* ***B.*** *Columns and bars represent the relative fold change of vehicle treated cells compared to VP79s treated cells of three independent experiments.*

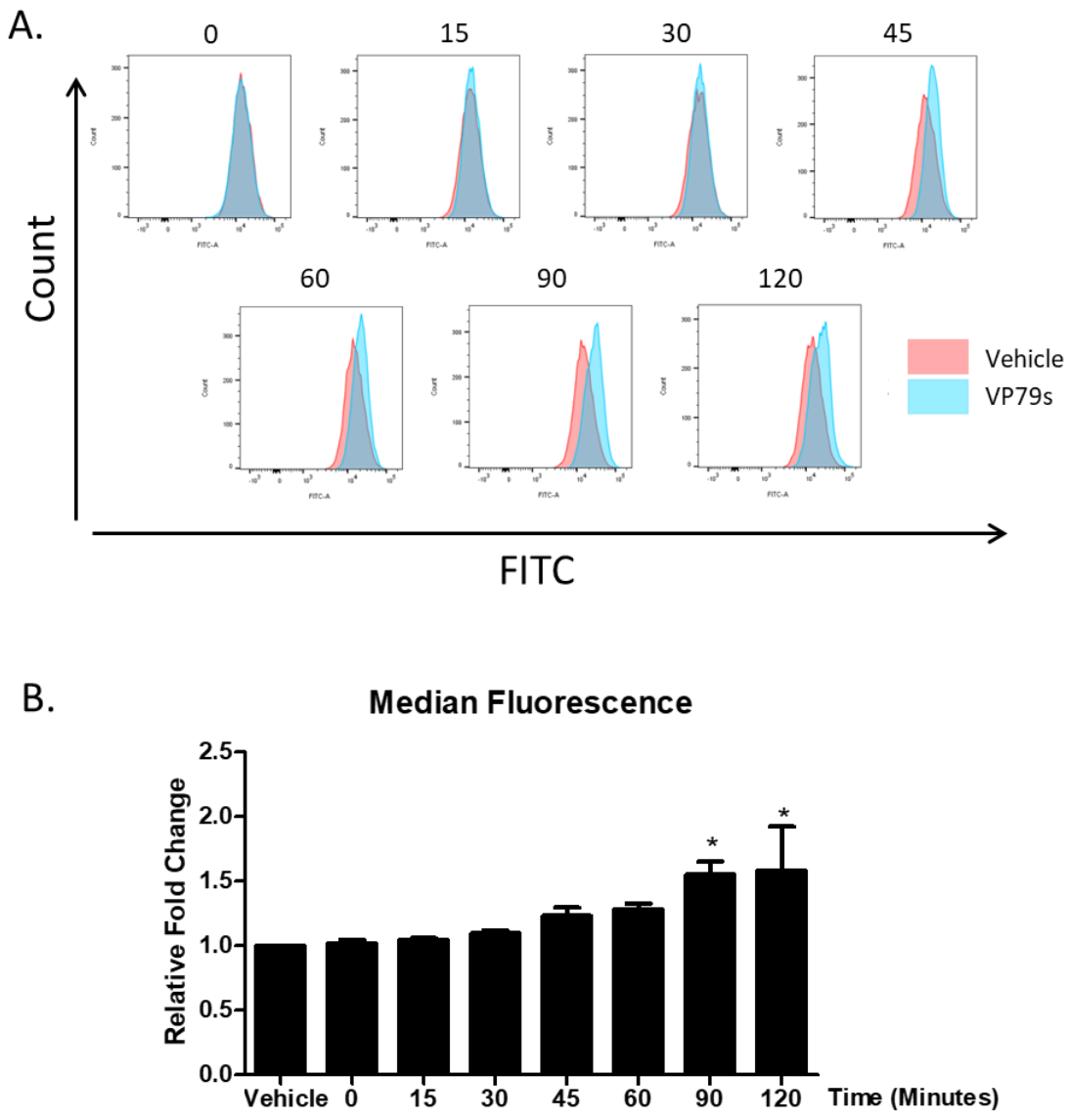

Figure 4. 29 VP79s induces ROS production in NCI-H929 cells.

15 x 10^4 cells/well of NCI-H929 cells were seeded in 24 well plates and were pre-stained with 20 µM DCF-DA for 30 minutes. Cells were then treated with either vehicle [0.5% EtOH (v/v)] or 10 µM VP79s for 0-120 minutes in duplicate. After the required treatment time cells were collected and analysed by flow cytometry. ***A.*** *Representative histograms of 10,000 single NCI-H929 cells gated on FITC.* ***B.*** *Columns and bars represent the relative fold change of vehicle treated cells compared to VP79s treated cells. Values represent the mean ± S.E.M. of three independent experiments. Statistical analysis was performed using one-way ANOVA with Dunnett's post hoc test. *p<0.05.*

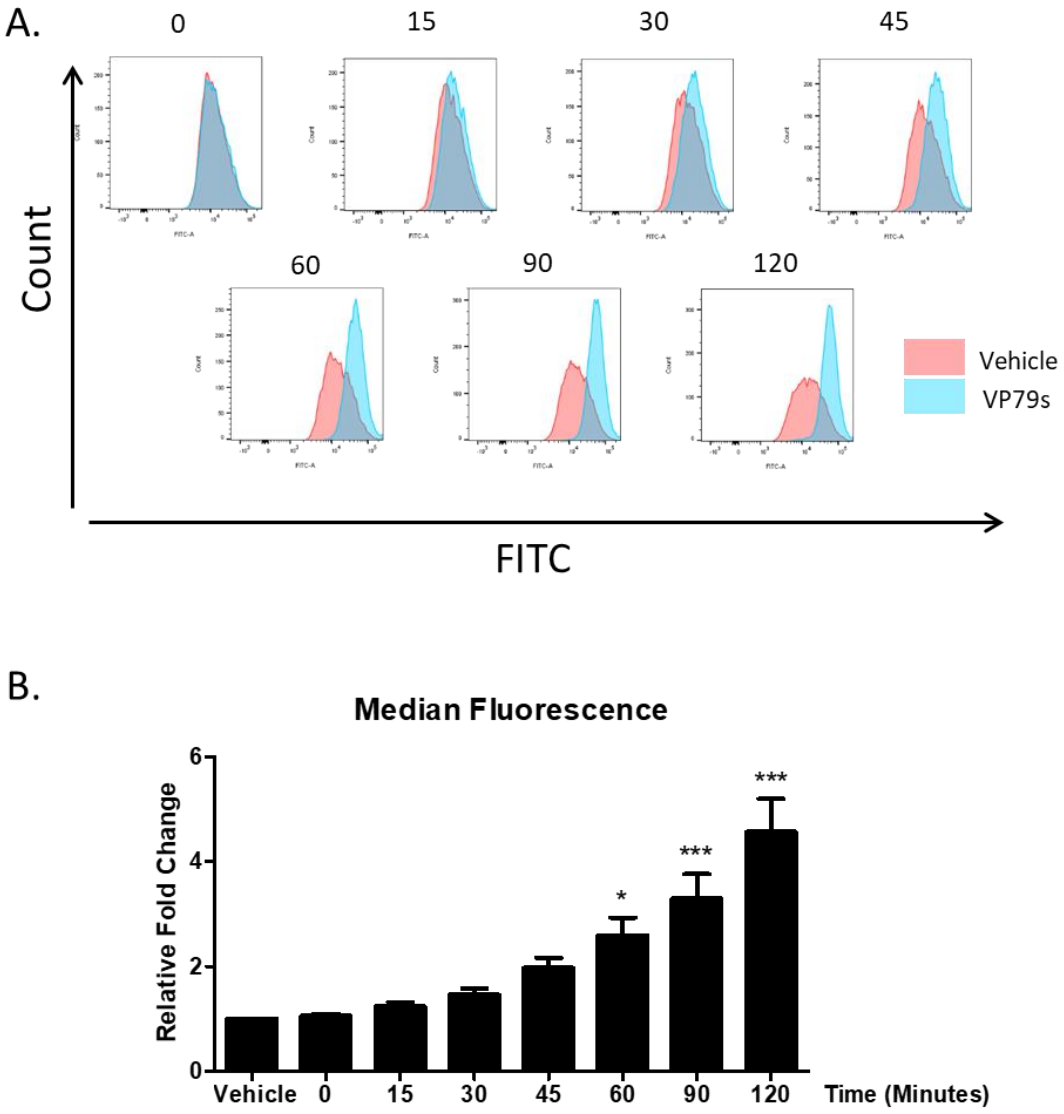

Figure 4. 30 VP79s induces ROS production in U266B1 cells.

15 x 10^4 cells/well of U266B1 cells were seeded in 24 well plates and were pre-stained with 20 µM DCF-DA for 30 minutes. Cells were then treated with either vehicle [0.5% EtOH (v/v)] or 10 µM VP79s for 0-120 minutes in duplicate. After the required treatment time cells were collected and analysed by flow cytometry. ***A.*** *Representative histograms of 10,000 single U266B1 cells gated on FITC.* ***B.*** *Columns and bars represent the relative fold change of vehicle treated cells compared to VP79s treated cells. Values represent the mean ± S.E.M. of three independent experiments. Statistical analysis was performed using one-way ANOVA with Dunnett's post hoc test. *p<0.05 and ***p<0.001.*

4.2.15. Inhibition of VP79s-induced ROS by NAC does not affect cell death

VP79s induced ROS production was demonstrated to occur just prior to mitochondrial depolarisation. Therefore, it was hypothesised that VP79s may induce cell death via induction of ROS. Consequently, NAC was used as a scavenger for ROS in order to determine its effects on cell death. U266B1 cells were pre-treated with 5 mM NAC prior to treatment with 10 µM VP79s for 16 hours. Menadione was used as a positive control for the production of intracellular ROS. After the treatment time, cells were collected, and apoptosis was analysed by flow cytometry using annexin V/PI staining.

Pre-treatment with NAC was shown to dramatically protect against the loss of cell viability induced by menadione, from 6.2% to 71%, thus validating that NAC is a ROS scavenger. In contrast, pre-treatment with NAC was shown to have no effect on VP79s induced cell death (Figure 4.31), suggesting that ROS does not play a significant role in VP79s induced cell death.

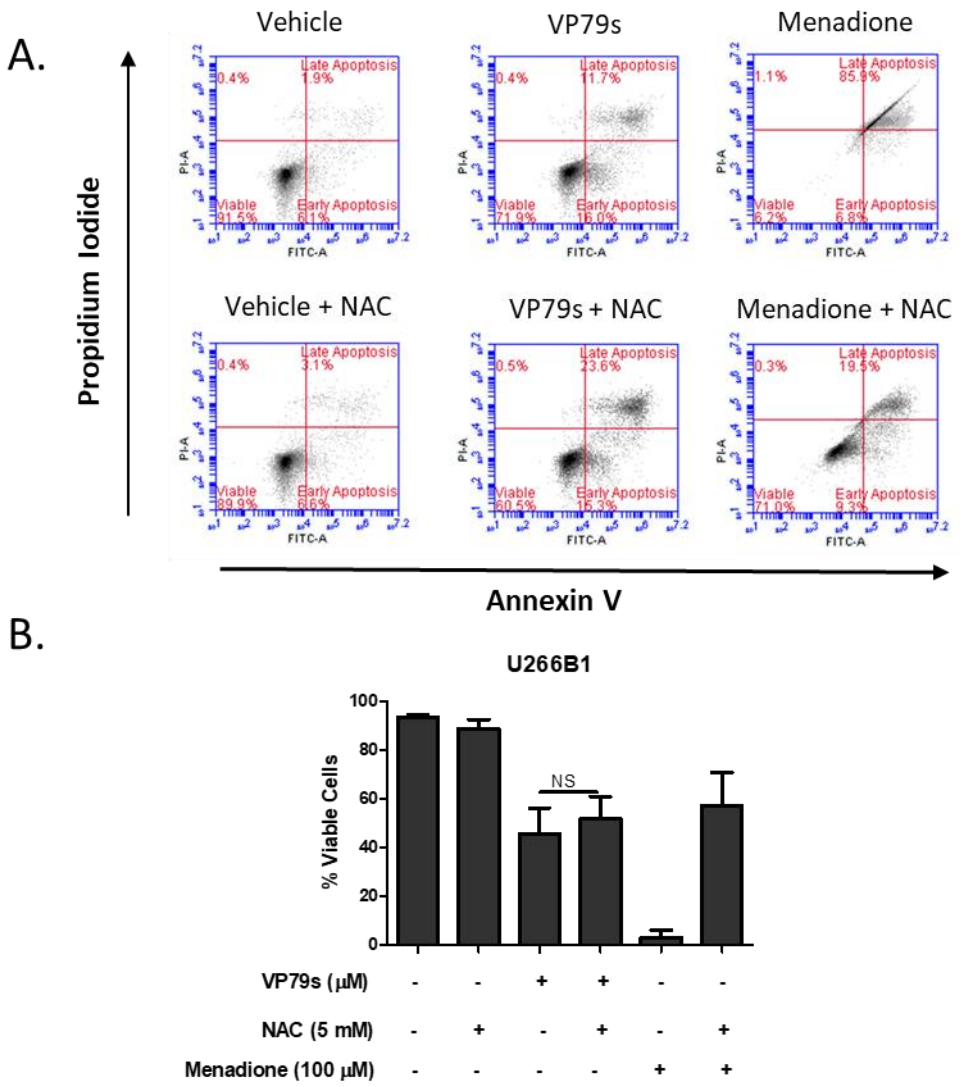

Figure 4. 31 N-Acetyl-L-Cysteine does not prevent VP79s induced cell death in U266B1 cells.

U266B1 cells were seeded at a density of 30x10^4 cells/mL. Cells were pre-treated with 5 mM N-acetyl-L-cysteine (NAC) for 1 hour prior to treatment with either vehicle [0.5% EtOH (v/v)] or VP79s (10 µM) for 16 hours. Menadione (100 µM) alone and in combination with NAC was used as a positive control. After incubation cells were harvested, stained with annexin V/PI and were analysed by flow cytometry using BD Accuri™ C6 software. 10,000 cells were gated on vehicle treated cells. ***A.*** *Representative dot plot of treated samples.* ***B.*** *Results are representative of 5 independent experiments for VP79s where values represent the mean ± S.E.M. and 2 independent experiments for menadione where values represent the range of two experiments. Statistical analysis was performed using a paired two-tailed t-test. NS = no significance.*

4.3. Discussion

Malignant plasma cells from MM patients display huge genetic heterogeneity not only from patient to patient but also in each individual where multiple clonal types can be present [285]. As such, while MM is classed as a single disease entity, the driving factors behind each individual patient can vary widely, making treating the disease with a single drug or treatment strategy unlikely [122]. Recent years have seen a remarkable increase in the range of novel drugs and treatments available to MM patients nearly doubling overall survival in the past 10 years. Despite this, MM is still a fatal malignancy which requires novel treatments. The activation of oncogenic signalling through both autonomous mutations and the BMM has been proven to play a critical role in the progression and pathogenesis of MM. Along with clonal diversity, the BMM plays an integral role in survival and drug resistance mediated by activation of the PI3K/AKT, JAK/STAT, RAS/RAF and NFκB pathways. Therefore, extensive research into novel strategies targeting these pathways is currently underway [253].

Since the aforementioned signalling pathways have been demonstrated to play an essential role in the survival of MM cells, the effect of VP79s on these oncogenic pathways was examined in MM cell lines. Previously, ED73a, a precursor of VP79s had been shown to inhibit phosphorylated ERK, STAT3 and AKT in colorectal cancer cell lines. Therefore, the effect VP79s had on these pathways as well as on the NFκB pathway was examined.

In the present study, in order to determine any effects on the PI3K/AKT pathway western blot analysis using antibodies against total AKT and AKT phosphorylated on serine 473 was performed. LY294002 is a PI3K inhibitor which has previously been shown to result in inhibition of AKT phosphorylation in MM cells [375]. Herein, LY294002 inhibited AKT phosphorylation on serine 473, in line with previous reports and thus validating the assay. VP79s induced transient, but not statistically significant, activation of phosphorylated AKT in both cell lines with peak phosphorylation observed around 30 minutes and 2 hours in the U266B1 and NCI-H929 cell lines, respectively. This was followed by a pronounced decrease in both phosphorylated and total AKT in the U266B1 cells. Phosphorylated AKT levels appeared to return to basal levels around 4 hours post treatment with VP79s in the

NCI-H929 cells. While traditionally the PI3K/AKT pathway is regarded as a cell survival pathway and inhibition of the pathway has been shown to induce apoptosis in cancers such as acute lymphoblastic leukaemia, cervical and MM [376-378]; reports in the literature have also demonstrated that activation of AKT may have a pro-death role. Thus, the PI3K/AKT pathway may play a dual role in both survival and cell death processes depending on the stimulus. AKT has been shown to be phosphorylated in response to the induction of ROS in prostate cancer cells [379, 380]. Moreover, it has been demonstrated that AKT activation sensitises cancer cells to ROS-mediated apoptosis by increasing oxidative stress through the enhancement of intracellular levels of ROS [381]. Activation of AKT was also associated with a decrease in the transcription factor FoxO which plays a role in the expression of antioxidant proteins [381]. Another study has reported that the viral protein apoptin induced cell death via activation and translocation of AKT to the nucleus where AKT participated in cell death [382]. Thus, nuclear AKT appeared to act as a positive regulator of apoptosis rather than a repressor. This may be due to its access to a new set of substrates in the nucleus. Of note, a study by Su *et al*. has demonstrated that treatment with the hsp90 inhibitor, geldanamycin, in HeLa cells leads to the transient phosphorylation of AKT on serine 473 followed by degradation of total AKT. The kinase activity of AKT depends on its association with hsp90 and hsp90 inhibition causes AKT degradation [383]. Pre-treatment with the PI3K inhibitor LY294002 resulted in delayed degradation of AKT indicating that phosphorylation of AKT is required for its degradation. It was also suggested that phosphorylation of AKT lead to enhanced binding of AKT to the E3 ligase C-terminal Hsp70-interacting protein (CHIP) leading to its ubiquitination and subsequent degradation by the proteasome [384]. Possibly, a similar mechanism could account for the transient activation and subsequent degradation of AKT observed in the U266B1 cells following treatment with VP79s but further studies would be required to confirm this. Furthermore, the lack of change in AKT in VP79s treated NCI-H929 cells would indicate that this pathway may not play a critical role in VP79s induced cell death.

The NFκB pathway has also been demonstrated to play a key role in the survival and proliferation of MM cells. Mutations in several components of the NFκB pathway in MM have been identified with around 17% of primary MM samples expressing mutations and

42% of all MM cell lines [144]. In MM, the NFκB pathway has been shown to be activated by two important MM cell survival factors, BAFF and A proliferation-inducing ligand (APRIL) [385]. Previous reports have demonstrated that activation of NFκB results in resistance to apoptosis in MM through upregulation of transcription factors involved in cell survival. For example, Meinel *et al*. have demonstrated that inhibition of the NFκB pathway by the novel proteasome inhibitor, V1810, induced apoptosis in MM cells via downregulation of Mcl-1 [386]. Conversely, bortezomib has previously been shown to activate the NFκB pathway in MM as demonstrated by degradation of its inhibitory subunit IκBα, therefore it was used as a positive control in this study [361, 387]. In agreement with previous reports, bortezomib was shown to robustly activate the NFκB pathway in U266B1 cells. In contrast, no effect was observed following VP79s treatment from 15 minutes up to 8 hours suggesting that the NFκB pathway does not play a critical role in VP79s induced cell death.

Having established that alterations in NFκB signalling did not appear to play a role in VP79s induced cell death, the effect of VP79s on the STAT3 signalling pathway was next examined. Activation of STAT3, both constitutive and microenvironmentally induced, has recently become a target for novel anti-cancer therapeutics [343]. In the present study, western blotting and flow cytometry were employed to examine the effects on STAT3 phosphorylation. It was determined that VP79s inhibited constitutively active STAT3 phosphorylation on tyrosine 705 but not serine 727 in U266B1 cells. Inhibition of tyrosine 705 phosphorylation has convincingly been shown to be essential for the transcriptional activity of STAT3 [388]. Furthermore, there is substantial evidence which supports the view that constitutive phosphorylation of STAT3 confers resistance to apoptosis in U266B1 cells [49, 389, 390]. A landmark study by Catlett-Falcone *el al*. demonstrated that constitutively active STAT3 phosphorylation on tyrosine 705 results in resistance to FAS mediated apoptosis in U266B1 cells due to high levels of Bcl-xL. The study found that blocking IL-6 receptor signalling from JAKs to STAT3 with the JAK inhibitor AG490 resulted in a decrease in Bcl-xL protein expression and the induction of apoptosis [49]. Similarly, another study by Alas *et al*. demonstrated that inhibition of STAT3 signalling with AG490 sensitised U266B1 cells to the activity of cisplatin, fludarabine, adriamycin, and vinblastine [390]. As previously discussed, the role of phosphorylation on serine 727 in MM is unclear. Previous

studies have correlated activation of serine phosphorylation with inhibition of phosphorylation on tyrosine [346], whilst others have demonstrated its role in fully activating the transcriptional activities of STAT3 [345]. Nevertheless, in the present study, VP79s was found to have minimal effect on serine 727 phosphorylation in either the U266B1 cells or NCI-H929 cells. These findings were consistent across both western blotting and flow cytometry results. The NCI-H929 cells do not possess constitutively phosphorylated STAT3 on tyrosine 705, therefore in order to induce STAT3 phosphorylation the cells were pre-treated with IL-6 prior to treatment with VP79s. Herein, it was shown that VP79s was also capable of inhibiting IL-6 induced STAT3 phosphorylation. The fact that VP79s could also induce apoptosis in the NCI-H929 cell line in the presence of the pro-survival cytokine IL-6 suggests that VP79s may be a promising treatment for MM. Previous studies in the literature have demonstrated that inhibition of STAT3 phosphorylation on tyrosine 705 induced cell death not only in MM cells but also in melanoma, breast, pancreatic and renal cancers [389, 391-394]. Drugs which selectively inhibit STAT3 phosphorylation on tyrosine but not serine have also been shown to induce cell death in MM cells [395]. For example, LLL12 is a small molecule which has been shown to directly inhibit STAT3 phosphorylation on tyrosine 705. Reports in the literature have shown that LLL12 can induce apoptosis via inhibition of STAT3 in MM, medulloblastoma, glioblastoma, osteosarcoma, rhabdomyosarcoma, breast cancer and others [389, 396-399]. Moreover, in MM, LLL12 was also shown to downregulate the gene and protein products of cyclin D1 and survivin [389]. Similarly, YL064, another direct STAT3 inhibitor, has been shown to selectively inhibit STAT3 phosphorylation on tyrosine 705 but not serine 727 in MM cells, thus inducing apoptosis. Treatment with YL064 resulted in a downregulation in the gene and protein expression of Mcl-1 and cyclin D1 [395]. Inhibition of upstream mediators of STAT3 phosphorylation by JAK inhibitors such as ruxolitinib, AZD1480 and AZD4205 have shown efficacy in cancers including MM, pancreatic, acute lymphoblastic leukaemia and non-small cell lung cancer (NCT03450330) [400-402]. These data support the findings herein that VP79s induces apoptosis in U266B1 cells via inhibition of STAT3 phosphorylation on tyrosine 705.

In chapter 3, four diverse MM cell lines which represent the heterogeneity of the disease were initially used to assess the anti-MM activity of VP79s. VP79s was found to induce almost equipotent apoptosis in all four cell lines; although, the NCI-H929 appeared to be slightly more sensitive. As discussed, there is a RAS/BRAF mutation cluster in MM with approximately 50% of patients presenting with mutations in the pathway [292]. All four of the MM cell lines used herein possess mutations in the RAS/RAF/MEK/ERK signalling pathway. NCI-H929 cells contain mutated *NRAS* [403], U266B1 possess mutated *BRAF* but are *RAS* wildtype [370, 404], whilst MM1.S and MM1.R possess mutated *KRAS* [405]. As well as mutations in this pathway, *TP53* mutations are extremely common in MM, however, in the panel used herein only the U266B1 cell line had a mutation in *TP53* [406]. To assess the effect of VP79s on signalling pathways known to play a role in the pathogenesis of MM, the NCI-H929 and U266B1 cells were used as a representative pair. One key difference observed between cell lines was the presence of constitutively active STAT3 phosphorylation on tyrosine 705 in the U266B1 cell line but not the NCI-H929 cell line. Although, flow cytometric analysis demonstrated a small population (5%) of NCI-H929 cells expressing phosphorylation on tyrosine 705. As previously discussed, mutations in *STAT3* and *JAK2* are rare in MM, therefore, the constitutive STAT3 signalling is likely caused by different mechanisms [74, 407]. Previously, it has been reported that constitutive STAT3 phosphorylation in U266B1 cells is dependent on an IL-6 autocrine loop [49]. Continuous activation of this pathway is likely due to perturbations in endogenous inhibitors of the pathway such as SOCS, protein inhibitor of activated STAT (PIAS) and Src homology containing protein 1 (SHP-1) and SHP-2 tyrosine phosphatases. Previously it has been reported that 79.4% of MM patients displayed hypermethylation of *SHP1*, and thus, epigenetic inactivation of SHP-1. Moreover, U266B1 cells displayed completely methylated *SHP1* and treatment with 5-azacytidine, a cytidine analogue, led to demethylation of *SHP1* concurrent with a decrease in STAT3 phosphorylation [408]. Similarly, aberrant SOCS-1 methylation has also been reported in 62.9% of MM patient samples and in U266B1 cells [363]. Treatment with 5-aza-2'-deoxycytidine, a demethylating agent, resulted in upregulation of SOCS-1 expression and enhanced sensitivity of the cells to the JAK inhibitor AG490 [363]. Therefore, it could be suggested that constitutive STAT3 phosphorylation in

U266B1 cell is due to methylation of *SHP1* and *SOCS1*. Interestingly, a study by Reddy *et al*. has demonstrated that while *SOCS1* and *SHP1* are methylated in U266B1 cells, only *SOCS1* is methylated in NCI-H929 cells. Herein, it was shown that IL-6 can induce sustained phosphorylation of STAT3 on tyrosine 705 in NCI-H929 cells, therefore it could be speculated that *SHP1* methylation may be more important for inhibition of the pathway. Previously, it has been shown that an increase SHP-1 expression can result in inhibition of STAT3 phosphorylation in MM cells [409]. This warrants investigation into SHP-1 expression following treatment with VP79s.

VP79s was initially designed to allosterically target BRAF, and since STAT3 is a transcription factor; upstream targets known to be involved in the activation of STAT3 were examined to assess the mechanism of action of VP79s. As mentioned above, SOCS-1 and SOCS-3 have the unique ability of inhibiting the kinase activity of JAKs by binding to their kinase inhibitory domain or by competing with STATs for phosphotyrosine binding sites on cytokine receptors [355, 410]. Furthermore, a study by Baek *et al.* has demonstrated that resveratrol inhibits STAT3 activation through the induction of SOCS-1 in head and neck cancer cells and resveratrol has also been shown to inhibit STAT3 phosphorylation in MM cells [411, 412]. Such reports prompted an examination into the role of SOCS-1 in VP79s induced STAT3 inhibition. In the present study, it was shown that VP79s had no effect on the protein expression level of SOCS-1 in U266B1 cells, indicating that the STAT3 inhibitory activity of VP79s was mediated through an alternative mechanism.

The JAK and SRC kinases have been shown to lie upstream of STAT3 and therefore may be involved in the mechanism by which VP79s inhibited STAT3 phosphorylation [257, 354]. SRC kinase activity is regulated by the phosphorylation of tyrosine residues. One of the major phosphorylation sites is tyrosine 529 (using the human SRC numbering system). Under basal conditions, phosphorylated tyrosine 529 binds to the SH2 domain of SRC resulting in the conformationally inactive form of the enzyme. Autophosphorylation on tyrosine 418 (tyrosine 416 in chicken SRC) results in the activation of the kinase [348]. Reports in the literature have also demonstrated that SRC can be phosphorylated on other sites including tyrosine 213 and 138 as well as serine and threonine residues [348]. Herein, it was established that VP79s had no effect on SRC phosphorylated on tyrosine 418.

However, at the later timepoints of 4 and 8 hours a band approximately 5-10 kilodaltons larger than total SRC appeared post treatment with VP79s. Give the size of the band, it is possible that it could represent phosphorylation or ubiquitination of SRC. Previous studies have demonstrated that while tyrosine 418 phosphorylation activates SRC, phosphorylation of a conserved tyrosine residue, tyrosine 529, has been demonstrated to result in inactivation of SRC through a conformational change [413, 414]. Possibly, the antibody may also react with the phosphorylated form of SRC on tyrosine 529. However, this would require further experimental examination. Previously, Hakak *et al*. have demonstrated that ubiquitin-proteasome-dependent degradation of SRC is another means of downregulating SRC activity [415]. The group examined whether the conformation and phosphorylation state of SRC affected its rate of ubiquitination by transiently co-transfecting HK-293 cells with a construct which expressed haemagglutinin (HA)-tagged ubiquitin with DNA encoding wild-type SRC, activated SRC or a catalytically inactive form of SRC. The study found that overexpression of wild-type SRC in the presence of HA-ubiquitin resulted in the formation of a 68 kilodalton form of SRC. This 68 kilodalton band had the same approximate molecular weight as the band probed with anti-HA and it was suggested that this band represents a monoubiquitinated form of SRC. Co-expression with the active form of SRC resulted in formation of the same 68 kD protein and also appeared to be polyubiquitinated. This result suggested that active SRC was more intensely ubiquitinated than the wild type-form. The catalytically inactive form of the kinase was not polyubiquitinated, suggesting that the active form of the enzyme is required for polyubiquitination [415]. This data suggests that phosphorylated, catalytically active SRC is required for ubiquitination of the protein or that active SRC initiates signalling pathways which are required for the targeted degradation of SRC. Another study by Lazlo and Cooper in 2009 has reported that active SRC is irreversibly destroyed by the E3 ubiquitin ligase component, cullin-5, via cullin-5-dependent ubiquitination and degradation [416]. These data suggest that the band that appears above SRC following treatment with VP79s may be a monoubiquitinated form of the kinase. The band is approximately 65-70 kDa in size which would align it with the reported monoubiquitinated SRC in Hakak's study. Further studies are therefore required to delineate this modulated form of SRC.

As aforementioned, the JAK family of kinases also lie upstream of STAT3 and play an important role in cytokine signalling with aberrant activation associated with many haematological malignancies. Previous studies have demonstrated that JAK-mediated inhibition of active STAT3 with selective inhibitors induces apoptosis in MM cells [76-78, 257, 352, 417]. For example, CYT387, a JAK1/2 inhibitor has been shown to induce apoptosis in MM cell lines and *ex vivo* patient samples [417]. Similarly, INCB16562, a JAK 1/2 inhibitor was shown to induce cell death in MM cells and overcome the protective effects of cytokines and stromal cells in *in vitro* models [352]. Single JAK2 inhibition has also been shown to result in MM cell death as TG101209, a selective JAK2 inhibitor, demonstrated selective cell death in MM cell lines and preferential cell death in CD45+ MM cells, which has been reported to be a negative prognostic factor [77, 418]. Herein, JAK2 rather than JAK1 appeared to be inhibited by VP79s and ruxolitinib, a known JAK 1/2 inhibitor. Ruxolitinib was used as a control as previous reports in the literature have shown that it induces apoptosis in MM cells and downregulates phosphorylated JAK2 on tyrosine 1007/1008 [76, 365]. Whilst ruxolitinib is known to be a JAK1 and JAK2 inhibitor [419], limited studies have shown inhibition of JAK1 by western blotting. One study by Lee *et al.* has demonstrated a paradoxical increase in JAK phosphorylation following treatment with ruxolitinib despite a decrease in STAT3 phosphorylation [420]. Similarly, other studies have also reported an increase in JAK2 phosphorylation despite inhibition of STAT3 phosphorylation in lymphomas [420]. Of note, a novel aryl-guanidino compound, DCZ3301, has been shown to inhibit JAK2 phosphorylation in large B cell lymphoma [421]. Similarly, DCZ3301 was also shown to induce apoptosis in MM cells via inhibition of STAT3, AKT and ERK [422]. These results support preliminary findings in this chapter which suggests that VP79s may inhibit JAK2 phosphorylation, and thus, STAT3 phosphorylation inducing cell death in U266B1 cells. Moreover, since VP79s was shown to inhibit IL-6 induced STAT3 signalling, it could be suggested that VP79s may overcome BMM induced drug resistance. The IL-6R/JAK/STAT3 pathway has been implicated in the multistep transformation process and pathogenesis of MM through upregulation of key angiogenic and anti-apoptotic proteins [16]. JAK inhibitors including ruxolitinib have been demonstrated to overcome IL-6

induced STAT3 phosphorylation and similarly, it has been suggested that this may be a potential mechanism for targeting BMM induced drug resistance [76, 256].

IL-6 can activate JAK/STAT signalling in MM through the *classical* signalling and *trans*-signalling pathways [67]. The *classical* signalling pathway involves the binding of IL-6 with the IL-6 receptor, CD126, on the cell surface. This complex then recruits CD130 to form an IL-6/CD126/CD130 complex which initiates downstream signalling through the JAKs and STAT3. Herein, it was demonstrated that VP79s rapidly downregulated the cell surface expression of CD126 and CD130. CD130 is key to both *classical* and *trans*-signalling as it is required to potentiate the signal in both pathways. The constitutive activation of CD130 has been shown to be a major event in the induction of a MM, as constitutive CD130/JAK/STAT3 signalling in a murine model has been shown facilitate the development of MM [108]. Similarly, a 2017 study by Burger *et al.* has shown that CD130 receptor blockade, with a specific antibody (B-R3), inhibits growth of the IL-6-dependent INA-6.Tu1 cell line completely in SCID mice whilst blockade of IL-6 only resulted in a delay in plasma cell growth, highlighting the importance of CD130 in IL-6 dependent MM cell growth [63]. Previous reports in the literature have also established the importance of CD130 in MM cell survival as pharmacological inhibition of CD130/JAK/STAT signalling with the histone deacetylase inhibitor; AR-42, the anti-microbial; atovaquone, and bortezomib led to the induction of apoptosis both *in vitro* and *in vivo* [161, 248, 423]. In the present study, VP79s induced a downregulation of CD126 and CD130 in a dose- and time-responsive manner in U266B1 cells with a visible downregulation of CD126 and CD130 beginning around 30 minutes post treatment with VP79s, although this did not reach significance until 60 minutes, consistent with inhibition of STAT3 phosphorylation. Therefore, an exact sequence of events could not be delineated. The exact mechanisms which regulate CD126 and CD130 are unknown. Surface expression can be regulated through shedding, downregulation and internalisation [424-427]. Jostock *et al.* has shown that this soluble form of CD130 can act as a natural inhibitor of IL-6 signalling as it forms a complex with sIL-6R and IL-6 [428]. How VP79s is reducing the surface expression of CD126 and CD130 is unknown; however, previous studies have demonstrated that IL-6 can upregulate expression of the CD126 through a positive feedback loop. Therefore, it could be

suggested that inhibition of the pathway may prevent this positive feedback loop or induce a negative feedback loop [429]. Dimerised STAT3 and STAT1 have been reported to bind to the promoter of CD130 resulting in its expression. Therefore, it could be speculated that inhibition of STAT3 by VP79s may result in downregulation of CD130 expression [430].

Having established that VP79s inhibits STAT3 phosphorylation, the effect of VP79s on downstream targets of STAT3 were next examined by quantitative PCR and western blotting. Numerous studies have established that cyclin D1, survivin, the anti-apoptotic Bcl-2 family members and many others are STAT3 target genes [100, 106, 431, 432]. Herein, VP79s was shown to cause an apparent downregulation in gene expression of *STAT3*, *MCL1* and *CCND1.* Western blot analysis of the anti-apoptotic Bcl-2 family members established that VP79s decreased the expression of Mcl-1 following treatment correlating with the qPCR results. Mcl-1 is considered a critical survival protein for MM [215] and Mcl-1 rather than Bcl-2 or Bcl-xL promotes myeloma cell survival [227]. Mcl-1 has been shown to lie downstream of STAT3 and other signalling pathways such as PI3K/AKT in MM [215, 222]. Myeloma cells rely heavily on signals from the BMM and in particular, IL-6 secreted from BMSCs [29]. IL-6 induces Mcl-1 upregulation mainly through the JAK/STAT pathway; thus targeting this pathway and Mcl-1 may be a promising treatment strategy for MM [230]. The induction of apoptosis through downregulation of Mcl-1 in MM and numerous other cancers by chemotherapeutics is well reported [57, 433, 434]. The transcriptional activity of *MCL1* does not always correlate with the protein levels as it can undergo many post translational modifications. Herein, VP79s caused possible cleavage of Mcl-1 in NCI-H929 cells. Cleavage of Mcl-1 has been shown to hinder the anti-apoptotic function of Mcl-1 as it halts its binding to pro-apoptotic partners thus preventing its ability to sequester their function. Other reports suggest that cleavage of Mcl-1 creates a pro-apoptotic form of Mcl-1 but this has been disputed [368, 435, 436]. Since the NCI-H929 cell line does not have constitutively active STAT3 phosphorylation on tyrosine 705, this downregulation of Mcl-1 could be mediated through another pathway such as the PI3K/AKT pathway which has been shown to play a role in mediating Mcl-1 expression [437, 438]. Nevertheless, cleavage of Mcl-1 has a role in preventing its anti-apoptotic functions. In contrast, levels of Bcl-2 and Bcl-xL remained relatively unchanged; however, a significant increase in a

putative cleaved Bcl-2 fragment was detected in U266B1 cells following treatment with VP79s. Similar to Mcl-1, it has been reported that caspase-dependent cleavage of Bcl-2 results in a pro-apoptotic form of the protein [439], thus, it may be suggested that VP79s is inducing cell death, in part, through cleavage of Bcl-2. Since Mcl-1 is considered to be a critical survival protein for MM, a time course was utilised to determine how quickly VP79s downregulated Mcl-1 expression. VP79s was shown to cause a decrease in protein expression from as early as 2 hours. Mcl-1 has a very short half-life of 30-90 minutes [440], therefore, this decrease in expression correlates with inhibition of STAT3 phosphorylation in the U266B1 cells.

Cyclin D1 is an important regulator of the cell cycle, regulating G1 to S phase progression in many cell types and its upregulation is an early and unifying event in MM [101]. In the present study, cyclin D1 was shown to be downregulated in both NCI-H929 and U266B1 cells following treatment with VP79s. As previously discussed, cyclin D1 is a downstream gene target of STAT3 [106]. Reports have shown downregulation of cyclin D1 following treatment with inhibitors of the STAT3 pathway in MM [395, 441, 442].

Survivin is a member of the inhibitor of apoptosis proteins family that has a dual role in mitosis and apoptosis. Studies have demonstrated that survivin plays an important role in MM progression and, therefore, inhibition of survivin may be a promising treatment strategy [97]. Herein, V7P9s was shown to significantly downregulate survivin protein expression in U266B1 cells but not NCI-H929 cells. This difference between cell lines could possibly be explained by the fact that survivin has been shown to lie downstream of STAT3 and NCI-H929 cells do not appear to possess constitutively active STAT3 [107].

Genomic studies have identified a mutation cluster of 15 RAS/MAPK associated genes in MM with up to 50% of patients presenting with mutations in this pathway (*NRAS*, *KRAS* and *BRAF*), suggesting that MM may be driven by mutations within the RAS signalling cascade [113]. Of note, all cell lines in the present study possess mutations in the pathway. Since ED73a, the precursor of VP79s was found to inhibit RAF kinase in colorectal cancer cells [259], the effect of VP79s on ERK phosphorylation was examined as a readout of the RAS/RAF/MEK/ERK pathway. Surprisingly, it was found that VP79s induced ERK phosphorylation in both the NCI-H929 and U266B1 cell lines. While this result was

unexpected, it did raise the possibility of ERK activation and oncogenic signalling pathway crosstalk being involved in VP79s-induced cell death. The prospect of ERK activation being involved in cell death is not a new concept. The pro-apoptotic functions of the RAS/RAF/MEK/ERK pathway in DNA damage-induced apoptosis are widely reported in a number of cancer cell types and by numerous chemotherapeutic drugs, including cisplatin, doxorubicin and taxol [443-445]. Furthermore, ERK activation has also been reported to be involved in TRAIL and ROS induced apoptosis [446].

Having observed the increase in ERK activation, p38 and JNK were also examined. ERK is generally activated in response to survival and mitogenic signalling whilst JNK and p38 are activated by various environmental stresses, osmotic shock, oxidative stress or heat shock inducing cell death [130, 447]. JNK and p38 phosphorylation has also been shown to be involved in both intrinsic and extrinsic apoptosis in response to a variety of stresses [130, 448]. In the present study, it has been shown that VP79s induced sustained phosphorylation of JNK and p38 in both the U266B1 and NCI-H929 cell line. Whether JNK is a tumour suppressive or activating factor in MM is still under debate. The JNK inhibitor, SP600125, was previously found to induce growth arrest in MM cell lines [449]. However, the cytotoxic activity of SP600125 in MM may be due to the inhibitor overstimulating NFκB activation independently of JNK inhibition [449]. Conversely, the proteasome inhibitor bortezomib has been shown to elicit its apoptotic effects, in part, through the activation of JNK and induction of ER stress [450]. Moreover, Hideshima *et al*. demonstrated that bortezomib's anti-myeloma activity could be inhibited with SP600125 [361]. A more recent 2016 study by Xie *et al.* has shown that pterostilbene inhibits myeloma cell growth, in part, through the activation of JNK and ERK [451]. One possible explanation for these conflicting reports is that different JNK proteins may function differently in the context of MM, although further research is required to elucidate these mechanisms. Like JNK, the role of p38 in MM is unclear. Inhibitors of p38 have shown efficacy in inducing cell death in MM cell lines, whilst p38 inhibition has been demonstrated to enhance the activity of bortezomib in MM cell lines and patient samples [452, 453]. Moreover, p38 inhibition has been shown to have a suppressive effect on the BMM leading to MM cell death [454, 455]. Conversely, p38 activation has been shown to play a role in cell death induced by the

antibiotic lidamycin and other compounds [456-458]. As with JNK activation, p38 activation or inhibition may induce cell death in MM cells depending on the circumstances or even cell line.

This activation of the MAPK signalling pathways may be in response to stress induced by VP79s and may act as a pro-survival mechanism. Activation of ERK signalling is classically seen as a proliferative pathway although, as previously discussed, ERK activation has been implicated in cell death [459]. Of note, the kinase inhibitor sorafenib has been found to induce activation of the pro-survival protein AKT in certain cancer cell types [120]. This activation can be sustained or transient and the exact function of this activation is unknown. Studies have shown that inhibition of this sorafenib-induced AKT activation can reverse acquired sorafenib resistance by inducing autophagic cell death [460], suggesting that AKT activation plays a role in resistance and survival. Interestingly, Ohta *et al*. demonstrated that ERK and AKT activation by platinum-based chemotherapy was indicative of favourable patient outcome [461]. These data suggest that activation of proliferative pathways by chemotherapeutics may have many consequences, both positive and negative, and that these effects may be specific to the drug, cancer type and even patient.

In order to elucidate the sequence of signalling events mediated by VP79s, a series of short time courses were carried out examining phosphorylation of proteins by western blotting, mitochondrial depolarisation and induction of ROS. Western blotting indicated that inhibition of STAT3 occurred earlier than activation of JNK and p38 but concurrently with ERK activation. DCZ3301, an aryl-guanidino compound, was shown to activate ERK and it was suggested that ERK phosphorylation may contribute to STAT3 inhibition as there is evidence of crosstalk between the pathways [422]. Crosstalk between MAPK activation and STAT3 inhibition may also exist since ERK activation by VP79s correlated with phospho-STAT3 inhibition. A study by Chung *et al.* has shown that ERK1/2 activation negatively regulates tyrosine 705 STAT3 phosphorylation through phosphorylation of STAT3 on serine 727 in a RAF-inducible fibroblast cell line [346]. It is thought that ERK activation leads to ERK-dependent phosphorylation of STAT3 on serine 727, which concurrently inhibits STAT3 phosphorylation on tyrosine 705 [346, 462]. In the present

study this is unlikely to be a mechanism as VP79s had minimal effects on serine 727 phosphorylation. Interestingly, a similar study demonstrated that ERK activation mediated the inhibition of IL-6-induced STAT3 phosphorylation in multiple cell lines, including the human liver cell line, Hep-G2, and the human myeloid cell line, MM6. Moreover, the MEK inhibitor PD98059 could abrogate this inhibition [463]. A further study by Gkouveris *et al*. demonstrated that pharmacological inhibition of ERK with U0126 in SCC9 oral squamous cell carcinoma cell line resulted in a moderate increase in STAT3 tyrosine phosphorylation, whilst induction of ERK activation by a selective MAPK (MEK 1/2) inducer resulted in inhibition of STAT3 phosphorylation on tyrosine 705, suggesting that there is crosstalk between ERK and STAT3 [464].

Crosstalk between JNK and STAT3 has also been previously demonstrated. A study by Wei *et al*. has shown that a novel anti-cancer agent activated the p38, JNK and ERK pathways; however, only inhibition of JNK abrogated apoptotic cell death [465]. Moreover, a later analogue of the drug was shown to inhibit STAT3 phosphorylation through activation of JNK, illustrating possible crosstalk between the pathways [466]. Similarly, a study by Bill *et al.* has shown that treatment with a novel curcumin analogue resulted in p38 activation which caused reciprocal inhibition of STAT3 phosphorylation [391]. These collective data establish crosstalk between the MAPK pathways and STAT3 signalling pathway and offer potential mechanistic avenues to explore in elucidating the anti-cancer activity of VP79s.

Pharmacological inhibitors of ERK, JNK and p38 were next employed to determine their role in VP79s induced cell death. Neither inhibition of ERK, JNK nor p38 was found to have any impact on VP79s induced cell death, suggesting their activation may be a consequence of other cellular processes and, whilst they were not found to be critical to cell death, may still play a role in part.

Examination of mitochondrial membrane potential by the JC-1 assay demonstrated that significant loss of membrane potential occurred at 90 and 120 minutes in U266B1 and NCI-H929 cells respectively. Prior to depolarisation of the membrane, the mitochondrial membranes appeared to become hyperpolarised. Previous reports have suggested that hyperpolarisation of the mitochondrial membrane is associated with an increase in ROS production [372, 467]. Indeed, in the present study hyperpolarisation of the mitochondrial

membrane was shown to correlate with the initiation of ROS in both cell lines. ROS has been established to be a mediator of cell death following treatment with a multitude of chemotherapeutics [468-471]. Having observed a significant increase in ROS production, the role of ROS in cell death was examined. N-Acetyl-L-Cysteine (NAC), an antioxidant which acts as a scavenger for free radicals, such as superoxide and hydrogen peroxide, was used to inhibit ROS production as NAC has been shown to abrogate cell death by chemotherapeutics such as dexamethasone and bortezomib [472]. In the present study, NAC was shown to have no effect on VP79s induced cell death. Therefore, it can be suggested that ROS is not integral to VP79s-induced cell death. Previous reports have shown that induction of ROS is associated with a marked increase in ERK, JNK and p38 activation however, how ROS activates these pathways is unclear [473]. One potential mechanism is that ROS has been shown to modify amino acid residues of proteins, therefore, it is suggested that this leads to oxidative modification of signalling molecules thereby activating them [473]. Nevertheless, activation of MAPKs and the induction of ROS was not shown to play a critical role in VP79s-induced cell death and rather, ROS induction is possibly a consequence of other cellular events.

To conclude, this study provides evidence for the first time that VP79s affects the JAK/STAT signalling pathway in MM cell lines. VP79s was shown to inhibit both constitutively active and IL-6 induced STAT3 signalling resulting in downregulation of STAT3 target genes. It appears that VP79s inhibits JAK2 phosphorylation and results in the downregulation of cell surface expression of the IL-6 receptors, CD126 and CD130. Of note, VP79s was shown to downregulate Mcl-1 a critical MM survival protein. These findings provide insights into the possible mechanism of VP79s-induced apoptosis in MM whilst also indicating that VP79s may be an effective therapy against MM, warranting further investigations. Therefore, the translational capabilities of VP79s were next examined.

Chapter 5:
Evaluation of the potential translational capacity of VP79s

5.1. Introduction

Multiple myeloma is the second most common haematological malignancy and accounts for approximately 1% of all cancers [474, 475]. The introduction of new classes of therapeutic agents such as monoclonal antibodies and proteasome inhibitors into the MM treatment arsenal has greatly improved survival rates with the median overall survival rate increasing from 2-3 years to 8-10 years over the past two decades [149, 476]. This improvement in survival is thought to be due to a better understanding of the pathology of MM, the introduction of autologous stem cell transplantation (ASCT) and the advancement in the range of therapeutics available. The therapeutic field in MM is rapidly changing with new drugs, combinations and strategies being frequently introduced. Currently, newly diagnosed MM patients are frequently treated with a doublet or triplet combinations such as lenalidomide, dexamethasone and bortezomib followed by ASCT or maintenance therapy for ASCT-ineligible patients [150]. How MM patients are treated depends on numerous factors including age, co-morbidities, eligibility for ASCT and the presence or absence of cytogenetic abnormalities [150]. Cytogenetic stratification of MM patients is based upon consensus from the international myeloma working group which divides them into three risk subgroups: standard, intermediate and high [477]. Based upon these groupings MM patients receive the most appropriate treatment. For example, based on available data from numerous clinical trials, proteasome inhibitors bortezomib and carfilzomib offer a promising treatment for patients with the t(4;14) translocation and deletion del(17/17p) [478].

Despite these advancements patients invariably relapse and become refractory to treatment necessitating the pursuit of novel treatments to combat the malignancy. The development of acquired or intrinsic drug resistance in MM is highly complex and varies from patient to patient. As mentioned above, MM is cytogenetically complex, therefore, intrinsic resistance to chemotherapeutics can arise in newly diagnosed patients depending on their karyotype. For example, some translocations can lead to the aberrant expression of oncogenes such as cyclin D and c-MYC. Acquired resistance in MM can arise through multiple mechanisms. Clonal evolution is one of the main mechanisms by which myeloma

cells evade chemotherapeutic cell death as during rounds of treatment patients can develop new translocations which confer resistance against previously effective drugs [194, 479]. Upregulation of the expression of multidrug resistance proteins such as p-glycoprotein has been shown to be a key player in myeloma drug resistance in myeloma cells [190]. One study has shown that up to 75% of MM patients treated with dexamethasone, vincristine and doxorubicin showed an increase in p-glycoprotein expression [480]. A unique aspect of MM, in contrast to many other malignancies, is its elaborate relationship with the bone marrow microenvironment (BMM). The BMM creates a niche environment which supports the survival of MM cells through direct contact with cells and soluble factors such as the cytokine IL-6 [43]. Therefore, disruption of BMM-MM cell interactions is becoming an increasing area of research for the treatment of MM for both single agent treatment and in combination treatments [343].

In chapter 4, VP79s was shown to inhibit both constitutively active and IL-6-induced STAT3 signalling resulting in downregulation of key STAT3 responsive proteins. Previous reports have established that STAT3 is overexpressed in MM and may in part be responsible for BMM mediated drug resistance [36, 49]. STAT3 has multiple downstream targets such as cell cycle proteins, proinflammatory cytokines, matrix metalloproteinases (MMP), growth factors and anti-apoptotic proteins. These downstream targets all play a vital role in MM cell survival. Increasing evidence has demonstrated that activation of the JAK/STAT3 signalling pathway in MM can confer resistance to apoptosis through upregulation of key survival proteins such as Mcl-1 [29, 57, 349].

The body of data presented herein has highlighted the role that the JAK/STAT3 pathway and upregulation of Mcl-1 plays in the survival of MM cells. Moreover, reports in the literature have demonstrated that the BMM plays a key role in the development of drug resistance to therapeutics such as dexamethasone and bortezomib [33, 36]. Therefore, in this chapter the effects of VP79s in combination with the proteasome inhibitor bortezomib were examined. Furthermore, the ability of VP79s to overcome bone marrow stromal cell-mediated drug resistance was assessed. The preclinical evaluation of novel therapeutics in normal, non-malignant cells is essential in order to determine if their cytotoxic selectivity; therefore, given the potent anti-myeloma activity of VP79s, the effects VP79s had on the

viability of PBMCs and lymphocytes from healthy donors was examined. In chapters 3 and 4, the use of *in vitro* cell line models demonstrated that VP79s elicited potent anti-MM activity. In the development of novel therapeutics, testing the novel agent in clinically relevant models is vital in understanding its potential. Therefore, the ability of VP79s to induce cell death in *ex vivo* MM patient samples was finally examined.

5.2. Experimental results

5.2.1. VP79s enhances bortezomib induced cell death in U266B1 cells

Bortezomib is a first-in-class proteasome inhibitor which is used for the treatment of newly diagnosed and relapsed MM. Since its introduction, patient survival has continued to increase, however, drug resistance following treatment remains inevitable. Activation of STAT3 by IL-6 and BMSCs in MM plays a role in the development of drug resistance [37] and previous studies have demonstrated that STAT3 inhibition can enhance cell death induced by bortezomib [353, 481]. Therefore, the affects of VP79s and bortezomib in combination were examined in the U266B1 cells as the U266B1 cells were shown to have constitutively active STAT3 phosphorylation on tyrosine 705.

Potential synergism between VP79s and bortezomib was assessed using multiple drug dose-effect calculations using the median effect method [279]. U266B1 cells were treated with a range of concentrations of VP79s (2-10 μM) and bortezomib (2-10 nM), both alone and in combination for 16 hours. A one to one ratio was utilised i.e. 6 μM VP79s to 6 nM bortezomib. Flow cytometric analysis of annexin V/PI stained cells was employed to determine the percentage of apoptotic and dead cells.

Cell death was shown to be significantly higher in combination versus single treatment at 3 and 7 μM:nM treatments (Figure 5.1). Analysis of synergism was carried out using the CompuSyn program. Combination indexes (CI) were generated for each combination treatment with CI values <1, =1 and >1 indicating synergistic, additive and antagonistic effects respectively. From these graphs the combination index can be evaluated. The combination treatment 7 μM:nM was found to be synergistic (Figure 5.2 and Table 5.1). Further optimisation of bortezomib in combination with VP79s is still required to improve on the results obtained herein.

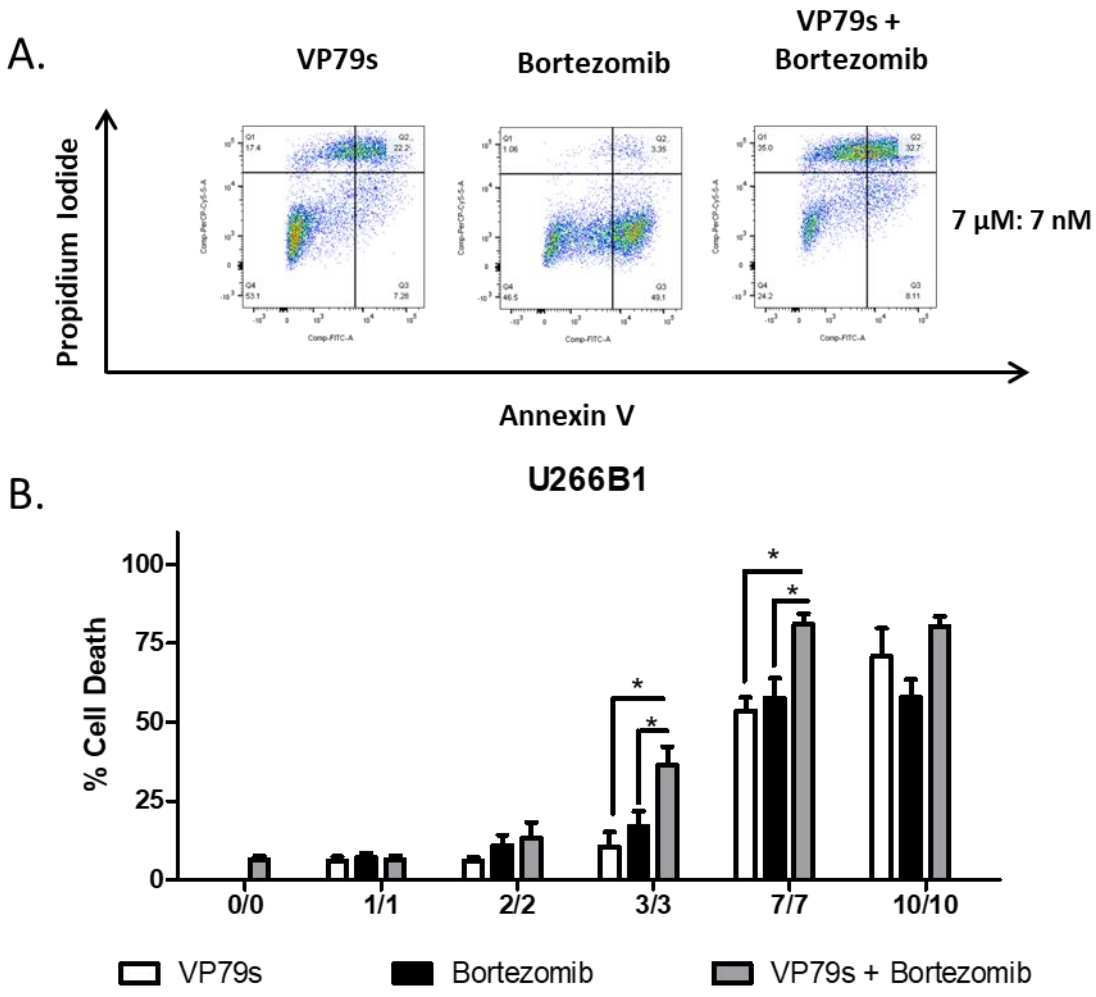

Figure 5. 1 VP79s and bortezomib in combination enhance cell death in U266B1 cells.

30 x 10^4 cells/mL U266B1 cells were seeded in 12 well plates and were treated in duplicate with either vehicle [0.01 % DMSO (v/v) and 0.5% EtOH (v/v)] or a range of concentrations of VP79s (1 -10 µM) and bortezomib (1-10 nM) alone and in combination. After 16 hours, cells were collected and stained with annexin V/propidium iodide. Cells were analysed by flow cytometry using the BD FACSCanto™ II flow cytometer. 10,000 single cells were gated on vehicle treated cells excluding debris and doublets. ***A.*** *Representative image of 7 µM VP79s and 7 nM bortezomib alone and in combination.* ***B.*** *Bars represent the mean ± S.E.M. of three independent experiments. Statistical analysis was performed using a paired two-tailed t-test. *p<0.05. The effect of VP79s or bortezomib alone was compared to their effects in combination.*

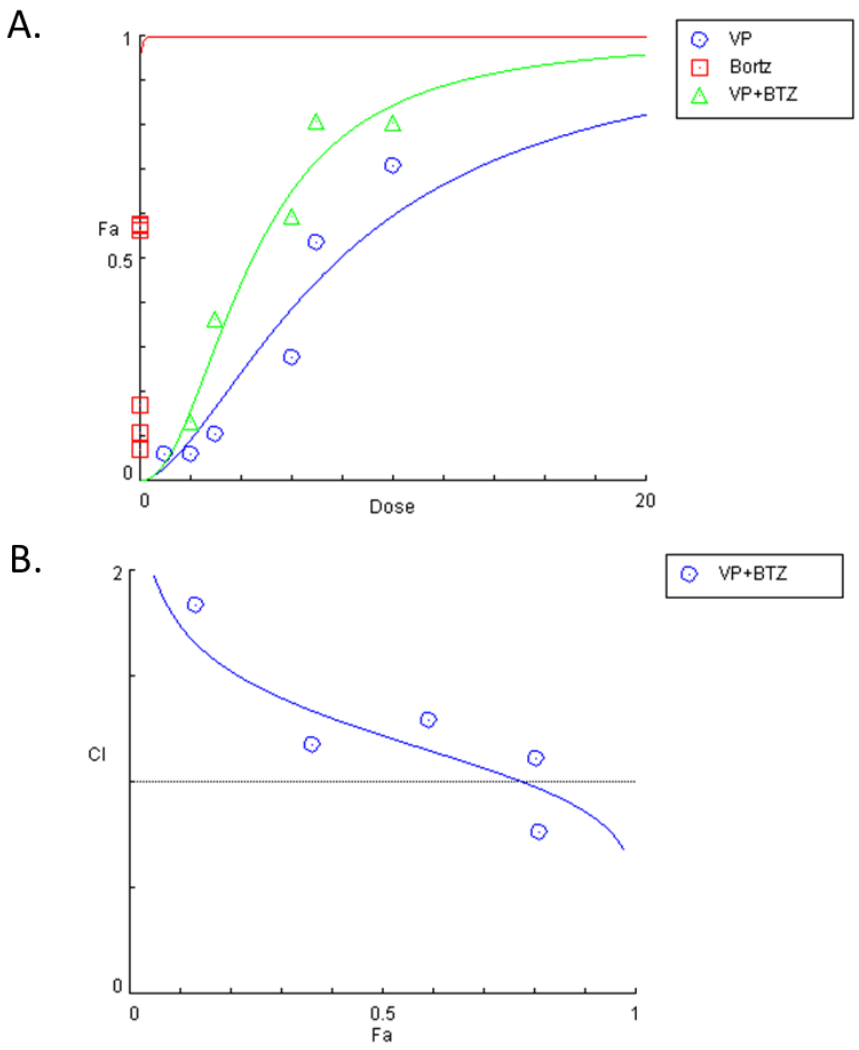

Figure 5. 2 Synergism between VP79s and bortezomib in U266B1 cells.

30 x 10^4 cells/mL U266B1 cells were seeded in 12 well plates were treated in duplicate with a range of concentrations of VP79s (VP) (1 - 10 µM) and bortezomib (Bortz) (1 - 10 nM) alone and in combination (VP + BTZ). After 16 hours, cells were collected and stained with annexin V-FITC or propidium iodide. Cells were analysed by flow cytometry using the BD FACSCanto™ II flow cytometer. 10,000 single cells were gated on vehicle treated cells excluding debris and doublets. The mean of three independent experiments, each of which was performed in duplicate, as indicated in Figure 5.1. was entered into compusyn. ***A****. Dose response curves for VP79s, bortezomib and both in combination.* ***B****. Combination index plot showing synergism between VP79s and bortezomib. CI values <1, =1 and >1 indicate synergistic, additive and antagonistic effects respectively.*

VP79s (µM)	Bortezomib (nM)	Fa	Combination Index	Description
1	1	0.06	1.5	Antagonism
2	2	0.13	1.8	Antagonism
3	3	0.37	1.17	Slight antagonism
7	7	0.81	0.76	Moderate Synergism
10	10	0.81	1.1	Nearly additive

Table 5. 1 Synergism between VP79s and bortezomib in U266B1 cells

30 x 10^4 cells/mL U266B1 cells were seeded in 12 well plates were treated in duplicate with a range of concentrations of VP79s (1 -10 µM) and bortezomib (2 -10 nM) alone and in combination. After 16 hours, cells were collected and stained with annexin V-FITC or propidium iodide. Cells were analysed by flow cytometry using the BD FACSCanto™ II flow cytometer. 10,000 single cells were gated on vehicle treated cells excluding debris and doublets. The mean of three independent experiments, each of which was performed in duplicate, as indicated in Figure 5.1 was entered into compusyn. CI values <1, =1 and >1 indicate synergistic, additive and antagonistic effects respectively.

5.2.2. VP79s can overcome bone marrow stromal cell induced resistance in NCI-H929 cells

Substantial study into the area of the BMM has elucidated the important role that it plays in MM cell differentiation, migration, proliferation, survival and drug resistance [28, 29]. BMSCs are a key component of the BMM which have been shown to be involved in the upregulation of adhesion molecules and pro-survival cytokines such as IL-6. Previously, VP79s was shown to inhibit constitutively active and IL-6-induced STAT3 phosphorylation in MM cell lines (Chapter 4). Following on from these promising results, the ability of VP79s to overcome BMM-induced resistance was examined. The bone marrow stromal cell line HS5 was used as an experimental model to mimic BMM induced resistance in MM cells [270]. The HS5 cell model is widely used in breast cancer, pancreatic cancer and MM research [37, 482-485]. These cells have been shown to produce many pro-survival cytokines and growth factors such as IL-6, granulocyte colony stimulating factor, granulocyte macrophage colony stimulating factor, macrophage colony stimulating factor, kit ligand, macrophage inhibitory protein-1 alpha, IL-1 alpha and beta, IL-8, IL-11, and leukaemia inhibitory factor [270]. Cell adhesion mediated drug resistance (CAM-DR) is a mechanism whereby MM cells avoid the cytotoxic effects of chemotherapeutics by binding to cells in the BMM via adhesion molecules [36]. Adhesion leads to upregulation of anti-apoptotic proteins, cell cycle proteins and drug transporters such as ATP-binding cassette transporters in MM cells [486]. Resistance to therapeutics such as doxorubicin is mainly mediated through adhesion to fibronectin or BMSCs. MM-BMSCs interactions are complex as they are mediated by several adhesion molecules present on both cell types [487].

Firstly, the alamar blue assay was employed in order to determine if VP79s elicited any cytotoxic effects on the HS5 cell line. VP79s had minimal effect on the viability of the HS5 cell line at concentrations below 6 µM following treatment for 24 hours (Figure 5.3). Consequently, 5 µM VP79s was used in subsequent experiments with the HS5 cells.

BMSCs have previously been shown to prevent MM cells from cell death induced by bortezomib [37, 488]. Therefore, in the present study, bortezomib was used as a positive control to validate that BMSCs elicit a pro-survival effect in MM cells. The NCI-H929 cells

were chosen for the co-culture experiments as they do not possess constitutive phosphorylation of STAT3 on tyrosine, but they are IL-6 responsive. Therefore, NCI-H929 cells were seeded either in monoculture or co-culture with the HS5 cells. Cells were then treated with 1.5 nM bortezomib for 24 hours. Cells were collected, stained and cell death was evaluated on CD138+ MM cells to exclude any HS5 cells which may have detached during the collection of cells for annexin V/PI staining and flow cytometry (see gating strategy Figure 5.4). The HS5 cell line was found to abrogate cell death induced by bortezomib in the NCI-H929 cells. Bortezomib was found to induce 27% apoptosis in NCI-H929 cells in monoculture whilst only inducing 8% apoptosis in the cells when in co-culture (Figure 5.5 A). This reduction in cell death was statistically significant (Figure 5.5 B).

Having validated the assay, the experiment above was repeated with VP79s. Initially, a transwell assay was utilised to determine if any drug resistance would be elicited from soluble factors released by the HS5 cells. Thereby, HS5 cells were seeded in a well of a 12 well plate with MM cells being seeded into a transwell. The transwell holds the NCI-H929 cells in suspension above the HS5 cells allowing for both cell lines to be in the presence of soluble factors without direct contact. Cells were then treated with 5 μM VP79s for 24 hours, collected, stained and cell death was evaluated in CD138+ cells using annexin V/PI staining and flow cytometry. No statistically significant differences in cell death were observed between the NCI-H929 cells in monoculture treated with VP79s compared to those in co-culture with HS5 cells and treated with VP79s. Therefore, HS5 cells did not induce a significant survival advantage (Figure 5.6).

Having shown that soluble factors secreted by HS5 cells had no impact on VP79s induced cell death, NCI-H929 cells were then cultured in direct contact with HS5 cells to assess CAM-DR. In contrast to the results obtained with bortezomib, the HS5 cells had no impact on cell death induced by VP79s in NCI-H929 cells. VP79s induced 37% and 41% cell death in monoculture and co-culture respectively (Figure 5.7).

To summarise, unlike bortezomib, VP79s can overcome the protective effects of HS5 cells in co-culture with NCI-H929 cells. This suggests that VP79s may be a promising anti-MM therapeutic warranting further investigation into its translational capabilities.

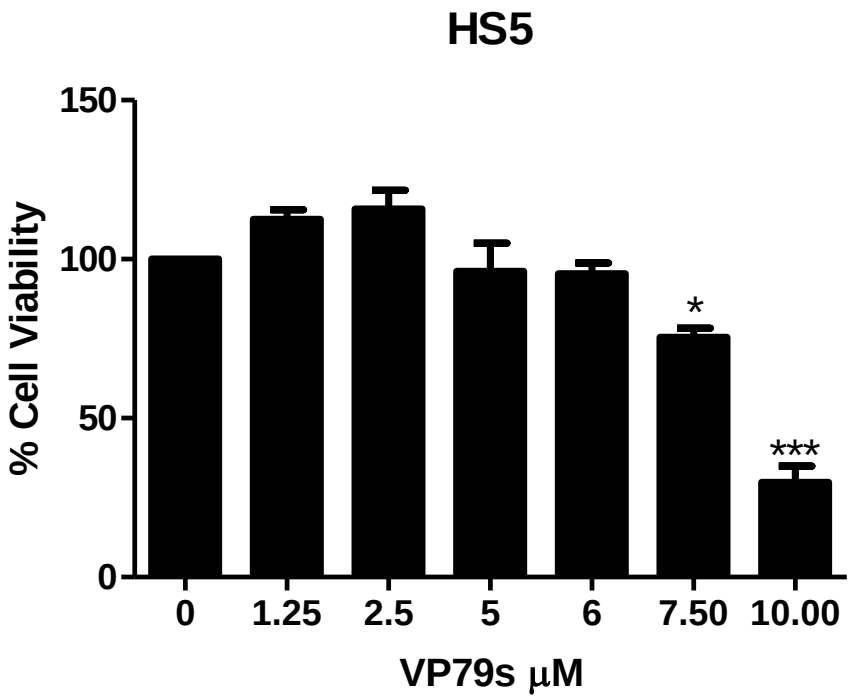

Figure 5. 3 Effect of VP79s on the viability of HS5 cells.

*HS5 cells were seeded at a density of 40,000 cells per well in a 96 well plate and left to adhere overnight. The following day cells were treated with either vehicle [0.5% EtOH (v/v)] or various concentrations of VP79s (1.25 – 10 μM). After 24 hours 10% alamar blue (v/v) was added to each well. Plates were incubated in the dark for up to 5 hours until a colour change was observed in the vehicle. Fluorescence was measured using a SpectraMax Gemini plate reader at excitation wavelength 544 nm and emission wavelength 590. Values represent the S.E.M. of three independent experiments. Statistical analysis was performed using one-way ANOVA with Dunnett's post hoc test. *p<0.05, ***p<0.001.*

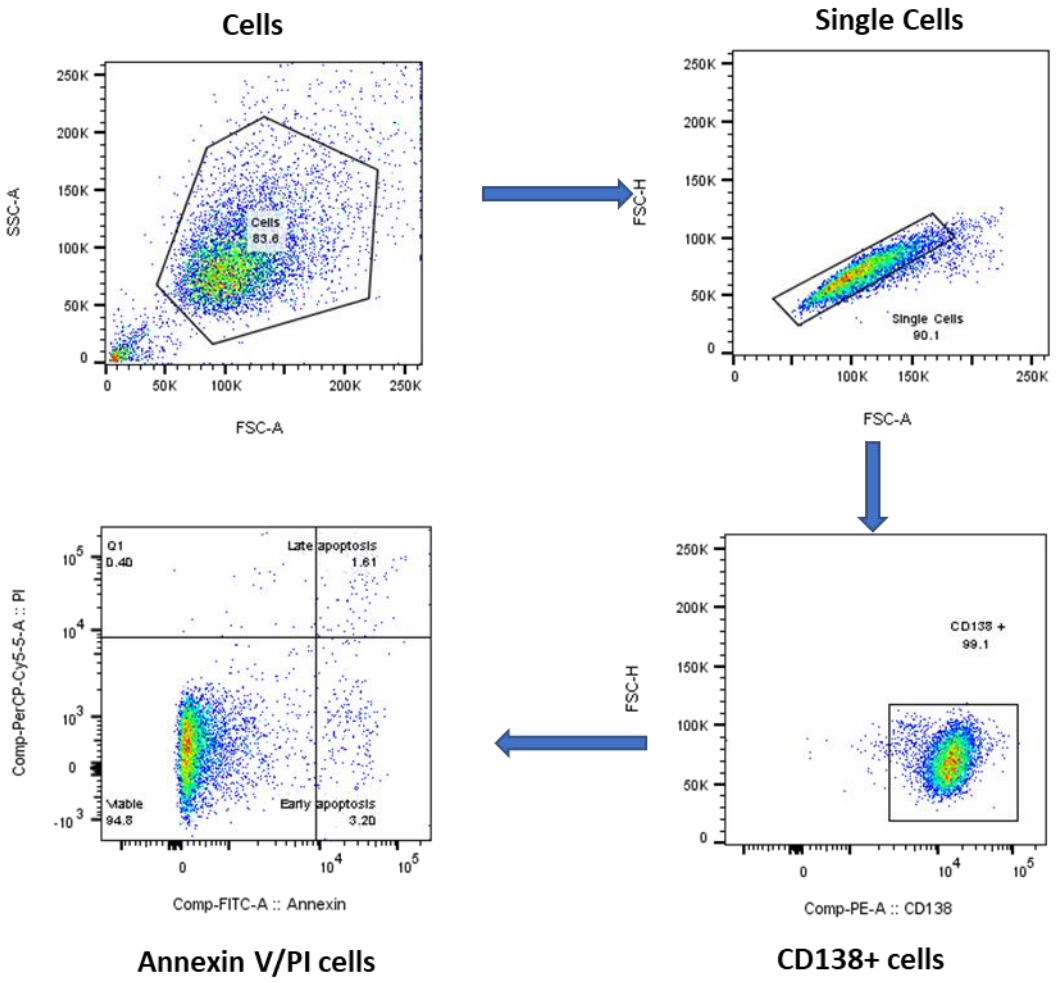

Figure 5. 4 Gating strategy for HS5 co-culture with the NCI-H929 cell line.

HS5 bone marrow stromal cells were seeded at a density of 10 x 10^4 cells in 12 well plates and left to adhere overnight. The next day NCI-H929 cells were seeded at a density of 30 x 10^4 cells/well either in monoculture or in co-culture with the HS5 cells. Following treatment cells were collected and stained with anti-CD138, annexin V and propidium iodide (PI). Cells were analysed by flow cytometry using the BD FACSCanto™ II flow cytometer. 10,000 single cells were gated on vehicle treated cells excluding debris and doublets, CD138+ cells were then selected for annexin V/PI analysis.

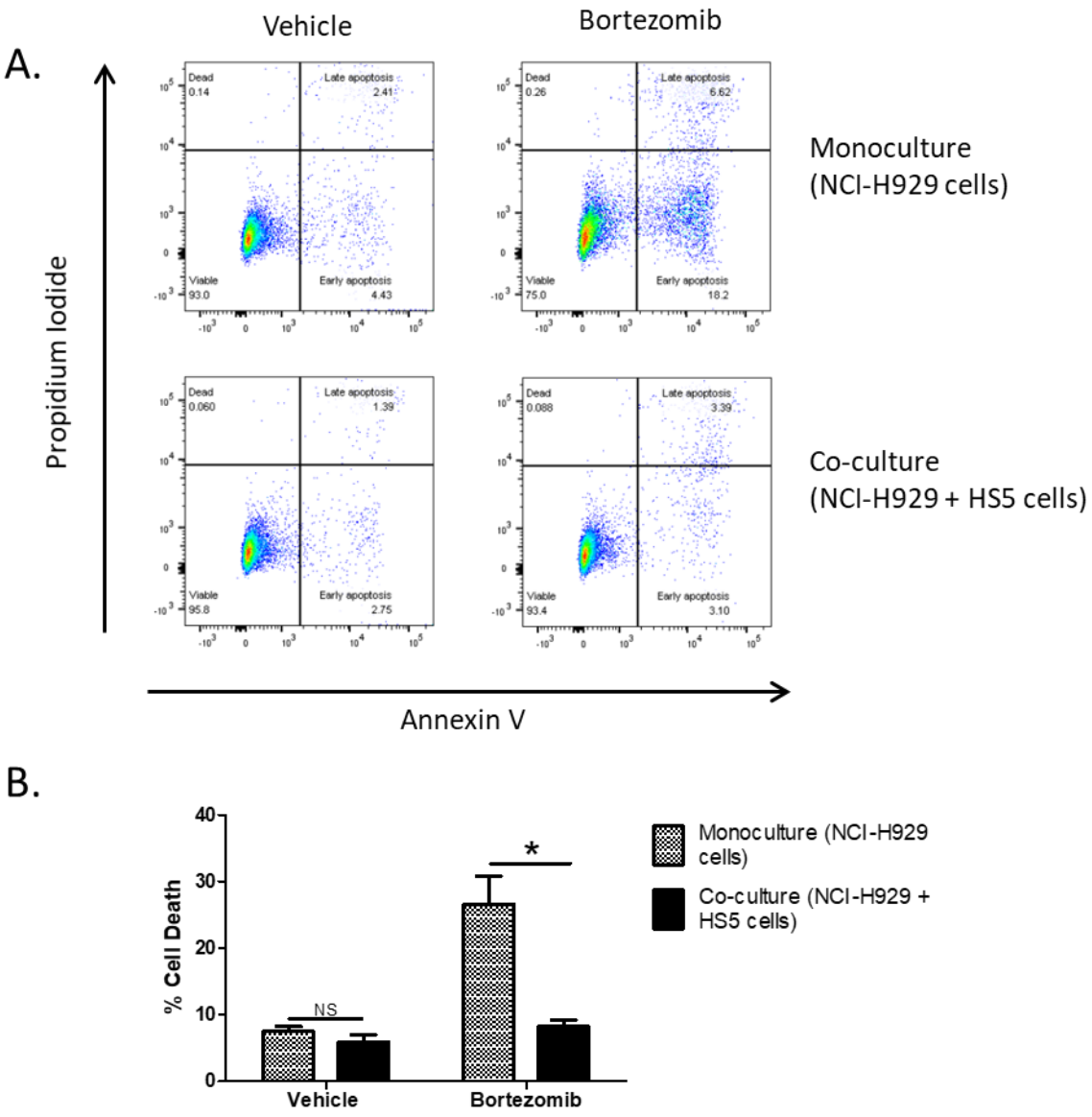

Figure 5. 5 HS5 cells induce bortezomib resistance in NCI-H929 cells.

HS5 bone marrow stromal cells were seeded at a density of 10 x 10^4 cells in 12 well plates and left to adhere overnight. The next day NCI-H929 cells were seeded at a density of 30 X 10^4 cells/well either in monoculture or co-culture with the HS5 cells. Cells were then treated with either vehicle [0.01% DMSO (v/v)] or 1.5 nM bortezomib for 24 hours. Samples were collected and analysed by flow cytometry. ***A.*** *Representative dot plots of CD138 positive cells gated on annexin V/PI positive cells.* ***B.*** *Bars represent the mean ± S.E.M of 3 independent experiments. Statistical analysis was performed using a paired two-tailed t-test. *p<0.05.*

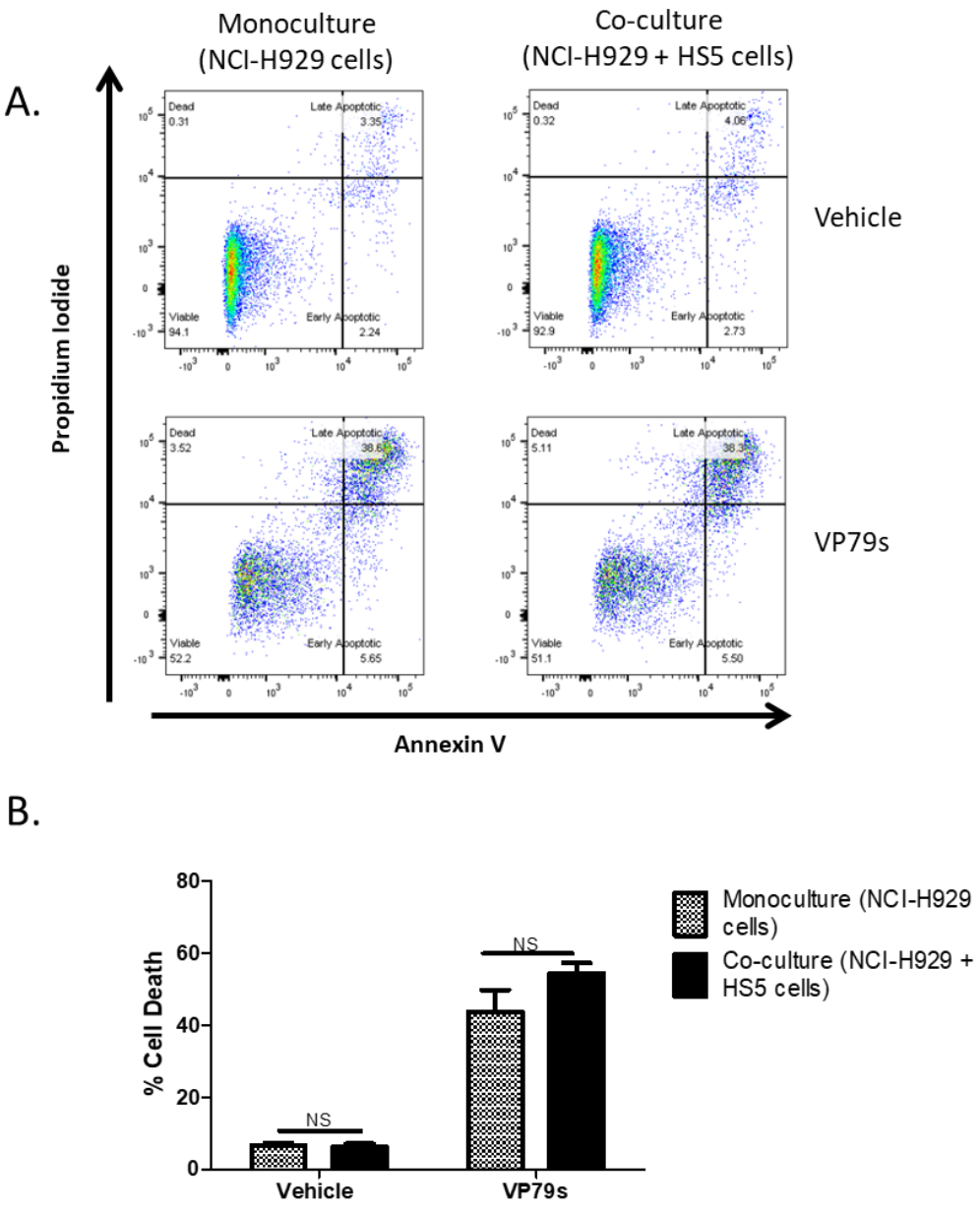

Figure 5. 6 VP79s can overcome soluble pro-survival factors secreted by HS5 cells and elicit cell death.

1.5 X 10^5 NCI-H929 cells were seeded in transwell inserts in 12 well plate wells either in monoculture or in co-culture with 1 x 10^5 HS5 bone marrow stromal cells seeded overnight in 12 well plate wells. Cells were treated with either vehicle [0.5% EtOH (v/v)] or 5 µM VP79s for 24 hours. NCI-H929 cells were collected and apoptosis was analysed by annexin V/propidium iodide (PI) staining of $CD138^+$cells. ***A.*** *Representative dot plots of $CD138^+$ cells gated on annexin V/PI positive cells.* ***B.*** *Bars represent the mean ± S.E.M of 3 independent experiments. Statistical analysis was performed using a paired two-tailed t-test. NS = no significance.*

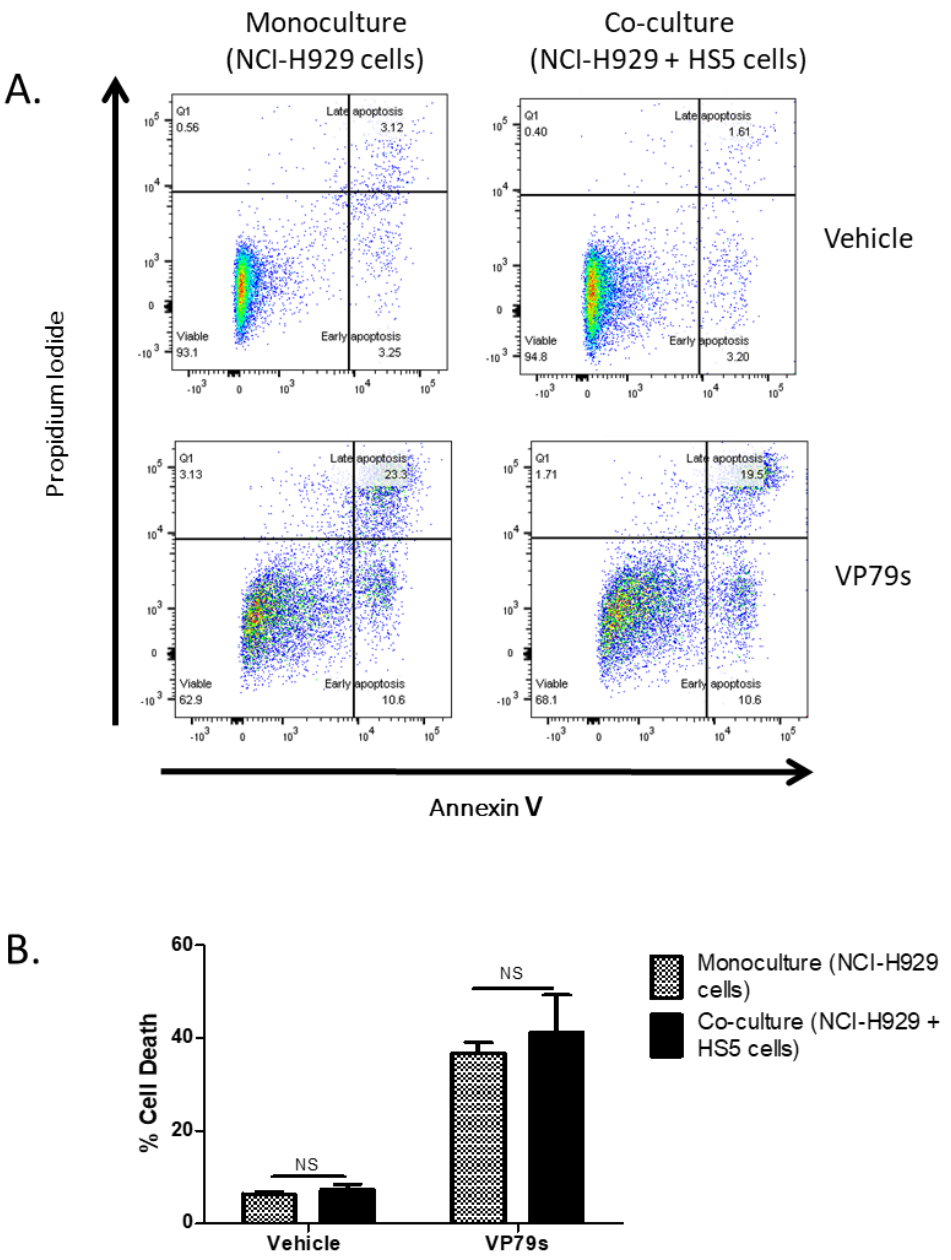

Figure 5. 7 VP79s can overcome HS5 induced resistance to cell death.

HS5 bone marrow stromal cells were seeded at a density of 10 x 10^4 cells in 12 well plates and left to adhere overnight. The next day NCI-H929 cells were seeded at a density of 30 X 10^4 cells/well either alone or in co-culture with the HS5 cells. Samples were treated with either vehicle [0.5% EtOH (v/v)] or 5 µM VP79s for 24 hours. Samples were collected and analysed by flow cytometry. ***A.*** *Representative dot plots of $CD138^+$ cells gated on annexin V/propidium iodide (PI) positive cells.* ***B.*** *Bars represent the mean ± S.E.M of 3 independent experiments. Statistical analysis was performed using a paired two-tailed t-test. NS = no significance.*

5.2.3. The effect of VP79s on the viability of lymphocytes from healthy donors

VP79s was shown to elicit potent anti-myeloma activity in MM cell lines. Therefore, the effect of VP79s on healthy cells was next examined. Since VP79s was shown to downregulate Mcl-1 in MM cells, the effect of VP79s on non-malignant lymphocytes was also examined as Mcl-1 has been shown to be important for their survival [489-491].

Peripheral blood mononuclear cells (PBMCs) were isolated from the blood of 6 healthy donors following informed consent. PBMCs were then seeded and treated with various concentrations of VP79s (0.625 – 10 μM) for 24 hours. After treatment, cells were collected, stained with antibodies against CD3, CD19 and CD56 for the gating of T cells, B cells and NK cells respectively (Figure 5.8). DAPI was used as an indicator of cell viability as DAPI cannot be taken up by healthy cells.

VP79s was found to elicit minimal effects on the viability of donor PBMCs up to a concentration of 5 μM. Treatment with 10 μM VP79s resulted in 13.7% cell death when compared to the vehicle. No significant cell death was observed at concentrations lower than 10 μM (Figure 5.9). The effect of VP79s on lymphocyte subclasses was then tested.

Similar to the results obtained with the PBMCs, VP79s did not significantly reduce the viability of the NK cells, T cells or B cells until the highest concentration of 10 μM was reached. Similar to the PBMCs, VP79s induced 15.9% cell death in NK cells at 10 μM but no significant cell death was observed at the lower concentrations tested (Figure 5.10). Similar results were obtained with T cells (Figure 5.11) and B cells (Figure 5.12).

To conclude, VP79s was found to induce minimal cell death in healthy donor PBMCs at concentrations up to 5 μM which are lethal to MM cell lines.

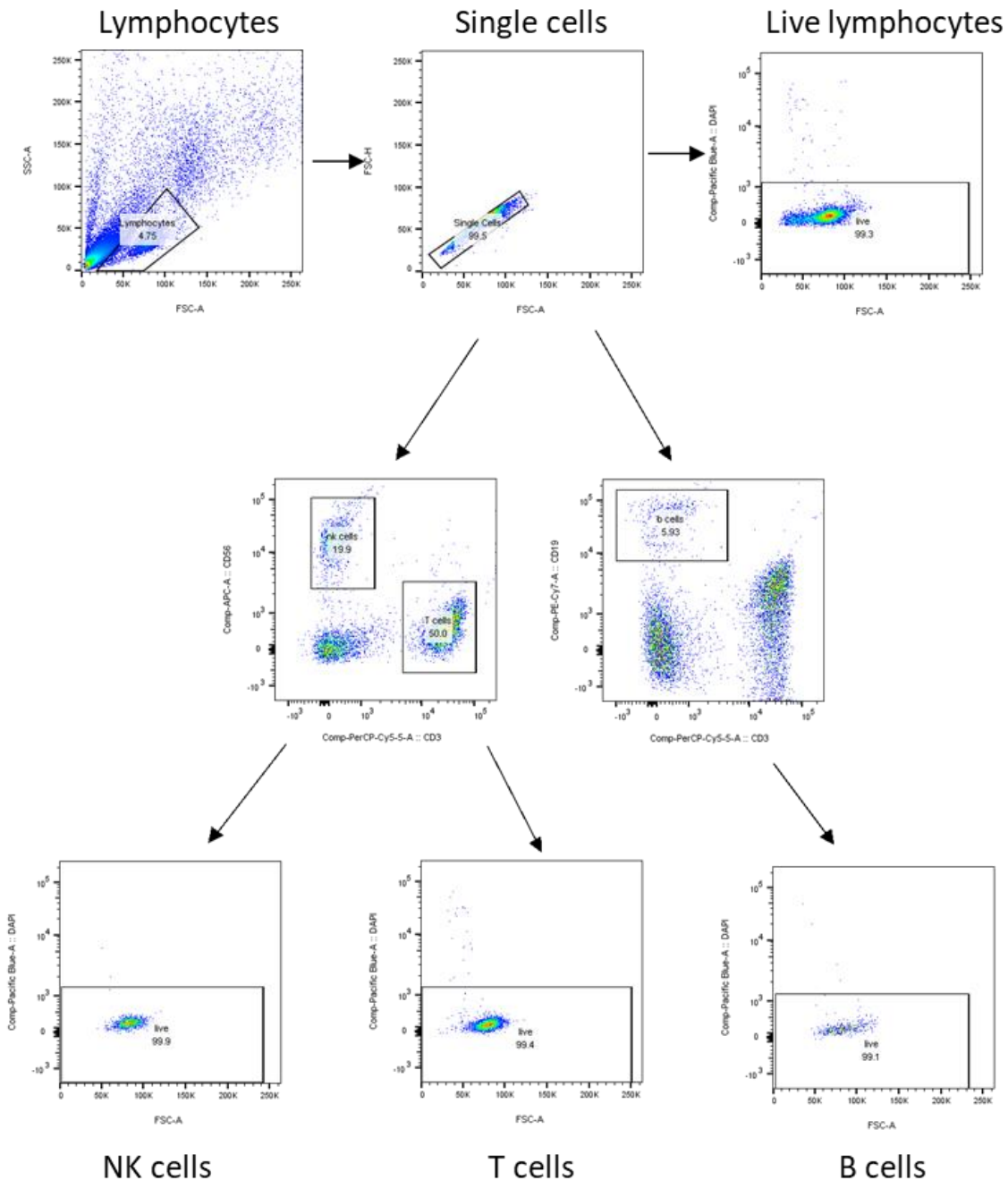

Figure 5. 8 Gating strategy for lymphocytes isolated from donor blood.

Peripheral blood mononuclear cells (PBMCs) were isolated from whole blood from healthy donors. 100,000 cells/well were seeded in a 96 well plate and after 24 hours cells were collected and were analysed by flow cytometry using the BD FACSCanto™ II flow cytometer 10,000 single cells were gated on vehicle treated lymphocytes excluding debris and doublets. NK cells were selected from CD56 positive cells, T cells were selected from CD3 positive cells and B cells were selected from CD19 positive cells as above.

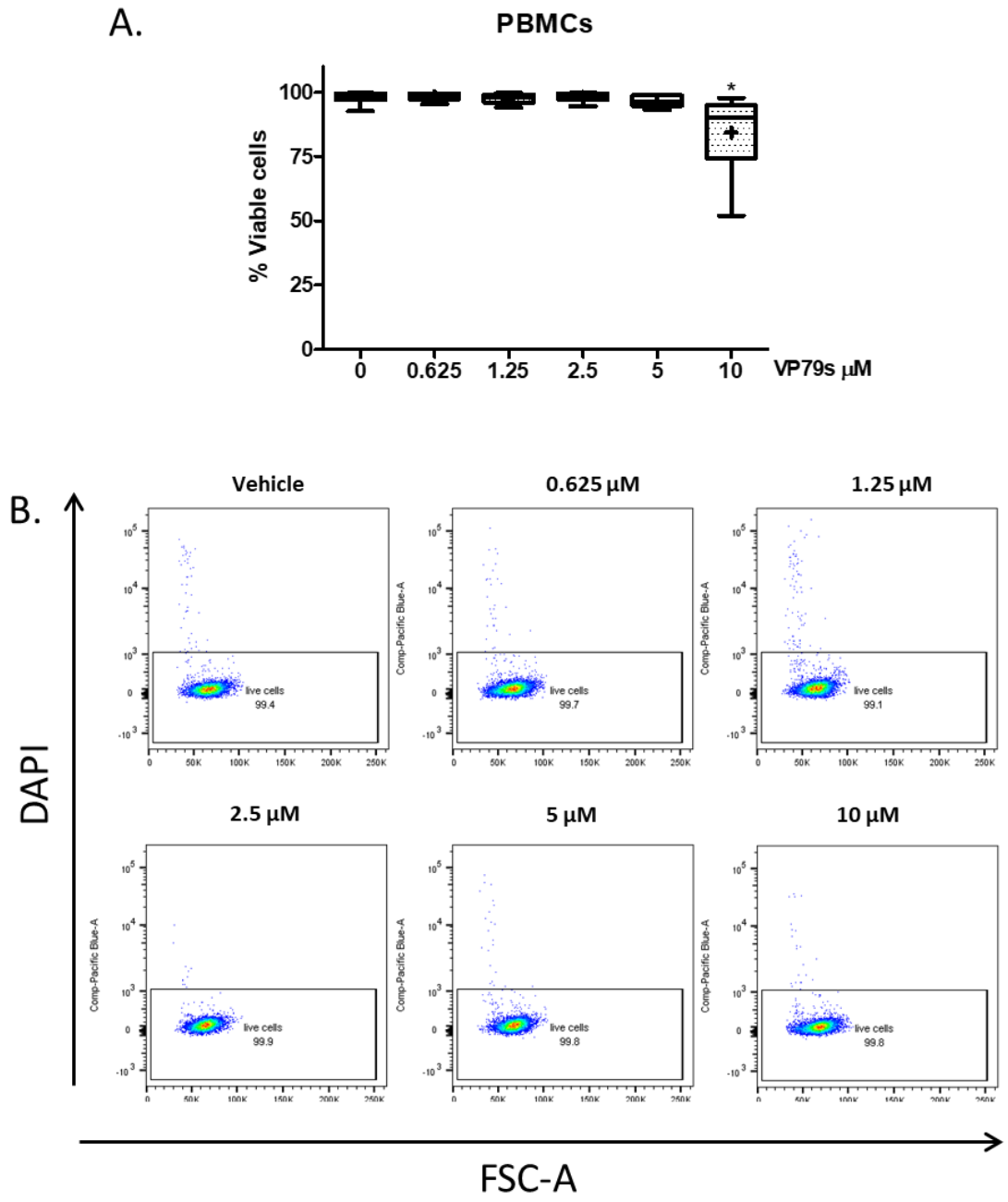

Figure 5. 9 Effect of VP79s on the viability of donor PBMCs.

Peripheral blood mononuclear cells (PBMCs) were isolated from whole blood from healthy donors. 100,000 cells/well were seeded in a 96 well plate and treated with either vehicle [0.5% EtOH (v/v)] or various concentrations of VP79s (0.625 – 10 µM) for 24 hours. After 24 hours cells were collected and analysed by flow cytometry, gating on total PBMCs, single cells and DAPI positive cells ***A.*** *Values represent the minimum to maximum viability of PBMCs from 6 healthy donors (N=6). Statistical analysis was performed using one-way ANOVA with Dunnett's post hoc test. *p<0.05* ***B.*** *Representative dot plots of effect of VP79s on total lymphocytes (Donor 4).*

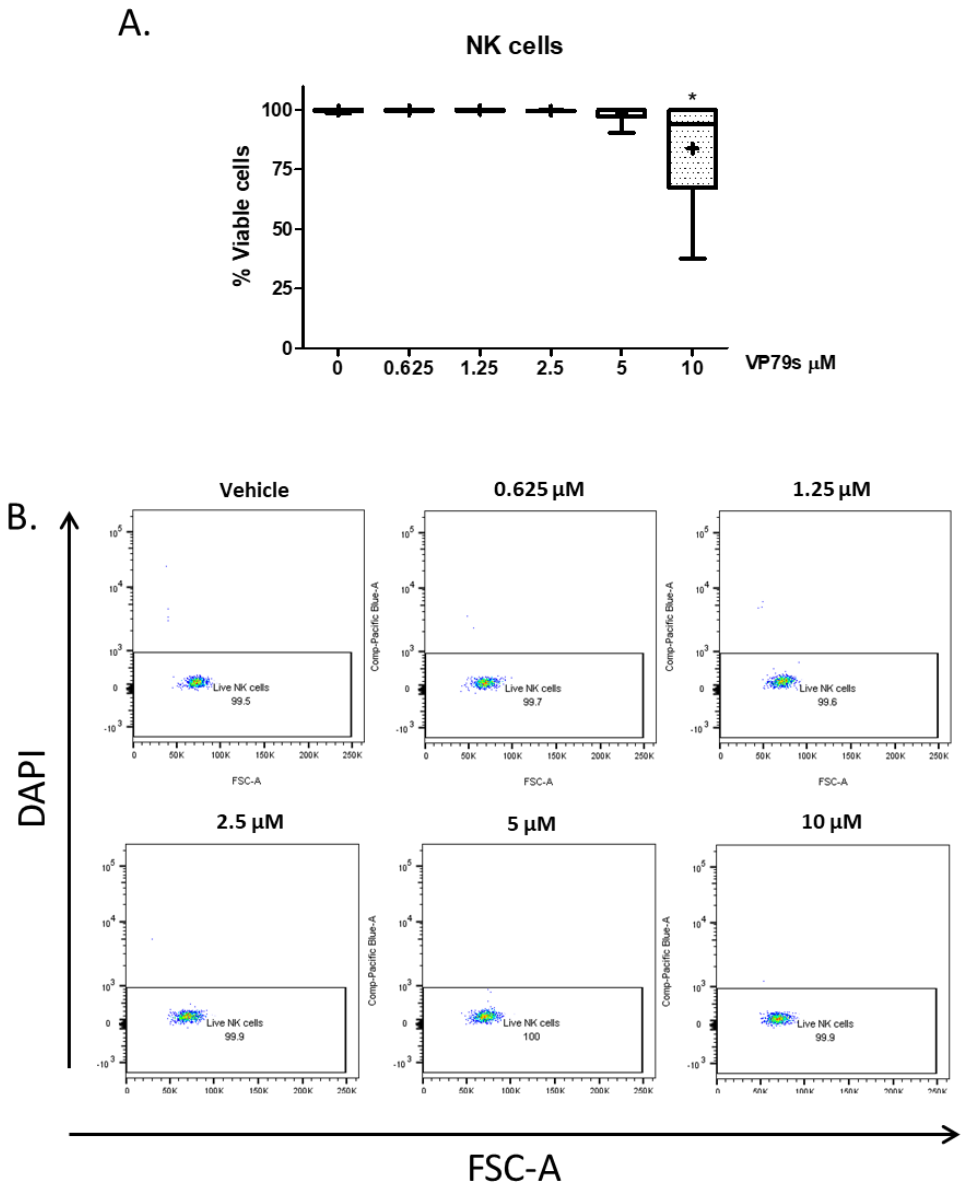

Figure 5. 10 Effect of VP79s on the viability of donor NK cells.

Peripheral blood mononuclear cells (PBMCs) were isolated from whole blood from healthy donors. 100,000 cells/well in a 96 well plate were seeded and treated with either vehicle [0.5% EtOH (v/v)] or various concentrations of VP79s (0.625 –10 µM) for 24 hours. After 24 hours cells were collected and analysed by flow cytometry, gating on total lymphocytes, single cells, CD56 positive, CD3 negative NK cells and DAPI positive cells ***A.*** *Values represent the minimum to maximum viability of NK cells from 6 healthy donors (N=6). Statistical analysis was performed using one-way ANOVA with Dunnett's post hoc test. *p<0.05* ***B.*** *Representative dot plots of effect of VP79s on total NK cells (Donor 4).*

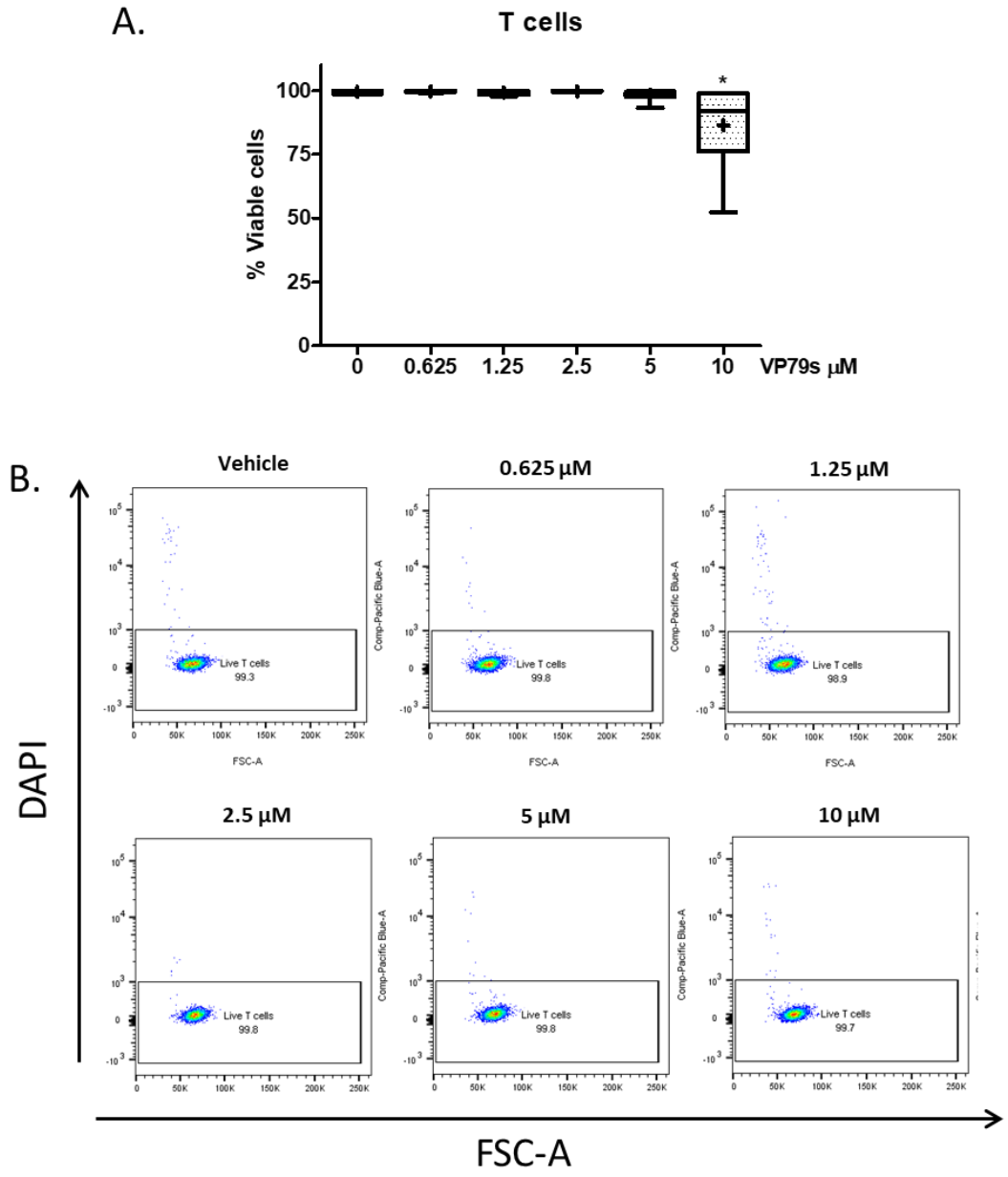

Figure 5. 11 Effect of VP79s on the viability of donor T cells.

*Peripheral blood mononuclear cells (PBMCs) were isolated from whole blood from healthy donors. 100,000 cells/well in a 96 well plate were seeded and treated with either vehicle [0.5% EtOH (v/v)] or various concentrations of VP79s (0.625 – 10 µM) for 24 hours. After 24 hours cells were collected and analysed by flow cytometry, gating on total lymphocytes, single cells, CD3 positive lymphocytes and DAPI positive cells A. Values represent the minimum to maximum viability of T cells from 6 healthy donors (N=6). Statistical analysis was performed using one-way ANOVA with Dunnett's post hoc test. *p<0.05 B. Representative dot plots of effect of VP79s on B cells (Donor 4).*

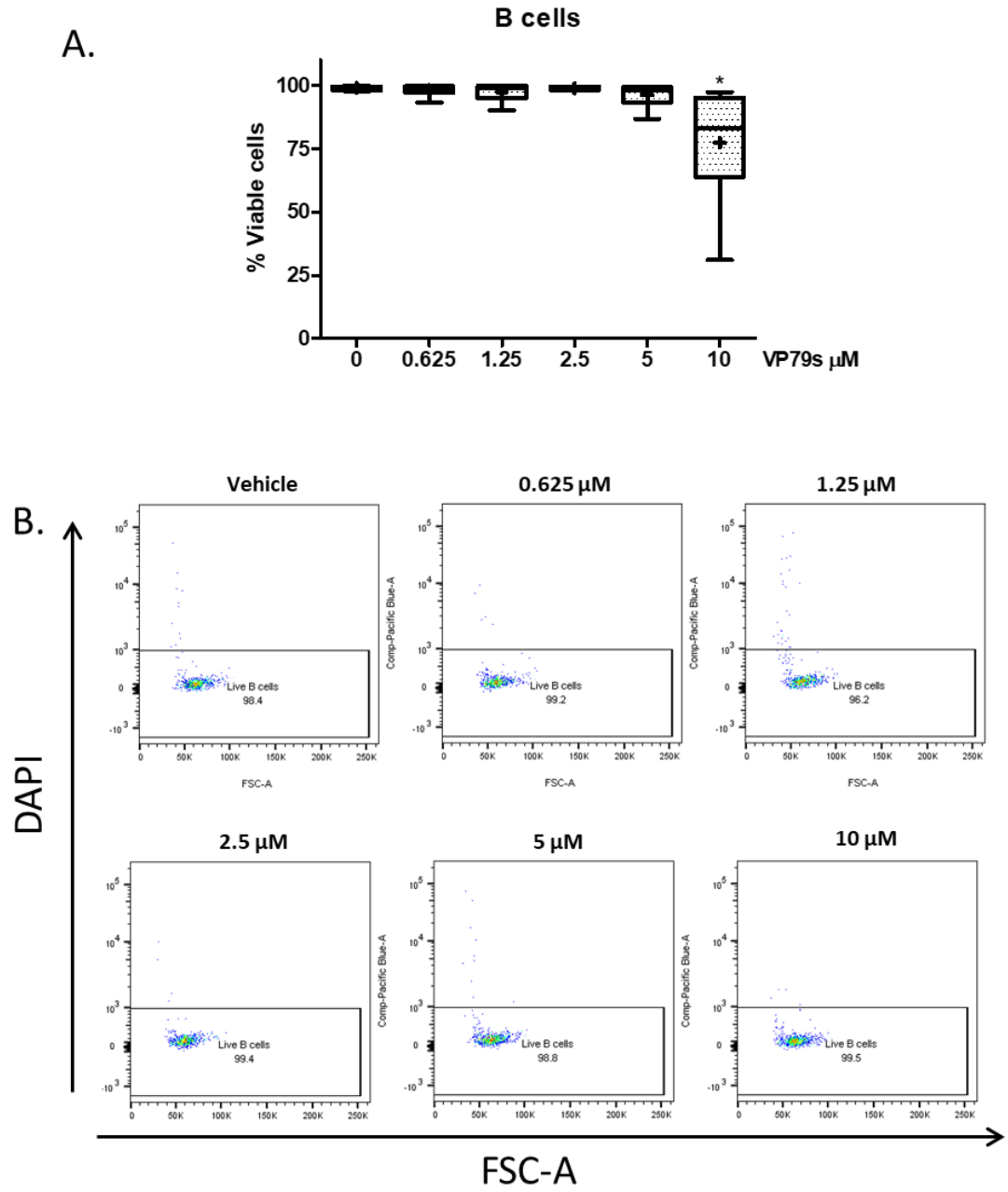

Figure 5. 12 Effect of VP79s on the viability of donor B cells.

Peripheral blood mononuclear cells (PBMCs) were isolated from whole blood from healthy donors. 100,000 cells/well in a 96 well plate were seeded and treated with either vehicle [0.5% EtOH (v/v)] or various concentrations of VP79s (0.625 – 10 µM) for 24 hours. After 24 hours cells were collected and analysed by flow cytometry, gating on total lymphocytes, single cells, CD19 positive lymphocytes and DAPI positive cells ***A.*** *Values represent the minimum to maximum viability of B cells from 6 healthy donors (N=6). Statistical analysis was performed using one-way ANOVA with Dunnett's post hoc test. *p<0.05* ***B.*** *Representative dot plots of effect of VP79s on B cells (Donor 4).*

5.2.4. VP79s induces cell death in *ex vivo* MM patient samples

Having demonstrated that VP79s can induce apoptosis in a panel of drug-sensitive and -resistant MM cell lines (Chapter 3), enhance bortezomib induced cell death and overcome BMM-induced drug resistance (Chapter 5), the ability of VP79s to induce cell death in *ex vivo* MM patient samples was next assessed. MM cells isolated from 5 patients at diagnosis were used in this study. These patient samples were obtained from the Trinity College Dublin/St James's Hospital Blood Cancer Biobank. The MM cells were purified from BM aspirates using CD138 positive selection and cryopreserved in liquid nitrogen. When required MM cells were thawed and viability was assessed, with cell exhibiting least 80% viable following thawing. Cells were then treated with VP79s (0.625 – 5 µM) for 24 hours. Since VP79s was shown to have no cytotoxic effects on donor PBMCs up to 5 µM, *ex vivo* MM patient samples were treated with concentrations to up 5 µM. After 24 hours, samples were collected, stained with annexin V/PI and apoptosis was assessed by flow cytometry. Due to the scarcity of patient samples and the gruelling means by which these samples are obtained, the number of samples used in this study was limited to 5.

As expected, VP79s was shown to elicit variable results at lower concentrations in *ex vivo* patient samples. A substantial decrease in viability was determined in patient samples MM1 and MM4 at the lowest concentration of 0.625 µM VP79s whilst MM2 and MM6 were not as sensitive (Figure 5.13 A). This is in agreement with reports on heterogeneity in newly diagnosed MM patients [492]. VP79s caused a dose-dependent reduction in when normalised to the vehicle (Figure 5.13 B). This reduction in viability was statistically significant at 5 µM. This suggests that VP79s can significantly reduce the viability of MM cells at a concentration which has no effect on healthy PBMCs.

In this present study, VP79s demonstrated the ability to overcome BMM induced resistance in NCI-H929 cells (Figure 5.6). Therefore, one *ex vivo* MM patient sample was co-cultured with HS5 cells to assess the ability of VP79s to overcome HS5 induced drug resistance. In vehicle treated cells, co-culture with the HS5 cells enhanced the percentage of viable cells from 51.9% to 67.6% thus validating the assay. At 2.5 µM VP79s did not enhance cell death in monocultured cells, however, in co-culture VP79s induced a 10%

increase in cell death relative to the vehicle. At 5 µM VP79s induced a 30% increase in cell death in monoculture and a 20% increase in co-culture relative to the vehicle (Appendix Figure 6).

These data suggest that VP79s can reduce the viability of *ex vivo* MM patient samples, warranting further investigation into the translational capacity of VP79s.

Patient characteristics		
Patient:	**Sex**	**Age**
MM 1	Male	63
MM 2	Female	80
MM 4	Male	55
MM 5	Female	83
MM 6	Male	69

Table 5. 2 Multiple myeloma patient characteristics.

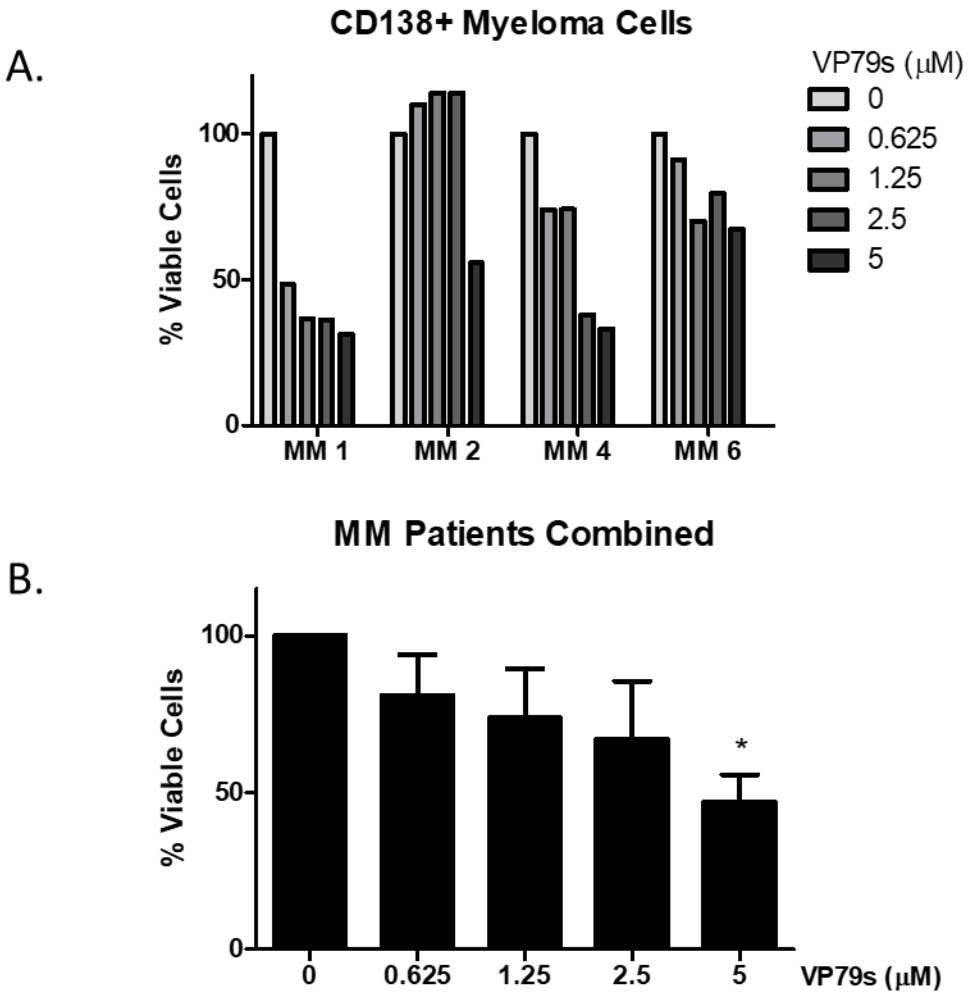

Figure 5. 13 VP79s induces cell death in a dose-responsive manner in ex vivo MM patient samples.

Ex vivo MM patient samples were seeded at 5x10^4 cells/well in round bottom 96 well plates and left to rest for 1 hour. Cells were then treated with either vehicle [0.25% EtOH (v/v)] or VP79s (0.625 – 5 μM) for 24 hours. After incubation, cells were collected, stained with annexin V/PI and analysed by flow cytometry using the BD FACSCanto™ II flow cytometer. 10,000 single cells were gated on vehicle treated cells excluding debris and doublets. ***A.*** *Relative cell viability following treatment with VP79s in individual ex vivo patient samples.* ***B.*** *Bars represent the mean and S.E.M. of four MM patient samples. Statistical analysis was performed using one-way ANOVA with Dunnett's post hoc test. *p<0.05.*

5.3. Discussion

Despite the advancements in the treatment and therapies available, MM is still incurable. Currently MM is managed by doublet and triplet combination therapies including corticosteroids, proteasome inhibitors, monoclonal antibodies and immunomodulators based upon the patient's risk group [493]. Combination treatments within the risk groups then vary based upon their eligibility for stem cell transplantation [105, 494]. Generally, transplant eligible patients undergo four rounds of an induction treatment of a doublet or triplet combination prior to transplantation. Ineligible patients usually undergo eight to twelve rounds of combination therapies such as lenalidomide and dexamethasone (Rd), bortezomib, lenalidomide and dexamethasone (VRD) or cyclophosphamide, bortezomib and dexamethasone (CyBorD) or more recently CyBorD with the addition of the monoclonal antibody daratumumab (CyBorD-DARA) [493, 495]. Whilst these front-line therapies usually result in remission, it is not permanent. Remission can last from months to years, however, patients invariably relapse necessitating the need for novel drugs and combination therapies to combat the malignancy. As previously discussed in detail, the heterogeneous nature of MM makes a treatment with a single drug unlikely and as such, targeting the JAK/STAT3 pathway in MM may be of therapeutic benefit in the treatment of MM. Previous reports in the literature have shown that MM relies heavily on the BMM and IL-6 for survival and drug resistance [43, 352]. Moreover, JAK2 upregulation due to the BMM has been shown to be present in approximately 57% of MM patients, making inhibition of the pathway a possible treatment strategy [76].

In chapter 4, VP79s was shown to inhibit the JAK2/STAT3 signalling pathway and thus downregulate the downstream anti-apoptotic Bcl-2 family member Mcl-1. The JAK/STAT3 signalling pathway has previously been implicated in the survival and proliferation of MM cells through upregulation of pro-survival proteins such as the anti-apoptotic Bcl-2 family members, cell cycle proteins, MMPs and IAPs [343]. As such, activation of JAK/STAT pathway has been associated with the development of drug resistance to chemotherapeutics such as cisplatin and paclitaxel as inhibition of the pathway abrogated cell death [496, 497].

The introduction of bortezomib into the MM treatment arsenal has greatly improved the overall survival rates of patients. Despite this, bortezomib resistance is a frequent problem in the clinic. The exact mechanisms of bortezomib resistance are unknown and likely to be caused by a variety of factors varying from patient to patient. However, the BMM and Mcl-1 have both been shown to play a role in proteasome inhibitor drug resistance in MM [498-500]. Moreover, inhibition of the proteasome by bortezomib led to an upregulation of Mcl-1 in pre-clinical models of cancer including MM [500]. Voorhees *et al.* have demonstrated that inhibition of IL-6 signalling by the mAb CNTO 328 enhances the activity of bortezomib in MM [501]. Therefore, in this present study, the effect of VP79s and bortezomib in combination was examined in U266B1 cells. VP79s was shown to enhance bortezomib induced cell death at the concentration of 7μM:nM following analysis with the compusyn programme. Similar effects were observed in a study by Zhang *et al.* who demonstrated that Mcl-1 downregulation with small interfering ribonucleic acid (siRNA) sensitised glioma cells to bortezomib [502]. Moreover, the anti-MM activity of AZD5991, a selective Mcl-1 inhibitor was enhanced when in combination with bortezomib in a xenograft MM mouse model [503]. Numerous studies have demonstrated that a JAK/STAT inhibitor in combination with bortezomib results in enhancement in cell death [504-506]. Oliveira *et al.* have also demonstrated that the JAK inhibitor ruxolitinib synergises with bortezomib to induce apoptosis in MM cell lines proposing a similar rationale to the present study [76]. Similarly, another study has shown that farnesol, a STAT3 inhibitor, synergises with bortezomib in a MM xenograft to reduce tumour volume [507], whilst arctiin and icariin, pharmacological inhibitors of STAT3 phosphorylation on tyrosine 705 were shown to potentiate the effects of bortezomib in U266B1 cells [508, 509]. These collective data support the findings described in this present study demonstrating that VP79s and bortezomib enhance cell death in U266B1 cells.

Accumulating evidence from chapter 4 and the present chapter have indicated that VP79s may be able to overcome BMM-induced drug resistance. As previously discussed, MM cells rely heavily on the BMM and in particular BMSCs in order to survive and proliferate [43]. The BMM creates an environment which protects MM cells from both drug-induced and immunological cell death. Herein, VP79s was shown to overcome both soluble and

adhesion mediated drug resistance when in co-culture with the stromal cell line HS5. Previous reports in the literature have shown that HS5 cells can induce drug resistance to bortezomib in MM cells which was confirmed in this study and used as a positive control to validate the assay [37]. Natan-Barr *et al*. have shown that co-culture of MM cells with BMSCs led to the upregulation of the oncoprotein MUC-1 which protects MM cells from cytotoxic damage [37]. MUC1 has been shown to be involved in tumourigenesis, resistance to apoptosis and invasion in MM cells as well as in other malignancies [510-512]. The same study also illustrated that MUC-1 is upregulated via the JAK/STAT3 signalling pathway by BMSC derived IL-6. Therefore, it could be suggested that VP79s may be able to overcome the resistance induced by BMSC through its ability to inhibit the JAK/STAT3 pathway. However, further studies examining MUC-1 expression would be required to confirm this. Interestingly, a peptide inhibitor of the MUC-1 C-terminal, GO-203, was shown to synergise with bortezomib to enhance cell death in MM cells supporting the combination study carried out in this chapter [513]. As mentioned before, DCZ3301, a aryl-guanidinio compound which inhibits JAK2 and STAT3, was also shown to overcome BMSC resistance in MM cells supporting the findings in this study [422]. Similarly, novel JAK inhibitors such as AZD1480 and INCB16562 have also been shown to overcome BMSC-induced drug resistance in MM cells [78, 352]. As VP79s was shown to induce apoptosis in the presence of IL-6 (Chapter 4) and BMSCs, the ability of VP79s to induce apoptosis in an *ex vivo* MM patient sample in co-culture with HS5 cells was examined in a preliminary experiment. HS5 cells produce a multitude of pro-survival cytokines and growth factors and also mediate resistance through MM-BMSC cell adhesion [514]. In the present study, HS5 cells were shown to offer a supportive environment for *ex vivo* MM cells as they enhanced the viability of MM cells by 15.7%. The supportive effects of HS5 cells in MM cell lines were not as observable as cell lines are highly proliferative and have very limited basal levels of spontaneous apoptosis unlike the *ex vivo* MM samples. Herein, VP79s was shown to induce apoptosis even in the presence of HS5 cells. As this experiment was only carried out in one patient sample no firm conclusions can be drawn; however, it does support the previous cell line findings in this study. In agreement with the results presented herein, there have been many reports that JAK/STAT3 pathway inhibitors induce apoptosis in *ex*

vivo MM samples [248, 352, 395, 515]. A study by Burger *et al*., demonstrated that the JAK inhibitor INCB20 could reduce the viability of *ex vivo* MM patient samples both alone and in the presence of BMSCs [516]. Another JAK1/2 inhibitor, INCB16562, induced apoptosis in *ex vivo* samples cultured with IL-6 [352]. These collective data support the evidence in this study that VP79s induces apoptosis in MM patient samples and NCI-H929 cells even in the presence of BMSCs

Having shown that VP79s induces cell death in MM cell lines and enhances cell death induced by the commonly used MM therapeutic bortezomib, the cytotoxic effects of VP79s in PBMCs isolated from healthy donors was next examined. VP79s was found to induce some cell death in PBMCs but only at the highest concentration tested of 10 µM. VP79s did not induce selective cell death against T cells, B cells or NK cells with significant cell death being observed only at 10 µM in all cell types. Collectively this suggests that VP79s exhibits greater selectivity for MM cells compared to healthy donor cells. However, off-target toxicity is still an issue with other standard and emerging treatments as toxicities are a common side effect associated with chemotherapeutics such as cisplatin and gemcitabine [517]. Historically, the dose and duration of therapeutics used for the treatment of MM depends greatly on adverse reactions such as peripheral neuropathy and myelosuppression [308]. Mcl-1 has been shown to be important for the survival of immune cells such as B and T cells and since VP79s has been shown to downregulate Mcl-1 such cytotoxicity may be unavoidable [490]. However, a 2016 study by Servier *et al*. has shown that Mcl-1 inhibition is tolerable in cancer models including *in vivo* mouse models despite inducing cell death in PBMCs from healthy donors [518]. Further examination in *in vivo* models is required to assess the true of toxicity of VP79s. Molecular optimisation of VP79s is also required to reduce off-target cytotoxic effects.

STAT3 activation has been shown to play an integral role in MM as previous reports have shown that CD138+ MM cells possess constitutively active STAT3 signalling which is not present in healthy controls [519]. Given the promising results on PBMCs, the effects of VP79s in *ex vivo* MM patient samples were next examined. Having previously established that VP79s elicits no cytotoxicity at 5 µM in PBMCs, the effects of VP79s on CD138+ MM cells up to 5 µM were examined. VP79s was shown to reduce the viability of four

treatment naïve *ex vivo* patient samples in a dose-responsive manner with a significant reduction observed at the 5 µM treatment when the results were combined. Three of the four MM samples responded to VP79s in a dose-responsive manner; however, MM2 showed no reduction in viability until the 5 µM treatment. This may be due to the heterogeneous nature of MM cells and patient to patient variability [285]. Previous studies have established that clonal heterogeneity is present at all stages of MM. For example, a 2014 study by Walker *et al*. has shown that intraclonal heterogeneity is present at all stages of MM, even the preceding stages of MGUS and SMM. The same study also demonstrated that there are an average of 23 non-synonymous mutations present in symptomatic MM patients [520]. Similarly, another study by Lohr *et al*. demonstrated that MM patients display around 5 subclones; therefore, targeted therapies affecting one subclone could have a limited therapeutic effect on the malignancy [281]. Therefore, the heterogeneous nature of MM would likely account for variations in the efficacy of VP79s between patient samples. These results indicate that VP79s may be a potential anti-MM therapeutic; however, given the limited number of samples examined in this study no firm conclusions can be drawn.

In conclusion, this study has demonstrated that VP79s may be a promising therapeutic for the treatment of MM. Additionally, it has been shown that VP79s can enhance bortezomib induced cell death, a standard MM treatment and overcome BMM-mediated drug resistance, possibly via inhibition of the JAK/STAT3 signalling pathway. VP79s was also shown to reduce the viability of *ex vivo* MM patient samples in a dose-responsive manner at concentrations that had no significant cytotoxic effect on PBMCs, T, B and NK cells from healthy donors. These data warrant further investigations into the anti-myeloma activity of VP79s.

Chapter 6:
General Discussion

Multiple myeloma (MM) is the second most common haematological malignancy and accounts for around 250-350 cancer diagnoses in Ireland each year [521]. In 2016, the global incidence of MM was 138,509 cases demonstrating a 126% increase since 1990. Generally, MM is a malignancy of the elderly with the median age for onset around 70-75 years. The highest incidences in MM are observed in western societies such as Australia, the United States of America and Western Europe [283]. There are no known unifying genetic or lifestyle factors which lead to development of MM but it is most likely due to the culmination of various factors including diet, obesity, exposure to toxins and stress throughout an individual's lifetime [522]. Recently, genome-wide association studies have identified common risk alleles at 24 independent loci [523] and a germline mutation in lysine-specific demethylase 1 which may predispose individuals to MM [524], however, to date, no definitive genetic risk factors have been identified. The surge in the incidence is more likely a result of increasing elderly populations and the availability of proper nutrition and modern drugs extending overall life expectancy. Therefore, the global incidence of MM is likely to increase whilst deaths due to MM are also expected to rise.

MM is still an incurable malignancy; however, it is treatable. MM therapy has advanced significantly over the past two decades with the introduction of novel therapeutics, namely proteasome inhibitors and immunomodulatory agents, which has led to durable treatment responses and an increase in progression free survival. Despite this, patients frequently experience multiple relapses and become refractory to treatment. Therefore, novel drugs and therapeutics are required to combat this unremitting malignancy. One of the biggest challenges impeding successful control of MM is the marked sub-clonal heterogeneity observed among patients. Whole exome sequencing of MM patients identified patients presenting with a median of 60 exonic mutations however, some individuals presented with up to 500 [525]. The most frequently mutated genes in MM include *TP53*, *NRAS*, *KRAS*, *BRAF* and *MYC.* However, there is growing evidence that suggests patients with *STAT3* mutations show significantly shortened progression free survival and overall survival using the Kaplan-Meier survival estimation when compared to patients with *NRAS*, *KRAS* and *TP53* mutations. In fact, these frequent mutations had no significant impact on survival [407]. It should be noted that of the 142 newly diagnosed patients screened only

3.5% of patients presented with *STAT3* mutations whereas other studies examining phosphorylated STAT3 in cell lines and patient samples have demonstrated active STAT3 at frequencies between 11 and 48% [519, 526-528]. Jung *et al.* has established that approximately 10% of MM patients in a cohort of 94 expressed STAT3 tyrosine phosphorylation and that those patients displayed inferior responses compared to phospho-STAT3 negative patients with significantly lower progression free survival and overall survival rates. Moreover, those with "strong" STAT3 staining displayed even worse outcomes [527]. The JAK/STAT signalling pathway has been shown to be upregulated in many other malignancies including breast, pancreatic, gastric and glioma cancers and, for the most part, STAT3 activation is a poor prognostic factor [529-533]. These collective data suggest that STAT3 phosphorylation negatively impacts patient overall survival and may be a possible therapeutic target.

Given the relatively low percentage of patients which display *STAT3* mutations compared to those who present with active STAT3, it could be speculated that STAT3 is activated through other endogenous or exogenous sources. Like *STAT3*, mutations in *JAK2* are frequently absent in MM [74, 75], therefore, constitutively active STAT3 phosphorylation is thought to be driven by other factors such as autocrine or paracrine IL-6 production from interactions with the bone marrow microenvironment (BMM). In normal cells, STAT3 phosphorylation is transient and tightly regulated by inhibitory proteins such as protein inhibitor of activated STATs (PIAS) and suppressor of cytokine signal transduction (SOCS) as well as the phosphatases (SHP-1 and SHP-2) which act to negatively regulate activation of the pathway [534]. Some MM cells may produce autocrine IL-6 due to perturbations in these regulatory proteins, for example, one study has demonstrated that these proteins are repressed in MM and this repression sustains the activation of the JAK/STAT3 pathway through autocrine IL-6 production [535]. It is widely accepted that the BMM supports MM cell growth and survival via activation of signalling pathways such as the PI3K/AKT, RAS/RAF/MEK/ERK and JAK/STAT3 signalling pathways. Bone marrow stromal cells (BMSCs) are particularly important and have also been implicated in the secretion of pro-survival factors into the BMM thus supporting MM cell survival and proliferation [35].

Given this accumulating evidence, numerous studies targeting the JAK/STAT3 signalling pathway are now underway not only in MM but other malignancies where STAT3 has been shown to play a detrimental role. For example, TTI-101 is a binaphthol-sulfonamide-based inhibitor of STAT3 whose efficacy is currently being examined in a phase 1 trial in advanced cancers (NCT03195699). JAK inhibitors such as ruxolitinib and WP1066 are also being examined alone or in combination for the treatment of breast cancer (NCT01594216), non-Hodgkin's lymphoma (NCT02164500), glioma and metastatic melanoma in the brain (NCT01904123).

The current project sought to assess the anti-myeloma activity of a series of novel guanidinium-based compounds which were rationally designed to target BRAF. As previously mentioned, there is a dominant mutation cluster in RAS/BRAF associated genes and it was therefore hypothesised that the compounds would exert their activity via inhibition of this pathway [292]. In this study, for the first time, a novel guanidinium-based compound, VP79s, was shown to reduce the viability of a panel of drug-sensitive (NCI-H929 and MM1.S) and -resistant (U266B1 and MM1.R) MM cell lines with no significant differences in efficacy exhibited between cell lines. The MM cell lines were found to be particularly sensitive to VP79s when compared to standard and emerging therapeutic agents, where in all cases, at least one MM cell line exhibited some degree of resistance in line with previous reports in the literature. The JAK 1/2 inhibitor, ruxolitinib, and the Bcl-2 inhibitor, venetoclax, were selected as representative emerging pharmacological agents for the treatment of MM as pre-clinical studies of both drugs have successfully paved the way for further clinical investigations [218, 401]. Overall, the results with VP79s compared favourably in comparison with drugs which are already used to treat MM; however, it should be noted that these agents are mainly used in combination and rarely as a single therapy.

In addition, VP79s was shown to induce apoptotic cell death in a dose- and time-responsive manner in the same panel of MM cell lines. The intrinsic and extrinsic apoptotic pathways were found to be involved in VP79s induced cell death as indicated by cleavage of pro-caspases 3, 8 and 9.

In the second part of this study, having established that VP79s induced apoptotic cell death in MM cell lines, further studies into signalling pathways known to play a key role in MM were undertaken. VP79s was found to rapidly inhibit constitutively active and IL-6 induced STAT3 phosphorylation on tyrosine 705 but not serine 727. Constitutively active STAT3 phosphorylation on tyrosine 705 has been implicated in survival and drug resistance in MM and other cancers [49, 536]. As previously mentioned, aberrant STAT3 activation has been identified in 70% of haematological and solid tumours and this activation has been implicated in the development and progression of cancer. For example, inhibition of STAT3 has been found to overcome cisplatin resistance in cervical, ovarian and breast cancers [537-539]. Evidence also suggests that BMM derived IL-6 may be a major mediator of BMM-induced drug resistance [48, 540, 541]. Examination of upstream mediators of STAT3 activation established that VP79s treatment resulted in a possible downregulation of phosphorylated JAK2 but not phosphorylated JAK1 or SRC. Interestingly, JAK2 overexpression has been reported in 57% of MM patients in two independent studies and, as previously discussed, numerous JAK2 inhibitors have been shown to induce apoptosis both in *in vitro* and *in vivo* MM models supporting highlighting the importance of the potential modulating of JAK2 activity by VP79s [76, 77, 352, 422, 542-544]. Inhibition of STAT3 also resulted in a downregulation of the IL-6 receptors, CD126 and CD130. The mechanism of how VP79s resulted in the downregulation of these receptors was not investigated in this present study. Previous reports in the literature have demonstrated that CD130 can be controlled through multiple mechanisms including internalisation of the receptor and shedding. A likely mechanism of receptor downregulation is through control of its own transcription. When activated, CD130 results in the phosphorylation and dimerisation of STAT3, which in turn binds to the promoter of CD130 gene resulting in increased expression. Therefore, it could be speculated that inhibition of STAT3 may result in downregulation of expression [430]. However, further studies are required to determine the mechanism of downregulation. Interestingly, it has previously been reported that phosphorylation of CD130 on serine 782 can lead to its downregulation [545]. Radtke *et al.* has reported that p38 activation resulted in phosphorylation of CD130 which in turn resulted in its internalisation and degradation [546]. In the present study, VP79s was

shown to activate the mitogen activated protein kinases (MAPKs) including p38. It was demonstrated that inhibition of these pathways had no impact on cell death induced by VP79s, however, MAPK activation could possibly lead to downregulation of CD130 as a secondary mechanism warranting further investigation [547, 548]. Internalisation of the IL-6 receptor has been reported to occur rapidly, and since CD126 and CD130 surface expression significantly decreased from 60 minutes post treatment with VP79s, VP79s could result in internalisation of the receptors [549].

Inhibition of STAT3 signalling in the U266B1 cells resulted in downregulation of STAT3 responsive genes Mcl-1 and cyclin D1 at both the gene and protein level. Survivin, another downstream target of STAT3 was also shown to be downregulated. Abrogation of STAT3 signalling by numerous pharmacological inhibitors has been shown to result in downregulation of these proteins and is associated with the induction of apoptosis [100, 550, 551]. VP79s was also shown to downregulate Mcl-1 and cyclin D1 in the NCI-H929 cell line despite the absence of detectable phosphorylated STAT3 on tyrosine 705 by western blotting suggesting another possible mechanism for VP79s induced cell death in this cell line. This warrants investigation into other signalling pathways known to play a role in MM pathogenesis such as the notch and Wnt signalling pathways [552, 553].

The activation of the MAPKs p38, JNK and ERK was not found to play a significant role in VP79s induced cell death. However, the activation of these pathways was shown to correlate with the induction of reactive oxygen species (ROS). Previous reports in the literature have demonstrated that mitochondrial depolarisation can results in the induction of reactive oxygen species or vice versa [554]. The induction of ROS has also been shown to lead to the activation of MAPKs [473] and AKT [379]. Therefore, it could be speculated that activation of these pathways are a result of ROS-induced activation of the pathways and may potentiate the activity of VP79s. WP1066, a JAK2/STAT3 inhibitor, was shown to also result in the activation of phosphorylated ERK [394, 555]. Similarly, DCZ3301, a JAK2/STAT3 inhibitor was also shown to result in the activation ERK [422]. Previous reports in the literature have shown that direct inhibitors of BRAF, AKT and JAK2 can result in the paradoxical upregulation of detectable phosphorylation of that kinase despite inhibition of downstream kinases [556-558]. One study found that a selective

$BRAF^{V600E}$ kinase inhibitor, vemurafenib, resulted in activation of ERK signalling in BRAF wild type melanoma cells via stimulation of CRAF. Conversely, vemurafenib inhibited ERK phosphorylation in melanoma cells which possessed the $BRAF^{V600E}$ mutation [559]. Another study by Andros *et al*. found that type I JAK inhibitors which target the active conformation of the kinase led to enhanced activation of phosphorylation in cell lines with wild type JAK2, but they did not lead to enhanced activation in mutant JAK2. Of note, type II kinase inhibitors, which target the inactive conformation, did not result in JAK2 phosphorylation in wild type cells [558]. In the present study, treatment with VP79s was shown to lead to enhanced activation of ERK and AKT. Further studies are required to elucidate the true involvement of MAPK and AKT activation in VP79s induced cell death.

In the final part of this study, the translational potential of VP79s was examined. VP79s was found to enhance cell death induced by the proteasome inhibitor bortezomib in U266B1 cells. Reports in the literature have provided evidence that simultaneous inhibition of the JAK/STAT3 pathway and proteasome inhibition with bortezomib enhances cell death in MM and other cancers [505, 507, 508]. For example, arctiin, an inhibitor of STAT3 phosphorylation on tyrosine 705, was found to synergise with bortezomib in U266B1 cells to enhance cell death [508]. Since MM cells display marked heterogeneity, combination therapies are the most promising therapeutic option for patients with the disease.

VP79s was found to induce minimal cytotoxicity in normal PBMCs and lymphocytes at concentrations which were lethal to MM cell lines and patient derived MM cells indicating that VP79s may be a potential anti-MM therapeutic. The benefit of VP79s inhibiting STAT3 activation was further demonstrated as VP79s was able to overcome BMSC induced resistance in NCI-H929 cells unlike bortezomib, a standard treatment for MM [37]. These results indicate that VP79s may be able to induce cell death in the cytoprotective environment of the BMM as previous reports in the literature have shown that inhibition of the STAT3 pathway can overcome BMM resistance in MM and AML [76, 560, 561].

In order to predict the clinical potential of VP79s, the ability of VP79s to induce cell death in primary *ex vivo* MM patient samples was essential. VP79s was shown to reduce the viability of MM cells by 53% at concentrations which had no effect on normal PBMCs from

healthy donors. Moreover, VP79s was able to induce cell death in a MM patient sample in the presence of HS5 stromal cells. It should be noted that although a limited number of patient samples were examined in this study, these results are a clear indication of the anti-MM activity exhibited by VP79s. These favourable results warrant further investigation into VP79s as a potential anti-MM therapy. The therapeutic efficacy of VP79s should also be examined in other malignancies, such as colorectal and breast cancer, where STAT3 activation has been shown to be a contributing factor in disease progression and drug resistance [562, 563].

In conclusion, the results presented herein demonstrate that VP79s, a novel guanidinium-based compound, was capable of inducing apoptosis in a panel of drug-sensitive and drug-resistant MM cell lines. It also reduced the viability of *ex vivo* MM patient samples whilst inducing limited cytotoxicity in PBMCs from healthy donors. VP79s appeared to rapidly inhibit the STAT3 signalling pathway and thus, its downstream targets Mcl-1, cyclin D1 and surviving (Figure 6.1). Furthermore, VP79s was able to enhance cell death when in combination with bortezomib, a standard MM treatment and overcome BMSC-induced drug resistance. This study provides novel insights into understanding the underlying mechanism of the anti-MM activity of VP79s, warranting further studies into VP79s and the development of further analogues.

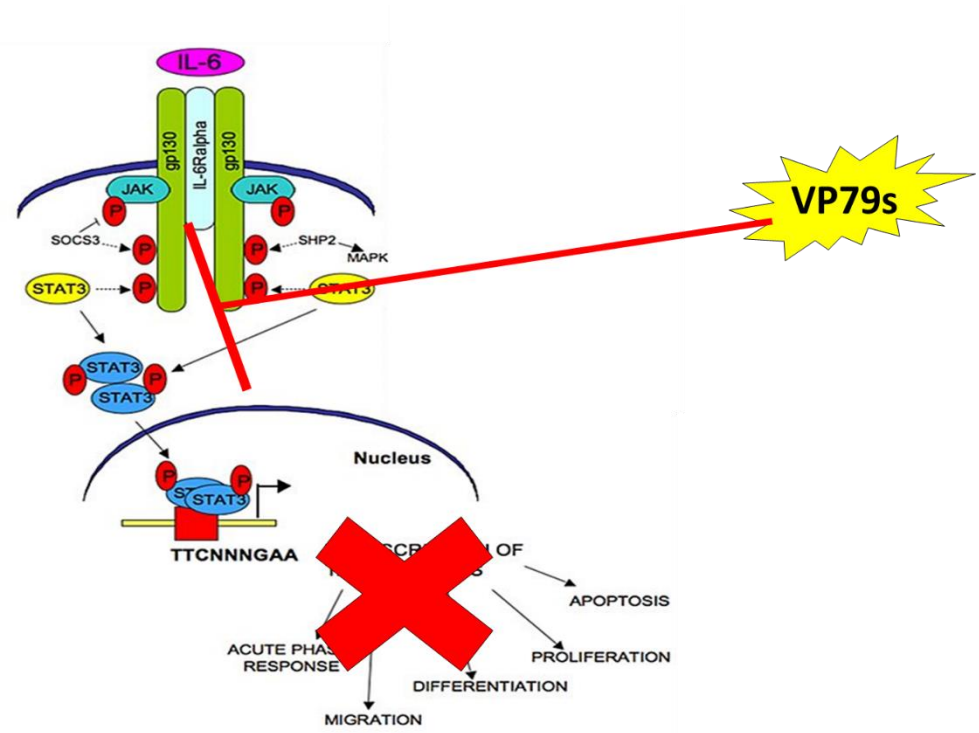

Figure 6. 1 Schematic of proposed mechanism of VP79s.

Image adapted from Camporeale et al., Frontiers in Bioscience, 2012 [70].

Chapter 7:
Future work

The present project has presented promising results demonstrating the potent anti-myeloma activity of VP79s in a panel of drug-sensitive and -resistant multiple myeloma (MM) cell lines at concentrations which were found to be sub-lethal in peripheral blood mononuclear cells (PBMCs) from healthy donors. VP79s was shown to inhibit the JAK/STAT3 signalling pathway in U266B1 cells and overcome IL-6 induced STAT3 signalling in NCI-H929 cells. Moreover, VP79s was shown to enhance bortezomib induced cell death and overcome bone morrow stromal cell-induced drug resistance. Therefore, in order to further progress this pre-clinical study, additional work is required to further elucidate the molecular mechanisms underlying VP79s induced cell death.

Given the body of data generated in this study, further optimisation of novel guanidinium-based compounds by the Rozas group could lead to the development of new drugs which elicit anti-myeloma activity at much lower concentrations with less toxicity to normal healthy cells. Herein, the cytotoxic effects of VP79s was examined in PBMCs. The effect of VP79s on other normal cell types should also be examined. In particular, osteoclasts and hepatocytes have been shown to express high levels of STAT3, therefore, it would be of interest to determine if VP79s elicits any cytotoxicity in these cell types [564, 565].

The data herein suggests that VP79s may elicit some of its anti-MM activity though targeting the kinase, JAK2. However, due to technical difficulties with western blotting of the phosphorylated form of JAK2 on tyrosine 1007/1008 no definitive conclusions could be drawn. Therefore, further experiments are required to confirm that VP79s is inhibiting JAK2 phosphorylation. As it can be quite difficult to detect phospho-proteins which are in low abundance [566], JAK2 and phosphorylated JAK2 could be co-immunoprecipitated or pulled down using a pull-down assay [567]. Sayyah *et al*. pulled down total JAK and then probed with antibodies against phospho-tyrosine and JAK2 phosphorylated on tyrosine 1007/1008 in BSC-40 cells [567]. The blots were then stripped and re-probed with total JAK2 to ensure equal loading. A similar experiment could be conducted on myeloma cells treated with VP79s. As previously discussed, VP79s was designed to target BRAF through an allosteric mechanism. Previous reports in the literature have demonstrated that JAK2 phosphorylation can actually be upregulated with kinase inhibitors [558, 568]. One study by Andraos *et al*. established that ATP competitive type I kinase inhibitors caused an

increase in JAK phosphorylation despite blocking downstream kinase function while, type II inhibitors, which bind to the inactive conformation led to a loss of phosphorylation [558]. This would indicate that VP79s may be inhibiting JAK2 phosphorylation through a type II or allosteric mechanism. However, further experimentation to confirm the mechanism of inhibition is required. Of note, it appears that the paradoxical increase in phosphorylation may only occur certain cell types as ruxolitinib, a type I kinase inhibitor, did not induce phosphorylation of JAK 1 or JAK 2 in the U266B1 cells. A kinase binding assay such as a LanthaScreen EU kinase assay could be used to measure the binding of VP79s to JAK2 and other kinases by monitoring the signal from a fluorescent tracer. Time Resolved-Fluorescence Resonance Energy Transfer (TR-FRET) assays such as a LanthaScreen, are less susceptible to compound interference than other assays. The assay requires a kinase protein (human recombinant), a fluorescent kinase tracer, and a europium (EU)-labelled antibody. The assay uses EU as a donor species and Alexa Fluor 647 as an acceptor species. When the donor and acceptor labelled molecules are in close proximity, energy transfer occurs resulting in an increase in acceptor fluorescence and a subsequent decrease in donor fluorescence. High FRET occurs when the tracer binds to the kinase. For example, the EU-labelled antibody binds to the kinase of interest, in this case JAK2, and if VP79s targets JAK2, the tracer is displaced. This results is FRET being reduced [569]. Kinases are available for both the inactive and active forms of the kinase making it possible to further elucidate if VP79s inhibits JAK2 in a type I or type II mechanism. A more expensive and complex method would involve x-ray crystallography in order to determine the binding mode of VP79s to both the active and inactive conformations of JAK2. Molecular modelling to determine how VP79s fits into JAK2 would also help to delineate how, and if, VP79s is inhibiting JAK2 phosphorylation. Previous JAK2 inhibitors have been identified using these virtual screening methods [570]. These experiments would provide further evidence that VP79s is targeting JAK2.

VP79s was found to activate AKT and mitogen-activated protein kinases (MAPKs) as evidenced by an increase in the phosphorylated forms of the proteins. Reports in the literature have shown that direct inhibitors of both AKT and BRAF can lead to paradoxical activation of those kinases [557, 571]. Further studies to determine if VP79s is an inhibitor

of these kinases or if the activation is due to other cellular processes should be undertaken to further enhance understanding of the anti-MM activity of VP79s. As with the JAK kinases; x-ray crystallography, molecular modelling and kinase assays could be undertaken to determine how VP79s is interacting with these kinases. As aforementioned, such kinase pathways may be activated through the generation of reactive oxygen species (ROS) as previous reports in the literature have shown that ROS can lead to the activation of AKT, ERK, JNK and p38 [473, 572]. In order to determine if ROS causes activation of these kinases, cells could be pre-treated with the ROS-scavenger, N-acetyl-L-cysteine (NAC) followed by VP79s. Samples could then be analysed by western blotting to assess the effect on the activated forms of the kinases.

The SRC kinases have been shown to play a critical role in the survival, proliferation, invasion and angiogenesis in cancer. In MM, SRC has been shown to play a role in bone destruction and hypercalcemia [257, 573]. SRC has been shown to lie upstream of STAT3 and therefore, the effect of VP79s on SRC and phosphorylated SRC was examined herein by western blotting. Phosphorylation of SRC on tyrosine 418 has been reported to be the main activating phosphorylation site on SRC [348]. The present study has shown that VP79s had no effect on phosphorylated SRC on tyrosine 418 but resulted in the formation of a band above total SRC approximately 5-10 kilodaltons (kDa) larger than total SRC. It is possible that the band could represent either a phosphorylated form or a ubiquitinated form of the protein. As previously discussed in chapter 4, reports in the literature have shown that whilst tyrosine 418 phosphorylation activates SRC, phosphorylation of a conserved tyrosine residue on tyrosine 529 results in the inactivation of SRC through a conformational change [413, 414]. Possibly, the antibody may also react with the phosphorylated form of SRC on tyrosine 529. In order to establish if the apparent band represents phosphorylation at tyrosine 529 western blotting could be carried out using an antibody specific for the phosphorylation on tyrosine 529. A study by Simekka *et al*. has shown that double phosphorylation of SRC in paediatric brain tumours led to an increase in SRC of approximately 15 kDa [574]. Similarly, another study has demonstrated that phosphorylation of Lck, a SRC family kinase, on serine 42 and 59 results in a shift of 7 kDa. Therefore, SRC may be phosphorylated at multiple sites resulting in the shift in the protein

warranting investigation into the possibility of phosphorylation [575]. Therefore, treatment of the sample with a phosphatase, such as calf intestinal alkaline phosphatase, to dephosphorylate SRC prior to immunoblotting would aid in determining whether the band shift is due to phosphorylation. It has previously been reported that active SRC can be ubiquitinated leading to its degradation [415, 416, 576]. To determine if SRC is ubiquitinated a number of experiments could be undertaken. Ubiquitination is the attachment of the polypeptide ubiquitin to a target protein via covalent bonds. The addition of ubiquitin to a protein is carried out by 3 enzymes: ubiquitin activating enzyme E1, ubiquitin conjugating enzyme E2, and ubiquitin ligase E3 [577]. Many proteins are post-translationally modified by monoubiqutination, multi-monoubiquination and polyubiquitination. Traditionally polyubiquitination has been demonstrated to lead to protein degradation, however, more recently it has been reported that several proteins can be targeted for degradation following monoubiquitination [578]. Monoubiquitination has been demonstrated to act as a signalling scaffold for non-proteolytic cellular functions such as histone modification, cytoskeleton arrangement, and budding of viruses [578]. Inhibitors of these enzymes are commercially available for example, PYR-41 is a well-established ubiquitin activating enzyme E1 inhibitor [579]. Cells could be pre-treated with the inhibitor prior to treatment with VP79s. Following incubation, treated cells could be analysed by western blotting for the appearance of the band above total SRC and cell death could be analysed by annexin V/PI staining. A possible limitation of this experiment could be the reported toxicity of PYR-41 to cells. Therefore, optimisation would be required along with controls for the detection of ubiquitin. The proteasome inhibitor MG-132 could also be used in a similar manner as PYR-41, as this should prevent SRC from being degraded if it is being targeted for degradation [415]. Another possible experiment would be to pull down SRC with a pull down assay and then probe with an antibody for ubiquitination. This would determine if treatment with VP79s results in ubiquitination of SRC. If SRC is being ubiquitinated, the type of ubiquitination being induced by VP79s could be determined by the pattern of ubiquitin as monoubiquitin appears as a single band, whilst polyubiquitin appears as a streak on the blot [580]. These collective experiments will

help to determine what type of post-translational modification occurs following treatment with VP79s.

Other signalling pathways known to play a role in MM pathogenesis should also be examined. The NCI-H929 cell line does not possess STAT3 phosphorylation on tyrosine 705, therefore it is unlikely that VP79s is eliciting cell death through this pathway. As well as the pathways examined in this study; the Wnt and notch signalling pathways have been shown to play a role in MM cell survival therefore, the effect of VP79s on these pathways should be examined [552, 581].

Another area of interest are the Pim kinases; a small family of kinases that are constitutively expressed in haematological malignancies and have been shown to play a role in drug resistance. In MM, Pim-2 has been shown to be required for maintaining MM cell growth [582]. Previously Pim-3 kinase has been shown to be positive regulator of STAT3 phosphorylation on tyrosine 705 in prostate cancer as selective Pim inhibitors resulted in inhibition of STAT3 [110]. Somewhat conversely, BMSCs have been shown to increase the expression of Pim-2 in MM cells via an IL-6-STAT3 mechanism and inhibition of STAT3 has been shown to result in a decrease in Pim-2 levels [583]. Therefore, Pim kinases may lie upstream or downstream of STAT3. Nevertheless, examination of the Pim kinases may be of benefit as a study by Paíno *et al.* demonstrated that all of the myeloma cell lines tested in their study expressed Pim-1, -2 and -3 and moreover, the pan-Pim kinase inhibitor, PIM447 induced apoptosis in all four cell lines [111]. Therefore, examination of the effect of VP79s on Pim kinases is warranted.

As VP79s is a completely novel compound, global gene expression profiling may be of benefit in examining early changes in gene expression in a panel of myeloma cell lines following treatment with VP79s. Differential gene expression using DESeq2 to analyse the gene expression profiles would identify statistical changes in gene expression. Combined analysis to determine overlap of down and upregulated genes across a panel of myeloma cell lines, could be used to indicate any common expression response to VP79s treatment. Heat maps of the top differentially expressed genes could then be generated and the top deregulated genes could be validated using real-time qPCR. Similarly, a commercially available protein profiler examining kinases could be employed to determine if any other

phosphorylation or dephosphorylation events occur post treatment with VP79s. Indeed, any significant differences obtained from the aforementioned assays should be examined by other means such as western blotting and qPCR to confirm these results.

The JAK/STAT3 signalling pathway has previously been implicated in the survival and proliferation of MM cells through upregulation of pro-survival proteins such as the anti-apoptotic Bcl-2 family members, cell cycle proteins, MMPs and IAPs [343]. As such, activation of JAK/STAT pathway has been associated with the development of drug resistance to chemotherapeutics such as cisplatin and paclitaxel as inhibition of the pathway abrogated cell death [496, 497]. Venetoclax is a specific oral inhibitor of Bcl-2 which has shown efficacy in CLL, AML and small lymphocytic lymphoma in recent years leading to FDA approval for these cancers. Since VP79s was shown herein to downregulate the Bcl-2 family member Mcl-1 and venetoclax specifically inhibits Bcl-2 it is hypothesised that dual inhibition of Mcl-1 and Bcl-2 would lead to enhanced cell death in the MM cell lines. Previous studies have demonstrated that combination treatment of Mcl-1 inhibition and venetoclax synergise to enhance cell death in acute myelogenous leukaemia, T-cell acute lymphoblastic leukaemia and neuroblastoma [584-586]. Moreover, venetoclax resistance has been shown to be mediated through stabilisation and upregulation of non-target Mcl-1 and Bcl-xL leading to drug resistance [587]. Whilst Mcl-1 is considered to be a critical survival protein in MM, there is a subset of MM patients where Bcl-2 inhibition could be highly effective. Reports in the literature have demonstrated that venetoclax is effective in MM cell lines and patients with the t(11;14) translocation; indeed, one trial (NCT01794520) demonstrated a 40% objective response rate with venetoclax monotherapy in patients with the translocation [219, 320]. Previously this translocation has been reported to present in patients with high Bcl-2 and low Mcl-1/Bcl-xL levels and also led to an increase in cyclin D1 expression [101, 588]. Studies by Puthier *et al.* have shown that IL-6 can upregulate Mcl-1 and Bcl-xL in MM and that upregulation of Mcl-1 by IL-6 is mediated through the JAK/STAT pathway rather than the RAS/MAPK pathway [50, 230]. Therefore, downregulation of Mcl-1 via inhibition of the JAK/STAT pathway with simultaneous inhibition of Bcl-2 may be a possible combination therapy which targets two subtypes of MM and is efficacious in the treatment of MM. Similarly, studies have also

demonstrated that Mcl-1 is upregulated by the bone marrow microenvironment (BMM) in MM and other haematological malignancies. Karjalainen *et al.* have shown that ruxolitinib can synergise with venetoclax to counteract BMSC induced protection in AML. The group found that in the presence of BMSCs or conditioned media, AML cells became resistant to many pharmacological inhibitors but became sensitive to JAK inhibitors such as ruxolitinib, highlighting the value of JAK inhibition in malignancies where the BMM offers cytoprotective effects [561].

As immunotherapy is a growing field in the treatment of MM and cancer, studies examining the efficacy of VP79s in combination with the anti-CD38 monoclonal antibody, daratumumab, should be undertaken. MM cells highly express CD38 and recent reports have demonstrated that daratumumab can mediate MM cell killing *in vivo* through diverse mechanisms including complement-dependent cytotoxicity (CDC), antibody-dependent cellular cytotoxicity (ADCC) and antibody-dependent cellular phagocytosis [589]. Daratumumab has also been shown to elicit some activity as a single agent through programmed cell death and modulation of enzymatic activity [188]. The JAK/STAT3 signalling pathway has been shown to regulate the expression of CD38 on MM cells. Induction of constitutively active STAT3 by transfection or co-culture with BMSC or IL-6, in MM cells resulted in downregulation of CD38. Interestingly, treatment with the JAK1/2 inhibitor ruxolitinib resulted in increased expression of CD38 [590]. Therefore, it could be suggested that inhibition of STAT3 by VP79s followed by treatment with daratumumab may enhance cell death. Previous reports have demonstrated that nanoparticles decorated with anti-CD38 monoclonal antibodies and loaded with a STAT3 inhibitor resulted in improved therapeutic efficacy in MM cell lines and a xenograft mouse model [591]. Any increase in cell death could be monitored by annexin V/PI staining. To monitor ADCC and CDC, VP79s treated MM cells could be stained with 5-6-carboxyfluorescein diacetate succinimidyl ester (CFSE), a cell permeable fluorescent dye [592]. The cells would be incubated with serial dilutions of daratumumab or isotype control antibodies. For assessment of ADCC, PBMCs from healthy donors would be added at an effector:target ratio of 50:1 and incubated together. For CDC, 10% normal human serum would be added,

and myeloma cell viability analysed by propidium iodide uptake. Combination indexes could then be calculated using the Chou-Talalay method as in Chapter 5.

Monoclonal immunoglobulin free light chains are produced by plasma cells and are present in serum and urine of 97% of patients with MM [593]. Kappa (κ) and lambda (λ) free light chain (FLC) assays measure total polyclonal and monoclonal FLC and the calculated κ/λ FLC ratio is a surrogate measure of clonality [594]. The ratio is considered a useful tool in measuring the response to treatment. Healthy individuals produce about 500 mg/day of FLCs with a κ/λ ratio of about 2/1, whilst an abnormal ratio is considered to be between 0.26-1.56 [593]. A decrease in the release of FLC from MM cells is considered to be key to a good therapeutic response. Levels of human immunoglobulin FLC, κ and λ, in culture supernatants from MM patient samples following treatment VP79s could be measured using a commercially available ELISA kit. This assay would provide a greater understanding of the translational capacity of VP79s.

In the present study, the anti-MM activity of VP79s was assessed in 5 treatment naïve *ex vivo* MM patient samples. While the results were promising, a much larger sample size is required to make any firm conclusions. As MM patients often experience multiple relapses and become refractory to treatment, testing the efficacy of VP79s in some of these patient samples would be useful in determining VP79s efficacy in drug resistant patients [595].

Another major avenue for future research is determining the translational efficacy of VP79s in an *in vivo MM* mouse model. This is an important step in the preclinical evaluation of novel therapeutics as it helps to understand any toxicities that VP79s may or may not have. It also helps to evaluate the efficacy of the compound when cancer cells are in the cytoprotective environment of the body. There are numerous myeloma murine models available including the spontaneous MM model, 5TMM, transgenic models, xenograft and severe combined immunodeficient (SCID) mice models [596]. Each of these models has their advantages and disadvantages which depend greatly on the research question being posed. For example, the 5TMM mouse model spontaneously develops a myeloma-like disease therefore, this model allows for the study of interactions between MM cells and the BMM. Unlike transgenic models, where a known oncogene drives the disease, the spontaneous 5T models have been shown to display a wide range of

mutations mimicking the human disease [597]. This model is useful for studying the effects of novel compounds in a cytoprotective environment; however, one major drawback is that the 5TMM model is a completely murine model. Xenograft models are therefore a possible alternative to overcoming the completely murine 5TMM. Xenograft models involve the engraftment of human MM cell lines subcutaneously or intravenously into SCID or non-obese diabetic/SCID mice. Subcutaneous injection of MM cells, usually into the flank, results in the formation of a visible tumour which is advantageous as it can be easily monitored following treatment. However, this model has major disadvantages. In order to allow for the formation of the tumour at the injection site, these mice are lacking T and B cells and have reduced NK cell function. As discussed, since the MM cells have such an intricate relationship with the BMM, the subcutaneous model lacks this interaction. Similarly, the lack of immune cells present in the mice will also have an impact on MM cell survival. Intravenous xenografts also have limitations as although they mimic the systemic aspect of MM and homing to the bone marrow is present in some cases, during the disease course, other mouse organs become host to the MM cells which is not present in the human version of the disease (Reviewed in [596]). Methods to overcome these limitations include the implantation of a foetal bone chip into the flank of the mouse followed by inoculation with an IL-6 dependent cell line. This model is known as SCID-Hu [598]. MM cells then nearly exclusively home to the bone fragment rather than the mouse BM, and the MM cells produce IL-6 mimicking the human malignancy. Moreover, the full extent of BM cells such as BMSCs, osteoclast and osteoblasts are present in the bone chip; therefore, bone destruction can be reproduced in this model. Access to foetal bone chips is limited and poses greater ethical questions than the exclusive use of mouse models, therefore, the SCID-Rab model was designed to overcome these issues whereby the foetal bone is replaced by a rabbit bone [599]. While this is an option, it still does not represent the human BMM. Therefore, in order to reproduce the human BMM within a mouse, synthetic scaffolds which resemble human bone can be loaded with human MM cells and other cells present in the BMM. These scaffolds can then be engrafted into the flank of the mouse creating a human BMM within the mouse [600]. A limiting aspect of the model is the lack of bone destruction due to the use of a synthetic bone, however, in terms of

testing the efficacy of a drug it is highly beneficial. Transgenic models such as the VK*MYC involves activation-induced cytidine deaminase (AID)-dependent overexpression of MYC in the B-cells of the mice [601]. VK*MYC mice develop an MM like disease with similar characteristics to human MM. This model is frequently used to study MM and to test drug efficacy, however a major limitation is that only one oncogene is overexpressed rather than multiple which is frequently seen in MM. These collective models show that no murine model is an ideal representation of the human malignancy; therefore, careful consideration must be taken when deciding which model is the most suitable for the experimental question.

In summary, this project shows promising pre-clinical efficacy for VP79s as an anti-MM agent. Further examination of the effect of VP79s on key signalling pathways known to play a role in MM pathogenesis should be carried out as well as studies into the translational capacity of VP79s by examining its ability to synergise with other therapeutics to combat the malignancy. The efficacy of VP79s in a MM mouse model should also be carried out to assess any unwanted cytotoxicity and the ability of VP79s to induce cell death in the presence of a cytoprotective environment. Further examination of VP79s in *ex vivo* MM patient samples that represent the wider MM community are also required to garner further evidence of the anti-myeloma activity of VP79s.

References:

1. Udd, K.A., T.M. Spektor, and J.R. Berenson, *Monitoring multiple myeloma.* Clin Adv Hematol Oncol, 2017. **15**(12): p. 951-961.
2. Moreau, P., et al., *Multiple myeloma: ESMO Clinical Practice Guidelines for diagnosis, treatment and follow-up.* Ann Oncol, 2017. **28**(suppl_4): p. iv52-iv61.
3. Kyle, R.A., et al., *A long-term study of prognosis in monoclonal gammopathy of undetermined significance.* N Engl J Med, 2002. **346**(8): p. 564-9.
4. Group, I.M.W., *Criteria for the classification of monoclonal gammopathies, multiple myeloma and related disorders: a report of the International Myeloma Working Group.* Br J Haematol, 2003. **121**(5): p. 749-57.
5. Solly, S., *Remarks on the pathology of mollities ossium; with cases.* Med Chir Trans, 1844. **27**: p. 435-498 8.
6. McDevitt, J. and P. Walsh, *Cancer in Ireland 1994-2015 with estimates for 2015-2017: Annual Report of the National Cancer Registry*. 2017, National Cancer Registry Ireland National Cancer Registry Ireland.
7. Wildes, T.M., A. Rosko, and S.A. Tuchman, *Multiple myeloma in the older adult: better prospects, more challenges.* J Clin Oncol, 2014. **32**(24): p. 2531-40.
8. Zingone, A. and W.M. Kuehl, *Pathogenesis of monoclonal gammopathy of undetermined significance and progression to multiple myeloma.* Semin Hematol, 2011. **48**(1): p. 4-12.
9. Rajkumar, S.V., *Updated Diagnostic Criteria and Staging System for Multiple Myeloma.* Am Soc Clin Oncol Educ Book, 2016. **35**: p. e418-23.
10. Kyle, R.A., *Monoclonal gammopathy of undetermined significance. Natural history in 241 cases.* Am J Med, 1978. **64**(5): p. 814-26.
11. Kyle, R.A. and S.V. Rajkumar, *Monoclonal Gammopathy of Undetermined Significance and Multiple Myeloma.* JAMA Oncol, 2015. **1**(2): p. 174-5.
12. Landgren, O., et al., *Monoclonal gammopathy of undetermined significance (MGUS) consistently precedes multiple myeloma: a prospective study.* Blood, 2009. **113**(22): p. 5412-7.
13. Korde, N., S.Y. Kristinsson, and O. Landgren, *Monoclonal gammopathy of undetermined significance (MGUS) and smoldering multiple myeloma (SMM): novel biological insights and development of early treatment strategies.* Blood, 2011. **117**(21): p. 5573-81.
14. Rajkumar, S.V., O. Landgren, and M.V. Mateos, *Smoldering multiple myeloma.* Blood, 2015. **125**(20): p. 3069-75.
15. Sundararajan, S., et al., *Smoldering Multiple Myeloma: Emerging Concepts and Therapeutics.* Curr Hematol Malig Rep, 2016. **11**(2): p. 102-10.
16. Riccardi, A., et al., *Treatment of multiple myeloma according to the extension of the disease: a prospective, randomised study comparing a less with a more aggressive cystostatic policy. Cooperative Group of Study and Treatment of Multiple Myeloma.* Br J Cancer, 1994. **70**(6): p. 1203-10.
17. Dispenzieri, A., et al., *Smoldering multiple myeloma requiring treatment: time for a new definition?* Blood, 2013. **122**(26): p. 4172-81.
18. Palumbo, A., et al., *Revised International Staging System for Multiple Myeloma: A Report From International Myeloma Working Group.* J Clin Oncol, 2015. **33**(26): p. 2863-9.
19. Tandon, N., et al., *Clinical utility of the Revised International Staging System in unselected patients with newly diagnosed and relapsed multiple myeloma.* Blood Cancer J, 2017. **7**(2): p. e528.
20. Teke, H., et al., *Serum Level of Lactate Dehydrogenase is a Useful Clinical Marker to Monitor Progressive Multiple Myeloma Diseases: A Case Report.* Turk J Haematol, 2014. **31**(1): p. 84-7.

21. Fernández de Larrea, C., et al., *Plasma cell leukemia: consensus statement on diagnostic requirements, response criteria and treatment recommendations by the International Myeloma Working Group.* Leukemia, 2013. **27**(4): p. 780-91.
22. Kumar, S.K., et al., *Multiple myeloma.* Nat Rev Dis Primers, 2017. **3**: p. 17046.
23. Hoyer, J.D., et al., *The (11;14)(q13;q32) translocation in multiple myeloma. A morphologic and immunohistochemical study.* Am J Clin Pathol, 2000. **113**(6): p. 831-7.
24. Morgan, G.J., B.A. Walker, and F.E. Davies, *The genetic architecture of multiple myeloma.* Nat Rev Cancer, 2012. **12**(5): p. 335-48.
25. Athanasiou, E., et al., *Cyclin D1 overexpression in multiple myeloma. A morphologic, immunohistochemical, and in situ hybridization study of 71 paraffin-embedded bone marrow biopsy specimens.* Am J Clin Pathol, 2001. **116**(4): p. 535-42.
26. Epstein, J., H.Q. Xiao, and X.Y. He, *Markers of multiple hematopoietic-cell lineages in multiple myeloma.* N Engl J Med, 1990. **322**(10): p. 664-8.
27. Rajkumar, S.V., *Multiple myeloma: 2016 update on diagnosis, risk-stratification, and management.* Am J Hematol, 2016. **91**(7): p. 719-34.
28. Kawano, Y., et al., *Targeting the bone marrow microenvironment in multiple myeloma.* Immunol Rev, 2015. **263**(1): p. 160-72.
29. Gupta, V.A., et al., *Bone marrow microenvironment-derived signals induce Mcl-1 dependence in multiple myeloma.* Blood, 2017. **129**(14): p. 1969-1979.
30. Merico, F., et al., *Cytokines involved in the progression of multiple myeloma.* Clin Exp Immunol, 1993. **92**(1): p. 27-31.
31. Fairfield, H., et al., *Multiple myeloma in the marrow: pathogenesis and treatments.* Ann N Y Acad Sci, 2016. **1364**: p. 32-51.
32. Wang, J., et al., *Bone marrow stromal cell-derived exosomes as communicators in drug resistance in multiple myeloma cells.* Blood, 2014. **124**(4): p. 555-66.
33. Markovina, S., et al., *Bone marrow stromal cells from multiple myeloma patients uniquely induce bortezomib resistant NF-kappaB activity in myeloma cells.* Mol Cancer, 2010. **9**: p. 176.
34. Wang, X., et al., *Myeloma cell adhesion to bone marrow stromal cells confers drug resistance by microRNA-21 up-regulation.* Leuk Lymphoma, 2011. **52**(10): p. 1991-8.
35. Chauhan, D., et al., *Multiple myeloma cell adhesion-induced interleukin-6 expression in bone marrow stromal cells involves activation of NF-kappa B.* Blood, 1996. **87**(3): p. 1104-12.
36. Di Marzo, L., et al., *Microenvironment drug resistance in multiple myeloma: emerging new players.* Oncotarget, 2016. **7**(37): p. 60698-60711.
37. Bar-Natan, M., et al., *Bone marrow stroma protects myeloma cells from cytotoxic damage via induction of the oncoprotein MUC1.* Br J Haematol, 2017. **176**(6): p. 929-938.
38. Gupta, D., et al., *Adherence of multiple myeloma cells to bone marrow stromal cells upregulates vascular endothelial growth factor secretion: therapeutic applications.* Leukemia, 2001. **15**(12): p. 1950-61.
39. Berenstein, R., et al., *Multiple myeloma cells modify VEGF/IL-6 levels and osteogenic potential of bone marrow stromal cells via Notch/miR-223.* Mol Carcinog, 2016. **55**(12): p. 1927-1939.
40. Fuhler, G.M., et al., *Bone marrow stromal cell interaction reduces syndecan-1 expression and induces kinomic changes in myeloma cells.* Exp Cell Res, 2010. **316**(11): p. 1816-28.
41. Tanaka, Y., et al., *Myeloma cell-osteoclast interaction enhances angiogenesis together with bone resorption: a role for vascular endothelial cell growth factor and osteopontin.* Clin Cancer Res, 2007. **13**(3): p. 816-23.

42. Karadag, A., et al., *Human myeloma cells promote the production of interleukin 6 by primary human osteoblasts.* Br J Haematol, 2000. **108**(2): p. 383-90.
43. Manier, S., et al., *Bone marrow microenvironment in multiple myeloma progression.* J Biomed Biotechnol, 2012. **2012**: p. 157496.
44. Musolino, C., et al., *Inflammatory and Anti-Inflammatory Equilibrium, Proliferative and Antiproliferative Balance: The Role of Cytokines in Multiple Myeloma.* Mediators Inflamm, 2017. **2017**: p. 1852517.
45. Tanaka, T., M. Narazaki, and T. Kishimoto, *IL-6 in inflammation, immunity, and disease.* Cold Spring Harb Perspect Biol, 2014. **6**(10): p. a016295.
46. Ludwig, H., et al., *Interleukin-6 is a prognostic factor in multiple myeloma.* Blood, 1991. **77**(12): p. 2794-5.
47. Frassanito, M.A., et al., *Autocrine interleukin-6 production and highly malignant multiple myeloma: relation with resistance to drug-induced apoptosis.* Blood, 2001. **97**(2): p. 483-9.
48. Matthes, T., B. Manfroi, and B. Huard, *Revisiting IL-6 antagonism in multiple myeloma.* Crit Rev Oncol Hematol, 2016. **105**: p. 1-4.
49. Catlett-Falcone, R., et al., *Constitutive activation of Stat3 signaling confers resistance to apoptosis in human U266 myeloma cells.* Immunity, 1999. **10**(1): p. 105-15.
50. Puthier, D., et al., *Mcl-1 and Bcl-xL are co-regulated by IL-6 in human myeloma cells.* Br J Haematol, 1999. **107**(2): p. 392-5.
51. Hideshima, T., et al., *Biologic sequelae of interleukin-6 induced PI3-K/Akt signaling in multiple myeloma.* Oncogene, 2001. **20**(42): p. 5991-6000.
52. Mahtouk, K., et al., *Growth factors in multiple myeloma: a comprehensive analysis of their expression in tumor cells and bone marrow environment using Affymetrix microarrays.* BMC Cancer, 2010. **10**: p. 198.
53. Weroha, S.J. and P. Haluska, *The insulin-like growth factor system in cancer.* Endocrinol Metab Clin North Am, 2012. **41**(2): p. 335-50, vi.
54. Nishida, N., et al., *Angiogenesis in cancer.* Vasc Health Risk Manag, 2006. **2**(3): p. 213-9.
55. Podar, K. and K.C. Anderson, *The pathophysiologic role of VEGF in hematologic malignancies: therapeutic implications.* Blood, 2005. **105**(4): p. 1383-95.
56. Kumar, S., et al., *Expression of VEGF and its receptors by myeloma cells.* Leukemia, 2003. **17**(10): p. 2025-31.
57. Le Gouill, S., et al., *VEGF induces Mcl-1 up-regulation and protects multiple myeloma cells against apoptosis.* Blood, 2004. **104**(9): p. 2886-92.
58. Lentzsch, S., et al., *PI3-K/AKT/FKHR and MAPK signaling cascades are redundantly stimulated by a variety of cytokines and contribute independently to proliferation and survival of multiple myeloma cells.* Leukemia, 2004. **18**(11): p. 1883-90.
59. Hideshima, T. and K.C. Anderson, *Molecular mechanisms of novel therapeutic approaches for multiple myeloma.* Nat Rev Cancer, 2002. **2**(12): p. 927-37.
60. Harmer, D., C. Falank, and M.R. Reagan, *Interleukin-6 Interweaves the Bone Marrow Microenvironment, Bone Loss, and Multiple Myeloma.* Front Endocrinol (Lausanne), 2018. **9**: p. 788.
61. Tefferi, A. and D.L. Longo, *Chapter 135, Less Common Hematological Malignancies*, in *Harrison's Principles of Internal Medicine, 19th Edition*, D.L. Casper, Editor. 2015.
62. Ramakrishnan, V. and A. D'Souza, *Signaling Pathways and Emerging Therapies in Multiple Myeloma.* Curr Hematol Malig Rep, 2016. **11**(2): p. 156-64.
63. Yu, H. and R. Jove, *The STATs of cancer--new molecular targets come of age.* Nat Rev Cancer, 2004. **4**(2): p. 97-105.

64. Wolf, J., S. Rose-John, and C. Garbers, *Interleukin-6 and its receptors: a highly regulated and dynamic system.* Cytokine, 2014. **70**(1): p. 11-20.
65. Heinrich, P.C., et al., *Interleukin-6-type cytokine signalling through the gp130/Jak/STAT pathway.* Biochem J, 1998. **334 (Pt 2)**: p. 297-314.
66. Imada, K. and W.J. Leonard, *The Jak-STAT pathway.* Mol Immunol, 2000. **37**(1-2): p. 1-11.
67. Rosean, T.R., et al., *Preclinical validation of interleukin 6 as a therapeutic target in multiple myeloma.* Immunol Res, 2014. **59**(1-3): p. 188-202.
68. Johnson, D.E., R.A. O'Keefe, and J.R. Grandis, *Targeting the IL-6/JAK/STAT3 signalling axis in cancer.* Nat Rev Clin Oncol, 2018. **15**(4): p. 234-248.
69. Burger, R., et al., *Due to interleukin-6 type cytokine redundancy only glycoprotein 130 receptor blockade efficiently inhibits myeloma growth.* Haematologica, 2017. **102**(2): p. 381-390.
70. Camporeale, A. and V. Poli, *IL-6, IL-17 and STAT3: a holy trinity in auto-immunity?* Front Biosci (Landmark Ed), 2012. **17**: p. 2306-26.
71. Babon, J.J., et al., *The molecular regulation of Janus kinase (JAK) activation.* Biochem J, 2014. **462**(1): p. 1-13.
72. O'Shea, J.J., et al., *The JAK-STAT pathway: impact on human disease and therapeutic intervention.* Annu Rev Med, 2015. **66**: p. 311-28.
73. Nielsen, C., et al., *The JAK2 V617F somatic mutation, mortality and cancer risk in the general population.* Haematologica, 2011. **96**(3): p. 450-3.
74. Fiorini, A., et al., *Screening of JAK2 V617F mutation in multiple myeloma.* Leukemia, 2006. **20**(10): p. 1912-3.
75. Huang, Q., et al., *Absence of JAK-2V617F point mutations in multiple myeloma.* Leukemia, 2007. **21**(4): p. 813-4; author reply 814-5.
76. de Oliveira, M.B., et al., *Anti-myeloma effects of ruxolitinib combined with bortezomib and lenalidomide: A rationale for JAK/STAT pathway inhibition in myeloma patients.* Cancer Lett, 2017. **403**: p. 206-215.
77. Ramakrishnan, V., et al., *TG101209, a novel JAK2 inhibitor, has significant in vitro activity in multiple myeloma and displays preferential cytotoxicity for CD45+ myeloma cells.* Am J Hematol, 2010. **85**(9): p. 675-86.
78. Scuto, A., et al., *The novel JAK inhibitor AZD1480 blocks STAT3 and FGFR3 signaling, resulting in suppression of human myeloma cell growth and survival.* Leukemia, 2011. **25**(3): p. 538-50.
79. Senkevitch, E. and S. Durum, *The promise of Janus kinase inhibitors in the treatment of hematological malignancies.* Cytokine, 2017. **98**: p. 33-41.
80. Lim, C.P. and X. Cao, *Structure, function, and regulation of STAT proteins.* Mol Biosyst, 2006. **2**(11): p. 536-50.
81. Siveen, K.S., et al., *Targeting the STAT3 signaling pathway in cancer: role of synthetic and natural inhibitors.* Biochim Biophys Acta, 2014. **1845**(2): p. 136-54.
82. Sansone, P. and J. Bromberg, *Targeting the interleukin-6/Jak/stat pathway in human malignancies.* J Clin Oncol, 2012. **30**(9): p. 1005-14.
83. Koppikar, P., et al., *Constitutive activation of signal transducer and activator of transcription 5 contributes to tumor growth, epithelial-mesenchymal transition, and resistance to epidermal growth factor receptor targeting.* Clin Cancer Res, 2008. **14**(23): p. 7682-90.
84. Xi, S., et al., *Constitutive activation of Stat5b contributes to carcinogenesis in vivo.* Cancer Res, 2003. **63**(20): p. 6763-71.

85. Bharadwaj U., K.M.M., Tweardy D.J., *STAT3 Inhibitors in Cancer: A Comprehensive Update.* 2016, Humana Press: C ancer Drug Discovery and Development In: Ward A. (eds) STAT Inhibitors in Cancer.
86. Chang, Q., et al., *The IL-6/JAK/Stat3 feed-forward loop drives tumorigenesis and metastasis.* Neoplasia, 2013. **15**(7): p. 848-62.
87. Kim, B.H., E.H. Yi, and S.K. Ye, *Signal transducer and activator of transcription 3 as a therapeutic target for cancer and the tumor microenvironment.* Arch Pharm Res, 2016. **39**(8): p. 1085-99.
88. Buettner, R., L.B. Mora, and R. Jove, *Activated STAT signaling in human tumors provides novel molecular targets for therapeutic intervention.* Clin Cancer Res, 2002. **8**(4): p. 945-54.
89. Srivastava, J. and J. DiGiovanni, *Non-canonical Stat3 signaling in cancer.* Mol Carcinog, 2016. **55**(12): p. 1889-1898.
90. Frank, D.A., S. Mahajan, and J. Ritz, *B lymphocytes from patients with chronic lymphocytic leukemia contain signal transducer and activator of transcription (STAT) 1 and STAT3 constitutively phosphorylated on serine residues.* J Clin Invest, 1997. **100**(12): p. 3140-8.
91. Hazan-Halevy, I., et al., *STAT3 is constitutively phosphorylated on serine 727 residues, binds DNA, and activates transcription in CLL cells.* Blood, 2010. **115**(14): p. 2852-63.
92. Sakaguchi, M., et al., *Role and regulation of STAT3 phosphorylation at Ser727 in melanocytes and melanoma cells.* J Invest Dermatol, 2012. **132**(7): p. 1877-85.
93. Gough, D.J., et al., *Mitochondrial STAT3 supports Ras-dependent oncogenic transformation.* Science, 2009. **324**(5935): p. 1713-6.
94. Yuan, Z.L., et al., *Stat3 dimerization regulated by reversible acetylation of a single lysine residue.* Science, 2005. **307**(5707): p. 269-73.
95. Nicholas, C. and G.B. Lesinski, *The JAK-STAT Signal Transduction Pathway in Melanoma*. 2011, Breakthroughs in Melanoma Research.
96. Fulda, S. and D. Vucic, *Targeting IAP proteins for therapeutic intervention in cancer.* Nat Rev Drug Discov, 2012. **11**(2): p. 109-24.
97. Romagnoli, M., et al., *Significant impact of survivin on myeloma cell growth.* Leukemia, 2007. **21**(5): p. 1070-8.
98. Ambrosini, G., C. Adida, and D.C. Altieri, *A novel anti-apoptosis gene, survivin, expressed in cancer and lymphoma.* Nat Med, 1997. **3**(8): p. 917-21.
99. Romagnoli, M., et al., *The imbalance between Survivin and Bim mediates tumour growth and correlates with poor survival in patients with multiple myeloma.* Br J Haematol, 2009. **145**(2): p. 180-9.
100. Gritsko, T., et al., *Persistent activation of stat3 signaling induces survivin gene expression and confers resistance to apoptosis in human breast cancer cells.* Clin Cancer Res, 2006. **12**(1): p. 11-9.
101. Bergsagel, P.L., et al., *Cyclin D dysregulation: an early and unifying pathogenic event in multiple myeloma.* Blood, 2005. **106**(1): p. 296-303.
102. Maes, A., et al., *The therapeutic potential of cell cycle targeting in multiple myeloma.* Oncotarget, 2017. **8**(52): p. 90501-90520.
103. Alao, J.P., *The regulation of cyclin D1 degradation: roles in cancer development and the potential for therapeutic invention.* Mol Cancer, 2007. **6**: p. 24.
104. Malumbres, M. and M. Barbacid, *Cell cycle, CDKs and cancer: a changing paradigm.* Nat Rev Cancer, 2009. **9**(3): p. 153-66.
105. Chesi, M. and P.L. Bergsagel, *Molecular pathogenesis of multiple myeloma: basic and clinical updates.* Int J Hematol, 2013. **97**(3): p. 313-23.

106. Leslie, K., et al., *Cyclin D1 is transcriptionally regulated by and required for transformation by activated signal transducer and activator of transcription 3.* Cancer Res, 2006. **66**(5): p. 2544-52.
107. Carpenter, R.L. and H.W. Lo, *STAT3 Target Genes Relevant to Human Cancers.* Cancers (Basel), 2014. **6**(2): p. 897-925.
108. Dechow, T., et al., *GP130 activation induces myeloma and collaborates with MYC.* J Clin Invest, 2014. **124**(12): p. 5263-74.
109. Holien, T., et al., *Addiction to c-MYC in multiple myeloma.* Blood, 2012. **120**(12): p. 2450-3.
110. Chang, M., et al., *PIM kinase inhibitors downregulate STAT3(Tyr705) phosphorylation.* Mol Cancer Ther, 2010. **9**(9): p. 2478-87.
111. Paíno, T., et al., *The Novel Pan-PIM Kinase Inhibitor, PIM447, Displays Dual Antimyeloma and Bone-Protective Effects, and Potently Synergizes with Current Standards of Care.* Clin Cancer Res, 2017. **23**(1): p. 225-238.
112. Prior, I.A., P.D. Lewis, and C. Mattos, *A comprehensive survey of Ras mutations in cancer.* Cancer Res, 2012. **72**(10): p. 2457-67.
113. Walker, B.A., et al., *Mutational Spectrum, Copy Number Changes, and Outcome: Results of a Sequencing Study of Patients With Newly Diagnosed Myeloma.* J Clin Oncol, 2015. **33**(33): p. 3911-20.
114. Liu, P., et al., *Activating mutations of N- and K-ras in multiple myeloma show different clinical associations: analysis of the Eastern Cooperative Oncology Group Phase III Trial.* Blood, 1996. **88**(7): p. 2699-706.
115. Mulligan, G., et al., *Mutation of NRAS but not KRAS significantly reduces myeloma sensitivity to single-agent bortezomib therapy.* Blood, 2014. **123**(5): p. 632-9.
116. Chng, W.J., et al., *Clinical and biological significance of RAS mutations in multiple myeloma.* Leukemia, 2008. **22**(12): p. 2280-4.
117. Heuck, C.J., et al., *Inhibiting MEK in MAPK pathway-activated myeloma.* Leukemia, 2016. **30**(4): p. 976-80.
118. Chapman, M.A., et al., *Initial genome sequencing and analysis of multiple myeloma.* Nature, 2011. **471**(7339): p. 467-72.
119. Gentile, M., et al., *Sorafenib for the treatment of multiple myeloma.* Expert Opin Investig Drugs, 2016. **25**(6): p. 743-9.
120. Ramakrishnan, V., et al., *Sorafenib, a dual Raf kinase/vascular endothelial growth factor receptor inhibitor has significant anti-myeloma activity and synergizes with common anti-myeloma drugs.* Oncogene, 2010. **29**(8): p. 1190-202.
121. Sharman, J.P., et al., *Vemurafenib response in 2 patients with posttransplant refractory BRAF V600E-mutated multiple myeloma.* Clin Lymphoma Myeloma Leuk, 2014. **14**(5): p. e161-3.
122. Rasche, L., et al., *The Impact of Tumor Heterogeneity on Diagnostics and Novel Therapeutic Strategies in Multiple Myeloma.* Int J Mol Sci, 2019. **20**(5).
123. Liu, J. and A. Lin, *Role of JNK activation in apoptosis: a double-edged sword.* Cell Res, 2005. **15**(1): p. 36-42.
124. Bode, A.M. and Z. Dong, *The functional contrariety of JNK.* Mol Carcinog, 2007. **46**(8): p. 591-8.
125. Bubici, C. and S. Papa, *JNK signalling in cancer: in need of new, smarter therapeutic targets.* Br J Pharmacol, 2014. **171**(1): p. 24-37.
126. Das, M., et al., *The role of JNK in the development of hepatocellular carcinoma.* Genes Dev, 2011. **25**(6): p. 634-45.

127. Barbarulo, A., et al., *Poly(ADP-ribose) polymerase family member 14 (PARP14) is a novel effector of the JNK2-dependent pro-survival signal in multiple myeloma.* Oncogene, 2013. **32**(36): p. 4231-42.
128. She, Q.B., et al., *Deficiency of c-Jun-NH(2)-terminal kinase-1 in mice enhances skin tumor development by 12-O-tetradecanoylphorbol-13-acetate.* Cancer Res, 2002. **62**(5): p. 1343-8.
129. Cellurale, C., et al., *Role of JNK in a Trp53-dependent mouse model of breast cancer.* PLoS One, 2010. **5**(8): p. e12469.
130. Dhanasekaran, D.N. and E.P. Reddy, *JNK-signaling: A multiplexing hub in programmed cell death.* Genes Cancer, 2017. **8**(9-10): p. 682-694.
131. Feng, Y., J. Wen, and C.C. Chang, *p38 Mitogen-activated protein kinase and hematologic malignancies.* Arch Pathol Lab Med, 2009. **133**(11): p. 1850-6.
132. Pramanik, R., et al., *p38 isoforms have opposite effects on AP-1-dependent transcription through regulation of c-Jun. The determinant roles of the isoforms in the p38 MAPK signal specificity.* J Biol Chem, 2003. **278**(7): p. 4831-9.
133. Pene, F., et al., *Role of the phosphatidylinositol 3-kinase/Akt and mTOR/P70S6-kinase pathways in the proliferation and apoptosis in multiple myeloma.* Oncogene, 2002. **21**(43): p. 6587-97.
134. Okkenhaug, K., M. Graupera, and B. Vanhaesebroeck, *Targeting PI3K in Cancer: Impact on Tumor Cells, Their Protective Stroma, Angiogenesis, and Immunotherapy.* Cancer Discov, 2016. **6**(10): p. 1090-1105.
135. Cantrell, D.A., *Phosphoinositide 3-kinase signalling pathways.* J Cell Sci, 2001. **114**(Pt 8): p. 1439-45.
136. Younes, H., et al., *Targeting the phosphatidylinositol 3-kinase pathway in multiple myeloma.* Clin Cancer Res, 2007. **13**(13): p. 3771-5.
137. Shiojima, I. and K. Walsh, *Role of Akt signaling in vascular homeostasis and angiogenesis.* Circ Res, 2002. **90**(12): p. 1243-50.
138. Menu, E., et al., *Specific roles for the PI3K and the MEK-ERK pathway in IGF-1-stimulated chemotaxis, VEGF secretion and proliferation of multiple myeloma cells: study in the 5T33MM model.* Br J Cancer, 2004. **90**(5): p. 1076-83.
139. Bieghs, L., et al., *The insulin-like growth factor system in multiple myeloma: diagnostic and therapeutic potential.* Oncotarget, 2016. **7**(30): p. 48732-48752.
140. Li, J., et al., *The mTOR signaling pathway is an emerging therapeutic target in multiple myeloma.* Curr Pharm Des, 2014. **20**(1): p. 125-35.
141. Adimonye, A., et al., *Analysis of the PI3K-AKT-mTOR pathway in penile cancer: evaluation of a therapeutically targetable pathway.* Oncotarget, 2018. **9**(22): p. 16074-16086.
142. Park, M.H. and J.T. Hong, *Roles of NF-κB in Cancer and Inflammatory Diseases and Their Therapeutic Approaches.* Cells, 2016. **5**(2).
143. Xia, Y., S. Shen, and I.M. Verma, *NF-κB, an active player in human cancers.* Cancer Immunol Res, 2014. **2**(9): p. 823-30.
144. Vrábel, D., L. Pour, and S. Ševčíková, *The impact of NF-κB signaling on pathogenesis and current treatment strategies in multiple myeloma.* Blood Rev, 2019. **34**: p. 56-66.
145. Rinkenbaugh, A.L. and A.S. Baldwin, *The NF-κB Pathway and Cancer Stem Cells.* Cells, 2016. **5**(2).
146. de Mel, S., et al., *Implications of heterogeneity in multiple myeloma.* Biomed Res Int, 2014. **2014**: p. 232546.
147. *Multiple myeloma: 2018 update on diagnosis, risk-stratification, and management.* Am J Hematol, 2018. **93**(8): p. 981-1114.

148. Mahajan, S., N. Tandon, and S. Kumar, *The evolution of stem-cell transplantation in multiple myeloma.* Ther Adv Hematol, 2018. **9**(5): p. 123-133.
149. Costa, L.J., et al., *Recent trends in multiple myeloma incidence and survival by age, race, and ethnicity in the United States.* Blood Adv, 2017. **1**(4): p. 282-287.
150. Rajkumar, S.V., *Multiple myeloma: Every year a new standard?* Hematol Oncol, 2019. **37 Suppl 1**: p. 62-65.
151. Palumbo, A., et al., *International Myeloma Working Group consensus statement for the management, treatment, and supportive care of patients with myeloma not eligible for standard autologous stem-cell transplantation.* J Clin Oncol, 2014. **32**(6): p. 587-600.
152. Al Hamed, R., et al., *Current status of autologous stem cell transplantation for multiple myeloma.* Blood Cancer J, 2019. **9**(4): p. 44.
153. Moreau, P., *How I treat myeloma with new agents.* Blood, 2017. **130**(13): p. 1507-1513.
154. Kubiczkova, L., et al., *Proteasome inhibitors - molecular basis and current perspectives in multiple myeloma.* J Cell Mol Med, 2014. **18**(6): p. 947-61.
155. Moreau, P., et al., *Proteasome inhibitors in multiple myeloma: 10 years later.* Blood, 2012. **120**(5): p. 947-59.
156. Crawford, L.J., B. Walker, and A.E. Irvine, *Proteasome inhibitors in cancer therapy.* J Cell Commun Signal, 2011. **5**(2): p. 101-10.
157. Tanaka, K., *The proteasome: overview of structure and functions.* Proc Jpn Acad Ser B Phys Biol Sci, 2009. **85**(1): p. 12-36.
158. Ciechanover, A., *The ubiquitin-proteasome pathway: on protein death and cell life.* EMBO J, 1998. **17**(24): p. 7151-60.
159. Cao, B. and X. Mao, *The ubiquitin-proteasomal system is critical for multiple myeloma: implications in drug discovery.* Am J Blood Res, 2011. **1**(1): p. 46-56.
160. Kisselev, A.F., W.A. van der Linden, and H.S. Overkleeft, *Proteasome inhibitors: an expanding army attacking a unique target.* Chem Biol, 2012. **19**(1): p. 99-115.
161. Hideshima, T., et al., *Proteasome inhibitor PS-341 abrogates IL-6 triggered signaling cascades via caspase-dependent downregulation of gp130 in multiple myeloma.* Oncogene, 2003. **22**(52): p. 8386-93.
162. Wallington-Beddoe, C.T. and S.M. Pitson, *Enhancing ER stress in myeloma.* Aging (Albany NY), 2017. **9**(7): p. 1645-1646.
163. *Chemical Structure of Bortezomib National Center for Biotechnology Information. PubChem Database. Bortezomib, CID=387447, https://pubchem.ncbi.nlm.nih.gov/compound/Bortezomib (accessed on Dec. 31, 2019)*.
164. Bayraktar, U.D., et al., *Fifty years of melphalan use in hematopoietic stem cell transplantation.* Biol Blood Marrow Transplant, 2013. **19**(3): p. 344-56.
165. Swift, L.H. and R.M. Golsteyn, *Genotoxic anti-cancer agents and their relationship to DNA damage, mitosis, and checkpoint adaptation in proliferating cancer cells.* Int J Mol Sci, 2014. **15**(3): p. 3403-31.
166. Damia, G. and M. D'Incalci, *Mechanisms of resistance to alkylating agents.* Cytotechnology, 1998. **27**(1-3): p. 165-73.
167. Powar, T.A. and A.A. Hajare, *Development and Validation of an HPLC-UV Method for the Determination of Melphalan from Lyophilized Nanosuspension*. 2019: Indian Journal of Pharmaceutical Research and Education.
168. Miller, W.L. and R.J. Auchus, *The molecular biology, biochemistry, and physiology of human steroidogenesis and its disorders.* Endocr Rev, 2011. **32**(1): p. 81-151.
169. Kyle, R.A. and S.V. Rajkumar, *An overview of the progress in the treatment of multiple myeloma.* Expert Rev Hematol, 2014. **7**(1): p. 5-7.

170. Keith, B.D., *Systematic review of the clinical effect of glucocorticoids on nonhematologic malignancy.* BMC Cancer, 2008. **8**: p. 84.
171. Greenstein, S., et al., *Mechanisms of glucocorticoid-mediated apoptosis in hematological malignancies.* Clin Cancer Res, 2002. **8**(6): p. 1681-94.
172. Duarte, C.A.R., F.J. Mano, and L. Reis, Rui, *Preparation of chitosan scaffolds loaded with dexamethasone for tissue engineering applications using supercritical fluid technology*. 2009: European Polymer Journal.
173. Holstein, S.A. and P.L. McCarthy, *Immunomodulatory Drugs in Multiple Myeloma: Mechanisms of Action and Clinical Experience.* Drugs, 2017. **77**(5): p. 505-520.
174. Singhal, S., et al., *Antitumor activity of thalidomide in refractory multiple myeloma.* N Engl J Med, 1999. **341**(21): p. 1565-71.
175. Lu, G., et al., *The myeloma drug lenalidomide promotes the cereblon-dependent destruction of Ikaros proteins.* Science, 2014. **343**(6168): p. 305-9.
176. Haslett, P.A., et al., *Thalidomide costimulates primary human T lymphocytes, preferentially inducing proliferation, cytokine production, and cytotoxic responses in the CD8+ subset.* J Exp Med, 1998. **187**(11): p. 1885-92.
177. Saxena, J., S. Saroj, and S. Rajput, *ESTIMATION OF LENALIDOMIDE IN BULK AND ITS DOSAGE FORM USING UV SPECTROPHOTOMETRIC AND RP-HPLC METHODS*. 2017, INDO American Journal of Pharmaceutical Research.
178. Michalak, E.M., et al., *The roles of DNA, RNA and histone methylation in ageing and cancer.* Nat Rev Mol Cell Biol, 2019. **20**(10): p. 573-589.
179. Baxter, E., et al., *Epigenetic regulation in cancer progression.* Cell Biosci, 2014. **4**: p. 45.
180. Choudhary, C., et al., *Lysine acetylation targets protein complexes and co-regulates major cellular functions.* Science, 2009. **325**(5942): p. 834-40.
181. Afifi, S., et al., *Role of Histone Deacetylase Inhibitors in Relapsed Refractory Multiple Myeloma: A Focus on Vorinostat and Panobinostat.* Pharmacotherapy, 2015. **35**(12): p. 1173-88.
182. West, A.C. and R.W. Johnstone, *New and emerging HDAC inhibitors for cancer treatment.* J Clin Invest, 2014. **124**(1): p. 30-9.
183. Harada, T., T. Hideshima, and K.C. Anderson, *Histone deacetylase inhibitors in multiple myeloma: from bench to bedside.* Int J Hematol, 2016. **104**(3): p. 300-9.
184. Mitsiades, C.S., et al., *Transcriptional signature of histone deacetylase inhibition in multiple myeloma: biological and clinical implications.* Proc Natl Acad Sci U S A, 2004. **101**(2): p. 540-5.
185. *National Center for Biotechnology Information. PubChem Database. Panobinostat, CID=6918837, https://pubchem.ncbi.nlm.nih.gov/compound/Panobinostat (accessed on Jan. 3, 2020)*.
186. Phipps, C., et al., *Daratumumab and its potential in the treatment of multiple myeloma: overview of the preclinical and clinical development.* Ther Adv Hematol, 2015. **6**(3): p. 120-7.
187. Rajkumar, S.V. and S. Kumar, *Multiple Myeloma: Diagnosis and Treatment.* Mayo Clin Proc, 2016. **91**(1): p. 101-19.
188. van de Donk, N.W., et al., *Monoclonal antibodies targeting CD38 in hematological malignancies and beyond.* Immunol Rev, 2016. **270**(1): p. 95-112.
189. Gottesman, M.M., *Mechanisms of cancer drug resistance.* Annu Rev Med, 2002. **53**: p. 615-27.
190. Dalton, W.S., *Detection of multidrug resistance gene expression in multiple myeloma.* Leukemia, 1997. **11**(7): p. 1166-9.

191. Xie, L., et al., *Drug resistance-related microRNAs in hematological malignancies: translating basic evidence into therapeutic strategies.* Blood Rev, 2015. **29**(1): p. 33-44.
192. Roccaro, A.M., et al., *MicroRNAs 15a and 16 regulate tumor proliferation in multiple myeloma.* Blood, 2009. **113**(26): p. 6669-80.
193. Yang, W.C. and S.F. Lin, *Mechanisms of Drug Resistance in Relapse and Refractory Multiple Myeloma.* Biomed Res Int, 2015. **2015**: p. 341430.
194. Abdi, J., G. Chen, and H. Chang, *Erratum: Drug resistance in multiple myeloma: latest findings and new concepts on molecular mechanisms.* Oncotarget, 2015. **6**(10): p. 7364.
195. Lü, S. and J. Wang, *The resistance mechanisms of proteasome inhibitor bortezomib.* Biomark Res, 2013. **1**(1): p. 13.
196. Zaal, E.A., et al., *Bortezomib resistance in multiple myeloma is associated with increased serine synthesis.* Cancer Metab, 2017. **5**: p. 7.
197. Chauhan, D. and K.C. Anderson, *Mechanisms of cell death and survival in multiple myeloma (MM): Therapeutic implications.* Apoptosis, 2003. **8**(4): p. 337-43.
198. Mohammad, R.M., et al., *Broad targeting of resistance to apoptosis in cancer.* Semin Cancer Biol, 2015. **35 Suppl**: p. S78-S103.
199. Kerr, J.F., A.H. Wyllie, and A.R. Currie, *Apoptosis: a basic biological phenomenon with wide-ranging implications in tissue kinetics.* Br J Cancer, 1972. **26**(4): p. 239-57.
200. Cohen, G.M., et al., *Key morphological features of apoptosis may occur in the absence of internucleosomal DNA fragmentation.* Biochem J, 1992. **286 (Pt 2)**: p. 331-4.
201. Pfeffer, C.M. and A.T.K. Singh, *Apoptosis: A Target for Anticancer Therapy.* Int J Mol Sci, 2018. **19**(2).
202. Nuñez, G., et al., *Caspases: the proteases of the apoptotic pathway.* Oncogene, 1998. **17**(25): p. 3237-45.
203. Donepudi, M. and M.G. Grütter, *Structure and zymogen activation of caspases.* Biophys Chem, 2002. **101-102**: p. 145-53.
204. Fulda, S., *Targeting extrinsic apoptosis in cancer: Challenges and opportunities.* Semin Cell Dev Biol, 2015. **39**: p. 20-5.
205. Huang, K., et al., *Cleavage by Caspase 8 and Mitochondrial Membrane Association Activate the BH3-only Protein Bid during TRAIL-induced Apoptosis.* J Biol Chem, 2016. **291**(22): p. 11843-51.
206. Czabotar, P.E., et al., *Control of apoptosis by the BCL-2 protein family: implications for physiology and therapy.* Nat Rev Mol Cell Biol, 2014. **15**(1): p. 49-63.
207. Xiong, S., et al., *Mitochondria-mediated apoptosis in mammals.* Protein Cell, 2014. **5**(10): p. 737-49.
208. Fulda, S. and K.M. Debatin, *Extrinsic versus intrinsic apoptosis pathways in anticancer chemotherapy.* Oncogene, 2006. **25**(34): p. 4798-811.
209. Marzban, H., et al., *Cellular commitment in the developing cerebellum.* Front Cell Neurosci, 2014. **8**: p. 450.
210. Giménez-Cassina, A. and N.N. Danial, *Regulation of mitochondrial nutrient and energy metabolism by BCL-2 family proteins.* Trends Endocrinol Metab, 2015. **26**(4): p. 165-75.
211. Adams, J.M. and S. Cory, *The BCL-2 arbiters of apoptosis and their growing role as cancer targets.* Cell Death Differ, 2018. **25**(1): p. 27-36.
212. Gahl, R.F., P. Dwivedi, and N. Tjandra, *Bcl-2 proteins bid and bax form a network to permeabilize the mitochondria at the onset of apoptosis.* Cell Death Dis, 2016. **7**(10): p. e2424.
213. Willis, S., et al., *The Bcl-2-regulated apoptotic pathway.* J Cell Sci, 2003. **116**(Pt 20): p. 4053-6.

214. Delbridge, A.R., et al., *Thirty years of BCL-2: translating cell death discoveries into novel cancer therapies.* Nat Rev Cancer, 2016. **16**(2): p. 99-109.
215. Zhang, B., I. Gojo, and R.G. Fenton, *Myeloid cell factor-1 is a critical survival factor for multiple myeloma.* Blood, 2002. **99**(6): p. 1885-93.
216. Tse, C., et al., *ABT-263: a potent and orally bioavailable Bcl-2 family inhibitor.* Cancer Res, 2008. **68**(9): p. 3421-8.
217. Leverson, J.D., et al., *Potent and selective small-molecule MCL-1 inhibitors demonstrate on-target cancer cell killing activity as single agents and in combination with ABT-263 (navitoclax).* Cell Death Dis, 2015. **6**: p. e1590.
218. Basali, D., et al., *Real-world data on safety and efficacy of venetoclax-based regimens in relapsed/refractory t(11;14) multiple myeloma.* 2020, British Society for Haematology and John Wiley and Sons Ltd.: British Journal of Haematology.
219. Kumar, S., et al., *Efficacy of venetoclax as targeted therapy for relapsed/refractory t(11;14) multiple myeloma.* Blood, 2017. **130**(22): p. 2401-2409.
220. Kozopas, K.M., et al., *MCL1, a gene expressed in programmed myeloid cell differentiation, has sequence similarity to BCL2.* Proc Natl Acad Sci U S A, 1993. **90**(8): p. 3516-20.
221. Beroukhim, R., et al., *The landscape of somatic copy-number alteration across human cancers.* Nature, 2010. **463**(7283): p. 899-905.
222. Le Gouill, S., et al., *Mcl-1 regulation and its role in multiple myeloma.* Cell Cycle, 2004. **3**(10): p. 1259-62.
223. Mojsa, B., I. Lassot, and S. Desagher, *Mcl-1 ubiquitination: unique regulation of an essential survival protein.* Cells, 2014. **3**(2): p. 418-37.
224. Thomas, L.W., C. Lam, and S.W. Edwards, *Mcl-1; the molecular regulation of protein function.* FEBS Lett, 2010. **584**(14): p. 2981-9.
225. Slomp, A., et al., *Multiple myeloma with 1q21 amplification is highly sensitive to MCL-1 targeting.* Blood Adv, 2019. **3**(24): p. 4202-4214.
226. Wuillème-Toumi, S., et al., *Mcl-1 is overexpressed in multiple myeloma and associated with relapse and shorter survival.* Leukemia, 2005. **19**(7): p. 1248-52.
227. Derenne, S., et al., *Antisense strategy shows that Mcl-1 rather than Bcl-2 or Bcl-x(L) is an essential survival protein of human myeloma cells.* Blood, 2002. **100**(1): p. 194-9.
228. Peperzak, V., et al., *Mcl-1 is essential for the survival of plasma cells.* Nat Immunol, 2013. **14**(3): p. 290-7.
229. Gong, J.N., et al., *Hierarchy for targeting prosurvival BCL2 family proteins in multiple myeloma: pivotal role of MCL1.* Blood, 2016. **128**(14): p. 1834-1844.
230. Puthier, D., R. Bataille, and M. Amiot, *IL-6 up-regulates mcl-1 in human myeloma cells through JAK / STAT rather than ras / MAP kinase pathway.* Eur J Immunol, 1999. **29**(12): p. 3945-50.
231. Peeters, S.D., et al., *Bcl-xl expression in multiple myeloma.* Med Oncol, 2005. **22**(2): p. 183-90.
232. Yang, H., et al., *The role of cellular reactive oxygen species in cancer chemotherapy.* J Exp Clin Cancer Res, 2018. **37**(1): p. 266.
233. Liou, G.Y. and P. Storz, *Reactive oxygen species in cancer.* Free Radic Res, 2010. **44**(5): p. 479-96.
234. Galadari, S., et al., *Reactive oxygen species and cancer paradox: To promote or to suppress?* Free Radic Biol Med, 2017. **104**: p. 144-164.
235. Storz, P., *KRas, ROS and the initiation of pancreatic cancer.* Small GTPases, 2017. **8**(1): p. 38-42.
236. Storz, P., *Reactive oxygen species in tumor progression.* Front Biosci, 2005. **10**: p. 1881-96.

237. Nikesitch, N., et al., *Endoplasmic reticulum stress in the development of multiple myeloma and drug resistance.* Clin Transl Immunology, 2018. **7**(1): p. e1007.
238. Obeng, E.A., et al., *Proteasome inhibitors induce a terminal unfolded protein response in multiple myeloma cells.* Blood, 2006. **107**(12): p. 4907-16.
239. Castella, M., C. Fernández de Larrea, and B. Martín-Antonio, *Immunotherapy: A Novel Era of Promising Treatments for Multiple Myeloma.* Int J Mol Sci, 2018. **19**(11).
240. D'Agostino, M. and N. Raje, *Anti-BCMA CAR T-cell therapy in multiple myeloma: can we do better?* Leukemia, 2020. **34**(1): p. 21-34.
241. Syed, Y.Y., *Selinexor: First Global Approval.* Drugs, 2019. **79**(13): p. 1485-1494.
242. Heo, T.H., J. Wahler, and N. Suh, *Potential therapeutic implications of IL-6/IL-6R/gp130-targeting agents in breast cancer.* Oncotarget, 2016. **7**(13): p. 15460-73.
243. Hunsucker, S.A., et al., *Blockade of interleukin-6 signalling with siltuximab enhances melphalan cytotoxicity in preclinical models of multiple myeloma.* Br J Haematol, 2011. **152**(5): p. 579-92.
244. San-Miguel, J., et al., *Phase 2 randomized study of bortezomib-melphalan-prednisone with or without siltuximab (anti-IL-6) in multiple myeloma.* Blood, 2014. **123**(26): p. 4136-42.
245. Brighton, T.A., et al., *Randomized, Double-Blind, Placebo-Controlled, Multicenter Study of Siltuximab in High-Risk Smoldering Multiple Myeloma.* Clin Cancer Res, 2019. **25**(13): p. 3772-3775.
246. Sebba, A., *Tocilizumab: the first interleukin-6-receptor inhibitor.* Am J Health Syst Pharm, 2008. **65**(15): p. 1413-8.
247. Dijkgraaf, E.M., et al., *A phase I trial combining carboplatin/doxorubicin with tocilizumab, an anti-IL-6R monoclonal antibody, and interferon-α2b in patients with recurrent epithelial ovarian cancer.* Ann Oncol, 2015. **26**(10): p. 2141-9.
248. Xiang, M., et al., *Gene expression-based discovery of atovaquone as a STAT3 inhibitor and anticancer agent.* Blood, 2016. **128**(14): p. 1845-1853.
249. Fang, Z., C. Grütter, and D. Rauh, *Strategies for the selective regulation of kinases with allosteric modulators: exploiting exclusive structural features.* ACS Chem Biol, 2013. **8**(1): p. 58-70.
250. Roskoski, R., *Properties of FDA-approved small molecule protein kinase inhibitors: a 2020 update.* Pharmacol Res, 2019: p. 104609.
251. Blair, H.A., *Fedratinib: First Approval.* Drugs, 2019. **79**(15): p. 1719-1725.
252. Manning, G., et al., *The protein kinase complement of the human genome.* Science, 2002. **298**(5600): p. 1912-34.
253. Abramson, H.N., *Kinase inhibitors as potential agents in the treatment of multiple myeloma.* Oncotarget, 2016. **7**(49): p. 81926-81968.
254. Zhang, J., P.L. Yang, and N.S. Gray, *Targeting cancer with small molecule kinase inhibitors.* Nat Rev Cancer, 2009. **9**(1): p. 28-39.
255. Wu, P., T.E. Nielsen, and M.H. Clausen, *FDA-approved small-molecule kinase inhibitors.* Trends Pharmacol Sci, 2015. **36**(7): p. 422-39.
256. Lam, C., et al., *Repurposing tofacitinib as an anti-myeloma therapeutic to reverse growth-promoting effects of the bone marrow microenvironment.* Haematologica, 2018. **103**(7): p. 1218-1228.
257. Honda, A., et al., *NS-018 reduces myeloma cell proliferation and suppresses osteolysis through inhibition of the JAK2 and Src signaling pathways.* Blood Cancer J, 2018. **8**(7): p. 62.
258. Heusschen, R., et al., *SRC kinase inhibition with saracatinib limits the development of osteolytic bone disease in multiple myeloma.* Oncotarget, 2016. **7**(21): p. 30712-29.

259. Diez-Cecilia, E., et al., *Probing a 3,4'-bis-guanidinium diaryl derivative as an allosteric inhibitor of the Ras pathway.* Bioorg Med Chem Lett, 2015. **25**(19): p. 4287-92.
260. Keating, G.M., *Sorafenib: A Review in Hepatocellular Carcinoma.* Target Oncol, 2017. **12**(2): p. 243-253.
261. White, P.T. and M.S. Cohen, *The discovery and development of sorafenib for the treatment of thyroid cancer.* Expert Opin Drug Discov, 2015. **10**(4): p. 427-39.
262. Arranz, J., et al., *Sorafenib in renal cell carcinoma.* Crit Rev Oncol Hematol, 2011. **80**(2): p. 314-22.
263. Hung, M.H., et al., *Downregulation of signal transducer and activator of transcription 3 by sorafenib: a novel mechanism for hepatocellular carcinoma therapy.* World J Gastroenterol, 2014. **20**(41): p. 15269-74.
264. Wilhelm, S.M., et al., *Preclinical overview of sorafenib, a multikinase inhibitor that targets both Raf and VEGF and PDGF receptor tyrosine kinase signaling.* Mol Cancer Ther, 2008. **7**(10): p. 3129-40.
265. Diez-Cecilia, E., et al., *Guanidinium-based derivatives: searching for new kinase inhibitors.* Eur J Med Chem, 2014. **81**: p. 427-41.
266. Gazdar, A.F., et al., *Establishment and characterization of a human plasma cell myeloma culture having a rearranged cellular myc proto-oncogene.* Blood, 1986. **67**(6): p. 1542-9.
267. Nilsson, K., et al., *Established immunoglobulin producing myeloma (IgE) and lymphoblastoid (IgG) cell lines from an IgE myeloma patient.* Clin Exp Immunol, 1970. **7**(4): p. 477-89.
268. Kawano, M., et al., *Autocrine generation and requirement of BSF-2/IL-6 for human multiple myelomas.* Nature, 1988. **332**(6159): p. 83-5.
269. Greenstein, S., et al., *Characterization of the MM.1 human multiple myeloma (MM) cell lines: a model system to elucidate the characteristics, behavior, and signaling of steroid-sensitive and -resistant MM cells.* Exp Hematol, 2003. **31**(4): p. 271-82.
270. Roecklein, B.A. and B. Torok-Storb, *Functionally distinct human marrow stromal cell lines immortalized by transduction with the human papilloma virus E6/E7 genes.* Blood, 1995. **85**(4): p. 997-1005.
271. Tessoulin, B., et al., *Whole-exon sequencing of human myeloma cell lines shows mutations related to myeloma patients at relapse with major hits in the DNA regulation and repair pathways.* J Hematol Oncol, 2018. **11**(1): p. 137.
272. Norris, E.J., et al., *Cytotoxic efficacy of filanesib and melphalan combination is governed by sequence of treatment in human myeloma cells.* Blood Cancer J, 2016. **6**(10): p. e480.
273. Khin, Z.P., et al., *A preclinical assay for chemosensitivity in multiple myeloma.* Cancer Res, 2014. **74**(1): p. 56-67.
274. Chauhan, D., et al., *Combination of novel proteasome inhibitor NPI-0052 and lenalidomide trigger in vitro and in vivo synergistic cytotoxicity in multiple myeloma.* Blood, 2010. **115**(4): p. 834-45.
275. Riccardi, C. and I. Nicoletti, *Analysis of apoptosis by propidium iodide staining and flow cytometry.* Nat Protoc, 2006. **1**(3): p. 1458-61.
276. Wlodkowic, D., et al., *Apoptosis and beyond: cytometry in studies of programmed cell death.* Methods Cell Biol, 2011. **103**: p. 55-98.
277. Kroemer, G., B. Dallaporta, and M. Resche-Rigon, *The mitochondrial death/life regulator in apoptosis and necrosis.* Annu Rev Physiol, 1998. **60**: p. 619-42.
278. Livak, K.J. and T.D. Schmittgen, *Analysis of relative gene expression data using real-time quantitative PCR and the 2(-Delta Delta C(T)) Method.* Methods, 2001. **25**(4): p. 402-8.

279. Chou, T.C., *Drug combination studies and their synergy quantification using the Chou-Talalay method.* Cancer Res, 2010. **70**(2): p. 440-6.
280. Kazandjian, D. and O. Landgren, *A look backward and forward in the regulatory and treatment history of multiple myeloma: Approval of novel-novel agents, new drug development, and longer patient survival.* Semin Oncol, 2016. **43**(6): p. 682-689.
281. Lohr, J.G., et al., *Widespread genetic heterogeneity in multiple myeloma: implications for targeted therapy.* Cancer Cell, 2014. **25**(1): p. 91-101.
282. Ferlay, J., et al., *Cancer incidence and mortality patterns in Europe: Estimates for 40 countries and 25 major cancers in 2018.* Eur J Cancer, 2018. **103**: p. 356-387.
283. Cowan, A.J., et al., *Global Burden of Multiple Myeloma: A Systematic Analysis for the Global Burden of Disease Study 2016.* JAMA Oncol, 2018. **4**(9): p. 1221-1227.
284. Mikhael, J., et al., *Treatment of Multiple Myeloma: ASCO and CCO Joint Clinical Practice Guideline.* J Clin Oncol, 2019. **37**(14): p. 1228-1263.
285. Bolli, N., et al., *Heterogeneity of genomic evolution and mutational profiles in multiple myeloma.* Nat Commun, 2014. **5**: p. 2997.
286. Larocca, A., et al., *Emerging drugs and combinations to treat multiple myeloma.* Oncotarget, 2017. **8**(36): p. 60656-60672.
287. Kumar, S.K., et al., *Continued improvement in survival in multiple myeloma: changes in early mortality and outcomes in older patients.* Leukemia, 2014. **28**(5): p. 1122-8.
288. Kumar, S.K., et al., *Early relapse after autologous hematopoietic cell transplantation remains a poor prognostic factor in multiple myeloma but outcomes have improved over time.* Leukemia, 2018. **32**(4): p. 986-995.
289. San Miguel, J.F., *Introduction to a series of reviews on multiple myeloma.* Blood, 2015. **125**(20): p. 3039-40.
290. João, C., et al., *Long-term survival in multiple myeloma.* Clin Case Rep, 2014. **2**(5): p. 173-9.
291. Raza, S., et al., *Optimizing current and emerging therapies in multiple myeloma: a guide for the hematologist.* Ther Adv Hematol, 2017. **8**(2): p. 55-70.
292. Xu, J., et al., *Molecular signaling in multiple myeloma: association of RAS/RAF mutations and MEK/ERK pathway activation.* Oncogenesis, 2017. **6**(5): p. e337.
293. Dervisis, N. and S. Klahn, *Therapeutic Innovations: Tyrosine Kinase Inhibitors in Cancer.* Vet Sci, 2016. **3**(1).
294. Muñoz-Couselo, E., et al., *NRAS-mutant melanoma: current challenges and future prospect.* Onco Targets Ther, 2017. **10**: p. 3941-3947.
295. Amanuel, B., et al., *Incidence of BRAF p.Val600Glu and p.Val600Lys mutations in a consecutive series of 183 metastatic melanoma patients from a high incidence region.* Pathology, 2012. **44**(4): p. 357-9.
296. Raje, N., *Vemurafenib in Patients With Relapsed Refractory Multiple Myeloma Harboring BRAF^{V600} Mutations: A cohort of the Histology Independent VE-BASKET Study*, I. Chau, et al., Editors. 2018, American Society of Clinical Oncology: JCO^{TM} Precision Oncology.
297. Zhao, Z., L. Xie, and P.E. Bourne, *Insights into the binding mode of MEK type-III inhibitors. A step towards discovering and designing allosteric kinase inhibitors across the human kinome.* PLoS One, 2017. **12**(6): p. e0179936.
298. Kharaziha, P., et al., *Sorafenib has potent antitumor activity against multiple myeloma in vitro, ex vivo, and in vivo in the 5T33MM mouse model.* Cancer Res, 2012. **72**(20): p. 5348-62.
299. O'Brien, J., et al., *Investigation of the Alamar Blue (resazurin) fluorescent dye for the assessment of mammalian cell cytotoxicity.* Eur J Biochem, 2000. **267**(17): p. 5421-6.

300. Lavik, A.R., et al., *A synthetic peptide targeting the BH4 domain of Bcl-2 induces apoptosis in multiple myeloma and follicular lymphoma cells alone or in combination with agents targeting the BH3-binding pocket of Bcl-2.* Oncotarget, 2015. **6**(29): p. 27388-402.
301. Hamouda, M.A., et al., *The small heat shock protein B8 (HSPB8) confers resistance to bortezomib by promoting autophagic removal of misfolded proteins in multiple myeloma cells.* Oncotarget, 2014. **5**(15): p. 6252-66.
302. Weiss, C., et al., *Differential downregulation of telomerase activity by bortezomib in multiple myeloma cells-multiple regulatory pathways in vitro and ex vivo.* Br J Cancer, 2012. **107**(11): p. 1844-52.
303. Vermes, I., et al., *A novel assay for apoptosis. Flow cytometric detection of phosphatidylserine expression on early apoptotic cells using fluorescein labelled Annexin V.* J Immunol Methods, 1995. **184**(1): p. 39-51.
304. Neri, P. and N.J. Bahlis, *Genomic instability in multiple myeloma: mechanisms and therapeutic implications.* Expert Opin Biol Ther, 2013. **13 Suppl 1**: p. S69-82.
305. Hideshima, T., et al., *Understanding multiple myeloma pathogenesis in the bone marrow to identify new therapeutic targets.* Nat Rev Cancer, 2007. **7**(8): p. 585-98.
306. Maginn, E.N., et al., *PBOX-15, a novel microtubule targeting agent, induces apoptosis, upregulates death receptors, and potentiates TRAIL-mediated apoptosis in multiple myeloma cells.* Br J Cancer, 2011. **104**(2): p. 281-9.
307. Alexanian, R., et al., *Primary dexamethasone treatment of multiple myeloma.* Blood, 1992. **80**(4): p. 887-90.
308. Delforge, M. and H. Ludwig, *How I manage the toxicities of myeloma drugs.* Blood, 2017. **129**(17): p. 2359-2367.
309. Moalli, P.A., et al., *A mechanism of resistance to glucocorticoids in multiple myeloma: transient expression of a truncated glucocorticoid receptor mRNA.* Blood, 1992. **79**(1): p. 213-22.
310. Rychak, E., et al., *Pomalidomide in combination with dexamethasone results in synergistic anti-tumour responses in pre-clinical models of lenalidomide-resistant multiple myeloma.* Br J Haematol, 2016. **172**(6): p. 889-901.
311. Rees-Unwin, K.S., et al., *Proteomic evaluation of pathways associated with dexamethasone-mediated apoptosis and resistance in multiple myeloma.* Br J Haematol, 2007. **139**(4): p. 559-67.
312. Kervoëlen, C., et al., *Dexamethasone-induced cell death is restricted to specific molecular subgroups of multiple myeloma.* Oncotarget, 2015. **6**(29): p. 26922-34.
313. Burwick, N. and S. Sharma, *Glucocorticoids in multiple myeloma: past, present, and future.* Ann Hematol, 2019. **98**(1): p. 19-28.
314. Quach, H., A. Kalff, and A. Spencer, *Lenalidomide in multiple myeloma: Current status and future potential.* Am J Hematol, 2012. **87**(12): p. 1089-95.
315. Zhu, Y.X., et al., *Identification of lenalidomide resistance pathways in myeloma and targeted resensitization using cereblon replacement, inhibition of STAT3 or targeting of IRF4.* Blood Cancer J, 2019. **9**(2): p. 19.
316. Moros, A., et al., *Antitumoral activity of lenalidomide in in vitro and in vivo models of mantle cell lymphoma involves the destabilization of cyclin D1/p27KIP1 complexes.* Clin Cancer Res, 2014. **20**(2): p. 393-403.
317. Jonas, B.A. and D.A. Pollyea, *How we use venetoclax with hypomethylating agents for the treatment of newly diagnosed patients with acute myeloid leukemia.* Leukemia, 2019. **33**(12): p. 2795-2804.

318. Wierda, W.G. and F.P. Tambaro, *How I Manage CLL with Venetoclax-Based Treatments.* Blood, 2020.
319. Mihalyova, J., et al., *Venetoclax: A new wave in hematooncology.* Exp Hematol, 2018. **61**: p. 10-25.
320. Touzeau, C., et al., *The Bcl-2 specific BH3 mimetic ABT-199: a promising targeted therapy for t(11;14) multiple myeloma.* Leukemia, 2014. **28**(1): p. 210-2.
321. Matulis, S.M., et al., *Dexamethasone treatment promotes Bcl-2 dependence in multiple myeloma resulting in sensitivity to venetoclax.* Leukemia, 2016. **30**(5): p. 1086-93.
322. Valdez, B.C., et al., *Panobinostat and venetoclax enhance the cytotoxicity of gemcitabine, busulfan, and melphalan in multiple myeloma cells.* Exp Hematol, 2020.
323. Punnoose, E.A., et al., *Expression Profile of BCL-2, BCL-XL, and MCL-1 Predicts Pharmacological Response to the BCL-2 Selective Antagonist Venetoclax in Multiple Myeloma Models.* Mol Cancer Ther, 2016. **15**(5): p. 1132-44.
324. Touzeau, C., et al., *BH3 profiling identifies heterogeneous dependency on Bcl-2 family members in multiple myeloma and predicts sensitivity to BH3 mimetics.* Leukemia, 2016. **30**(3): p. 761-4.
325. Moreau, P., et al., *Promising efficacy and acceptable safety of venetoclax plus bortezomib and dexamethasone in relapsed/refractory MM.* Blood, 2017. **130**(22): p. 2392-2400.
326. Greenfield, G., et al., *The ruxolitinib effect: understanding how molecular pathogenesis and epigenetic dysregulation impact therapeutic efficacy in myeloproliferative neoplasms.* J Transl Med, 2018. **16**(1): p. 360.
327. San Miguel, J.F., et al., *Bortezomib plus melphalan and prednisone for initial treatment of multiple myeloma.* N Engl J Med, 2008. **359**(9): p. 906-17.
328. Murray, M.Y., M.J. Auger, and K.M. Bowles, *Overcoming bortezomib resistance in multiple myeloma.* Biochem Soc Trans, 2014. **42**(4): p. 804-8.
329. Shabaneh, T.B., et al., *Molecular basis of differential sensitivity of myeloma cells to clinically relevant bolus treatment with bortezomib.* PLoS One, 2013. **8**(2): p. e56132.
330. Dolloff, N.G., *Emerging Therapeutic Strategies for Overcoming Proteasome Inhibitor Resistance.* Adv Cancer Res, 2015. **127**: p. 191-226.
331. Ramakrishnan, V. and D.E. Mager, *Network-Based Analysis of Bortezomib Pharmacodynamic Heterogeneity in Multiple Myeloma Cells.* J Pharmacol Exp Ther, 2018. **365**(3): p. 734-751.
332. Darzynkiewicz, Z., H.D. Halicka, and H. Zhao, *Analysis of cellular DNA content by flow and laser scanning cytometry.* Adv Exp Med Biol, 2010. **676**: p. 137-47.
333. Galluzzi, L., et al., *Molecular definitions of cell death subroutines: recommendations of the Nomenclature Committee on Cell Death 2012.* Cell Death Differ, 2012. **19**(1): p. 107-20.
334. Candé, C., et al., *Apoptosis-inducing factor (AIF): caspase-independent after all.* Cell Death Differ, 2004. **11**(6): p. 591-5.
335. McCafferty-Grad, J., et al., *Arsenic trioxide uses caspase-dependent and caspase-independent death pathways in myeloma cells.* Mol Cancer Ther, 2003. **2**(11): p. 1155-64.
336. Rudolf, E., K. Rudolf, and M. Cervinka, *Selenium activates p53 and p38 pathways and induces caspase-independent cell death in cervical cancer cells.* Cell Biol Toxicol, 2008. **24**(2): p. 123-41.
337. Tor, Y.S., et al., *Induction of Apoptosis in MCF-7 Cells via Oxidative Stress Generation, Mitochondria-Dependent and Caspase-Independent Pathway by Ethyl Acetate Extract of Dillenia suffruticosa and Its Chemical Profile.* PLoS One, 2015. **10**(6): p. e0127441.
338. Barwick, B.G., et al., *Cell of Origin and Genetic Alterations in the Pathogenesis of Multiple Myeloma.* Front Immunol, 2019. **10**: p. 1121.

339. Dehghanifard, A., et al., *Various Signaling Pathways in Multiple Myeloma Cells and Effects of Treatment on These Pathways.* Clin Lymphoma Myeloma Leuk, 2018. **18**(5): p. 311-320.
340. Nefedova, Y., T.H. Landowski, and W.S. Dalton, *Bone marrow stromal-derived soluble factors and direct cell contact contribute to de novo drug resistance of myeloma cells by distinct mechanisms.* Leukemia, 2003. **17**(6): p. 1175-82.
341. Fowler, J.A., et al., *Bone marrow stromal cells create a permissive microenvironment for myeloma development: a new stromal role for Wnt inhibitor Dkk1.* Cancer Res, 2012. **72**(9): p. 2183-9.
342. Chang-Yew Leow, C., S. Gerondakis, and A. Spencer, *MEK inhibitors as a chemotherapeutic intervention in multiple myeloma.* Blood Cancer J, 2013. **3**: p. e105.
343. Chong, P., W. Chng, and S. De Mel, *STAT3: A promising therapeutic target in multiple myeloma*. 2019, MDPI: Cancers (Basel). p. 713.
344. Nishimoto, N., et al., *Oncostatin M, leukemia inhibitory factor, and interleukin 6 induce the proliferation of human plasmacytoma cells via the common signal transducer, gp130.* J Exp Med, 1994. **179**(4): p. 1343-7.
345. Wen, Z., Z. Zhong, and J.E. Darnell, *Maximal activation of transcription by Stat1 and Stat3 requires both tyrosine and serine phosphorylation.* Cell, 1995. **82**(2): p. 241-50.
346. Chung, J., et al., *STAT3 serine phosphorylation by ERK-dependent and -independent pathways negatively modulates its tyrosine phosphorylation.* Mol Cell Biol, 1997. **17**(11): p. 6508-16.
347. Silva, C.M., *Role of STATs as downstream signal transducers in Src family kinase-mediated tumorigenesis.* Oncogene, 2004. **23**(48): p. 8017-23.
348. Roskoski, R., *Src kinase regulation by phosphorylation and dephosphorylation.* Biochem Biophys Res Commun, 2005. **331**(1): p. 1-14.
349. Jourdan, M., et al., *A major role for Mcl-1 antiapoptotic protein in the IL-6-induced survival of human myeloma cells.* Oncogene, 2003. **22**(19): p. 2950-9.
350. Jourdan, M., et al., *Regulation of Bcl-2-family proteins in myeloma cells by three myeloma survival factors: interleukin-6, interferon-alpha and insulin-like growth factor 1.* Cell Death Differ, 2000. **7**(12): p. 1244-52.
351. Liu, T., et al., *Interleukin-6 and JAK2/STAT3 signaling mediate the reversion of dexamethasone resistance after dexamethasone withdrawal in 7TD1 multiple myeloma cells.* Leuk Res, 2013. **37**(10): p. 1322-8.
352. Li, J., et al., *INCB16562, a JAK1/2 selective inhibitor, is efficacious against multiple myeloma cells and reverses the protective effects of cytokine and stromal cell support.* Neoplasia, 2010. **12**(1): p. 28-38.
353. Yao, Y., et al., *Piperlongumine induces apoptosis and reduces bortezomib resistance by inhibiting STAT3 in multiple myeloma cells.* Oncotarget, 2016. **7**(45): p. 73497-73508.
354. Garcia, R., et al., *Constitutive activation of Stat3 by the Src and JAK tyrosine kinases participates in growth regulation of human breast carcinoma cells.* Oncogene, 2001. **20**(20): p. 2499-513.
355. Liau, N.P.D., et al., *The molecular basis of JAK/STAT inhibition by SOCS1.* Nat Commun, 2018. **9**(1): p. 1558.
356. Keats, J.J., et al., *Promiscuous mutations activate the noncanonical NF-kappaB pathway in multiple myeloma.* Cancer Cell, 2007. **12**(2): p. 131-44.
357. Annunziata, C.M., et al., *Frequent engagement of the classical and alternative NF-kappaB pathways by diverse genetic abnormalities in multiple myeloma.* Cancer Cell, 2007. **12**(2): p. 115-30.

358. Demchenko, Y.N. and W.M. Kuehl, *A critical role for the NFkB pathway in multiple myeloma.* Oncotarget, 2010. **1**(1): p. 59-68.
359. Demchenko, Y.N., et al., *Classical and/or alternative NF-kappaB pathway activation in multiple myeloma.* Blood, 2010. **115**(17): p. 3541-52.
360. Wang, Q., et al., *Potentiation of (-)-epigallocatechin-3-gallate-induced apoptosis by bortezomib in multiple myeloma cells.* Acta Biochim Biophys Sin (Shanghai), 2009. **41**(12): p. 1018-26.
361. Hideshima, T., et al., *Bortezomib induces canonical nuclear factor-kappaB activation in multiple myeloma cells.* Blood, 2009. **114**(5): p. 1046-52.
362. Al Zaid Siddiquee, K. and J. Turkson, *STAT3 as a target for inducing apoptosis in solid and hematological tumors.* Cell Res, 2008. **18**(2): p. 254-67.
363. Galm, O., et al., *SOCS-1, a negative regulator of cytokine signaling, is frequently silenced by methylation in multiple myeloma.* Blood, 2003. **101**(7): p. 2784-8.
364. Yu, C.L., et al., *Enhanced DNA-binding activity of a Stat3-related protein in cells transformed by the Src oncoprotein.* Science, 1995. **269**(5220): p. 81-3.
365. de Melo Campos, P., et al., *IRS2 silencing increases apoptosis and potentiates the effects of ruxolitinib in JAK2V617F-positive myeloproliferative neoplasms.* Oncotarget, 2016. **7**(6): p. 6948-59.
366. Han, E.S., et al., *Ruxolitinib synergistically enhances the anti-tumor activity of paclitaxel in human ovarian cancer.* Oncotarget, 2018. **9**(36): p. 24304-24319.
367. Denley, S.M., et al., *Activation of the IL-6R/Jak/stat pathway is associated with a poor outcome in resected pancreatic ductal adenocarcinoma.* J Gastrointest Surg, 2013. **17**(5): p. 887-98.
368. Ryu, Y., et al., *Caspase-dependent Mcl-1 cleavage and effect of Mcl-1 phosphorylation in ABT-737-induced apoptosis in human acute lymphoblastic leukemia cell lines.* Exp Biol Med (Maywood), 2014. **239**(10): p. 1390-402.
369. Kirsch, D.G., et al., *Caspase-3-dependent cleavage of Bcl-2 promotes release of cytochrome c.* J Biol Chem, 1999. **274**(30): p. 21155-61.
370. Lionetti, M., et al., *Molecular spectrum of BRAF, NRAS and KRAS gene mutations in plasma cell dyscrasias: implication for MEK-ERK pathway activation.* Oncotarget, 2015. **6**(27): p. 24205-17.
371. Elefantova, K., et al., *Detection of the Mitochondrial Membrane Potential by the Cationic Dye JC-1 in L1210 Cells with Massive Overexpression of the Plasma Membrane ABCB1 Drug Transporter.* Int J Mol Sci, 2018. **19**(7).
372. Hsiao, C.H., et al., *Honokiol induces apoptotic cell death by oxidative burst and mitochondrial hyperpolarization of bladder cancer cells.* Exp Ther Med, 2019. **17**(5): p. 4213-4222.
373. Yu, T., J.L. Robotham, and Y. Yoon, *Increased production of reactive oxygen species in hyperglycemic conditions requires dynamic change of mitochondrial morphology.* Proc Natl Acad Sci U S A, 2006. **103**(8): p. 2653-8.
374. Choi, K., et al., *Oxidative stress-induced necrotic cell death via mitochondira-dependent burst of reactive oxygen species.* Curr Neurovasc Res, 2009. **6**(4): p. 213-22.
375. Tong, Y., et al., *PI3K inhibitor LY294002 inhibits activation of the Akt/mTOR pathway induced by an oncolytic adenovirus expressing TRAIL and sensitizes multiple myeloma cells to the oncolytic virus.* Oncol Rep, 2014. **31**(4): p. 1581-8.
376. Song, I.S., et al., *Pharmacologic inhibition of AKT leads to cell death in relapsed multiple myeloma.* Cancer Lett, 2018. **432**: p. 205-215.

377. Kuttikrishnan, S., et al., *Curcumin Induces Apoptotic Cell Death via Inhibition of PI3-Kinase/AKT Pathway in B-Precursor Acute Lymphoblastic Leukemia.* Front Oncol, 2019. **9**: p. 484.
378. Rashmi, R., et al., *AKT inhibitors promote cell death in cervical cancer through disruption of mTOR signaling and glucose uptake.* PLoS One, 2014. **9**(4): p. e92948.
379. Chetram, M.A., et al., *ROS-mediated activation of AKT induces apoptosis via pVHL in prostate cancer cells.* Mol Cell Biochem, 2013. **376**(1-2): p. 63-71.
380. Chetram, M.A., A.S. Don-Salu-Hewage, and C.V. Hinton, *ROS enhances CXCR4-mediated functions through inactivation of PTEN in prostate cancer cells.* Biochem Biophys Res Commun, 2011. **410**(2): p. 195-200.
381. Nogueira, V., et al., *Akt determines replicative senescence and oxidative or oncogenic premature senescence and sensitizes cells to oxidative apoptosis.* Cancer Cell, 2008. **14**(6): p. 458-70.
382. Maddika, S., et al., *Akt is transferred to the nucleus of cells treated with apoptin, and it participates in apoptin-induced cell death.* Cell Prolif, 2007. **40**(6): p. 835-48.
383. Basso, A.D., et al., *Akt forms an intracellular complex with heat shock protein 90 (Hsp90) and Cdc37 and is destabilized by inhibitors of Hsp90 function.* J Biol Chem, 2002. **277**(42): p. 39858-66.
384. Su, C.H., et al., *Phosphorylation accelerates geldanamycin-induced Akt degradation.* Arch Biochem Biophys, 2013. **536**(1): p. 6-11.
385. Neri, P., et al., *Neutralizing B-cell activating factor antibody improves survival and inhibits osteoclastogenesis in a severe combined immunodeficient human multiple myeloma model.* Clin Cancer Res, 2007. **13**(19): p. 5903-9.
386. Meinel, F.G., et al., *The novel, proteasome-independent NF-kappaB inhibitor V1810 induces apoptosis and cell cycle arrest in multiple myeloma and overcomes NF-kappaB-mediated drug resistance.* Mol Cancer Ther, 2010. **9**(2): p. 300-10.
387. Kawaguchi, T., et al., *Combined treatment with bortezomib plus bafilomycin A1 enhances the cytocidal effect and induces endoplasmic reticulum stress in U266 myeloma cells: crosstalk among proteasome, autophagy-lysosome and ER stress.* Int J Oncol, 2011. **38**(3): p. 643-54.
388. Johnston, P.A. and J.R. Grandis, *STAT3 signaling: anticancer strategies and challenges.* Mol Interv, 2011. **11**(1): p. 18-26.
389. Lin, L., et al., *A small molecule, LLL12 inhibits constitutive STAT3 and IL-6-induced STAT3 signaling and exhibits potent growth suppressive activity in human multiple myeloma cells.* Int J Cancer, 2012. **130**(6): p. 1459-69.
390. Alas, S. and B. Bonavida, *Inhibition of constitutive STAT3 activity sensitizes resistant non-Hodgkin's lymphoma and multiple myeloma to chemotherapeutic drug-mediated apoptosis.* Clin Cancer Res, 2003. **9**(1): p. 316-26.
391. Bill, M.A., et al., *The small molecule curcumin analog FLLL32 induces apoptosis in melanoma cells via STAT3 inhibition and retains the cellular response to cytokines with anti-tumor activity.* Mol Cancer, 2010. **9**: p. 165.
392. Li, Y., et al., *Inhibition of Stat3 Signaling Pathway by Natural Product Pectolinarigenin Attenuates Breast Cancer Metastasis.* Front Pharmacol, 2019. **10**: p. 1195.
393. Huang, C., et al., *Inhibition of STAT3 activity with AG490 decreases the invasion of human pancreatic cancer cells in vitro.* Cancer Sci, 2006. **97**(12): p. 1417-23.
394. Horiguchi, A., et al., *STAT3 inhibitor WP1066 as a novel therapeutic agent for renal cell carcinoma.* Br J Cancer, 2010. **102**(11): p. 1592-9.

395. Wang, Y., et al., *YL064 directly inhibits STAT3 activity to induce apoptosis of multiple myeloma cells.* Cell Death Discov, 2018. **4**: p. 44.
396. Ball, S., et al., *The small molecule, LLL12, inhibits STAT3 phosphorylation and induces apoptosis in medulloblastoma and glioblastoma cells.* PLoS One, 2011. **6**(4): p. e18820.
397. Wei, C.C., et al., *Two small molecule compounds, LLL12 and FLLL32, exhibit potent inhibitory activity on STAT3 in human rhabdomyosarcoma cells.* Int J Oncol, 2011. **38**(1): p. 279-85.
398. Onimoe, G.I., et al., *Small molecules, LLL12 and FLLL32, inhibit STAT3 and exhibit potent growth suppressive activity in osteosarcoma cells and tumor growth in mice.* Invest New Drugs, 2012. **30**(3): p. 916-26.
399. Lin, L., et al., *A novel small molecule, LLL12, inhibits STAT3 phosphorylation and activities and exhibits potent growth-suppressive activity in human cancer cells.* Neoplasia, 2010. **12**(1): p. 39-50.
400. Hurwitz, H.I., et al., *Randomized, Double-Blind, Phase II Study of Ruxolitinib or Placebo in Combination With Capecitabine in Patients With Metastatic Pancreatic Cancer for Whom Therapy With Gemcitabine Has Failed.* J Clin Oncol, 2015. **33**(34): p. 4039-47.
401. Berenson, J.R., et al., *A Phase 1 Study of Ruxolitinib, Lenalidomide and Steroids for Patients with Relapsed/Refractory Multiple Myeloma.* Clin Cancer Res, 2020.
402. Suryani, S., et al., *Evaluation of the in vitro and in vivo efficacy of the JAK inhibitor AZD1480 against JAK-mutated acute lymphoblastic leukemia.* Mol Cancer Ther, 2015. **14**(2): p. 364-74.
403. Holstein, S.A., H. Tong, and R.J. Hohl, *Differential activities of thalidomide and isoprenoid biosynthetic pathway inhibitors in multiple myeloma cells.* Leuk Res, 2010. **34**(3): p. 344-51.
404. Bolick, S.C., et al., *The farnesyl transferase inhibitor, FTI-277, inhibits growth and induces apoptosis in drug-resistant myeloma tumor cells.* Leukemia, 2003. **17**(2): p. 451-7.
405. Steinbrunn, T., et al., *Mutated RAS and constitutively activated Akt delineate distinct oncogenic pathways, which independently contribute to multiple myeloma cell survival.* Blood, 2011. **117**(6): p. 1998-2004.
406. Yue, Z., et al., *p53 Deletion promotes myeloma cells invasion by upregulating miR19a/CXCR5.* Leuk Res, 2017. **60**: p. 115-122.
407. Kortuem, K.M., et al., *Panel sequencing for clinically oriented variant screening and copy number detection in 142 untreated multiple myeloma patients.* Blood Cancer J, 2016. **6**: p. e397.
408. Chim, C.S., et al., *SOCS1 and SHP1 hypermethylation in multiple myeloma: implications for epigenetic activation of the Jak/STAT pathway.* Blood, 2004. **103**(12): p. 4630-5.
409. Kim, J.H. and B. Park, *Triptolide blocks the STAT3 signaling pathway through induction of protein tyrosine phosphatase SHP-1 in multiple myeloma cells.* Int J Mol Med, 2017. **40**(5): p. 1566-1572.
410. Jiang, M., et al., *Dysregulation of SOCS-Mediated Negative Feedback of Cytokine Signaling in Carcinogenesis and Its Significance in Cancer Treatment.* Front Immunol, 2017. **8**: p. 70.
411. Bhardwaj, A., et al., *Resveratrol inhibits proliferation, induces apoptosis, and overcomes chemoresistance through down-regulation of STAT3 and nuclear factor-kappaB-regulated antiapoptotic and cell survival gene products in human multiple myeloma cells.* Blood, 2007. **109**(6): p. 2293-302.
412. Baek, S.H., et al., *Resveratrol inhibits STAT3 signaling pathway through the induction of SOCS-1: Role in apoptosis induction and radiosensitization in head and neck tumor cells.* Phytomedicine, 2016. **23**(5): p. 566-77.

413. Cooper, J.A., et al., *Tyr527 is phosphorylated in pp60c-src: implications for regulation.* Science, 1986. **231**(4744): p. 1431-4.
414. Tang, H., et al., *Inactivation of SRC family tyrosine kinases by reactive oxygen species in vivo.* J Biol Chem, 2005. **280**(25): p. 23918-25.
415. Hakak, Y. and G.S. Martin, *Ubiquitin-dependent degradation of active Src.* Curr Biol, 1999. **9**(18): p. 1039-42.
416. Laszlo, G.S. and J.A. Cooper, *Restriction of Src activity by Cullin-5.* Curr Biol, 2009. **19**(2): p. 157-62.
417. Monaghan, K.A., et al., *The novel JAK inhibitor CYT387 suppresses multiple signalling pathways, prevents proliferation and induces apoptosis in phenotypically diverse myeloma cells.* Leukemia, 2011. **25**(12): p. 1891-9.
418. Gonsalves, W.I., et al., *The prognostic significance of CD45 expression by clonal bone marrow plasma cells in patients with newly diagnosed multiple myeloma.* Leuk Res, 2016. **44**: p. 32-9.
419. Quintás-Cardama, A., et al., *Preclinical characterization of the selective JAK1/2 inhibitor INCB018424: therapeutic implications for the treatment of myeloproliferative neoplasms.* Blood, 2010. **115**(15): p. 3109-17.
420. Lee, S., et al., *Ruxolitinib significantly enhances in vitro apoptosis in Hodgkin lymphoma and primary mediastinal B-cell lymphoma and survival in a lymphoma xenograft murine model.* Oncotarget, 2018. **9**(11): p. 9776-9788.
421. Sun, X., et al., *DCZ3301, a novel cytotoxic agent, inhibits proliferation in diffuse large B-cell lymphoma via the STAT3 pathway.* Cell Death Dis, 2017. **8**(10): p. e3111.
422. Gao, M., et al., *Preclinical activity of DCZ3301, a novel aryl-guanidino compound in the therapy of multiple myeloma.* Theranostics, 2017. **7**(15): p. 3690-3699.
423. Zhang, S., et al., *The novel histone deacetylase inhibitor, AR-42, inhibits gp130/Stat3 pathway and induces apoptosis and cell cycle arrest in multiple myeloma cells.* Int J Cancer, 2011. **129**(1): p. 204-13.
424. Vermes, C., et al., *Shedding of the interleukin-6 (IL-6) receptor (gp80) determines the ability of IL-6 to induce gp130 phosphorylation in human osteoblasts.* J Biol Chem, 2002. **277**(19): p. 16879-87.
425. Thiel, S., et al., *Termination of IL-6-induced STAT activation is independent of receptor internalization but requires de novo protein synthesis.* FEBS Lett, 2000. **470**(1): p. 15-9.
426. Jiang, X.P., et al., *Down-regulation of expression of interleukin-6 and its receptor results in growth inhibition of MCF-7 breast cancer cells.* Anticancer Res, 2011. **31**(9): p. 2899-906.
427. Müllberg, J., et al., *The soluble interleukin-6 receptor is generated by shedding.* Eur J Immunol, 1993. **23**(2): p. 473-80.
428. Jostock, T., et al., *Soluble gp130 is the natural inhibitor of soluble interleukin-6 receptor transsignaling responses.* Eur J Biochem, 2001. **268**(1): p. 160-7.
429. Bauer, J., et al., *Regulation of interleukin-6 receptor expression in human monocytes and hepatocytes.* FEBS Lett, 1989. **249**(1): p. 27-30.
430. O'Brien, C.A. and S.C. Manolagas, *Isolation and characterization of the human gp130 promoter. Regulation by STATS.* J Biol Chem, 1997. **272**(23): p. 15003-10.
431. Alvarez, J.V. and D.A. Frank, *Genome-wide analysis of STAT target genes: elucidating the mechanism of STAT-mediated oncogenesis.* Cancer Biol Ther, 2004. **3**(11): p. 1045-50.
432. Slomp, A. and V. Peperzak, *Role and Regulation of Pro-survival BCL-2 Proteins in Multiple Myeloma.* Front Oncol, 2018. **8**: p. 533.
433. Belmar, J. and S.W. Fesik, *Small molecule Mcl-1 inhibitors for the treatment of cancer.* Pharmacol Ther, 2015. **145**: p. 76-84.

434. Gomez-Bougie, P., et al., *Noxa up-regulation and Mcl-1 cleavage are associated to apoptosis induction by bortezomib in multiple myeloma.* Cancer Res, 2007. **67**(11): p. 5418-24.
435. Clohessy, J.G., J. Zhuang, and H.J. Brady, *Characterisation of Mcl-1 cleavage during apoptosis of haematopoietic cells.* Br J Haematol, 2004. **125**(5): p. 655-65.
436. Han, J., et al., *Disruption of Mcl-1.Bim complex in granzyme B-mediated mitochondrial apoptosis.* J Biol Chem, 2005. **280**(16): p. 16383-92.
437. Longo, P.G., et al., *The Akt/Mcl-1 pathway plays a prominent role in mediating antiapoptotic signals downstream of the B-cell receptor in chronic lymphocytic leukemia B cells.* Blood, 2008. **111**(2): p. 846-55.
438. Wang, J.M., et al., *The antiapoptotic gene mcl-1 is up-regulated by the phosphatidylinositol 3-kinase/Akt signaling pathway through a transcription factor complex containing CREB.* Mol Cell Biol, 1999. **19**(9): p. 6195-206.
439. Mi, Z., et al., *Bcl-2-mediated potentiation of neocarzinostatin-induced apoptosis: requirement for caspase-3, sulfhydryl groups, and cleavable Bcl-2.* Cancer Chemother Pharmacol, 2006. **57**(3): p. 357-67.
440. Stewart, D.P., et al., *Ubiquitin-independent degradation of antiapoptotic MCL-1.* Mol Cell Biol, 2010. **30**(12): p. 3099-110.
441. Akhtar, S., et al., *Sanguinarine Induces Apoptosis Pathway in Multiple Myeloma Cell Lines via Inhibition of the JaK2/STAT3 Signaling.* Front Oncol, 2019. **9**: p. 285.
442. Pathak, A.K., et al., *Ursolic acid inhibits STAT3 activation pathway leading to suppression of proliferation and chemosensitization of human multiple myeloma cells.* Mol Cancer Res, 2007. **5**(9): p. 943-55.
443. DeHaan, R.D., E.M. Yazlovitskaya, and D.L. Persons, *Regulation of p53 target gene expression by cisplatin-induced extracellular signal-regulated kinase.* Cancer Chemother Pharmacol, 2001. **48**(5): p. 383-8.
444. Tang, D., et al., *ERK activation mediates cell cycle arrest and apoptosis after DNA damage independently of p53.* J Biol Chem, 2002. **277**(15): p. 12710-7.
445. Bacus, S.S., et al., *Taxol-induced apoptosis depends on MAP kinase pathways (ERK and p38) and is independent of p53.* Oncogene, 2001. **20**(2): p. 147-55.
446. Shenoy, K., Y. Wu, and S. Pervaiz, *LY303511 enhances TRAIL sensitivity of SHEP-1 neuroblastoma cells via hydrogen peroxide-mediated mitogen-activated protein kinase activation and up-regulation of death receptors.* Cancer Res, 2009. **69**(5): p. 1941-50.
447. Burotto, M., et al., *The MAPK pathway across different malignancies: a new perspective.* Cancer, 2014. **120**(22): p. 3446-56.
448. Liu, J., et al., *p38 MAPK signaling mediates mitochondrial apoptosis in cancer cells induced by oleanolic acid.* Asian Pac J Cancer Prev, 2014. **15**(11): p. 4519-25.
449. Hideshima, T., et al., *Biologic sequelae of c-Jun NH(2)-terminal kinase (JNK) activation in multiple myeloma cell lines.* Oncogene, 2003. **22**(54): p. 8797-801.
450. Hideshima, T., et al., *Molecular mechanisms mediating antimyeloma activity of proteasome inhibitor PS-341.* Blood, 2003. **101**(4): p. 1530-4.
451. Xie, B., et al., *Pterostilbene Inhibits Human Multiple Myeloma Cells via ERK1/2 and JNK Pathway In Vitro and In Vivo.* Int J Mol Sci, 2016. **17**(11).
452. Hideshima, T., et al., *p38 MAPK inhibition enhances PS-341 (bortezomib)-induced cytotoxicity against multiple myeloma cells.* Oncogene, 2004. **23**(54): p. 8766-76.
453. Ishitsuka, K., et al., *p38 mitogen-activated protein kinase inhibitor LY2228820 enhances bortezomib-induced cytotoxicity and inhibits osteoclastogenesis in multiple myeloma; therapeutic implications.* Br J Haematol, 2008. **141**(5): p. 598-606.

454. Hideshima, T., et al., *Targeting p38 MAPK inhibits multiple myeloma cell growth in the bone marrow milieu.* Blood, 2003. **101**(2): p. 703-5.
455. Nguyen, A.N., et al., *Normalizing the bone marrow microenvironment with p38 inhibitor reduces multiple myeloma cell proliferation and adhesion and suppresses osteoclast formation.* Exp Cell Res, 2006. **312**(10): p. 1909-23.
456. Seo, S.K., et al., *Sulindac-derived reactive oxygen species induce apoptosis of human multiple myeloma cells via p38 mitogen activated protein kinase-induced mitochondrial dysfunction.* Apoptosis, 2007. **12**(1): p. 195-209.
457. Zhen, Y.Z., et al., *Enediyne lidamycin induces apoptosis in human multiple myeloma cells through activation of p38 mitogen-activated protein kinase and c-Jun NH2-terminal kinase.* Int J Hematol, 2009. **90**(1): p. 44-51.
458. Kobayashi, T., et al., *Galectin-9 exhibits anti-myeloma activity through JNK and p38 MAP kinase pathways.* Leukemia, 2010. **24**(4): p. 843-50.
459. Sun, Y., et al., *Signaling pathway of MAPK/ERK in cell proliferation, differentiation, migration, senescence and apoptosis.* J Recept Signal Transduct Res, 2015. **35**(6): p. 600-4.
460. Zhai, B., et al., *Inhibition of Akt reverses the acquired resistance to sorafenib by switching protective autophagy to autophagic cell death in hepatocellular carcinoma.* Mol Cancer Ther, 2014. **13**(6): p. 1589-98.
461. Ohta, T., et al., *The Akt and ERK activation by platinum-based chemotherapy in ovarian cancer is associated with favorable patient outcome.* Anticancer Res, 2009. **29**(11): p. 4639-47.
462. Tian, Z.J. and W. An, *ERK1/2 contributes negative regulation to STAT3 activity in HSS-transfected HepG2 cells.* Cell Res, 2004. **14**(2): p. 141-7.
463. Sengupta, T.K., et al., *Rapid inhibition of interleukin-6 signaling and Stat3 activation mediated by mitogen-activated protein kinases.* Proc Natl Acad Sci U S A, 1998. **95**(19): p. 11107-12.
464. Gkouveris, I., et al., *Erk1/2 activation and modulation of STAT3 signaling in oral cancer.* Oncol Rep, 2014. **32**(5): p. 2175-82.
465. Wei, X., et al., *Inhibiting JNK dephosphorylation and induction of apoptosis by novel anticancer agent NSC-741909 in cancer cells.* J Biol Chem, 2009. **284**(25): p. 16948-55.
466. Guo, W., et al., *Antitumor activity of a novel oncrasin analogue is mediated by JNK activation and STAT3 inhibition.* PLoS One, 2011. **6**(12): p. e28487.
467. Zorov, D.B., M. Juhaszova, and S.J. Sollott, *Mitochondrial reactive oxygen species (ROS) and ROS-induced ROS release.* Physiol Rev, 2014. **94**(3): p. 909-50.
468. Arihara, Y., et al., *Small molecule CP-31398 induces reactive oxygen species-dependent apoptosis in human multiple myeloma.* Oncotarget, 2017. **8**(39): p. 65889-65899.
469. Jang, K.Y., et al., *Activation of reactive oxygen species/AMP activated protein kinase signaling mediates fisetin-induced apoptosis in multiple myeloma U266 cells.* Cancer Lett, 2012. **319**(2): p. 197-202.
470. Mizutani, H., et al., *Mechanism of apoptosis induced by doxorubicin through the generation of hydrogen peroxide.* Life Sci, 2005. **76**(13): p. 1439-53.
471. Ruefli, A.A., et al., *The histone deacetylase inhibitor and chemotherapeutic agent suberoylanilide hydroxamic acid (SAHA) induces a cell-death pathway characterized by cleavage of Bid and production of reactive oxygen species.* Proc Natl Acad Sci U S A, 2001. **98**(19): p. 10833-8.
472. Salem, K., et al., *Combination chemotherapy increases cytotoxicity of multiple myeloma cells by modification of nuclear factor (NF)-κB activity.* Exp Hematol, 2013. **41**(2): p. 209-18.

473. Son, Y., et al., *Mitogen-Activated Protein Kinases and Reactive Oxygen Species: How Can ROS Activate MAPK Pathways?* J Signal Transduct, 2011. **2011**: p. 792639.
474. Kazandjian, D., *Multiple myeloma epidemiology and survival: A unique malignancy.* Semin Oncol, 2016. **43**(6): p. 676-681.
475. Pinto, V., et al., *Multiple Myeloma: Available Therapies and Causes of Drug Resistance.* Cancers (Basel), 2020. **12**(2).
476. Fonseca, R., et al., *Trends in overall survival and costs of multiple myeloma, 2000-2014.* Leukemia, 2017. **31**(9): p. 1915-1921.
477. Sonneveld, P., et al., *Treatment of multiple myeloma with high-risk cytogenetics: a consensus of the International Myeloma Working Group.* Blood, 2016. **127**(24): p. 2955-62.
478. Bianchi, G., P.G. Richardson, and K.C. Anderson, *Best treatment strategies in high-risk multiple myeloma: navigating a gray area.* J Clin Oncol, 2014. **32**(20): p. 2125-32.
479. Pandey MK, et al., *Resistance in Multiple Myeloma: How to Cross the Border*. 2015: Annals of Hematology and Oncology. p. 1025.
480. Grogan, T.M., et al., *P-glycoprotein expression in human plasma cell myeloma: correlation with prior chemotherapy.* Blood, 1993. **81**(2): p. 490-5.
481. Li, C., et al., *Bortezomib up-regulates activated signal transducer and activator of transcription-3 and synergizes with inhibitors of signal transducer and activator of transcription-3 to promote head and neck squamous cell carcinoma cell death.* Mol Cancer Ther, 2009. **8**(8): p. 2211-20.
482. Wan, S., et al., *BMP9 regulates cross-talk between breast cancer cells and bone marrow-derived mesenchymal stem cells.* Cell Oncol (Dordr), 2014. **37**(5): p. 363-75.
483. Windus, L.C., T.T. Glover, and V.M. Avery, *Bone-stromal cells up-regulate tumourigenic markers in a tumour-stromal 3D model of prostate cancer.* Mol Cancer, 2013. **12**(1): p. 112.
484. Ramasamy, K., et al., *Fluorescence-based experimental model to evaluate the concomitant effect of drugs on the tumour microenvironment and cancer cells.* Br J Haematol, 2012. **157**(5): p. 564-79.
485. Perez, L.E., et al., *Bone marrow stroma confers resistance to Apo2 ligand/TRAIL in multiple myeloma in part by regulating c-FLIP.* J Immunol, 2008. **180**(3): p. 1545-55.
486. Furukawa, Y. and J. Kikuchi, *Epigenetic mechanisms of cell adhesion-mediated drug resistance in multiple myeloma.* Int J Hematol, 2016. **104**(3): p. 281-92.
487. Damiano, J.S., et al., *Cell adhesion mediated drug resistance (CAM-DR): role of integrins and resistance to apoptosis in human myeloma cell lines.* Blood, 1999. **93**(5): p. 1658-67.
488. Hao, M., et al., *Bone marrow stromal cells protect myeloma cells from bortezomib induced apoptosis by suppressing microRNA-15a expression.* Leuk Lymphoma, 2011. **52**(9): p. 1787-94.
489. Ottina, E., M. Pellegrini, and A. Villunger, *Guarding effector T-cell survival: all for one, Mcl-1 for all?* Cell Death Differ, 2013. **20**(8): p. 969-71.
490. Vikstrom, I., et al., *Mcl-1 is essential for germinal center formation and B cell memory.* Science, 2010. **330**(6007): p. 1095-9.
491. Sathe, P., et al., *Innate immunodeficiency following genetic ablation of Mcl1 in natural killer cells.* Nat Commun, 2014. **5**: p. 4539.
492. Merz, M., et al., *Prognostic significance of cytogenetic heterogeneity in patients with newly diagnosed multiple myeloma.* Blood Adv, 2018. **2**(1): p. 1-9.
493. Alanazi, F., et al., *New Generation Drugs for Treatment of Multiple Myeloma*. 2020: Drug Discovery Today.

494. Dingli, D., et al., *Therapy for Relapsed Multiple Myeloma: Guidelines From the Mayo Stratification for Myeloma and Risk-Adapted Therapy.* Mayo Clin Proc, 2017. **92**(4): p. 578-598.
495. O'Dwyer, M., et al., *CyBorD-DARA is potent initial induction for MM and enhances ADCP: initial results of the 16-BCNI-001/CTRIAL-IE 16-02 study.* Blood Adv, 2019. **3**(12): p. 1815-1825.
496. Hu, Y., et al., *Inhibition of the JAK/STAT pathway with ruxolitinib overcomes cisplatin resistance in non-small-cell lung cancer NSCLC.* Apoptosis, 2014. **19**(11): p. 1627-36.
497. Seo, H.S., et al., *SH003 reverses drug resistance by blocking signal transducer and activator of transcription 3 (STAT3) signaling in breast cancer cells.* Biosci Rep, 2017. **37**(6).
498. Farrell, M.L. and M.R. Reagan, *Soluble and Cell-Cell-Mediated Drivers of Proteasome Inhibitor Resistance in Multiple Myeloma.* Front Endocrinol (Lausanne), 2018. **9**: p. 218.
499. Hu, J., et al., *Activation of ATF4 mediates unwanted Mcl-1 accumulation by proteasome inhibition.* Blood, 2012. **119**(3): p. 826-37.
500. Nencioni, A., et al., *Evidence for a protective role of Mcl-1 in proteasome inhibitor-induced apoptosis.* Blood, 2005. **105**(8): p. 3255-62.
501. Voorhees, P.M., et al., *Inhibition of interleukin-6 signaling with CNTO 328 enhances the activity of bortezomib in preclinical models of multiple myeloma.* Clin Cancer Res, 2007. **13**(21): p. 6469-78.
502. Zhang, Y., et al., *Mcl-1 downregulation sensitizes glioma to bortezomib-induced apoptosis.* Oncol Rep, 2015. **33**(5): p. 2277-84.
503. Tron, A.E., et al., *Discovery of Mcl-1-specific inhibitor AZD5991 and preclinical activity in multiple myeloma and acute myeloid leukemia.* Nat Commun, 2018. **9**(1): p. 5341.
504. Kim, S.H., et al., *Janus activated kinase 2/signal transducer and activator of transcription 3 pathway mediates icariside II-induced apoptosis in U266 multiple myeloma cells.* Eur J Pharmacol, 2011. **654**(1): p. 10-6.
505. Kim, H.J., et al., *Decursin chemosensitizes human multiple myeloma cells through inhibition of STAT3 signaling pathway.* Cancer Lett, 2011. **301**(1): p. 29-37.
506. Nam, D., et al., *8-hydrocalamenene, derived from Reynoutria elliptica, suppresses constitutive STAT3 activation, inhibiting proliferation and enhancing chemosensitization of human multiple myeloma cells.* J Med Food, 2014. **17**(3): p. 365-73.
507. Lee, J.H., et al., *Farnesol inhibits tumor growth and enhances the anticancer effects of bortezomib in multiple myeloma xenograft mouse model through the modulation of STAT3 signaling pathway.* Cancer Lett, 2015. **360**(2): p. 280-93.
508. Lee, J.H., et al., *Arctiin is a pharmacological inhibitor of STAT3 phosphorylation at tyrosine 705 residue and potentiates bortezomib-induced apoptotic and anti-angiogenic effects in human multiple myeloma cells.* Phytomedicine, 2019. **55**: p. 282-292.
509. Jung, Y.Y., et al., *Anti-myeloma Effects of Icariin Are Mediated Through the Attenuation of JAK/STAT3-Dependent Signaling Cascade.* Front Pharmacol, 2018. **9**: p. 531.
510. Ren, J., et al., *Human MUC1 carcinoma-associated protein confers resistance to genotoxic anticancer agents.* Cancer Cell, 2004. **5**(2): p. 163-75.
511. Tagde, A., et al., *MUC1-C drives MYC in multiple myeloma.* Blood, 2016. **127**(21): p. 2587-97.
512. Kawano, T., et al., *MUC1 oncoprotein promotes growth and survival of human multiple myeloma cells.* Int J Oncol, 2008. **33**(1): p. 153-9.
513. Yin, L., et al., *Targeting MUC1-C is synergistic with bortezomib in downregulating TIGAR and inducing ROS-mediated myeloma cell death.* Blood, 2014. **123**(19): p. 2997-3006.

514. Feng, Y., et al., *Bone marrow stromal cells from myeloma patients support the growth of myeloma stem cells.* Stem Cells Dev, 2010. **19**(9): p. 1289-96.
515. Pedranzini, L., et al., *Pyridone 6, a pan-Janus-activated kinase inhibitor, induces growth inhibition of multiple myeloma cells.* Cancer Res, 2006. **66**(19): p. 9714-21.
516. Burger, R., et al., *Janus kinase inhibitor INCB20 has antiproliferative and apoptotic effects on human myeloma cells in vitro and in vivo.* Mol Cancer Ther, 2009. **8**(1): p. 26-35.
517. Sakai, H., et al., *Effects of anticancer agents on cell viability, proliferative activity and cytokine production of peripheral blood mononuclear cells.* J Clin Biochem Nutr, 2013. **52**(1): p. 64-71.
518. Kotschy, A., et al., *The MCL1 inhibitor S63845 is tolerable and effective in diverse cancer models.* Nature, 2016. **538**(7626): p. 477-482.
519. Bharti, A.C., et al., *Nuclear factor-kappaB and STAT3 are constitutively active in CD138+ cells derived from multiple myeloma patients, and suppression of these transcription factors leads to apoptosis.* Blood, 2004. **103**(8): p. 3175-84.
520. Walker, B.A., et al., *Intraclonal heterogeneity is a critical early event in the development of myeloma and precedes the development of clinical symptoms.* Leukemia, 2014. **28**(2): p. 384-390.
521. Cuffe, C., *Patients' experience of living with multiple myeloma*. 2020, Mark Allen Publishing Ltd: British Journal of Nursing.
522. Boyle, E.M., et al., *Understanding the multiple biological aspects leading to myeloma.* Haematologica, 2014. **99**(4): p. 605-12.
523. Pertesi, M., et al., *Genetic predisposition for multiple myeloma.* Leukemia, 2020.
524. Wei, X., et al., *Germline Lysine-Specific Demethylase 1 (LSD1/KDM1) Mutations Confer Susceptibility to Multiple Myeloma.* Cancer Res, 2018. **78**(10): p. 2747-2759.
525. Corre, J., et al., *Multiple myeloma clonal evolution in homogeneously treated patients.* Leukemia, 2018. **32**(12): p. 2636-2647.
526. Quintanilla-Martinez, L., et al., *Analysis of signal transducer and activator of transcription 3 (Stat 3) pathway in multiple myeloma: Stat 3 activation and cyclin D1 dysregulation are mutually exclusive events.* Am J Pathol, 2003. **162**(5): p. 1449-61.
527. Jung, S.H., et al., *STAT3 expression is associated with poor survival in non-elderly adult patients with newly diagnosed multiple myeloma.* Blood Res, 2017. **52**(4): p. 293-299.
528. Vikova, V., et al., *Comprehensive characterization of the mutational landscape in multiple myeloma cell lines reveals potential drivers and pathways associated with tumor progression and drug resistance.* Theranostics, 2019. **9**(2): p. 540-553.
529. Segatto, I., G. Baldassarre, and B. Belletti, *STAT3 in Breast Cancer Onset and Progression: A Matter of Time and Context.* Int J Mol Sci, 2018. **19**(9).
530. Corcoran, R.B., et al., *STAT3 plays a critical role in KRAS-induced pancreatic tumorigenesis.* Cancer Res, 2011. **71**(14): p. 5020-9.
531. Wang, Z., et al., *Activation of STAT3 in human gastric cancer cells via interleukin (IL)-6-type cytokine signaling correlates with clinical implications.* PLoS One, 2013. **8**(10): p. e75788.
532. Ganguly, D., et al., *The critical role that STAT3 plays in glioma-initiating cells: STAT3 addiction in glioma.* Oncotarget, 2018. **9**(31): p. 22095-22112.
533. Wu, P., et al., *Prognostic role of STAT3 in solid tumors: a systematic review and meta-analysis.* Oncotarget, 2016. **7**(15): p. 19863-83.
534. Wu, M., et al., *Negative regulators of STAT3 signaling pathway in cancers.* Cancer Manag Res, 2019. **11**: p. 4957-4969.

535. Beldi-Ferchiou, A., et al., *Abnormal repression of SHP-1, SHP-2 and SOCS-1 transcription sustains the activation of the JAK/STAT3 pathway and the progression of the disease in multiple myeloma.* PLoS One, 2017. **12**(4): p. e0174835.
536. Malara, N., et al., *Simultaneous inhibition of the constitutively activated nuclear factor kappaB and of the interleukin-6 pathways is necessary and sufficient to completely overcome apoptosis resistance of human U266 myeloma cells.* Cell Cycle, 2008. **7**(20): p. 3235-45.
537. Xu, H., et al., *Tumor-derived mesenchymal-stem-cell-secreted IL-6 enhances resistance to cisplatin via the STAT3 pathway in breast cancer.* Oncol Lett, 2018. **15**(6): p. 9142-9150.
538. Morgan, E.L. and A. Macdonald, *JAK2 Inhibition Impairs Proliferation and Sensitises Cervical Cancer Cells to Cisplatin-Induced Cell Death.* Cancers (Basel), 2019. **11**(12).
539. Ji, T., et al., *Abrogation of constitutive Stat3 activity circumvents cisplatin resistant ovarian cancer.* Cancer Lett, 2013. **341**(2): p. 231-9.
540. Hardin, J., et al., *Interleukin-6 prevents dexamethasone-induced myeloma cell death.* Blood, 1994. **84**(9): p. 3063-70.
541. Hönemann, D., et al., *The IL-6 receptor antagonist SANT-7 overcomes bone marrow stromal cell-mediated drug resistance of multiple myeloma cells.* Int J Cancer, 2001. **93**(5): p. 674-80.
542. Tatekawa, S., et al., *Epigenetic repression of miR-375 is the dominant mechanism for constitutive activation of the PDPK1/RPS6KA3 signalling axis in multiple myeloma.* Br J Haematol, 2017. **178**(4): p. 534-546.
543. Zhang, Z., et al., *A novel small molecule agent displays potent anti-myeloma activity by inhibiting the JAK2-STAT3 signaling pathway.* Oncotarget, 2016. **7**(8): p. 9296-308.
544. De Vos, J., et al., *JAK2 tyrosine kinase inhibitor tyrphostin AG490 downregulates the mitogen-activated protein kinase (MAPK) and signal transducer and activator of transcription (STAT) pathways and induces apoptosis in myeloma cells.* Br J Haematol, 2000. **109**(4): p. 823-8.
545. Gibson, R.M., et al., *Phosphorylation of human gp130 at Ser-782 adjacent to the Di-leucine internalization motif. Effects on expression and signaling.* J Biol Chem, 2000. **275**(29): p. 22574-82.
546. Radtke, S., et al., *Cross-regulation of cytokine signalling: pro-inflammatory cytokines restrict IL-6 signalling through receptor internalisation and degradation.* J Cell Sci, 2010. **123**(Pt 6): p. 947-59.
547. Bonito, N.A., et al., *Control of gp130 expression by the mitogen-activated protein kinase ERK2.* Oncogene, 2014. **33**(17): p. 2255-63.
548. Terstegen, L., et al., *The inhibition of interleukin-6-dependent STAT activation by mitogen-activated protein kinases depends on tyrosine 759 in the cytoplasmic tail of glycoprotein 130.* J Biol Chem, 2000. **275**(25): p. 18810-7.
549. Thiel, S., et al., *Internalization of the interleukin 6 signal transducer gp130 does not require activation of the Jak/STAT pathway.* Biochem J, 1998. **330 (Pt 1)**: p. 47-54.
550. Nakaya, A., et al., *The gold compound auranofin induces apoptosis of human multiple myeloma cells through both down-regulation of STAT3 and inhibition of NF-κB activity.* Leuk Res, 2011. **35**(2): p. 243-9.
551. Luo, J., et al., *Constitutive activation of STAT3 and cyclin D1 overexpression contribute to proliferation, migration and invasion in gastric cancer cells.* Am J Transl Res, 2017. **9**(12): p. 5671-5677.
552. Colombo, M., et al., *Notch signaling deregulation in multiple myeloma: A rational molecular target.* Oncotarget, 2015. **6**(29): p. 26826-40.

553. Spaan, I., et al., *Wnt signaling in multiple myeloma: a central player in disease with therapeutic potential.* J Hematol Oncol, 2018. **11**(1): p. 67.
554. Murphy, M.P., *How mitochondria produce reactive oxygen species.* Biochem J, 2009. **417**(1): p. 1-13.
555. Judd, L.M., et al., *Inhibition of the JAK2/STAT3 pathway reduces gastric cancer growth in vitro and in vivo.* PLoS One, 2014. **9**(5): p. e95993.
556. Pratilas, C.A., et al., *(V600E)BRAF is associated with disabled feedback inhibition of RAF-MEK signaling and elevated transcriptional output of the pathway.* Proc Natl Acad Sci U S A, 2009. **106**(11): p. 4519-24.
557. Han, E.K., et al., *Akt inhibitor A-443654 induces rapid Akt Ser-473 phosphorylation independent of mTORC1 inhibition.* Oncogene, 2007. **26**(38): p. 5655-61.
558. Andraos, R., et al., *Modulation of activation-loop phosphorylation by JAK inhibitors is binding mode dependent.* Cancer Discov, 2012. **2**(6): p. 512-523.
559. Halaban, R., et al., *PLX4032, a selective BRAF(V600E) kinase inhibitor, activates the ERK pathway and enhances cell migration and proliferation of BRAF melanoma cells.* Pigment Cell Melanoma Res, 2010. **23**(2): p. 190-200.
560. Meads, M.B., L.A. Hazlehurst, and W.S. Dalton, *The bone marrow microenvironment as a tumor sanctuary and contributor to drug resistance.* Clin Cancer Res, 2008. **14**(9): p. 2519-26.
561. Karjalainen, R., et al., *JAK1/2 and BCL2 inhibitors synergize to counteract bone marrow stromal cell-induced protection of AML.* Blood, 2017. **130**(6): p. 789-802.
562. Kusaba, T., et al., *Activation of STAT3 is a marker of poor prognosis in human colorectal cancer.* Oncol Rep, 2006. **15**(6): p. 1445-51.
563. Qin, J.J., et al., *STAT3 as a potential therapeutic target in triple negative breast cancer: a systematic review.* J Exp Clin Cancer Res, 2019. **38**(1): p. 195.
564. Yang, Y., et al., *STAT3 controls osteoclast differentiation and bone homeostasis by regulating NFATc1 transcription.* J Biol Chem, 2019. **294**(42): p. 15395-15407.
565. Wang, H., et al., *Signal transducer and activator of transcription 3 in liver diseases: a novel therapeutic target.* Int J Biol Sci, 2011. **7**(5): p. 536-50.
566. Robertson, S.A., et al., *Regulation of Jak2 function by phosphorylation of Tyr317 and Tyr637 during cytokine signaling.* Mol Cell Biol, 2009. **29**(12): p. 3367-78.
567. Sayyah, J., et al., *Z3, a novel Jak2 tyrosine kinase small-molecule inhibitor that suppresses Jak2-mediated pathologic cell growth.* Mol Cancer Ther, 2008. **7**(8): p. 2308-18.
568. Tvorogov, D., et al., *Accumulation of JAK activation loop phosphorylation is linked to type I JAK inhibitor withdrawal syndrome in myelofibrosis.* Sci Adv, 2018. **4**(11): p. eaat3834.
569. Ma, H., S. Deacon, and K. Horiuchi, *The challenge of selecting protein kinase assays for lead discovery optimization.* Expert Opin Drug Discov, 2008. **3**(6): p. 607-621.
570. Lin, T.E., et al., *A Novel Selective JAK2 Inhibitor Identified Using Pharmacological Interactions.* Front Pharmacol, 2018. **9**: p. 1379.
571. Hatzivassiliou, G., et al., *RAF inhibitors prime wild-type RAF to activate the MAPK pathway and enhance growth.* Nature, 2010. **464**(7287): p. 431-5.
572. Wong, C.H., et al., *Simultaneous induction of non-canonical autophagy and apoptosis in cancer cells by ROS-dependent ERK and JNK activation.* PLoS One, 2010. **5**(4): p. e9996.
573. Lee, Y.C., et al., *Src family kinase/abl inhibitor dasatinib suppresses proliferation and enhances differentiation of osteoblasts.* Oncogene, 2010. **29**(22): p. 3196-207.
574. Sikkema, A.H., et al., *Kinome profiling in pediatric brain tumors as a new approach for target discovery.* Cancer Res, 2009. **69**(14): p. 5987-95.

575. Winkler, D.G., et al., *Phosphorylation of Ser-42 and Ser-59 in the N-terminal region of the tyrosine kinase p56lck.* Proc Natl Acad Sci U S A, 1993. **90**(11): p. 5176-80.
576. Harris, K.F., et al., *Ubiquitin-mediated degradation of active Src tyrosine kinase.* Proc Natl Acad Sci U S A, 1999. **96**(24): p. 13738-43.
577. Swatek, K.N. and D. Komander, *Ubiquitin modifications.* Cell Res, 2016. **26**(4): p. 399-422.
578. Livneh, I., et al., *Monoubiquitination joins polyubiquitination as an esteemed proteasomal targeting signal.* Bioessays, 2017. **39**(6).
579. Yang, Y., et al., *Inhibitors of ubiquitin-activating enzyme (E1), a new class of potential cancer therapeutics.* Cancer Res, 2007. **67**(19): p. 9472-81.
580. Lai, Z., et al., *Human mdm2 mediates multiple mono-ubiquitination of p53 by a mechanism requiring enzyme isomerization.* J Biol Chem, 2001. **276**(33): p. 31357-67.
581. van Andel, H., et al., *Aberrant Wnt signaling in multiple myeloma: molecular mechanisms and targeting options.* Leukemia, 2019. **33**(5): p. 1063-1075.
582. Lu, J., et al., *Pim2 is required for maintaining multiple myeloma cell growth through modulating TSC2 phosphorylation.* Blood, 2013. **122**(9): p. 1610-20.
583. Asano, J., et al., *The serine/threonine kinase Pim-2 is a novel anti-apoptotic mediator in myeloma cells.* Leukemia, 2011. **25**(7): p. 1182-8.
584. Bate-Eya, L.T., et al., *High efficacy of the BCL-2 inhibitor ABT199 (venetoclax) in BCL-2 high-expressing neuroblastoma cell lines and xenografts and rational for combination with MCL-1 inhibition.* Oncotarget, 2016. **7**(19): p. 27946-58.
585. Li, Z., S. He, and A.T. Look, *The MCL1-specific inhibitor S63845 acts synergistically with venetoclax/ABT-199 to induce apoptosis in T-cell acute lymphoblastic leukemia cells.* Leukemia, 2019. **33**(1): p. 262-266.
586. Ramsey, H.E., et al., *A Novel MCL1 Inhibitor Combined with Venetoclax Rescues Venetoclax-Resistant Acute Myelogenous Leukemia.* Cancer Discov, 2018. **8**(12): p. 1566-1581.
587. Tahir, S.K., et al., *Potential mechanisms of resistance to venetoclax and strategies to circumvent it.* BMC Cancer, 2017. **17**(1): p. 399.
588. Touzeau, C., et al., *Targeting Bcl-2 for the treatment of multiple myeloma.* Leukemia, 2018. **32**(9): p. 1899-1907.
589. Sanchez, L., et al., *Daratumumab: a first-in-class CD38 monoclonal antibody for the treatment of multiple myeloma.* J Hematol Oncol, 2016. **9**(1): p. 51.
590. Ogiya, D., et al., *Jak-STAT3 Pathway Regulates CD38 Expression on Multiple Myeloma Cells*. 2018, Blood: Blood (2018).
591. Huang, Y.H., et al., *Decoration of Anti-CD38 on Nanoparticles Carrying a STAT3 Inhibitor Can Improve the Therapeutic Efficacy Against Myeloma.* Cancers (Basel), 2019. **11**(2).
592. Quah, B.J. and C.R. Parish, *The use of carboxyfluorescein diacetate succinimidyl ester (CFSE) to monitor lymphocyte proliferation.* J Vis Exp, 2010(44).
593. Tosi, P., et al., *Serum free light-chain assay for the detection and monitoring of multiple myeloma and related conditions.* Ther Adv Hematol, 2013. **4**(1): p. 37-41.
594. Tate, J., et al., *Quantitative serum free light chain assay--analytical issues.* Clin Biochem Rev, 2009. **30**(3): p. 131-40.
595. Bazarbachi, A.H., et al., *Relapsed refractory multiple myeloma: a comprehensive overview.* Leukemia, 2019. **33**(10): p. 2343-2357.
596. Rossi, M., et al., *Mouse models of multiple myeloma: technologic platforms and perspectives.* Oncotarget, 2018. **9**(28): p. 20119-20133.
597. Maes, K., et al., *The genetic landscape of 5T models for multiple myeloma.* Sci Rep, 2018. **8**(1): p. 15030.

598. Urashima, M., et al., *The development of a model for the homing of multiple myeloma cells to human bone marrow.* Blood, 1997. **90**(2): p. 754-65.
599. Yata, K. and S. Yaccoby, *The SCID-rab model: a novel in vivo system for primary human myeloma demonstrating growth of CD138-expressing malignant cells.* Leukemia, 2004. **18**(11): p. 1891-7.
600. Calimeri, T., et al., *A unique three-dimensional SCID-polymeric scaffold (SCID-synth-hu) model for in vivo expansion of human primary multiple myeloma cells.* Leukemia, 2011. **25**(4): p. 707-11.
601. Chesi, M., et al., *AID-dependent activation of a MYC transgene induces multiple myeloma in a conditional mouse model of post-germinal center malignancies.* Cancer Cell, 2008. **13**(2): p. 167-80.

Appendix:

Chromatogram : vp-79-s_channel1

System : HPLC-PDA
Method : Gradient1
User : Daniel

Acquired : 26/05/2015 17:27:57
Processed : 26/05/2015 18:15:26
Printed : 15/07/2015 13:12:26

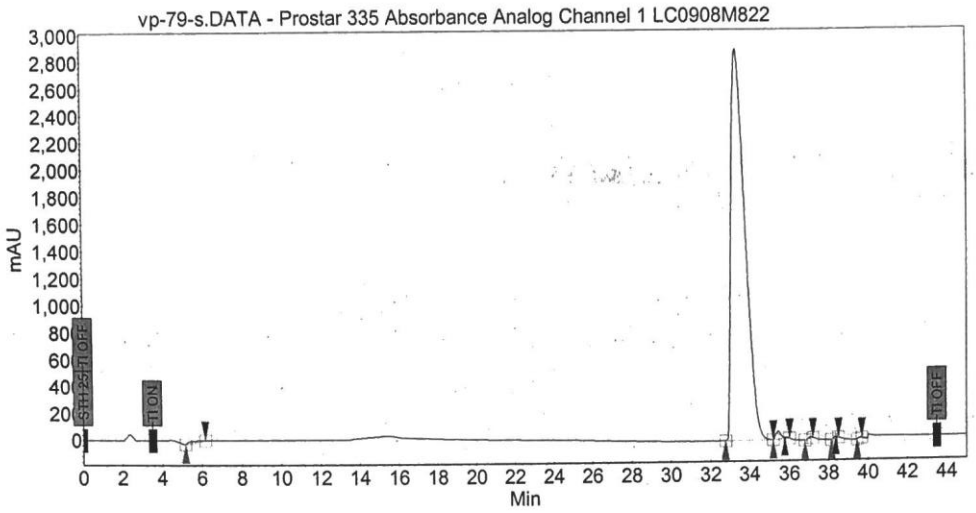

Peak results :

Index	Name	Time [Min]	Quantity [% Area]	Height [mAU]	Area [mAU.Min]	Area % [%]
1	UNKNOWN	5.44	0.40	16.7	9.6	0.403
2	UNKNOWN	33.32	98.60	2899.1	2361.7	98.605
3	UNKNOWN	35.44	0.75	60.7	17.9	0.746
4	UNKNOWN	35.84	0.04	7.0	1.0	0.041
5	UNKNOWN	37.08	0.07	9.8	1.7	0.069
6	UNKNOWN	38.31	0.07	12.8	1.6	0.067
7	UNKNOWN	38.35	0.03	10.7	0.8	0.033
8	UNKNOWN	39.57	0.04	5.7	0.9	0.036
Total			100.00	3022.4	2395.1	100.000

Appendix figure 1 Assessment of the purity of VP79s by high-performance liquid chromatography.

HPLC for VP79s 26/05/2015. High-performance liquid chromatography (HPLC) analysis was carried out using a Varian ProStar system in order to assess the purity of each batch of VP79s used in this study. The system is equipped with a Varian Prostar 335 diode array detector and a manual injector. In order to detect the purity of VP79s, detection was performed at 254 nm and peak purity was assessed using a purity channel. The stationary phase consisted of an ACE 5 C18-AR column (150 × 4.6 mm), and the mobile phase used the following gradient system, eluting at 1 mL/min: aqueous formate buffer (30 mM, pH 3.0) for 10 minutes, linear ramp to 85% methanol buffered with the same system over 25 minutes, hold at 85% buffered methanol for 10 minutes. HPLC: 98.6% (tR: 33.3 min).

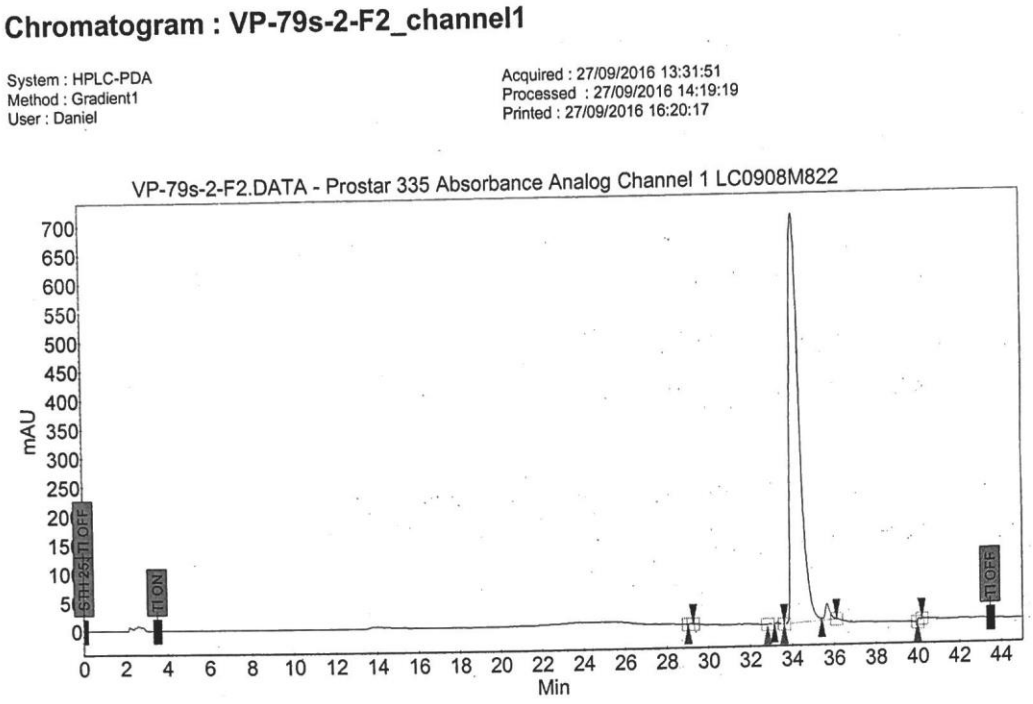

Peak results :

Index	Name	Time [Min]	Quantity [% Area]	Height [mAU]	Area [mAU.Min]	Area % [%]
1	UNKNOWN	29.15	0.03	0.9	0.1	0.025
2	UNKNOWN	32.93	0.04	1.3	0.2	0.045
3	UNKNOWN	33.29	0.13	3.1	0.5	0.126
4	UNKNOWN	34.12	97.81	706.6	379.6	97.809
5	UNKNOWN	35.67	1.86	27.6	7.2	1.856
6	UNKNOWN	40.00	0.14	5.3	0.5	0.139
Total			100.00	744.7	388.1	100.000

Appendix figure 2 Assessment of the purity of VP79s by high-performance liquid chromatography.

HPLC for VP79s 27/09/2016. High-performance liquid chromatography (HPLC) analysis was carried out using a Varian ProStar system in order to assess the purity of each batch of VP79s used in this study. The system is equipped with a Varian Prostar 335 diode array detector and a manual injector. In order to detect the purity of VP79s, detection was performed at 254 nm and peak purity was assessed using a purity channel. The stationary phase consisted of an ACE 5 C18-AR column (150 × 4.6 mm), and the mobile phase used the following gradient system, eluting at 1 mL/min: aqueous formate buffer (30 mM, pH 3.0) for 10 minutes, linear ramp to 85% methanol buffered with the same system over 25 minutes, hold at 85% buffered methanol for 10 minutes. HPLC: 97.8% (tR: 34.1 min).

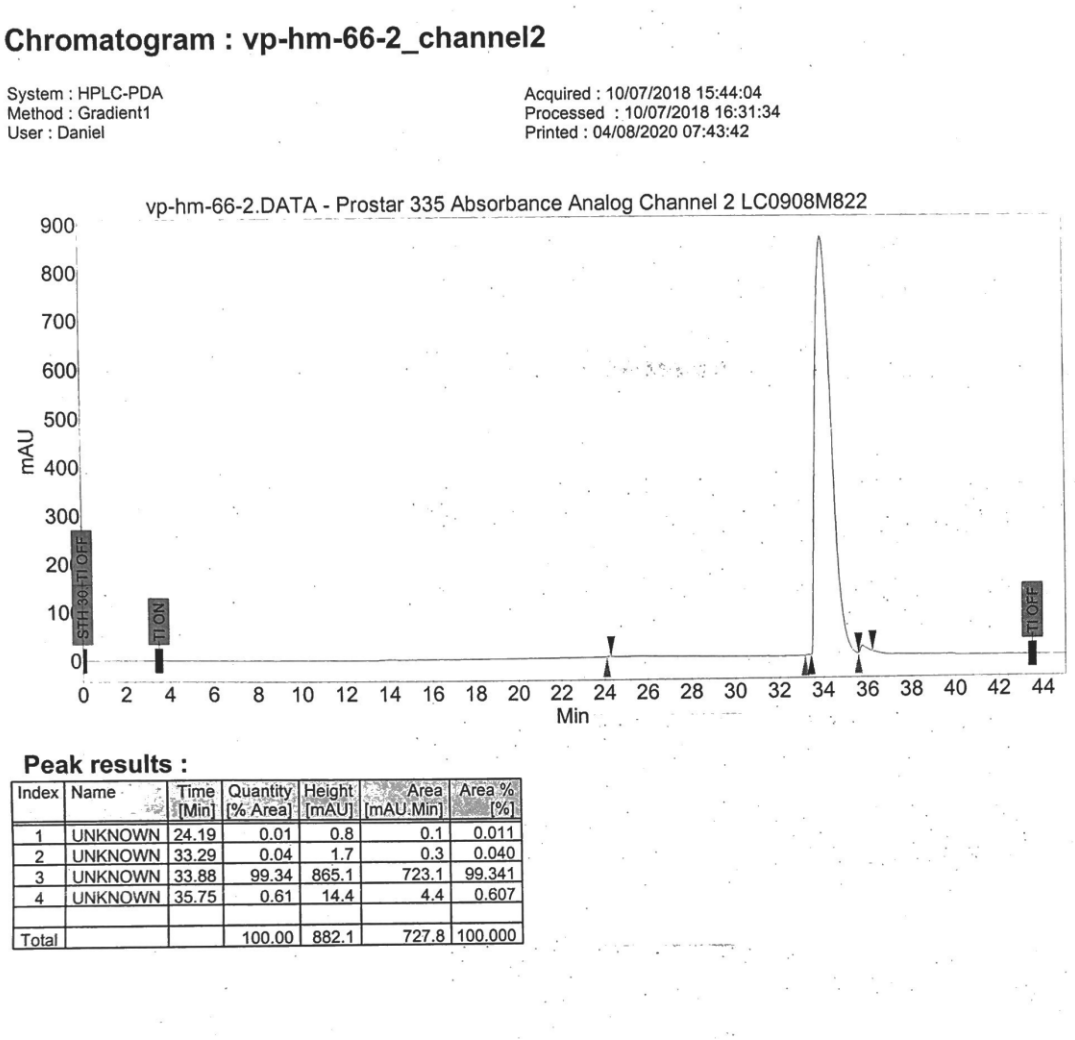

Index	Name	Time [Min]	Quantity [% Area]	Height [mAU]	Area [mAU.Min]	Area % [%]
1	UNKNOWN	24.19	0.01	0.8	0.1	0.011
2	UNKNOWN	33.29	0.04	1.7	0.3	0.040
3	UNKNOWN	33.88	99.34	865.1	723.1	99.341
4	UNKNOWN	35.75	0.61	14.4	4.4	0.607
Total			100.00	882.1	727.8	100.000

Appendix figure 3 Assessment of the purity of VP79s by high-performance liquid chromatography.

HPLC for VP79s 10/07/2018. High-performance liquid chromatography (HPLC) analysis was carried out using a Varian ProStar system in order to assess the purity of each batch of VP79s used in this study. The system is equipped with a Varian Prostar 335 diode array detector and a manual injector. In order to detect the purity of VP79s, detection was performed at 254 nm and peak purity was assessed using a purity channel. The stationary phase consisted of an ACE 5 C18-AR column (150 × 4.6 mm), and the mobile phase used the following gradient system, eluting at 1 mL/min: aqueous formate buffer (30 mM, pH 3.0) for 10 minutes, linear ramp to 85% methanol buffered with the same system over 25 minutes, hold at 85% buffered methanol for 10 minutes. HPLC: 99.3% (tR: 33.9 min).

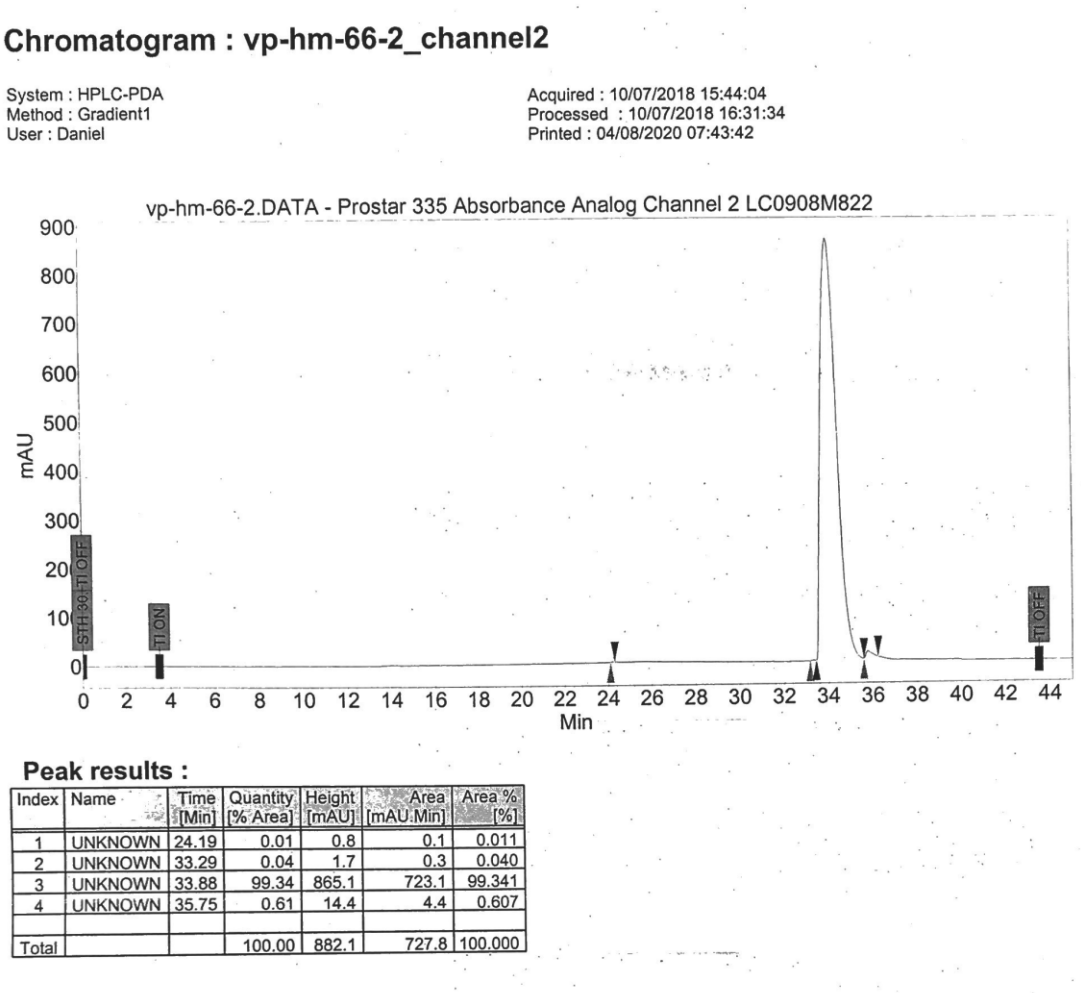

Index	Name	Time [Min]	Quantity [% Area]	Height [mAU]	Area [mAU.Min]	Area % [%]
1	UNKNOWN	24.19	0.01	0.8	0.1	0.011
2	UNKNOWN	33.29	0.04	1.7	0.3	0.040
3	UNKNOWN	33.88	99.34	865.1	723.1	99.341
4	UNKNOWN	35.75	0.61	14.4	4.4	0.607
Total			100.00	882.1	727.8	100.000

Appendix figure 4 Assessment of the purity of VP79s by high-performance liquid chromatography.

HPLC for VP79s 09/10/2018. High-performance liquid chromatography (HPLC) analysis was carried out using a Varian ProStar system in order to assess the purity of each batch of VP79s used in this study. The system is equipped with a Varian Prostar 335 diode array detector and a manual injector. In order to detect the purity of VP79s, detection was performed at 254 nm and peak purity was assessed using a purity channel. The stationary phase consisted of an ACE 5 C18-AR column (150 × 4.6 mm), and the mobile phase used the following gradient system, eluting at 1 mL/min: aqueous formate buffer (30 mM, pH 3.0) for 10 minutes, linear ramp to 85% methanol buffered with the same system over 25 minutes, hold at 85% buffered methanol for 10 minutes. HPLC: 99.2% (tR: 34 min).

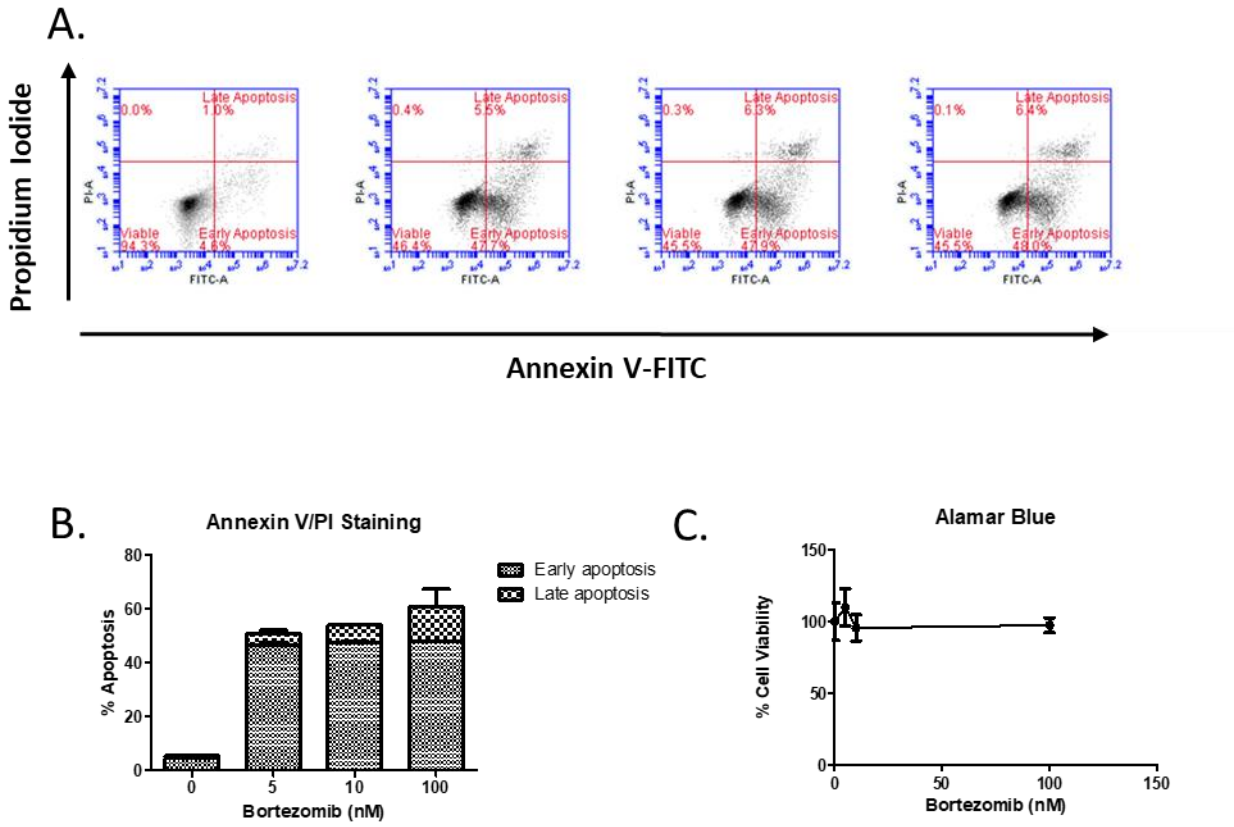

Appendix figure 5 Validation of results obtained with the alamar blue assay.

U266B1 cells were seeded at 5 x 10^4 cells/well on 96 well plates or 30 x 10^4 cells/mL in 12 well plates from the same passage of cells on the same day. Cells were then treated with either vehicle (0.01% DMSO) or bortezomib (5, 10 or 100 nM) for 24 hours. After 24 hours cells were collected and stained with annexin V/PI and analysed by flow cytometry or 10% alamar blue (v/v) was added to each well and plates were incubated in the dark for up to 5 hours until a colour change was observed. ***A.*** *Representative flow plots of annexin V/PI stained cells.* ***B.*** *Average percentage apoptosis of replicates analysed by flow cytometry.* ***C.*** *Percentage cell viability of cells analysed by alamar blue assay.*

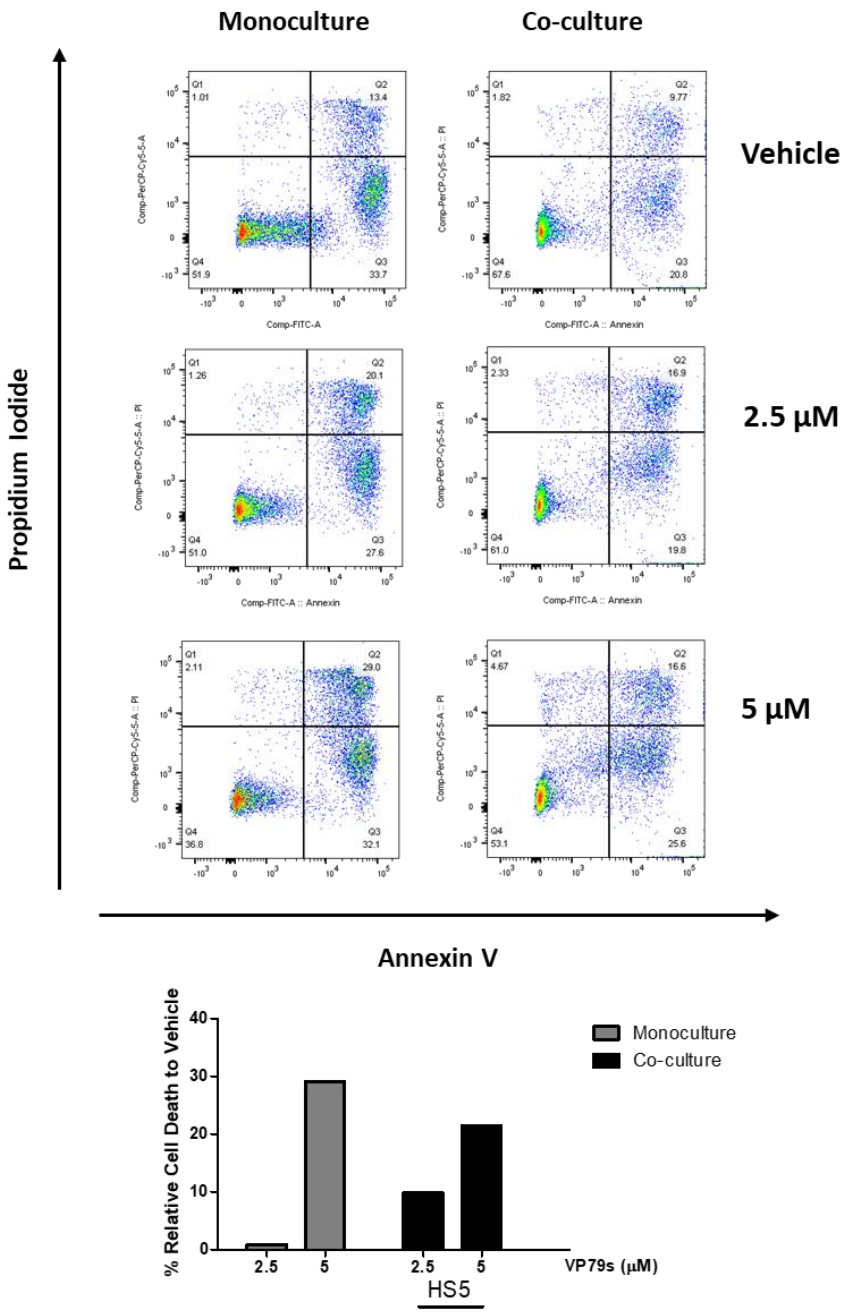

Appendix figure 6 VP79s induces cell death in an ex vivo MM patient sample in the presence of HS5 cells.

HS5 cells were seeded at 2 x 10^4 cells/well in flat bottom 96 well plates and left to adhere overnight. The following day, 50,000 ex vivo MM cells were seeded on top of the HS5 cells and left to rest for 1 hour. Cells were then treated with either vehicle [0.25% EtOH (v/v)] or VP79s (2.5 or 5 µM) for 24 hours. After incubation, cells were collected, stained with annexin V/PI and analysed by flow cytometry using the BD FACSCanto™ II flow cytometer. 10,000 single cells were gated on vehicle treated cells excluding debris and doublets. Bars represent relative cell death compared to vehicle.

List of clinical trials

Clinical trial numbers listed below can be found at: http://www.clinicaltrials.gov

- NCT03135171 - Trastuzumab and Pertuzumab in Combination with Tocilizumab in Subjects With Metastatic HER2 Positive Breast Cancer Resistant to Trastuzumab.
- NCT03999749 - A Phase II Study of the Interleukin-6 Receptor Inhibitor Tocilizumab in Combination with Ipilimumab and Nivolumab in Patients with Unresectable Stage III or Stage IV Melanoma.
- NCT03110822 - A Phase 1 Study of Ruxolitinib, Steroids and Lenalidomide for Relapsed/Refractory Multiple Myeloma (RRMM) Patients.
- NCT01524978 - A Study of Vemurafenib in Participants with BRAF V600 Mutation-Positive Cancers.
- NCT02834364 - BRAF/MEK Inhibition in Relapsed/Refractory Multiple Myeloma (BIRMA) (GMMG-BIRMA).
- NCT03539744 - A Study of Venetoclax and Dexamethasone Compared with Pomalidomide and Dexamethasone in Subjects with Relapsed or Refractory Multiple Myeloma (CANOVA).
- NCT03314181 - A Study of Combination Therapy with Venetoclax, Daratumumab and Dexamethasone (With and Without Bortezomib) in Subjects with Relapsed or Refractory Multiple Myeloma.
- NCT03450330 - Assessing an Oral Janus Kinase Inhibitor, AZD4205, in Combination with Osimertinib in Patients Who Have Advanced Non-small Cell Lung Cancer (JACKPOT1).
- NCT03195699 - Oral STAT3 Inhibitor, TTI-101, in Patients with Advanced Cancers.
- NCT01594216 - Ruxolitinib in Estrogen Receptor Positive Breast Cancer.
- NCT02164500 - JAK-inhibition in Recurrent Classical Hodgkin Lymphoma (JeRiCHO).
- NCT01904123 - STAT3 Inhibitor WP1066 in Treating Patients with Recurrent Malignant Glioma or Progressive Metastatic Melanoma in the Brain.
- NCT01794520 - Study Evaluating ABT-199 in Subjects with Relapsed or Refractory Multiple Myeloma.

Publications:

MedChemComm

RESEARCH ARTICLE

Cite this: *Med. Chem. Commun.*, 2018, **9**, 735

Effect of isouronium/guanidinium substitution on the efficacy of a series of novel anti-cancer agents†

Viola Previtali,[a] Cristina Trujillo,[a] Rebecca Amet,[b] Daniela M. Zisterer[b] and Isabel Rozas *[a]

Received 15th February 2018,
Accepted 19th March 2018

DOI: 10.1039/c8md00089a

rsc.li/medchemcomm

Considering our hypothesis that the guanidinium moiety in the protein kinase type III inhibitor **1** interacts with a phosphate of ATP within the hinge region, the nature of the interactions established between a model isouronium and the phosphate groups of ATP was computationally analysed indicating that an isouronium derivative of **1** will interact in a similar manner with ATP. Thus, a number of compounds were prepared to assess the effect of the guanidinium/isouronium substitution on cancer cell growth; additionally, the molecular shortening and conformational change induced by replacing the di-substituted guanidine-linker of **1** by an amide was explored. The effect of these compounds on cell viability was tested in human leukaemia, breast cancer and cervical cancer cell lines and the resulting IC_{50} values were compared with those of the lead compound **1**. Replacement of the di-substituted guanidine-linker by an amide results in the loss of cytotoxicity; however, substitution of the mono-substituted guanidinium by an isouronium cation seems to be beneficial for cell growth inhibition. Additionally, the effect of these compounds on the MAPK/ERK pathway was studied by means of Western blotting and the results indicate that the isouronium derivative **2** decreases the levels of phosphorylated, and thus activated, ERK (pERK) both in leukaemia and breast cancer cells, whereas lead compound **1** only shows an effect on pERK levels in breast cancer cells. This confirms that both compounds could interfere with the MAPK/ERK pathway although other targets cannot be ruled out.

Introduction

Protein kinases, important components of intracellular cascades, have emerged as one of the most central targets in drug discovery for anticancer therapies.[1] To date, the FDA has approved 31 small-molecule protein kinase inhibitors (PKIs), half of which have been approved in the past three years.[2] However, most of the known PKIs are competitive (type I), targeting the ATP site which is highly conserved amongst most of the kinases and this makes cross-reactivity a very common problem.[3] Other PKIs comprise type II inhibitors, which bind to the inactive form of the kinase, and type III inhibitors, which bind exclusively in an allosteric pocket. Such allosteric modulators bind to sites that are less conserved across the kinome and are likely to be specific for a particular family of kinases, not facing the limitations of ATP-competitive inhibition that challenge the translation of current generation PKIs to the clinic.[4,5]

The Ras/Raf/MEK/ERK pathway (MAPK/ERK pathway) is a kinase cascade that transmits signals from cell surface receptors to promote cell proliferation, differentiation and survival. Although much understanding has been gained in the last few years about the complicated regulatory steps that govern this signalling pathway, much remains to be elucidated about the pathway and its components.[6] Under physiological conditions, ERK signalling is controlled at multiple levels essential for maintaining regulated cell growth and homeostasis, but when hyper-activated, it can play a causative role in the development of different types of tumours.[7,8] Raf and MEK kinases also play a central role in cancer and their therapeutic opportunities have been intensely studied, both in terms of single kinase inhibition and interference in protein–protein interaction.[9–11] In particular, their constitutive activation in many tumours indicates the urgent need for new inhibitors with an alternative mechanism of action.[12,13] Trametinib (GSK) is the only allosteric type III inhibitor (MEK inhibitor) of the MAPK/ERK pathway approved for B-Raf(V600E) melanoma,[8,14] while Ras, Raf and ERK still

[a] *School of Chemistry, Trinity Biomedical Sciences Institute, Trinity College Dublin, 152-160 Pearse Street, Dublin 2, Ireland. E-mail: rozasi@tcd.ie*
[b] *School of Biochemistry and Immunology, Trinity Biomedical Sciences Institute, Trinity College Dublin, 152-160 Pearse Street, Dublin 2, Ireland*

† Electronic supplementary information (ESI) available: Computational results, synthetic general procedures and preparation of intermediates, NMR spectra and HPLC chromatogram of final compounds and calculated physicochemical properties. See DOI: 10.1039/c8md00089a

remain untargeted through a pure type III allosteric mechanism.

Previous studies in Rozas' group identified compound **1** (Fig. 1) as a PKI capable of inhibiting the MAPK/ERK pathway through a type-III allosteric mechanism providing a new lead for further refinement of kinase selectivity and potency.[15,16] Earlier and on-going molecular-modelling studies carried out in our laboratory indicate that this compound forms hydrogen bonds (HBs) and electrostatic interactions with the phosphate chain of ATP through the mono-substituted guanidinium cation, thus positioning the lipophilic (4-Cl-3-CF_3)-Ph moiety (see compound **1** in Fig. 1) in a hydrophobic pocket of the enzyme.[15,17]

Guanidine's high basicity (pK_{aH} in water is 13.6 (ref. 18)) indicates that at physiological pH, it will be protonated forming the guanidinium cation. Even though appropriate substitution of this cation decreases its basicity (*e.g.* pK_{aH} of phenylguanidine in water is 10.9 (ref. 19)) and this functional group is present in many current therapies such as zanamivir,[20] cimetidine[21] or clonidine,[22] guanidinium derivatives are sometimes discarded as useful drugs because of potential pharmacokinetic problems. Regardless of its basicity, the guanidinium cation has important features very useful for target binding such as forming strong HBs and ionic interactions.[23–25] Interestingly, the related isouronium cation retains these two binding features and, additionally, is less basic (pK_{aH} = 9.8 (ref. 18)); hence, this cation is very promising as a functional substitute in guanidinium derivatives with therapeutic potential.[26]

Over the past 20 years we have prepared a large number of symmetric and asymmetric di-aromatic isouronium derivatives that, in some cases, showed rather promising cytotoxic activity against diverse cancer cell lines.[27,28] Given these encouraging results and the possibility for isouronium to overcome the pharmacokinetic problems associated with guanidinium, we decided to explore the effect of substituting the guanidinium cation hypothetically involved in HBs and electrostatic interactions with the ATP's phosphate chain of protein kinases, by an isouronium.

Hence, we present in this article, first, the computational study of the potential interactions between a simple arylisouronium system and the phosphates in the ATP molecule. Although kinase active site structure limitations need to be considered for a deep understanding of the mode of action of our inhibitors, the aim of this first part of the study is to obtain a theoretical comparative description of all possible interacting modes between ATP and isouronium/guanidinium. Next, the preparation of isouronium **2** (Fig. 1) is presented; in this derivative of **1** the (4-Cl-3-CF_3)-Ph lipophilic moiety was retained because its importance in keeping potent kinase inhibition.[16] In addition, the synthesis of compounds **3** and **4** (Fig. 1) is reported to explore optimal length and conformation in these molecules by changing the di-substituted guanidinium in compounds **1** and **2** by an amide functionality.

This change orients the lipophilic moiety to a different position providing information on the structural requirements for improved kinase affinity.

Finally, we present the study of the effect of these compounds on cancerous cell growth, which was assessed on human leukaemia (HL-60), breast cancer (MCF-7) and cervical cancer (HeLa) cell lines by means of cell viability experiments. Additionally, the effect of these compounds on the MAPK/ERK kinase pathway, which was explored by Western blot experiments in HL-60 and MCF-7 cells, is also presented.

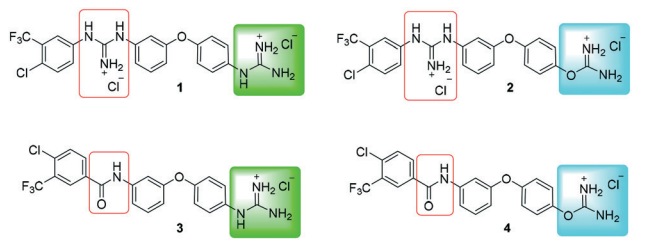

Fig. 1 Structure of compounds **1**, **2**, **3** and **4**, highlighting the comparison of the two cationic moieties (guanidinium in the green box and isouronium in the blue box). The guanidine and amide linkers are indicated by the red boxes.

Results and discussion

Computational studies

We have previously computationally studied the interactions between some arylguanidinium systems and the different phosphate groups of ATP to understand their possible mode of action in kinase inhibition; as a result, a theoretical model was proposed.[17] Now, we have carried out a similar study with 4-phenoxyphenyl-*O*-isouronium (simplified model of the molecules proposed in this work, see Fig. S1, ESI†) interacting with the different ATP phosphates.

In our previous study,[17] the most stable interaction formed between ATP and 4-phenoxyphenyl-*N*-guanidinium, was the one simultaneously established between two H atoms of the guanidinium moiety and two O atoms of the phosphate. Thus, with the aim of comparing isouronium and guanidinium contacts, only those interactions involving H2 and H3 of the isouronium (see Fig. S1†) and two O atoms of a phosphate were considered.

Calculated interaction energies (E_i, kJ mol^{-1}) between ATP and 4-phenyloxyphenyl-*O*-isouronium are presented in Table S1 (ESI†); those with the 4-phenyloxyphenyl-*N*-guanidium cation (in brackets in Table S1†) have been included for comparison purposes. The E_i values calculated for the 4-phenyloxyphenyl-*O*-isouronium···ATP complexes are larger than those previously reported by our group for 4-phenyloxyphenyl-*N*-guanidinium (Table S1†).[17] However, an exception to this trend is found in complexes that form multiple simultaneous interactions with different phosphates (Fig. S2, ESI†). Since the larger the number of interactions, the larger the E_i values, it is clear from Table S1† that these complexes are more stable than similar dimers with interactions at only one of the ATP phosphates.

All the interactions established within the 4-phenyloxyphenyl-*O*-isouronium–ATP complexes were characterized by analysing their electron density topology using the atoms in molecules (AIM) theory.[29] Thus, the electron density characteristics found in the bond critical points (BCPs) between the interacting moieties (ρ_{BCP} and $\nabla^2\rho_{BCP}$, a.u.), were calculated and are presented in Tables S2 and S3 (ESI†). The ρ_{BCP} values and positive Laplacians, indicate that all the interactions established within the complexes studied are of a non-covalent nature and can be classified as HBs. All the AIM molecular graphs are presented in Fig. S2 (ESI†).

In summary, the theoretical studies performed clearly indicate that the proposed isouronium derivatives can form similar interactions with the ATP phosphates as those proposed for the guanidinium lead compound **1** potentially exhibiting similar biological activity.

Synthetic procedures

Based on the positive results from the computational studies, we proceeded to the preparation of compounds **2** to **4** (Fig. 1). Synthesis of compound **2** required the preliminary preparation of a conveniently functionalised phenol (Scheme 1); thus, the phenol moiety was introduced by the initial protection of iodophenol **5** with pyridinium *p*-toluenesulfonate (PPTS) and 3,4-dihydro-2*H*-pyran in dry CH_2Cl_2 to yield compound **6**.[30] PPTS is the most common catalyst for the tetrahydropyranylation of alcohols, and seems to be superior to other catalysts such as hydrochloric acid, phosphoryl chloride, and boron trifluoride etherate.[31] Furthermore, since the THP protecting group was stable under the conditions of the next reaction, compound **6** was used in the subsequent Ullman coupling with commercially available 3-aminophenol **7**, CuI and picolinic acid in DMSO at 80 °C to obtain compound **8** (Scheme 1).[32]

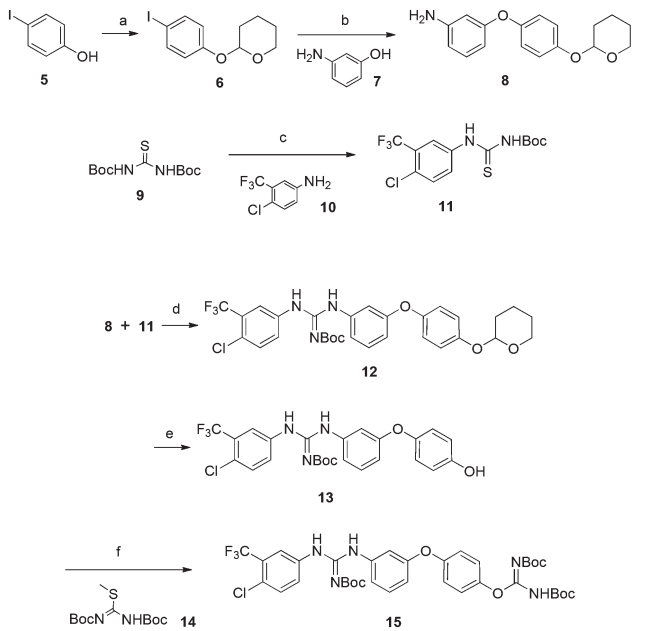

Scheme 1 Reagents and conditions: (a) PPTS, 3,4-dihydro-2*H*-pyran, CH_2Cl_2, rt, 2 h, 82%; (b) CuI, picolinic acid, K_3PO_4, DMSO, 80 °C, 24 h, 86%; (c) NaH, TFAA, THF, 0 °C, 5 h, 61%; (d) $HgCl_2$, Et_3N, CH_2Cl_2, rt, overnight, 58%; (e) montmorillonite KSF, MeOH, 50 °C, 4 h, 65%; (f) $HgCl_2$, Et_3N, CH_2Cl_2, rt, overnight, 55%.

Following the procedure already described by our group,[16] Boc-protected thiourea **9** was reacted with the commercially available aniline **10** to yield the corresponding amidylating agent **11** (Scheme 1). Coupling **8** with the synthesized thiourea **11**, in presence of $HgCl_2$ and triethylamine, afforded **12** in good yield (58%).

The OH free phenol derivative was then amidylated using standard conditions previously described by us[27] and others[34] using *N*,*N*′-bis-(*tert*-butoxycarbonyl)-*S*-methylisothiourea **14**, mercury(II) chloride and triethylamine to yield the corresponding Boc-protected isouronium **15** (Scheme 1). Compound **12** was then deprotected with montmorillonite KSF to obtain the corresponding phenol **13** (Scheme 1). Montmorillonite clays have been extensively used as efficient catalysts for a variety of organic reactions and they are a mild and efficient alternative procedure for the deprotection of THPEs.[33]

The rationale behind the preparation of compounds **3** and **4** was that introduction of the amido functionality will not only shorten the total length of these potential PKIs, but also will position the lipophilic group in a different orientation due to the strict *trans* conformation of the CO–NH arrangement. Therefore, commercially available dianiline **16** was reacted with Boc-protected thiourea **9** in the presence of $HgCl_2$ and triethylamine to yield aniline **17**.[16] Next, aniline **17**, was reacted with acid chloride **18** (previously prepared by reacting the corresponding benzoic acid and oxalyl chloride in the presence of catalytic DMF) to yield the Boc-protected guanidine **19** (Scheme 2).[35]

Finally, for the preparation of the amide-linked phenol precursor of isouronium **4**, the THP-protected compound **8** was reacted with the acid chloride **18** to yield compound **20** which was deprotected using montmorillonite KSF, as previously described, to obtain compound **21**. This phenol was subsequently amidylated with *N*,*N*′-bis-(*tert*-butoxycarbonyl)-*S*-methylisothiourea **14** to produce compound **22** in a very good yield (97%) (Scheme 3).

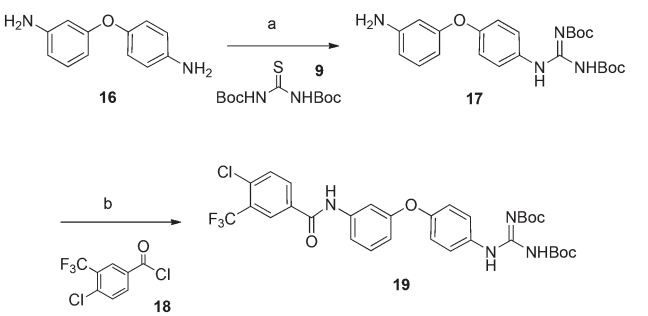

Scheme 2 Reagents and conditions: (a) $HgCl_2$, Et_3N, CH_2Cl_2, 25 °C, 12 h, 51%; (b) Et_3N, CH_2Cl_2, overnight, 51%.

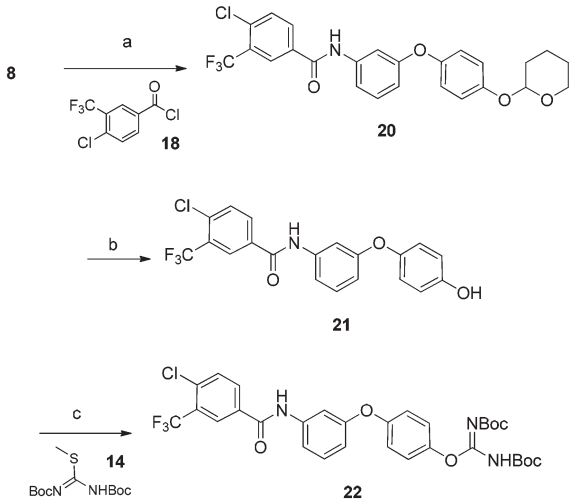

Scheme 3 Reagents and conditions: (a) Et_3N, CH_2Cl_2, overnight, 43%; (b) montmorillonite KSF, MeOH, 50 °C, 4 h, 74%; (c) $HgCl_2$, Et_3N, CH_2Cl_2, 25 °C, 12 h, 97%.

Boc-deprotection of isourea **15** was carried out following standard conditions within our lab to yield the final hydrochloride salt **2**; thus, **15** was treated with TFA, followed by chloride anion exchange, to afford the hydrochloride salt **2** in an excellent yield (95%). In the case of Boc-protected compounds **19** and **22**, a different approach was considered. Although heat is often required to cleave an amide bond, as it is not very nucleophilic, it was thought that the amide link present in these compounds is particularly labile due to the electron withdrawing nature of the Ph–O–Ph oxygen and the electronegative halogen substituents present on the adjacent phenyl ring. These two elements lead to the electron donating capabilities of the NH in the amide bond to be somewhat diminished leaving the CO carbon atom more open to nucleophilic attack. Hence, use of HCl or TFA was not considered appropriate for such substrates and, hence, deprotection of **19** and **22** was carried out with the use of $SnCl_4$ in EtOAc (as described by Miel *et al.*[36]) to obtain final hydrochloride salts **3** (47%) and **4** (51%).

Biological results and physicochemical properties

As mentioned, we had previously identified 4-chloro-3-trifluoromethylphenyl substituted 3,4′-bis-guanidinium phenoxyphenyl derivatives with potential as MAPK/ERK type III allosteric inhibitors. Compound **1** in particular was found to be the best cell growth inhibitor for the human leukemia HL-60 cancer cell line with an IC_{50} of 9.72 μM.[15,16] In order to assess the effect of the guanidinium/isouronium substitution as well as the effect of the conformational change, induced by an amide linker, on the growth inhibition properties of compound **1**, the cytotoxicity of the newly synthesised compounds **2**, **3** and **4** as well as that of the lead compound **1** was evaluated *in vitro* against the HL-60 (leukemia), MCF-7 (breast) and HeLa (cervical) cancer cell lines using the known type II kinase inhibitor sorafenib as a control (Table 1 and Fig. 2).

In these assays, compound **1** produced very similar results in the three cancer cell lines with IC_{50} values ranging from 9.48 to 9.84 μM. In contrast, compound **2** showed an improved effect on cell viability with low IC_{50} values of 5.49, 4.68 and 3.35 μM in the HL-60, MCF-7 and HeLa cell lines, respectively (Table 1 and Fig. 2). Moreover, the amide-linked guanidinium derivative **3**, a shorter analogue of the lead **1**, has a 2–3 fold decrease in activity compared to **1** and shows very similar cytotoxicity to the also short isouronium compound **4** (4–9 fold drop in activity). From these results we can deduce, firstly, that the amide linker present in compounds **3** and **4** probably orientates the lipophilic moiety in a different direction to that of the guanidinium link for compounds **1** or **2** resulting in the loss of activity. Secondly, the isouronium moiety seems to establish similar interactions to the monosubstituted guanidinium cation, resulting in related IC_{50} values.

Even though the difference in growth inhibitory activity between isouronium (**2**) and guanidinium (**1**) derivatives is small, it is still interesting to note that compound **2** shows slightly better results probably due to improved pharmacokinetic properties. Accordingly, we have calculated different relevant physicochemical parameters such as the clog*P* (lipophilicity), PSA (polar surface area), calculated pK_{aH} (basicity) or calculated solubility (in water) with the help of the Chemaxon's Marvin package[37] and the results are shown in Table 1.

The difference between isouronium and guanidinium is evident with the PSA, which is an indicator of HB formation and a commonly used metric for the optimisation of a drug's ability to permeate cells, since molecules with a polar surface area >140 Å^2 tend to be poor at permeating cell membranes.[38] In our case, compounds **3** and **4** have lower PSA values (100.2 and 97.4 Å^2, respectively) than compounds **1** and **2** (119.0 and 116.2 Å^2, respectively), but similar to

Table 1 Inhibition of cell viability, expressed as IC_{50} (μM ± SEM) values, in HL-60, MCF-7 and HeLa cells and calculated properties (clog*P*; PSA, Å^2; pK_{aH} and aqueous solubility, mg mL^{-1})[37] obtained for the guanidiniums **1** (ref. 15) and **3**, isouroniums **2** and **4** and sorafenib as a positive control. IC_{50} values are mean ± S.E.M. representatives of at least three independent experiments performed in triplicate

Comp	HL-60 IC_{50}	MCF-7 IC_{50}	HeLa IC_{50}	clog*P*	PSA	pK_{aH}	Solubility
1	9.72 ± 0.9 (ref. 15)	9.84 ± 1.8	9.48 ± 0.2	5.09	119.0	8.71, 7.02	0.0106
2	5.49 ± 0.10	4.68 ± 0.2	3.35 ± 0.3	5.46	116.2	8.34, 7.03	0.0102
3	28.16 ± 0.6	20.75 ± 2.3	11.28 ± 0.4	5.02	100.2	8.71	0.0092
4	35.60 ± 1.1	28.72 ± 1.4	83.57 ± 8.3	5.39	97.4	8.32	0.0091
Sorafenib	2.59 ± 0.40	3.07 ± 0.1	4.59 ± 0.5	4.34	92.4	2.03	0.0100

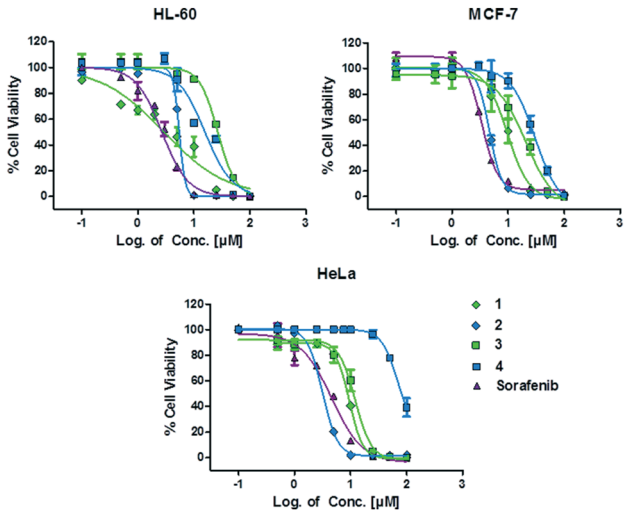

Fig. 2 Effect of compounds **1**, **2**, **3** and **4** on the viability of HL-60, MCF-7 and HeLa cells determined by the AlamarBlue® assay. Cells were seeded at a density of 4×10^4 (HL-60), 5×10^3 (MCF-7) and 5×10^3 (HeLa) cells per well on a 96-well plate and treated with vehicle alone [1% (v/v) EtOH or 0.1% (v/v) DMSO], or the compounds at 0.1–100 μM. Sorafenib was used as control. Cells were incubated for 72 h at 37 °C after which they were treated with AlamarBlue® and left in darkness in an incubator for 4–5 h. The resulting fluorescence was read using a plate reader from which percentage viability was calculated. The points on the three graphs represent mean values ± S.E.M. from at least three independent experiments performed in triplicate.

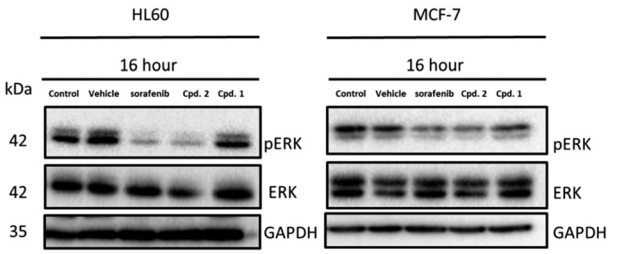

Fig. 3 Effect of compounds **1**, **2** and sorafenib (as a control) on the level of expression of phosphorylated (activated) and total ERK. HL-60 and MCF-7 cells were treated with either vehicle (0.1% EtOH), sorafenib (10 μM), compound **1** (10 μM) or compound **2** (10 μM) for 16 hours. Cells were lysed and 20 μg protein was loaded, separated on 12% SDS-page gel and transferred to PVDF membrane. The membrane was then blocked and probed with anti-ERK and anti-pERK [1 : 1000] and anti-rabbit secondary antibodies. Anti-GAPDH [1 : 2500] was used as a loading control and probed with anti-mouse secondary. HL-60 and MCF-7 results are representative of 4 and 2 independent experiments respectively.

sorafenib (92.4 Å^2). Moreover, isouroniums **2** and **4** have lower PSA values than their guanidinium analogues (**1** and **2**). This optimal profile for the isouroniums is countered by a slight gain in clog *P* compared to **1**, **3** and sorafenib which are still far from the optimal value of 3. Correlation between clog *P* and PSA is presented in Fig. S4 (ESI†), where all compounds are found in a similar region.

Looking at the calculated basicity, compounds **1** and **2** present two pK_{aH} values due to the di-substituted guanidine linker. Despite the difference in basicity of the isolated cations (guanidinium is approximately 4 units more basic than isouronium), both sets of derivatives have very similar pK_{aH} values (~8.3 and ~8.7, respectively) and will be protonated at physiological pH. Finally, the calculated aqueous solubility of these compounds is in the range of moderate (**1**, **2** and sorafenib) to low (**3** and **4**) and no particular advantage in this property can be seen for the use of one cation over another.

Summarising, taking into account the cell viability results and calculated physicochemical parameters, both isouronium and guanidinium cations show very similar profiles and should be considered as interchangeable in drug design.

Next, the effect on the MAPK/ERK pathway of compounds **1** and **2** (the most cytotoxic agents for each family) and sorafenib was studied in HL-60 and MCF-7 cells by means of Western blotting (Fig. 3). From these experiments it can be reasoned that, after 16 hours in HL-60 cells, compound **2** has a similar effect to sorafenib in decreasing the levels of pERK, indicative of a decrease in activated ERK. However, lead compound **1** does not show any change compared to control and vehicle. These results are in agreement with the IC_{50} values obtained (Table 1). Furthermore, after 16 hours in MCF-7 cells, the effect on decreasing pERK expression is again very similar between compound **2** and sorafenib, but also a weak effect is now observed for compound **1**. Expression of total ERK remained unaffected by any of the three compounds.

In summary, we can conclude that compound **2** clearly affects the MAPK/ERK pathway both in HL-60 and MCF-7, which directly correlates with its potent inhibition of cancer cell growth. However, the actual interactions established with the target will only be identified if the crystal structure of the corresponding complex is resolved. Furthermore, regarding the mechanism of action of compound **1**, even though targeting of the MAPK/ERK pathway cannot be completely ruled out, other mechanisms may be involved and, thus, further studies will be pursued.

Experimental

Computational details

The geometry of the monomers and the complexes were fully optimized at DFT ωB97XD/6-31+G(d,p)[39] and then MP2/6-311+G(d,p) to obtain binding energies. All these calculations were carried out with Gaussian09 program.[40] Frequency calculations were performed at the same computational level to confirm that the resulting optimized structures are energetic minima. Interaction energies, E_i, (kJ mol^{-1}) were calculated as the difference between the total energy of the complex and the sum of the isolated monomers. The effect of water solvation was then accounted for using the SCFR-PCM approach implemented in the Gaussian09 package including dispersing, repulsing and cavitation energy terms of the solvent in the optimization. For the sake of clarity during the discussion, the atoms involved in each interaction have been labelled as indicated in Fig. S1.† The bonding characteristics were analysed by means of the atoms in molecules (AIM)

theory.[29] For this purpose we have located the most relevant bond critical points (BCP) and evaluated the electron density at each of them, by means of AIMAll program.[41] Electron density shift maps (EDS) have been obtained in order to provide an insight into the changes in the electron density of the monomers upon complexation. All the EDS maps have been obtained following the procedure previously reported.[42]

Synthetic procedures

All commercially available chemicals were obtained from Sigma-Aldrich or Fluka and used without further purification. Deuterated solvents for NMR use were purchased from Apollo and Euriso-top. Chromatographic columns were run using silica gel 60 (230–400 mesh ASTM). Solvents for synthesis purposes were used at GPR grade. Analytical TLC was performed using Merck Kieselgel 60 F_{254} silica gel plates or Polygram Alox N/UV254 aluminium oxide plates. Visualisation was by UV light (254 nm). NMR spectra were recorded on Agilent and Bruker Avance spectrometers, operating at 400.13 MHz and 600.1 MHz for ^{1}H NMR; 100.6 MHz and 150.9 MHz for ^{13}C NMR. Shifts are referenced to the internal solvent signals. NMR data were processed using MestreNova software. HRMS spectra were measured on a Micromass LCT electrospray TOF instrument with a WATERS 2690 autosampler and methanol as carrier solvent. Melting points were determined using a Stuart Scientific Melting Point SMP1 apparatus and are uncorrected. Infrared spectra were recorded on a Perkin Elmer Spectrum One FTIR spectrometer equipped with a Universal ATR sampling accessory. HPLC purity analysis was carried out using a Varian ProStar system equipped with a Varian Prostar 335 diode array detector and a manual injector (20 μL). For purity assessment, UV detection was performed at 245 nm and peak purity was confirmed using a purity channel. The stationary phase consisted of an ACE 5 C18-AR column (150 × 4.6 mm), and the mobile phase used the following gradient system, eluting at 1 mL min^{-1}: aqueous formate buffer (30 mM, pH 3.0) for 10 min, linear ramp to 85% methanol buffered with the same system over 25 min, hold at 85% buffered methanol for 10 min. Minimum requirement for purity was set at 95%.

4-{3-[3-(4-Chloro-3-trifluoromethylphenyl)guanidino]-phenoxy}phenylcarbamimidate dihydrochloride (2). A solution of the corresponding Boc-protected precursor **15** (100 mg, 0.13 mmol) in 10 mL of a 50% v/v solution of TFA and CH_2Cl_2 was stirred at room temperature. Once disappearance of starting material was observed by TLC (3 h), the excess of TFA and CH_2Cl_2 were removed under vacuum to generate the trifluoroacetate salt. The residue was dissolved in water (10 mL) and 500 mg of IRA400 Amberlite resin in its chloride-activated form was added, allowing the reaction to proceed overnight. The resin was then removed by filtration and the aqueous solution washed with CH_2Cl_2 (2 × 5 mL). Removal of water under vacuum yielded the final isouronium hydrochloride **2** as a white/yellow solid (67 mg, 95%). Absence of the trifluoroacetate salt was confirmed by ^{19}F NMR. Mp: decomposes over 120 °C. δ_H (400 MHz, CD_3OD): 7.02 (dd, J = 8.2, 2.0 Hz, 1H, Ar), 7.09 (t, J = 2.1 Hz, 1H, Ar), 7.17 (dd, J = 8.0, 1.3 Hz, 1H, Ar), 7.20 (d, J = 9.0 Hz, 2H, Ar), 7.35 (d, J = 9.0 Hz, 2H, Ar), 7.47 (t, J = 8.1 Hz, 1H, Ar), 7.60 (dd, J = 8.6, 2.4 Hz, 1H, Ar), 7.70 (d, J = 8.6 Hz, 1H, Ar), 7.75 (d, J = 2.3 Hz, 1H, Ar). δ_C (100 MHz, CD_3OD): 116.5 (CH, Ar), 118.6 (CH, Ar), 121.1 (CH, Ar), 122.2 (2 CH, Ar), 123.8 (d, J = 271.0 Hz, qCF_3), 124.0 (2 CH, Ar), 125.3 (q, J = 4.3 Hz, CH, Ar), 130.5 (d, J = 31.8 Hz, qC), 130.8 (CH, Ar), 131.3 (qC), 132.5 (CH, Ar), 134.3 (CH, Ar), 136.1 (qC), 137.9 (qC), 146.8 (qC), 156.3 (qC), 157.5 (qC), 159.5 (qC), 163.3 (qC). δ_F (376 MHz, CD_3OD): −64.33 (s). ν_{max} (ATR)/cm^{-1}: 3183 (NH), 2963 (CH), 1574 (C═N), 1477, 1250 (CF_3), 1096, 1030 (C–O), 1012 (C–Cl), 785, 667. HRMS (m/z ES$^+$) calcd for $C_{21}H_{17}ClF_3N_5O_2$ ([M + H]$^+$): 464.1096, found 464.1101. HPLC: 98.4% (t_R 27.01 min).

4-[3′-(4-Chloro-3-trifluoromethylbenzamido)phenoxy]-phenyl guanidine hydrochloride (3). To a stirred solution of **19** (90 mg, 0.14 mmol) in EtOAc was added $SnCl_4$ (0.06 mL, 0.56 mmol). After 1 h of stirring at room temperature, the solvent and the excess of $SnCl_4$ were evaporated *in vacuum*. The product was purified by flash chromatography (silica gel, $CHCl_3$: MeOH, 100 : 0 → 95 : 5) and the purified fraction was then dissolved in MeOH and recrystallized from Et_2O to obtain **3** as a white solid (32 mg, 47%). Mp: decomposes over 120 °C. δ_H (400 MHz, CD_3OD): 6.86 (d, J = 7.8 Hz, 1H, Ar), 7.12 (d, J = 8.6 Hz, 2H, Ar), 7.30 (d, J = 8.7 Hz, 2H, Ar), 7.35–7.43 (m, 2H, Ar), 7.62 (s, 1H, Ar), 7.77 (d, J = 8.3 Hz, 1H, Ar), 8.16 (dd, J = 8.3, 1.5 Hz, 1H, Ar), 8.32 (s, 1H, Ar). δ_C (100 MHz, CD_3OD): 112.9 (CH, Ar), 116.3 (CH, Ar), 117.3 (CH, Ar), 121.0 (2 CH, Ar), 124.0 (d, J = 272.5 Hz, qCF_3), 128.2 (q, J = 5.5 Hz, CH, Ar), 128.9 (2 CH Ar), 129.4 (d, J = 31.6, qC), 130.9 (qC), 131.2 (CH, Ar), 133.1 (CH, Ar), 133.6 (CH, Ar), 135.3 (qC), 136.5 (qC), 141.2 (qC), 158.1 (qC), 158.3 (qC), 158.4 (qC), 166.0 (qC). δ_F (376 MHz, CD_3OD): −64.11 (s). ν_{max} (ATR)/cm^{-1}: 3413 (NH), 3343 (NH), 1602 (C═O), 1504 (C═N), 1450, 1412, 1261 (C–N), 1216 (C–O), 1134 (CF_3), 1035 (C–Cl), 924, 845. HRMS (m/z ES$^+$) calcd for $C_{21}H_{16}ClF_3N_4O_2$ ([M + H]$^+$): 449.0987, found 449.0988. HPLC: 98.9% (t_R 32.25 min).

4-{3-[4-Chloro-3-(trifluoromethyl)benzamido]phenoxy}-phenyl carbamimidate hydrochloride (4). To a stirred solution of **22** (47 mg, 0.07 mmol) in EtOAc was added $SnCl_4$ (0.033 mL, 0.28 mmol). After 1 h of stirring at room temperature, the solvent and the excess of $SnCl_4$ were evaporated *in vacuum*. The product was purified by flash chromatography (silica gel, $CHCl_3$: MeOH, 100 : 0 → 95 : 5) to afford the final hydrochloride salt **4** (17 mg, 51%) as a white/yellow gum. δ_H (400 MHz, CD_3OD): 6.84 (dd, J = 8.0, 1.8 Hz, 1H, Ar), 7.13 (d, J = 8.8 Hz, 2H, Ar), 7.30 (d, J = 8.9 Hz, 2H, Ar), 7.35 (t, J = 8.1 Hz, 1H, Ar), 7.44 (d, J = 8.0 Hz, 1H, Ar), 7.60 (s, 1H, Ar), 7.74 (d, J = 8.3 Hz, 1H, Ar), 8.17 (dd, J = 8.3, 1.6 Hz, 1H, Ar), 8.29 (d, J = 1.5 Hz, 1H, Ar), 8.66 (bs, NH). δ_C (150 MHz, CD_3OD): 113.0 (CH, Ar), 116.3 (CH, Ar); 117.5 (CH, Ar), 121.6 (2 CH, Ar), 122.2 (qC), 124.1 (d, J = 272.5 Hz, qCF_3), 123.8 (2 CH, Ar), 128.2 (q, J = 5.4 Hz, CH, Ar), 129.5 (d, J = 31.7 Hz, qC), 131.3 (CH, Ar), 133.1 (CH, Ar), 133.7 (CH, Ar), 135.4 (qC), 136.6 (qC), 141.3 (qC), 146.4 (qC), 158.2 (qC), 158.4 (qC), 166.1

(qC). δ_F (376 MHz, CD_3OD): −62.22 (s). ν_{max} 3329 (NH), 1695, 1648, 1602 (C═O), 1482 (C═N), 1249 (C–O), 1192 (CF_3), 1131, 1111 (C–Cl), 780, 660. HRMS (*m*/*z* ES^+) calcd for $C_{21}H_{15}ClF_3N_3O_3$ ($[M + H]^+$): 450.0827, found 450.0835. HPLC: 97.69% (t_R 31.72 min).

Biochemical methods

Preparation of stock solution. Stock solutions (10 mM) of the compounds were prepared in sterile EtOH or DMSO and were then sterile filtered (0.2 μM filters). Required concentration ranges (10–0.01 mM) of each drug were prepared in sterile EtOH or DMSO/ddH_2O and stored at −20 °C until required. Sorafenib was purchased from LC laboratories.

HL-60 cell line. The HL-60 (human caucasian promyelocytic leukemia) cell line was purchased from Sigma-Aldrich. They were maintained between 200 000 and 2 000 000 cells per mL in Roswell Park Memorial Institute (RPMI) 1640 medium with stable glutamate (GlutaMax I) supplemented with 10% (v/v) foetal bovine serum (FBS) and 50 μg mL^{-1} penicillin/streptomycin (pen–strep). The growth medium was stored in the fridge at 4 °C and heated to 37 °C prior to culture work. Cells were grown at 37 °C in a humidified environment maintained at 95% O_2 and 5% CO_2 and passaged at least twice weekly depending on their levels of confluency. When required for sub-culturing, cells were transferred to a sterile tube and centrifuged at 300 × *g* for 5 min. The supernatant was discarded and the cell pellet was re-suspended in 15 mL of fresh medium. Cells were then counted and seeded at a density of 200 000 cells per mL (200 μL per well or 4 × 10^4 cells per well) in complete medium.

HeLa cell line. The HeLa (human epithelioid cervix carcinoma) cell line was purchased from ECACC. They were maintained in Dulbecco's modified Eagle's medium (DMEM) supplemented with 10% (v/v) foetal bovine serum (FBS) and 50 μg mL^{-1} penicillin/streptomycin (pen–strep). The growth medium was stored in the fridge at 4 °C and heated to 37 °C prior to culture work. Cells were grown at 37 °C in a humidified environment maintained at 95% O_2 and 5% CO_2 and passaged at least twice weekly depending on their levels of confluency. When required for sub-culturing, cells were trypsinised and transferred to a sterile tube and centrifuged at 300 × *g* for 5 min. The supernatant was discarded and the cell pellet was re-suspended in 15 mL of fresh medium. HeLa cells were then counted and seeded in 96-well plates at a density of 2.5 × 10^4 cells per mL (200 μL per well or 5 × 10^3 cells per well) in complete medium.

MCF-7 cell line. The MCF-7 (human breast tumour) cell line was purchased from ATCC and maintained in Roswell Park Memorial Institute (RPMI) 1640 medium with stable glutamate (GlutaMax I) supplemented with 10% (v/v) foetal bovine serum (FBS), 50 μg mL^{-1} penicillin/streptomycin (pen–strep) and 2 mM L-glutamine. The growth medium was stored in the fridge at 4 °C and heated to 37 °C prior to culture work. Cells were grown at 37 °C in a humidified environment maintained at 95% O_2 and 5% CO_2 and passaged at least twice weekly depending on their levels of confluency. When required for sub-culturing, cells were trypsinised and transferred to a sterile tube and centrifuged at 300 × *g* for 5 min. The supernatant was discarded and the cell pellet was re-suspended in 15 mL of fresh medium. MCF-7 cells were then counted and seeded in 96-well plates at a density of 2.5 × 10^4 cells per mL (200 μL per well or 5 × 10^3 cells per well) in complete medium.

Cell viability (Alamar Blue®). The 96 well plates were then treated with a 1 : 100 dilution of stock concentrations of drugs or EtOH (1% v/v)/DMSO (0.1% v/v) as vehicle control in triplicate. Three blank wells containing 200 μL RPMI with no cells were also set-up as blank wells. After a 72 h incubation, 20 μL of Alamar Blue was added to each well. The plates were incubated in darkness at 37 °C for 4–5 h. Using a molecular devices microplate reader, the fluorescence (*F*) was then read at an excitation wavelength of 544 nm and an emission wavelength of 590 nm. Cell viability was then determined by subtracting the mean blank fluorescence (F_b) from the treated sample fluorescence (F_s) and expressing this as a percentage of the fluorescence of the blanked vehicle control (F_c). This is demonstrated in eqn (1). The results were then plotted as a nonlinear regression, sigmoidal dose–response curves on Prism, from which the IC_{50} value for each drug was determined.

$$(F_s - F_b)/(F_c - F_b) \times 100 = \%\text{Cell Viability} \quad (1)$$

MAPK/Erk pathway analysis (Western blotting). MCF-7 and HL-60 cells were seeded in T25 flasks at a density of 50 × 10^4 cells per mL for HL-60 and 25 × 10^4 cells per mL for MCF-7. Cells were then treated with either vehicle [0.1% ethanol (v/v)], sorafenib (10 μM), compound **1** (10 μM) or compound **2** (10 μM). Cells were harvested and washed with PBS. Cell pellets were re-suspended in ice-cold radioimmunoprecipitation assay buffer (RIPA buffer), supplemented with 1% (v/v) phosphatase inhibitor cocktail 2 and 3 (Sigma) and 10% (v/v) protease inhibitor (Roche). Lysis was carried out for 30 minutes on ice. Cellular lysates were clarified by centrifugation for 10 minutes at 14 000 × *g* at 4 °C. Protein concentration was determined and normalized using a BCA assay. Lysates were boiled with Laemmli sample buffer [Tris-HCl 50 mM (pH 6.7), glycerol 10% (w/v), sodium dodecyl sulphate 2% (w/v), bromophenol blue 0.02% (w/v)] containing DTT 50 μM for 10 minutes at 90 °C. Equal protein concentrations of lysates were resolved by sodium dodecyl sulphate polyacrylamide gel electrophoresis (SDS-PAGE) and transferred onto PVDF transfer membrane (EMD Millipore, Germany). The membranes were blocked in 5% non-fat milk and probed with primary antibodies for ERK, phospho-ERK (Cell Signalling, Danvers, MA) and GAPDH (Calbiochem) at 4 °C overnight and secondary antibodies the next day.

Conclusions

In this study, we have computationally characterised and analysed the nature of the interactions potentially established

upon complexation of 4-phenoxyphenyl-*O*-isouronium derivative with the ATP molecule and compared them with results previously obtained for a similar arylguanidinium. Considering our hypothesis that the guanidinium moiety of the previously identified lead compound **1** interacts with the γ-phosphate of ATP within the hinge region of an active protein kinase, our results now indicate that an isouronium analogue will be able to interact in a similar manner with the ATP molecule inhibiting kinase activity.

To evaluate the effect on antitumor activity of the guanidinium/isouronium substitution as well as the molecular shortening and conformational change, compounds **2**, **3** and **4** were prepared. Compound **3** is an amide-linked (shorter) version of the guanidine-linked lead compound **1** that will place the lipophilic 4-(Cl)-3-(CF_3)-Ph group in a different orientation, whereas compounds **2** and **4** are the corresponding isouronium analogues of **1** and **3**, respectively. Compounds **2**, **3** and **4** were successfully prepared through the amidylation of the corresponding aromatic amines or phenols by reaction with *N*,*N*′-bis-(*tert*-butoxycarbonyl)-*S*-methylisothiourea in the presence of mercury(II) chloride and triethylamine followed by Boc-deprotection to yield the corresponding hydrochloride salts in good to excellent yields.

The effect of all these compounds on cell viability was tested in human leukaemia (HL-60), breast cancer (MCF-7) and cervical cancer (HeLa) cell lines and the corresponding IC_{50} values were compared with those of the lead compound **1**. It was observed that the replacement of the di-substituted guanidine by an amide results in lower activity probably due to the wrong orientation of the lipophilic moiety of the molecules. However, replacement of the mono-substituted guanidinium by an isouronium cation seems to be beneficial for this activity probably due to improved pharmacokinetic properties. Accordingly, a number of physicochemical parameters (PSA, clog*P*, pK_{aH} and aqueous solubility) were calculated and the values obtained were in agreement with the cytotoxicity observed.

Finally, the effect of compounds **1** and **2** on the Ras–Raf–MEK–ERK pathway was explored by means of Western blot experiments measuring the effect of these compounds on the expression of phosphorylated ERK (pERK) and total ERK both in HL-60 and MCF-7 cancer cells. These experiments showed that compound **2** clearly inhibits the expression of pERK in both cell lines, whereas compound **1** only affects the expression of pERK in MCF-7 cells. This indicates that the most likely mechanism of anticancer action of compound **2** involves targeting of the MAPK/ERK pathway; however, for compound **1**, even though this mechanism of action cannot be discarded for MCF-7 cells, other targets are likely for HL-60 cancer cells. Even though the exact mode of action and/or targeting of the compounds in the MAPK/ERK pathway cannot be accurately determined with these experiments, a clear indication of their interference with this pathway is obtained and further studies are being pursued.

Taking all these results together we can conclude that the isouronium functionality is a good alternative to guanidinium and they can be interchanged for potential type III allosteric kinase inhibitors.

Conflicts of interest

The authors declare no competing interest.

Acknowledgements

Thanks are given to the School of Chemistry (V. P.) and the John Scott PhD fellowship from the School of Biochemistry & Immunology and the School of Medicine (R. A.) at Trinity College Dublin for postgraduate support. Thanks are given to the Irish Centre for High-End Computing (ICHEC) for the provision of computational facilities and to Dr. Goar Sanchez (ICHEC) for the AIM graphical outputs.

Notes and references

1 P. Cohen, *Nat. Rev. Drug Discovery*, 2002, **1**, 309–315.
2 P. Wu, T. E. Nielsen and M. H. Clausen, *Trends Pharmacol. Sci.*, 2015, **36**, 422–439.
3 M. A. Fabian, W. H. Biggs, D. K. Treiber, C. E. Atteridge, M. D. Azimioara, M. G. Benedetti, T. A. Carter, P. Ciceri, P. T. Edeen, M. Floyd, J. M. Ford, M. Galvin, J. L. Gerlach, R. M. Grotzfeld, S. Herrgard, D. E. Insko, M. A. Insko, A. G. Lai, J. M. Lelias, S. A. Mehta, Z. V. Milanov, A. M. Velasco, L. M. Wodicka, H. K. Patel, P. P. Zarrinkar and D. J. Lockhart, *Nat. Biotechnol.*, 2005, **23**, 329–336.
4 J. Zhang, P. L. Yang and N. S. Gray, *Nat. Rev. Cancer*, 2009, **9**, 28–39.
5 Z. Fang, C. Grutter and D. Rauh, *ACS Chem. Biol.*, 2013, **8**, 58–70.
6 W. Kolch, *Biochem. J.*, 2000, **351**, 289–305.
7 P. J. Roberts and C. J. Der, *Oncogene*, 2007, **26**, 3291–3310.
8 A. A. Samatar and P. I. Poulikakos, *Nat. Rev. Drug Discovery*, 2014, **13**, 928–942.
9 G. Maurer, B. Tarkowski and M. Baccarini, *Oncogene*, 2011, **30**, 3477–3488.
10 J. Hu, E. C. Stites, H. Yu, E. A. Germino, H. S. Meharena, P. J. Stork, A. P. Kornev, S. S. Taylor and A. S. Shaw, *Cell*, 2013, **154**, 1036–1046.
11 G. Hatzivassiliou, J. R. Haling, H. Chen, K. Song, S. Price, R. Heald, J. F. M. Hewitt, M. Zak, A. Peck, C. Orr, M. Merchant, K. P. Hoeflich, J. Chan, S.-M. Luoh, D. J. Anderson, M. J. C. Ludlam, C. Wiesmann, M. Ultsch, L. S. Friedman, S. Malek and M. Belvin, *Nature*, 2013, **501**, 232–236.
12 C. A. Hall-Jackson, P. A. Eyers, P. Cohen, M. Goedert, F. T. Boyle, N. Hewitt, H. Plant and P. Hedge, *Chem. Biol.*, 1999, **6**, 559–568.
13 A. D. Cox and C. J. Der, *Cancer Cell*, 2010, **17**, 221–223.
14 A. G. Gilmartin, M. R. Bleam, A. Groy, K. G. Moss, E. A. Minthorn and S. G. Kulkarni, *Clin. Cancer Res.*, 2012, **18**, 2413.
15 E. Diez-Cecilia, R. Carson, B. Kelly, S. van Schaeybroeck, J. T. Murray and I. Rozas, *Bioorg. Med. Chem. Lett.*, 2015, **25**, 4287–4292.

16 E. Diez-Cecilia, B. Kelly, C. Perez, D. M. Zisterer, D. K. Nevin, D. G. Lloyd and I. Rozas, *Eur. J. Med. Chem.*, 2014, **81**, 427–441.
17 C. Trujillo, V. Previtali and I. Rozas, *Theor. Chem. Acc.*, 2016, **135**, 260.
18 T. Ishikawa, *Superbases for Organic Synthesis*, John Wiley & Sons, Ltd, Edition edn, 2009, pp. 93–143.
19 C. Dardonville, B. A. Caine, M. Navarro de la Fuente, G. Martin Herranz, B. Corrales Mariblanca and P. L. A. Popelier, *New J. Chem.*, 2017, **41**, 11016–11028.
20 C. J. Heneghan, I. Onakpoya, M. Thompson, E. A. Spencer, M. Jones and T. Jefferson, *BMJ*, 2014, **348**, g2547.
21 R. C. Young, G. J. Durant, J. C. Emmett, C. R. Ganellin, M. J. Graham, R. C. Mitchell, H. D. Prain and M. L. Roantree, *J. Med. Chem.*, 1986, **29**, 44–49.
22 B. Rouot, G. Leclerc, C. G. Wermuth, F. Miesch and J. Schwartz, *J. Med. Chem.*, 1976, **19**, 1049–1054.
23 I. Rozas, G. Sanchez-Sanz, I. Alkorta and J. Elguero, *J. Phys. Org. Chem.*, 2013, **26**, 378–385.
24 I. Rozas, I. Alkorta and J. Elguero, *Struct. Chem.*, 2008, **19**, 923–933.
25 I. Rozas and P. E. Kruger, *J. Chem. Theory Comput.*, 2005, **1**, 1055–1062.
26 P. S. Nagle, A. Kahvedzic, T. McCabe and I. Rozas, *Struct. Chem.*, 2012, **23**, 315–323.
27 A. Kahvedzic-Seljubac, S. M. Nathwani, D. M. Zisterer and I. Rozas, *Eur. J. Med. Chem.*, 2016, **117**, 269–282.
28 A. Goonan, A. Kahvedzic, F. Rodriguez, P. S. Nagle, T. McCabe, I. Rozas, A. M. Erdozain, J. J. Meana and L. F. Callado, *Bioorg. Med. Chem.*, 2008, **16**, 8210–8217.
29 R. F. W. Bader, *Atoms in Molecules: A Quantum Theory*, Clarendon Press, Oxford, 1990.
30 Y. Li, A. Urbas and Q. Li, *J. Org. Chem.*, 2011, **76**, 7148–7156.
31 M. Miyashita, A. Yoshikoshi and P. A. Grieco, *J. Org. Chem.*, 1977, **42**, 3772–3774.
32 D. Maiti and S. L. Buchwald, *J. Am. Chem. Soc.*, 2009, **131**, 17423–17429.
33 T. S. Li, Z. H. Zhang and T. S. Jin, *Synth. Commun.*, 1999, **29**, 181–188.
34 K. S. Kim and L. G. Qian, *Tetrahedron Lett.*, 1993, **34**, 7677–7680.
35 X. J. Du, Q. Bian, H. X. Wang, S. J. Yu, J. J. Kou, Z. P. Wang, Z. M. Li and W. G. Zhao, *Org. Biomol. Chem.*, 2014, **12**, 5427–5434.
36 H. Miel and S. Rault, *Tetrahedron Lett.*, 1997, **38**, 7865–7866.
37 *MarvinSketch 15.9.7* (http://www.chemaxon.com), ChemAxon, 2015.
38 P. Ertl, B. Rohde and P. Selzer, *J. Med. Chem.*, 2000, **43**, 3714–3717.
39 M. J. Frisch, J. A. Pople and J. S. Binkley, *J. Chem. Phys.*, 1984, **80**, 3265–3269.
40 M. J. Frisch, G. W. Trucks, H. B. Schlegel, G. E. Scuseria, M. A. Robb, J. R. Cheeseman, G. Scalmani, V. Barone, B. Mennucci, G. A. Petersson, H. Nakatsuji, M. Caricato, X. Li, H. P. Hratchian, A. F. Izmaylov, J. Bloino, G. Zheng, J. L. Sonnenberg, M. Hada, M. Ehara, K. Toyota, R. Fukuda, J. Hasegawa, M. Ishida, T. Nakajima, Y. Honda, O. Kitao, H. Nakai, T. Vreven, J. A. Montgomery, Jr., J. E. Peralta, F. Ogliaro, M. Bearpark, J. J. Heyd, E. Brothers, K. N. Kudin, V. N. Staroverov, R. Kobayashi, J. Normand, K. Raghavachari, A. Rendell, J. C. Burant, S. S. Iyengar, J. Tomasi, M. Cossi, N. Rega, J. M. Millam, M. Klene, J. E. Knox, J. B. Cross, V. Bakken, C. Adamo, J. Jaramillo, R. Gomperts, R. E. Stratmann, O. Yazyev, A. J. Austin, R. Cammi, C. Pomelli, J. W. Ochterski, R. L. Martin, K. Morokuma, V. G. Zakrzewski, G. A. Voth, P. Salvador, J. J. Dannenberg, S. Dapprich, A. D. Daniels, Ö. Farkas, J. B. Foresman, J. V. Ortiz, J. Cioslowski and D. J. Fox, *Gaussian 09*, Gaussian, Inc., Wallingford CT, 2009.
41 T. A. Keith, *AIMAll, TK Gristmill Software, Version 17.01.25*, 2017.
42 G. Sanchez-Sanz, C. Trujillo, I. Alkorta and J. Elguero, *Comput. Theor. Chem.*, 2012, **991**, 124–133.

European Journal of Medicinal Chemistry 162 (2019) 290–320

Contents lists available at ScienceDirect

European Journal of Medicinal Chemistry

journal homepage: http://www.elsevier.com/locate/ejmech

Research paper

Structure-activity relationships, biological evaluation and structural studies of novel pyrrolonaphthoxazepines as antitumor agents

Margherita Brindisi [a, b], Cristina Ulivieri [b, c], Gloria Alfano [a, b], Sandra Gemma [a, b], Francisco de Asís Balaguer [d], Tuhina Khan [a], Alessandro Grillo [a, b], Giulia Chemi [a, b], Grégory Menchon [e, f], Andrea E. Prota [e, f], Natacha Olieric [e, f], Daniel Lucena-Agell [d], Isabel Barasoain [d], J. Fernando Diaz [d], Angela Nebbioso [g], Mariarosaria Conte [h], Ludovica Lopresti [b, c], Stefania Magnano [i], Rebecca Amet [i], Paula Kinsella [i], Daniela M. Zisterer [i], Ola Ibrahim [j], Jeff O'Sullivan [j], Lucia Morbidelli [b, c], Roberta Spaccapelo [k], Cosima Baldari [b, c], Stefania Butini [a, b, *], Ettore Novellino [l], Giuseppe Campiani [a, b, **], Lucia Altucci [g], Michel O. Steinmetz [e, f], Simone Brogi [a, b, l]

[a] European Research Centre for Drug Discovery and Development (NatSynDrugs), University of Siena, Department of Biotechnology, Chemistry and Pharmacy, DoE Department of Excellence 2018-2022, via Aldo Moro 2, I-53100, Siena, Italy
[b] Istituto Toscano Tumori, University of Siena, via Aldo Moro 2, I-53100, Siena, Italy
[c] Department of Life Sciences, via Aldo Moro 2, I-53100, Siena, Italy
[d] Department of Physical and Chemical Biology, Centro de Investigaciones Biologicas, Consejo Superior de Investigaciones Cientificas, Ramiro de Maeztu 9, 28040, Madrid, Spain
[e] Laboratory of Biomolecular Research, Division of Biology and Chemistry, Paul Scherrer Institut, 5232, Villigen, Switzerland
[f] University of Basel, Biozentrum, 4056 Basel, Switzerland
[g] Department of Precision Medicine, University of Campania Luigi Vanvitelli, Vico L. de Crecchio 7, 80138, Naples, Italy
[h] IRCCS, SDN, Via E. Gianturco 113, 80143, Naples, Italy
[i] School of Biochemistry and Immunology, Trinity Biomedical Sciences Institute, Trinity College Dublin, 152-160, Pearse Street, Dublin 2, Ireland
[j] School of Dental Science, Trinity College Dublin, Lincoln Place, Dublin 2, Ireland
[k] Department of Experimental Medicine, University of Perugia, P.le Gambuli, I-06132, Perugia, Italy
[l] Department of Pharmacy, University of Napoli Federico II, DoE Department of Excellence 2018-2022, Via D. Montesano 49, 80131, Napoli, Italy

ARTICLE INFO

Article history:
Received 16 July 2018
Received in revised form
11 October 2018
Accepted 2 November 2018
Available online 3 November 2018

Keywords:
Apoptosis
Antitumor agents
Microtubule-targeting agent
Tubulin
X-ray crystallography
Molecular modeling

ABSTRACT

Microtubule-targeting agents (MTAs) are a class of clinically successful anti-cancer drugs. The emergence of multidrug resistance to MTAs imposes the need for developing new MTAs endowed with diverse mechanistic properties. Benzoxazepines were recently identified as a novel class of MTAs. These anti-cancer agents were thoroughly characterized for their antitumor activity, although, their exact mechanism of action remained elusive. Combining chemical, biochemical, cellular, bioinformatics and structural efforts we developed improved pyrrolonaphthoxazepines antitumor agents and their mode of action at the molecular level was elucidated. Compound **6j**, one of the most potent analogues, was confirmed by X-ray as a colchicine-site MTA. A comprehensive structural investigation was performed for a complete elucidation of the structure-activity relationships. Selected pyrrolonaphthoxazepines were evaluated for their effects on cell cycle, apoptosis and differentiation in a variety of cancer cells, including multidrug resistant cell lines. Our results define compound **6j** as a potentially useful optimized hit for the development of effective compounds for treating drug-resistant tumors.

* Corresponding author. European Research Centre for Drug Discovery and Development (NatSynDrugs), University of Siena, Department of Biotechnology, Chemistry and Pharmacy, DoE Department of Excellence 2018-2022, via Aldo Moro 2, I-53100, Siena, Italy.
** Corresponding author. European Research Centre for Drug Discovery and Development (NatSynDrugs), University of Siena, Department of Biotechnology, Chemistry and Pharmacy, DoE Department of Excellence 2018-2022, via Aldo Moro 2, I-53100, Siena, Italy.
E-mail addresses: butini3@unisi.it (S. Butini), campiani@unisi.it (G. Campiani).

https://doi.org/10.1016/j.ejmech.2018.11.004
0223-5234/

1. Introduction

Microtubules (MTs) are the principal component of the cell cytoskeleton involved in a variety of crucial cell processes in eukaryotes such as growth, proliferation, trafficking, motility and autophagy [1–3]. In particular, MTs are found in mammalian cells and are involved in two different mitosis phases: interphase and division [1]. MTs consist of αβ-tubulin heterodimers that polymerize in a polarized way by a nucleation-elongation mechanism non-covalently adding dimers at the ends of MTs and forming hollow tubes. The terminal parts of the MT (denoted the plus- and minus-end) are continuously alternating between elongation and shortening periods - a property denoted dynamic instability [4] and which is highly regulated by accessory proteins in cells. It is well-known that cancer cells display an altered mitosis rate. Therefore, interfering with MT dynamics by microtubule-targeting agents (MTAs), represents one of the most important targets in cancer therapy [5]. MTAs can display different interaction sites on both α- and β-tubulin [6,7]. The most well-characterized sites include: i) the well-known taxane site, targeted by compounds such as taxol (**1**), located on β-tubulin in a profound hydrophobic cleft; ii) the site targeted by laulimalide (**2**) that binds to β-tubulin in a different pocket from the taxane site; iii) the vinca site located at the plus-end edge near the GTP binding site of β-tubulin, targeted by compounds such as vinblastine (**3**); and iv) the colchicine site situated at the tubulin intradimer interface between the α- and β-tubulin subunit and targeted by MTAs such as colchicine (**4**) and nocodazole (**5**) (Fig. 1) [8]. Additional very well characterized sites are the maytansine site [9] and the pironetin site [10]. The colchicine site is one of the most important binding pockets for MTAs and compounds acting on this site (e.g. **5**) are well-known microtubule-destabilizing agents (MDAs).

Alteration of MT dynamics can lead to cell cycle arrest and consequently to cell death by apoptosis in dividing cells. Additionally, the capability of MTAs to interact with the autophagy process, could suggest an additional therapeutic benefit by blocking or stimulating the process. Part of the cytotoxic effect of compound **1**, indeed, comprises the capability of blocking autophagosome maturation [11], while the other MTAs such as **3** and **4** are able to stimulate autophagy. This latter mechanism could contribute to their anticancer activity [12–15]. In this scenario, following our interest in the field, pyrrolo-1,5-benzoxazepines, typified by the 4-acetoxy-5-(1-naphthyl)naphtho[2,3-*b*]pyrrolo[2,1-*d*][1,4]oxazepine, (**PNOX**, Table 1) were developed as MDAs and were thoroughly characterized assessing their antitumor activity [16–18]. In particular, compound **PNOX** and related analogues were shown to inhibit the growth of a number of cancer cell lines such as ovarian carcinoma cell lines, oral squamous carcinoma cells, acute lymphoblastic leukemia cells, neuroblastoma cells, human colon cancer cells, malignant hematopoietic cells, breast tumor cells, prostate cancer cells, embryo cell lines and other myeloma and leukemia cells [17,19–26]. With the aim of further improving the class of benzoxazepine anticancers (antitumor potency and drug-like properties) and to fully elucidate their mechanism of action, we extended our studies by further decorating and/or modifying the original scaffold at different levels [27]. In particular, taking into account the high lipophilicity of the early developed analogues, typified by **PNOX** (cocrystallization/soaking of **PNOX** and related molecules with tubulin was unsuccessful), we attempted to attenuate lipophilicity by introducing specific structural modifications such as polar groups and/or heteroatoms. We herein present a multidisciplinary approach to the discovery of novel naphthoxazepine analogues with improved physicochemical properties, and a crystallographic study to unveil the binding site and mode of action on tubulin and microtubules of the novel analogues is discussed. A set of pyrrolonaphth(benz)oxazepine was synthesized (**6a-r**, Table 1) and appropriate biochemical studies were undertaken for establishing the affinity of selected analogues on isolated tubulin. The effects of the novel compounds were also evaluated against a relevant panel of different types of cancer cells including MDR cell lines. Finally, we carried out studies to assess the influence of the newly developed derivatives on the cell cycle, apoptosis and differentiation and to establish their effect on the autophagy process. These studies provided essential insight into the mechanism of action of the new PNOX derivatives and useful hints for the future design of improved analogues. A structure-activity relationship (SAR) study is discussed. This work identified compound **6j** as the most promising anticancer agent of the whole series, potentially useful as a novel interesting hit for the development of effective compounds for treating drug-resistant tumors.

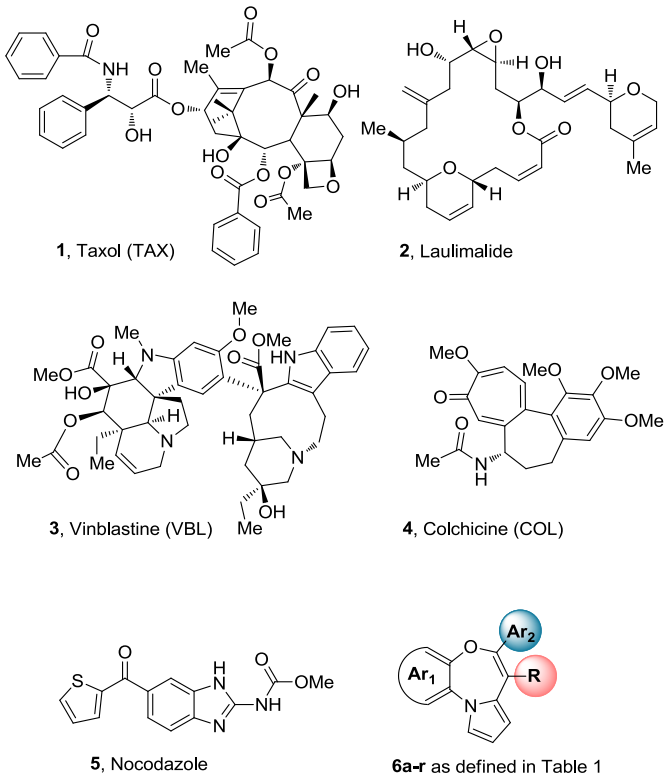

Fig. 1. Representative MTAs (**1**–**5**) and general structure of title compounds **6a-r**.

2. Results and discussion

2.1. Chemistry

The general retrosynthetic scheme for the synthesis of the novel compounds **6a-r** is described in Fig. 2. The synthesis of the key pyrrolonaphth(benz)oxazepinone template could derive from an alkylation reaction between pyrrolylphenol derivatives (**8**) and the suitable α-bromo esters (**9a-e**) providing the arylalkyl ether skeleton to undergo intramolecular cyclization generating key ketones **7**.

Due to the lengthy and often problematic synthesis of α-bromobenzyl derivatives and in order to identify a more general and expedite chemical route to target compounds, we subsequently envisioned a novel straightforward Mitsunobu-based route for the construction of the key aryl-alkyl ether template. Accordingly, a glioxylate intermediate could represent a convenient access to the required α-hydroxyester derivatives (**10a-g**) to undergo Mitsunobu

Table 1
Novel **PNOX** derivatives **6a-r**.

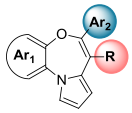

Cpd	Ar_1	Ar_2	R	Cpd	Ar_1	Ar_2	R
PNOX	naphtho [2,3]		OCOMe	**6j**	naphtho [2,3]		OCOMe
6a	naphtho[2,3]		OCOMe	**6k**	naphtho[2,3]	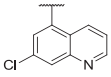	OCOMe
6b	naphtho[2,3]		$OCONMe_2$	**6l**	naphtho[2,3]	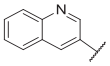	OCOMe
6c	naphtho[2,3]		$OCONEt_2$	**6m**	naphtho[2,3]		OCOMe
6d	naphtho[2,3]		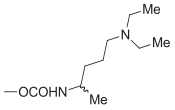	**6n**	naphtho[2,3]	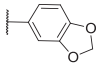	OCOMe
6e	naphtho[2,3]	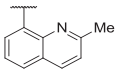	OCOMe	**6o**	naphtho[2,3]		OCOMe
6f	naphtho[2,3]	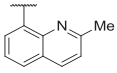	$OCONEt_2$	**6p**	benzo		OCOMe
6g	naphtho[2,3]	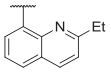	OCOMe	**6q**	naphtho[2,3]		NHCOMe
6h	naphtho[2,3]	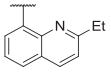	$OCONMe_2$	**6r**	naphtho[2,3]		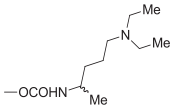
6i	naphtho[2,3]	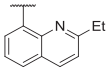	$OCONEt_2$				

reaction with the pyrrolylphenol derivatives (**8**). This revised path also provided a 3-step shorter route to the desired pyrrolobenzoxazepinone template **7**. In Fig. 2 we also reported the fragments engaged for the construction of the key cyclic ketone **7** subgrouped according to the employed route.

Scheme 1 reports the synthetic route for the construction of the quinoline-based α-bromoderivatives **9a-c** bearing an 8-, 5- and 3-quinolyl aromatic portion, respectively. In a first instance, 8-bromoquinoline **13a** was obtained by Skraup reaction on 2-bromoaniline **11** in the presence of glycerol, nitrobenzene and Fe(II) sulfate under strongly acidic conditions. Due to the poor yields provided by this method, a second route was envisaged, employing 8-aminoquinoline **12**, Cu(II) bromide and *tert*-butyl nitrite [28]. 8-Bromoquinoline **13a** and the commercially available 5-bromoquinoline **13b** were reacted with *N,N*-dimethylformamide (DMF) in the presence of *n*-butyllithium at −78 °C providing the corresponding formyl derivatives **14a,b**. Subsequently, aldehyde homologation was performed by reacting intermediates **14a,b** with (methoxymethyl)triphenylphosphonium chloride in the presence of sodium *bis*(trimethylsilyl)amide as the base. The resulting enol ethers **15a,b** were effectively cleaved in acidic medium providing the homologated aldehydes **16a,b** [29]. Oxidation with *N*-iodosuccinimide (NIS), in the presence of potassium carbonate and methanol [30], led to the corresponding methyl esters **17a,b**, which underwent radicalic bromination in the presence of *N*-bromosuccinimide (NBS), thus providing the desired bromo-derivatives **9a,b**.

The chemical route employed for the synthesis of compound **9c** entirely traced that adopted for the synthesis of compounds **9a,b**. Accordingly, formylation of the bromoderivative **18** followed by homologation of the resulting aldehyde **19** provided the corresponding enol ether finally hydrolyzed to the corresponding homologated aldehyde **20**. The oxidation of this latter to methyl ester, followed by radicalic bromination, led to intermediate compound **9c**.

The synthesis of compound **9d** is reported in Scheme 2. 8-Aminoquinoline **12** was brominated at 5-position with *N*-bromosuccinimide (NBS) in acetonitrile providing intermediate **21**. This latter was reacted with *N*-chlorosuccinimide (NCS) to afford the 5-bromo-7-chloro-8-aminoquinoline **22**. Reductive deamination in the presence of sodium nitrite and hypophosphorous acid provided 5-bromo-7-chloroquinoline **23** [31]. Conversion of **23** into the

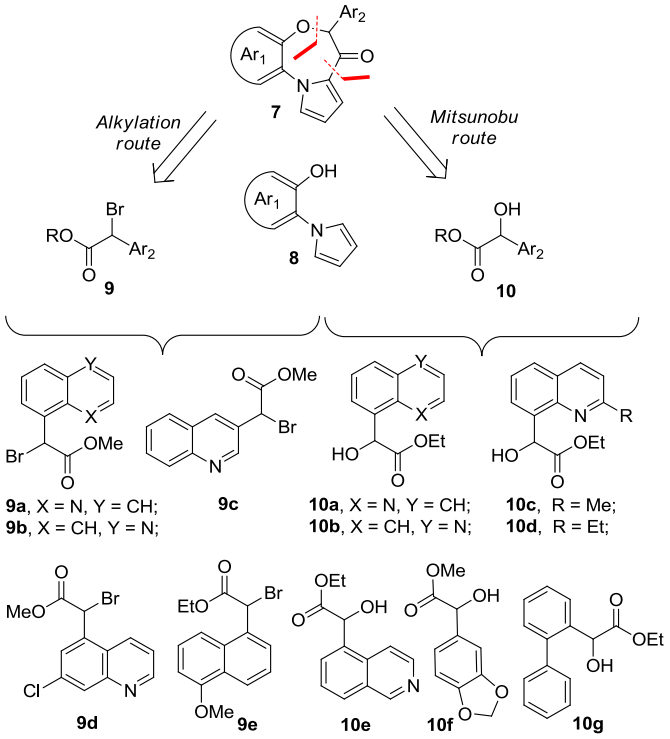

Fig. 2. Retrosynthetic pathways for the construction of the pyrrolonaphth(benz)oxazepinone core **7** and representation of α-bromoester derivatives **9a-e** and α-hydroxyesters **10a-g**.

formation of enol ether **25** was followed by hydrolysis to the corresponding homologated aldehyde **26**. Oxidation of this latter to methyl ester **27** followed by radicalic bromination led to bromoderivative **9d**.

Compound **9e** was synthesized as reported in Scheme 3. 5-Methoxytetralone **28** was treated with dry ethyl acetate in the presence of lithium *bis*(trimethylsilyl)amide. The resulting β-hydroxyester **29** was dehydrated in the presence of trifluoroacetic acid providing a mixture of regioisomers **30** and **31**, both submitted to catalytic hydrogenation, employing cyclohexene as hydrogen source to afford intermediate **32**, immediately submitted to oxidation with DDQ in order to provide the corresponding aromatic derivative **33** [32]. Radicalic bromination with NBS led to bromoderivative **9e**.

The synthesis of α-hydroxyesters **10a-d** is reported in Scheme 4. Bromoquinolines **13a,b** were converted into their corresponding ethyl glyoxylates derivatives **34a,b** by treatment with diethyl oxalate in the presence of *n*-butyllithium [33]. Selective reduction of the ketone functionality was achieved by reaction with sodium borohydride in dry tetrahydrofuran (THF), providing α-hydroxyester derivatives **10a,b**. The synthesis of compounds **10c,d** bearing 2-alkyl substituted quinoline rings started from 8-bromo-2-methylquinoline **35** prepared from 2-bromoaniline and crotonaldehyde as previously reported [34]. 8-Bromo-2-ethylquinoline **36** was derived from **35** by treatment with methyl iodide after deprotonation with lithium diisopropylamide (LDA). Both bromoquinoline derivatives **35** and **36** were reacted with diethyl oxalate in the presence of *n*-butyllithium providing glyoxalyl derivatives **37a,b**. Reduction of the ketone functionality in the presence of

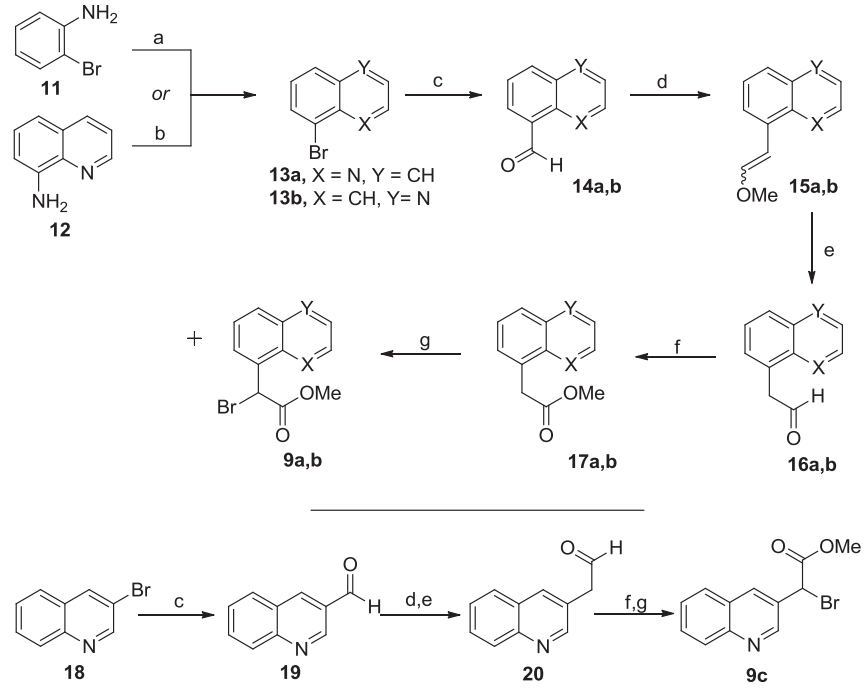

Scheme 1. Synthesis of α-bromoester derivatives **9a-c**. Reagents and conditions: (a) Glycerol, $PhNO_2$, $FeSO_4 \cdot 7H_2O$, conc. H_2SO_4, 150 °C, 7 h; (b) $CuBr_2$, *t*-BuONO, dry MeCN, 75 °C, 12 h; (c) *n*-BuLi (2.5 M solution in *n*-hexane), DMF, dry THF, −78 °C, 10 min; (d) (methoxymethyl)triphenylphosphonium chloride, $NaN(TMS)_2$, dry THF, 0 °C, 2 h; (e) 6 N HCl, acetone, 50 °C, 3 h; (f) NIS, K_2CO_3, MeOH, rt, 3 h; (g) NBS, AIBN, CCl_4, 85 °C, 12 h.

corresponding aldehyde derivative **24** was achieved by treatment with DMF in the presence of *n*-butyllithium. The following steps for the synthesis of compound **9d** entirely traced those reported in Scheme 1 for the synthesis of compounds **9a-c**. Accordingly, sodium borohydride led to the corresponding alcohols **10c,d**.

The synthesis of compounds **10e-g** is described in Scheme 5. Isoquinoline **38** was brominated at C-5 by treatment with NBS in the presence of sulfuric acid providing bromoderivative **39** [35].

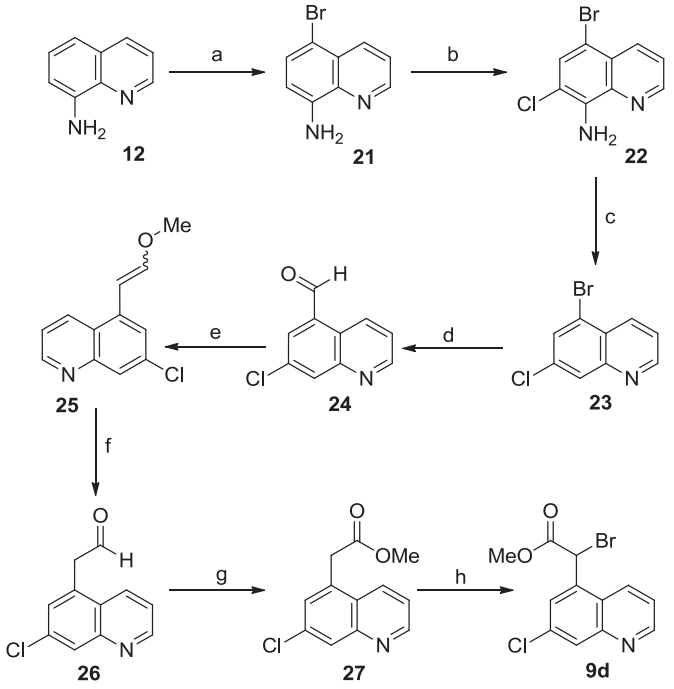

Scheme 2. Synthesis of α-bromoester derivative **9d**. Reagents and conditions: (a) NBS, MeCN, 25 °C, 1 h; (b) NCS, MeCN, 75 °C, 12 h; (c) H_3PO_2, $NaNO_2$, conc.H_2SO_4, water, from 25 °C to 60 °C, 3 h; (d) *n*-BuLi (2.5 M solution in *n*-hexane), dry DMF, dry THF, −78 °C, 15 min; (e) (methoxymethyl)triphenylphosphonium chloride, $NaN(TMS)_2$, dry THF, 0 °C, 3 h; (f) 6 N HCl, acetone, 25 °C, 4 h; (g) NIS, K_2CO_3, MeOH, 25 °C, 3 h; (h) NBS, AIBN, CCl_4, 85 °C, 8 h.

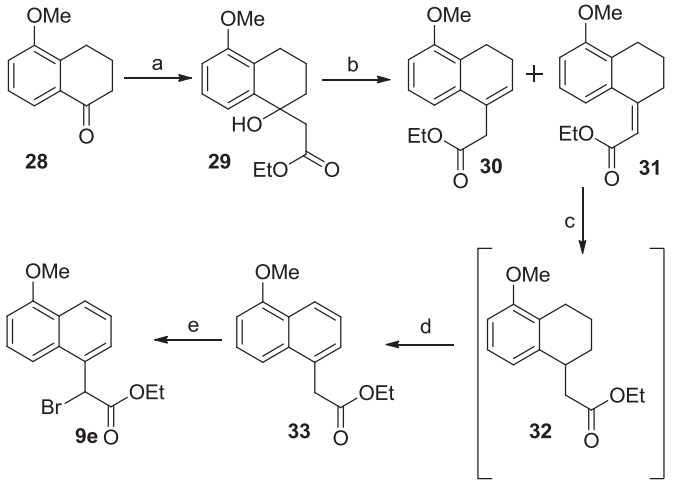

Scheme 3. Synthesis of α-bromoester derivative **9e**. Reagents and conditions: (a) $LiN(TMS)_2$, dry EtOAc, dry THF, from −78 °C to −70 °C, 1 h; (b) toluene, TFA, 110 °C, 3 h; (c) cyclohexene, 1,4-dioxane, 10% Pd/C, 101 °C, 12 h; (d) toluene, DDQ, 110 °C, 3 h; (e) NBS, AIBN, CCl_4, 80 °C, 12 h.

Reaction with diethyl oxalate in the presence of *n*-butyllithium followed by reduction in the presence of sodium borohydride led to alcohol **10e**.

For the synthesis of compound **10f**, piperonylic acid **40** was converted into the corresponding Weinreb amide that was reacted with methylmagnesium bromide in dry THF readily providing the desired methyl ketone **41**. This latter compound was then submitted to intramolecular Cannizzaro reaction performed with selenium dioxide in the presence of Amberlyst A-26 in a dioxane/water mixture providing the α-hydroxyacid derivative [36], immediately converted to the corresponding methyl ester **10f** with methyl iodide in the presence of potassium carbonate.

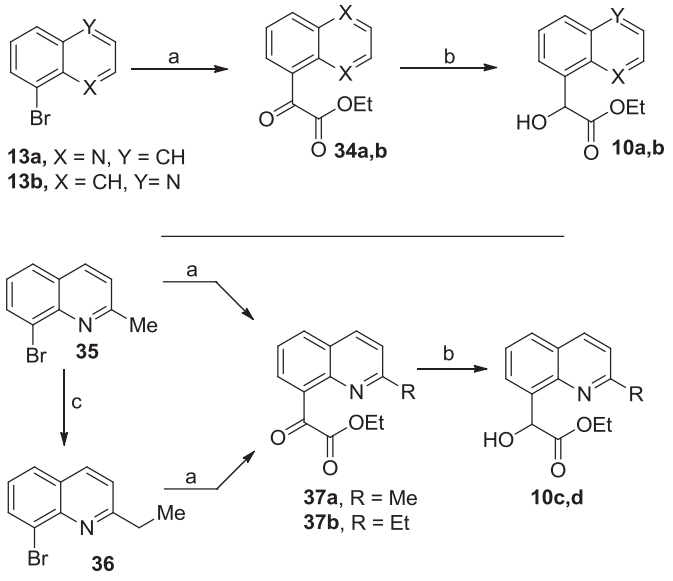

Scheme 4. Synthesis of α-hydroxyesters **10a-d**. Reagents and conditions: a) *n*-BuLi, (2.5 M solution in *n*-hexane), diethyl oxalate, dry THF, −78 °C, 10 min; b) $NaBH_4$, dry THF, 25 °C, 30 min; (c) LDA, MeI, dry THF, from −78 °C to 0 °C, 5 h.

The biphenyl derivative **10g** was prepared starting from bromoderivative **42**. This latter compound was converted into its glyoxylate derivative **43** and to alcohol **10g** as previously described.

The synthesis of final compounds **6a-p** is reported in Scheme 6. Arylpyrroles **8a,b** were submitted to alkylation or Mitsunobu reaction according to the availability of α-bromo- or α-hydroxyester derivatives providing aryl-alkyl ethers **44a-j**. Key compounds **6a** and **6j** were synthesized employing both the original alkylation route and then the shorter Mitsunobu route, in order to scale up

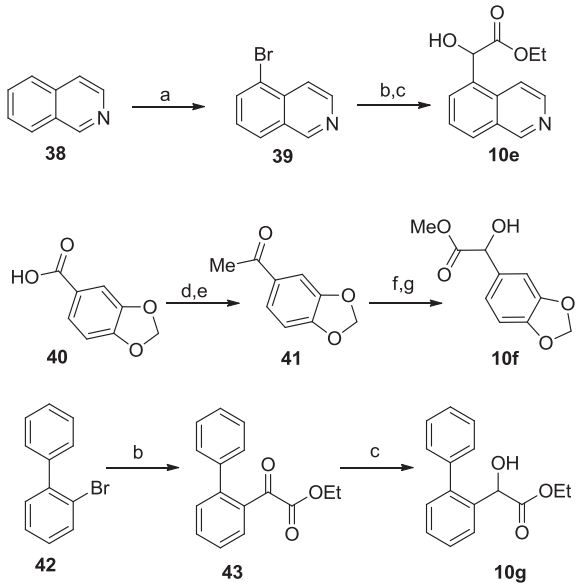

Scheme 5. Synthesis of α-hydroxyesters **10e-g**. Reagents and conditions: (a) NBS, H_2SO_4, from −25 C° to 25 °C, 24 h (b) *n*-BuLi (2.5 M in *n*-hexane), diethyl oxalate, dry THF, −78 °C, 10 min; (c) $NaBH_4$, dry THF, 25 °C, 4 h; (d) *N,O*-dimethylhydroxylamine hydrochloride, EDCI, HOBT, DIPEA, dry dichloromethane (DCM), 0 °C, 12 h; (e) MeMgBr (3 M solution in THF), dry THF, 1 h, 0 °C; (f) SeO_2, Amberlyst A-26, dioxane, water, 24 h, 90 °C; (g) MeI, K_2CO_3, dry DMF, 25 °C, 3 h.

molecules for further biological assays. Subsequently, alkaline hydrolysis with aqueous sodium hydroxide afforded carboxylic acid derivatives **45a-j**. These latter intermediates were submitted to intramolecular Friedel-Crafts reaction in the presence of phosphorous pentachloride providing key cyclic ketones **7a-j**. Final compound **6a** was obtained by adding acetyl chloride to the potassium enolate deriving by treatment of the cyclic ketone **7a** with potassium *tert*-butoxide. Carbamate-containing compounds **6b** and **6c** were obtained by treatment of the same potassium enolate with dimethylcarbamoyl chloride and diethylcarbamoyl chloride, respectively. Compound **6d** was obtained by reacting the potassium enolate of ketone **7a** with N^1,N^1-diethylpentane-1,4-diamine and triphosgene in the presence of *N,N*-DIPEA. Compounds **6e-i** were also obtained by enolization of suitable ketones **7f,g** employing potassium *tert*-butoxide and following reactions with acetyl chloride, dimethyl- or diethylcarbamoyl chloride.

In the case of the cyclic ketone **7b**, bearing the 5-substituted quinolyl moiety, the enolization in the presence of potassium *tert*-butoxide led to complete decomposition of the ketone. Therefore, after a series of attempts, the use of sodium *bis*(-trimethylsilyl)amide at −78 °C was identified as the best condition to efficiently form the enolate, subsequently reacted with acetyl chloride providing final compound **6j**. The same enolization protocol was also successfully applied to final compounds **6k-p**.

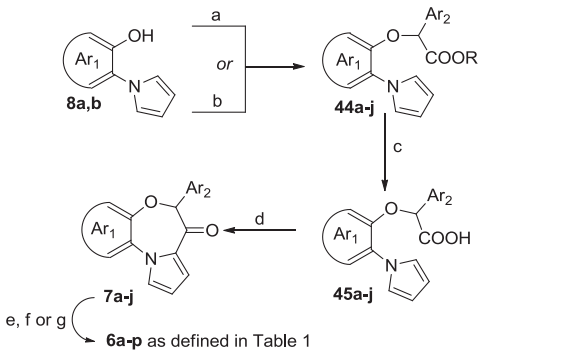

Cpd	Ar_1	Ar_2	R	Cpd	Ar_1	Ar_2	R
44a	naphtho[2,3]	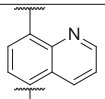	Me	44f	naphtho[2,3]	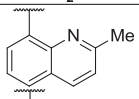	Et
44b	naphtho[2,3]	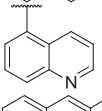	Me	44g	naphtho[2,3]	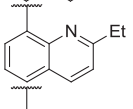	Et
44c	naphtho[2,3]	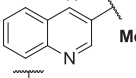	Me	44h	naphtho[2,3]	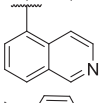	Et
44d	naphtho[2,3]	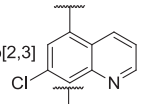	Me	44i	naphtho[2,3]	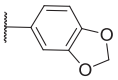	Me
44e	naphtho[2,3]	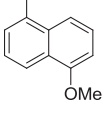	Et	44j	benzo	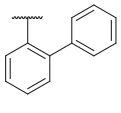	Et

Scheme 6. Synthesis of final compounds **6a-p**. Reagents and conditions: (a) K_2CO_3, 18-crown-6, dry DMF, 90 °C, 12 h for **44a-e**; (b) PPh_3, DIAD, dry DCM, from 0 °C to 25 °C, 24 h for **44a,b** and **44f-j**; (c) 5% $NaOH_{aq}$, THF, MeOH, rt, 2 h for **45 a-c, e-h,j**, 0.25 N LiOH, MeCN, 25 °C for **45d,i**; (d) PCl_5, dry DCM, 40 °C, 12 h; (e) KO-*t*-Bu, acetyl chloride, dry THF, rt, 8 h for **6a,e,g** or NaN(TMS)$_2$, acetyl chloride, dry THF, −78 °C, 4 h for **6j-p**; (f) KO-*t*-Bu, dimethylcarbamoyl chloride, dry THF, rt, 8 h, for **6b,h** or KO-*t*-Bu, diethylcarbamoyl chloride, dry THF, rt, 8 h, for **6c,f,i**; (g) KO-*t*-Bu, triphosgene, N^1,N^1-diethylpentane-1,4-diamine, *N,N*-DIPEA, 25 °C, 14 h, for **6d**.

The preparation of compounds **6q,r** is reported in Scheme 7. Ketone **46** [37] was converted into the corresponding oxime **47** by treatment with hydroxylamine hydrochloride in the presence of pyridine. Conversion to the corresponding enamide-containing compound **6q** was performed with acetic anhydride in the presence of sodium bisulfite [38]. Ketone **46** was also treated with potassium hydride, and the corresponding potassium enolate was reacted with triphosgene and *N,N*-dietilbutan-1,3-diamine, finally providing final compound **6r**.

Solubility for **6j** and **PNOX** was experimentally measured. *In silico* we determined the solubility values of a series of MTAs. Calculations performed by QikProp (QikProp, version 4.3, Schrödinger, LLC, New York, NY, 2015) highlighted the improved solubility of **6j** (−6.272 mol/dm^3) over **PNOX** (−6.814 mol/dm^3) and other well-known drugs such as tivantinib (−6.277 mol/dm^3), DJ-101 (−6.685 mol/dm^3) and lexibulin (−6.499 mol/dm^3). On the other hand, experimental data from literature and calculated solubility of **6j** proved to be lower than combretastatin (calculated −4.517 mol/dm^3) and colchicine (**4**) (calculated −4.961 mol/dm^3, experimental 7 mg/mL).

The water solubility of **6j** and **PNOX** were experimentally determined also by HPLC analysis [39]. HPLC experiments demonstrated that the introduction of a specific structural modification has improved water solubility of **6j** over PNOX (solubility at pH = 7.4 was 26.04 μM for **PNOX**, and 458.26 μM for **6j** (0.2 mg/mL), see Table S1), being similar to those reported for nocodazole (<1 mg/mL) and tivatinib (<1 mg/mL).

2.2. Biological investigation

2.2.1. Cell based assays in HL-60 and GIST-T1 cells

As a preliminary approach to determine the potential of the newly synthesized derivatives we performed a screening on the HL-60 cell line to determine the cell viability following treatment (Table 2). This preliminary investigation was performed on a small set of quinolyl-derivatives (**6a-c,j,l**) and also ketone intermediates **7a,b** were included. Cell viability was assessed using an AlamarBlue cell viability assay (cells were seeded at 4000/well in a 96-well plate and cell viability measured after 72 h of drug treatment). This test highlighted an exceptional potency for some of the tested compounds which exhibited very promising IC_{50} values in the high nanomolar range (**6a**, IC_{50} = 262.7 nM; **6b**, IC_{50} = 299.5 nM; **6j**, IC_{50} = 294.5 nM).

HL-60 cells (300,000 cells/mL) were seeded into 96-well plates and were treated in triplicate with vehicle (0.1% (v/v) DMSO) or the indicated compounds for 72 h. The cells were then incubated in 10% (v/v) AlamarBlue™ and its reduction to a fluorescent state measured at excitation 544 nm and emission 590 nm using a multi-well fluorimeter. IC_{50} values are the mean of at least three separate determinations. Standard errors were all within 10% of the mean.

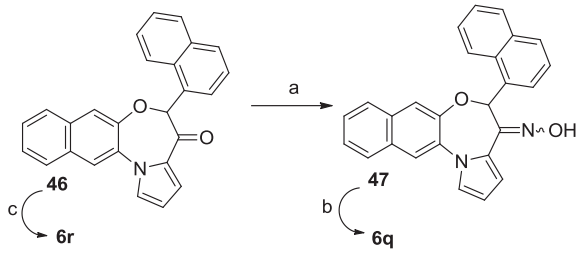

Scheme 7. Synthesis of compounds **6q,r**. Reagents and conditions: (a) $NH_2OH{\cdot}HCl$, piridine, dry MeOH, 120 °C, 12 h; (b) Ac_2O, $NaHSO_3$, CuI, 1,2-DCE, 120 °C, 12 h; (c) KH (30% suspension in mineral oil), triphosgene, N^1,N^1-diethylpentane-1,4-diamine, *N,N*-DIPEA, dry THF, 25 °C, 12 h.

Table 2
Viability tests as IC_{50} (μM) values for a panel of compounds tested in HL-60 cells.

Cmpd	HL-60 IC_{50} (μM)
6a	0.2627
6b	0.2995
6c	4.582
6j	0.2945
6l	6.462
7a	1.075
7b	2.767

Based on these data we sought to explore the efficacy of the best performing analogues in inhibiting the survival of the gastrointestinal stromal tumor cell line GIST-T1. The results indicated that the compounds were active in inhibiting cell viability already at 1 μM. Viability was further inhibited by applying a concentration of an order of magnitude higher (Fig. 3).

This preliminary investigation prompted us to expand the SARs at both the C4 and C5 of the pyrrolonaphthoxazepine nucleus, to systematically interrogate the ability of our compounds to interfere with cell cycle progression and to evaluate the potential pro-apoptotic effect in HL-60 cells. Thus, intranucleosomal DNA fragmentation was determined by flow cytometry [40] on HL-60 cells treated with a 10 μM concentration of the new derivatives in comparison with **PNOX** (Fig. 4A). The results show that most compounds induced a significant enhancement in the percentage of apoptotic cells (with hypodiploid or "sub-G_0/G_1" DNA content) compared to vehicle. Flow cytometric analysis of cell cycle progression also determined that the pro-apoptotic effects of the new compounds correlate with the blockage of the cell cycle in the G2M phase (Fig. 4B), further suggesting that compounds-induced apoptosis is secondary to cell cycle arrest.

From these preliminary tests we found that the improvement of the water solubility was achieved while leaving unaltered or even improving the pro-apoptotic potential of the new analogues.

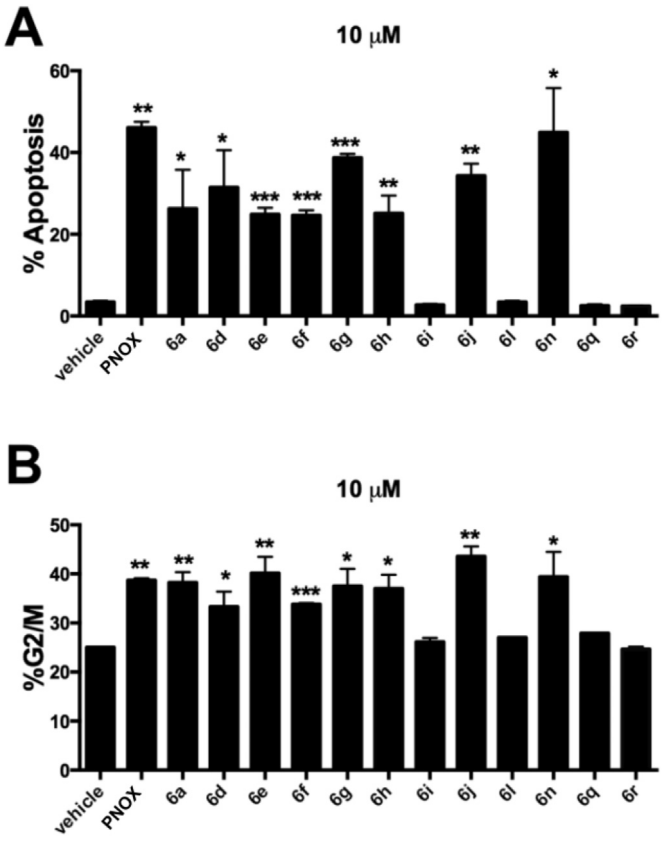

Fig. 4. Effect of compounds **PNOX**, **6a**,**d-j**,**l**,**n**,**q**,**r** on apoptosis in HL-60 cells. Cells were treated with 10 μM of the tested compounds for 24 h and DNA content was measured by flow cytometry. Control samples were treated with vehicle (0.1% DMSO). The bar graphs show the percentage of cells in the sub-G_0/G_1 peak (% apoptosis) (A) and the percentage of cells in the G2M phase (B). Data are mean ± SD (n > 3), *p < 0.05, **p < 0.01, ***p < 0.001 *vs* vehicle.

2.2.2. Effect of selected compounds on tubulin polymerization

The effect of the selected compounds (**PNOX** and **6a**,**d**,**f**,**g**,**h**,**j**,**m**,**n**) on tubulin polymerization was monitored by performing turbidity time course experiments to monitor absorbance at 350 nm (Figs. 5–7 and Table 3). Since microtubules are large structures, their formation is reflected in turbidity of the

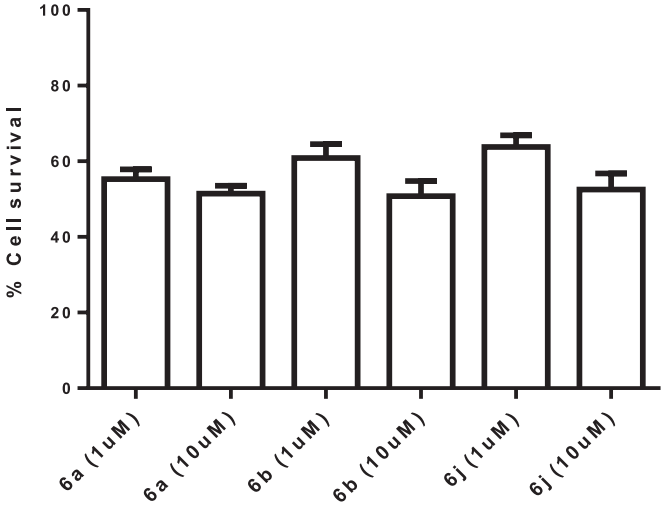

Fig. 3. Percentage of cell viability in a gastrointestinal stromal tumor cell line (GIST-T1) treated with **6a**, **6b** and **6j** each tested at 1 μM and 10 μM. Viability was assessed using an AlamarBlue cell viability assay cells were seeded at 4000/well in a 96-well plate and cell viability was measured after 48 h of drug treatment. Data represents mean ± the S.E.M of three biological replicates.

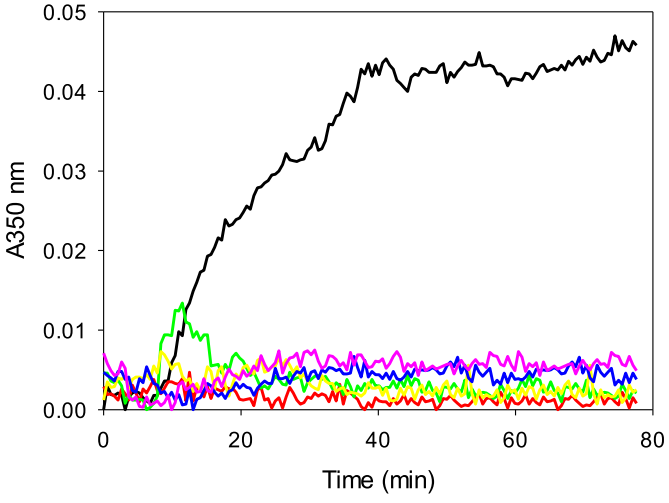

Fig. 5. Turbidity time course for the assembly of 25 μM tubulin at 37 °C in the presence of 27.5 μM of the compounds followed at 350 nm. Black line (DMSO, vehicle), red line (**PNOX**), blue line (**6a**), green line (**6e**), pink line (**6g**), yellow line (**6j**). (For interpretation of the references to color in this figure legend, the reader is referred to the Web version of this article.)

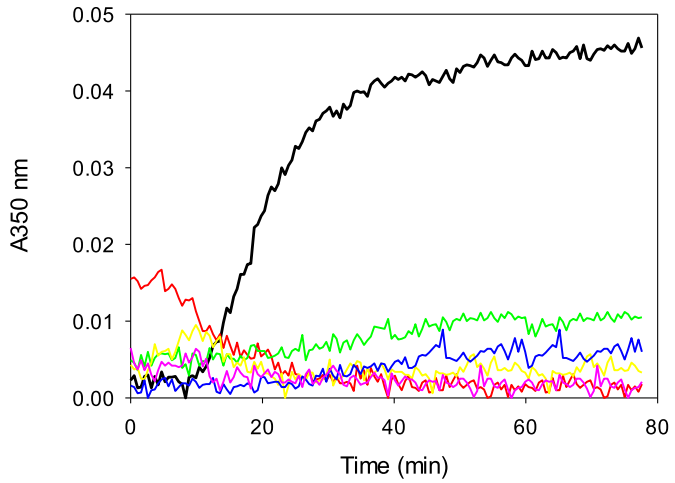

Fig. 6. Turbidity time course for the assembly of 25 μM tubulin at 37 °C in the presence of 27.5 μM of the compounds followed at 350 nm. Black line (DMSO, vehicle), green line (**6d**), yellow line (**6f**), pink line (**6h**), red line (**6m**), blue line (**6n**). (For interpretation of the references to color in this figure legend, the reader is referred to the Web version of this article.)

solution, allowing to follow the assembly reaction [41].

As can be seen in Figs. 5 and 6, when added stoichiometrically all the compounds tested were able to inhibit the polymerization of pure tubulin in conditions in which the protein is able to assembly into microtubules (black lines) indicating that they directly interact with tubulin and that the interaction results in the inhibition of the polymerization capacity of the protein.

Following on, we wanted to estimate the stoichiometry needed to inhibit the assembly reaction. As shown in Fig. 7, all the compounds are able to inhibit the assembly of tubulin at sub-stoichiometric ratios with tubulin in a colchicine-like manner, suggesting that they may inhibit the tubulin association by binding to the colchicine site. To support this hypothesis, we planned to determine the binding constant by competition experiments. In view of the chemical structure of the compounds it was possible to

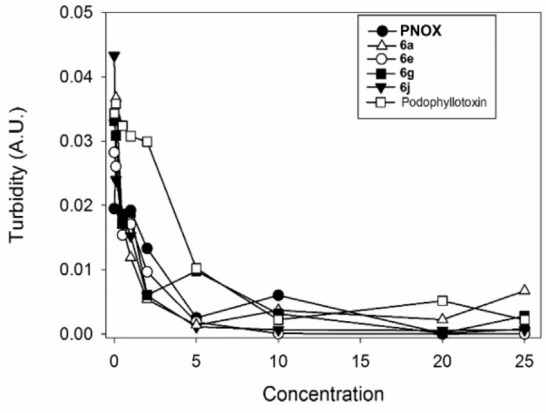

Fig. 7. Stoichiometry of the tubulin depolymerization in the presence of compounds: **PNOX**, **6a**, **6e**, **6g**, **6j** and the reference compound podophyllotoxin.

hypothesize that they would exhibit fluorescent behavior in the near UV. Accordingly, it was found that the compounds were fluorescent at 450 nm upon excitation at 320 nm. Upon addition of an excess of tubulin, the fluorescence of the compounds increased. We then tried to use this property to determine the binding constant by a competition assay with the colchicine site MDA podophyllotoxin [42]. However, it was found that upon podophyllotoxin addition the samples became turbid. We attributed this behavior to the low solubility of the compounds in the medium, which we found to be lower than 5 μM in our test conditions. To overcome the problem, we designed a method based on analytical ultracentrifugation in which the compounds dissociated by competition with podophyllotoxin were sedimented and we could measure the amount of compound bound in the presence of podophyllotoxin at the solubility limits of the compound, which are of the order of sub-μM (see Experimental Section). From these measurements, the binding constants of the compounds could be determined (Table 3) and the binding site was confirmed to be the one of **4**, because of the competition with podophyllotoxin (Fig. S1).

2.2.3. *Structural insight into the **6j**-tubulin complex*

We sought to solve the **6j**-tubulin complex structure by X-ray crystallography (Fig. 8A) in order to define the mode of interaction of the novel analogues at the molecular level. To this end, we soaked **6j** into a crystal formed by a protein complex composed of two αβ-tubulin heterodimers (T_2), the stathmin-like protein RB3 (R) and tubulin tyrosine ligase (TTL); the complex is denoted T_2R-TTL [43,44]. Using this approach, the **6j**-tubulin structure was determined to 2.4 Å resolution (Figs. 8B and 9A; Table S2). Any attempt using **PNOX** was unsuccessful mainly due to its poor solubility.

6j binds to the colchicine site of tubulin, which is formed by residues of helices H7 and H8, strands S8 and S9 and loop T7 of β-tubulin and of loop T5 of α-tubulin (Fig. 9A). The superimposition of the β-tubulin chains of the free (PDB ID 4I55 [43]) and **6j**-bound tubulin structures revealed a flip of the T7 loop of β-tubulin as well as a change in the conformation of the T5 loop of α-tubulin upon ligand binding (Fig. S2). These structural adaptations are necessary to accommodate the ligand in its binding site and have already been observed for other colchicine-site ligands [45,46].

We then investigated the detailed **6j**-tubulin binding mode. The fused system, acetoxyl and quinolyl moieties of **6j** are buried into the colchicine site, making most of the hydrophobic interactions with the β-tubulin part of the dimer (Fig. 8A and B). The interaction is further stabilized by a hydrogen-bond formed between the carbonyl of the acetoxyl group of **6j** and βQ247 of the T7 loop of β-tubulin, as well as a water-mediated contact between the nitrogen of the quinolyl moiety of **6j** and the main chain carbonyl of βG237 and amine groups of βT240 and βC241 from the H7 helix of β-tubulin. Moreover, the pyrrolonaphthoxazepine moiety is stacked between the sidechains of both K254 and K352 residues of β-tubulin. The NZ nitrogen of K352 is 5.7 Å distant from the center of the pyrrole ring of **6j**, suggesting that a cation-π stacking interaction can be established (Fig. 9).

To compare the tubulin-binding mode of **6j** with that of **4**, we superimposed the β-tubulin chains from the **4**-tubulin (PDB ID 4O2B [45]) and **6j**-tubulin structures (RMSD chain D of **4** onto chain D of **6j** 0.29 Å over 2732 atoms; Fig. 9B). We observed no functional

Table 3
Binding constants (*Kb*) of the compounds to dimeric tubulin calculated by AUC at 25 °C (10^7 M^{-1}).

Cpd	**PNOX**	**6a**	**6d**	**6e**	**6f**	**6g**	**6h**	**6j**	**6m**	**6n**
Kb	4.4 ± 1.5	115 ± 37	114 ± 48	4.4 ± 1.1	9 ± 5	0.3 ± 0.1	5 ± 1	7 ± 3	16 ± 4	2 ± 1

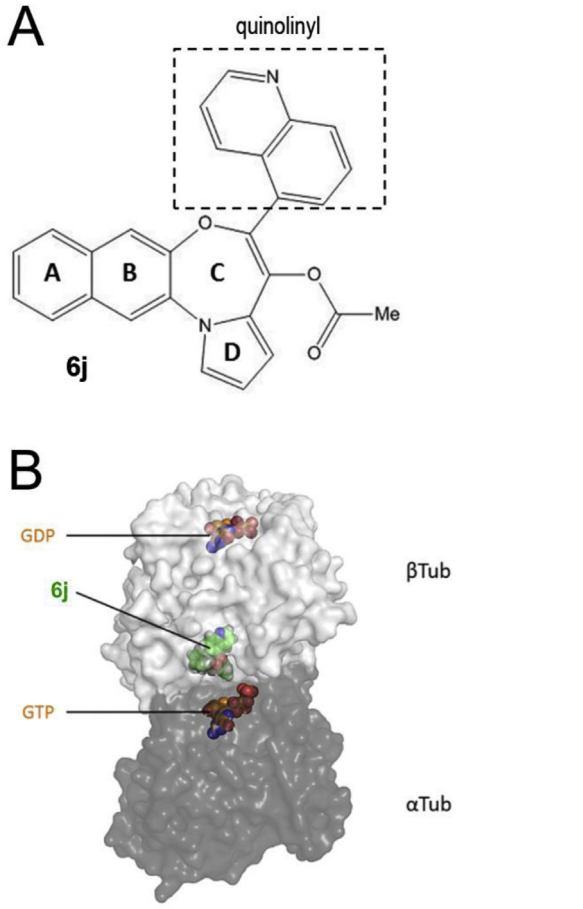

Fig. 8. X-ray crystallographic studies on **6j**. (A) Chemical structure of **6j**. The A, B, C and D cycles are part of the naphto-pyrrolo-benzoxazepine moiety. The quinolinyl moiety is highlighted by a dashed box. (B) Overall view of the X-ray crystal structure of the **6j**-tubulin complex. The α- and β-tubulin subunits are represented in dark and light gray surface representation, respectively. **6j** and the guanosine nucleotide molecules are shown in green and orange spheres representation, respectively. (For interpretation of the references to color in this figure legend, the reader is referred to the Web version of this article.)

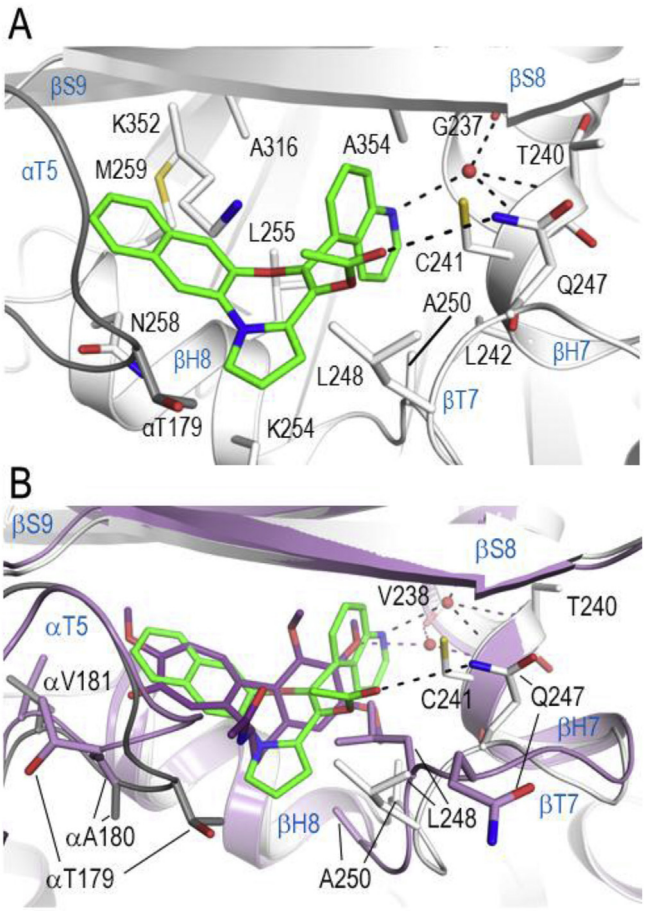

Fig. 9. Detailed interactions between tubulin and **6j**. (A) Close-up view of the interaction mode between **6j** and tubulin. **6j** and interacting tubulin residues are shown in green and grey sticks representation, respectively. Tubulin secondary structural elements are labeled with blue letters. (B) Superimposition of the **6j**-tubulin (**6j** in green sticks) and **4**-tubulin (PDB ID 4O2B; **4** in violet sticks) complex structures. In both figures, oxygen, nitrogen and sulfur atoms are colored in red, blue and yellow, respectively. Hydrogen bonds are represented by black dotted lines, and the water molecules are displayed as a red sphere. Tubulin secondary structural elements are labeled with blue letters. (For interpretation of the references to color in this figure legend, the reader is referred to the Web version of this article.)

common groups between **4** and **6j** molecules that occupy the same position in their respective binding pockets. The major differences are observed for the conformations of both the αT5 and βT7 loops. Compared to **4**, the bulky pyrrolonaphthoxazepine moiety of **6j** induces a flip of αT179 by establishing more hydrophobic contacts to the αT5-loop (Fig. 9B). The conformational flip of the βT7 loop is induced by the acetoxyl moiety of **6j** by displacing the side chain of L248. Together with L255 this residue is involved in the stabilization of the trimethoxy-substituted A ring of **4**. The hepta-membered C ring moiety of **4** superimposes with the naphthyl group of the naphthoxazepine moiety of **6j**, thereby establishing comparable hydrophobic contacts to tubulin. One common feature is a water-mediated contact between the 2-methoxy group of **4** and the main chain carbonyl group of βV238 and the main chain amine group of βC241 of β-tubulin; in the vicinity, a water-mediated contact is also formed with the nitrogen of the quinolyl moiety of **6j** (see above and Fig. 9A). βA250 appears to be largely involved in hydrophobic contacts with both compounds (with pyrrole moiety of **6j** and with the hepta-membered ring and the trimethoxyphenyl moiety of **4**) (for an overall view of superposition between compounds **4** and **6j** see Fig. S3).

Together, these results define **6j** as a new tubulin colchicine binder. It is well established that colchicine-site ligands inhibit microtubule polymerization by preventing the "curved-to-straight" conformational switch accompanying tubulin assembly into microtubules [45,46]. Inspection of the **6j** binding mode in the "curved" (T_2R-TTL) and "straight" (PDB ID 1JFF) tubulin states revealed that the ligand destabilizes microtubules by a similar mechanism (not shown).

Moreover, for providing a comprehensive analysis about the binding mode of the new compound **6j** into the colchicine binding site, in addition to the above performed analysis with the colchicine (PDB ID 4O2B), we further analyzed 40 tubulin-ligand complexes in which the ligands targeted the colchicine binding site (PDB IDs: 3DU7, 3HKC, 3HKD, 3N2G, 3N2K, 4O2A, 4YJ2, 4YJ3, 5CA0, 5CA1, 5CB4, 5C8Y, 5GON, 5H7O, 5JCB, 5JVD, 5LYJ, 5NG1, 5M7E, 5M7G, 5M8G, 5OSK, 5O7A, 5XAF, 5XAG, 5XLZ, 5XKF, 5XKG, 5XKH, 5XLT, 5YLJ, 5YLS, 5YL2, 5Z4U, 6BRF, 6BR1, 6BRY, 6BS2, 6FKL, 6FKJ). The analysis highlighted the crucial role of the hydrophobic contacts for interacting with the colchicine binding site. Accordingly, the quinoline moiety and the tricyclic portion of **6j** were overlapped by the hydrophobic portions of the examined ligands to strongly interact with the binding site. Notably, with respect to the selected ligands, **6j** is the only compound able to target the residue βQ247 by

a H-bond with its acetoxyl group. In fact, none of the other examined ligands is able to form the mentioned contact. This further investigation pointed out the novel pattern of interaction that could be useful for the rational design of ligands able to maximize the contacts into the colchicine binding site on tubulin.

2.2.4. Molecular Dynamics (MD) simulation on the **6j**-tubulin complex

In order to assess the contribution of structural moieties to the affinity of **6j** for tubulin in the colchicine site, and to evaluate the stability of the binding mode found by crystallographic studies, we performed a Molecular Dynamics (MD) simulation employing Desmond software on the **6j**-tubulin complex (Fig. 10). The MD study could also be able to establish the role of the water molecule in the binding mode of **6j**. For the calculation we used chains C and D from the crystal structure after appropriate preparation (see the Experimental Section for further details). During the MD simulation, after about 20 ns, the complex showed an overall stability with low Root Mean Square Deviation (RMSD) of the protein and the ligand (Fig. 10A). Regarding the pattern of interaction of **6j** with tubulin, we noted that the main contacts were maintained as underlined by the dynamic analysis of the simulation interaction diagram (Fig. 10B). In particular, the pyrrolonaphthoxazepine moiety is involved in i) strong contacts with the α-tubulin V181 with additional hydrophobic contacts with M259, A316, and I318 of β-tubulin and ii) a strong cation-π stacking with K352 of β-tubulin. The quinoline nucleus interacts by several hydrophobic contacts with C241, L242, L248, A250, L255, A354 and I378 of β-tubulin. Hydrophobic interactions are the main contacts that govern the affinity of **6j** for the colchicine site. In fact, as reported in Fig. 10C and D we noted a limited number of polar contacts, mainly water mediated, as confirmed by the crystal structure. The nitrogen of quinoline nucleus is able to maintain the water mediated H-bonds with G237, C241 and T240 and in addition can form a water mediated H-bond with the backbone of V238. The acetyl function lacks a direct H-bonding with Q247 that becomes sporadically water mediated.

2.2.5. Structure-activity relationship studies

Combining the experimental data (*Kb* and ΔG_{bind}; in the following discussion ΔG_{bind} values are referred to $\Delta G_{bind25°C}$) and molecular docking studies, a systematic and inclusive SAR study of the synthesized compounds (**6a-r**) was performed for investigating the behavior of the developed compounds within the colchicine binding site of the β-tubulin and to explain their activity and potency. Regarding **6j**, we found that the adopted molecular docking protocol (scoring function GoldScore implemented in GOLD software) was able to correctly accommodate the ligand into the active site with low RMSD (0.45) with respect to the crystal structure (Fig. S4). For **6j**, the ΔG_{bind} value confirms its strong binding to the colchicine binding site of β-tubulin ($Kb = 7 \pm 3 \times 10^7\ M^{-1}$; $\Delta G_{bind} = -10.7$ kcal/mol). The effect of different positioning of the heterocyclic nitrogen atom was explored and, in general, with respect to the original members, an increase of binding affinity was found, although to different extents. In fact, compounds **6a** and **6m** (8-substituted quinoline and 5-substituted isoquinoline,

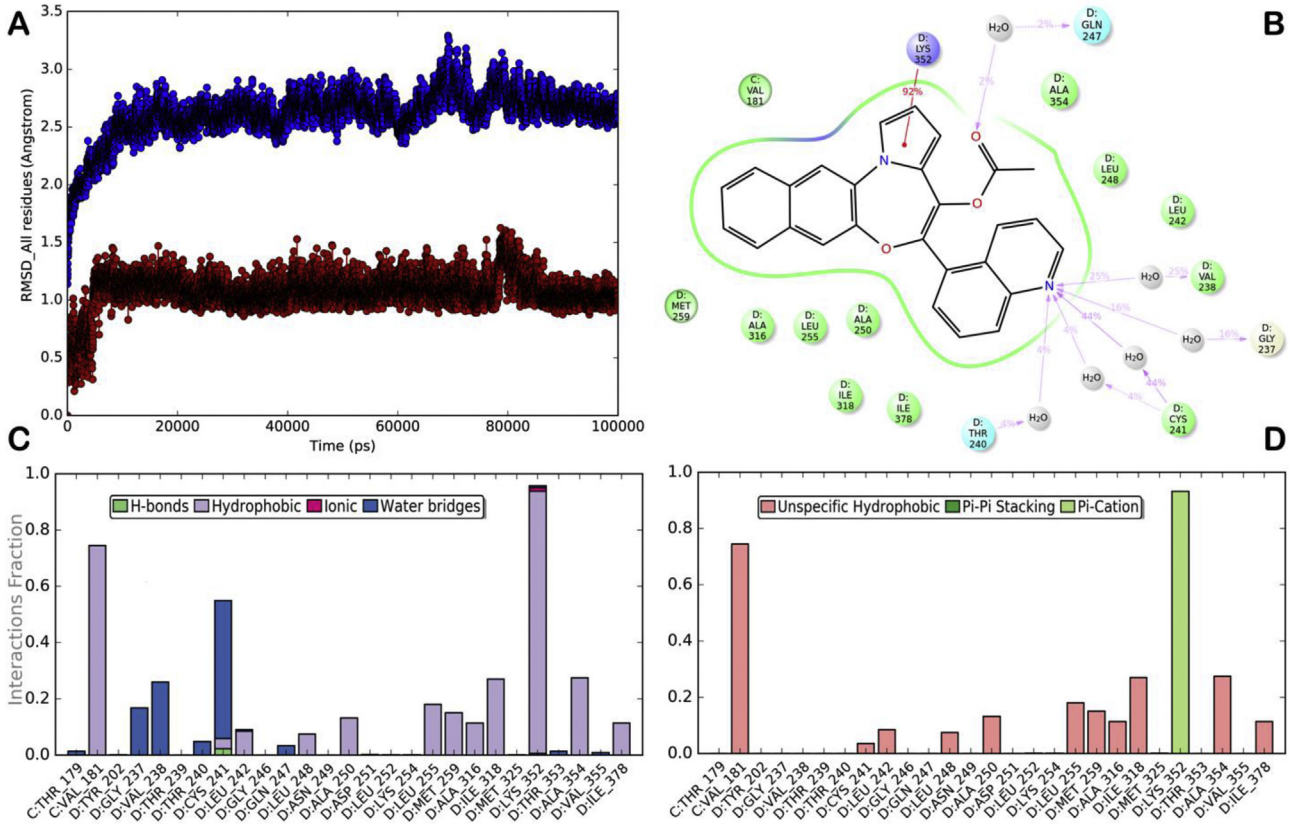

Fig. 10. Molecular dynamics of **6j**-tubulin complex outputs. (A) RMSD of the complex **6j**-tubulin (RMSD of the protein in a line formed by blue circles; RMSD of the ligand in a line formed by red circles). RMSD were calculated between the final conformation and the starting conformation through the 100 ns of the MD simulation. (B) **6j**-tubulin interactions monitored throughout the simulation. The represented water molecule interacting with G237, V238, T240 and C241 is the same, different to the water molecule interacting with Q247. (C) Protein-ligand interactions are categorized into four types: H-bonds, hydrophobic, ionic and water bridges. (D) Hydrophobic contacts of the ligand into the colchicine binding site over the course of the trajectory. (For interpretation of the references to color in this figure legend, the reader is referred to the Web version of this article.)

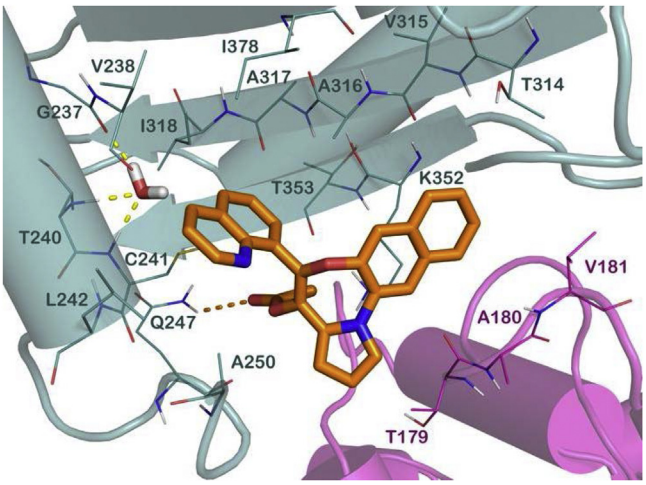

Fig. 11. Complex of **6a**-tubulin (orange sticks, α-tubulin in magenta cartoon and β-tubulin in dark green cartoon) as found by means of molecular docking calculation. (For interpretation of the references to color in this figure legend, the reader is referred to the Web version of this article.)

respectively) act as low and high nanomolar tubulin binders, respectively (*Kb* **6a** $= 115 \pm 37 \times 10^7\ M^{-1}$; *Kb* **6m** $= 16 \pm 4 \times 10^7\ M^{-1}$). Notably, compound **6a** was found to be one of the most potent tubulin-binders of the series. Even though compounds **6a** and **6m** are accommodated in a similar fashion as found for **6j** (Fig. 11 and Fig. S5 respectively), the different position of the nitrogen atom on quinoline nucleus clearly influences their binding mode. Although **6a,m** cannot form the water mediated contacts shown by **6j**, they display a higher hydrophobic contribution which is responsible for the increased tubulin affinity especially in the case of **6a**. In fact, compound **6a** is able to maximize the hydrophobic contacts with the residues V238, L242, I318 and I378. The reported data highlight the strong binding behavior with a reduction of ΔG_{bind} (ΔG_{bind} **6a** $= -12.4$ kcal/mol and ΔG_{bind} **6m** $= -11.2$ kcal/mol (Table 3).

In contrast, the introduction of an ethyl group on the quinoline ring of **6a** at 2-position (compound **6g** in Fig. S6) significantly decreased potency against tubulin (**6g**, *Kb* $= 0.3 \pm 0.1 \times 10^7\ M^{-1}$; $\Delta G_{bind} = -8.8$ kcal/mol). This could most likely be ascribed to the increment of the steric hindrance on the quinoline substituent. For this reason, the docking study on the mentioned compounds highlighted a slightly different orientation of the core of the molecules with reduced interaction with K352. This binding mode brings the oxygen atom of the carbonyl group at 3.5 Å from the sidechain of Q247 precluding the specific polar contacts. The introduction of a Me group on the quinoline ring of **6a** at C-2 led to a compound, **6e**, with a significant binding affinity against tubulin (*Kb* $= 4.4 \pm 1.1 \times 10^7\ M^{-1}$). This confirms the relevant role of the hydrophobic patch at the colchicine binding site targeted by the quinoline substituted ring (Fig. S7), maintaining interaction with Q247. The ΔG_{bind} of -10.4 kcal/mol also supports its high affinity for the colchicine binding site.

The introduction of more hydrophobic nuclei as in compounds **PNOX** and **6e** seems to be well tolerated, although with a slight decrease of binding affinity. This observation supports the easier displacement of the water molecule when more hydrophobic nuclei were introduced (**PNOX** and **6e**), without a significant decrease of affinity, indicating that the water molecules should not be fundamental for the activity of the ligands based on the scaffold herein described. In fact, these compounds present comparable binding affinities to tubulin, although slightly lower, to that found for **6j**. Remarkably, the introduction of a nitrogen atom at C-5 as in **6j** led to a more soluble compound with respect to **PNOX** (hydrophobic analogue) while maintaining tubulin affinity (Fig. S8 and Table 3; ΔG_{bind} **PNOX** $= -10.4$ kcal/mol). The introduction of a different fused ring such as benzodioxole at a different position as in **6n** (Fig. S9) seems to be well tolerated, with a slight decrease of binding affinity (**6n**, *Kb* $= 2 \pm 1 \times 10^7\ M^{-1}$; $\Delta G_{bind} = -10.0$ kcal/mol) with respect to **6j**, while the 3-quinoline moiety of **6l** is not tolerated as confirmed by the docking calculation (Fig. S10). This is due to the different interactions showed for the two compounds (**6l** and **6n**). In particular, **6n** forms water mediated H-bond as found for **6j** but the different orientation of the R_1 substituent did not allow the compound to reach an optimal accommodation to establish polar contacts with Q247, due to the fact that the oxygen from the carbonyl group was found at 3.6 Å from the Q247 side chain (Fig. S9). On the contrary, **6l** with a quinolin-3-yl substituent differently oriented with respect to that of **6j**, showed a limited potency mainly due to the steric hindrance and the absence of the water mediated interactions. In particular, the different orientation of the quinoline moiety did not allow compound **6l** to establish efficient hydrophobic interactions with V238, L242, I318 and I378, the stacking with K352 and H-bonding with the Q247 side chain (carbonyl group at 3.9 Å) (Fig. S10). Modification of the R_2 site (carbamates) led to a sub-series of analogues with different affinity against tubulin. The introduction of the dimethylamino group (**6h**) gave a potency similar to **PNOX** (**6h**, *Kb* $= 5 \pm 1 \times 10^7\ M^{-1}$; $\Delta G_{bind} = -10.5$ kcal/mol). Compound **6h** is accommodated into the colchicine binding site in a similar fashion found for **6j** (Fig. S11). The diethylamino derivative **6f** showed a potency similar to **6j** (Fig. S12) (**6f**, *Kb* $= 9 \pm 5 \times 10^7\ M^{-1}$; $\Delta G_{bind} = -10.9$ kcal/mol). Further, the elongation of the chain at R_2 position as in compound **6d**, bearing a urethane functionality containing a flexible lateral chain with extra protonatable nitrogen, led to one of the best compounds in term of binding affinity towards tubulin. Additionally, both enantiomers of **6d** showed a similar accommodation into the colchicine binding site, indicating the lack of a stereoselective interaction. As depicted in Fig. S13, despite the flexible chain, **6d** showed a relevant number of docked solutions of both the *R*- (82%) and *S*-enantiomer (74%), with a further polar contact established between the protonated nitrogen of the flexible lateral chain and the backbone of T353 by both enantiomers. Accordingly, compound **6d** showed a *Kb* $= 114 \pm 48 \times 10^7\ M^{-1}$ and a ΔG_{bind} of -12.3 kcal/mol.

2.2.6. Effect of selected compounds on tumor cell lines

A subset of the most promising analogues was characterized for their potential anticancer properties in different tumor cell lines, including both sensitive and multidrug resistant cells.

2.2.6.1. Effect on A2780 and A2780AD human ovarian carcinoma cells, NIH3T3 and P-gp overexpressing NIH-MDR-G185 cells. The effects of compounds **PNOX**, **6a**,**d-h**,**j**,**l-n** on A2780 and A2780AD human ovarian carcinoma cells, mouse embryo NIH 3T3 and P-gp overexpressing NIH-MDR-G185 (3T3Col) cells was investigated. A2780 and 3T3 cells are sensitive to chemotherapy, whereas A2780AD and 3T3Col cells have acquired resistance by means of P-glycoprotein overexpression. We determined the IC_{50} values of the aforementioned compounds and compared them with those measured for **1**, **3** and **4** (Table 4).

As it can be seen all the compounds are effective in killing cancer cells in the low micro/high nanomolar ranges, which is in agreement with the binding affinities in the high nanomolar range. It should be noticed that the IC_{50} values determined are within the solubility range of the drugs (except for **6g**, whose IC_{50} 1 μM is far over the determined solubility 0.064 μM) thus the values obtained

Table 4
Cytotoxicity assessment of different compounds on the growth of two human ovarian carcinoma cell lines (A2780 and A2780AD) and two embryo cell lines (NIH 3T3 and NIH-MDR-G185).[a]

Cpd	A2780[b]	A2780AD	R/S[c]	3T3	3T3col	R/S
PNOX	249 ± 17	240 ± 33	0.96	126 ± 4	306 ± 24	2.42
6a	76 ± 13	79 ± 15	1.03	34 ± 4	68 ± 13	2
6d	1900 ± 200	1350 ± 50	0.71	2300 ± 300	2500 ± 600	1.08
6e	285 ± 26	310 ± 24	1.08	126 ± 10	278 ± 19	2.20
6f	3050 ± 250	2250 ± 50	0.73	4950 ± 750	9000 ± 100	1.81
6g	1000 ± 0.03	950 ± 5	0.95	540 ± 79	790 ± 100	1.46
6h	900 ± 100	826.5 ± 17	0.91	408.5 ± 7	1051.5 ± 148	2.57
6j	80 ± 12	92 ± 16	1.15	42 ± 9	84 ± 16	2
6m	300.75 ± 122	810 ± 48	2.69	375.3 ± 1	876 ± 144	2.33
6n	2050 ± 50	7100 ± 2600	3.46	2775 ± 375	2040 ± 520	0.73
1	3.3 ± 0.5	700 ± 79	212.12	25 ± 3	4875 ± 1000	195
3	0.5 ± 0.01	44 ± 3	88	1 ± 0.02	70.4 ± 7	70.4
4	13.1 ± 4	500 ± 20	38.2	25 ± 4	1117 ± 117	44.7

[a] IC_{50} values of the ligands determined in ovarian carcinoma cells A2780, P-gp overexpressing A2780AD cells, mouse embryo NIH 3T3 and P-gp overexpressing NIH-MDR-G185. IC_{50} value is the concentration that gives 50% inhibition of cell growth.
[b] IC_{50} values (nM) are the mean ± SE of three independent assays.
[c] The relative resistance of the resistant cell lines obtained by dividing the IC_{50} of the resistant cell line by that of the parental cell line.

should be considered with this limitation and are probably overestimated being the actual values lower than those resulting from the assay. Interestingly all the compounds are extremely effective against the resistant cell lines, indicating that either they are poor substrates for P-glycoprotein (one of the main reasons for antitumoral drug resistance) [47] or that their affinity for tubulin is stronger than that for P-glycoprotein [48].

2.2.6.2. Effect on A549, B16F10, B16F1, PC9 and HCC827 cells. We further characterized **PNOX** in primary human melanocytes (HEMA), human primary melanoma cell line A375 and metastatic melanoma 501MEL cell lines on their cell cycle profile (Figs. S14–S16), and we engaged further cell-based assays for a subseries of new compounds with different binding affinity against tubulin. In particular, we assessed efficacy for **PNOX**, **6a**, **6j** and **6l** against the following tumor cell lines: A549, lung adenocarcinoma; B16F10, mouse melanoma (metastatic); B16F1, mouse melanoma; PC9, lung adenocarcinoma; HCC827, lung adenocarcinoma with EGFR mutation (Fig. 12).

The efficacy of **6a**, **6j** and **6l** on cell survival was investigated on different tumor cell lines both of mouse and human origin, representative of melanoma and lung tumors. Cells were exposed to increasing concentrations (0.1, 1 and 10 μM) in medium containing 5% serum. Cell viability was evaluated by the MTT assay after 18 h of incubation. **PNOX** was kept as reference compound. Data demonstrate that **6a** and **6j** showed an inhibitory effect overlapping the one elicited by **PNOX**, while **6l** was not active. The inhibitory effect was marked in all tumor cell lines except HCC827, characterized by a doubling time of ca. 50–60 h (Fig. 12).

Based on the computational and experimental data, we observed that the tubulin affinity correlates with growth inhibition of tumor cell lines. In fact, we noted that **6a**, possessing a strong affinity against tubulin, is able to behave as tumor cell growth inhibitor at higher concentration with respect to compounds **PNOX** and **6j**. Compound **6l**, containing the 3-substituted quinoline is almost inactive against all the selected tumor cell lines. This is fully consistent with the predicted lack of affinity towards tubulin of **6l** that is not able to correctly accommodate the quinoline nucleus into the colchicine binding site.

For PC9 and HCC827 cell lines we also performed a western blot analysis in order to gain additional information regarding their possible mechanism of action as pro-apoptotic agents. As shown in Fig. 13A, compounds **PNOX** and **6j** were able to promote caspase 3-mediated apoptosis in the tested cell lines. Moreover, the western blot reported in Fig. 13B documented an increase of the inhibitory protein of cell cycle p21 and reduction of cyclin D1. Based on these results we can conclude that our developed compounds are able to block tumor cell cycle (increasing p21 and reducing cyclin D1 expression) and induce apoptosis, being as effective as **PNOX**.

2.2.6.3. Effects on cell cycle and differentiation in NB4 cell line. To extend the investigation of their biological effects, compounds **6a**, **6e**, **6j**, and **6n** were also evaluated in the promyelocytic leukemia (APL) NB4 cell line in terms of cell cycle progression, cell death and cell differentiation. NB4 cells were treated with four different concentrations (50 and 100 nM, 1 and 10 μM) for 24 h, in comparison with **PNOX**.

The compounds were able to induce a dose-dependent block in G1 phase, compared to the control (Fig. S17A) indicating that compounds are able to affect cell cycle progression. Interestingly, in the APL context the cell cycle block is mainly in G1 phase (**PNOX**, **6a**, **6e**, **6j**), suggesting a context-dependent effect on the type of cell cycle block. Furthermore, compound **6n**, which in this context is less potent in cell death induction, induces a G2M block, indicating a possible link with cell death and cell cycle blocks. In addition, treatment for 24 h induced cell death, revealed by the percentage of cells in pre-G1 phase (Fig. S17B). Flow cytometric analysis of propidium iodide stained cells showed the capability of the compounds to induce dose-dependent cell death (Fig. 14A). Compound **6n** was not able to affect cell-cycle progression as well as cell death (Fig. 14A and S17A,B). Moreover, effects on granulocytic differentiation, revealed by CD11c staining, were also tested in a dose dependent manner. The differentiation induction reached a maximum value at 1 μM concentration and, then, decreased likely due to the occurrence of cell death (Fig. 14B). To better understand the role of these compounds on cell differentiation, NB4 cells were treated with these drugs at a concentration of 500 nM and in co-treatment with ATRA (All Trans Retinoic Acid), a known differentiation modulator. While as expected in these timeframes, cell cycle progression and cell death were less affected by ATRA co-treatment (Fig. 15A and S18A,B), NB4 differentiation was strongly regulated by ATRA, and high values were reached in combination, particularly for **6j**. A strong differentiating effect was obtained after combination with **6j** (Fig. 15B). This biological effect indicates potential therapeutic applications in differentiation therapy.

2.2.6.4. Effect on tongue carcinoma (SCC4), multiple myeloma (NCI-H929), and Ca9.22 gingival squamous carcinoma (p53 mutated) cell lines. Compounds **PNOX**, **6j** and **6p** were also evaluated in for their effect on viability on tongue carcinoma (SCC4) and multiple myeloma (NCI-H929), and Ca9.22 gingival squamous carcinoma (p53 mutated) cell lines (Table 5). As shown, compounds **PNOX** and **6j** demonstrated comparable efficacy in SCC4 and NCI-H929 cells, while, compound **6p** demonstrated negligible efficacy in both cell lines.

As **PNOX** and **6j** had promising IC_{50} values these compounds were further tested for their pro-apoptotic ability through flow cytometric analysis of Annexin V/Propidium iodide stained cells. This dual staining method can distinguish between early apoptosis and late apoptosis. As can be seen from Fig. 16 (panels A and B), both compounds induced substantial apoptosis (over 40%) following a 48 h treatment in SCC4 and NCI-H929 cells. Regarding Ca9.22 cells (Fig. 16, panel C), **6j** does not seem to be effective at 500 nM when compared to the other cell lines, while **6p** displays only modest efficacy.

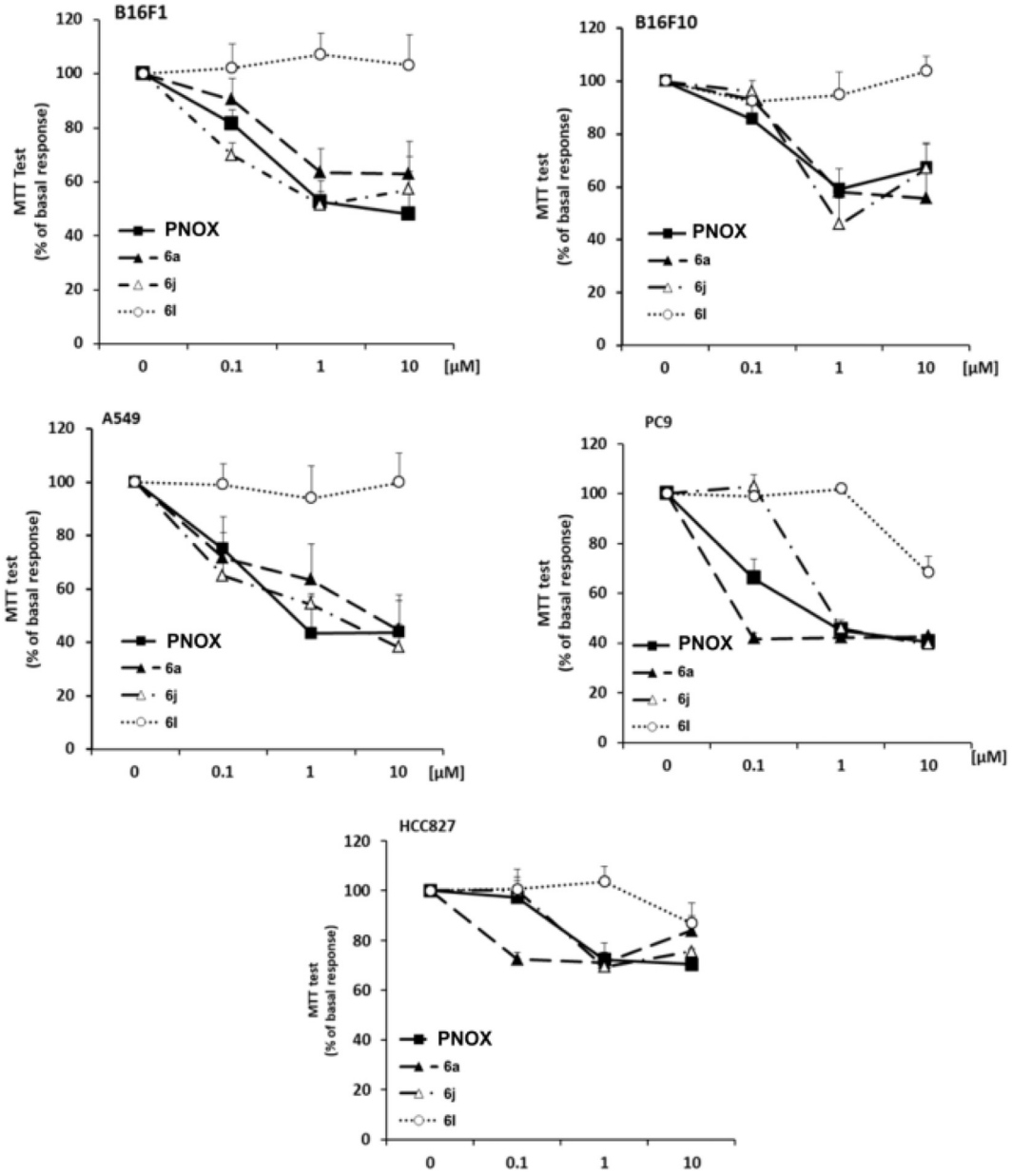

Fig. 12. Effect of compounds **PNOX**, **6a**, **6j** and **6l** against the following cell lines: A549, lung adenocarcinoma; B16F10, mouse melanoma (metastatic); B16F1, mouse melanoma; PC9, lung adenocarcinoma; HCC827, lung adenocarcinoma with EGFR mutation. Cells were exposed to the test substances for 18 h in presence of 5% serum.

After incubation cells were harvested and stained with Annexin V/Propidium Iodide (PI) and were analyzed by flow cytometry using BD FACs Accuri software. 10,000 cells were gated on vehicle treated cells. Values represent the mean ± S.E.M of three independent experiments (n = 3). Statistical analysis was performed using a T-test. **p = 0.001".

2.2.7. Autophagy studies

Dysfunction of autophagy is implied in several diseases including cancer where it may either inhibit or promote cancer cell proliferation depending on the tumor setting [49]. To address the impact of compounds on both basal and induced autophagy we measured the accumulation of the LC3B-II protein by immunoblot. LC3B-II is indeed exclusively located on autophagic vesicles and it is one of the most widely used markers to monitor autophagy since LC3B-II levels are considered directly correlated to the abundance of autophagosomes in the cells. However, since autophagy is a dynamic process, accumulation of LC3B-II within the cells does not necessarily correspond to an increase of autophagy but could reflect a reduction in autophagosome turnover. We therefore compared the amount of LC3B-II in compound-treated samples both in presence or absence of chloroquine (CQ), a well-known inhibitor of lysosomal activity and autophagy (Fig. 17).

HL-60 cells were treated with the tested compounds for 1 h 45 min and accumulation of LC3B-II was measured by immunoblot (Fig. 17A). Significant higher levels of LC3B-II, which were further increased in presence of the lysosomal inhibitor CQ, were found in samples treated with **PNOX**, **6g** and **6j** compared with cells maintained in full medium indicating that these compounds are able to induce accumulation of autophagosomes in HL-60 cells in basal condition (Fig. 17A). Moreover, **6g** and **6j** appeared to be more effective when compared with **PNOX** (Fig. 17A). To investigate the

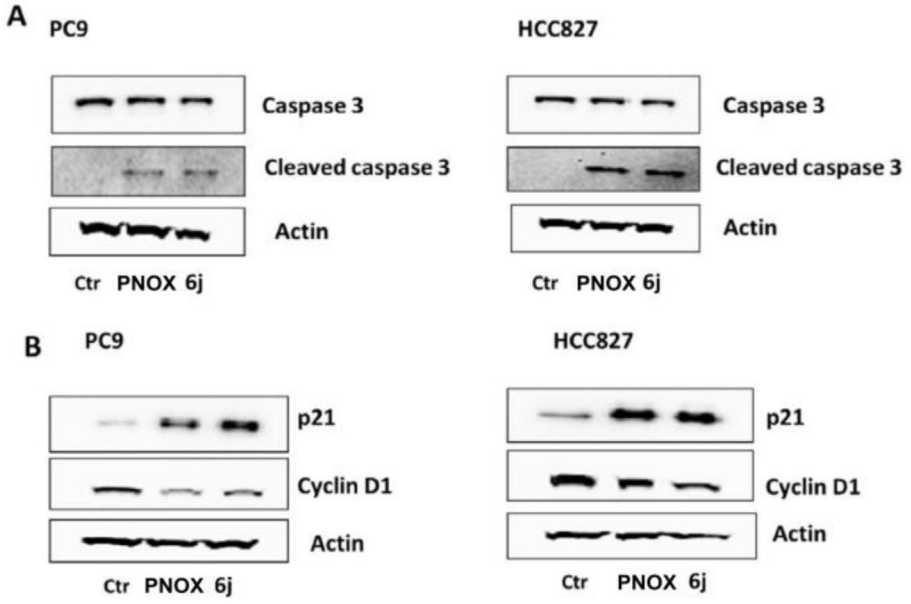

Fig. 13. Western blot analysis. (A) caspase 3 activation; (B) cell cycle proteins. Cells were exposed to **PNOX** and **6j** (10 μM) for 18 h in presence of 5% serum.

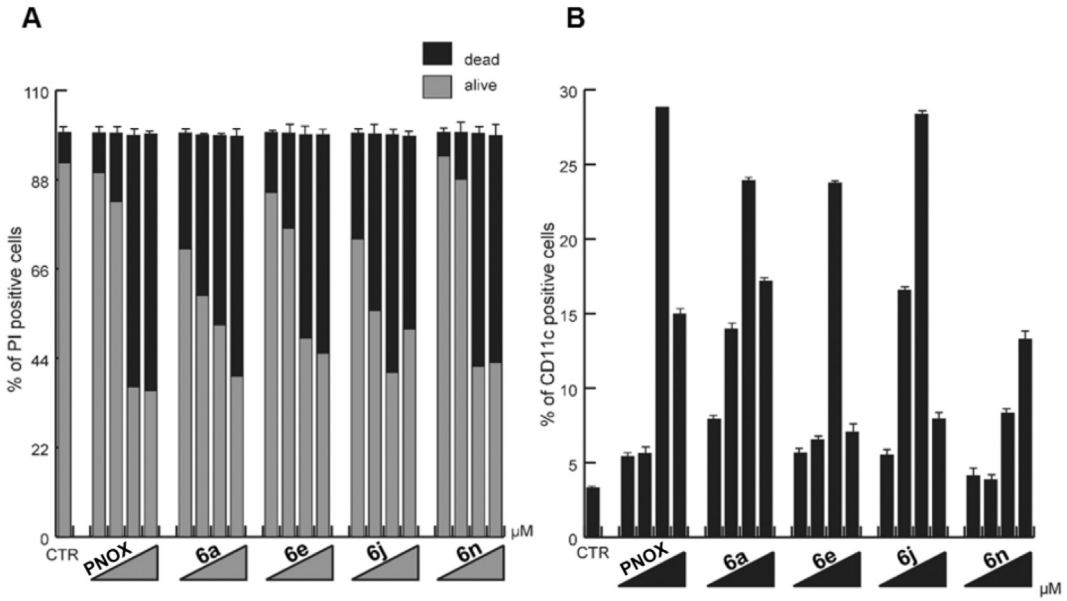

Fig. 14. Biological assays on NB4 cells. (A) propidium iodide assay (B) CD11c expression levels at 24 h after treatment with compounds **PNOX**, **6a**, **6e**, **6j** and **6n** used at 50 and 100 nM, 1 and 10 μM. Data are represented as mean ± S.E.M of biological triplicates.

effect of these compounds on autophagy induced by serum deprivation, cells were starved for 15 min before the addition of the compounds and the levels of LC3B-II measured in presence or absence of CQ after 1 h 45 min of treatment. Accumulation of LC3B-II was significantly higher in serum starved samples co-treated with **6g**, **6j** and **6n** compared with untreated and **PNOX**-treated samples indicating that **6g** and **6j** are the most effective derivatives on the autophagic process in both basal and serum starved conditions. Moreover, a reduction of the LC3B-II protein was found in treated samples, but not in the same samples co-treated with CQ, following longer treatment (16 h) in serum supplemented medium compared with untreated cells. The enhancement of LC3B-II accumulation in samples treated with CQ, a lysosomal inhibitor, compared with CQ-untreated samples may be indicative of a pro-autophagic effect of compounds rather than of an inhibitory effect on the autophagic process. In support of a pro-autophagic effect of the novel analogues in HL-60 cells, short treatment (1 h 45 min) with compounds in serum supplemented samples resulted in the increase of LC3II-B levels which is further enhanced in samples co-treated with CQ (Fig. 17A). Despite this analysis of the autophagic flux (difference in the levels of LC3II-B in presence or absence of lysosomal inhibitors) which reflects the net amount of LC3II-B delivered to lysosomes, suggests a pro-autophagic effect, additional assays are required to better characterize the pro-autophagic effect of novel compounds. Our preliminary data demonstrated that our novel analogues are able to target the autophagic process and that **6g** and **6j** are the best performing analogues so far identified when tested at 10 μM.

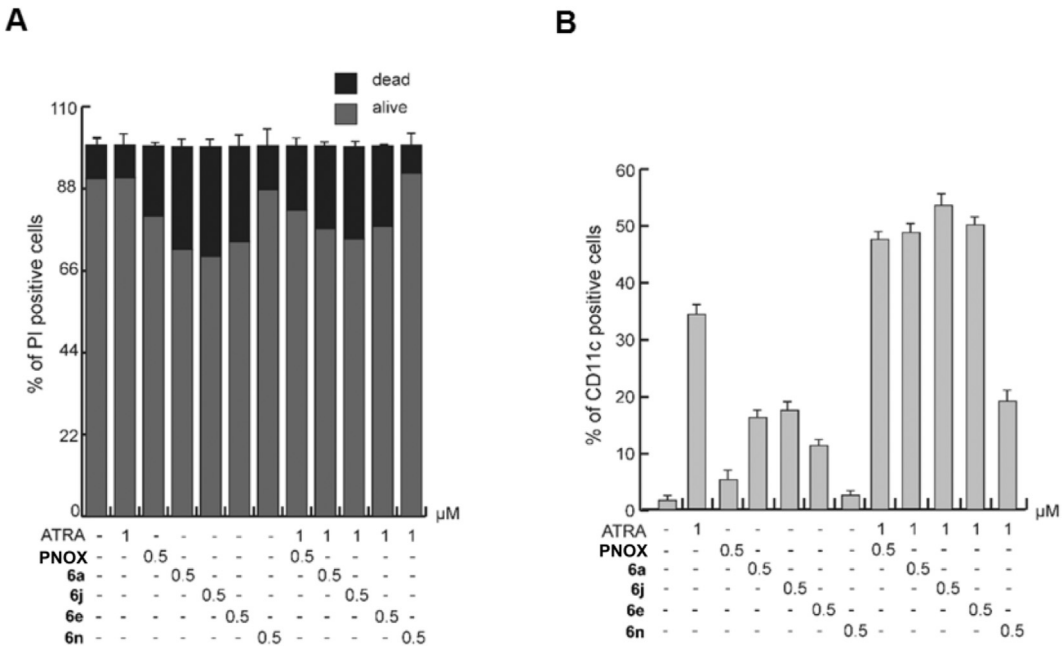

Fig. 15. Biological assays on the promyelocytic leukemia NB4 with and without ATRA treatment. (A) Propidium iodide assay and (B) CD11c expression levels at 24 h after treatment with compounds **PNOX**, **6a**, **6e**, **6j** and **6n** used at the concentration of 0.5 μM with and without ATRA used at the concentration of 1 μM. Data are represented as mean ± S.E.M. of biological triplicates.

Table 5
Cytotoxicity assessment of compounds **PNOX** and **6j** and **6p** on the growth on tongue carcinoma (SCC4) and multiple myeloma (NCI-H929), and Ca9.22 gingival squamous carcinoma (p53 mutated) cell lines.

Cpd	h	SCC4[a]	IC_{50} (μM) NCI-H929[b]	Ca9.22[c]
PNOX	24	nt	nt	0.210
	48	0.160	0.376	0.170
	72	nt	nt	0.083
6j	24	nt	nt	31.6
	48	0.222	0.363	13.4
	72	nt	nt	4.5
6p	24	nt	nt	8.0
	48	9.37	>50	6.3
	72	nt	nt	4.5

[a] IC_{50} values determined in tongue carcinoma (SCC4) cells; cells were treated with increasing concentrations of each compound for 48 h. Data represent the mean of three independent experiments.
[b] IC_{50} values determined in multiple myeloma (NCI-H929) cells; cells were treated with increasing concentrations of each compound for 48 h. Data represent the mean of three independent experiments.
[c] IC_{50} values determined in Ca9.22 gingival squamous carcinoma (p53 mutated) cells; cells were treated with increasing concentrations of each compound for 24 h, 48 h and 72 h. Data represent the mean of three independent experiments. We have previously reported the IC_{50} values for **PNOX** in Ca9.22 cells [21] and they are shown here again for comparison purposes.

3. Conclusion

In summary, we explored the SARs of a pyrrolonaphthoxazepine class of anticancer agents, and described the development of a series of potent pro-apoptotic MDAs with nanomolar affinity. Compounds were characterized by crystallographic, biological, bioinformatics and medicinal chemistry studies. In particular, we have assessed the binding affinity to tubulin for selected compounds and we have solved the X-ray structure of one of the most promising compounds in complex with tubulin. This allowed us to unveil the binding site on tubulin for this class of MDAs, thus gaining insights into their binding mode and mechanism of action. We assessed their ability to inhibit the growth of a large group of tumor cells, including multidrug-resistant cell lines and we investigated the mechanism of action of a sub-series of compounds on cell cycle in different cell lines, unveiling for some of them the activation of caspase 3-mediated apoptosis. Finally, the role of selected compounds on the autophagic process was investigated by the quantification of LC3B-II protein. The obtained data suggested a relevant therapeutic potential for the newly developed compound **6j** and some of its analogues as effective anticancer agents displaying efficacy on multiple cancer cell lines. Additionally, the molecular insight derived from analysis of the X-ray structure of **6j** in complex with tubulin will pave the way to the discovery of novel optimized compounds as potential antitumor agents.

4. Experimental Section

4.1. Chemistry

4.1.1. General remarks

Unless otherwise specified, materials were purchased from commercial suppliers and used without further purification. Reaction progress was monitored by TLC using silica gel 60 F254 (0.040–0.063 μm) with detection by UV. Silica gel 60 (0.040–0.063 μm) was used for column chromatography. ^{1}H NMR and ^{13}C NMR spectra were recorded on a Varian 300 MHz spectrometer or a Bruker 400 MHz spectrometer by using the residual signal of the deuterated solvent as internal standard. Splitting patterns are described as singlet (s), doublet (d), triplet (t), quartet (q), and broad (br); the value of chemical shifts (δ) are given in ppm and coupling constants (*J*) in Hertz (Hz). ESI-MS spectra were performed by an Agilent 1100 Series LC/MSD spectrometer. IR spectra were recorded on a Agilent Cary 630 FTIR spectrophotometer and are reported as cm^{-1}. Melting points were determined in Pyrex capillary tubes using an Electrothermal 8103 apparatus and are uncorrected. Yields refer to purified products and are not

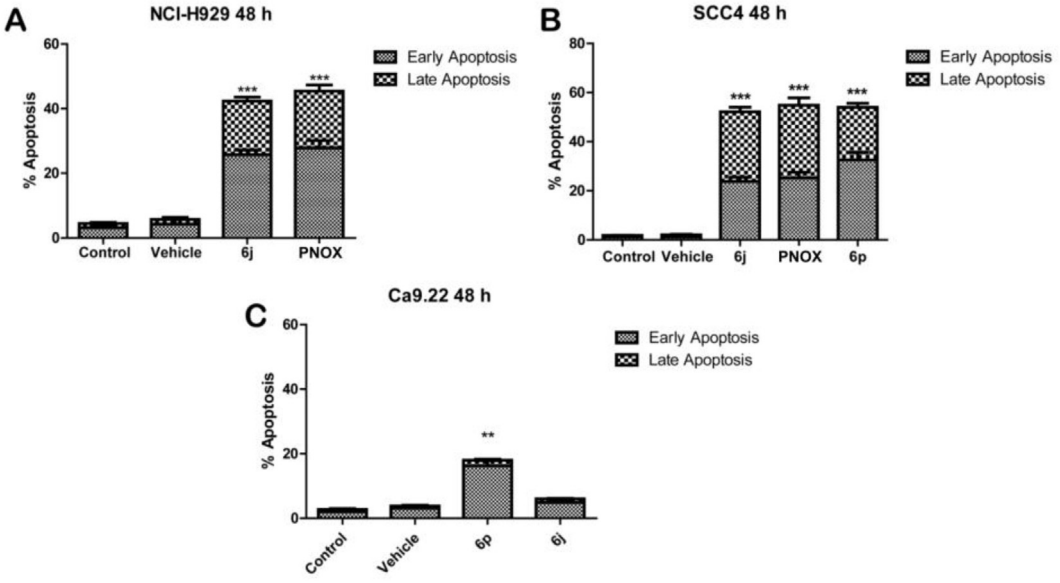

Fig. 16. (A) NCI-H929 cells were seeded at a density of 30×104 cells/mL and were left untreated (control) or treated with either vehicle (1% EtOH (v/v)) or 500 nM of **PNOX** and **6j** for 48 h (B) SCC4 cells were seeded at a density of 15×10^4 cells/mL and were treated with either vehicle control (1% EtOH (v/v)) or 500 nM of **6j** or **PNOX** or 50 μM **6p** for 48 h (C) Ca9.22 cells were seeded at a density of 30×10^4 cells/mL and were treated with either vehicle control (1% EtOH (v/v)) or 500 nM **6p**, or 500 nM of **6j** for 48 h.

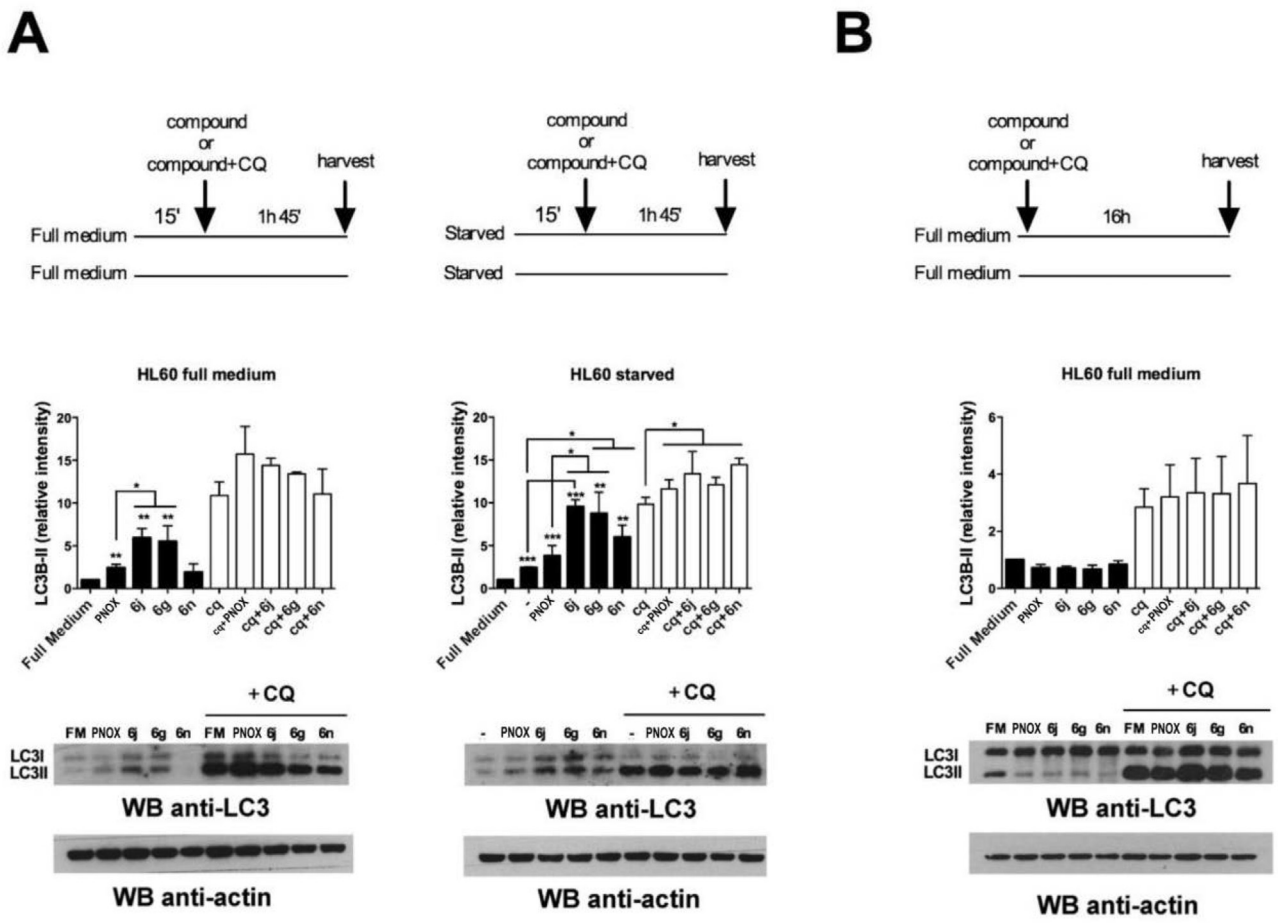

Fig. 17. Immunoblot analysis of LC3B-II levels in HL-60 cells cultured in serum supplemented RPMI 1640 (full medium) or in Earle's Balanced Salts (EBS) medium (starved) and treated with 10 μM of compounds **PNOX**, **6g**, **6j** or **6n** in presence or absence of 40 μM chloroquine (CQ) for 1 h 45 min (A) or 16 h (B). Control immunoblot with anti-actin antibodies of the same filters are shown. Densitometric analysis of LC3B-II amount from three independent experiments was performed and normalized with actin level. Bar graphs show the relative intensity of LC3B-II. *, $p < 0.05$ **, $p < 0.01$ versus full medium as calculated by Student's T-test.

optimized. All moisture-sensitive reactions were performed under argon atmosphere using oven-dried glassware and anhydrous solvents. Final compounds were analyzed by combustion analysis (CHN) to confirm purity > 95% (Table S3).

4.1.2. 8-Bromoquinoline (13a)

Method 1. $FeSO_4 \cdot 7H_2O$ (121 mg, 0.44 mmol) and nitrobenzene (1.78 g, 14.53 mmol) were heated at 110 °C. In a separate flask 2-bromoaniline **11** (2.50 g, 14.53 mmol) and glycerol were sequentially added to conc. H_2SO_4 and the resulting mixture heated at 70 °C. This solution was then added to the $PhNO_2$ $FeSO_4 \cdot 7H_2O$ at 110 °C and the mixture was heated at 150 °C for 7 h. After cooling to room temperature, the mixture was poured into ice and neutralized to pH = 8 with 4 N NaOH. The aqueous phase was extracted 10 times with EtOAc. The combined organic layers were dried over anhydrous sodium sulfate, filtered and concentrated. The residue was purified by flash chromatography on silica gel (50% petroleum ether in DCM) to afford the title compound as a brown oil (60% yield).

Method 2. To a solution of copper (II) bromide (7.00 g, 31.36 mmol) and *tert*-butyl nitrite (5.40 g, 52.28 mmol) in dry acetonitrile (90 mL) was added 8-aminoquinoline **12** (3.77 mg, 26.14 mmol) at room temperature and the mixture was stirred at 65 °C for 12 h. Acetonitrile was evaporated, then Et_2O and water were added and the precipitate filtered. The aqueous phase was extracted 3 times with Et_2O. The combined organic layers were dried over anhydrous sodium sulfate, filtered and concentrated. The residue was purified by flash chromatography on silica gel (30% EtOAc in petroleum ether) to afford the title compound as a brown oil (76% yield). ^{1}H NMR ($CDCl_3$, 300 MHz) δ 9.05 (dd, 1H, J_1 = 1.5 Hz, J_2 = 4.2 Hz), 8.18 (dd, 1H, J_1 = 1.5 Hz, J_2 = 8.4 Hz), 8.05 (dd, 1H, J_1 = 1.2 Hz, J_2 = 7.2 Hz), 7.78 (d, 1H, J = 7.8 Hz), 7.50–7.38 (m, 2H); ESI-MS *m/z* 209.9 $[M+H]^+$, 231.9 $[M+Na]^+$.

4.1.3. Quinoline-8-carbaldehyde (14a)

To a solution of **13a** (100 mg, 0.48 mmol) in dry THF (1.5 mL) at −78 °C *n*BuLi (2.5 M in *n*-hexane, 300 μL, 0.72 mmol) was added dropwise. The resulting solution turned to red and DMF (192 μL, 2.49 mmol) was added. After 10 min at −78 °C the mixture was quenched with water. The reaction was poured into a saturated aqueous solution of $NaHCO_3$ (10 mL) and extracted with EtOAc (3 × 10 mL). The combined organic layers were dried over anhydrous sodium sulfate, filtered and concentrated. The residue was purified by flash chromatography on silica gel (10% EtOAc in *n*-hexane) to afford the title compound as a yellow solid (53% yield). ^{1}H NMR ($CDCl_3$, 300 MHz) δ 11.44 (s, 1H), 9.03 (dd, J_1 = 1.8 Hz, J_2 = 4.2 Hz, 1H), 8.31 (dd, J_1 = 1.2 Hz, J_2 = 7.2 Hz, 1H), 8.23 (dd, J_1 = 1.8 Hz, J_2 = 8.1 Hz, 1H), 8.08 (dd, J_1 = 1.5 Hz, J_2 = 8.4 Hz, 1H), 7.66 (t, J = 7.8 Hz, 1H), 7.50 (dd, J_1 = 4.5 Hz, J_2 = 8.4 Hz, 1H); ESI-MS *m/z* 158 $[M+H]^+$; 180 $[M+Na]^+$.

4.1.4. Quinoline-5-carbaldehyde (14b)

Compound **14b** was obtained from **13b** (500 mg, 2.4 mmol) following the procedure described for the preparation of **14a**. The residue was purified by flash chromatography on silica gel (16% EtOAc in *n*-hexane) to afford the title compound as a yellow solid (66% yield). ^{1}H NMR ($CDCl_3$, 300 MHz) δ 10.37 (s, 1H), 9.62 (d, 1H, J = 8.7 Hz), 9.02 (t, 1H, J = 2.1 Hz), 8.38 (d, 1H, J = 8.7 Hz), 8.07 (dd, 1H, J_1 = 5.4 Hz, J_2 = 7.2 Hz), 7.92–7.88 (m, 1H), 7.58 (dd, 1H, J_1 = 4.5 Hz, J_2 = 8.7 Hz); ESI-MS *m/z* 158 $[M+H]^+$.

4.1.5. 8-(2-Methoxyvinyl)quinoline (15a)

(Methoxymethyl)triphenylphosphonium chloride (76 mg, 0.223 mmol) was suspended in dry THF (1.0 mL) and then sodium *bis*(trimethylsilyl)amide (1 M solution in THF, 300 μL, 0.3 mmol) was added at 0 °C. The solution immediately became dark red colored. After 30 min at 0 °C, aldehyde **14a** (40 mg, 0.255 mmol) dissolved in dry THF (1.0 mL) was added and the resulting mixture was stirred at 0 °C for 30 min. The reaction was monitored by TLC. After 1 h stirring at room temperature, H_2O was added and the aqueous layer was extracted twice with EtOAc. The combined organic layers were dried over anhydrous sodium sulfate, filtered and concentrated. The residue was purified by flash chromatography on silica gel (10% EtOAc in *n*-hexane) to afford the title compound as a yellow oil (63% yield). ^{1}H NMR ($CDCl_3$, 300 MHz) (mixture of *cis* and *trans* isomers) δ 8.91 (td, 1H J_1 = 1.8 Hz, J_2 = 3.9 Hz), 8.43 (dd, 1H, J_1 = 1.5 Hz, J_2 = 7.5 Hz), 8.12 (dt, 1H, J_1 = 2.1 Hz, J_2 = 8.1 Hz), 7.69 (dd, 1H, J_1 = 1.2 Hz, J_2 = 7.5 Hz), 7.62 (dd, 1H, J_1 = 1.2 Hz, J_2 = 8.1 Hz), 7.54–7.36 (m, 3H), 6.96 (d, 1H, J = 13.2 Hz), 6.71 (d, J = 7.2 Hz), 6.45 (d, 1H, J = 7.2 Hz, 1H), 3.85 (s, 3H), 3.84 (s, 3H); ESI-MS *m/z* 186 $[M+H]^+$.

4.1.6. 5-(2-Methoxyvinyl)quinoline (15b)

Compound **15b** was obtained from **14b** (400 mg, 2.55 mmol) following the procedure described for the preparation of **15a**. The residue was purified by flash chromatography on silica gel (30% EtOAc in *n*-hexane) to afford the title compound as a yellow oil (84% yield). ^{1}H NMR ($CDCl_3$, 300 MHz) (mixture of *cis* and *trans* isomers) δ 8.91–8.87 (m, 1H), 8.41 (d, 1H, J = 8.4 Hz), 8.05 (d, 1H, J = 7.2 Hz), 7.95 (dd, 1H, J_1 = 5.4 Hz, J_2 = 8.1 Hz), 7.70–7.60 (m, 1H), 7.48–7.36 (m, 2H), 7.00 (dd, 1H, J_1 = 1.2 Hz, J_2 = 12.6 Hz), 6.42–6.36 (m, 1H), 5.81 (d, 1H, J = 6.9 Hz), 3.81–3.79 (m, 3H); ESI-MS *m/z* 186 $[M+H]^+$.

4.1.7. 2-(Quinolin-8-yl)acetaldehyde (16a)

Compound **15a** (30 mg, 0.162 mmol) was dissolved in acetone (1.0 mL) and then 6 N HCl (405 μL) was added dropwise. The mixture was refluxed for 3 h. The solvent was evaporated and the resulting aqueous mixture was taken to pH = 8 with saturated aqueous $NaHCO_3$. The aqueous layer was extracted with EtOAc (3 × 20 mL). The combined organic layers were dried over anhydrous sodium sulfate, filtered and concentrated. The residue was purified by flash chromatography on silica gel (30% EtOAc in *n*-hexane) to afford the title compound as a red oil (54% yield). ^{1}H NMR ($CDCl_3$, 300 MHz) δ 9.93 (s, 1H), 8.91 (dd, 1H, J_1 = 1.8 Hz, J_2 = 4.2 Hz), 8.18 (dd, 1H, J_1 = 1.2 Hz, J_2 = 8.1 Hz), 7.80 (d, 1H, J = 8.1 Hz), 7.61–7.41 (m, 3H), 4.28 (s, 2H); ESI-MS *m/z* 180 $[M+Na]^+$.

4.1.8. 2-(Quinolin-5-yl)acetaldehyde (16b)

Compound **16b** was obtained starting from **15b** (500 mg, 2.68 mmol) following the procedure described for the preparation of **16a**. The title compound was obtained as a dark yellow oil (94% yield). ^{1}H NMR ($CDCl_3$, 300 MHz) δ 9.80–9.78 (m, 1H), 8.95 (d, 1H, J = 3.6 Hz), 8.22 (d, 1H, J = 8.7 Hz), 8.10 (d, 1H, J = 8.4 Hz), 7.71 (t, 1H, J = 7.8 Hz), 7.49–7.44 (m, 2H), 4.14 (s, 2H); ESI-MS *m/z* 180 $[M+Na]^+$.

4.1.9. Methyl 2-(quinolin-8-yl)acetate (17a)

To a solution of compound **16a** (300 mg, 1.75 mmol) in MeOH (2.0 mL) *N*-iodosuccinimide (987 mg, 4.38 mmol) and potassium carbonate (605 mg, 4.38 mmol) were sequentially added. The reaction was performed in a dark room. The resultant dark brown mixture was stirred for 3 h at 25 °C. Subsequently, water (1.0 mL) and $Na_2S_2O_3 \cdot 5H_2O$ (900 mg) were added. The aqueous phase was extracted with EtOAc (3 × 50 mL). The combined organic layers were dried over anhydrous sodium sulfate, filtered and concentrated. The residue was purified by flash chromatography on silica gel (30% EtOAc in *n*-hexane) to afford the title compound as a pale yellow oil (57% yield). ^{1}H NMR ($CDCl_3$, 300 MHz) δ 8.92 (dd, J_1 = 1.8 Hz, J_2 = 4.2 Hz, 1H), 8.14 (d, 1 H, J = 8.1 Hz), 7.76 (d, 1 H,

$J = 8.1$ Hz), 7.64 (d, 1 H, $J = 6.9$ Hz), 7.52–7.38 (m, 2H), 4.30 (s, 3H), 3.70 (s, 2H); ESI-MS *m/z* 202 $[M+H]^+$, 224 $[M+Na]^+$.

4.1.10. Methyl 2-(quinolin-5-yl)acetate ***(17b)***

Compound **17b** was obtained from **16b** (450 mg, 2.63 mmol) following the procedure described for the preparation of **17a**. The residue was purified by flash chromatography on silica gel (33% EtOAc in *n*-hexane) to afford the title compound as a pale yellow amorphous solid (70% yield). ^{1}H NMR ($CDCl_3$, 300 MHz) δ 8.94 (t, 1H, $J = 2.4$ Hz), 8.38 (d, 1H, $J = 8.7$ Hz), 8.08 (d, 1H, $J = 8.7$ Hz), 7.68 (t, 1H, $J = 7.5$ Hz), 7.50–7.44 (m, 2H), 4.08 (s, 2H), 3.69 (s, 3H); ESI-MS *m/z* 202 $[M+H]^+$, 224 $[M+Na]^+$.

4.1.11. Methyl 2-bromo-2-(quinolin-8-yl)acetate ***(9a)***

To a solution of compound **17a** (130 mg, 0.64 mmol) in CCl_4 (10 mL) NBS (126 mg, 0.71 mmol) and a catalytic amount of AIBN were added in sequence. The mixture was refluxed for 24 h in the presence of a lamp (radicalic reaction). Subsequently the solvent was evaporated and DCM was added. The organic layer was washed twice with water (10 mL) and then dried over anhydrous sodium sulfate, filtered and concentrated. The residue was purified by flash chromatography on silica gel (30% EtOAc in petroleum ether) to afford the title compound as a colorless oil (60% yield). ^{1}H NMR ($CDCl_3$, 300 MHz) δ 8.96 (dd, 1H, $J_1 = 2.4$ Hz, $J_2 = 4.2$ Hz), 8.20–8.12 (m, 2H), 7.84 (dd, 1H, $J_1 = 1.5$ Hz, $J_2 = 8.1$ Hz), 7.58 (t, $J = 8.1$ Hz, 1 H), 7.45 (dd, 1H, $J_1 = 3.9$ Hz, $J_2 = 8.1$ Hz), 6.95 (s, 1H), 3.79 (s, 3H); ESI-MS *m/z* 281 $[M+H]^+$.

4.1.12. Methyl 2-bromo-2-(quinolin-5-yl)acetate ***(9b)***

Compound **9b** was obtained from **17b** (350 mg, 1.74 mmol) following the procedure described for the preparation of **9a**. The mixture was refluxed for 2 h. The residue was purified by flash chromatography on silica gel (33% EtOAc in *n*-hexane) to afford the title compound as a colorless oil (51% yield). ^{1}H NMR ($CDCl_3$, 300 MHz) δ 8.95 (d, 1H, $J = 3.6$ Hz), 8.50 (d, 1H, $J = 8.4$ Hz), 8.12 (d, 1H, $J = 8.4$ Hz), 7.80–7.78 (m, 1H), 7.69–7.66 (m, 1H), 7.49–7.46 (m, 1H), 6.05 (s, 1H), 3.77 (s, 3H); ESI-MS *m/z* 280 $[M+H]^+$.

4.1.13. Quinoline-3-carbaldehyde ***(19)***

Compound **19** was obtained starting from **18** (500 mg, 2.40 mmol) following the procedure described for the preparation of **14a**. The residue was purified by flash chromatography on silica gel (16% EtOAc in *n*-hexane) to afford the title compound as a yellow solid (45% yield). ^{1}H NMR ($CDCl_3$, 300 MHz) δ 10.23 (s, 1H), 9.34 (s, 1H), 8.61 (s, 1H), 8.17 (d, 1H, $J = 8.7$ Hz), 7.97 (d, 1H, $J = 7.8$ Hz), 7.86 (t, 1H, $J = 7.2$ Hz), 7.64 (t, 1H, $J = 7.8$ Hz); ESI-MS *m/z* 158 $[M+H]^+$.

4.1.14. 2-(Quinolin-3-yl)acetaldehyde ***(20)***

Starting from **19** (600 mg, 3.82 mmol) *3-(2-methoxyvinyl)quinoline* was obtained following the procedure described for the preparation of **15a**. The residue was purified by flash chromatography on silica gel (20% EtOAc in *n*-hexane) to afford *3-(2-methoxyvinyl)quinoline* as a yellow oil (500 mg, 70% yield). ^{1}H NMR ($CDCl_3$, 300 MHz) (mixture of *cis* and *trans* isomers) δ 8.97 (s, 1H), 8.85 (s, 1H), 8.42 (s, 1H), 8.03 (d, 2H, $J = 8.7$ Hz), 7.88 (s, 1H), 7.78–7.43 (m, 15H), 7.21 (d, 1H, $J = 1.5$ Hz), 6.35 (dd, 1H, $J_1 = 1.8$ Hz, $J_2 = 7.2$ Hz), 5.92 (d, 2H, $J = 12.9$ Hz), 5.37 (d, 1H, $J = 6.0$ Hz), 3.88 (d, 3H, $J = 1.8$ Hz), 3.76 (d, 3H, $J = 1.5$ Hz); ESI-MS *m/z* 186 $[M+H]^+$. Compound **20** was obtained starting from *3-(2-methoxyvinyl) quinoline* (1.0 g, 5.41 mmol) following the procedure described for the preparation of **16a**. The title compound was obtained as a yellow oil (97% yield). ^{1}H NMR ($CDCl_3$, 300 MHz) δ 9.88 (s, 1H), 8.74 (d, 1H, $J = 2.1$ Hz), 8.10 (d, 1H, $J = 8.1$ Hz), 8.01 (s, 1H), 7.80 (d, 1H, $J = 8.1$ Hz), 7.71 (t, 1H, $J = 1.2$ Hz), 7.58 (t, 1H, $J = 1.2$ Hz), 3.92 (s, 2H); ESI-MS *m/z* 180 $[M+Na]^+$.

4.1.15. Methyl 2-bromo-2-(quinolin-3-yl)acetate ***(9c)***

Starting from **20** (1.0 g, 5.85 mmol) compound *methyl 2-(quinolin*-3-yl*)acetate* was obtained following the procedure described for the preparation of **17a**. The residue was purified by flash chromatography on silica gel (33% EtOAc in *n*-hexane) to afford the title compound as a pale yellow oil (29% yield). ^{1}H NMR ($CDCl_3$, 300 MHz) δ 8.84 (d, 1H, $J = 1.8$ Hz), 8.11–8.07 (m, 2H), 7.79 (d, 1H, $J = 7.8$ Hz), 7.69 (dt, 1H, $J_1 = 1.8$ Hz, $J_2 = 8.7$ Hz), 7.54 (dt, 1H, $J_1 = 1.2$ Hz, $J_2 = 7.2$ Hz), 3.82 (s, 2H), 3.72 (s, 3H); ESI-MS *m/z* 202 $[M+H]^+$, 224 $[M+Na]^+$. Starting from *methyl 2-(quinolin*-3-yl*)acetate* (350 mg, 1.74 mmol) compound **9c** was obtained following the procedure described for the preparation of **9a**. The mixture was refluxed for 2 h. The residue was purified by flash chromatography on silica gel (25% EtOAc in *n*-hexane) to afford the title compound as a brown oil (71% yield). ^{1}H NMR ($CDCl_3$, 300 MHz) δ 9.03 (d, 1H, $J = 1.8$ Hz), 8.35 (s, 1H), 8.11 (d, 1H, $J = 8.4$ Hz), 7.83 (d, 1H, $J = 7.8$ Hz), 7.75 (dt, 1H, $J_1 = 0.6$ Hz, $J_2 = 6.9$ Hz), 7.57 (dt, 1H, $J_1 = 0.9$ Hz, $J_2 = 6.9$ Hz), 5.54 (d, 1H, $J = 1.5$ Hz), 3.82 (d, 3H, $J = 2.4$ Hz); ESI-MS *m/z* 280.9 $[M+H]^+$.

4.1.16. 5-Bromo-8-aminoquinoline ***(21)***

To solution of compound **12** (1.0 g, 6.94 mmol) in 46.0 mL of acetonitrile, a portion of NBS (605 mg, 3.40 mmol) was added. The reaction mixture was stirred at 25 °C for 15 min, then a second portion of NBS (667 mg, 3.75 mmol) was added. The reaction was stirred for 1 h at 25 °C. The solvent was evaporated under reduced pressure and the residue taken up with EtOAc and washed with water (3 × 50 mL). The organic layer was dried over anhydrous sodium sulfate, filtered and concentrated. The residue was purified by flash chromatography on silica gel (10% EtOAc in petroleum ether) to afford the title compound as an amorphous yellow solid (51% yield). ^{1}H NMR (300 MHz, $CDCl_3$) δ 8.76 (d, 1H, $J = 6.0$ Hz), 8.43 (d, 1H, $J = 9.0$ Hz), 7.56 (d, 1H, $J = 12.0$), 7.48 (q, 1H, $J = 3.0$ Hz), 6.80 (d, 1H, $J = 6.0$ Hz); ESI-MS *m/z* 222.9 $[M+H]^+$.

4.1.17. 5-Bromo-7-choro-8-aminoquinoline ***(22)***

To a solution of compound **21** (800 mg, 3.61 mmol) in 77.0 mL of acetonitrile, NCS (458 mg, 3.43 mmol) was added at 25 °C. The reaction mixture was then stirred at 75 °C for 12 h. After cooling to room temperature, acetonitrile was removed under reduced pressure. The residue was taken up with EtOAc, and washed with water (3 × 70 mL). The organic layer was dried over anhydrous sodium sulfate, filtered and concentrated. The residue was purified by flash chromatography on silica gel (7% EtOAc in petroleum ether) to afford the title compound as an amorphous orange solid (70% yield). ^{1}H NMR (300 MHz, $CDCl_3$) δ 8.78 (d, 1H, $J = 4.2$ Hz), 7.69 (s, 1H), 8.43 (d, 1H, $J = 8.7$ Hz), 7.50 (q, 1H, $J = 4.2$), 5.46 (br, 2H); ^{13}C NMR (75 MHz, $CDCl_3$) δ 148.5, 148.4, 135.5, 133.0, 130.7, 127.4, 126.3, 122.3, 121.9. ESI-MS *m/z* 258.0 $[M+H]^+$.

4.1.18. 5-Bromo-7-chloroquinoline ***(23)***

To a suspension of compound **22** (650 mg, 2.52 mmol) in 25 mL of water, concentrated H_2SO_4 was added dropwise at 0 °C until complete dissolution of the starting material was achieved. A solution of $NaNO_2$ (348 mg, 5.05 mmol) in 6.5 mL of water at 0 °C was added to the resulting bright yellow solution. The mixture was stirred for 15 min and subsequently it was added via cannula to a 50% aqueous solution of H_3PO_2 (6.0 mL) at 65 °C. The resulting mixture was stirred at 60 °C for 3 h. After cooling to room temperature, H_2SO_4 was neutralized through addition of 5 mL of a 4 N NaOH solution. The aqueous layer was extracted with EtOAc (3 × 30 mL) and the organic layers dried over anhydrous sodium sulfate, filtered and concentrated. The residue was purified by flash

chromatography on silica gel (7% EtOAc in petroleum ether) to afford the title compound as a yellow amorphous solid (12% yield). ^{1}H NMR (400 MHz, $CDCl_3$) δ 8.84 (d, 1H, $J = 3.2$ Hz), 8.40 (d, 1H, $J = 8.4$ Hz), 8.00 (s, 1H), 7.73 (s, 1H), 7.41 (q, 1H, $J = 4.4$ Hz); ESI-MS *m/z* 243.9 $[M+H]^+$.

*4.1.19. 7-Chloroquinoline-5-carbaldehyde **(24)***

Compound **24** was obtained from **23** following the procedure described for the preparation of **14a**. The residue was purified by flash chromatography on silica gel (11% EtOAc in petroleum ether) to afford the title compound as a yellow amorphous solid (48% yield). ^{1}H NMR (400 MHz, $CDCl_3$) δ 10.22 (s, 1H), 9.46 (d, 1H, $J = 8.8$ Hz), 8.94 (dd, 1H, $J_1 = 1.2$ Hz, $J_2 = 4.0$ Hz), 8.30 (d, 1H, $J = 1.6$ Hz), 7.94 (d, 1H, $J = 2.0$ Hz), 7.52 (q, 1H, $J = 4.4$ Hz); ESI-MS *m/z* 192.0 $[M+H]^+$.

*4.1.20. 7-Chloro-5-(2-methoxyvinyl)quinoline **(25)***

Compound **25** was obtained from **24** following the procedure described for the preparation of **15a**. The residue was purified by flash chromatography on silica gel (25% EtOAc in petroleum ether) to afford the title compound as a yellow amorphous solid (62% yield). ^{1}H NMR (300 MHz, $CDCl_3$), mixture of *cis* - *trans* isomers, δ 8.91–8.87 (m, 2H), 8.39 (t, 3H, $J = 6.9$ Hz), 8.09 (d, 1H, $J = 2.1$ Hz), 7.97 (s, 1H), 7.45–7.38 (m, 3H), 7.02 (d, 1H, $J = 12.6$ Hz), 6.46 (d, 1H, $J = 6.9$ Hz), 6.31 (d, 1H, $J = 6.3$ Hz), 5.77 (d, 1H, $J = 6.9$ Hz), 3.86 (s, 3H), 3.81 (s, 3H); ESI-MS *m/z* 220.0 $[M+H]^+$.

*4.1.21. 2-(7-Chloroquinolin-5-yl)acetaldehyde **(26)***

Compound **26** was obtained from **25** following the procedure described for the preparation of **16a**. The product was isolated as a brown oil and submitted to the next step without further purification (73% yield). ^{1}H NMR (300 MHz, $CDCl_3$), δ 9.83 (s, 1H), 8.97 (d, 1H, $J = 6.0$ Hz), 8.28–8.25 (m, 2H), 7.55–7.51 (m, 2H), 4.15 (s, 2H); ESI-MS *m/z* 206.0 $[M+H]^+$.

*4.1.22. Methyl 2-(7-chloroquinolin-5-yl)acetate **(27)***

Compound **27** was obtained from **26** following the procedure described for the preparation of **17a**. The residue was purified by flash chromatography on silica gel (20% EtOAc in petroleum ether) to afford the title compound as a white amorphous solid (59% yield). ^{1}H NMR (300 MHz, $CDCl_3$), δ 8.93 (dd, 1H, $J_1 = 1.5$ Hz, $J_2 = 4.2$ Hz), 8.32 (d, 1H, $J = 7.8$ Hz), 8.07 (d, 1H, $J = 1.5$ Hz), 7.47–7.43 (m, 2H), 4.04 (s, 2H), 3.70 (s, 3H); ESI-MS *m/z* 236.0 $[M+H]^+$.

*4.1.23. Metil 2-bromo-2-(7-chloroquinolin-5-yl)acetate **(9d)***

Compound **9d** was obtained starting from **27** following the procedure described for the preparation of **9a**. The residue was purified by flash chromatography on silica gel (20% EtOAc in petroleum ether) to afford the title compound as a colorless oil (65% yield). ^{1}H NMR (300 MHz, $CDCl_3$), δ 8.97 (dd, 1H, $J_1 = 1.5$ Hz, $J_2 = 4.5$ Hz), 8.52 (d, 1H, $J = 1.5$ Hz), 8.21 (d, 1H, $J = 1.5$ Hz), 7.83 (d, 1H, $J = 2.1$ Hz), 7.54 (q, 1H, $J_1 = 4.5$ Hz, $J_2 = 8.7$ Hz), 5.98 (s, 1H), 3.70 (s, 3H); ESI-MS *m/z* 315.9 $[M+H]^+$.

*4.1.24. Ethyl 2-(1-hydroxy-5-methoxy-1,2,3,4-tetrahydronaphthalen-1-yl)acetate **(29)***

To a solution of LHMDS (1M in THF, 14.74 mL, 14.74 mmol) in dry THF (15.8 mL) cooled to −78 °C, a solution of dry EtOAc (1.34 mL, 13.64 mmol) in dry THF (1.36 mL) was added dropwise. A solution of tetralone **28** (2.0 g, 11.34 mmol) in dry THF (2.6 mL) was added while maintaining an internal temperature below −70 °C. The resulting mixture was stirred at −70 °C for 1 h, quenched with 2 N HCl (10 mL), and allowed to warm up to 25 °C. The mixture was extracted with EtOAc (2 × 10 mL) and the combined organic layers were washed with brine, dried over anhydrous sodium sulfate, filtered and concentrated. The residue was purified by flash chromatography on silica gel (10% EtOAc in *n*-hexane) to afford the title compound as a yellow oil (76% yield). ^{1}H NMR (400 MHz, $CDCl_3$) δ 7.20 (m, 2H), 6.75 (m, 1H), 4.2 (q, $J = 6.4$ Hz, 2H), 3.80 (s, 3H), 2.70 (m, 4H), 2.10 (m, 1H), 1.85 (m, 1H), 1.25 (t, $J = 7.2$ Hz, 3H); ESI-MS *m/z* 287.0 $[M+H]^+$.

*4.1.25. Ethyl 2-(5-methoxy-3,4-dihydronaphthalen-1-yl)acetate (**30**) and ethyl 2-(5-methoxy-3,4-dihydronaphthalen-1(2H)-ylidene)acetate **(31)***

Hydroxyester **29** (2270 mg, 8.6 mmol) was dissolved in toluene/TFA (17 mL/0.4 mL) and the mixture was stirred at 110 °C for 3 h. The mixture was then cooled to 25 °C, diluted with EtOAc and washed with a 1 N NaOH solution (5 mL) and water (5 mL). The organic layer was washed with brine, dried over anhydrous sodium sulfate, filtered and concentrated. The resulting dark yellow residue containing a 1:2 mixture of olefins **30** and **31** was directly used in the next step (quantitative yield). ^{1}H NMR (300 MHz, $CDCl_3$) δ 7.25 (m, 0.5H), 7.15 (m, 1H), 6.80 (m, 1.5H), 6.35 (s, 0.3H), 6.00 (t, 0.7H), 4.20 (m, 2H), 3.80 (s, 3H), 3.40 (s, 1.5H), 3.20 (m, 0.5H), 2.80 (m, 2H), 2.30 (m, 1.5H), 1.85 (m, 0.5H), 1.25 (t, 1H), 1.20 (t, 2H).

*4.1.26. Ethyl 2-(5-methoxynaphthalen-1-yl)acetate **(33)***

A mixture of olefins **31** and **32** (1866 mg, 7.58 mmol) was dissolved in cyclohexene/dioxane (7.7 mL/2.6 mL). A catalytic amount of 10% Pd-C was then added and the mixture heated to reflux for 12 h. The mixture was cooled to 25 °C, filtered through a pad of celite and, after carefully washing the pad with EtOAc, concentrated under reduced pressure. The above residue containing intermediate **32** was dissolved in toluene (16.4 mL). To this was added DDQ (3614 mg, 7.96 mmol), and the mixture heated at reflux for 3 h. The mixture was then cooled to 25 °C, and the resulting solids were removed by filtration using EtOAc as the solvent. The filtrate was concentrated to dryness and the product was purified by flash chromatography on silica gel (4% EtOAc in petroleum ether) to afford the title compound as a yellow oil (30% yield). ^{1}H NMR (400 MHz, $CDCl_3$) δ 8.27 (t, $J = 5.2$ Hz, 1H), 7.55 (d, $J = 8.6$ Hz 1H), 7.48–7.41 (m, 3H), 6.85 (d, $J = 7.6$ Hz, 1H), 4.15 (q, $J = 7.2$ Hz, 2H), 4.09 (s, 2H), 4.00 (s, 3H), 1.20 (t, $J = 7.2$ Hz, 3H); ^{13}C NMR (75 MHz, $CDCl_3$) δ 171.6, 155.8, 133.1, 130.3, 128.5, 126.3, 125.9, 124.7, 121.8, 116.0, 103.8, 60.9, 55.5, 39.6, 14.1. ESI-MS *m/z* 245.2 $[M+H]^+$, 267.3 $[M+Na]^+$.

*4.1.27. Ethyl 2-bromo-2-(5-methoxynaphthalen-1-yl)acetate **(9e)***

Compound **9e** was obtained starting from **33** following the procedure described for the preparation of **9a**. The residue was purified by flash chromatography on silica gel (5% Et_2O in petroleum ether) to afford title compound as a yellow oil (30% yield). ^{1}H NMR (400 MHz, $CDCl_3$) δ 8.32 (d, $J = 8.4$ Hz, 1H), 7.79 (d, $J = 7.2$ Hz, 1H), 7.64 (d, $J = 8.4$ Hz, 1H), 7.50 (t, $J = 8.0$ Hz, 1H), 7.42 (t, $J = 8.0$ Hz, 1H), 6.85 (d, $J = 7.6$ Hz, 1H), 6.11 (s, 1H), 4.25 (q, $J = 7.6$ Hz, 2H), 3.99 (s, 3H), 1.22 (t, $J = 7.2$ Hz, 3H); ESI-MS *m/z* 325.0 $[M+H]^+$.

*4.1.28. Ethyl 2-oxo-2-(quinolin-8-yl)acetate **(34a)***

To a solution of compound **13a** (250 mg, 1.22 mmol) in dry THF (2.5 mL), *n*-BuLi (2.5 M solution in *n*-hexane, 1.50 mmol) was added dropwise at −78 °C. After 10 min diethyl oxalate (165 μL, 1.22 mmol) was added at −78 °C. The reaction mixture was stirred at −78 °C for 10 min (TLC monitoring) and then quenched with 3 mL of a saturated solution of $NaHCO_3$. The aqueous layer was extracted with EtOAc (3 × 5 mL). The combined organic layers were dried over anhydrous sodium sulfate, filtered and concentrated. The residue was purified by flash chromatography on silica gel (7% EtOAc in petroleum ether) to afford the title compound as a yellow amorphous solid (20% yield). ^{1}H NMR ($CDCl_3$, 300 MHz) δ 8.89 (dd,

1H, $J_1 = 1.5$ Hz, $J_2 = 3.9$ Hz), 8.34 (dd, 1H, $J_1 = 1.5$ Hz, $J_2 = 7.2$ Hz), 8.23 (dd, 1H, $J_1 = 1.5$ Hz, $J_2 = 8.4$ Hz), 8.10 (dd, 1H, $J_1 = 1.2$ Hz, $J_2 = 8.1$ Hz), 7.69 (t, 1H, $J = 7.8$ Hz), 7.50–7.46 (m, 1H), 4.44 (m, 2H), 1.42 (t, 3H, $J = 6.9$ Hz); ESI-MS *m/z* 230.0 $[M+H]^+$, 252.0 $[M+Na]^+$, 481.0 $[2M+Na]^+$.

4.1.29. Ethyl 2-oxo-2-(quinolin-5-yl)acetate (34b)

Compound **34b** was prepared stating from **13b** following the procedure described for the preparation of **34a**. The residue was purified by flash chromatography on silica gel (20%–50% EtOAc in *n*-hexane) to afford the title compound as a yellow amorphous solid (22% yield). ^{1}H NMR (300 MHz, $CDCl_3$) δ 9.39 (d, $J = 8.7$ Hz, 1H), 9.01 (d, $J = 4.1$ Hz, 1H), 8.40 (d, $J = 8.4$ Hz, 1H), 8.08 (d, $J = 7.2$ Hz, 1H), 7.81 (t, $J = 7.9$ Hz, 1H), 7.60 (dd, $J_1 = 8.7$, $J_2 = 4.1$ Hz, 1H), 4.50 (q, $J = 7.1$ Hz, 2H), 1.46 (t, $J = 8$ Hz, 3H); ESI-MS *m/z* 230.1 $[M+H]^+$.

4.1.30. Ethyl 2-hydroxy-2-(quinolin-8-yl)acetate (10a)

To a solution of compound **34a** (130 mg, 0.57 mmol) in dry THF (5 mL), $NaBH_4$ (13 mg, 0.34 mmol) was added at 25 °C. The reaction mixture was stirred at 25 °C for 30 min (TLC monitoring), and then quenched with saturated aqueous NH_4Cl (1 mL). THF was evaporated under reduced pressure and the aqueous residue extracted with EtOAc (3 × 10 mL). The combined organic layers were dried over anhydrous sodium sulfate, filtered and concentrated. The residue was purified by flash chromatography on silica gel (10%–20% EtOAc in *n*-hexane) to afford the title compound as a pale yellow amorphous solid (26% yield). ^{1}H NMR ($CDCl_3$, 300 MHz) δ 8.87 (dd, 1H, $J_1 = 1.8$ Hz, $J_2 = 4.5$ Hz), 8.20 (dd, 1H, $J_1 = 1.8$ Hz, $J_2 = 8.4$ Hz), 7.80 (dd, 1H, $J_1 = 1.5$ Hz, $J_2 = 8.1$ Hz), 7.71 (d, 1H, $J = 6.9$ Hz), 7.57–7.52 (m, 1H), 7.44 (q, 1H, $J = 3.9$ Hz), 5.66 (s, 1H), 4.26–4.05 (m, 2H), 1.12 (t, 3H, $J = 4.2$ Hz); ESI-MS *m/z* 232.0 $[M+H]^+$, 254.0 $[M+Na]^+$, 485.0 $[2M+Na]^+$.

4.1.31. Ethyl 2-hydroxy-2-(quinolin-5-yl)acetate (10b)

Compound **10b** was prepared starting from **34b** following the procedure described for the preparation of **10a**. The residue was purified by flash chromatography on silica gel (50% DCM in acetone) to afford the title compound as a yellow amorphous solid (21% yield). ^{1}H NMR (300 MHz, $CDCl_3$) δ 8.83 (d, $J = 4.2$ Hz, 1H), 8.56 (d, $J = 8.7$ Hz, 1H), 8.05 (d, $J = 8.4$ Hz, 1H), 7.67–7.52 (m, 2H), 7.39 (dd, $J = 8.6$, 4.2 Hz, 1H), 5.76 (s, 1H), 4.27–4.03 (m, 2H), 1.10 (t, $J = 7.2$ Hz, 3H); ESI-MS *m/z* 231.9 $[M+H]^+$.

4.1.32. 8-Bromo-2-ethylquinoline (36)

To a solution of freshly distilled diisopropylamine (428 μL, 3.06 mmol) in dry THF (10 mL), *n*-BuLi (1.6 M solution in *n*-hexane, 2.90 mmol) was added dropwise at 0 °C. The solution was stirred for 30 min and then cooled to −78 °C. The cold solution was added dropwise to a solution of compound **35** (500 mg, 2.25 mmol) in dry THF (1 mL). The reaction mixture immediately turned dark red and it was kept stirring at −78 °C for 1 h. Methyl iodide (270 μL, 4.34 mmol) was then added and the mixture was stirred while slowly reaching 0 °C, and then poured into crushed ice and neutralized with saturated aqueous NH_4Cl. The aqueous layer was extracted with EtOAc (3 × 10 mL). The combined organic layers were dried over anhydrous sodium sulfate, filtered and concentrated. The residue was purified by flash chromatography on silica gel (10% EtOAc in petroleum ether) to afford the title compound as a yellow oil (48% yield). ^{1}H NMR (300 MHz, $CDCl_3$) δ 8.03 (d, 1H, $J = 8.6$ Hz), 8.01 (dd, 1H, $J_1 = 7.8$ Hz, $J_2 = 1.6$ Hz), 7.73 (dd, 1H, $J_1 = 8.2$ Hz, $J_2 = 1.2$ Hz), 7.34 (d, 1H, $J = 8.2$ Hz), 7.30 (t, 1H, $J = 7.8$ Hz), 3.12–3.05 (m, 2H), 1.43 (t, 3H, $J = 7.4$ Hz); ESI-MS *m/z* 237.0 $[M+H]^+$.

4.1.33. Ethyl 2-(2-methylquinolin-8-yl)-2-oxoacetate (37a)

Compound **37a** was prepared stating from **35** following the procedure described for the preparation of **34a**. The residue was purified by flash chromatography on silica gel (7% EtOAc in petroleum ether) to afford the title compound as a yellow amorphous solid (18% yield). ^{1}H NMR (300 MHz, $CDCl_3$) δ 8.29 (d, $J = 7.2$ Hz, 1H), 8.12–7.96 (m, 2H), 7.65–7.54 (m, 1H), 7.38–7.21 (m, 1H), 4.47 (q, $J = 7.1$ Hz, 2H), 2.68 (s, 3H), 1.41 (t, $J = 7.2$ Hz, 3H); ESI-MS *m/z* 244.0 $[M+H]^+$.

4.1.34. Ethyl 2-(2-ethylquinolin-8-yl)-2-oxoacetate (37b)

Compound **37b** was prepared stating from **36** following the procedure described for the preparation of **34a**. The residue was purified by flash chromatography on silica gel (10% EtOAc in petroleum ether) to afford the title compound as a yellow amorphous solid (38% yield). ^{1}H NMR (300 MHz, $CDCl_3$) δ 8.23 (d, $J = 7.3$ Hz, 1H), 8.05 (d, $J = 8.5$ Hz, 1H), 7.98 (d, $J = 8.1$ Hz, 1H), 7.54 (t, $J = 7.7$ Hz, 1H), 7.30 (d, $J = 8.5$ Hz, 1H), 4.43 (q, $J = 7.5$ Hz, 2H), 2.92 (q, $J = 7.6$ Hz, 2H), 1.42–1.29 (m, 6H).

4.1.35. Ethyl 2-hydroxy-2-(2-methylquinolin-8-yl)acetate (10c)

Compound **10c** was prepared starting from **37a** following the procedure described for the preparation of **10a**. The residue was purified by flash chromatography on silica gel (10% EtOAc in *n*-hexane) to afford the title compound as a yellow amorphous solid (50% yield). ESI-MS *m/z* 246.0 $[M+H]^+$, 268.0 $[M+Na]^+$.

4.1.36. Ethyl 2-(2-ethylquinolin-8-yl)-2-hydroxyacetate (10d)

Compound **10d** was prepared starting from **37b** following the procedure described for the preparation of **10a**. The residue was pure enough to be directly employed for the subsequent step (97% yield). ^{1}H NMR (300 MHz, $CDCl_3$) δ 8.07 (d, $J = 8.5$ Hz, 1H), 7.74 (d, $J = 8.2$ Hz, 1H), 7.65 (d, $J = 7.1$ Hz, 1H), 7.45 (t, $J = 7.6$ Hz, 1H), 7.33–7.23 (m, 1H), 6.80 (br s, 1H), 5.53 (s, 1H), 4.26–4.02 (m, 2H), 3.00 (q, $J = 7.6$ Hz, 2H), 1.41 (t, $J = 7.5$ Hz, 3H), 1.15 (t, $J = 7.1$ Hz, 3H); ESI-MS *m/z* 260.0 $[M+H]^+$, 281.9 $[M+Na]^+$.

4.1.37. 5-Bromoisoquinoline (39)

Isoquinoline **38** (1156 mg, 8.95 mmol) was suspended in conc. H_2SO_4 (9.7 mL) at 0 °C. After cooling to −25 °C, NBS (1912 mg, 10.74 mmol) was added. The reaction mixture was stirred at −25 °C for 2 h and then at 25 °C for additional 24 h. Subsequently, ice was added and the mixture was treated with conc. NH_4OH (10 mL) to pH = 8–10. The resulting solution was extracted with EtOAc (3 × 10 mL). The combined organic layers were dried over anhydrous sodium sulfate, filtered and concentrated. The residue was purified by flash chromatography on silica gel (20% EtOAc in petroleum ether) to afford the title compound as a pale pink solid (71% yield). ^{1}H NMR (300 MHz, $CDCl_3$) δ 9.24 (s, 1H), 8.65 (d, $J = 5.9$ Hz, 1H), 8.00–7.95 (m, 3H), 7.48 (t, $J = 7.8$ Hz, 1H); ESI-MS *m/z* 209.1 $[M+H]^+$.

4.1.38. Ethyl 2-hydroxy-2-(isoquinolin-5-yl)acetate (10e)

Ethyl 2-(isoquinolin-5-yl*)-2-oxoacetate* was prepared starting from **39** following the procedure described for the preparation of **34a**. The residue was purified by flash chromatography on silica gel (25% EtOAc in petroleum ether) to afford the title compound as a pale orange amorphous solid (40% yield). ^{1}H NMR (400 MHz, $CDCl_3$) δ 9.32 (s, 1H), 8.79 (d, $J = 6.0$ Hz, 1H), 8.70 (d, $J = 6.1$ Hz, 1H), 8.27–8.17 (m, 2H), 7.69 (t, $J = 7.6$ Hz, 1H), 4.47 (q, $J = 7.2$ Hz, 2H), 1.43 (t, $J = 6.8$ Hz, 3H); ESI-MS *m/z* 230.1 $[M+H]^+$. Compound **10e** was obtained starting from *ethyl 2-(isoquinolin*-5-yl*)-2-oxoacetate* following the procedure described for **10a**. The residue was purified by flash chromatography on silica gel (50% EtOAc in petroleum ether) to afford title compound as a pale yellow amorphous solid

(53% yield). ^{1}H NMR (400 MHz, $CDCl_3$) δ 9.24 (s, 1H), 8.54 (d, $J = 6.0$ Hz, 1H), 7.95–7.91(m, 2H), 7.75 (d, $J = 7.2$ Hz, 1H), 7.58 (t, $J = 7.6$ Hz, 1H), 5.73 (s, 1H), 4.31–4.06 (m, 2H), 3.76 (s, 1H), 1.11 (t, $J = 7.2$ Hz, 3H); ESI-MS *m/z* 232.1 $[M+H]^+$.

4.1.39. 1-(Benzo[d][1,3]dioxol-5-yl)ethanone (41)

N-methoxy-N-methylbenzo[d][1,3]dioxole-5-carboxamide. To a solution of acid **40** (1.0 g, 6.01 mmol) in dry DCM (20 mL), EDCI (1382 mg, 7.21 mmol), HOBt (974 mg, 7.21 mmol) and *N,N*-DIPEA (2 mL, 12.01 mmol) were added at 0 °C. The reaction mixture was stirred at 0 °C for 30 min, then *N,O*-dimethylhydroxylamine hydrochloride (703 mg, 7.21 mmol) and *N,N*-DIPEA (1.00 mL, 6.01 mmol) were added. The reaction mixture was stirred at 25 °C for 12 h, then quenched with saturated aqueous $NaHCO_3$. The reaction was extracted with DCM (3 × 20 mL) and the combined organic layers were washed with saturated aqueous $NaHCO_3$, dried over anhydrous sodium sulfate, filtered and concentrated. The residue was purified by flash chromatography on silica gel (100% chloroform) to afford the title compound as a colorless oil (73% yield). ^{1}H NMR (300 MHz, $CDCl_3$), δ 7.30 (dd, 1H, $J_1 = 0.9$ Hz, $J_2 = 0.9$ Hz), 7.22 (s, 1H), 6.81 (d, 1H, $J = 8.7$ Hz), 6.00 (s, 2H), 3.55 (s, 3H), 3.34 (s, 3H); ESI-MS *m/z* 210.0 $[M+H]^+$, 231.9 $[M+Na]^+$, 425.0 $[2M+H]^+$, 440.9 $[2M+Na]^+$. To a solution of *N-methoxy-N-methylbenzo[d][1,3]dioxole-5-carboxamide* (920 mg, 4.40 mmol) in dry THF (20 mL) MeMgBr (3 M solution in Et_2O, 2.2 mL, 6.60 mmol) was added at 0 °C. The reaction mixture was stirred at 0 °C for 1 h, and then quenched with saturated aqueous NH_4Cl. THF was evaporated under reduced pressure and the residue was partitioned between DCM and water. The aqueous layer was extracted with DCM (3 × 30 mL). The combined organic layers were dried over anhydrous sodium sulfate, filtered and concentrated. The obtained residue was submitted to the next step without further purification (85% yield). ^{1}H NMR (300 MHz, $CDCl_3$) δ 7.53 (dd, 1H, $J_1 = 1.8$ Hz, $J_2 = 8.1$ Hz), 7.41 (s, 1H), 6.83 (d, 2H, $J = 8.4$ Hz), 6.02 (s, 1H), 2.52 (s, 3H); ESI-MS *m/z* 165.0 $[M+H]^+$.

4.1.40. Methyl 2-(benzo[d][1,3]dioxol-5-yl)-2-hydroxyacetate (10f)

*2-(Benzo[d][1,3]dioxol-*5-yl*)-2-hydroxyacetic acid.* To a suspension of compound **41** (2,8 g, 16.96 mmol) in a 3:1 mixture of 1,4-dioxane and water (24 mL), Amberlyst A-26 (1696 mg, 16.96 mmol) and SeO_2 (3763 mg, 33.92 mmol) were added at 25 °C. The reaction was heated to 90 °C and stirred for 24 h. After cooling to room temperature, the mixture was filtered and the filtrate was further filtered over a celite pad to remove residual SeO_2. The reaction mixture was treated with 1 N NaOH (20 mL) and extracted with DCM (3 × 20 mL). The aqueous layer was then acidified to pH = 1 with 6 N HCl and extracted with EtOAc (3 × 25 mL). The combined organic layers were dried over anhydrous sodium sulfate, filtered and concentrated. The obtained yellow solid residue was submitted to the next step without further purification (84% yield). ^{1}H NMR (300 MHz, $(CD_3)_2CO$) δ 6.97 (m, 2H), 6.81 (d, 1H, $J = 8.4$ Hz), 5.98 (s, 2H), 5.10 (s, 1H); ESI-MS *m/z* 194.9 $[M-H]^-$. To a solution of the crude *2-(benzo[d][1,3]dioxol-*5-yl*)-2-hydroxyacetic acid* (465 mg, 2.37 mmol) in dry DMF (12 mL), anhydrous K_2CO_3 (818 mg, 5.92 mmol) and methyl iodide (442 μL, 7.11 mmol) were added at 25 °C. The resulting mixture was stirred at 25 °C for 3 h, and then poured in water (10 mL) and extracted with DCM (3 × 20 mL). The combined organic layers were dried over anhydrous sodium sulfate, filtered and concentrated. The residue was purified by flash chromatography on silica gel (10% EtOAc in petroleum ether) to afford title compound as an amorphous white solid (29% yield). ^{1}H NMR (300 MHz, $CDCl_3$) δ 6.94–6.87 (m, 2H), 6.79 (d, 1H, $J = 8.7$ Hz), 5.96 (s, 2H), 5.07 (s, 2H), 3.76 (s, 3H); ESI-MS *m/z* 232.9 $[M+Na]^+$.

4.1.41. Ethyl 2-([1,1'-biphenyl]-2-yl)-2-oxoacetate (43)

Compound **43** was prepared stating from **42** following the procedure described for the preparation of **34a**. The residue was purified by flash chromatography on silica gel (2% EtOAc in petroleum ether) to afford the title compound as a yellow oil (18%). ^{1}H NMR (300 MHz, $CDCl_3$) δ 7.82 (d, $J = 7.5$ Hz, 1H), 7.63 (t, $J = 7.4$ Hz, 1H), 7.52–7.25 (m, 7H), 3.75 (t, $J = 6.9$ Hz, 2H), 1.25 (q, $J = 7.2$ Hz, 3H); ESI-MS *m/z* 276.9 $[M+Na]^+$.

4.1.42. Ethyl 2-([1,1'-biphenyl]-2-yl)-2-hydroxyacetate (10g)

Compound **10g** was obtained starting from **43** following the procedure described for **10a**. The residue was purified by column chromatography on silica gel (10% EtOAc in petroleum ether) to afford the title compound as a yellow oil (56%). ^{1}H NMR (300 MHz, $CDCl_3$) δ 7.55–7.28 (m, 9H), 5.35 (d, $J = 5.1$ Hz, 1H), 4.19–4.02 (m, 2H), 1.12 (t, $J = 7.2$ Hz, 3H); ESI-MS *m/z* 279.9 $[M+Na]^+$.

4.1.43. General Procedure A. Alkylation protocol employed for the synthesis of aryl-alkyl ethers 44a-e

To a stirred solution of pyrrolylphenol compounds (**8a** or **8b**, 1.0 mmol) in dry DMF (10 mL/mmol) were added K_2CO_3 (1.5 mmol) and a catalytic amount of 18-crown-6. The mixture was stirred at 25 °C for 2 h, then the suitable α-bromoderivative (1.2 mmol) dissolved in dry DMF (3 mL/mmol) was added. The reaction mixture was stirred for 12 h at 90 °C. Then DMF was evaporated and the residue was dissolved in EtOAc. The organic layer was washed with water and dried over anhydrous sodium sulfate, filtered and concentrated. The residue was purified by flash chromatography on silica gel.

4.1.44. General Procedure B. Mitsunobu protocol employed for the synthesis of aryl-alkyl ethers 44f-j

The suitable α-hydroxyester derivative (1.0 mmol) was dissolved in dry THF (10 mL/mmol), then triphenylphosphine (1.5 mmol) and DIAD (1.0 mmol) were added at 0 °C. The mixture was stirred at 0 °C for 10 min, then a solution of pyrrolylphenol compounds **8a** or **8b** (1.0 mmol) dissolved in dry THF (8 mL/mmol) was added. The reaction mixture was stirred at 25 °C for 24 h, then THF was evaporated under reduced pressure. The residue was taken up with DCM and washed with water and brine. The organic layer was dried over anhydrous sodium sulfate, filtered and concentrated. The residue was purified by flash chromatography on silica gel.

4.1.45. Methyl 2-[(3-(1H-pyrrol-1-yl)naphthalen-2-yl)oxy]-2-(quinolin-8-yl)acetate (44a)

The title compound was prepared following General Procedure A. The residue was purified by flash chromatography on silica gel (30% EtOAc in *n*-hexane) to afford the title compound as a white solid (68% yield). ^{1}H NMR ($CDCl_3$, 300 MHz) δ 9.05 (t, $J = 2.4$ Hz, 1H), 8.20 (dd, $J_1 = 1.5$ Hz, $J_2 = 8.1$ Hz, 1H), 7.94 (d, 1H, $J = 7.5$ Hz), 7.83 (d, 1H, $J = 8.1$ Hz), 7.73 (m, 2H), 7.65 (d, 1H, $J = 8.1$ Hz), 7.60–7.37 (m, 6H), 7.27 (t, 2H, $J = 2.4$ Hz), 6.35 (t, 2H, $J = 1.5$ Hz), 3.70 (s, 3H); ^{13}C NMR (75 MHz, $CDCl_3$) δ 170.3, 150.1, 149.2, 145.3, 136.4, 133.3, 132.3, 131.5, 128.9, 128.9, 128.5, 128.1, 127.2, 126.6, 126.5, 126.2, 124.8, 123.7, 122.6 (2), 121.4, 109.9, 109.0 (2), 73.3, 52.6. ESI-MS *m/z* 409 $[M+H]^+$.

4.1.46. Methyl 2-[(3-(1H-pyrrol-1-yl)naphthalen-2-yl)oxy]-2-(quinolin-5-yl)acetate (44b)

The title compound was prepared following General Procedure A. The residue purified by flash chromatography on silica gel (33% EtOAc in *n*-hexane) to afford the title compound as a yellow solid (49% yield). ^{1}H NMR ($CDCl_3$, 300 MHz) δ 8.93 (d, 1H, $J = 3.9$ Hz), 8.62 (d, 1H, $J = 8.7$ Hz), 8.12 (d, 1H, $J = 8.1$ Hz), 7.77–7.66 (m, 5H), 7.48–7.36 (m, 4H), 7.12 (t, 2H, $J = 2.1$ Hz), 6.32 (t, 2H, $J = 2.1$ Hz), 6.27

(s, 1H), 3.67 (s, 3H); ESI-MS *m/z* 409 $[M+H]^+$, 431 $[M+Na]^+$, 447 $[M+K]^+$.

4.1.47. Methyl 2-[(3-(1H-pyrrol-1-yl)naphthalen-2-yl)oxy]-2-(quinolin-3-yl)acetate (44c)

The title compound was prepared following General Procedure A. The residue was purified by flash chromatography on silica gel (25% EtOAc in *n*-hexane) to afford the title compound as a yellow solid (39% yield). ^{1}H NMR ($CDCl_3$, 300 MHz) δ 9.03 (d, 1H, $J = 2.4$ Hz), 8.27 (d, 1H, $J = 2.1$ Hz), 8.11 (d, 1H, $J = 8.7$ Hz), 7.83–7.72 (m, 5H), 7.58 (t, 1H, $J = 6.6$ Hz), 7.51–7.40 (m, 2H), 7.36 (s, 1H), 7.21 (t, 2H, $J = 2.1$ Hz), 6.42 (t, 2H, $J = 2.1$ Hz), 5.94 (s, 1H), 3.73 (s, 3H); ESI-MS *m/z* 409 $[M+H]^+$, 431 $[M+Na]^+$, 447 $[M+K]^+$.

4.1.48. Methyl 2-((3-(1H-pyrrol-1-yl)naphthalen-2-yl)oxy)-2-(7-chloroquinolin-5-yl)acetate (44d)

The title compound was prepared following General Procedure A. The residue was purified by flash chromatography on silica gel (33% EtOAc in petroleum ether) to afford the title compound as a brown oil (44% yield). ^{1}H NMR (300 MHz, $CDCl_3$), δ 8.92 (d, 1H, $J = 2.7$ Hz), 8.66 (s, 1H), 8.24 (s, 1H), 7.81 (t, 4H, $J = 3.0$ Hz), 7.52–7.40 (m, 4H), 7.07 (t, 2H, $J = 1.8$ Hz), 6.33 (t, 2H, $J = 2.1$ Hz), 6.16 (s, 1H), 3.68 (s, 3H); ESI-MS *m/z* 443.0 $[M+H]^+$, 465.0 $[M+Na]^+$, 481.0 $[M+K]^+$.

4.1.49. Ethyl 2-((3-(1H-pyrrol-1-yl)naphthalen-2-yl)oxy)-2-(5-methoxynaphthalen-1-yl)acetate (44e)

The title compound was prepared following General Procedure A. The residue was purified by flash chromatography on silica gel (30% EtOAc in petroleum ether) to afford the title compound as an amorphous orange solid (75% yield). ^{1}H NMR (400 MHz, $CDCl_3$) δ 8.30 (d, $J = 8.4$ Hz, 1H), 7.86 (d, $J = 8.7$ Hz, 1H), 7.76–7.72 (m, 3H), 7.65 (d, $J = 7.6$ Hz, 1H), 7.51–7.33 (m, 4H), 7.30 (s, 1H), 7.21 (s, 2H), 6.84 (d, $J = 7.6$ Hz, 1H), 6.40 (s, 1H), 6.33 (s, 2H), 4.12 (q, $J = 3.6$ Hz, 2H), 3.99 (s, 3H), 1.11 (t, $J = 6.8$ Hz, 3H); ^{13}C NMR (75 MHz, $CDCl_3$) δ 169.3, 155.8, 149.1, 134.3, 132.2, 131.6, 131.6, 130.1, 129.0, 127.3, 127.2, 126.8, 126.6, 126.3, 125.3, 125.0, 124.8, 124.7, 124.1, 123.5, 122.5, 115.8, 110.2, 109.1, 108.9, 103.9, 61.7, 55.5, 13.9. ESI-MS *m/z* 452.2 $[M+H]^+$.

4.1.50. Ethyl 2-((3-(1H-pyrrol-1-yl)naphthalen-2-yl)oxy)-2-(2-methylquinolin-8-yl)acetate (44f)

The title compound was prepared following General Procedure B. The residue was purified by flash chromatography on silica gel (10% EtOAc in *n*-hexane) to afford the title compound as a white amorphous solid (66% yield). ^{1}H NMR (300 MHz, $CDCl_3$) δ 8.04 (d, $J = 8.4$ Hz, 1H), 7.86 (d, $J = 7.3$ Hz, 1H), 7.81–7.64 (m, 3H), 7.64 (d, $J = 7.6$ Hz, 1H), 7.59 (s, 1H), 7.51–7.22 (m, 6H), 6.33 (t, $J = 2.2$ Hz, 2H), 4.25–4.07 (m, 3H), 2.81 (s, 3H), 1.18 (t, $J = 7.1$ Hz, 3H); ESI-MS *m/z* 437.0 $[M+H]^+$, 458.9 $[M+Na]^+$, 474.9 $[M+K]^+$.

4.1.51. Ethyl 2-((3-(1H-pyrrol-1-yl)naphthalen-2-yl)oxy)-2-(2-ethylquinolin-8-yl)acetate (44g)

The title compound was prepared following General Procedure B. The residue was purified by flash chromatography on silica gel (5% EtOAc in petroleum ether) to afford the title compound as an amorphous light pink solid (55% yield). ^{1}H NMR (300 MHz, $CDCl_3$) δ 8.06 (d, $J = 8.4$ Hz, 1H), 7.87 (d, $J = 7.2$ Hz, 1H), 7.78–7.72 (m, 3H), 7.63 (d, $J = 8.1$ Hz, 1H) 7.56 (s, 1H), 7.48 (s, 1H), 7.45 (s, 1H), 7.43–7.32 (m, 3H), 7.29 (t, $J = 3.0$ Hz, 2H), 6.35 (t, $J = 2.1$, 2H), 4.26–4.12 (m, 2H), 3.09 (q, $J = 7.5$, 2H), 1.48 (t, $J = 7.2$, 3H), 1.19 (t, $J = 7.5$); ESI-MS *m/z* 450.9 $[M+H]^+$, 473.0 $[M+Na]^+$.

4.1.52. Ethyl 2-((3-(1H-pyrrol-1-yl)naphthalen-2-yl)oxy)-2-(isoquinolin-5-yl)acetate (44h)

The title compound was prepared following General Procedure B. The residue was purified by flash chromatography on silica gel (1% MeOH in DCM) to afford the title compound as colorless oil (35% yield). ^{1}H NMR (400 MHz, $CDCl_3$) δ 9.25 (s, 1H), 8.56 (d, $J = 6.0$ Hz, 1H), 8.06 (d, $J = 6.0$ Hz, 1H), 7.94 (dd, $J_1 = 11.2$, $J_2 = 7.8$ Hz, 2H), 7.77 (s, 1H), 7.74 (s, 1H), 7.70 (d, $J = 8.0$ Hz, 1H), 7.58 (t, $J = 8$ Hz, 1H), 7.46–7.36 (m, 2H), 7.34 (s, 1H), 7.16 (s, 2H), 6.34 (s, 2H), 6.30 (s, 1H), 4.21–4.05 (m, 2H), 1.11 (t, $J = 7.1$ Hz, 3H); ESI-MS *m/z* 423.0 $[M+H]^+$, 445.0 $[M+Na]^+$.

4.1.53. Methyl 2-((3-(1H-pyrrol-1-yl)naphthalen-2-yl)oxy)-2-(benzo[d][1,3]dioxol-5-yl)acetate (44i)

The title compound was prepared following General Procedure B. The residue was purified by flash chromatography on silica gel (7% Et_2O in petroleum ether) to afford the title compound as a white amorphous solid (18% yield). ^{1}H NMR (300 MHz, $CDCl_3$) δ 7.78–7.72 (m, 3H), 7.48–7.38 (m, 3H), 7.22–7.20 (m, 2H), 7.01–6.96 (m, 2H), 6.78 (d, 2H, $J = 8.1$ Hz), 6.39–6.37 (m, 2H), 5.96 (s, 2H), 3.71 (s, 3H); ESI-MS *m/z* 402.0 $[M+H]^+$, 404.0 $[M+Na]^+$, 440.0 $[M+K]^+$.

4.1.54. Ethyl 2-(2-(1H-pyrrol-1-yl)phenoxy)-2-([1,1'-biphenyl]-2-yl)acetate (44j)

The title compound was prepared following General Procedure B. The residue was purified by column chromatography on alumina (4% EtOAc in petroleum ether) to provide the title compound as a colorless oil (56%).^{1}H NMR (300 MHz, $CDCl_3$) δ 7.81–7.76 (m, 1H), 7.47–7.30 (m, 8H), 7.19–7.01 (m, 4H), 6.72 (t, $J = 7.8$ Hz, 1H), 6.39 (dd, $J_1 = 1.8$ Hz, $J_2 = 2.7$ Hz, 2H), 5.81 (d, $J = 11.4$ Hz, 1H), 4.31–4.16 (m, 2H), 1.31–1.21 (m, 3H); ESI-MS *m/z* 398.0 $[M+H]^+$, 420.9 $[M+Na]^+$.

4.1.55. 2-[(3-(1H-Pyrrol-1-yl)naphthalen-2-yl)oxy]-2-(quinolin-8-yl)acetic acid (45a)

To a stirred solution of compound **44a** (100 mg, 0.24 mmol) in a THF/MeOH mixture (3.5 mL/4.0 mL), 5% aqueous NaOH (1.7 mL) was added dropwise and the mixture was stirred at 25 °C for 2 h. The organic solvents were evaporated and the aqueous layer acidified to pH = 2 with a 1 N solution of HCl and extracted twice with DCM. The organic layer was dried over anhydrous sodium sulfate, filtered and concentrated. The title compound was obtained as a yellow amorphous solid and was submitted to the next step without further purification. (85% yield). ^{1}H NMR ($CDCl_3$, 300 MHz) δ 8.93 (d, 1H, $J = 4.5$ Hz), 8.35 (d, 1H, $J = 8.4$ Hz), 8.00 (d, 1H, $J = 7.2$ Hz), 7.86 (d, 1H, $J = 8.4$ Hz), 7.78–7.74 (m, 3H), 7.62–7.56 (m, 2H), 7.45–7.39 (m, 3H), 7.26–7.23 (m, 2H), 6.72 (s, 1H), 6.36 (s, 2H); ESI-MS *m/z* 395 $[M+H]^+$, 417 $[M+Na]^+$.

4.1.56. 2-[(3-(1H-Pyrrol-1-yl)naphthalen-2-yl)oxy]-2-(quinolin-5-yl)acetic acid (45b)

Compound **45b** was obtained following the procedure described for **45a**. The title compound was obtained as a yellow amorphous solid and submitted to the next step without further purification (88% yield). ^{1}H NMR (300 MHz, CD_3OD) δ 8.88 (dd, $J_1 = 11.5$ Hz, $J_2 = 6.5$ Hz, 1H), 8.04 (d, $J = 8.5$ Hz, 1H), 7.90 (d, $J = 6.6$ Hz, 1H), 7.84–7.74 (m, 4H), 7.65 (s, 1H), 7.55–7.35 (m, 4H), 7.14–7.09 (m, 2H), 6.61 (s, 1H), 6.25–6.21 (m, 2H); ^{13}C NMR (75 MHz, DMSO) δ 171.1, 150.5, 149.7, 148.3, 135.1, 134.4, 132.5, 131.2, 129.7, 129.1, 128.6, 127.7, 127.1, 126.7 (2C), 126.5, 124.8, 123.4, 122.7 (2C), 121.4, 109.8, 109.1 (2C), 78.2. ESI-MS *m/z* 395 $[M+H]^+$, 417 $[M+Na]^+$.

*4.1.57. 2-[(3-(1H-Pyrrol-1-yl)naphthalen-2-yl)oxy]-2-(quinolin-3-yl)acetic acid **(45c)***

Compound **45c** was obtained following the procedure described for **45a**. The title compound was obtained as an orange amorphous solid and submitted to the next step without further purification (83% yield). ^{1}H NMR ($CDCl_3$, 300 MHz) δ 10.66 (br s, 1H), 9.27 (s, 1H), 8.42 (s, 1H), 8.01 (d, 1H, J = 8.1 Hz), 7.65–7.57 (m, 4H), 7.51–7.38 (m, 3H), 7.29–7.19 (m, 4H), 6.31 (d, 2H, J = 1.5 Hz), 5.98 (s, 1H); ESI-MS *m/z* 395 $[M+H]^+$.

*4.1.58. 2-((3-(1H-Pyrrol-1-yl)naphthalen-2-yl)oxy)-2-(7-chloroquinolin-5-yl)acetic acid **(45d)***

To a solution of compound **44d** (80 mg, 0.189 mmol) in acetonitrile (2.5 mL), a 0.25 N solution of LiOH (1 mL) was added dropwise. The reaction was stirred at 25 °C for 30 min, then acetonitrile was evaporated under reduced pressure and the residue partitioned between EtOAc and water. The aqueous layer was acidified to pH = 1 with 2 N HCl and extracted with EtOAc. The organic layer was dried over anhydrous sodium sulfate, filtered and concentrated. The title compound was obtained as a brown oil and was submitted to the next step without further purification (78% yield). ^{1}H NMR (300 MHz, CD_3OD), δ 8.86 (s, 1H), 8.01 (d, 1H, J = 1.5 Hz), 7.88 (d, 1H, J = 1.8 Hz), 7.82–7.79 (m, 3H), 7.67 (s, 1H), 7.52–7.39 (m, 4H), 7.11 (t, 2H, J = 1.8 Hz), 6.63 (s, 1H), 6.26 (t, 2H, J = 2.10 Hz); ESI-MS *m/z* 429.0 $[M+H]^+$.

*4.1.59. 2-((3-(1H-Pyrrol-1-yl)naphthalen-2-yl)oxy)-2-(5-methoxynaphthalen-1-yl)acetic acid **(45e)***

Compound **45e** was obtained following the procedure described for **45a**. The title compound was obtained as an orange amorphous solid and submitted to the next step without further purification (99% yield). ^{1}H NMR (300 MHz, $CDCl_3$) δ 8.32 (d, J = 8.1 Hz, 1H), 7.82–7.68 (m, 4H), 7.59 (d, J = 7.6 Hz, 1H), 7.52–7.34 (m, 5H), 7.25 (s, 2H), 7.15 (s, 1H), 6.86 (d, J = 8.2 Hz, 1H), 6.37 (s, 2H), 3.99 (s, 3H); ESI-MS *m/z* 424.0 $[M+H]^+$, 446.0 $[M+Na]^+$.

*4.1.60. 2-((3-(1H-Pyrrol-1-yl)naphthalen-2-yl)oxy)-2-(2-methylquinolin-8-yl)acetic acid **(45f)***

Compound **45f** was obtained following the procedure described for **45a**. The title compound was obtained as a dark yellow oil and submitted to the next step without further purification (98% yield). ^{1}H NMR (300 MHz, CD_3OD) δ 8.42 (d, J = 8.9 Hz, 2H), 7.96 (t, J = 8.6 Hz, 2H), 7.76 (t, J = 8.6 Hz, 2H), 7.72–7.40 (m, 4H), 7.40–7.33 (m, 1H), 7.16–7.02 (m, 2H), 6.94 (s, 1H), 6.29–6.10 (m, 2H), 2.76 (s, 3H); ESI-MS *m/z* 409.0 $[M+H]^+$, 431.0 $[M+Na]^+$.

*4.1.61. 2-((3-(1H-Pyrrol-1-yl)naphthalen-2-yl)oxy)-2-(2-ethylquinolin-8-yl)acetic acid **(45g)***

Compound **45g** was obtained following the procedure described for **45a**. The title compound was obtained as an orange solid and submitted to the next step without further purification (99% yield). ^{1}H NMR (300 MHz, $CDCl_3$) δ 8.26 (d, J = 8.5 Hz, 1H), 7.97 (d, J = 7.3 Hz, 1H), 7.85–7.73 (m, 4H), 7.54 (t, J = 7.4 Hz, 1H), 7.50–7.35 (m, 4H), 7.23–7.20 (m, 2H), 6.59 (s, 1H), 6.37–6.31 (m, 2H), 3.14 (q, J = 7.8 Hz, 2H), 1.48 (t, J = 7.1 Hz, 3H); ESI-MS *m/z* 422.0 $[M+H]^+$, 445.0 $[M+Na]^+$.

*4.1.62. 2-((3-(1H-Pyrrol-1-yl)naphthalen-2-yl)oxy)-2-(isoquinolin-5-yl)acetic acid **(45h)***

Compound **45h** was obtained following the procedure described for **45a**. The title compound was obtained as an orange amorphous solid and submitted to the next step without further purification (98% yield). ^{1}H NMR (400 MHz, CD_3OD) δ 9.24 (s, 1H), 8.36 (d, J = 6.4 Hz, 1H), 8.28 (d, J = 6.4 Hz, 1H), 8.10 (d, J = 8.4 Hz, 1H), 8.04 (d, J = 7.2 Hz, 1H), 7.80–7.74 (m, 3H), 7.66 (t, J = 7.6 Hz, 1H), 7.62 (s, 1H), 7.40 (dt, J_1 = 15.2 Hz, J_2 = 7.2 Hz, 2H), 7.12 (s, 2H), 6.50 (s, 1H), 6.20 (s, 2H); ^{13}C NMR (75 MHz, CD_3OD) δ 175.6, 148.7, 136.3, 136.1, 135.9, 132.6, 131.6, 131.0, 130.9, 130.1, 129.4, 129.3, 127.0 (2), 126.5, 126.3, 124.9, 124.3, 122.4 (2), 122.0, 110.6, 108.6 (2), 77.1. ESI-MS *m/z* 395.0 $[M+H]^+$.

*4.1.63. 2-((3-(1H-Pyrrol-1-yl)naphthalen-2-yl)oxy)-2-(benzo[d][1,3]dioxol-5-yl)acetic acid **(45i)***

Compound **45i** was obtained following the procedure described for **45d**. The title compound was obtained as an orange amorphous solid and submitted to the next step without further purification (98% yield). ^{1}H NMR (300 MHz, $CDCl_3$) δ 7.90–7.82 (m, 3H), 7.58 (s, 1H), 7.54–7.40 (m, 2H), 7.33 (s, 2H), 7.18–7.10 (m, 2H), 6.86 (d, 1H, J = 6.00 Hz), 6.29 (s, 2H), 6.06 (s, 1H), 6.01 (s, 2H); ESI-MS *m/z* 386.0 $[M-H]^-$, 773.0 $[2M-H]^-$.

*4.1.64. 2-(2-(1H-Pyrrol-1-yl)phenoxy)-2-([1,1'-biphenyl]-2-yl) acetic acid **(45j)***

Compound **45j** was obtained following the procedure described for **45a**. The title compound was obtained as a brown amorphous solid and submitted to the next step without further purification (quantitative yield). ^{1}H NMR (300 MHz, $CDCl_3$) δ 9.83 (s, 1H), 7.70–7.67 (m, 9H), 7.45–7.27 (m, 9H), 7.11–7.02 (m, 4H), 6.63 (d, 1H, J = 7.5 Hz), 6.35–6.33 (m, 2H), 5.74 (s, 1H); ^{13}C NMR (75 MHz, $CDCl_3$) δ 174.7, 149.3, 142.6, 139.6, 132.2, 131.6, 130.2, 129.6 (2), 129.1, 128.3 (2), 128.2, 127.7, 127.6, 127.0, 125.8, 122.9, 121.9 (2), 116.2, 109.1 (2), 75.2. ESI-MS *m/z* 369.9 $[M+H]^+$.

*4.1.65. 5-(Quinolin-8-yl)naphtho[2,3-b]pyrrolo[1,2-d][1,4]oxazepin-4(5H)-one **(7a)***

To a stirred solution of acid **45a** (80 mg, 0.20 mmol) in dry DCM (50.0 mL) phosphorus pentachloride (46 mg, 0.22 mmol) was added in 5 small portions. The reaction was refluxed for 12 h. Then saturated aqueous $NaHCO_3$ was added dropwise and the aqueous layer was extracted with DCM (3 × 20 mL). The combined organic layers were dried over anhydrous sodium sulfate, filtered and concentrated. The residue was purified by flash chromatography on silica gel (25% EtOAc in *n*-hexane) to afford the title compound as a yellow amorphous solid (52% yield). ^{1}H NMR ($CDCl_3$, 300 MHz) δ 8.81(s, 1H), 8.14 (dd, 1H, J_1 = 1.2 Hz, J_2 = 8.1 Hz), 7.87–7.78 (m, 4H), 7.62–7.26 (m, 8H), 6.86 (br s, 1H), 6.58 (q, 1H, J_1 = 2.4 Hz, J_2 = 4.2 Hz); ESI-MS *m/z* 377 $[M+H]^+$, 399 $[M+Na]^+$.

*4.1.66. 5-(Quinolin-5-yl)naphtho[2,3-b]pyrrolo[1,2-d][1,4]oxazepin-4(5H)-one **(7b)***

Compound **7b** was obtained following the procedure described for **7a**. The residue was purified by chromatography on Al_2O_3 (10% EtOAc in *n*-hexane) to afford the title compound as a white amorphous solid (42% yield). ^{1}H NMR ($CDCl_3$, 300 MHz) δ 8.97 (d, 1H, J = 3.9 Hz), 8.53 (d, 1H, J = 8.1 Hz), 8.09 (d, 1H, J = 8.7 Hz), 7.88–7.82 (m, 2H), 7.60–7.36 (m, 9H), 6.64–6.61 (m, 1H), 6.13 (s, 1H); ^{13}C NMR (75 MHz, $CDCl_3$) δ 189.2, 150.4, 148.6, 147.3, 133.2, 132.9, 132.8, 132.1, 131.2, 131.1, 131.0, 128.5, 127.9, 127.4 (2C), 127.1, 126.7, 126.5, 121.6, 121.4, 120.6, 120.4, 112.5, 89.0. ESI-MS *m/z* 377 $[M+H]^+$.

*4.1.67. 5-(Quinolin-3-yl)naphtho[2,3-b]pyrrolo[1,2-d][1,4]oxazepin-4(5H)-one **(7c)***

Compound **7c** was obtained following the procedure described for **7a**. The residue was purified by flash chromatography on silica gel (25% EtOAc in petroleum ether) to afford the title compound as a brown solid (53% yield). ^{1}H NMR ($CDCl_3$, 300 MHz) δ 9.02 (d, 1H, J = 2.1 Hz), 8.19 (d, 1H, J = 0.9 Hz), 8.12 (d, 1H, J = 8.7 Hz), 7.85–7.69 (m, 5H), 7.65 (s, 1H), 7.56–7.46 (m, 4H), 7.39 (d, 1H, J = 3.3 Hz), 6.58 (t, 1H, J = 3.9 Hz), 5.73 (s, 1H); ESI-MS *m/z* 377 $[M+H]^+$, 399 $[M+Na]^+$, 775 $[2M+Na]^+$.

*4.1.68. 5-(7-Chloroquinolin-5-yl)naphtho[2,3-b]pyrrolo[1,2-d][1,4] oxazepin-4(5H)-one **(7d)***

Compound **7d** was obtained following the procedure described for **7a**. The residue was purified by flash chromatography on silica gel (20% EtOAc in *n*-hexane) to afford the title compound as a white amorphous solid (19% yield). ^{1}H NMR (300 MHz, $CDCl_3$), δ 8.95 (dd, 1H, $J_1 = 1.50$ Hz, $J_2 = 4.20$ Hz), 8.43 (d, 1H, $J = 8.70$ Hz), 8.15 (s, 1H), 7.91–7.86 (m, 2H), 7.69 (d, 1H, $J = 7.50$ Hz), 7.55–7.43 (m, 7H), 6.64–6.62 (m, 1H), 5.98 (s, 1H); ESI-MS *m/z* 411.0 $[M+H]^+$.

*4.1.69. 5-(5-Methoxynaphthalen-1-yl)naphtho[2,3-b]pyrrolo[1,2-d] [1,4]oxazepin-4(5H)-one **(7e)***

Compound **7e** was obtained following the procedure described for **7a**. The residue was purified by flash chromatography on silica gel (10% Et_2O in petroleum ether) to afford the title compound as a pale yellow amorphous solid (40% yield). ^{1}H NMR (400 MHz, $CDCl_3$) δ 8.22 (d, 1H, $J = 8.0$ Hz), 7.82 (s, 2H), 7.79 (d, 1H, $J = 8.7$ Hz), 7.54–7.45 (m, 5H), 7.33–7.44 (m, 4H), 6.87 (d, 1H, $J = 8.0$ Hz), 6.59 (t, 1H, $J = 3.2$ Hz), 6.24 (s, 1H), 3.99 (s, 3H); ESI-MS *m/z* 406.2 $[M+H]^+$, 427.9 $[M+Na]^+$, 443.1 $[M+K]^+$.

*4.1.70. 5-(2-Methylquinolin-8-yl)naphtho[2,3-b]pyrrolo[1,2-d][1,4] oxazepin-4(5H)-one **(7f)***

Compound **7f** was obtained following the procedure described for **7a**. The residue was purified by flash chromatography on silica gel (20% EtOAc in *n*-hexane) to afford the title compound as a yellow amorphous solid (62% yield). ^{1}H NMR (300 MHz, $CDCl_3$) δ 8.00–7.66 (m, 5H), 7.58–7.29 (m, 6H), 7.25 (s, 2H), 7.09 (s, 1H), 6.62–6.54 (m, 1H), 2.36 (s, 3H); ESI-MS *m/z* 391.0 $[M+H]^+$, 412.9 $[M+Na]^+$.

*4.1.71. 5-(2-Ethylquinolin-8-yl)naphtho[2,3-b]pyrrolo[1,2-d][1,4] oxazepin-4(5H)-one **(7g)***

Compound **7g** was obtained following the procedure described for **7a**. The residue was purified by flash chromatography on Al_2O_3 (5% EtOAc in petroleum ether) to afford the title compound as an orange amorphous solid (56% yield). ^{1}H NMR (300 MHz, $CDCl_3$) δ 7.95 (d, $J = 8.4$ Hz, 1H), 7.86–7.72 (m, 4H), 7.56 (d, $J = 7.5$ Hz, 1H), 7.52 (s, 1H), 7.50–7.46 (m, 2H), 7.46–7.28 (m, 4H), 7.15 (d, $J = 8.3$ Hz, 1H), 6.62–6.56 (m, 1H), 2.79–2.59 (m, 2H), 1.15 (t, $J = 7.4$ Hz, 3H); ^{13}C NMR (75 MHz, $CDCl_3$) δ 190.8, 162.8, 148.0, 145.0, 136.0, 134.8, 134.5, 134.3, 131.9, 130.9, 130.8, 128.9, 127.3, 127.0, 126.5, 126.1, 125.9, 125.9, 125.7, 125.2, 121.0, 120.6, 119.9, 119.8, 111.6, 31.5, 12.7.

*4.1.72. 5-(Isoquinolin-5-yl)naphtho[2,3-b]pyrrolo[1,2-d][1,4] oxazepin-4(5H)-one **(7h)***

Compound **7h** was obtained following the procedure described for **7a**. The residue was purified by flash chromatography on silica gel (10% EtOAc in *n*-hexane) to afford the title compound as a white amorphous solid (60% yield). ^{1}H NMR (400 MHz, $CDCl_3$) δ 9.26 (s, 1H), 8.60 (d, $J = 5.6$ Hz, 1H), 7.96–7.91 (m, 2H), 7.85–7.80 (m, 3H), 7.59–7.35 (m, 7H), 6.61 (dd, $J_1 = 4$ Hz, $J_2 = 2.8$ Hz, 1H), 6.13 (s, 1H); ESI-MS *m/z* 377.0 $[M+H]^+$.

*4.173. 5-(Benzo[d][1,3]dioxol-5-yl)naphtho[2,3-b]pyrrolo[1,2-d] [1,4]oxazepin-4(5H)-one **(7i)***

Compound **7i** was obtained following the procedure described for **7a**. The residue was purified by flash chromatography on silica gel (10% EtOAc in *n*-hexane) to afford the title compound as a white amorphous solid (13% yield). ^{1}H NMR (300 MHz, $CDCl_3$) δ 7.86–7.83 (m, 2H), 7.76–7.73 (m, 1H), 7.58 (s, 1H), 7.52–7.44 (m, 3H), 7.37–7.35 (m, 1H), 6.86–6.74 (m, 2H), 6.57–6.55 (m, 1H), 5.94 (s, 1H), 5.49 (s, 1H); ESI-MS *m/z* 370.0 $[M+H]^+$, 392.0 $[M+Na]^+$, 408.0 $[M+K]^+$.

*4.1.74. 6-([1,1'-Biphenyl]-2-yl)benzo[b]pyrrolo[1,2-d][1,4]oxazepin-7(6H)-one **(7j)***

Compound **7j** was obtained following the procedure described for **7a**. The residue was purified by column chromatography on Al_2O_3 (5% EtOAc in petroleum ether) to afford the title compound as a yellow oil (37%). ^{1}H NMR (300 MHz, $CDCl_3$) δ 7.59–7.52 (m, 2H), 7.45–7.27 (m, 12H), 7.08–7.02 (m, 1H), 6.49 (dd, $J_1 = 3.0$ Hz, $J_2 = 0.9$ Hz, 1H), 5.61 (s, 1H); ^{13}C NMR (75 MHz, $CDCl_3$) δ 190.8, 149.0, 142.7, 140.4, 139.8, 135.0, 133.6, 130.1, 129.5 (2), 128.6, 128.4, 128.2 (2), 127.7, 127.6, 127.4, 126.1, 125.8, 123.6, 122.2, 120.5, 111.8, 88.0. ESI-MS *m/z* 352.0 $[M+H]^+$, 374.9 $[M+Na]^+$.

*4.1.75. 5-(Quinolin-8-yl)naphtho[2,3-b]pyrrolo[1,2-d][1,4] oxazepin-4-yl acetate **(6a)***

To a suspension of potassium *tert*-butoxide (30 mg, 0.26 mmol) in dry THF (1.0 mL) a solution of compound **7a** (40 mg, 0.11 mmol) in dry THF (1.0 mL) was added, and the solution immediately turned orange. After 1 h acetyl chloride (15 μL, 0.21 mmol) was added dropwise. The mixture was stirred at 25 °C for 8 h, then saturated aqueous NH_4Cl was added dropwise and the resulting mixture was extracted with EtOAc (3 × 15 mL). The combined organic layers were dried over anhydrous sodium sulfate, filtered and concentrated. The residue was purified by flash chromatography on silica gel (16% EtOAc in *n*-hexane) to afford the title compound as a pale yellow solid (18% yield). ^{1}H NMR ($CDCl_3$, 300 MHz) δ 9.02–9.04 (m, 1H), 8.22 (dd, 1H, $J_1 = 1.5$ Hz, $J_2 = 8.4$ Hz), 7.90–7.83 (m, 4H), 7.69 (dt, 1H, $J_1 = 1.5$ Hz, $J_2 = 7.2$ Hz), 7.62 (d, 1H, 7.8 Hz), 7.54–7.38(m, 7H), 6.50–6.43 (m, 2H), 1.92 (s, 3H); ^{13}C NMR ($CDCl_3$, 75 MHz) δ 169.3, 151.3, 151.0, 146.7, 145.4, 136.5, 134.6, 133.2, 132.6, 132.4, 131.5, 130.5, 130.4, 129.8, 128.9, 127.8, 127.7, 127.3, 126.3, 126.2, 122.3, 121.7, 120.9, 119.6, 111.2, 110.7, 20.9; FT-IR (neat) $\nu_{max} = 1751$ cm^{-1}. ESI-MS *m/z* 419 $[M+H]^+$, 441 $[M+Na]^+$, 457 $[M+K]^+$. Anal. ($C_{27}H_{18}N_2O_3$) C, H, N.

*4.1.76. 5-(Quinolin-8-yl)naphtho[2,3-b]pyrrolo[1,2-d][1,4] oxazepin-4-yl dimethylcarbamate **(6b)***

To a suspension of KO-*t*-Bu (23 mg, 0.20 mmol) in dry THF (2.0 mL), a solution of compound **7a** (30 mg, 0.08 mmol) in dry THF (2.0 mL) was added. After 1 h dimethylcarbamoyl chloride (15 μL, 0.16 mmol) was added dropwise. The mixture was stirred at 25 °C for 8 h, then saturated aqueous NH_4Cl was added dropwise and the resulting mixture was extracted EtOAc (3 × 10 mL). The combined organic layers were dried over anhydrous sodium sulfate, filtered and concentrated. The residue was purified by chromatography on Al_2O_3 (50% DCM in petroleum ether) to afford the title compound as a pale yellow solid (8% yield). ^{1}H NMR ($CDCl_3$, 300 MHz) δ 9.07 (d, 1H, $J = 3.6$ Hz), 8.24 (d, 1H, $J = 7.8$ Hz), 7.91–7.81 (m, 3H), 7.61–7.31 (m, 8H), 6.45 (dd, 2H, $J_1 = 5.1$ Hz, $J_2 = 8.1$ Hz), 2.75 (d, 6H, $J = 26.7$ Hz); ^{13}C NMR ($CDCl_3$, 75 MHz) δ 154.7, 151.5, 150.7, 137.5, 133.3, 132.4, 131.5, 131.2, 131.1, 130.0, 129.9, 129.5, 128.8, 127.7, 127.3, 126.4, 126.2, 126.1, 124.3, 122.1, 121.6, 120.9, 119.5 (2), 111.1, 110.5, 36.5, 29.9; ESI-MS *m/z* 448 $[M+H]^+$. Anal. ($C_{28}H_{21}N_3O_3$) C, H, N.

*4.1.77. 5-(Quinolin-8-yl)naphtho[2,3-b]pyrrolo[1,2-d][1,4] oxazepin-4-yl ethylcarbamate **(6c)***

To a suspension of potassium *tert*-butoxide (23 mg, 0.20 mmol) in dry THF (2.0 mL) was added a solution of compound **7a** (30 mg, 0.08 mmol) in dry THF (2.0 mL). After 1 h diethylcarbamoyl chloride (22 μL, 0.16 mmol) was added dropwise. The mixture was stirred at 25 °C for 8 h, then saturated aqueous NH_4Cl was added dropwise and the resulting mixture was extracted with EtOAc (3 × 10 mL). The combined organic layers were dried over anhydrous sodium sulfate, filtered and concentrated. The residue was purified by chromatography on silica gel (17% EtOAc in *n*-hexane) to afford the title compound as a pale yellow solid (16% yield). ^{1}H NMR ($CDCl_3$,

300 MHz) δ 9.05 (d, 1H, $J = 2.4$ Hz), 8.21 (d, 1H $J = 8.4$ Hz), 7.89–7.78 (m, 4H), 7.60 (d, 1H, $J = 8.1$ Hz), 7.51–7.32 (m, 6H), 6.45 (d, 2H, $J = 5.7$ Hz), 3.09 (dd, 4H $J_1 = 6.6$ Hz, $J_2 = 40.8$ Hz), 0.98 (t, 3H, $J = 6.6$ Hz), 0.68 (t, 3H, $J = 6.6$ Hz); ^{13}C NMR ($CDCl_3$, 75 MHz) δ 154.0, 151.6, 150.9, 146.9, 145.4, 136.4, 135.1, 133.3, 132.9, 132.4, 131.5, 130.8, 129.4, 128.8, 128.6, 127.6, 127.3, 126.2, 126.1, 122.1, 122.0, 121.6, 120.9, 119.5, 111.1, 110.43, 42.3, 41.7, 13.9, 13.5; ESI-MS *m/z* 477 $[M+H]^+$, 498 $[M+Na]^+$, 514 $[M+K]^+$. Anal. ($C_{30}H_{25}N_3O_3$) C, H, N.

4.1.78. 5-(Quinolin-8-yl)naphtho[2,3-b]pyrrolo[1,2-d][1,4] oxazepin-4-yl (5-(diethylamino)pentan-2-yl)carbamate (6d)

A solution of compound **7a** (50 mg, 0.13 mmol) in dry THF (2 mL) was added to a two-necked round bottom flask containing KO-*t*-Bu in 2 mL of dry THF. The resulting suspension immediately turned dark orange. The reaction mixture was stirred for 30 min at 25 °C, and then added *via* cannula to a solution containing triphosgene (39 mg, 0.13 mmol) in dry THF (1 mL). After 5 min stirring, N_1,N_1-diethylbutan-1,3-diamine (52 μL, 0.27 mmol) and *N*,*N*-DIPEA (91 μL, 0.52 mmol) were sequentially added. The reaction mixture was stirred for 14 h at 25 °C, and then neutralized with saturated aqueous $NaHCO_3$. THF was evaporated under reduced pressure and the residue was extracted with EtOAc (2 × 10 mL). The combined organic layers were dried over anhydrous sodium sulfate, filtered and concentrated. The residue was purified by chromatography on silica gel (10% EtOAc in *n*-hexane) to afford title compound as an amorphous white solid (15% yield). ^{1}H NMR (300 MHz, $CDCl_3$) δ 9.03 (s, 1H), 8.24 (m, 1H), 8.16 (m, 1H), 7.91–7.75 (m, 5H), 7.62–7.27 (m, 5H), 6.47 (d, 2H, $J = 13.1$ Hz), 5.59 (br, 1H), 3.53 (m, 1H), 2.66–2.17 (m, 4H), 1.69–1.58 (m, 2H), 1.43–1.11 (m, 6H), 0.86 (m, 6H); ESI-MS *m/z* 560.8 $[M+H]^+$. Anal. ($C_{35}H_{36}N_4O_3$) C, H, N.

4.1.79. 5-(2-Methylquinolin-8-yl)naphtho[2,3-b]pyrrolo[1,2-d][1,4] oxazepin-4-yl acetate (6e)

Compound **6e** was obtained following the procedure described for **6a**. The residue was purified by flash chromatography on silica gel (20% EtOAc in *n*-hexane) to afford the title compound as a pale yellow amorphous solid (77% yield). ^{1}H NMR (300 MHz, $CDCl_3$ δ 8.05 (d, $J = 8.2$ Hz, 1H), 7.97–7.71 (m, 4H), 7.64 (d, $J = 7.1$ Hz, 1H), 7.57–7.14 (m, 6H), 6.47 (s, 2H), 2.54 (s, 3H), 1.93 (s, 3H); ^{13}C NMR (75 MHz, $CDCl_3$) δ 169.3, 159.6, 151.7, 146.4, 146.0, 136.1, 134.0, 133.2, 132.4, 131.4, 130.8, 129.5, 128.0, 127.7, 127.3, 127.0, 126.2, 126.1, 125.56, 125.1, 122.6, 122.2, 120.6, 120.4, 111.2, 110.6, 25.7, 21.0; FT-IR (neat) $\nu_{max} = 1751$ cm^{-1}. ESI-MS *m/z* 433.9 $[M+H]^+$. Anal. ($C_{28}H_{20}N_2O_3$) C, H, N.

4.1.80. 5-(2-Methylquinolin-8-yl)naphtho[2,3-b]pyrrolo[1,2-d][1,4] oxazepin-4-yl diethylcarbamate (6f)

Compound **6f** was obtained following the procedure described for **6c**. The residue was purified by flash chromatography on silica gel (10% EtOAc in *n*-hexane) to afford the title compound as a pale yellow amorphous solid (46% yield). ^{1}H NMR (300 MHz, $CDCl_3$) δ 8.04 (d, $J = 8.3$ Hz, 1H), 7.87–7.74 (m, 4H), 7.65 (d, $J = 7.7$ Hz, 1H), 7.48–7.36 (m, 4H), 7.34–7.20 (m, 2H), 6.46 (d, $J = 1.8$ Hz, 2H), 3.21–2.92 (m, 4H), 2.56 (s, 3H), 0.99 (t, $J = 6.5$ Hz, 3H), 0.66 (t, $J = 6.5$ Hz, 3H); ^{13}C NMR (75 MHz, $CDCl_3$) δ 159.4, 154.0, 151.9, 146.7, 146.2, 136.0, 134.4, 133.4, 132.6, 132.3, 131.4, 131.3, 129.2, 128.9, 127.6, 127.3, 126.9, 126.1, 126.0, 125.1, 122.4, 121.8, 120.6, 120.3, 111.2, 110.4, 42.3, 41.7, 25.9, 13.9, 13.5; FT-IR (neat) $\nu_{max} = 2923, 1711$ cm^{-1}. ESI-MS *m/z* 490.0 $[M+H]^+$, 527.9 $[M+K]^+$. Anal. ($C_{31}H_{27}N_3O_3$) C, H, N.

4.1.81. 5-(2-Ethylquinolin-8-yl)naphtho[2,3-b]pyrrolo[1,2-d][1,4] oxazepin-4-yl acetate (6g)

Compound **6g** was obtained following the procedure described for **6a**. The residue was purified by flash chromatography on silica gel (20% EtOAc in *n*-hexane) to afford the title compound as a colorless oil (77% yield). ^{1}H NMR (300 MHz, $CDCl_3$) δ 8.08 (d, $J = 8.4$ Hz, 1H), 7.86–7.82 (m, 3H), 7.77 (d, $J = 7.2$ Hz, 1H), 7.65 (d, $J = 7.7$ Hz, 1H), 7.51–7.38 (m, 5H), 7.37–7.23 (m, 2H), 6.48 (d, $J = 2.2$ Hz, 2H), 2.79 (q, $J = 7.6$ Hz, 2H), 1.88 (s, 3H), 1.11 (t, $J = 8.1$ Hz, 3H); ^{13}C NMR (75 MHz, $CDCl_3$) δ 169.3, 164.3, 151.8, 146.4, 146.1, 136.2, 133.9, 133.2, 132.5, 132.4, 131.4, 131.2, 130.8, 129.5, 129.2, 128.0, 127.7, 127.6, 126.4, 125.2, 122.2, 121.4, 120.6, 120.3, 111.2, 110.5, 32.2, 20.9, 13.5; ESI-MS *m/z* 447.8 $[M+H]^+$. Anal. ($C_{29}H_{22}N_2O_3$) C, H, N.

4.1.82. 5-(2-Ethylquinolin-8-yl)naphtho[2,3-b]pyrrolo[1,2-d][1,4] oxazepin-4-yl dimethylcarbamate (6h)

Compound **6h** was obtained following the procedure described for **6b**. The residue was purified by flash chromatography on silica gel (10% EtOAc in *n*-hexane) to afford the title compound as a pale yellow amorphous solid (50% yield). ^{1}H NMR (300 MHz, $CDCl_3$); δ 8.07 (d, $J = 8.5$ Hz, 1H), 7.89–7.79 (m, 4H), 7.64 (m, 1H), 7.50–7.36 (m, 4H), 7.34–7.30 (m, 2H), 6.51–6.44 (m, 2H), 2.89–2.76 (m, 5H), 2.63(s, 3H), 1.19 (t, $J = 7.6$ Hz, 3H); ^{13}C NMR (75 MHz, $CDCl_3$) δ 164.1, 154.7, 152.0, 146.6, 146.0, 136.2, 134.5, 133.3, 132.7, 132.4, 131.4, 131.2, 129.2, 128.8, 127.6, 127.3, 127.1, 126.1, 126.0, 125.1, 121.9, 121.2, 120.6, 120.1, 111.2, 110.3, 36.8, 36.3, 32.3, 13.7; FT-IR (neat) $\nu_{max} = 1718$ cm^{-1}. ESI-MS *m/z* 475.8 $[M+H]^+$, 513.7 $[M+K]^+$. Anal. ($C_{30}H_{25}N_3O_3$) C, H, N.

4.1.83. 5-(2-Ethylquinolin-8-yl)naphtho[2,3-b]pyrrolo[1,2-d][1,4] oxazepin-4-yl diethylcarbamate (6i)

Compound **6i** was obtained following the procedure described for **6c**. The residue was purified by flash chromatography on silica gel (10% EtOAc in *n*-hexane) to afford the title compound as a yellow amorphous solid (33% yield). ^{1}H NMR (300 MHz, $CDCl_3$) δ 8.07 (d, $J = 8.5$ Hz, 1H), 7.89–7.77 (m, 4H), 7.65 (d, $J = 7.4$ Hz, 1H), 7.48–7.37 (m, 4H), 7.37–7.28 (m, 2H), 7.26 (s, 1H), 6.53–6.43 (m, 2H), 3.21–2.91 (m, 4H), 2.82 (q, $J = 7.6$ Hz, 2H), 1.18 (t, $J = 7.6$ Hz, 3H), 1.03–0.84 (m, 3H), 0.69–0.53 (m, 3H); ^{13}C NMR (75 MHz, $CDCl_3$) δ 164.1, 154.0, 152.1, 146.6, 146.0, 136.1, 134.4, 133.4, 132.8, 132.4, 131.4, 131.2, 130.0, 129.1, 128.9, 127.6, 127.3, 127.1, 126.0, 126.0, 125.1, 121.8, 121.2, 120.6, 120.0, 111.2, 110.4, 42.2, 41.7, 32.3, 29.9, 13.8, 13.6, 13.5; ESI-MS *m/z* 503.9 $[M+H]^+$. Anal. ($C_{32}H_{29}N_3O_3$) C, H, N.

4.1.84. 5-(Quinolin-5-yl)naphtho[2,3-b]pyrrolo[1,2-d][1,4] oxazepin-4-yl acetate (6j)

To a solution of **46b** (20 mg, 0.053 mmol) in dry THF (1.0 mL) sodium *bis*(trimethylsilyl)amide (1 M solution in THF, 133 μL, 0.13 mmol) was added dropwise at −78 °C. After 45 min at −78 °C acetyl chloride (8 μL, 0.11 mmol) was added. The mixture was stirred for 4 h at −78 °C. Subsequently 1 mL of aqueous saturated NH_4Cl was added. The aqueous phase was extracted with EtOAc. The organic layer was dried over anhydrous sodium sulfate, filtered and concentrated. The residue was purified by chromatography on Al_2O_3 (30% petroleum ether in DCM) to afford the title compound as a white solid (17% yield). ^{1}H NMR ($CDCl_3$, 300 MHz) δ 8.97 (dd, 1H, $J_1 = 1.5$ Hz, $J_2 = 3.9$ Hz), 8.52 (d, 1H, $J = 8.4$ Hz), 8.21 (d, 1H, $J = 8.4$ Hz), 7.85–7.87 (m, 2H), 7.38–7.72 (m, 7H), 7.31 (s, 1H), 6.50 (t, 2H, $J = 1.2$ Hz), 1.88 (s, 3H); ^{13}C NMR ($CDCl_3$, 75 MHz) δ 168.8, 150.9, 150.2, 135.0, 132.7, 132.4, 131.6, 131.3, 130.8, 129.3, 128.0, 127.7 (2), 127.4, 127.3, 126.9, 126.6 (2), 122.8, 121.6, 121.7, 121.1, 119.3, 111.5, 111.1, 104.4, 20.7; FT-IR (neat) $\nu_{max} = 1756$ cm^{-1}. ESI-MS *m/z* 419 $[M+H]^+$, 441 $[M+Na]^+$, 457 $[M+K]^+$. HRMS-ESI (*m/z*): $[M+H]^+$ calcd for $C_{27}H_{19}N_2O_3$ 419,13957; found 419,13815. Anal. ($C_{27}H_{18}N_2O_3$) C, H, N.

4.1.85. 5-(7-Chloroquinolin-5-yl)naphtho[2,3-b]pyrrolo[1,2-d][1,4]oxazepin-4-yl acetate (6k)

Compound **6k** was obtained following the procedure described for **6j**. The residue was purified by flash chromatography on silica gel (4% acetone in DCM) to afford the title compound as an amorphous white solid (27% yield). ^{1}H NMR (300 MHz, $CDCl_3$) δ 8.97 (dd, 1H, $J_1 = 1.8$ Hz, $J_2 = 4.5$ Hz), 8.53 (d, 1H, $J = 8.4$ Hz), 8.24 (s, 1H), 7.86–7.88 (m, 2H), 7.66 (d, 1H, $J = 7.8$ Hz), 7.40–7.55 (m, 5H), 7.32 (s, 1H), 6.51 (d, 2H, $J = 2.40$ Hz), 1.94 (s, 1H); ^{13}C NMR (75 MHz, $CDCl_3$), δ 168.7, 150.7, 132.5, 132.4 (2), 131.6 (2), 128.9, 127.7 (2), 127.5 (2), 126.8 (2), 125.5, 123.3, 121.7 (2), 121.3 (2), 119.3 (2), 111.6, 29.9, 20.7; ESI-MS *m/z* 452.9 $[M+H]^+$, 475.0 $[M+Na]^+$, 491.0 $[M+K]^+$. Anal. ($C_{27}H_{17}ClN_2O_3$) C, H, N.

4.1.86. 5-(Quinolin-3-yl)naphtho[2,3-b]pyrrolo[1,2-d][1,4]oxazepin-4-yl acetate (6l)

Compound **6l** was obtained following the procedure described for **6j**. The residue was purified by flash chromatography on silica gel (0.5% methanol in DCM) to afford the title compound as a yellow oil (28% yield). ^{1}H NMR ($CDCl_3$, 300 MHz) δ 9.32 (s, 1H), 8.62 (s, 1H), 8.13 (d, 1H, $J = 8.7$ Hz), 7.92 (d, 1H, $J = 7.8$ Hz), 7.72–7.85 (m, 4H), 7.68 (s, 1H), 7.61 (t, 1H, $J = 7.5$ Hz), 7.42–7.50 (m, 2H), 7.37 (s, 1H), 6.49–6.53 (m, 2H), 2.26 (s, 3H); ^{13}C NMR ($CDCl_3$,75 MHz) δ 168.8, 150.8, 148.2, 142.1, 135.0, 134.6, 132.6, 132.4, 131.6, 130.9, 128.7, 128.6, 127.9 (2), 127.7, 127.6, 127.5, 127.4, 127.1, 126.8, 126.7, 123.1, 121.1, 119.0, 111.8, 111.7, 21.3; ESI-MS *m/z* 419 $[M+H]^+$, 441 $[M+Na]^+$. Anal. ($C_{27}H_{18}N_2O_3$) C, H, N.

4.1.87. 5-(Isoquinolin-5-yl)naphtho[2,3-b]pyrrolo[1,2-d][1,4]oxazepin-4-yl acetate (6m)

Compound **6m** was obtained following the procedure described for **6j**. The residue was purified by flash chromatography on silica gel (1% acetone in DCM) to afford the title compound as a colorless oil (30% yield). ^{1}H NMR (300 MHz, $CDCl_3$) δ 9.34 (s, 1H), 8.54 (d, $J = 6.4$ Hz, 1H), 8.06 (d, $J = 8.2$ Hz, 1H), 7.98 (d, $J = 6.4$ Hz, 1H), 7.87–7.85 (m, 2H), 7.74 (d, $J = 6.7$ Hz, 1H), 7.65–7.61 (m, 3H), 7.49–7.35 (m, 4H), 7.31 (s, 1H), 6.50 (d, $J = 3.2$ Hz, 2H), 1.87 (s, 3H); ^{13}C NMR ($CDCl_3$, 75 MHz) δ 168.6, 152.4, 150.7, 143.7, 142.9, 134.7, 134.2, 132.5, 132.1, 131.5, 131.3, 130.0, 129.3, 128.87, 127.4, 127.1, 127.0, 126.8, 126.4 (2), 122.6, 120.9, 119.4, 119.0, 111.2, 110.9, 20.5; ESI-MS *m/z* 419.1 $[M+H]^+$. Anal. ($C_{27}H_{18}N_2O_3$) C, H, N.

4.1.88. 5-(Benzo[d][1,3]dioxol-5-yl)naphtho[2,3-b]pyrrolo[1,2-d][1,4]oxazepin-4-yl acetate (6n)

Compound **6n** was obtained following the procedure described for **6j**. The residue was purified by flash chromatography on silica gel (10% EtOAc in *n*-hexane) to afford the title compound as a white amorphous solid (37% yield). ^{1}H NMR (300 MHz, $CDCl_3$) δ 7.84–7.73 (m, 3H), 7.63 (s, 1H), 7.46–7.43 (m, 2H), 7.36–7.26 (m, 3H), 6.87 (d, 1H, $J = 8.4$ Hz), 6.45–6.42 (m, 2H), 6.02 (s, 2H), 2.22 (s, 3H); ^{13}C NMR (75 MHz, $CDCl_3$) δ 169.0, 151.0, 148.2, 145.0, 144.6, 132.9, 132.5, 132.4, 131.5, 128.2, 127.7, 127.4, 127.2, 126.6 (2), 122.2, 121.7, 120.7, 118.9, 111.3, 110.7, 108.5, 107.6, 101.6, 21.3; ESI-MS *m/z* 411.9 $[M+H]^+$, 433.8 $[M+Na]^+$, 449.9 $[M+K]^+$. Anal. ($C_{25}H_{17}NO_5$) C, H, N.

4.1.89. 5-(5-Methoxynaphthalen-1-yl)naphtho[2,3-b]pyrrolo[1,2-d][1,4]oxazepin-4-yl acetate (6o)

Compound **6o** was obtained following the procedure described for **6j**. The residue was purified by flash chromatography on silica gel (5% EtOAc in *n*-hexane) to afford the title compound as a colorless oil (65% yield). ^{1}H NMR (400 MHz, $CDCl_3$) δ 8.35 (d, $J = 8.0$ Hz, 1H), 7.84 (d, $J = 7.7$ Hz, 1H), 7.69 (d, $J = 8.5$ Hz, 1H), 7.61 (d, $J = 8.0$ Hz, 1H), 7.47–7.34 (m, 6H), 7.31 (s, 2H), 6.86 (d, $J = 7.6$ Hz, 1H), 6.47 (s, 2H), 4.02 (s, 3H), 1.84 (s, 3H); ^{13}C NMR ($CDCl_3$, 75 MHz) δ 168.8, 155.5, 150.9, 145.9, 134.1, 132.7, 132.4, 132.2, 131.3, 130.2, 127.8, 127.5, 127.4, 127.2, 126.5, 126.2, 126.1, 126.0, 124.4, 123.7, 122.2, 120.7, 119.3, 118.7, 111.1, 110.4, 104.1, 55.6, 20.8; ESI-MS *m/z* 448.3 $[M+H]^+$, 470.2 $[M+Na]^+$. Anal. ($C_{29}H_{21}NO_4$) C, H, N.

4.1.90. 6-([1,1'-Biphenyl]-2-yl)benzo[b]pyrrolo[1,2-d][1,4]oxazepin-7-yl acetate (6p)

Compound **6p** was obtained following the procedure described for **6j**. The residue was purified by flash chromatography on silica gel (5% EtOAc in petroleum ether) to afford the title compound as a yellow oil (84%).^{1}H NMR (300 MHz, $CDCl_3$) δ 7.49–7.41 (m, 5H), 7.37–7.30 (m, 1H), 7.28–7.18 (m, 4H), 7.12–7.05 (m, 2H), 6.95 (td, $J_1 = 6.6$ Hz, $J_2 = 1.2$ Hz, 1H), 6.58 (d, $J = 7.2$ Hz, 1H), 6.33 (m, 1H), 6.26 (dd, $J_1 = 1.5$ Hz, $J_2 = 2.1$ Hz, 1H), 1.99 (s, 3H); ^{13}C NMR (300 MHz, $CDCl_3$) δ 168.6, 152.1, 146.4, 141.7, 141.2, 132.8, 132.5, 131.6, 130.6, 130.4, 129.4, 128.6, 128.2, 127.2, 127.1, 126.8, 126.7, 125.2, 122.3, 122.2, 121.3, 110.6, 109.9, 20.6; ESI-MS *m/z* 416.1 $[M+Na]^+$. Anal. ($C_{26}H_{19}NO_3$) C, H, N.

4.1.91. 5-(Naphthalen-1-yl)naphtho[2,3-b]pyrrolo[1,2-d][1,4]oxazepin-4(5H)-one oxime (47)

To a solution of compound **46** (50 mg, 0.13 mmol) in dry MeOH (1 mL) hydroxylamine hydrochloride (185 mg, 2.66 mmol) and pyridine (1.06 mL, 2.66 mmol) were sequentially added. The reaction mixture was stirred at reflux for 12 h, then methanol was evaporated under reduced pressure. The residue was partitioned between water and EtOAc. The organic layer was dried over anhydrous sodium sulfate, filtered and concentrated. The residue was purified by chromatography on silica gel (1% acetone in DCM) to afford the title compound as a yellow amorphous solid (60% yield). ^{1}H NMR (300 MHz, $CDCl_3$) δ 8.51 (d, 1H, $J = 8.4$ Hz), 8.40 (s, 1H), 7.91 (d, 1H, $J = 8.1$ Hz), 7.78–7.72 (m, 3H), 7.74–7.55 (m, 4H), 7.50–7.40 (m, 4H), 7.13 (s, 1H), 6.81 (m, 1H), 6.45 (t, 1H, $J = 3.0$ Hz); ESI-MS *m/z* 390.9 $[M+H]^+$, 413.9 $[M+Na]^+$.

4.1.92. N-(5-(Naphthalen-1-yl)naphtho[2,3-b]pyrrolo[1,2-d][1,4]oxazepin-4-yl)acetamide (6q)

To a solution of **47** (70 mg, 0.18 mmol) in 1,2-dichloroethane (4 mL), acetic anhydride (42 μL, 0.45 mmol), sodium bisulfite (56 mg, 0.54 mmol) and copper(I) iodide (10 mol%) were added in sequence at 25 °C. The reaction mixture was heated to reflux and stirred for 12 h. The mixture was then cooled to room temperature and extracted with EtOAc (3 × 10 mL). The combined organic layers were dried over anhydrous sodium sulfate, filtered and concentrated. The residue was purified by chromatography on silica gel (36% EtOAc in *n*-hexane) to afford the title compound as a yellow amorphous solid (22% yield). ^{1}H NMR (300 MHz, $CDCl_3$) δ 8.11–8.04 (m, 1H), 7.84 (m, 4H), 7.62–7.29 (m, 9H), 6.60–6.37 (m, 3H), 1.79 (s, 3H); ^{13}C NMR (75 MHz, $CDCl_3$) δ 134.0, 133.2, 132.4, 132.0, 131.5 (2), 131.2, 129.8, 129.0, 128.6, 127.7 (2), 127.4, 126.9, 126.6, 126.4, 126.3, 125.5 (2), 123.3, 122.6, 121.0, 119.2, 111.3, 111.2, 23.5; FT-IR (neat) $\nu_{max} = 1733$ cm^{-1}. ESI-MS *m/z* 417.0 $[M+H]^+$, 439.0 $[M+Na]^+$, 455.0 $[M+K]^+$. Anal. ($C_{28}H_{20}N_2O_2$) C, H, N.

4.1.93. 5-(Naphthalen-1-yl)naphtho[2,3-b]pyrrolo[1,2-d][1,4]oxazepin-4-yl (5-(diethylamino)pentan-2-yl)carbamate (6r)

A solution of compound **46** (100 mg, 0.26 mmol) in dry THF (3 mL) was added to a two-necked round bottom flask containing potassium hydride (30% suspension in mineral oil, 40 mg, 0.26 mmol). The resulting suspension immediately turned dark orange. The reaction mixture was stirred for 1 h at 25 °C, and then added via cannula to a solution containing triphosgene (78 mg, 0.26 mmol) in dry THF (1 mL). After 5 min stirring, N^1,N^1-diethylbutan-1,3-diamine (103 μL, 0.53 mmol) and *N*,*N*-DIPEA (185 μL, 1.06 mmol) were sequentially added. The reaction mixture was stirred for 14 h at 25 °C, and then neutralized with saturated

aqueous $NaHCO_3$. THF was evaporated under reduced pressure and the residue was extracted with EtOAc (3 × 8 mL). The combined organic layers were dried over anhydrous sodium sulfate, filtered and concentrated. The residue was purified by chromatography on silica gel (100% EtOAc to 5% MeOH/5% trimethylamine in EtOAc) to afford the title compound as yellow oil (10% yield). ^{1}H NMR (300 MHz, $CDCl_3$) δ 8.09 (d, 1H, J = 8.0 Hz), 8.04 (s, 1H), 7.93 (d, 3H, J = 7.6 Hz), 7.70 (d, 1H, J = 8.0 Hz), 7.27–7.53 (m, 8H), 6.43 (d, 2H, J = 13.2 Hz), 3.38 (s, 1H), 2.40 (q, 2H, J = 7.2 Hz), 2.31 (q, 4H, J = 6.8 Hz), 1.26 (s, 2H), 0.83 (t, 6H, J = 6.8 Hz); ESI-MS m/z 561.0 $[M+H]^+$. Anal. ($C_{36}H_{37}N_3O_3$) C, H, N.

4.2. Crystallization, data collection, and structure solution

Crystals of T_2R-TTL were grown as previously described [43,44] and soaked 30 min or 3 h at 20 °C in the reservoir solution (10% PEG 4k, 12.5% glycerol) containing 5 mM of **6j**. Crystals were fished directly from the drop and flash-cooled in a nitrogen stream at the beamline after a transfer into cryo-solution containing 20% glycerol. Standard data collection at beamline x06DA at the Swiss Light Source (Paul Scherrer Institut, Villigen, Switzerland), data processing, and structure solution using the difference Fourier method were performed as described previously [43,44]. Data collection and refinement statistics are given in the Table S2. Chains in the T_2R-TTL complex were defined as follows: chain A, α-tubulin-1; chain B, β-tubulin-1; chain C, α-tubulin-2; chain D, β-tubulin-2; chain E, RB3; and chain F, TTL. Chains B and D were used throughout for the structural analyses and figure preparation.

4.3. Computational details

4.3.1. Protein and ligands preparation

The crystal structure of **6j**-tubulin was prepared by means of Protein Preparation Wizard protocol implemented in Maestro (Maestro, version 10.1, Schrödinger, LLC, New York, NY, 2015) for acquiring an appropriate starting complex for the subsequent computational analyses [16,50–52]. Regarding the **6j**-tubulin used in MD simulation we maintained the chain C and D of the complex removing the water molecules and the compounds used for the crystallization but maintaining the co-factors such as GDP and GTP. The **6j**-tubulin used in molecular docking studies was prepared in a similar way reported for **6j**-tubulin employed in MD simulation maintaining the structural water molecules obtained by the crystallographic study. The derivatives used in molecular docking calculation were generated by using the building panel in Maestro. Molecules were treated by means of MacroModel (MacroModel, version 10.7, Schrödinger, LLC, New York, NY, 2015) for retrieving the lower energy conformers [53] to use as input in molecular docking experiments. The calculation was performed using the Optimized Potentials for Liquid Simulations-all atom (OPLS-AA) force field 2005 [54,55] and the Generalized-Born/Surface-Area (GB/SA) model to simulate the solvent effects [56]. No cutoff for non-bonded interactions was used. Polak-Ribiere conjugate gradient (PRCG) method was employed with 2500 maximum iterations and 0.001 gradient convergence threshold for performing the molecular energy minimizations. MCMM (Monte Carlo Multiple Minimum) was employed as torsional sampling method for the conformational searches, performing automatic setup with 21 kJ/mol (5.02 kcal/mol) in the energy window for saving structure and 0.5 Å was used as cutoff distance for redundant conformers. The lower conformers were treated by LigPrep application (LigPrep, version 3.3, Schrödinger, LLC, New York, NY, 2015), generating the most plausible ionization state at cellular pH value (7.4 ± 0.2) [57].

All the compounds presented in this study were evaluated for their potential capability to behave as Pan Assay Interference Compounds (PAINS) by FAF-Drugs4 web server. The compounds filtered for PAINS indicated that none of them contain substructural features that would label them as “frequent hitters” in high throughput screens (http://fafdrugs4.mti.univ-paris-diderot.fr/).

4.3.2. Molecular Dynamics simulation

MD simulations studies were performed by means of Desmond 4.8 academic version, providing by D. E. Shaw Research (“DESRES”), using Maestro as graphical interface (Desmond Molecular Dynamics System, version 4.8, D. E. Shaw Research, New York, NY, 2016. Maestro-Desmond Interoperability Tools, version 4.8, Schrödinger, New York, NY, 2016). The calculation was performed using the Compute Unified Device Architecture (CUDA) API [58] employing two NVIDIA GPU. The calculation was performed on a system comprising 72 Intel Xeon E5-2695 v4@2.10 GHz processors and two NVIDIA GeForce 1070 GTX GPU. The complex **6j**-tubulin was prepared as above reported. The complex was positioned into an orthorhombic box filled with water (TIP3P model). OPLS_2005 force field was used in MD calculation. The physiological concentration of monovalent ions (0.15 M) was simulated by adding Na^+ and Cl^- ions. Constant temperature (300 K) and pressure (1.01325 bar) were employed with NPT (constant number of particles, pressure, and temperature) as ensemble class. RESPA integrator [59] was used in order to integrate the equations of motion, with an inner time step of 2.0 fs for bonded interactions and nonbonded interactions within the short-range cutoff. Nose-Hoover thermostats [60] were used to maintain the constant simulation temperature, and the Martyna-Tobias-Klein method [61] was used to control the pressure. Long-range electrostatic interactions were evaluated adopting particle-mesh Ewald method (PME). The cut-off for van der Waals and short-range electrostatic interactions was set at 9.0 Å. The equilibration of the system was performed with the default protocol provided in Desmond, which consists of a series of restrained minimizations and MD simulations used to slowly relax the system. By following this protocol, a single trajectory of 100 ns was obtained. We performed five independent MD runs for the mentioned complex with an aggregate simulation time of 0.5 μs to provide a more reliable result. The trajectory files were investigated by simulation interaction diagram tools, simulation quality analysis and simulation event. The described applications were used to generate all plots regarding MD simulations analysis included in the manuscript (Fig. 10).

4.3.3. Molecular docking

Genetic Optimization for Ligand Docking (GOLD, version 5.2, Cambridge Crystallographic Data Center, UK) software was employed in molecular docking studies using the Genetic algorithm (GA) [62,63]. This technique allows a partial flexibility of protein and full flexibility of ligand. For each of the 100 independent GA runs, a maximum number of 125,000 GA operations were performed. The default search efficiency value was employed. The active site radius of 4 Å was chosen from the ligand (**6j**) of the crystal structure of **6j**-tubulin. Default cutoff values of 2.5 Å (dH-X) for hydrogen bonds and 4.0 Å for van der Waals distance were used. When the top three solutions attained RMSD values within 1.5 Å, GA docking was terminated. The fitness function GoldScore was evaluated. The main contacts of ligands with tubulin were calculated employing ligand-interaction diagram and a script for displaying hydrophobic interactions (*display_hydrophobic_interactions.py*) downloaded from Schrödinger website and implemented in Maestro. The RMSD between the docked pose and the crystal structure of compound **6j** was calculated by using the script *rmsd.py* available in Maestro.

4.3.4. Pictures preparation

Figs. 8, 9 and 11 were prepared by means of PyMOL (The PyMOL Molecular Graphics System, v1.8.4.0, Schrödinger LLC, New York, 2015).

4.4. Biological evaluation

4.4.1. Cell lines

Human ovarian carcinomas A2780, A2780AD (MDR overexpressing P-glycoprotein) and Human promyelocytic leukemia cells HL-60 were cultured in RPMI1640 medium supplemented with 10% fetal calf serum (FCS), glutamine (2 mM), gentamycin (40 μg/mL) penicillin (100 IU/mL), streptomycin (100 μg/mL) and 0.25 units/mL of bovine insulin. NIH3T3 Mouse fibroblasts and NIH-MDR-G185 3T3 cells (colchicine resistant fibroblasts) were maintained in Dulbecco's modified Eagle's medium (DMEM) supplemented with 10% FCS, glutamine (2 mM), penicillin (100 IU/mL), streptomycin (100 μg/mL) and **4** (60 ng/mL) and were a generous gift of Carol O. Cardarelli and Michael. M. Gottesman [64].

The human lung carcinoma A549 cells were obtained from European Collection of Cell Cultures (Salisbury, UK). The mouse melanoma cells B16F1 and B16F10 (metastatic), the non-small cell lung carcinoma cells PC9, and the NSC lung adenocarcinoma with EGFR mutation HCC827, were obtained from the American Type Culture Collection. Cells were maintained in DMEM (Sigma-Aldrich) supplemented with 10% fetal bovine serum (FBS) (Hyclone, Celbio, Milan, Italy) and 2 mM glutamine, 100 units penicillin and 0.1 mg/l streptomycin (Sigma Aldrich, St. Louis, MO, USA).

NB4 is a cell line derived from human acute promyelocytic leukemia and has been obtained from ATCC. The cells were grown at 37 °C in a humidified atmosphere containing 5% CO_2 in RPMI-1640 medium (SIGMA) supplemented with 10% heat-inactivated fetal bovine serum (HYCLONE), penicillin G (100 units/mL), streptomycin (100 μg/mL), L-glutamine (2 mM), amphotericin B (250 mg/mL).

Human multiple myeloma cell line NCI-H929 was obtained from the DSMZ cell bank (Braunschweig, Germany) and were cultured in RPMI-1640 GlutaMAX™. The SCC4 cell line was cultured in DMEM GlutaMAX™ from Gibco (Grand Island, NY, USA). All media was supplemented with 10% (v/v) foetal bovine serum (FBS) (Gibco) and 100 U/mL penicillin and cells were incubated at 37 °C containing 5% CO_2.

4.4.2. Flow cytometry analysis

Differentiation: the cells were resuspended in 10 μL of conjugate phycoerythrine CD11c (CD11c-PE, PharMingen). Control samples were incubated 10 μL of mouse IgG1 PE conjugated; after incubation for 1 h at 4 °C in the dark, the cells were washed in PBS and resuspended in 500 μL PBS containing propidium iodide (0.25 μg/mL). The samples were then analyzed according to standard flow cytometry (FACSCalibur, BD). In particular, it has been applied statistics, Kolmogorov-Smirnov (KS) for data validation. Histograms obtained represent the distribution of real data obtained from the cells.

4.4.3. Cell cycle analysis and apoptosis

Cells were plated (2×10^5 cells/mL) and collected after treatment with title compounds. Then they were centrifuged and suspended in a solution containing 1X PBS, sodium citrate 0.1%, NP40 0.1% and propidium iodide 50 mg/mL. After 30 min of incubation at room temperature in the dark, cell cycle was evaluated by flow cytometry (FACSCalibur, Becton Dickinson Inc.) and analyzed with the program Mod Fit V3 (Verity). Apoptosis was quantified by propidium iodide staining and evaluated by flow cytometry. Alternatively, cell cycle distribution was quantified by flow cytometric analysis of propidium iodide (PI Invitrogen UK) stained cells. Briefly, cells treated with 10 μM **6a-r** for 24 h or DMSO were fixed and permeabilized with 70% ethanol o.n. at 4 °C and incubated with 100 μg RNAsi and 20 μg/mL PI (Sigma) for 30 min. Samples were acquired in a GUAVA flow cytometer (Merck) and analyzed with the FlowJo software. Doublets were excluded and 20,000 events were acquired for each sample.

4.4.4. Short term cytotoxicity assays

B16F1, B16F10, A549, PC9 and HCC827 were seeded at the density of 2500 cells/well in 96 multiwell plates in medium with 10% serum. After adhesion, cells were treated with **PNOX** and **6a,j,l** (0.1, 1 and 10 μM) in presence of 5% serum. After 18 h, medium was removed and cells were incubated for 4 h with fresh medium in the presence of 1.2 mM MTT (3-(4,5-dimethylthiazol-2-yl)-2,5-diphenyltetrazolium bromide) (Sigma, Milan, Italy). Alive cells reduce MTT to a strongly pigmented formazan product. After solubilization in DMSO, absorbance of the formazan was measured with a microplate reader at 540 nm. Data are expressed as % of basal response.

4.4.5. Long term cytotoxicity assays

Cells were seeded in 96-well plates at a density of 12,000 to 17,000 cells in 0.08 mL per well depending on the cell line and incubated overnight. Next day cells were exposed to serial dilutions of ligands for 48 h and then MTT at 2.5 mg/mL was added to each well. MTT was incubated for 4 h at 37 °C and then treated with an MTT solubilizer (10% SDS, 45% dimethylformamide, pH 5.5). Plates were incubated overnight at 37 °C in order to solubilize the formazan precipitate and the next day absorbance were measured at 595/690 nm in an automated Appliskan microplate reader (Thermo Scientific). Control Wells containing medium were used as blanks. The IC_{50} was calculated from the log-dose response curves.

4.4.6. Tubulin polymerization assay

Polymerization of tubulin in the presence of the different compounds was monitored by absorbance at 355 nm (Filter A00019x) in 96 well plates (Falcon, transparent, flat bottom) with an Appliskan (Thermo Scientific). 25 μM of Tubulin in GAB buffer (10 mM Sodium Phosphate, 30% Glycerol, 1 mM EGTA, 6 mM $MgCl_2$ and 1 mM GTP, pH 6.7) was supplemented with 27.5 μM of the compounds or DMSO as vehicle control. The turbidity was measured for 70 min at 37 °C. Data was exported using Thermo Scientific SKanIt Software for Appliskan (version 2.3) and SigmaPlot 13.0 was used to plot the charts. In order to correct the absorbance of the compounds at 350 nm data were normalized to absorbance value of the initial stable plateau.

4.4.7. Binding constant determination

In order to determine the binding constant, we first attempted a fluorometric assay. Firstly, the spectroscopy properties of each compound were determined. Their ultraviolet−visible absorbance spectrum was determined in 10 mM NaPi 1% SDS it show a maximal absorbance of 320 nm. Absorbance was measured in a double haz Evolution 201 (Thermo Scientific) in 1 cm path length quartz cuvettes at 25 °C. Fluorescence was measured in a Horiba Jovin Yvon Fluoromax-2 at 25 °C. The fluorescence spectra with 10 μM of each compound exciting at 320 nm (10 mM NaPi and 0.1 mM GTP) showed a maximum emission around 450 nm. When incubated with an excess of tubulin, the compounds an increment of the fluorescence intensity was observed. However, when a displacement assay using podophyllotoxin was attempted, turbidity due to precipitation was observed, which we attributed to the insolubility of the compounds. To determine the solubility of each compound in 10 mM NaPi, different concentrations (5, 10,

25, 50 and 100 μM) were centrifugated for 20 min at 50 krpms (110.00 g) in a Beckman Optima TLX in 1 mL polycarbonate tubes. Concentration of compound was determined spectrophotometrically before and after centrifugation. None of the compound were soluble at the lower concentration assayed, so we had to design an experiment in which the displaced insoluble compound does not interfere with the measurement. We decided to determine the binding constants using analytical ultracentrifugation. In this experiment the compound bound to tubulin is soluble and the non-bound compound will precipitate allowing determining the bound concentration without the interference of the free compound. Samples of 10 μM GTP-tubulin equilibrated in 10 mM Sodium Phosphate and 1 mM GTP were incubated with 15 μM of the different derivatives (**PNOX**, **6a**-**h**, **6j**, **6m**, **6n**) compounds and growing amounts of podophyllotoxin (5, 10, 25, 50 and 100 μM). Displacement of the compound by podophyllotoxin was measured by using analytical ultracentrifugation. Analysis were performed in a Beckman Optima XL-I ultracentrifuge equipped with dual detection system, one of UV–visible absorbance and another by Rayleigh interference [65]. An angular speed of 45 krpm (163.300 g) and a An50Ti rotor equipped with a 1.2 cm optical pathway double sector cells with quartz windows. The sedimentation profiles were analyzed as described [66,67] and the average sedimentation coefficient c(s) was calculated using *Sedfit* [68]. The data obtained were corrected by the density and viscosity of the media using *Sednterp* [69]. The concentration of the compound-tubulin complex was measured by the absorbance at 320 nm of the peak which contains the protein (this at 6S). Given the concentrations of ligand and tubulin, and the outcome of preliminary experiments that indicate that the binding is saturated at these concentrations, the absorbance of the peak in the absence of podophyllotoxin can be considered the absorbance of 10 μM ligand-tubulin complex. Then, since the concentrations of tubulin and podophyllotoxin are far over the dissociation constant of podophyllotoxin (54 nM [70]) it could be also considered that all the sites not bound to the compound are bound to podophyllotoxin allowing determining the concentration of the podophyllotoxin-tubulin complex. The free concentration of podophyllotoxin (soluble at the conditions of the assay) can be the determined from the difference between the total podophyllotoxin added and the bound podophyllotoxin. In this way we just need the free concentration of the ligands. To measure it the samples with 15 μM of each compound in 10 mM NaPi buffer were centrifuged for 20 min at 70 krpms (163.300 g) in a Beckman Optima TLX in 1 mL polycarbonate tubes. We prepared duplicated samples without centrifugation. Supernatants were collected and 10 μM docetaxel was added as internal standard to the supernatant and the samples which were not centrifuged. The compounds were extracted with three volumes of DCM. The extracts were dried and solved in the mobile phase to analyze with an Agilent 1100 chromatograph connected to a reverse phase column Zorbax Eclipse XDB-C18 (mobile phase gradient 50–100% acetonitrile) with detection at 220, 2890 and 320 nm. In the assay conditions, the concentration remaining in the supernatant was considered the maximal free concentration of the ligand in solution, and the apparent solubility of it (**PNOX** 0.62 μM, **6a** 0.36 μM, **6d** 2.89 μM, **6e** 0.34 μM, **6f** 0.39 μM, **6g** 0.064 μM, **6h** 0.27 μM, **6j** 0.17 μM, **6m** 0.22 μM, **6n** 0.14 μM). *Kb* of each compound can be calculated using the next equation:

$$\frac{Kc}{Kp} = \frac{\frac{[C]b}{[T]f.[C]f}}{\frac{[P]b}{[T]f.[P]f}}$$

$$Kc = \frac{[C]b.[P]f}{[P]b.[C]f}.Kp$$

Kc is the binding constant of the compound, *Kp* the binding constant of podophyllotoxin, *[C]b* the concentration of bound compound, *[C]f* the concentration of free compound, *[P]b* the concentration of bound podophyllotoxin and *[P]f* the free concentration of podophyllotoxin. The previous described experimental procedure result in the values of all the data requested considering *Kb* of podophyllotoxin ($185 \pm 7 \times 10^5\ M^{-1}$) [70].

4.4.8. Alamar blue viability assay

NCI-H929 cells were seeded at 5×10^4 cells/well in 96 well plates while SCC4 cells were seeded at 5×10^3 cells/well in 96 well plates. Cells were treated in triplicate with either vehicle (1% (v/v) ethanol) or a range of concentrations (6-5000 nM) of the indicated compound. After 48 h, 10% alamar blue (v/v) was added to each well. Plates were incubated in the dark for up to 5 h until a color change was observed in the vehicle. Fluorescence was measured using a SpectraMax Gemini plate reader at excitation wavelength 544 nm and emission wavelength 590 nm.

4.4.9. Flow cytometric analysis of Annexin V/PI stained cells

The Annexin V/Propidium iodidie (PI) double stain assay was employed to detect both early and late stage apoptosis using flow cytometry. Early stage apoptosis is detected by the presence of phosphatidyl serine (PS) on the outer surface of the cell membrane which is bound by the phospholipid binding protein Annexin V. Early stage apoptotic cells have an intact cell membrane and therefore stain Annexin V^+/PI^-. Late stage apoptosis is characterized by the ability of PI to permeate the cell membrane therefore these cells stain Annexin V^+/PI^+. For this apoptosis assay, SCC4 cells were seeded at a density of 15×10^4 cells/mL while NCI-H929 cells were seeded at a density of 30×10^4 cells/mL. Cells were treated with either vehicle control (1% EtOH (v/v)) or 500 nM of **PNOX** or **6j** for 48 h. After incubation, cells were harvested and stained with Annexin V/Propidium Iodide (PI) and were analyzed by flow cytometry using BD FACs Accuri software. 10,000 cells were gated on vehicle treated cells.

4.4.10. Autophagy

HL-60 cells (1×10^6 cells/sample) were resuspended in RPMI1640 medium supplemented with 10% bovine calf serum (BCS) or in Earle's Balanced Salts (EBS) medium incubated at 37 °C for 15 min and treated with 10 μM of compounds **PNOX**, **6g**, **6j** or **6n** in presence or absence of 40 μM chloroquine (CQ) for 1 h 45 min. Alternatively, cells were resuspended in RPMI1640 medium supplemented with 10% BCS and treated as above for 16 h. Cells were harvested and lysed in 1% (v/v) Triton X-100 in 20 mM Tris-HCl (pH 8), 150 mM NaCl (in the presence of 0.2 mg/mL Na orthovanadate; 1 mg/mL pepstatin, leupeptin, and aprotinin; 10 mM phenyl methyl sulfonyl fluoride; and 50 mM NaF), resolved by SDS-PAGE, and transferred to nitrocellulose. Immunoblot analysis was carried out by chemiluminescence (SuperSignal West Pico Chemiluminescent Substrate kit from Pierce) using anti-LC3B (D11) XP (Cell Signaling Technology), as well as control anti-actin mAb (catalogue MAB1501; Millipore) and secondary peroxidase-labeled Abs (Amersham Pharmacia Biotech). Immunoblots were scanned and quantitated using ImageJ software.

4.4.11. Western blot for cell cycle and apoptosis proteins

PC9 and HCC827 were seeded at the density of 300,000 cells/well in 6 multiwell plates in medium with 10% serum. After adhesion, cells were treated with **PNOX** and **6j** (10 μM) in presence

of 5% serum. After 18 h of incubation, cells were lysed as described [71]. Cell lysates were centrifuged at 15,000×*g* for 20 min at 4 °C. Following gel electrophoresis, proteins were blotted onto activated nitrocellulose membranes. Non-specific protein-binding sites were blocked by incubation with 5% milk 0.5% Tween-20 in PBS for 1 h at room temperature and membranes were then incubated overnight at 4 °C with appropriate dilutions of specific primary antibodies: anti p21 (1:1000, Cell Signaling, Celbio, Milan, Italy), anti-cyclin D1 (1:1000, Cell Signaling), anti-cleaved-caspase-3 (1:1000, Cell Signaling), anti-caspase-3 (1:1000, Cell Signaling) monoclonal antibodies. Membranes were then washed with PBS/0.1% Tween-20 and incubated for 1 h at room temperature with horseradish peroxidase-conjugated anti-mouse (1:2500, Promega, Madison, USA) or anti-rabbit (1:10,000, Merck Millipore) secondary antibody, followed by enhanced chemiluminescence detection system (Bio-Rad, Hercules, USA). As an internal control for protein loading, membranes were reprobed with antibodies for the house-keeping protein β-actin (mouse anti β-actin Ab 1:1000, Sigma). Images were digitalized with Image Quant LAS4000.

Additional information

The atomic coordinates and structure factors of the T_2R-TTL-**6j** complex have been deposited to the RCSB PDB (www.rcsb.org) with the PDB ID 6GJ4. Authors will release the atomic coordinates and the experimental data upon article publication.

Acknowledgements

This work was supported in part by a grant from the Swiss National Science Foundation (31003A_166608; to M.O.S), grant BFU2016-75319-R (AEI/FEDER, EU) from Ministerio de Economia y Competitividad, Blueprint 282510, AIRC-17217. The authors acknowledge networking contribution by the COST Action CM1407 “Challenging organic syntheses inspired by nature - from natural products chemistry to drug discovery” (to M.O.S. and J.F.D.) and the COST Action EPICHEMBIO CM-1406 (to L.A. and G.C.). This work has also received partial funding from the European Union’s Horizon 2020 (EU) research and innovation programme under the Marie Sklodowska-Curie grant agreement No 721906. Finally, this work was partially funded by MIUR-PRIN project n. 2015Y3C5KP (to L.M.).

The Authors thank V. Olieric and M. Wang for excellent technical assistance with the collection of X-ray data at beamlines X06DA of the Swiss Light Source (Paul Scherrer Institut, Villigen, Switzerland). We also thank Dr. Federica Finetti for technical assistance on cell biology studies and Dr. Nicola Gaggelli for technical support during IR experiments.

Appendix A. Supplementary data

Supplementary data to this article can be found online at https://doi.org/10.1016/j.ejmech.2018.11.004.

References

[1] E. Mukhtar, V.M. Adhami, H. Mukhtar, Targeting microtubules by natural agents for cancer therapy, Mol. Canc. Therapeut. 13 (2014) 275–284.
[2] C. Dumontet, M.A. Jordan, Microtubule-binding agents: a dynamic field of cancer therapeutics, Nat. Rev. Drug Discov. 9 (2010) 790–803.
[3] R. Mackeh, D. Perdiz, S. Lorin, P. Codogno, C. Pous, Autophagy and microtubules - new story, old players, J. Cell Sci. 126 (2013) 1071–1080.
[4] T. Mitchison, M. Kirschner, Dynamic instability of microtubule growth, Nature 312 (1984) 237–242.
[5] E. Pasquier, M. Kavallaris, Microtubules: a dynamic target in cancer therapy, IUBMB Life 60 (2008) 165–170.
[6] J. Yang, Y. Wang, T. Wang, J. Jiang, C.H. Botting, H. Liu, Q. Chen, J.H. Naismith, X. Zhu, L. Chen, Pironetin reacts covalently with cysteine-316 of alpha-tubulin to destabilize microtubule, Nat. Commun. 7 (2016) 12103.
[7] P.G. Morris, M.N. Fornier, Microtubule active agents: beyond the taxane frontier, Clin. Canc. Res. 14 (2008) 7167–7172.
[8] Y. Lu, J. Chen, M. Xiao, W. Li, D.D. Miller, An overview of tubulin inhibitors that interact with the colchicine binding site, Pharm. Res. (N. Y.) 29 (2012) 2943–2971.
[9] A.E. Prota, K. Bargsten, J.F. Diaz, M. Marsh, C. Cuevas, M. Liniger, C. Neuhaus, J.M. Andreu, K.H. Altmann, M.O. Steinmetz, A new tubulin-binding site and pharmacophore for microtubule-destabilizing anticancer drugs, Proc. Natl. Acad. Sci. U. S. A. 111 (2014) 13817–13821.
[10] A.E. Prota, J. Setter, A.B. Waight, K. Bargsten, J. Murga, J.F. Diaz, M.O. Steinmetz, Pironetin binds covalently to alphaCys316 and perturbs a major loop and helix of alpha-tubulin to inhibit microtubule formation, J. Mol. Biol. 428 (2016) 2981–2988.
[11] R.A. Veldhoen, S.L. Banman, D.R. Hemmerling, R. Odsen, T. Simmen, A.J. Simmonds, D.A. Underhill, I.S. Goping, The chemotherapeutic agent paclitaxel inhibits autophagy through two distinct mechanisms that regulate apoptosis, Oncogene 32 (2013) 736–746.
[12] B.R. Acharya, S. Bhattacharyya, D. Choudhury, G. Chakrabarti, The microtubule depolymerizing agent naphthazarin induces both apoptosis and autophagy in A549 lung cancer cells, Apoptosis 16 (2011) 924–939.
[13] R. Kochl, X.W. Hu, E.Y. Chan, S.A. Tooze, Microtubules facilitate autophagosome formation and fusion of autophagosomes with endosomes, Traffic 7 (2006) 129–145.
[14] S. Bhattacharya, A. Das, S. Datta, A. Ganguli, G. Chakrabarti, Colchicine induces autophagy and senescence in lung cancer cells at clinically admissible concentration: potential use of colchicine in combination with autophagy inhibitor in cancer therapy, Tumour Biol 37 (2016) 10653–10664.
[15] S. He, Q. Li, X. Jiang, X. Lu, F. Feng, W. Qu, Y. Chen, H. Sun, Design of small molecule autophagy modulators: a promising druggable strategy, J. Med. Chem. (2017), https://doi.org/10.1021/acs.jmedchem.1027b01019.
[16] M. Brindisi, S. Maramai, S. Brogi, E. Fanigliulo, S. Butini, E. Guarino, A. Casagni, S. Lamponi, C. Bonechi, S.M. Nathwani, F. Finetti, F. Ragonese, P. Arcidiacono, P. Campiglia, S. Valenti, E. Novellino, R. Spaccapelo, L. Morbidelli, D.M. Zisterer, C.D. Williams, A. Donati, C. Baldari, G. Campiani, C. Ulivieri, S. Gemma, Development of novel cyclic peptides as pro-apoptotic agents, Eur. J. Med. Chem. 117 (2016) 301–320.
[17] M.M. Mc Gee, S. Gemma, S. Butini, A. Ramunno, D.M. Zisterer, C. Fattorusso, B. Catalanotti, G. Kukreja, I. Fiorini, C. Pisano, C. Cucco, E. Novellino, V. Nacci, D.C. Williams, G. Campiani, Pyrrolo[1,5]benzoxa(thia)zepines as a new class of potent apoptotic agents. Biological studies and identification of an intracellular location of their drug target, J. Med. Chem. 48 (2005) 4367–4377.
[18] M. Brindisi, S. Maramai, A. Grillo, S. Brogi, S. Butini, E. Novellino, G. Campiani, S. Gemma, Development of a practical and scalable route for the preparation of the deacetoxytubuvaline (dTuv) fragment of pretubulysin and analogs, Tetrahedron Lett. 57 (2016) 920–923.
[19] S.M. Nathwani, L.M. Greene, S. Butini, G. Campiani, D.C. Williams, A. Samali, E. Szegezdi, D.M. Zisterer, The pyrrolo-1,5-benzoxazepine, PBOX-15, enhances TRAILinduced apoptosis by upregulation of DR5 and downregulation of core cell survival proteins in acute lymphoblastic leukaemia cells, Int. J. Oncol. 49 (2016) 74–88.
[20] S.M. Nathwani, S. Butler, D. Fayne, N.N. McGovern, B. Sarkadi, M.J. Meegan, D.G. Lloyd, G. Campiani, M. Lawler, D.C. Williams, D.M. Zisterer, Novel microtubule-targeting agents, pyrrolo-1,5-benzoxazepines, induce apoptosis in multi-drug-resistant cancer cells, Cancer Chemother. Pharmacol. 66 (2010) 585–596.
[21] K. O'Callaghan, E. Palagano, S. Butini, G. Campiani, D.C. Williams, D.M. Zisterer, J. O'Sullivan, Induction of apoptosis in oral squamous carcinoma cells by pyrrolo-1,5-benzoxazepines, Mol. Med. Rep. 12 (2015) 3748–3754.
[22] J.C. Lennon, S. Butini, G. Campiani, A. O'Meara, D.C. Williams, D.M. Zisterer, Involvement of AMP-activated protein kinase in mediating pyrrolo-1,5-benzoxazepine-induced apoptosis in neuroblastoma cells, Invest. N. Drugs 34 (2016) 663–676.
[23] L.M. Greene, D.P. Nolan, D. Regan-Komito, G. Campiani, D.C. Williams, D.M. Zisterer, Inhibition of late-stage autophagy synergistically enhances pyrrolo-1,5-benzoxazepine-6-induced apoptotic cell death in human colon cancer cells, Int. J. Oncol. 43 (2013) 927–935.
[24] F.T. Bane, J.H. Bannon, S.R. Pennington, G. Campiani, D.C. Williams, D.M. Zisterer, M.M. Mc Gee, The microtubule-targeting agents, PBOX-6 [pyrrolobenzoxazepine 7-[(dimethylcarbamoyl)oxy]-6-(2-naphthyl)pyrrolo-[2,1-d] (1,5)-benzoxazepine] and paclitaxel, induce nucleocytoplasmic redistribution of the peptidyl-prolyl isomerases, cyclophilin A and pin1, in malignant hematopoietic cells, J. Pharmacol. Exp. Therapeut. 329 (2009) 38–47.
[25] L.M. Greene, M. Fleeton, J. Mulligan, C. Gowda, B.J. Sheahan, G.J. Atkins, G. Campiani, V. Nacci, M. Lawler, D.C. Williams, D.M. Zisterer, The pyrrolo-1,5-benzoxazepine, PBOX-6, inhibits the growth of breast cancer cells in vitro independent of estrogen receptor status and inhibits breast tumour growth in vivo, Oncol. Rep. 14 (2005) 1357–1363.
[26] L.M. Greene, S. Butini, G. Campiani, D.C. Williams, D.M. Zisterer, Pre-clinical evaluation of a novel class of anti-cancer agents, the Pyrrolo-1, 5-benzoxazepines, J. Canc. 7 (2016) 2367–2377.
[27] M. Brindisi, S. Gemma, G. Alfano, G. Kshirsagar, E. Novellino, G. Campiani, S. Butini, A stereoselective route to 6-substituted pyrrolo-1,5-benzoxazepinones and their analogues, Tetrahedron Lett. 54 (2013)

5387–5390.
[28] K. Wada, T. Mizutani, S. Kitagawa, Synthesis of functionalized porphyrins as oxygen ligand receptors, J. Org. Chem. 68 (2003) 5123–5131.
[29] S. Gemma, S. Brogi, P.R. Patil, S. Giovani, S. Lamponi, A. Cappelli, E. Novellino, A. Brown, M.K. Higgins, K. Mustafa, T. Szestak, A.G. Craig, G. Campiani, S. Butini, M. Brindisi, From (+)-epigallocatechin gallate to a simplified synthetic analogue as a cytoadherence inhibitor for P. falciparum, RSC Adv. 4 (2014) 4769–4781.
[30] C. Mcdonald, H. Holcomb, K. Kennedy, E. Kirkpatrick, T. Leathers, P. Vanemon, N-Iodosuccinimide-Mediated conversion of aldehydes to methyl-esters, J. Org. Chem. 54 (1989) 1213–1215.
[31] S. Lin, C.P. Stevenson, E.R. Parmee, L. Xu, X. Liao, E. Metzger, R. Liang, F. Zhang, J.E. Stelmach, Glucagon receptor antagonist compounds, compositions containing such compounds and methods of use, in: PCT Int. Appl., 2010030722, 2010 March 18.
[32] W.B. Choi, D.S. Menaldino, D.I. Kim, M. Bouygues, M.W. Hager, Gram-positive carbapenem antibacterials and processes for their preparation, in: WO 2005123069, 2005 December 29.
[33] A. Crespo-Pena, D. Monge, E. Martin-Zamora, E. Alvarez, R. Fernandez, J.M. Lassaletta, Asymmetric formal carbonyl-ene reactions of formaldehyde tert-butyl hydrazone with alpha-keto esters: dual activation by bis-urea catalysts, J. Am. Chem. Soc. 134 (2012) 12912–12915.
[34] A.M. Lord, M.F. Mahon, M.D. Lloyd, M.D. Threadgill, Design, synthesis, and evaluation in vitro of quinoline-8-carboxamides, a new class of poly(adenosine-diphosphate-ribose)polymerase-1 (PARP-1) inhibitor, J. Med. Chem. 52 (2009) 868–877.
[35] W.D. Brown, A.H. Gouliaev, Bromination of Isoquinoline, Quinoline, Quinazoline and Quinoxaline in Strong Acid, Synthesis-Stuttgart, 2002, pp. 83–86.
[36] M.G. Shen, S.B. Shang, Z.Q. Song, D. Wang, X.P. Rao, H. Gao, H. Liu, Amberlyst A-26: an efficient and reusable heterogeneous catalyst for a one-pot oxidation-Cannizarro reaction, J. Chem. Res. (2013) 51–52.
[37] D.C. Williams, D.M. Zisterer, V. Nacci, G. Campiani, Apoptosis-inducing compounds, in, WO 2001058904 A1, 2001 August 16.
[38] Z.H. Guan, Z.Y. Zhang, Z.H. Ren, Y.Y. Wang, X. Zhang, Synthesis of enamides via CuI-catalyzed reductive acylation of ketoximes with NaHSO3, J. Org. Chem. 76 (2011) 339–341.
[39] S. Gemma, C. Camodeca, M. Brindisi, S. Brogi, G. Kukreja, S. Kunjir, E. Gabellieri, L. Lucantoni, A. Habluetzel, D. Taramelli, N. Basilico, R. Gualdani, F. Tadini-Buoninsegni, G. Bartolommei, M.R. Moncelli, R.E. Martin, R.L. Summers, S. Lamponi, L. Savini, I. Fiorini, M. Valoti, E. Novellino, G. Campiani, S. Butini, Mimicking the intramolecular hydrogen bond: synthesis, biological evaluation, and molecular modeling of benzoxazines and quinazolines as potential antimalarial agents, J. Med. Chem. 55 (2012) 10387–10404.
[40] C.M. Henry, E. Hollville, S.J. Martin, Measuring apoptosis by microscopy and flow cytometry, Methods 61 (2013) 90–97.
[41] M. Mirigian, K. Mukherjee, S.L. Bane, D.L. Sackett, Measurement of in vitro microtubule polymerization by turbidity and fluorescence, Methods Cell Biol. 115 (2013) 215–229.
[42] J.F. Diaz, R.M. Buey, Characterizing ligand-microtubule binding by competition methods, Methods Mol. Med. 137 (2007) 245–260.
[43] A.E. Prota, K. Bargsten, D. Zurwerra, J.J. Field, J.F. Diaz, K.H. Altmann, M.O. Steinmetz, Molecular mechanism of action of microtubule-stabilizing anticancer agents, Science 339 (2013) 587–590.
[44] A.E. Prota, M.M. Magiera, M. Kuijpers, K. Bargsten, D. Frey, M. Wieser, R. Jaussi, C.C. Hoogenraad, R.A. Kammerer, C. Janke, M.O. Steinmetz, Structural basis of tubulin tyrosination by tubulin tyrosine ligase, J. Cell Biol. 200 (2013) 259–270.
[45] A.E. Prota, F. Danel, F. Bachmann, K. Bargsten, R.M. Buey, J. Pohlmann, S. Reinelt, H. Lane, M.O. Steinmetz, The novel microtubule-destabilizing drug BAL27862 binds to the colchicine site of tubulin with distinct effects on microtubule organization, J. Mol. Biol. 426 (2014) 1848–1860.
[46] R.B. Ravelli, B. Gigant, P.A. Curmi, I. Jourdain, S. Lachkar, A. Sobel, M. Knossow, Insight into tubulin regulation from a complex with colchicine and a stathmin-like domain, Nature 428 (2004) 198–202.
[47] J.A. Shabbits, R. Krishna, L.D. Mayer, Molecular and pharmacological strategies to overcome multidrug resistance, Expert Rev. Anticancer Ther. 1 (2001) 585–594.
[48] R. Matesanz, I. Barasoain, C.G. Yang, L. Wang, X. Li, C. de Ines, C. Coderch, F. Gago, J.J. Barbero, J.M. Andreu, W.S. Fang, J.F. Diaz, Optimization of taxane binding to microtubules: binding affinity dissection and incremental construction of a high-affinity analog of paclitaxel, Chem. Biol. (Lond.) 15 (2008) 573–585.
[49] E. White, The role for autophagy in cancer, J. Clin. Invest. 125 (2015) 42–46.
[50] S. Brogi, S. Butini, S. Maramai, R. Colombo, L. Verga, C. Lanni, E. De Lorenzi, S. Lamponi, M. Andreassi, M. Bartolini, V. Andrisano, E. Novellino, G. Campiani, M. Brindisi, S. Gemma, Disease-modifying anti-alzheimer's drugs: inhibitors of human cholinesterases interfering with beta-amyloid aggregation, CNS Neurosci. Ther. 20 (2014) 624–632.
[51] S. Butini, M. Brindisi, S. Brogi, S. Maramai, E. Guarino, A. Panico, A. Saxena, V. Chauhan, R. Colombo, L. Verga, E. De Lorenzi, M. Bartolini, V. Andrisano, E. Novellino, G. Campiani, S. Gemma, Multifunctional cholinesterase and amyloid Beta fibrillization modulators. Synthesis and biological investigation, ACS Med. Chem. Lett. 4 (2013) 1178–1182.
[52] L. Zaccagnini, S. Brogi, M. Brindisi, S. Gemma, G. Chemi, G. Legname, G. Campiani, S. Butini, Identification of novel fluorescent probes preventing PrP(Sc) replication in prion diseases, Eur. J. Med. Chem. 127 (2017) 859–873.
[53] S. Gemma, S. Kunjir, S.S. Coccone, M. Brindisi, V. Moretti, S. Brogi, E. Novellino, N. Basilico, S. Parapini, D. Taramelli, G. Campiani, S. Butini, Synthesis and antiplasmodial activity of bicyclic dioxanes as simplified dihydroplakortin analogues, J. Med. Chem. 54 (2011) 5949–5953.
[54] W.L. Jorgensen, D.S. Maxwell, J. TiradoRives, Development and testing of the OPLS all-atom force field on conformational energetics and properties of organic liquids, J. Am. Chem. Soc. 118 (1996) 11225–11236.
[55] G.A. Kaminski, R.A. Friesner, J. Tirado-Rives, W.L. Jorgensen, Evaluation and reparametrization of the OPLS-AA force field for proteins via comparison with accurate quantum chemical calculations on peptides, J. Phys. Chem. B 105 (2001) 6474–6487.
[56] W.C. Still, A. Tempczyk, R.C. Hawley, T. Hendrickson, Semianalytical treatment of solvation for molecular mechanics and dynamics, J. Am. Chem. Soc. 112 (1990) 6127–6129.
[57] M. Brindisi, S. Gemma, S. Kunjir, L. Di Cerbo, S. Brogi, S. Parapini, S. D'Alessandro, D. Taramelli, A. Habluetzel, S. Tapanelli, S. Lamponi, E. Novellino, G. Campiani, S. Butini, Synthetic spirocyclic endoperoxides: new antimalarial scaffolds, Medchemcomm 6 (2015) 357–362.
[58] J. Nickolls, I. Buck, M. Garland, K. Skadron, Scalable parallel programming with CUDA, Queue 6 (2008) 40–53.
[59] D.D. Humphreys, R.A. Friesner, B.J. Berne, A multiple-time-step molecular-dynamics algorithm for macromolecules, J. Phys. Chem. 98 (1994) 6885–6892.
[60] W.G. Hoover, Canonical dynamics - equilibrium phase-space distributions, Phys. Rev. 31 (1985) 1695–1697.
[61] G.J. Martyna, D.J. Tobias, M.L. Klein, Constant-pressure molecular-dynamics algorithms, J. Chem. Phys. 101 (1994) 4177–4189.
[62] G. Jones, P. Willett, Docking small-molecule ligands into active sites, Curr. Opin. Biotechnol. 6 (1995) 652–656.
[63] A. Gasser, S. Brogi, K. Urayama, T. Nishi, H. Kurose, A. Tafi, N. Ribeiro, L. Desaubry, C.G. Nebigil, Discovery and cardioprotective effects of the first non-Peptide agonists of the G protein-coupled prokineticin receptor-1, PloS One 10 (2015) e0121027.
[64] C.O. Cardarelli, I. Aksentijevich, I. Pastan, M.M. Gottesman, Differential effects of P-glycoprotein inhibitors on NIH3T3 cells transfected with wild-type (G185) or mutant (V185) multidrug transporters, Cancer Res. 55 (1995) 1086–1091.
[65] J.S. Philo, A critical review of methods for size characterization of non-particulate protein aggregates, Curr. Pharmaceut. Biotechnol. 10 (2009) 359–372.
[66] P. Schuck, Size-distribution analysis of macromolecules by sedimentation velocity ultracentrifugation and lamm equation modeling, Biophys. J. 78 (2000) 1606–1619.
[67] P.H. Brown, P. Schuck, A new adaptive grid-size algorithm for the simulation of sedimentation velocity profiles in analytical ultracentrifugation, Comput. Phys. Commun. 178 (2008) 105–120.
[68] P. Schuck, B. Demeler, Direct sedimentation analysis of interference optical data in analytical ultracentrifugation, Biophys. J. 76 (1999) 2288–2296.
[69] T.M. Laue, B.D. Shah, T.M. Ridgeway, S.L. Pelletier, Computer-aided interpretation of analytical sedimentation data for proteins, in: S.E. Harding, A.J. Rowe, J.C. Horton (Eds.), Analytical Ultracentrifugation in Biochemistry and Polymer Science, Royal Society of Chemistry, Cambridge [England], 1992, pp. 90–125.
[70] M. Antunez-Mojica, J. Rodriguez-Salarichs, M. Redondo-Horcajo, A. Leon, I. Barasoain, A. Canales, F.J. Canada, J. Jimenez-Barbero, L. Alvarez, J.F. Diaz, Structural and biochemical characterization of the interaction of tubulin with potent natural analogues of podophyllotoxin, J. Nat. Prod. 79 (2016) 2113–2121.
[71] F. Finetti, E. Terzuoli, S. Donnini, M. Uva, M. Ziche, L. Morbidelli, Monitoring endothelial and tissue responses to cobalt ferrite nanoparticles and hybrid hydrogels, PloS One 11 (2016), e0168727.